



UNIVERSITY OF BURGOS
SCHOOL OF ENGINEERING
DEPARTMENT OF CIVIL ENGINEERING

DOCTORAL THESIS

**FLEXURAL FATIGUE OF HIGH-STRENGTH PLAIN
AND FIBER-REINFORCED CONCRETE: INFLUENCE OF
MESOSTRUCTURE AND STUDY OF SIZE EFFECT**

PhD candidate

Álvaro Mena Alonso

Thesis directors

Miguel Ángel Vicente Cabrera

Dorys Carmen González Cabrera

Burgos, June 2023

UNIVERSITY OF BURGOS
SCHOOL OF ENGINEERING
DEPARTMENT OF CIVIL ENGINEERING
AREA OF CONTINUUM MECHANICS AND THEORY OF
STRUCTURES

DOCTORAL THESIS

**FLEXURAL FATIGUE OF HIGH-STRENGTH PLAIN
AND FIBER-REINFORCED CONCRETE: INFLUENCE OF
MESOSTRUCTURE AND STUDY OF SIZE EFFECT**

PhD candidate

Álvaro Mena Alonso

MSc Civil Engineer

Thesis directors

Miguel Ángel Vicente Cabrera

PhD Civil Engineer

Dorys Carmen González Cabrera

PhD Civil Engineer

2023

TABLE OF CONTENTS

1	INTRODUCTION	27
1.1	Motivation	27
1.2	Problem statement and objectives	28
1.3	Structure of the document	29
2	STATE OF THE ART	31
2.1	Steel fiber-reinforced concrete	31
2.1.1	Introduction.....	31
2.1.2	Components	33
2.1.3	Mix design	37
2.1.4	Resistance mechanism	39
2.1.5	Mechanical properties	42
2.1.6	Applications	46
2.2	Fatigue in concrete	48
2.2.1	Introduction.....	48
2.2.2	General concepts of fatigue	51
2.2.3	Factors affecting fatigue	57
2.2.4	Fatigue damage	62
2.3	Size effect on the mechanical response of concrete.....	74
2.3.1	Introduction.....	74
2.3.2	Causes of the size effect in concrete	76
2.3.3	Size effect in bending	81
2.3.4	Size effect in compression	82
2.3.5	Size effect in fatigue	84
2.3.6	Influence of mesostructure on size effect	86
2.4	Analysis of the mesostructure of concrete with micro-computed tomography	89

2.4.1	Introduction	89
2.4.2	Fibers in SFRC	95
2.4.3	Porosity.....	97
2.4.4	Cracking	98
3	MATERIALS AND METHODS	101
3.1	Concrete manufacturing	101
3.1.1	Materials.....	101
3.1.2	Concrete mix design.....	104
3.1.3	Concreting of test specimens.....	109
3.2	Experimental campaign	115
3.2.1	Description	115
3.2.2	Flexural fatigue test design	121
3.2.3	Facilities and equipment.....	127
3.2.4	Test plan	135
3.2.5	Post-processing of results.....	135
3.3	Mesostructural study with micro-computed tomography and image analysis	139
3.3.1	Scanning of specimens	139
3.3.2	Image post-processing.....	141
4	RESULTS.....	145
4.1	Characterization tests.....	145
4.1.1	Slump test.....	145
4.1.2	Compressive strength	148
4.1.3	Modulus of elasticity	150
4.1.4	Flexural strength.....	152
4.2	Flexural fatigue tests.....	163
4.2.1	S-size specimens	163

4.2.2	L-size specimens	185
4.3	Study of the mesostructure	202
4.3.1	Geometric parameters of the fibers	202
4.3.2	Geometric parameters of the pores	208
5	ANALYSIS OF RESULTS AND DISCUSSION	213
5.1	Influence of fibers on the flexural fatigue response of SFRC.....	214
5.1.1	Orientation	215
5.1.2	Spatial distribution	224
5.1.3	Fatigue life estimation	237
5.2	Influence of pores on the flexural fatigue response of plain concrete	240
5.2.1	Porosity and pore distribution.....	241
5.2.2	Pore volume	246
5.2.3	Fatigue life estimation	249
5.3	Size effect on the flexural fatigue behavior of concrete	252
5.3.1	Fatigue life	252
5.3.2	CMOD vs N diagrams	259
5.3.3	Secondary crack opening rate	272
6	CONCLUSIONS AND FUTURE LINES OF RESEARCH	279
6.1	Influence of fibers on the flexural fatigue response of SFRC.....	280
6.2	Influence of pores on the flexural fatigue response of plain concrete	285
6.3	Size effect on the flexural fatigue behavior of concrete	287
6.4	Future lines of research	291
	APPENDIX. FATIGUE TEST SHEETS.....	293
	REFERENCES.....	373

LIST OF TABLES

Table 2.1-1. Common properties of steel fibers for SFRC.....	37
Table 3.1-1. Characteristics of the steel fibers used.	103
Table 3.1-2. Materials used in the manufacture of concrete, together with their typology.	104
Table 3.1-3. Requirements for self-compactness in the slump test [3].....	105
Table 3.1-4. Initial dosage of the experimental dosage study.	106
Table 3.1-5. Verification of the criteria of Annex 17 in the initial dosage.....	106
Table 3.1-6. Definitive dosage after the experimental dosage study.....	107
Table 3.1-7. Final dosages (per m ³) for the four series of concrete.....	108
Table 3.1-8. Verification of the criteria of Annex 17 in the final dosage.....	108
Table 3.1-9. Distribution of specimens per batch, in each series.	110
Table 3.1-10. Relative error in a 2-month experimental campaign when taking $f_{c,28}$ and $f_{c,365}$ as reference, respectively.	115
Table 3.2-1. Geometric parameters of the 3-point bending tests for the two sizes of prismatic specimens.	119
Table 3.2-2. Bibliographic consultation of experimental work on flexural fatigue of fiber-reinforced concrete.....	124
Table 3.2-3. Parameters of flexural fatigue tests.	127
Table 3.2-4. Summary table of the experimental campaign.	135
Table 4.1-1. Results of the slump test.....	145
Table 4.1-2. Compressive strength.	148
Table 4.1-3. Modulus of elasticity in compression.....	151
Table 4.1-4. Maximum flexural strength.	154
Table 4.1-5. Strength corresponding to the limit of proportionality.....	155
Table 4.1-6. Residual flexural strengths of SFRC series.....	156
Table 4.1-7. Maximum flexural strength.	160
Table 4.1-8. Strength corresponding to the limit of proportionality.....	161
Table 4.1-9. Residual flexural strengths of SFRC series.....	162
Table 4.2-1. Fatigue life N.....	163
Table 4.2-2. Fit parameters λ and β of the Weibull distribution function.	166
Table 4.2-3. Fatigue life, distinguishing between the part corresponding to matrix fatigue (N_{mat}) and that associated with fiber fatigue (N_{fib}).	175

Table 4.2-4. Stress corresponding to LOP and maximum stress from loading cycles in flexural fatigue tests.	176
Table 4.2-5. Fatigue life N.	185
Table 4.2-6. Fit parameters λ and β of the Weibull distribution function.	188
Table 4.2-7. Fatigue life, distinguishing between the part corresponding to matrix fatigue (N_{mat}) and that associated with fiber fatigue (N_{fib}).	195
Table 4.2-8. Stress corresponding to LOP and maximum stress from loading cycles in flexural fatigue tests.	196
Table 4.3-1. Fiber orientation efficiency indexes.	205
Table 4.3-2. Number of fibers and density in the crack plane.	207
Table 4.3-3. Porosity and pore density in A0-S series.	210
Table 5.1-1. Adjustment coefficients for prediction formulation of fatigue results.	238
Table 5.1-2. R^2 coefficients of determination for prediction formulation of fatigue results.	239
Table 5.2-1. Adjustment coefficients for prediction formulation of fatigue results.	250
Table 5.2-2. R^2 coefficients of determination for the prediction formulation of fatigue results.	251
Table 5.3-1. Fatigue life N of plain concrete series.	252
Table 5.3-2. Fatigue life N of fiber-reinforced concrete series.	253
Table 5.3-3. Fit parameters λ and β , and correlation coefficient R^2 of the Weibull distribution function.	256
Table 5.3-4. Fatigue lives in A0-S and A0-L series.	261
Table 5.3-5. Fatigue lives in A1-S and A1-L series.	265
Table 5.3-6. Fatigue lives in A2-S and A2-L series.	268
Table 5.3-7. Fatigue lives in A3-S and A3-L series.	271
Table 5.3-8. Crack opening rate in A0-S and A0-L series.	273
Table 5.3-9. Crack opening rate in A1-S and A1-L series.	273
Table 5.3-10. Crack opening rate in A2-S and A2-L series.	274
Table 5.3-11. Crack opening rate in A3-S and A3-L series.	274
Table 6.1-1. Adjustment coefficients for estimation formulation of fatigue life.	284
Table 6.1-2. R^2 coefficients of determination for the estimation formulation of fatigue life.	284

LIST OF FIGURES

Figure 1.3-1. Conceptual outline of the doctoral thesis.....	30
Figure 2.1-1. Glued steel fibers with shaped ends.....	32
Figure 2.1-2. Effect of aggregate size on fiber distribution in a 40 mm square with 40 mm fibers (adapted from [4]).....	34
Figure 2.1-3. Some of the most common types of steel fibers. From left to right, straight, crimped and hooked ends.	35
Figure 2.1-4. Wall effect on fiber orientation in specimens of different size with the same dosage and fiber length.....	36
Figure 2.1-5. Comparison of straight fiber and hooked end strength mechanisms.	41
Figure 2.1-6. Indicative force vs displacement diagrams in pull-out test of straight and hooked-end fibers without or with inclination.	42
Figure 2.1-7. Three-point bending test setup according to [7].	44
Figure 2.1-8. Load vs CMOD diagram in static flexural test with the behaviors that plain concrete (PC) and fiber reinforced concrete (SFRC) can show.....	44
Figure 2.1-9. Execution of lining, in this case of a slope, with projected fiber concrete.....	46
Figure 2.2-1. Stress range in a fatigue test and S-N curve for characterizing the fatigue response of a material.	49
Figure 2.2-2. FPZ in materials with brittle (a), ductile (b) and quasi-brittle (c) behavior (adapted from [24]). F indicates the fracture zone and N the zone of nonlinear or ductile behavior.	50
Figure 2.2-3. Fatigue classes as a function of the number of cycles [25].....	50
Figure 2.2-4. Example of S-N-P curve [31].....	53
Figure 2.2-5. Comparison of S-N curves for flexural fatigue, according to several authors.....	54
Figure 2.2-6. Aas-Jackobsen S-N curves [21] for flexural fatigue, considering different loading ratios.....	58
Figure 2.2-7. Number of cycles to failure vs loading frequency, according to different fatigue models [52].	59
Figure 2.2-8. S-N curves for plain concrete and SFRC with 0.5% and 1.0% fibers [54].....	60

Figure 2.2-9. Load vs CMOD curve in static flexural tensile test of SFRC with strain-hardening behavior. Example of the underestimation of fatigue loads that could be committed by considering P_L instead of P_{max} as reference.	61
Figure 2.2-10. Cracking growth processes in a concrete element subjected to flexural fatigue [63].	63
Figure 2.2-11. Load-CMOD curve in a flexural fatigue test in SFRC, indicating residual crack opening ($CMOD_{pi}$) and stiffness decrease with the number of cycles (Δk_i).	65
Figure 2.2-12. Monotonic envelope failure criterion in flexural fatigue [37].	66
Figure 2.2-13. CMOD-N diagram in flexural fatigue test in SFRC, showing damage stages and secondary crack opening rate.	67
Figure 2.2-14. Crack opening rate versus fatigue life in concretes with fiber contents of 0, 0.5 and 1.0% [54].	68
Figure 2.2-15. CMOD-N curve in flexural fatigue test in SFRC, showing the fatigue mechanisms of uncracked and cracked concrete.	69
Figure 2.2-16. Schematic representation of the determination of residual stiffness for each load cycle [65].	70
Figure 2.2-17. Variation of stiffness with the number of cycles in SFRC with different fiber contents (0.25% or 20 kg/m ³ , 0.50% or 40 kg/m ³ and 0.75% or 60 kg/m ³) [57].	70
Figure 2.2-18. Stiffness vs CMOD for SFRC with different fiber contents: (a) zoom in the range 0-0.06 mm, (b) general view [66].	71
Figure 2.2-19. Model proposed by Mínguez [41] for the evolution of the residual compressive strength over the fatigue life.	72
Figure 2.2-20. Increased post-fatigue flexural strength in specimens that have exceeded the runout limit [37].	73
Figure 2.3-1. Strength-size curve in concrete structures (adapted from [24]).	75
Figure 2.3-2. Transition from ductile to brittle behavior with increasing size in concrete subjected to flexural stress (adapted from [24]).	76
Figure 2.3-3. Fracture process in plain concrete with identification of main zones.	77
Figure 2.3-4. FPZ in materials with brittle (a), ductile (b) and quasi-brittle (c) behavior (adapted from [24]).	78
Figure 2.3-5. Wall effect on fiber orientation in different size specimens with the same fiber dosage and fiber length.	80

Figure 2.3-6. Fracture process in SFRC with identification of main zones.....	81
Figure 2.3-7. Size effect on flexural strength in SFRC with different fiber content [86].....	82
Figure 2.3-8. Size effect on SFRC compressive strength. The dosages of the series vary in cement and fiber content; as an example, the C100 series has 500 kg/m ³ and 0.75%, while the C175 has 750 kg/m ³ and 1.75%.....	83
Figure 2.3-9. Weibull fit of the fatigue life of series of cubic and cylindrical specimens of different sizes. All specimens were fabricated with the same SFRC and subjected to the same stress levels (20%-85% f_c) [42,97].	86
Figure 2.3-10. MicroCT analysis of a concrete specimen subjected to compressive fatigue: (a) pores before testing, (b) pores and cracks after testing [31].	87
Figure 2.3-11. Crack patterns in indirect tensile test on cylindrical specimens with diameters ranging from 74 to 290 mm [115].....	88
Figure 2.4-1. Interior of a microCT unit and identification of main elements.	90
Figure 2.4-2. Simple thresholding of fibers in a SFRC specimen and identification of errors due to connected fibers.....	92
Figure 2.4-3. Process of the segmentation technique of watershed transform.	93
Figure 2.4-4. Fiber segmentation: (a) applying watershed transform and (b) applying watershed transform together with an artificial intelligence model.	94
Figure 2.4-5. Correlation between fiber distribution and orientation, and flexural strength. [125].....	96
Figure 2.4-6. MicroCT images showing the bridging effect of fibers on cracks caused by compressive fatigue [61]......	96
Figure 2.4-7. Porosity in specimens with different content of air-entraining agent; from left to right, 0, 0.1% and 0.2%. [129].....	98
Figure 2.4-8. In situ microCT system, with Skyscan 1173 microCT scanner mounted on an Instron 5569 50 kN testing machine [123].....	99
Figure 2.4-9. Segmentation of the different concrete phases (coarse aggregate, matrix and pores) for the development of finite element models [135].	100
Figure 2.4-10. Identification of pores and cracks in cubic specimens subjected to compressive fatigue (pores < 1 mm in red, 1-2 mm in green and > 2 mm in blue) [68].....	100
Figure 3.1-1. Superplasticizer admixture (left) and nanosilica suspension (right).	102
Figure 3.1-2. Dramix RC-80/30-CP steel fibers.	102

Figure 3.1-3. Comparison of the slump flow: (a) starting dosage and (b) final dosage.....	107
Figure 3.1-4. Vertical-axis concrete mixer used.	109
Figure 3.1-5. Types of molds used: cylindrical 150x300 mm, prismatic 150x150x600 mm and prismatic 100x100x400 mm with reductions.	110
Figure 3.1-6. Weighing of solid materials and pouring into the concrete mixer.	111
Figure 3.1-7. Mixing of solid materials and addition of water with admixtures.....	112
Figure 3.1-8. Appearance of concrete with fibers at the end of the mixing time.....	113
Figure 3.1-9. Curing chamber used.	113
Figure 3.1-10. Evolution of the compressive strength with time in HA-60 concrete, according to the formulation proposed in [3].	114
Figure 3.2-1. Example of a slump test.	116
Figure 3.2-2. Compressive strength test on a fiber-reinforced concrete specimen.	117
Figure 3.2-3. Test to determine the modulus of elasticity in compression.	118
Figure 3.2-4. Flexural strength test on a specimen of size S.....	118
Figure 3.2-5. Flexural strength test on a specimen of size L, with identification of the main elements.....	120
Figure 3.2-6. Flexural fatigue test, showing the data acquisition system in the foreground.	121
Figure 3.2-7. Identification of reference parameters in a static flexural tensile test.	122
Figure 3.2-8. Load vs CMOD diagram in static flexural test with the behaviors that plain concrete (PC) and fiber-reinforced concrete (SFRC) can show.....	123
Figure 3.2-9. Main entrance of the School of Engineering and access to the Laboratory of Large Structures of Civil Works.	128
Figure 3.2-10. Inside view of the Large Structures of Civil Works Laboratory.	128
Figure 3.2-11. 300 T testing machine.	129
Figure 3.2-12. 50 kN actuator positioned in its reaction frame.....	129
Figure 3.2-13. Bending fixtures for size S (left) and L (right) specimens.	130
Figure 3.2-14. Fixture for size S specimens.....	131
Figure 3.2-15. Laser distance meters and axial extensometer placed on a specimen of size L.	133
Figure 3.2-16. Data acquisition with QuantumX module and Catman software.	133
Figure 3.2-17. Example of the error due to the ratio between data acquisition frequency and loading frequency in a fatigue test.....	134

Figure 3.2-18. CMOD-N curve in flexural fatigue test in SFRC, showing the fatigue mechanisms of uncracked and cracked concrete.	138
Figure 3.3-1. TESCAN CoreTOM microCT equipment.	139
Figure 3.3-2. Specimen inside the microCT equipment.	140
Figure 3.3-3. 3D reconstruction of specimen with indication of the coordinate axis system.	141
Figure 3.3-4. Fiber segmentation: (a) applying watershed transform and (b) applying watershed transform together with an artificial intelligence model.	143
Figure 4.1-1. Slump vs fiber content.	146
Figure 4.1-2. Time t_{50} vs fiber content.	146
Figure 4.1-3. Appearance of the slump flow: (a) A0, (b) A1, (c) A2 and (d) A3.	147
Figure 4.1-4. Compressive strength vs fiber content.	149
Figure 4.1-5. Stress-strain curves in compressive strength tests: (a) A0, (b) A1, (c) A2 and (d) A3.	150
Figure 4.1-6. Modulus of elasticity vs fiber content.	151
Figure 4.1-7. Nominal stress vs CMOD diagram of A0-S series.	152
Figure 4.1-8. Nominal stress vs CMOD diagram of A1-S series.	152
Figure 4.1-9. Nominal stress vs CMOD diagram of A2-S series.	153
Figure 4.1-10. Nominal stress vs CMOD diagram of A3-S series.	153
Figure 4.1-11. Comparison of the nominal stress vs CMOD diagrams for the series of S-size specimens.	154
Figure 4.1-12. Maximum stress and stress corresponding to the LOP in the flexural tensile test, vs fiber content.	155
Figure 4.1-13. Residual flexural strengths of SFRC series.	157
Figure 4.1-14. Nominal stress vs CMOD diagram of A0-L series.	158
Figure 4.1-15. Nominal stress vs CMOD diagram of A1-L series.	158
Figure 4.1-16. Nominal stress vs CMOD diagram of A2-L series.	159
Figure 4.1-17. Nominal stress vs CMOD diagram of A3-L series.	159
Figure 4.1-18. Comparison of the nominal stress vs CMOD diagrams for the L-size specimen series.	160
Figure 4.1-19. Maximum stress and stress corresponding to LOP in the flexural tensile test, vs fiber content.	161
Figure 4.1-20. Residual flexural strengths of SFRC series.	162
Figure 4.2-1. Fit to the Weibull distribution of the fatigue life of A0-S series.	164

Figure 4.2-2. Fit to the Weibull distribution of the fatigue life of A1-S series.....	164
Figure 4.2-3. Fit to the Weibull distribution of the fatigue life of A2-S series.....	165
Figure 4.2-4. Fit to the Weibull distribution of the fatigue life of A3-S series.....	165
Figure 4.2-5. Fit to the Weibull distribution of the fatigue life of the S-size series.....	166
Figure 4.2-6. CMOD vs fatigue life in A0-S series fatigue tests.	168
Figure 4.2-7. CMOD vs fatigue life in A0-S series fatigue tests (detail view).....	168
Figure 4.2-8. CMOD vs relative fatigue life in A0-S series fatigue tests.	169
Figure 4.2-9. CMOD vs relative fatigue life in A0-S series fatigue tests (detail view).....	169
Figure 4.2-10. CMOD vs fatigue life in A1-S series fatigue tests.	170
Figure 4.2-11. CMOD vs fatigue life in A1-S series fatigue tests (detail view).....	170
Figure 4.2-12. CMOD vs relative fatigue life in A1-S series fatigue tests.	171
Figure 4.2-13. CMOD vs relative fatigue life in A1-S series fatigue tests (detail view).....	171
Figure 4.2-14. CMOD vs fatigue life in A2-S series fatigue tests.	172
Figure 4.2-15. CMOD vs fatigue life in A2-S series fatigue tests (detail view).....	172
Figure 4.2-16. CMOD vs relative fatigue life in A2-S series fatigue tests.	173
Figure 4.2-17. CMOD vs relative fatigue life in A2-S series fatigue tests (detail view).....	173
Figure 4.2-18. CMOD vs fatigue life in A3-S series fatigue tests.	174
Figure 4.2-19. CMOD vs relative fatigue life in A3-S series fatigue tests.	174
Figure 4.2-20. Secondary crack opening rate due to matrix fatigue versus total number of cycles. A0-S series.....	178
Figure 4.2-21. Secondary crack opening rate due to matrix fatigue vs number of cycles due to matrix fatigue. A1-S series.....	179
Figure 4.2-22. Secondary crack opening rate due to matrix fatigue versus total number of cycles. A1-S series.....	179
Figure 4.2-23. Secondary crack opening rate due to fiber fatigue vs number of cycles due to fiber fatigue. A1-S series.....	180
Figure 4.2-24. Secondary crack opening rate due to fiber fatigue versus total number of cycles. A1-S series.....	180
Figure 4.2-25. Secondary crack opening rate due to matrix fatigue vs number of cycles due to matrix fatigue. A2-S series.....	181

Figure 4.2-26. Secondary crack opening rate due to matrix fatigue versus total number of cycles. A2-S series.	181
Figure 4.2-27. Secondary crack opening rate due to fiber fatigue versus number of cycles due to fiber fatigue. A2-S series.	182
Figure 4.2-28. Secondary crack opening rate due to fiber fatigue versus total number of cycles. A2-S series.	182
Figure 4.2-29. Secondary crack opening rate due to fiber fatigue versus total number of cycles. A3-S series.	183
Figure 4.2-30. Secondary crack opening rate versus number of cycles, distinguishing between the two fatigue mechanisms.....	184
Figure 4.2-31. Fit to the Weibull distribution of the fatigue life of A0-L series.....	186
Figure 4.2-32. Fit to the Weibull distribution of the fatigue life of A1-L series.....	186
Figure 4.2-33. Fit to the Weibull distribution of the fatigue life of A2-L series.....	187
Figure 4.2-34. Fit to the Weibull distribution of the fatigue life of A3-L series.....	187
Figure 4.2-35. Fit to the Weibull distribution of the fatigue life of the L-size specimen series.	188
Figure 4.2-36. CMOD vs fatigue life in A0-L series fatigue tests.....	190
Figure 4.2-37. CMOD vs relative fatigue life in A0-L series fatigue tests.....	190
Figure 4.2-38. CMOD vs fatigue life in A1-L series fatigue tests.....	191
Figure 4.2-39. CMOD vs fatigue life in A1-S series fatigue tests (detail view).	191
Figure 4.2-40. CMOD vs relative fatigue life in A1-L series fatigue tests.....	192
Figure 4.2-41. CMOD vs relative fatigue life in A1-L series fatigue tests (detail view).	192
Figure 4.2-42. CMOD vs fatigue life in A2-L series fatigue tests.....	193
Figure 4.2-43. CMOD vs relative fatigue life in A2-L series fatigue tests.....	193
Figure 4.2-44. CMOD vs fatigue life in A3-L series fatigue tests.....	194
Figure 4.2-45. CMOD vs relative fatigue life in A3-L series fatigue tests.....	194
Figure 4.2-46. Secondary crack opening rate due to matrix fatigue versus total number of cycles. A0-L series.	197
Figure 4.2-47. Secondary crack opening rate due to matrix fatigue vs number of cycles due to matrix fatigue. A1-L series.	198
Figure 4.2-48. Secondary crack opening rate due to matrix fatigue versus total number of cycles. A1-L series.	198

Figure 4.2-49. Secondary crack opening rate due to fiber fatigue vs number of cycles due to fiber fatigue. A1-L series.....	199
Figure 4.2-50. Secondary crack opening rate due to fiber fatigue versus total number of cycles. A1-L series.....	199
Figure 4.2-51. Secondary crack opening rate due to fiber fatigue versus total number of cycles. Series A2-L.....	200
Figure 4.2-52. Secondary crack opening rate due to fiber fatigue versus total number of cycles. A3-L series.....	200
Figure 4.2-53. Secondary crack opening rate versus number of cycles, distinguishing between the two fatigue mechanisms.	201
Figure 4.3-1. Histogram of fiber orientation with respect to the X-axis.....	203
Figure 4.3-2. Histogram of fiber orientation with respect to the Y-axis.....	203
Figure 4.3-3. Histogram of fiber orientation with respect to the Z-axis.	204
Figure 4.3-4. Indication of the coordinate system used.	204
Figure 4.3-5. Histogram of X-coordinate of the center of gravity of the fibers.....	206
Figure 4.3-6. Histogram of Y-coordinate of the center of gravity of the fibers.....	206
Figure 4.3-7. Histogram of Z-coordinate of the center of gravity of the fibers.	207
Figure 4.3-8. Porosity curve of A0-S series.	209
Figure 4.3-9. Cumulative pore volume curve of A0-S series.....	209
Figure 4.3-10. Histogram of pore volume versus number of pores. A0-S series.....	210
Figure 4.3-11. Histogram of pore volume versus total volume of pores. A0-S series.	211
Figure 4.3-12. Histogram of pore length in relation to the number of pores. A0-S series.....	212
Figure 4.3-13. Histogram of pore length in relation to the total volume of pores. A0-S series.....	212
Figure 4.3-1. Indication of the coordinate system used.	213
Figure 5.1-1. Linear regression (per series) between the mean fiber orientation with respect to the Z-axis and the total number of cycles.	216
Figure 5.1-2. Linear regression (global) between the mean fiber orientation with respect to the Z-axis and the total number of cycles.	216
Figure 5.1-3. Linear regression (per series) between the mean fiber orientation with respect to the Z-axis and the number of fiber fatigue cycles.	217

Figure 5.1-4. Linear regression (global) between the mean fiber orientation with respect to the Z-axis and the number of fiber fatigue cycles.	217
Figure 5.1-5. Linear regression (per series) between the mean fiber orientation with respect to the Z-axis and the secondary crack opening rate of fiber fatigue.....	218
Figure 5.1-6. Linear regression (global) between the mean fiber orientation with respect to the Z-axis and the secondary crack opening rate of fiber fatigue.....	218
Figure 5.1-7. Linear regression (per series) between the mean efficiency index on the Z-axis and the total number of cycles.	220
Figure 5.1-8. Linear regression (global) between the mean efficiency index on the Z-axis and the total number of cycles.	220
Figure 5.1-9. Linear regression (per series) between the mean efficiency index on the Z-axis and the number of fiber fatigue cycles.	221
Figure 5.1-10. Linear regression (global) between the mean efficiency index on the Z-axis and the number of fiber fatigue cycles.	221
Figure 5.1-11. Linear regression (per series) between the mean efficiency index on the Z-axis and the secondary crack opening rate of fiber fatigue.	222
Figure 5.1-12. Linear regression (global) between the mean efficiency index on the Z-axis and the secondary crack opening rate of fiber fatigue.	222
Figure 5.1-13. Relationship between orientation and efficiency index.	224
Figure 5.1-14. Linear regression (per series) between the relative density of fibers passing through the crack plane and the total number of cycles.	225
Figure 5.1-15. Linear regression (global) between the relative density of fibers passing through the crack plane and the total number of cycles.	225
Figure 5.1-16. Linear regression (per series) between the relative density of fibers passing through the crack plane and the number of fiber fatigue cycles.....	226
Figure 5.1-17. Linear regression (global) between the relative density of fibers passing through the crack plane and the number of fiber fatigue cycles.....	226
Figure 5.1-18. Linear regression (per series) between the relative density of fibers crossing the crack plane and the secondary crack opening rate of fiber fatigue.....	227
Figure 5.1-19. Linear regression (global) between the relative density of fibers crossing the crack plane and the secondary crack opening rate of fiber fatigue.....	227
Figure 5.1-20. Linear regression (per series) between weighted average fiber height and total number of cycles.	230

Figure 5.1-21. Linear regression (global) between weighted average fiber height and total number of cycles.	230
Figure 5.1-22. Linear regression (per series) between the weighted average fiber height and the number of fiber fatigue cycles.	231
Figure 5.1-23. Linear regression (global) between the weighted average fiber height and the number of fiber fatigue cycles.	231
Figure 5.1-24. Linear regression (per series) between weighted average fiber height and secondary crack opening rate of fiber fatigue.	232
Figure 5.1-25. Linear regression (global) between weighted average fiber height and secondary crack opening rate of fiber fatigue.	232
Figure 5.1-26. Linear regression (per series) between median fiber height and total number of cycles.	234
Figure 5.1-27. Linear regression (global) between median fiber height and total number of cycles.	234
Figure 5.1-28. Linear regression (per series) between median fiber height and number of fiber fatigue cycles.....	235
Figure 5.1-29. Linear regression (global) between median fiber height and number of fiber fatigue cycles.	235
Figure 5.1-30. Linear regression (per series) between median fiber height and secondary crack opening rate of fiber fatigue.	236
Figure 5.1-31. Linear regression (global) between median fiber height and secondary crack opening rate of fiber fatigue.	236
Figure 5.2-1. View of the pore study region in a A0-S series specimen tested under fatigue.....	241
Figure 5.2-2. Linear regression between porosity and number of cycles.	242
Figure 5.2-3. Linear regression between porosity and secondary crack opening rate.	242
Figure 5.2-4. Linear regression between pore density and number of cycles.....	243
Figure 5.2-5. Linear regression between pore density and secondary crack opening rate.	243
Figure 5.2-6. Linear regression between mean neighborhood distance and number of cycles.....	245
Figure 5.2-7. Linear regression between mean neighborhood distance and secondary crack opening rate.	245

Figure 5.2-8. Linear regression between mean pore volume and number of cycles. ...	247
Figure 5.2-9. Linear regression between mean pore volume and secondary crack opening rate.....	247
Figure 5.2-10. Linear regression between maximum pore volume and number of cycles.	248
Figure 5.2-11. Linear regression between maximum pore volume and secondary crack opening rate.....	248
Figure 5.3-1. Weibull fitting of fatigue life of plain concrete series.	254
Figure 5.3-2. Weibull fitting of fatigue life of SFRC series with 0.3% fibers.	254
Figure 5.3-3. Weibull fitting of fatigue life of SFRC series with 0.6% fibers.	255
Figure 5.3-4. Weibull fitting of fatigue life of SFRC series with 1.0% fibers.	255
Figure 5.3-5. Weibull fitting of fatigue life of all series.....	257
Figure 5.3-6. CMOD vs fatigue life in A0-S and A0-L series.....	259
Figure 5.3-7. CMOD vs fatigue life in A0-S and A0-L series (detail view).	260
Figure 5.3-8. CMOD vs relative fatigue life in A0-S and A0-L series.....	260
Figure 5.3-9. CMOD vs fatigue life in A1-S and A1-L series.....	263
Figure 5.3-10. CMOD vs fatigue life in A1-S and A1-L series (detail view).	263
Figure 5.3-11. CMOD vs relative fatigue life in A1-S and A1-L series.....	264
Figure 5.3-12. CMOD vs relative fatigue life in A1-S and A1-L series (detail view).	264
Figure 5.3-13. CMOD vs fatigue life in A2-S and A2-L series.....	267
Figure 5.3-14. CMOD vs relative fatigue life in A2-S and A2-L series.....	267
Figure 5.3-15. CMOD vs fatigue life in A3-S and A3-L series.....	270
Figure 5.3-16. CMOD vs relative fatigue life in A3-S and A3-L series.....	270
Figure 5.3-17. Secondary crack opening rate versus number of cycles, both associated with fatigue of uncracked concrete, in all series.	275
Figure 5.3-18. Secondary crack opening rate versus number of cycles, both associated with fatigue of cracked concrete, in all series.	276
Figure 5.3-19. Secondary crack opening rate versus number of cycles in all series, distinguishing between fatigue of uncracked concrete (dashed line) and cracked concrete (solid line).	277
Figure 6.1-1. Linear regression between the relative density of fibers passing through the crack plane and the total number of cycles.	282

Figure 6.1-2. Linear regression between the average efficiency index on the Z-axis and the total number of cycles.....	282
Figure 6.1-3. Linear regression between the median fiber height and the total number of cycles.	283
Figure 6.2-1. Linear regression between the mean neighborhood distance and the number of cycles.	286
Figure 6.2-2. Linear regression between the maximum pore volume and the number of cycles.....	286
Figure 6.3-1. Weibull fitting of fatigue life of all series.	288
Figure 6.3-2. CMOD vs relative fatigue life in A1-S and A1-L series.	289
Figure 6.3-3. Secondary crack opening rate versus number of cycles in all series, distinguishing between fatigue of uncracked concrete (dashed line) and cracked concrete (solid line).....	290

ACKNOWLEDGMENTS

This doctoral thesis is not the result of the efforts of a single person, so I would like to acknowledge all those persons or entities that, in one way or another, have contributed to its development.

My thanks to the *Ministerio de Universidades* of the Government of Spain for the funding received through its grants *Formación del Profesorado Universitario*. I would also like to thank the University of Burgos, and especially the Department of Civil Engineering, for allowing me to use its magnificent facilities.

I want to express my gratitude to my thesis directors, Miguel Ángel Vicente and Dorys González, as well as to Jesús Mínguez. Their extensive experience has been a great asset, but equally important has been their full disposition and the sincere and kind treatment they have always offered me.

Thanks to the technicians of the School of Engineering for their help and professionalism during the testing campaign. My special recognition goes to Antonio Fernández, who has always given me his unconditional support.

Finally, I would like to thank my parents, my brother and my partner for always being by my side, encouraging me not to give up and to keep going forward.

ABSTRACT

Equal fatigue tests in concrete, meaning those performed on exactly equal or homothetic specimens subjected to the same stress levels, present two problems yet to be solved. On the one hand, the high dispersion of the results, which causes the fatigue life in two apparently identical elements to vary by up to two or more orders of magnitude. On the other hand, the size effect, whereby fatigue strength decreases with increasing element size.

The aim of this research work is to study these two issues in depth. Regarding the first one, the influence of the dispersion of concrete mesostructure on the dispersion of fatigue results will be studied; in particular, it will be evaluated whether the stochastic arrangement of fibers (in fiber concrete) or pores (in plain concrete) explains the variability of fatigue life. As for the size effect, fatigue tests will be performed on geometrically similar specimens subjected to the same equivalent stress levels. Macroscopic damage indicators, such as crack opening, will be used to determine the magnitude of the size effect and its variation according to the type of concrete (plain concrete and fiber-reinforced with different fiber contents).

The results reveal that the arrangement of fibers and pores varies significantly in apparently identical specimens, and that this partly explains the dispersion of fatigue results. However, the estimation of the fatigue response of concrete from its mesostructure requires complex models, comprising several geometrical parameters of various components. In this work, a methodological approach to the problem is made, proposing mesostructure parameters that are reasonably predictive. With respect to the size effect, it is observed that the presence of fibers reduces the size effect on fatigue life, almost nullifying it. Furthermore, it is concluded that the secondary crack opening rate ($dCMOD/dn$) is an adequate parameter to explain the fatigue life in general, and the size effect in particular.

1 INTRODUCTION

1.1 Motivation

Fatigue in concrete is a tremendously interesting phenomenon, since it implies that a given element can collapse without ever exceeding its maximum load under static conditions. This type of action is the order of the day in structural codes, since, with the progress of high-strength concrete, structures are becoming increasingly slender. As a result, the importance of variable loads (traffic, wind, etc.), which are cyclic in nature and therefore susceptible to fatigue, is increasing.

There are two issues related to equal fatigue tests, understood as those performed on identical or homothetic specimens subjected to the same stress levels, that the scientific community has not yet been able to resolve. The first of these is the high dispersion of the results, it being common for fatigue life to vary by two or more orders of magnitude. In other words, it is accepted that two identical specimens, with the same shape and size and subjected to the same stress levels, can withstand, for example, a number of cycles of 10,000 and 1,000,000 cycles, respectively. This lack of knowledge of the phenomenon means that the safety margins for fatigue testing in current codes are very conservative. For example, according to Eurocode 2 [1], in a concrete with a characteristic compressive strength f_{ck} of 80 MPa, its design fatigue strength $f_{cd, fat}$ barely reaches 36 MPa [2]. Therefore, with regard to structures whose design is determined by fatigue (such as wind turbine concrete towers, and to a lesser extent, high-speed railroad viaducts), it is very interesting to advance in the investigation of fatigue dispersion. In this way, it will be possible to reduce the safety coefficients and thus optimize the strength of the concrete.

The second issue is the size effect; that is, the reduction of mechanical strength in homothetic or geometrically similar elements as their size increases. This problem is not exclusive to fatigue, but to the structural response of concrete in general. The study of the size effect is of great interest because normally the experimental determination of the strength of concrete (compressive strength, fatigue strength, etc.) is made on specimens that are several orders of magnitude smaller than the real elements. Therefore, if the results are not properly corrected, an overestimation of the capacity of the concrete is incurred, with the consequent risk for our structures.

Therefore, this doctoral thesis aims to make a small contribution to the knowledge of these problems affecting fatigue in concrete.

1.2 Problem statement and objectives

As mentioned above, this research work attempts to shed some light on the high dispersion of results, firstly, and the size effect, secondly, in equal fatigue tests in concrete. On the one hand, with respect to the high dispersion of the results, the influence of the mesostructure on this phenomenon is going to be studied; in particular, of the fibers in steel fiber reinforced concrete and of the pores in plain concrete. On the other hand, as regards the size effect in fatigue, macroscopic damage indicators will be analyzed, based on the crack opening (CMOD) vs fatigue life (N) diagrams, comparing them between tests carried out on specimens of different sizes.

The general objectives of the doctoral thesis are described below:

1. To study the influence of the dispersion of the distribution and orientation of the fibers on the dispersion of the flexural fatigue response of steel fiber-reinforced concrete. In other words, the aim is to find out whether the stochastic dispersion of the fibers within the matrix is related to the fatigue response of "apparently" identical specimens.

To this end, numerous flexural fatigue tests have been carried out on identical specimens made with the same dosage and fiber content. Prior to the tests, the specimens were scanned by micro-computed tomography (μ CT) to obtain the geometrical properties of the fibers (distribution, position, orientation, etc.). This process has been repeated with three fiber contents (0.3%, 0.6% and 1.0%), so that it is possible to know if the impact of fibers on the dispersion of fatigue results changes with their content.

2. Analogously to the previous one, to analyze the influence of the dispersion in the morphological parameters of the pores on the dispersion of the fatigue response of plain concrete. The aim is to answer whether the stochastic nature of the pore morphology is related to the fatigue response in a priori equal specimens.

For this purpose, fatigue tests have been carried out with the same load levels on plain concrete specimens of the same size and the same dosage. Previously, the specimens were scanned with μ CT to obtain the geometrical properties of the pores (porosity volume, spatial distribution, pore size distribution, etc.).

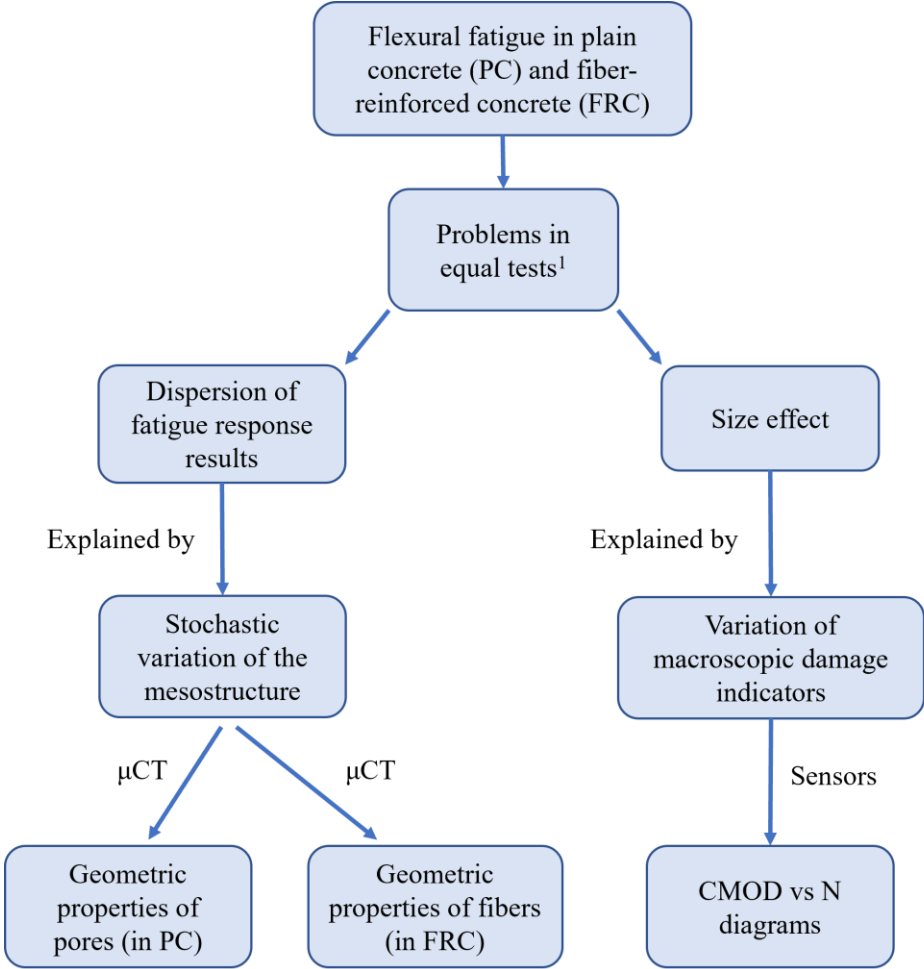
3. To study the size effect on the fatigue life of plain concrete and fiber-reinforced concrete.

To this end, fatigue tests have been carried out on two different specimen sizes and with four concrete dosages (plain concrete and with 0.3%, 0.6% and 1.0% of fibers). In this way, it can be determined whether the size effect varies according to the presence of fibers and their quantity.

1.3 Structure of the document

This doctoral thesis is divided into 6 sections. Section 2 discusses the state of the art, distinguishing between fiber-reinforced concrete, fatigue in concrete, size effect and computed tomography. This is followed by a description of materials and methods in Section 3. Then, in Section 4, the results are presented. In Section 5, the results are discussed in depth. Finally, the main conclusions are presented in Section 6.

The following figure shows the conceptual diagram of this doctoral thesis.



¹Tests performed under the same stress levels on exactly or geometrically similar (homothetic) specimens.

Figure 1.3-1. Conceptual outline of the doctoral thesis.

2 STATE OF THE ART

2.1 Steel fiber-reinforced concrete

This section describes the main characteristics of the material used in this research work: steel fiber reinforced concrete (SFRC). First, the material is defined. Then, the components are described. Next, the most significant parameters involved in its dosage are listed, as well as their recommended values. At this point, it should be taken into account that a non-conventional SFRC has been designed, which has two singular properties: high strength and self-compacting. Therefore, the influence of these qualities on the design of the dosages is highlighted. Next, the main mechanical properties of SFRC are described, explaining first its strength mechanism. Finally, the most relevant current applications are indicated.

2.1.1 Introduction

According to Annex 7 of the Spanish Structural Code [3], fiber-reinforced concretes are defined as those concretes that include in their composition short, discrete and randomly distributed fibers in their mass. It should be added that this is intended to improve the brittle behavior of the concrete; in particular, by increasing the tensile strength in the cracked state.

The addition of fibers to improve the properties of construction materials is an ancient technique. The first indications date back more than 10,000 years ago in the Middle East, where blocks or mud bricks reinforced with straw, known as adobe, have been found. In the case of concrete, the use of fibers to improve its load-bearing capacity is linked to its very origin, since the Romans used natural fibers in their primitive lime mortar (1st century B.C.).

The use of fibers in modern concrete made with Portland cement did not emerge until the beginning of the 20th century. Until then, the most significant breakthrough was the patent recorded by Berard in 1874 in the USA, where he proposed the addition of granular steel residues to concrete. The first patents using steel fibers to improve the mechanical response of concrete were the ones by Graham (1911, USA) and Alfsen (1918, France). Over the next two decades, patents for fiber-reinforced concrete, mainly steel and glass, continued to be published in the USA, France and Germany.

In the 1950s and especially the 1960s, the research and development of this material took a new impulse, seeking to perfect the geometry of the fibers in order to solve the problems of workability (formation of balls, etc.) and adherence to the matrix, which were very common in these early stages. Romualdi's work with Batson and Mandel in 1963 and 1964, respectively, is noteworthy. At this time, SFRC began to be commonly used in applications such as high-performance pavements, heavy machinery foundations, air raid shelters, etc.

During the following decades and up to the present day, very significant advances have been made in the performance of SFRC. With respect to steel fibers, the most relevant innovations were fibers with shaped ends and gluing (Figure 2.1-1). On the one hand, shaped ends increase the fiber-matrix adhesion in a critical area, which allows an increase in toughness with the same number of fibers. On the other hand, gluing ensures that the "combs" or groups of laterally joined fibers are less slender than the individual fibers. In this way, the risk of balling up during mixing is greatly reduced.



Figure 2.1-1. Glued steel fibers with shaped ends.

It is not only the improvement of steel fibers that has contributed to the development of SFRC, but also the appearance of other admixtures. For example, superplasticizer admixtures make it possible to compensate for the reduction in workability caused by the fibers without increasing the water/cement (w/c) ratio, and thus without compromising the mechanical response of the concrete. Another case is the silica fume, a pozzolanic admixture that, among other aspects, improves the strength, cohesion and impermeability of concrete.

This set of advances has made it possible to expand the field of application of SFRC, from the construction of pavements to support heavy loads and impacts, to the lining of subway works using the shotcrete technique.

This material is currently attracting a great deal of scientific interest. There are still significant technical and psychological barriers that prevent the fibers from being given a greater structural responsibility, so that they can partially or totally replace conventional rebar reinforcement. Consequently, the scientific community continues to move forward with the common goal of making SFRC a reality in the design of structural elements.

2.1.2 Components

Concretes reinforced with steel fibers are, in essence, conventional concretes to which fibers are added. Therefore, the matrix components are the usual ones: cement, water, aggregates, additions and admixtures. However, the introduction of fibers affects to some extent the requirements of the rest of the components.

The most relevant aspects of the materials that constitute the SFRC are described below.

Cement

The cements used in the manufacture of SFRC are the same as those used in conventional concrete. If high strength is to be achieved, it is recommended to use cements with a strength class equal to or higher than 42.5, the most common types being CEM I 42.5 R and CEM I 52.5 R.

Water

The water used in SFRC is the same as in conventional concrete. It is simply recommended to avoid water that is susceptible to corroding the fibers and eventual reinforcements, such as seawater.

Aggregates

The design of a proper aggregate granulometry is especially important in the manufacture of SFRC, not only because it conditions the strength properties of the hardened concrete, but also because it directly affects the consistency and workability of the fresh concrete.

As for the coarse aggregate, it should be small enough to ensure an adequate distribution of the fibers within the matrix, avoiding their grouping (Figure 2.1-2). In this regard, it is recommended that the ratio between the maximum aggregate size and the length of the fibers be a maximum of 1/2, which can be reduced to 1/3 or less [3]. Consequently, it is not usual to use coarse aggregate with a maximum size greater than 20 mm.

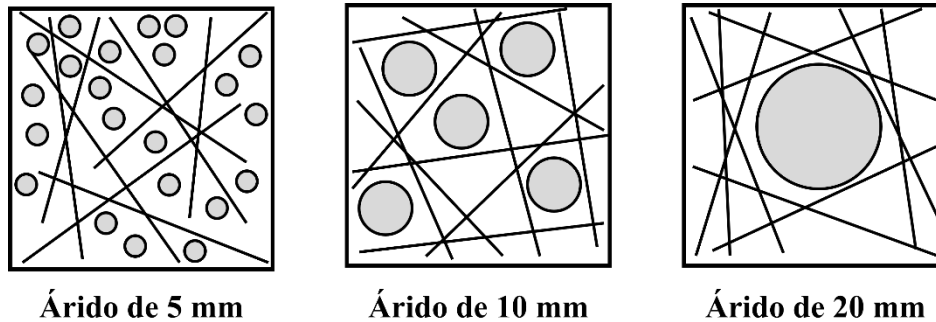


Figure 2.1-2. Effect of aggregate size on fiber distribution in a 40 mm square with 40 mm fibers (adapted from [4]).

As for the fine aggregate, it is generally recommended to increase its quantity by increasing the fine aggregate/coarse aggregate ratio. This improves the workability and cohesion of the concrete, reducing the risk of segregation.

Admixtures

The incorporation of fibers in concrete significantly reduces its workability. Therefore, the use of superplasticizers or water-reducing admixtures is recommended, since they improve the workability of concrete without increasing the w/c ratio, i.e., without affecting its final strength.

These admixtures are also used to achieve liquid consistencies or even self-compacting properties, especially in applications such as tunnel or mine lining, where SFRC is applied in the form of pumped or shotcrete.

Additions

The most recommended additions in the manufacture of SFRC are pozzolanic materials. These are siliceous or silicoaluminous substances that, finely ground and in the presence of water, are capable of reacting with the hydration products of cement (mainly $\text{Ca}(\text{OH})_2$) to create resistant compounds (silicates and calcium aluminates).

The most common pozzolanic materials used in the manufacture of concrete are natural pozzolans, fly ash and silica fume. These additions improve concrete cohesion and thus fiber-matrix adhesion.

Fibers

Fibers are the differentiating element of SFRC with respect to conventional concrete. They are linear elements of short length (in the order of 10-50 mm) and very small section (in general, 0.2-1.5 mm) that are added to the concrete matrix to improve some of its properties. Although only steel fibers are discussed here, it is worth mentioning that there are other types on the market, such as synthetic fibers (polypropylene, glass, carbon, etc.) and natural fibers (wood, sisal, etc.).

Depending on the manufacturing process, steel fibers can be obtained by cold drawing (Type I), by cutting into sheets (Type II), extracted by hot scraping (Type III) or obtained by other procedures (Type IV) [5]. The most common fibers are cold-drawn.

In terms of shape, there is a wide variety of typologies: straight, wavy, serrated, twisted, hooked-end, flat-end, etc. (Figure 2.1-3). Fiber geometry directly influences fiber-matrix adhesion, and therefore the mechanical response of the SFRC. The higher the adhesion, the higher the energy absorption by the fibers and therefore the higher the fracture toughness. Therefore, this wide range of fiber shapes is the result of manufacturers' efforts to achieve better adhesion. At present, the most common fibers are straight and hooked-end fibers.



Figure 2.1-3. Some of the most common types of steel fibers. From left to right, straight, crimped and hooked ends.

The geometrical properties that characterize the fibers are the type of cross-section (circular, rectangular, etc.), diameter (or equivalent diameter), length and slenderness. Length is one of the most important parameters, and certain recommendations should be

taken into account when choosing it. As already mentioned, to facilitate the mobility of the fibers during mixing, the maximum aggregate size/fiber length ratio should be a maximum of 1/2. In addition, it is recommended that the ratio of fiber length to minimum mold size be a maximum of 1/3 [6,7]. The objective is to reduce as much as possible the wall effect, whereby the fibers closest to the mold or formwork tend to be oriented parallel to their faces. In the laboratory, it is especially important to control this phenomenon, since small molds are normally used. Moreover, by combining the wall effect with the pouring direction of the concrete, preferred fiber orientations can be induced, which could lead to overestimate the strength of SFRC with respect to larger elements [8]. A clear example is that of prismatic specimens subjected to flexural bending (Figure 2.1-4).

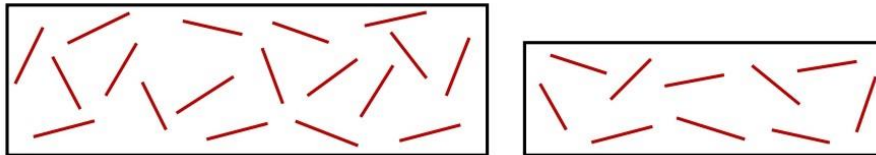


Figure 2.1-4. Wall effect on fiber orientation in specimens of different size with the same dosage and fiber length.

Another fundamental parameter that characterizes the geometry of the fibers is the slenderness, defined as the ratio between the length and the diameter (l/d or λ). The slenderness of the fibers is directly related to their mechanical efficiency, so that the higher its value, the greater the fiber-matrix adhesion and therefore the fracture toughness. However, caution must be taken since excessive slenderness leads to a significant reduction in the workability of the concrete and the risk of the formation of fiber balls. These disadvantages can be solved to some extent by gluing, which artificially reduces the slenderness of the fibers during mixing. In any case, the usual range is between 45 and 80, and it is not advisable to exceed 100.

As regards the mechanical properties of the fibers, the most relevant are the modulus of elasticity, tensile strength and elongation at break. The tensile strength is usually very high; the minimum values are around 500 MPa, although in practice it is common to find steel fibers on the market that reach 3,000 MPa.

A table with the average values of the main geometrical and mechanical properties of steel fibers is given below.

Table 2.1-1. Common properties of steel fibers for SFRC.

Geometrical properties	Length (mm)	10 – 60
	Equivalent diameter (mm)	0.2 – 1.0
	Slenderness	45 – 80
Material and mechanical properties	Modulus of elasticity (GPa)	> 200
	Tensile strength (MPa)	500 – 3,000
	Elongation at break (%)	2 – 7
	Density (kN/m ³)	78.5

2.1.3 Mix design

The type of concrete used is a SFRC with two singularities: it is high strength and self-compacting. This means that it combines the advantages of its 3 main properties, which gives it great potential as a construction material. However, this also implies a certain complexity in the design of the dosages. The addition of fibers reduces the workability and consistency of the concrete, but a self-compacting concrete requires good cohesion of its components and a very liquid consistency. In addition, high strength means low w/c ratios, so the reduction in workability added by fibers cannot be compensated for by adding water.

The design of concretes with these characteristics, and in particular of self-compacting concretes, has attracted some scientific interest in recent years [9]. However, to date there are no standardized mix design methods. Therefore, it is usual to start with the dosage of a conventional concrete and make modifications following certain indicative recommendations set out in the standards [5].

The most relevant factors to be taken into account when proportioning a high-strength, self-compacting steel fiber concrete are described below.

Cement content

The cement content must be higher than conventional concretes for several reasons. First, it is a fundamental requirement for achieving high strength. Second, the increased volume of cement paste increases workability by counteracting the effect of fibers. Finally, self-compacting concretes require a large quantity of fine aggregates to maintain the cohesion of the mix and avoid segregation problems.

In general, it is recommended a minimum cement dosage of 350-400 kg/m³.

Water/cement ratio

The w/c ratio is limited by the high strength condition. High w/c ratios imply a greater volume of water that does not react with the cement, an increase in porosity and consequently a decrease in strength. Therefore, in these situations the w/c ratios will be low, of about 0.4.

On the other hand, in order to achieve self-compacting properties with such low w/c ratios, additives must necessarily be used, as will be indicated below; otherwise, the consistency obtained would be very dry.

It is worth mentioning that, given the sensitivity of these dosages to small variations in their components, special attention must be paid to the moisture content of the aggregates and this must be included in the calculation of the w/c ratio.

Aggregates

One of the most important characteristics of this type of concrete is that it has a high content of the finest aggregates (particles < 0.063 mm in size, including the cement itself). These aggregates contribute to improve workability, increase cohesion and avoid segregation, so they are ideal both when fibers are added and when a self-compacting consistency is desired. The minimum fines content will be in the range of $500\text{-}600$ kg/m³, so filler or other additions, such as silica fume, will normally be added.

As for the coarse aggregate, it will have a reduced maximum size and its content will not be high. On the one hand, the smaller its size, the easier it will be for the fibers to be distributed uniformly throughout the matrix and be perfectly enveloped by the cement paste, ensuring its adherence (Figure 2.1-2). On the other hand, high coarse aggregate contents favor segregation and inhomogeneity problems, especially if the fiber content is high [4]. Considering the above, it is recommended that the amount of coarse aggregate with respect to the total aggregates be a maximum of 50% [5,10].

Fiber content

The fiber content is usually expressed as the percentage of fiber volume with respect to the total volume of concrete, or as the weight of fibers per unit volume of concrete (in kg/m³). The minimum fiber dosage is determined by its contribution to the strength performance of the concrete, which varies greatly depending on the characteristics of the fibers and the properties of the matrix. In general, it is recommended that the content of

steel fibers when they fulfill structural functions should not be less than 0.25% (20 kg/m³) [3]. As for the maximum fiber content, it is set according to the decrease in workability of the concrete and the risk of balling or hedgehog formation. In this respect, very slender fibers (> 100) are particularly problematic. As an order of magnitude, the recommended maximum fiber content is approximately 2% (160 kg/m³).

Finally, it can be stated that the most common range of steel fiber dosages is between 0.30% (25 kg/m³) and 1.20% (95 kg/m³).

With respect to the self-compacting condition, it should be noted that, although in principle the fibers reduce the workability of the concrete, the stiffness they provide helps to some extent to maintain the cohesion of the mix. However, this benefit is significantly dependent on the characteristics and amount of fibers. In general, the best results are obtained for contents that are not very high ($\leq 1\%$).

Superplasticizer admixtures

In this type of concrete, the use of superplasticizer admixtures is particularly indicated, since they contribute directly to obtaining the 3 properties sought: high strength (maintaining a low w/c ratio), self-compactness (improving consistency) and addition of fibers (maintaining or improving workability).

The dosage will depend on the type of admixture used, but it is not usual to exceed 5% by weight of cement. In general, in experimental concretes it is usual to exceed the maximum amounts recommended by the manufacturers, which are usually conservative. In these cases, it is important to check that there is no loss of homogeneity in the mix. When the quantity of superplasticizer is excessive, the cement paste becomes fluid and drips between the fibers and the coarse aggregate, losing cohesion. Therefore, the most common pathologies are exudation of the paste and segregation of the aggregates.

2.1.4 Resistance mechanism

The main contribution of the fibers to the strength response of concrete is the support of tensile stresses, causing an increase in fracture toughness.

When a SFRC element is subjected to tensile stresses, as long as the stresses are low, they are supported jointly by the matrix and the fibers. In fact, due to strain compatibility, the fibers assume very little stress and in practice almost all the stress is resisted by the matrix. However, as the tensile stress increases, and in particular as soon as the first crack

appears, a progressive transfer of tensile stresses from the matrix to the fibers begins. Finally, in the fully cracked state, the fibers are the only mechanism that resists tensile stresses. From this, it is concluded that fibers do not cause significant increases in the first crack resistance, at least for moderate contents.

Steel fibers have two main failure mechanisms: pull-out, due to the depletion of the tangential bond stresses ($\tau > \tau_{\max}$) and breakage, due to the depletion of the normal tensile stresses ($\sigma > \sigma_{\max}$). Whether one or the other type of failure occurs basically depends on 3 factors: the ultimate pull-out bond tangential stress τ_{\max} (which in turn depends on the fiber-matrix bond), the ultimate tensile normal stress σ_{\max} and the fiber slenderness λ (l/d). If the equilibrium condition between the two modes of failure is developed, the following relationship between these factors is obtained [11]:

$$\tau_{\max} \cdot \lambda = \sigma_{\max} \quad (2.1-1)$$

The slenderness of the fibers normally used is usually low, reaching a maximum value of 100. This limitation is explained by the workability problems caused by the slender fibers. Therefore, considering equation (2.1-1), this implies that fiber depletion in the SFRC is mostly due to pull-out. This failure mode has an important advantage: it is more progressive, more ductile, than that which would occur if the fibers failed due to excessive normal stresses.

The pull-out strength of steel fibers depends significantly on the geometry of the fibers. A distinction will be made between the two most common types: straight and hooked-end shaped. In addition, their response also depends on the inclination of the fibers with respect to the crack plane, since, being randomly distributed, they are not expected to be perfectly orthogonal to the crack plane.

In straight fibers, the mechanisms that are mobilized when the fibers are subjected to traction are: adhesion, friction and mechanical anchorage due to inclination [12] (Figure 2.1-5). Adhesion is the force that holds the fiber to the matrix and depends largely on the microstructure of the fiber-matrix interface. Friction is the force that is mobilized when the fiber starts to detach from the matrix. Finally, when the fiber has a certain inclination, the force acting in the direction of its axis is only a part of the total pull-out force, so that a mechanical anchoring effect is necessarily generated.

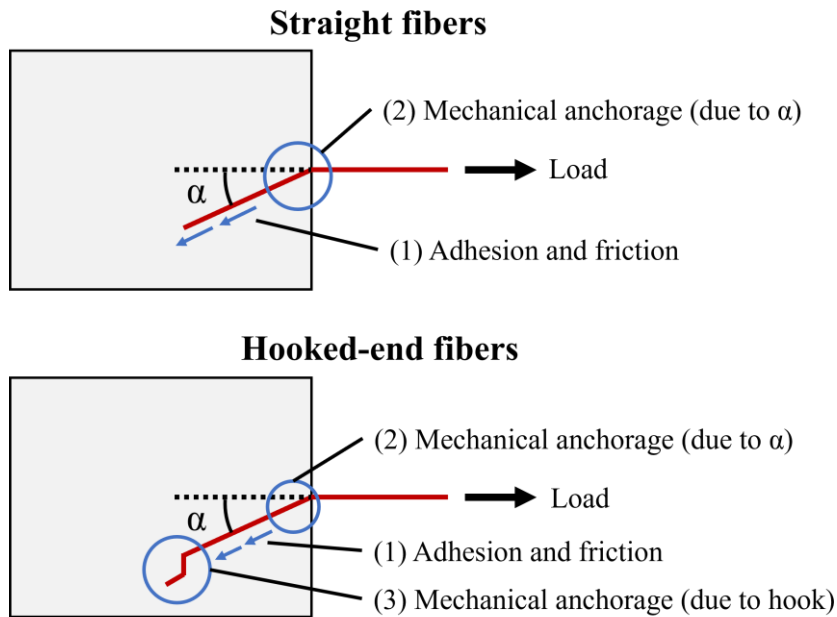


Figure 2.1-5. Comparison of straight fiber and hooked end strength mechanisms.

The mechanical anchorage contributes significantly to the pull-out resistance, which means that the inclination with respect to the crack plane has a significant influence on the pull-out resistance. When the fibers are perfectly orthogonal (0°), the mechanical anchorage is not mobilized and only adhesion and friction act. As the inclination increases, the effect of the mechanical anchorage increases and thus also the pull-out resistance (Figure 2.1-6). Finally, an optimum value of inclination is reached for which the maximum resistance is obtained, after which it decreases. The optimum inclination angle depends on both the geometric properties of the fibers and the matrix; according to the literature consulted, it can be estimated that common values range between 30° and 60° [13,14]. When the inclination is very high, failure occurs by detachment of the matrix coating, resulting in low strength values.

In hooked-end fibers, the mechanisms involved when the fibers are subjected to tensile stress are the same as for straight fibers (adhesion, friction and mechanical anchoring by inclination) and, in addition, mechanical anchoring by the hooked end (Figure 2.1-5). Both mechanical anchors contribute substantially to the pull-out resistance. However, the largest contribution is that of the anchorage due to the hooked-end, so it is observed that the fiber inclination has less influence on the pull-out resistance of hooked-end fibers than of straight fibers. In fact, for not very high inclinations (0° - 30°), and depending on the characteristics of the fibers and the matrix, the pull-out resistance can be kept constant [13,15]. In this sense, it is worth mentioning that, although the inclination does not always

produce an increase in resistance, it does increase the energy absorbed by the fibers. The latter is observed for both types of fibers (Figure 2.1-6).

Comparing the two types of fibers, it is concluded that hooked-end fibers are much more efficient, since the additional strength mechanism generated by the hook leads to an increase in both pull-out strength and fracture toughness.

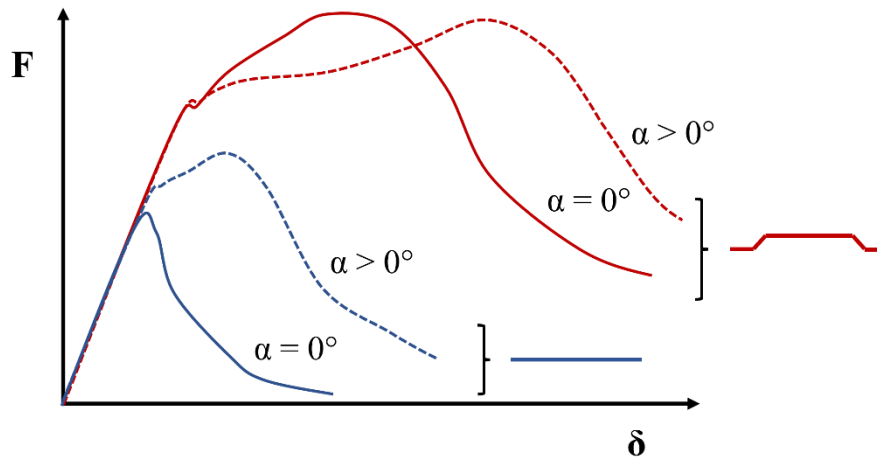


Figure 2.1-6. Indicative force vs displacement diagrams in pull-out test of straight and hooked-end fibers without or with inclination.

2.1.5 Mechanical properties

Plain concrete is characterized by high compressive strength, very low tensile strength and brittle behavior at breakage. The addition of steel fibers radically modifies its mechanical behavior, affecting both these and other properties. The main mechanical properties of SFRC are described below.

Compressive strength

It is generally accepted that the presence of fibers does not significantly improve compressive strength, at least for the usual contents ($< 2\%$). However, they do affect the stress-strain diagram (σ - ϵ). In particular, the strain under maximum load is higher in SFRC than in plain concrete, due to the ductility provided by the fibers. Moreover, during the unloading branch, while in plain concrete there is a steep drop, in SFRC the slope is much smoother; i.e., the fibers contribute a large increase in toughness and residual compressive strength.

The greater or lesser toughness depends on multiple factors, among which the fiber content, slenderness, fiber-matrix adhesion or fiber orientation with respect to the direction of load application, among others, stand out.

Modulus of elasticity

It is observed that the usual fiber contents do not produce relevant improvements in the value of the modulus of elasticity, so it can be assumed that it remains constant.

Tensile strength

In general, the addition of fibers does not contribute to increase the ultimate direct or uniaxial tensile strength, at least for moderate contents ($\leq 1\%$). However, it is found that high dosages of very slender fibers can cause significant increases in tensile strength.

The σ - ε diagram under uniaxial tension varies significantly as a function of fiber content, slenderness and shape, among other aspects. When the content and/or slenderness are low (low-performance SFRC), the diagram is very similar to that of plain concrete, with a sharp drop in stress after reaching the maximum value. The difference is that, after that drop, the fibers are able to support a certain level of load, providing ductility to the material; this is known as strain-softening. As the performance of the SFRC improves (more slender fibers and/or in greater quantity), the stress drop after cracking of the concrete is reduced until it reaches a point where it disappears and the material deforms plastically (plastic deformation). Finally, for very high contents and/or very slender fibers, strain-hardening occurs, i.e., after reaching the cracking stress, the fibers can support more load.

Finally, it follows from the above that in all cases the addition of fibers causes an increase in fracture toughness, which is all the greater the slimmer the fibers and the higher their content.

Flexural strength

The addition of fibers greatly affects the flexural behavior of concrete. In relation to plain concrete, the flexural strength can be maintained or increased, which depends on the performance of the SFRC, i.e. on a set of factors such as the number of fibers, their slenderness, their geometrical shape or the fiber-matrix bond. In this regard, it is worth mentioning that the presence of fibers has a much greater influence on the flexural response of concrete than on the uniaxial tensile or compressive response [16]. It is

observed that the flexural strength can be increased even for relatively low contents, whereas in the case of tensile strength a larger volume is required.

The flexural strength of SFRC can be evaluated in different ways, although in practice all normative tests are summarized in prismatic specimens, with or without notch, subjected to bending at 3 or 4 points. In the first case, the load is applied in the center of the span, and in the second, in the central thirds. The type of bending test taken as reference in this document is the one described in the UNE-EN 14651 standard [7] (Figure 2.1-7), equivalent to the RILEM TC 162-TDF [17].

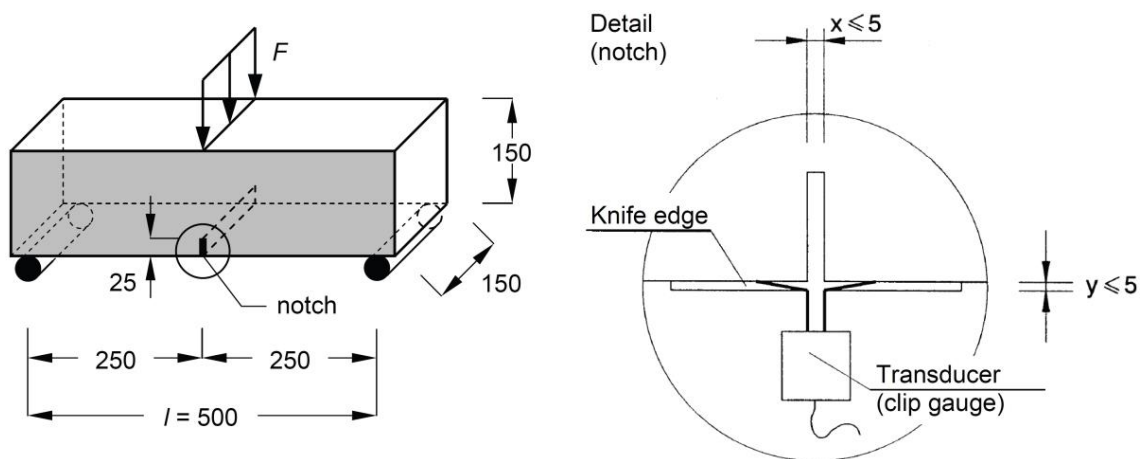


Figure 2.1-7. Three-point bending test setup according to [7].

The flexural behavior of SFRC can be analyzed through the load-CMOD (crack mouth opening displacement) diagram obtained from the above mentioned tests. Figure 2.1-8 shows this diagram for plain concrete and different types of SFRC.

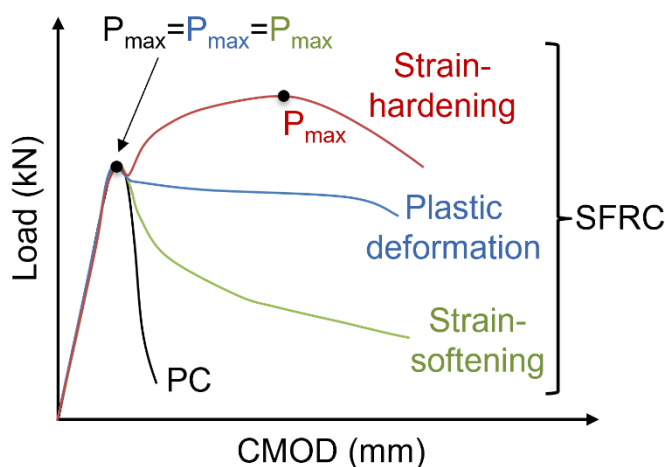


Figure 2.1-8. Load vs CMOD diagram in static flexural test with the behaviors that plain concrete (PC) and fiber reinforced concrete (SFRC) can show.

The first linear-elastic section is identical in all cases, since it is governed by the matrix, which bears practically all the stresses. The resistance mechanism of the fibers does not begin to mobilize until cracks appear. This means that the first crack resistance (P_f) depends almost exclusively on the matrix, so that the usual fiber contents hardly improve it. Once the concrete starts to crack, instead of a sudden drop in load and specimen failure, as would occur in plain concrete, 3 situations can occur:

- a) Strain-softening: The fibers do not resist more load, so the load decreases with crack opening. However, they provide a large increase in toughness compared to plain concrete. Consequently, the maximum flexural strength coincides with the first crack strength ($P_{\max} = P_f$).
- b) Plastic deformation: The fibers maintain the load up to high CMOD levels (> 0.1 - 0.2 mm), after which it decreases. In this case, again it is fulfilled that the maximum flexural strength coincides with that of first crack ($P_{\max} \approx P_f$), or at most increases slightly. However, the difference in relation to the strain-softening situation is that the fibers absorb more energy and therefore the fracture toughness is higher.
- c) Strain-hardening: The strength mechanism of the fibers is able to take more load than that of the matrix, causing an increase in flexural strength. The fibers provide ductility to the concrete, so the maximum load occurs for high CMOD values. Therefore, it is satisfied that $P_{\max} > P_f$. This is the only situation in which there are really significant increases in flexural strength with respect to plain concrete, which can be more than 100%.

Fatigue

The response of SFRC to dynamic fatigue loading will be discussed in subsection 2.2, with emphasis on bending fatigue.

Other mechanical properties

Steel fibers help to control cracking by distributing it and reducing crack width. This means that they can improve the durability of concrete (reduction of reinforcement corrosion, increased resistance to chloride attack, etc.). In addition, fibers improve other properties of concrete, such as impact resistance, abrasion resistance or control of cracking due to thermal actions. In other situations, steel fibers are not as suitable, as in the case of fire resistance, where polypropylene fibers are more effective.

2.1.6 Applications

SFRC began to be used in the building and civil engineering sectors in the 1970s. Its traditional applications, which are still in use today, are pavements, subway lining and water retaining structures.

In pavements, steel fiber concrete is used to control and reduce cracking, which allows for increased joint spacing. In addition, due to improved flexural behavior, thicknesses can be reduced. SFRC is also commonly used in the construction of high-performance pavements, such as those in airports and military areas, which require high resistance to impact and abrasion. Finally, another common use is the repair of existing pavements by means of overlays.

In subway works, such as tunnels or mines, SFRC is used to execute the resurfacing, either in the form of shotcrete or to manufacture precast segments. The fibers provide very interesting properties, such as increased stiffness and reduced cracking, preventing possible leaks.



Figure 2.1-9. Execution of lining, in this case of a slope, with projected fiber concrete.

In hydraulic works, the most interesting property of SFRC is the control of cracking, which leads to a reduction in leakage and an increase in durability. Consequently, it is used in the construction of water containment structures, such as canals and reservoirs. In addition, it is also used in dam spillways, as it offers good resistance to cavitation and erosion. Finally, another application in dams is the construction or repair of stilling basins, due to its high resistance to impact.

Although fiber-reinforced concrete is a material that has been known for more than 50 years, so far its most common applications do not have a great structural responsibility, or even it is usual that they are not taken into account for the strength calculation. The explanation is due, on the one hand, to the lack of systematic design procedures such as those that exist for reinforced and prestressed concrete and, on the other hand, to the inertia to change that the construction industry has always had.

However, it is to be expected that, with the advances in the research of this material and the increase in published experiences, the applications with a structural role of fibers will become more widespread. Some recent examples are the construction of slabs in which the traditional reinforcement is completely replaced or the construction of wind turbine foundations.

2.2 Fatigue in concrete

This section describes fatigue in concrete; specifically, bending fatigue in steel fiber-reinforced concrete, since this is the field of research in which this doctoral thesis is framed. First, the phenomenon is described, highlighting its current interest. Secondly, some general concepts related to fatigue are introduced. Thirdly, the factors influencing fatigue are indicated, distinguishing between those related to loads and those due to the presence of fibers. Finally, the fatigue damage process is described, including its main indicators.

Most of the fatigue research in concrete is focused on uniaxial compressive fatigue, so very relevant references addressing the state of the art of this field can be found in the literature [18–20]. In contrast, flexural fatigue has been studied much less, although it is true that there is a growing interest, especially in the case of SFRC. Therefore, despite the fact that flexural fatigue will be addressed, in some aspects it will be unavoidable to refer to compressive fatigue.

2.2.1 Introduction

Fatigue is defined as a process of mechanical degradation of a material leading to its failure, produced when it is subjected to a cyclic action whose maximum value is lower than the static strength. This phenomenon can occur in any building material (steel, aluminum, concrete, etc.) and under repetitive stresses of any nature (compressive fatigue, bending fatigue, torsional fatigue, etc.).

The study of fatigue of materials began in the mid-19th century, motivated by a series of structural failures that apparently could not be explained by classical mechanics. The best known is the Versailles railway accident of 1842, due to the sudden breakage of one of the axles of a locomotive. The Scottish engineer W. Rankine discovered that the failure had not been caused by excessive overloading, but by the birth of a crack at a point of stress concentration, which had been growing due to the repeated action of the loads. During the following decades, the first research on fatigue was carried out, focused exclusively on metals. Of particular note was the work of Wöhler, who laid the foundations of the theory of fatigue in metals, demonstrating that fatigue depended on the range of stresses and not on the maximum stress, and proposing the use of stress-number of cycles (S-N) curves to evaluate the fatigue response of the elements.

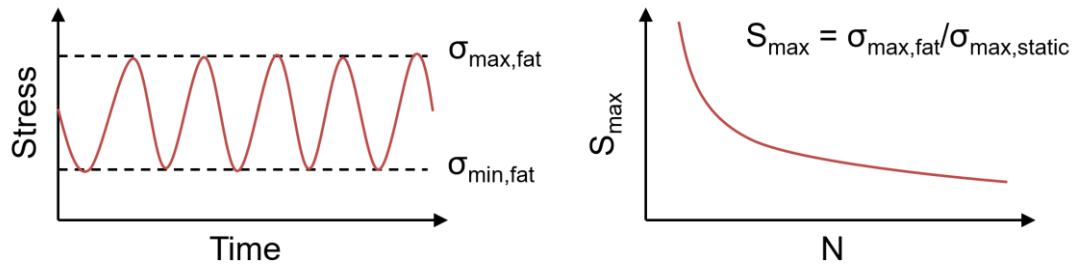


Figure 2.2-1. Stress range in a fatigue test and S-N curve for characterizing the fatigue response of a material.

The first investigations of fatigue in concrete date back to the end of the 19th century, although it is true that the most significant advances did not occur until the 1970s. Aas-Jakobsen and Lenschow [21] adapted Wöhler's S-N curves for metals to concrete, determining that fatigue life depends not only on the stress range ($\Delta\sigma$), but also on the stress level (S_{\max}). From that time on, the most relevant research works on fatigue in concrete began to be developed, which will be cited throughout this section.

Concrete fatigue is very different from that of metals. A first difference is that in steel, tensile fatigue is usually studied, since it is normally the limiting stress, critical in some aspects such as welds. In concrete, on the other hand, compressive fatigue is more interesting.

The mechanisms of tensile failure in metals, on the one hand, and compression failure in concrete, on the other, are radically different. On the one hand, steel is a homogeneous, isotropic material with linear-elastic behavior. Cyclic loads cause a crack to develop from imperfections in the material at the crystalline level. When the crack reaches a critical length, failure occurs. In the scientific literature there are a good number of crack growth equations that allow estimating the fatigue life of metals, such as the Paris Law [22], one of the first and most widely accepted. All of them propose that the fatigue response depends fundamentally on the stress range ($\Delta\sigma$).

On the other hand, concrete is a heterogeneous, anisotropic material with nonlinear behavior. It therefore requires a fracture mechanics model different from that of metals. When a crack appears in a concrete or steel element, a zone of non-negligible size with non-linear behavior develops at its face. In the case of metals, most of this zone is totally plasticized due to nonlinear hardening mechanisms, containing only a small area of fracture generation. In contrast, in concrete this fracture process zone (FPZ) is much larger and is surrounded by a small ductile zone or zone of nonlinear behavior, as shown in

Figure 2.2-2 [23]. Consequently, concrete is considered a quasi-brittle material. With respect to fatigue behavior, this implies that the response of concrete depends on both the stress range ($\Delta\sigma$) and the stress level (S_{\max}), which is a fundamental difference with respect to metal fatigue.

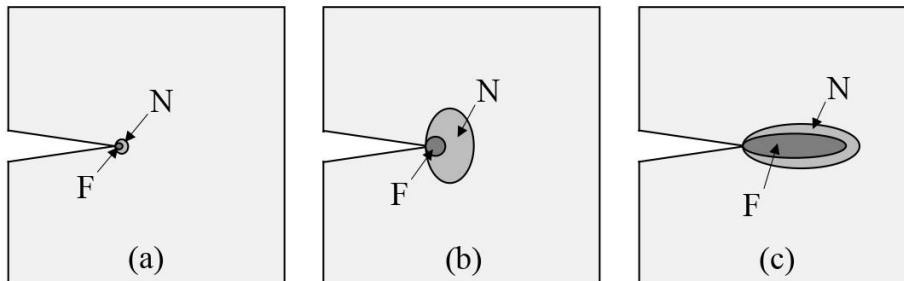


Figure 2.2-2. FPZ in materials with brittle (a), ductile (b) and quasi-brittle (c) behavior (adapted from [24]). F indicates the fracture zone and N the zone of nonlinear or ductile behavior.

The study of fatigue in concrete is of great interest for several reasons. Firstly, practically all concrete structures are subjected to cyclic loading, to a greater or lesser extent. Depending on the number of load cycles that occur during the lifetime of the structures, a distinction is made between low, high and very high cycle fatigue (Figure 2.2-3).

Low-cycle fatigue			High-cycle fatigue				Very high-cycle fatigue		
1	10^1	10^2	10^3	10^4	10^5	10^6	10^7	10^8	10^9
Structures subject to earthquakes			Airport pavements and bridges		Highway and railroad bridges and highway pavements		Structures belonging to the subway or metropolitan railroad		Marine structures

Figure 2.2-3. Fatigue classes as a function of the number of cycles [25].

Thus, there are structures that undergo few load cycles, but with very high stress levels (such as a building during an earthquake), while others withstand a large number of cycles of small amplitude and low stress levels (for example, a dam or an offshore wind turbine subjected to waves). In addition, there are intermediate situations, such as a railway viaduct subjected to the passage of trains.

Secondly, fatigue, as an Ultimate Limit State, is gaining increasing prominence and in fact in some situations is a conditioning factor for structural design. The main reason is the development of high performance concretes, which leads to new structures requiring less concrete volume and therefore being slenderer. As a result, variable loads (use

overload, wind, waves, etc.), which are capable of producing fatigue due to their cyclic nature, are increasingly accounting for a higher percentage of the total loads, to the detriment of permanent loads (self-weight, dead loads, etc.). Some examples of concrete structures in which the fatigue ULS is of great importance are wind turbine towers or high-speed railroad viaducts.

Moreover, the way in which the fatigue phenomenon is approached in current standards is too simplistic and conservative, and a large part of the mechanical capacity of concrete is wasted. Therefore, advances in concrete fatigue are very important in order to develop more efficient standards that take into account the complexity of this mechanism.

Finally, with respect to the particular case of flexural fatigue, it is a phenomenon that is as or more interesting than compressive fatigue, since, although concrete is mainly intended to withstand compression, it is not very common for failure to occur for this reason. The field where flexural fatigue is of greatest interest is fiber-reinforced concrete (specifically, SFRC), due to the residual strength they provide to resist tensile stresses. In plain concrete, on the other hand, it is not so relevant, and is reduced almost exclusively to its application in pavements.

2.2.2 General concepts of fatigue

The most important general concepts related to concrete fatigue are described below.

Fatigue life, stress levels and S-N curves

The most common parameter to represent the fatigue behavior of a concrete element is the fatigue life, i.e. the number of load cycles (N) it is able to withstand until failure. However, the fatigue life depends on the stress levels between which the cycles oscillate, referred to as S_{\max} and S_{\min} . These are defined as the quotient between the maximum or minimum stress of the cycles and the static reference parameter. In the case of compressive fatigue, this parameter is the compressive strength (f_c), whereby:

$$S_{c,\max} = \frac{\sigma_{c,\max}}{f_c} \quad (2.2-1)$$

$$S_{c,\min} = \frac{\sigma_{c,\min}}{f_c} \quad (2.2-2)$$

In the case of flexural fatigue in SFRC, the definition of stress levels is somewhat more complex. First, they are usually defined in terms of load, or equivalent stress at the

most tensioned point, being the ratio between these parameters (for the case of 3-point bending):

$$\sigma_{eq,fl} = \frac{3 \cdot P_{fl} \cdot l}{2 \cdot b \cdot (h_{sp})^2} \quad (2.2-3)$$

Where $\sigma_{eq,fl}$ is the equivalent stress, P_{fl} is the load applied at the center of the span, l is the length of the specimen, b is its width and h_{sp} is its depth at the center of the span, minus the notch depth.

Secondly, there are several possibilities for the static reference parameter. The most common ones are the maximum stress over the whole test ($\sigma_{eq,max}$) and the stress corresponding to the limit of proportionality ($\sigma_{eq,L}$) [7]. In the case where $\sigma_{eq,max}$ is considered, as in this work, the stress levels of the flexural fatigue tests are defined as:

$$S_{fl,max} = \frac{\sigma_{eq,max,fat}}{\sigma_{eq,max}} \quad (2.2-4)$$

$$S_{fl,min} = \frac{\sigma_{eq,min,fat}}{\sigma_{eq,max}} \quad (2.2-5)$$

Where $\sigma_{eq,max}$ and $\sigma_{eq,min}$ are the maximum and minimum cycle loads, respectively.

Regardless of the type of fatigue (compression or bending), it is found that, given a S_{min} , the higher the S_{max} , the lower the fatigue life. Furthermore, given an S_{max} , the lower the S_{min} , the lower the fatigue life. Therefore, the fatigue life decreases with the increase of the cycle stress level and with the increase of the difference between S_{max} and S_{min} .

It follows from the above that to fully characterize the fatigue behavior of a concrete it is necessary to perform a good number of tests systematically varying the stress levels. The way to represent the results are the so-called S-N curves, which relate the maximum stress level S_{max} to the number of cycles N . Moreover, since there are different minimum stress levels S_{min} , in fact a family of curves is obtained, and not a single one.

There are different expressions for S-N curves for fatigue in concrete, although most of the research is focused on compressive fatigue. The main S-N curves related to flexural fatigue are summarized below.

The equation proposed by Aas-Jackobsen [26], developed from Whöler curves for metals, was the first to take into account the minimum stress level (S_{min}) in the form of the stress ratio ($R = S_{min} / S_{max}$).

$$S_{\max} = 1 - \beta \cdot (1 - R) \cdot \log(N) \quad (2.2-6)$$

Where β is an experimental adjustment parameter. Aas-Jackobsen [26] and Tepfers [27] recommended values for β in compressive fatigue in plain concrete of 0.064 and 0.0685, respectively. In flexural fatigue in plain concrete, Oh [28] proposed a value of 0.0690.

Naaman and Hammoud [29] performed an experimental flexural fatigue campaign on SFRC with hooked-end fibers. They applied 3 maximum load levels (70%, 80% and 90% of the ultimate load in static bending), keeping the minimum load level at 10%. Therefore, they proposed an expression for the S-N curve in which only S_{\max} is taken into account.

$$S_{\max} = 0.9302 - 0.0368 \cdot \log(N) \quad (2.2-7)$$

Singh and Kaushik [30] carried out a large number of 4-point flexural fatigue tests on SFRC specimens containing 1.5% corrugated fibers. As a result, they developed an equation incorporating the effects of the maximum load level S_{\max} , the ratio between the maximum and minimum loads R and the survival probability L_R .

$$S_{\max} = C_1 \cdot (N)^{-C_2 \cdot (1-R)} \quad (2.2-8)$$

Where C_1 and C_2 are experimental coefficients that also depend on the chosen survival probability. Since fatigue results have a large scatter, this probabilistic approach is very interesting, giving rise to S-N-P curves; i.e., stress-number of cycles-failure probability (Figure 2.2-4).

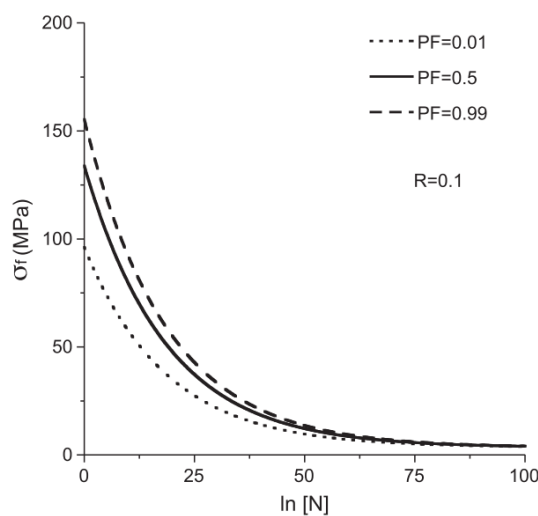


Figure 2.2-4. Example of S-N-P curve [31].

More recently, Banjara and Ramanjaneyulu [32] presented an S-N curve expression for flexural fatigue in SFRC considering the average effect of various fiber contents. Since S_{min} was kept constant with a value of 20% of the ultimate load in static bending, this equation does not take into account its effect.

$$S_{max} = 1.1633 - 0.0783 \cdot \log(N) \tag{2.2-9}$$

It is worth mentioning that there are other classical S-N curve formulations, but they have not been included because they are focused on pure compressive or tensile fatigue; among them, those of Hsu [32], that of Eurocode 2 [1], or that of Petkovic, on which the 2010 Model Code [33] is based, stand out.

A comparative plot of the S-N curves for flexural fatigue described is included below. In those cases where the formulation contemplates it, the average parameters corresponding to this research work have been included.

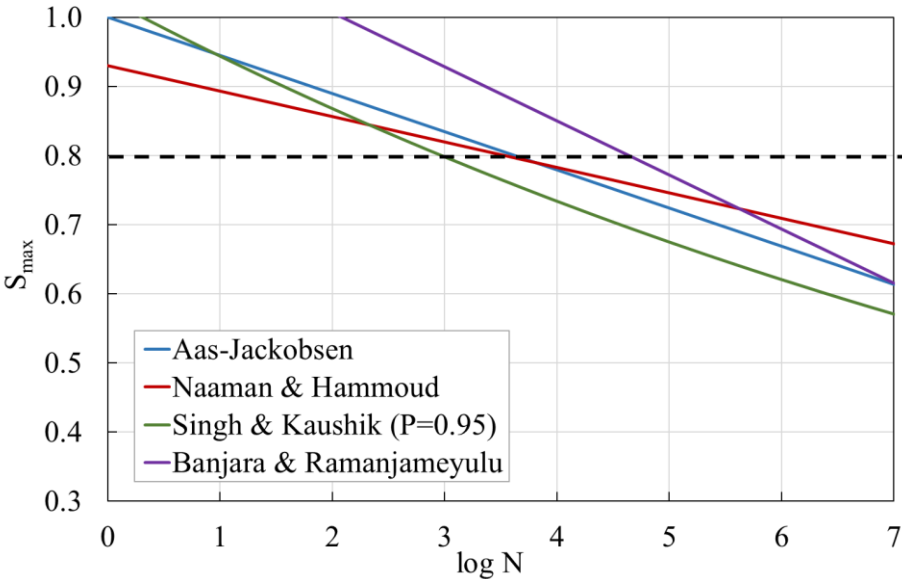


Figure 2.2-5. Comparison of S-N curves for flexural fatigue, according to several authors.

It is observed that, for the maximum stress level S_{max} of 0.80 considered in this work, the most conservative S-N curve is that of Singh and Kaushik, with an estimated fatigue life of 1,000 cycles. The Aas-Jackobsen and Naaman & Hammoud expressions give practically identical results of about 3,500 cycles. Finally, the Banjara & Ramanjameyulu equation is the one that estimates a higher fatigue life of about 40,000 cycles.

In addition, new regression models have been developed in recent years to describe both fatigue life and cumulative damage evolution, mostly based on probabilistic or

Bayesian approaches. Some of these works propose new mathematical methods for fatigue analysis [31,34,35].

Endurance limit

In flexural fatigue, the endurance limit or fatigue limit is the maximum load level at which crack growth does not occur and thus the concrete has an infinite life under cyclic loading. However, at present it is not clear whether the endurance limit really exists, since it has been found that even very low load levels are capable of producing damage in concrete. Furthermore, research in this field has the major drawback that fatigue tests can be very time-consuming.

Consequently, for practical purposes, the endurance limit is defined as the maximum load level for which, after a certain number of cycles, the accumulated fatigue damage is not sufficient to cause material failure. This implies that it is necessary to specify a minimum number of cycles for which it is assumed that the fatigue life of the material is infinite; that is, that even if it continues to be subjected to cycles of the same load level, the element will not collapse. In the usual situations in concrete, it is accepted that, if the element is able to withstand $2 \cdot 10^6$ without failure, its fatigue life can be considered infinite for those load levels [29,36].

In the case of flexural fatigue in SFRC, some authors have set the endurance limit at around 65% of the ultimate load in the static flexural tensile test [29,37], although its value is sensitive to the characteristics of the concrete matrix and fibers. In addition, there are some experimental methods that allow estimating the endurance limit, being very useful for the design of fatigue test campaigns; the most widely used are the Locati and Staircase methods [19].

Cumulative damage. Palmgren-Miner rule

Throughout their service life, concrete structures are subjected to cyclic loads of varying magnitude and for varying periods of time. For example, a wind turbine under wind action. However, to date, most of the fatigue research has been carried out under loading cycles with constant stress levels, and very few have studied the effects of random loading cycles.

When it is intended to estimate the fatigue life of a concrete element that has a certain loading history (i.e., it has withstood a certain number of cyclic load series with different

maximum and minimum stress levels), it is usual to resort to the Palmgren-Miner rule or linear damage accumulation hypothesis [38].

This hypothesis is based on the concept of cumulative damage. Each series of cyclic loads causes a certain percentage of damage, calculated as the quotient between the number of cycles applied and the maximum number of cycles to collapse for that type of cycles, which is determined from the S-N curves. The total accumulated damage is the sum of the damage caused by each series of cyclic loads, and when this reaches 100%, fatigue failure occurs (Eq. (2.2-10)):

$$D = \sum_{i=1}^n D_i = \sum_{i=1}^n \frac{n_i}{N_i} \quad (2.2-10)$$

Where D is the global cumulative damage (fatigue collapse occurs when it reaches 1 or 100%), n_i is the number of cycles applied at certain stress levels and N_i is the number of cycles that cause failure at those stress levels.

Traditionally, the Palmgren-Miner rule has been widely used because of its simplicity; in fact, it appears in structural codes such as the 2010 Model Code [33]. However, there are numerous publications showing that this hypothesis does not fit too well to the fatigue response of concrete elements subjected to different series of cyclic loads [39,40]. This can be explained for several reasons. On the one hand, the damage superposition principle is assumed (i.e., the damage caused by a given series of cyclic loads is independent of the previous loading history), which is not fulfilled in concrete due to its nonlinear behavior in fatigue. On the other hand, very relevant aspects are not taken into account, such as the negative effect of isolated load peaks, the positive effect of maintained loads (as long as they do not exceed a certain value) or the positive effect of fatigue maturation [41,42], which will be discussed later.

Fatigue dispersion. Weibull distribution

A singular characteristic of fatigue tests on concrete is that, even when performed on apparently identical specimens (same dosage and even batch) and under the same load levels, they show a very high dispersion of results, which in some cases can reach 2 or more orders of magnitude. This is verified in both compressive and flexural fatigue, and in both plain concrete and fiber-reinforced concrete. Therefore, when designing an experimental fatigue campaign, it is essential to perform a sufficient number of identical tests, obtaining the statistical distribution of the results and their representative values. In this

sense, it is very interesting the work of Ortega et al. [43], which performs a statistical study on a large specimen of experimental data of fatigue by compression, determining the number of tests to be performed to obtain a certain error in the fatigue life, also considering the probability of failure. In practice, due to time and cost constraints, in most experimental concrete fatigue campaigns between 10 and 15 tests per series are performed.

Different mathematical probability models exist to describe fatigue outcomes statistically. The log-normal distribution function was widely used, although it was finally discarded because its hazard function decreases with increasing fatigue life, which is not consistent with the progressive deterioration observed in concrete subjected to cyclic loading [44]. Currently, the two-parameter Weibull distribution function is the most commonly used to statistically describe fatigue data, due to its physically valid assumptions, robust experimental verification, relative ease of use, and better developed statistics, among other aspects [45]. Moreover, numerous papers reveal that this function fits reasonably well to both compressive and flexural fatigue data, and in both plain concrete and SFRC [37,46].

The Weibull cumulative distribution function can be expressed as:

$$F(x)=1-\exp\{-(x/\lambda)^\beta\} \quad (2.2-11)$$

Where x is the specific value of the random variable $\log(N)$ (number of cycles to failure), β is the Weibull shape parameter and λ is the scale parameter. The shape parameter β is related to the dispersion, so that the higher its value, the lower the variability of the results. On the other hand, the scale parameter λ is related to the characteristic fatigue life, so that, the larger it is, the greater the fatigue life.

Finally, there are other probabilistic models that have proven to have a very good fit to fatigue data, as is the case of the three-parameter Weibull distribution proposed by Saucedo et al. [31] in compressive fatigue, and successfully applied later by Ríos et al. [47] in flexural fatigue.

2.2.3 Factors affecting fatigue

The fatigue response of concrete is conditioned by a series of factors, which can be divided into those related to the load and those due to the presence of fibers, in the particular case of fiber-reinforced concrete.

2.2.3.1 Related to loading

The load-related variables that most affect the fatigue behavior of concrete are load levels and frequency.

Load levels and range

The maximum and minimum load levels S_{\max} and S_{\min} are the parameters that most influence the fatigue life of concrete elements. In fact, as already discussed in detail in the previous subsection, the fatigue response of concrete is characterized by the S-N curves, which precisely relate the load levels to the number of cycles to failure. It is found that the fatigue life decreases with increasing maximum load level S_{\max} . Equivalently, the lower the load ratio $R = S_{\min}/S_{\max}$, the lower the fatigue life (Figure 2.2-6). In consequence, the choice of loading levels is a fundamental aspect in the design of any experimental fatigue campaign.

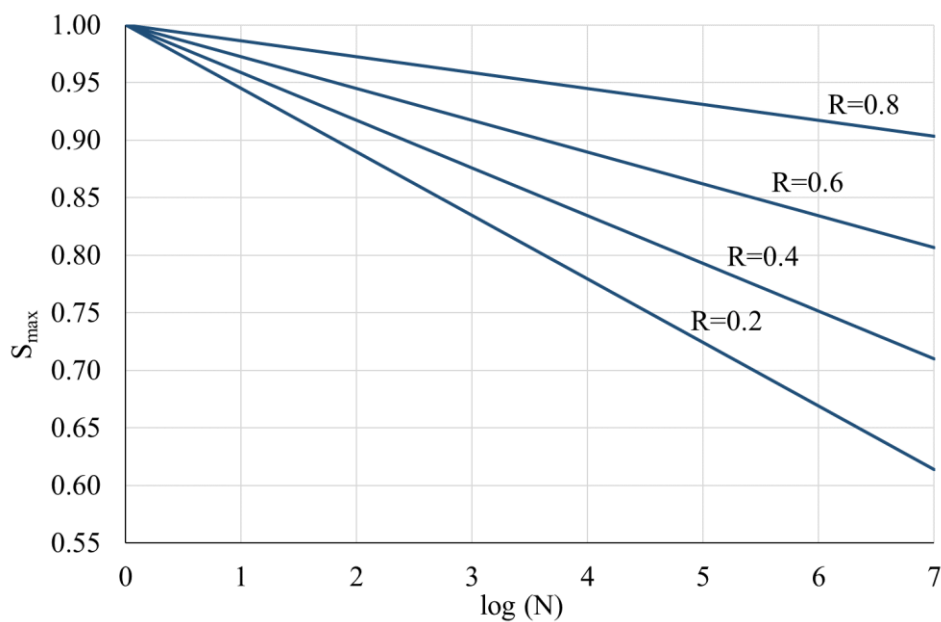


Figure 2.2-6. Aas-Jackobsen S-N curves [21] for flexural fatigue, considering different loading ratios.

Frequency

The frequency of load cycles influences the fatigue life of concrete. A large number of investigations have been carried out in this respect, although most of them are focused on compressive fatigue in plain concrete. Some authors suggest that, when S_{\max} is less than 75% of f_c , frequencies between 1 and 15 Hz have little influence on fatigue life [48,49].

The first concrete fatigue model in which the loading frequency was analytically considered was the one developed by Hsu [25], who proposed two S-N curves considering low and high number of cycles fatigue, respectively. Other later models that took this factor into account were those of Furtak [50] and Zhang [51]. More recently, Saucedo et al. [31] developed a probabilistic fatigue model, applicable to both plain concrete and fiber-reinforced concrete. It is worth mentioning that in all the above models it is established that, as the frequency decreases, so does the fatigue life (Figure 2.2-7). Medeiros et al. [52] found that the fatigue life of plain concrete could be up to an order of magnitude lower at low frequencies (1/16 Hz) than at high frequencies (4 Hz).

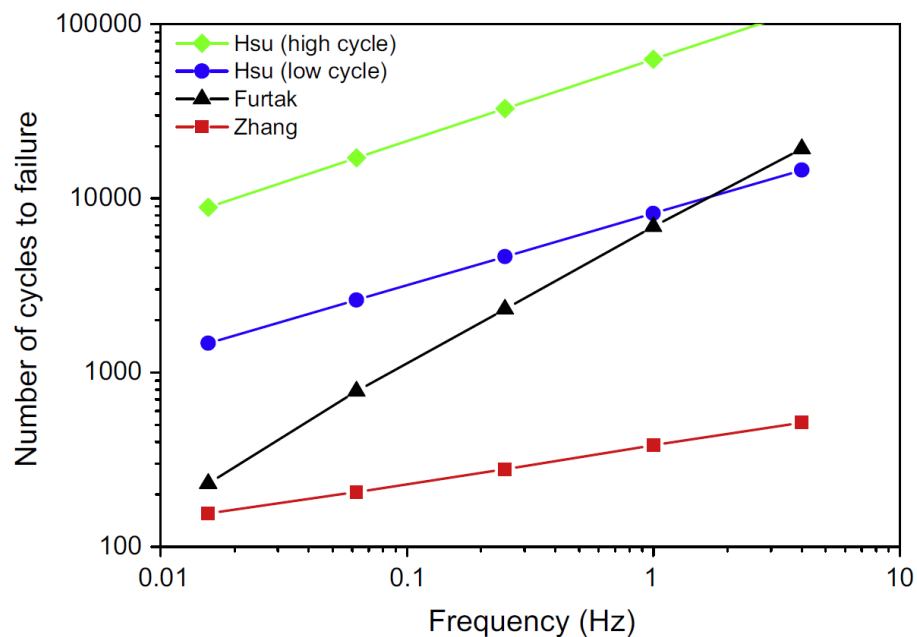


Figure 2.2-7. Number of cycles to failure vs loading frequency, according to different fatigue models [52].

Regarding SFRC, the work of Medeiros et al. is also very interesting, since it is observed that the presence of steel fibers practically eliminates the influence of frequency on fatigue life, at least for the range studied (1/16 to 4 Hz).

2.2.3.2 Presence of fibers

The addition of fibers modifies the mechanical characteristics of concrete, and therefore its fatigue response. In this sense, Johnston et al. [53] concluded that the most determinant factor in the fatigue life of SFRC is the fiber content, while other factors, such as slenderness or shape, are secondary.

Germano et al. [54] carried out an experimental study of flexural fatigue in SFRC, considering different load levels (15-65%, 25-75% and 35-85%) and fiber contents (0%, 0.5% and 1.0%). The results were very interesting (Figure 2.2-8). On the one hand, it is observed that the presence of fibers improves fatigue life for high load levels (low-cycle fatigue). However, this effect fades with decreasing load, to the point that fibers worsen the fatigue life for load levels of 15-65%. On the other hand, the fatigue strength is higher in specimens with the fiber content of 0.5% than 1.0%, and furthermore this is true for all load levels. This suggests that there is an optimum fiber content in terms of fatigue response.

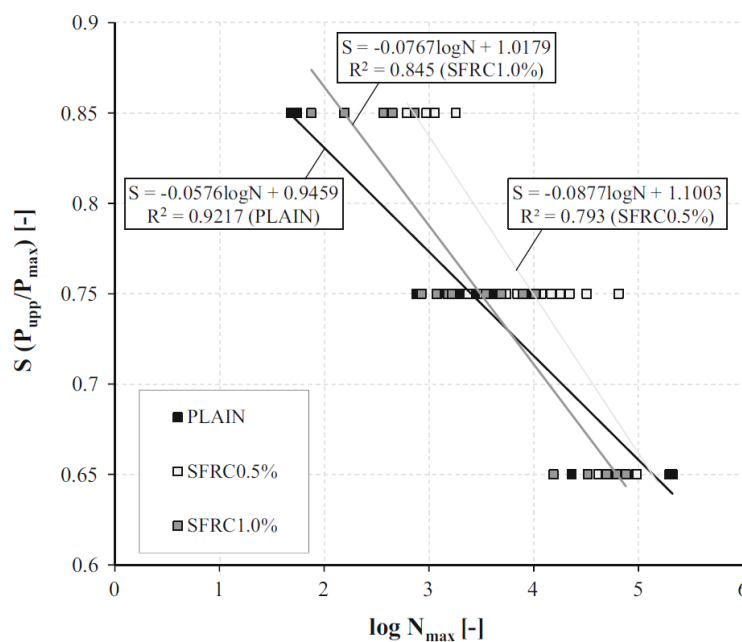


Figure 2.2-8. S-N curves for plain concrete and SFRC with 0.5% and 1.0% fibers [54].

Other works have been published that conclude that fibers improve the fatigue life of concrete, but only up to a certain volume [46,55,56]. Vicente et al. [55] performed flexural fatigue tests on pre-cracked specimens with 1% and 2% fiber contents. He observed that, while the residual flexural strength increased with fiber dosage, the fatigue life remained practically constant. Poveda et al. [46] studied the effect of different fiber contents (0, 0.2, 0.4, 0.6 and 0.8%) on the compressive fatigue response of self-compacting concrete. They concluded that low amounts do not produce significant improvements; however, intermediate dosages are able to increase the fatigue life by up to five times compared to that of plain concrete. They found that the optimum fiber content is 0.6%, and that above 0.8% there is a significant deterioration in fatigue behavior. This is attributed

to the fact that high fiber contents distort the matrix, producing pores and imperfections that favor the development of cracks.

In conclusion, it can be stated that the addition of fibers improves the fatigue response of concrete, both in flexure and compression, but only under certain conditions of load levels and fiber contents. Further research is required in this field, so it is advisable to make a detailed study of each particular case.

Additionally, a nuance should be made in relation to flexural fatigue studies in SFRC. Sometimes, the static parameter taken as a reference to establish the load levels is not the absolute maximum load of the flexural tensile test (P_{max}), but the load corresponding to the limit of proportionality (P_L) or similar (Figure 2.2-9) [37,57]. This is not a problem when the SFRC behavior is strain-softening, since in that case $P_{max} \approx P_L$. However, when strain-hardening occurs ($P_{max} > P_L$), this leads to overestimation of the fatigue life of the SFRC, since a critical failure parameter is not taken as a reference. Consequently, to state in these cases that fibers improve fatigue life is not scientifically rigorous, since this fact is explained by an improvement in static flexural strength that is not taken into account when defining fatigue loads (Figure 2.2-9).

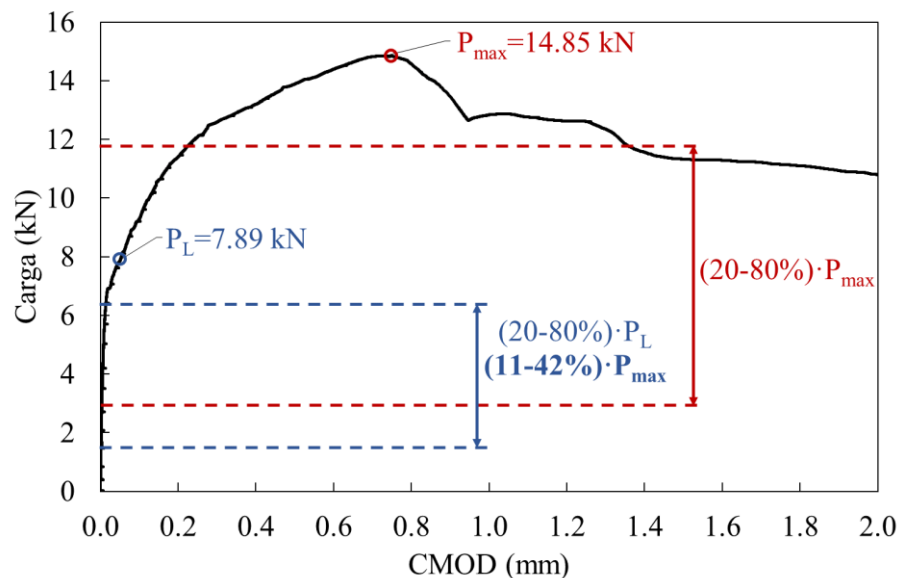


Figure 2.2-9. Load vs CMOD curve in static flexural tensile test of SFRC with strain-hardening behavior. Example of the underestimation of fatigue loads that could be committed by considering P_L instead of P_{max} as reference.

As can be noticed, the parameter related to the fibers that has been most studied in relation to fatigue strength is the content, while in others (shape, slenderness, orientation, etc.) the works are much smaller.

In the case of orientation, most publications analyze its influence on the static response of concrete. There are numerous investigations that show that the residual flexural strength is higher when the fibers are oriented perpendicular to the crack plane [58,59]. A very interesting work is that of Mínguez et al. [58], in which the distribution of the fibers is studied by means of micro-computed tomography, proposing an expression that relates the residual flexural strength to the orientation and density of the fibers located in the vicinity of the crack plane. A similar conclusion is obtained in González et al. [60], from the same research group, although this time linking the fiber orientation with the fracture energy and tensile strength of SFRC according to the wedge splitting test. With respect to fatigue, one of the few published articles is that of Vicente et al. [61], which studies the effect of orientation on the compressive fatigue of SFRC. It is concluded that the fatigue life is higher when the fibers are more perpendicular to the loading axis, which is explained by the bridging effect of the vertical cracks produced by the Poisson effect.

In general, the works that analyze the influence of the geometrical parameters of the fibers on the fatigue response of concrete are scarce. This is because, in order to establish robust correlations, it is essential to know the exact location and position of the fibers in each specimen, which is only possible by means of techniques such as micro-computed tomography, which are not always accessible. Any other method, such as inductive testing, which provides average values of the number and orientation of fibers, has an inherent scatter which, added to that of the fatigue tests themselves, usually leads to inconclusive results.

2.2.4 Fatigue damage

2.2.4.1 Fatigue damage mechanism

Cyclic fatigue loading causes progressive internal damage in concrete that can be evaluated according to three levels [62]: microstructural, mesostructural and macrostructural. The last two are the most interesting in relation to this work, since the first one is related to the physical and chemical bonding mechanisms of hydrated calcium silicate crystals, which is outside the scope of concrete fracture mechanics.

Mesostructural level

At the mesostructural scale, SFRC consists of the following phases [63]: matrix (cement paste and coarse aggregate), fibers, fiber-matrix interface, and coarse aggregate-

cement paste interface. When cyclic fatigue loads are applied, these phases suffer some damage, the most common being:

- Crack formation and growth at the coarse aggregate-cement paste interface due to the difference in stiffness between the components and to stress concentration phenomena. Some authors argue that part of this microcracking appears even before the application of loads, as a result of the cement hydration process itself.
- Relative movements of the fibers with respect to the matrix, resulting in surface abrasion and damage at the fiber-matrix interface as a result of the cyclic sliding process.

Consequently, it can be stated that the weakest zones of the SFRC are the coarse aggregate-matrix and fibers-matrix interfaces, and thus are the locations where fatigue cracks originate and grow [63].

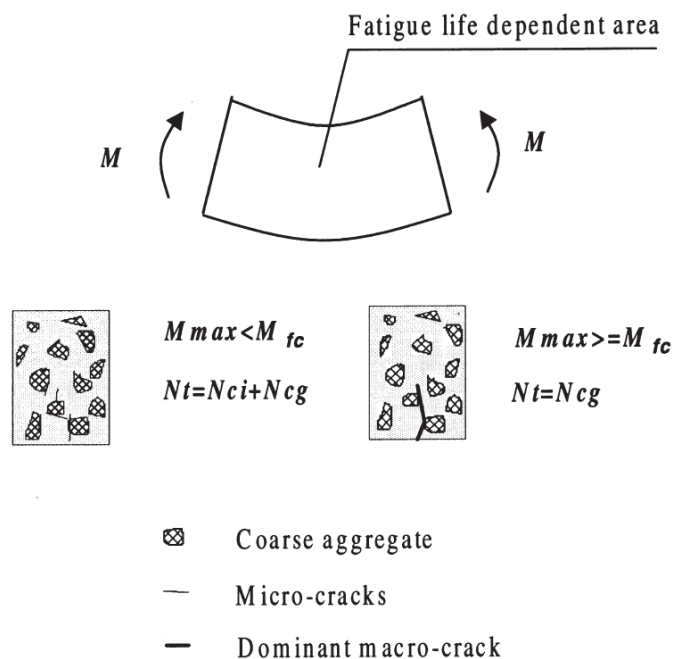


Figure 2.2-10. Cracking growth processes in a concrete element subjected to flexural fatigue [63].

The fatigue crack growth process determines the fatigue life of SFRC elements, and according to Zhang et al. [63] it can be divided into two stages: crack initiation and crack growth (Figure 2.2-10). As an example, an SFRC beam subjected to 3-point flexural fatigue with cycles of constant amplitude ranging from a maximum (M_{max}) to a minimum (M_{min}) moment can be taken. When $M_{max} > M_{fc}$, where M_{fc} is the cracking moment, the fatigue life of the beam is given by:

$$N_t = N_{ci} + N_{cg} \quad (2.2-12)$$

On the other hand, when $M_{max} > M_{fc}$, it follows that:

$$N_t = N_{cg} \quad (2.2-13)$$

Where N_t is the total fatigue life, N_{ci} is the fraction of fatigue life corresponding to crack initiation and N_{cg} is the part due to crack growth. The first term depends mainly on the characteristics of the concrete matrix, and therefore on aspects such as aggregate properties or pore structure (size distribution, porosity volume, etc.). On the other hand, the second term depends to a large extent on the cohesion forces in the fracture process zone (FPZ), located upstream of the crack front. In the case of SFRC, this mechanism is mainly governed by the bridging effect generated by the fibers themselves.

In summary, the flexural fatigue life of a SFRC element can be divided into two parts: a first in a non-cracked situation governed by the concrete matrix, and a second in a cracked situation dominated mainly by the fibers. Depending on the fatigue load levels, both phases or only the second one may appear.

Macrostructural level

The damage mechanisms at the mesostructural level described above result in changes in the macroscopic properties of the concrete. The main indicators of damage in flexural fatigue are the variation of crack opening or CMOD, the variation of stiffness and the post-fatigue flexural strength. These aspects are discussed in detail in the following subsection.

2.2.4.2 Fatigue damage indicators

Variation of crack opening (CMOD)

In compressive fatigue, cyclic loading causes progressive changes in the stress-strain diagram (σ - ε) throughout the fatigue life of the element. These modifications are basically summarized in an increase of the plastic or residual strain and a reduction of the dynamic modulus of elasticity [64]. Equivalently, in flexural fatigue, the load (or equivalent stress) versus crack opening diagram is taken as a reference, observing that the fatigue cycles produce an increase in the residual crack opening ($CMOD_{pl,i}$) and a decrease in stiffness (k_i) in each cycle, defined as the straight line joining the reloading point with the intersection between the loading and unloading branches (Figure 2.2-11) [37,54,65,66].

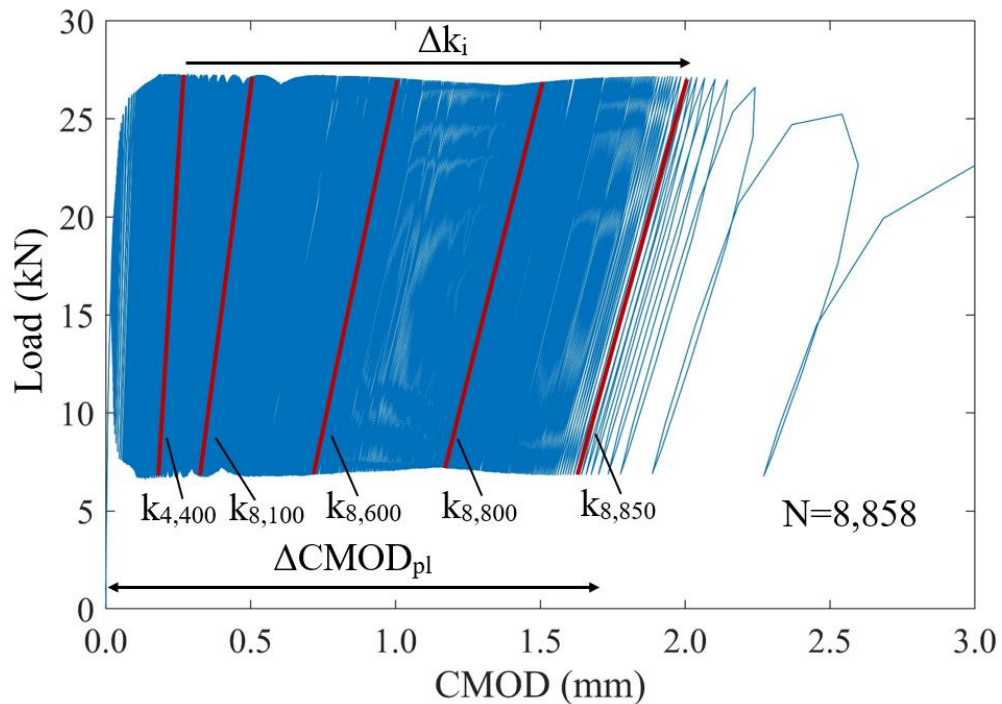


Figure 2.2-11. Load-CMOD curve in a flexural fatigue test in SFRC, indicating residual crack opening ($CMOD_{pl}$) and stiffness decrease with the number of cycles (Δk_i).

In relation to this diagram, it is worth mentioning the envelope paradigm, according to which the ultimate crack opening ($CMOD_f$) of an element subjected to flexural fatigue is reached when the fatigue load-CMOD curve reaches the equivalent curve of the monotonic flexural fatigue test (Figure 2.2-12). This paradigm is used as a failure criterion in many concrete fatigue models, and several authors have tried to verify it experimentally [37,54]. Carlesso et al. [37] propose that the increase in crack opening is constant with the number of cycles until the CMOD reaches the monotonic envelope ($CMOD_e$), at which point the damage process accelerates to failure ($CMOD_f$). Based on this, it is suggested that $CMOD_e$ depends mainly on the maximum load level (P_{upp}), while the load amplitude ($P_{upp}-P_{low}$) is strongly related to the number of cycles to failure. However, the envelope approach is not widely accepted in the scientific community, with several papers questioning its validity in both compressive and flexural fatigue [63,67,68].

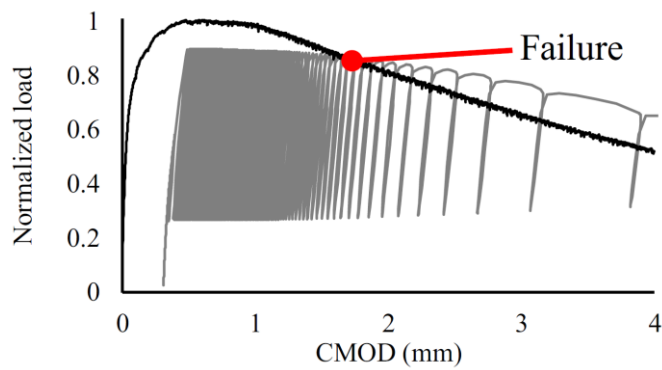


Figure 2.2-12. Monotonic envelope failure criterion in flexural fatigue [37].

Another very interesting diagram that allows the analysis of mechanical degradation in concrete due to flexural fatigue is the cyclic creep curve, which represents the crack opening versus the number of cycles (Figure 2.2-13). In general, in tests with uncracked specimens, this curve consists of three damage phases:

- I.** Initially, there is a rapid increase in CMOD due to the emergence of microcracks at the edge of the notch.
- II.** Afterwards, the CMOD increases appreciably steadily as a result of stable crack growth. Therefore, at this stage the upper envelope of the curve approaches a straight line, the slope of which is called the crack mouth opening rate ($d\text{CMOD}/dn$).
- III.** Finally, unstable crack propagation occurs, resulting in a rapid increase in CMOD until failure.

The slope of the upper envelope of the second phase is a very interesting parameter, since it is closely related to the fatigue life. In compressive fatigue, it is expressed in terms of strain, referred to as secondary strain rate ($d\varepsilon/dn$). Sparks & Menzies [49] showed that there is a linear correlation between the logarithms of the secondary strain rate and the fatigue life, so that the higher the $d\varepsilon/dn$, the lower the fatigue life. Numerous works have verified this relationship, known as Sparks and Menzies' law, proving that it is a property of the material, and therefore independent of the test parameters (load levels, frequency, etc.) [31,46]. This leads to the fact that $d\varepsilon/dn$ can be used as a basis for establishing fatigue failure criteria, as already proposed by Poveda et al. [46]. In this regard, it is worth mentioning that some authors claiming that the upper envelope of the CMOD vs N curve actually follows a continuous expression, fitting very well to Weibull-type cumulative distribution functions [69].

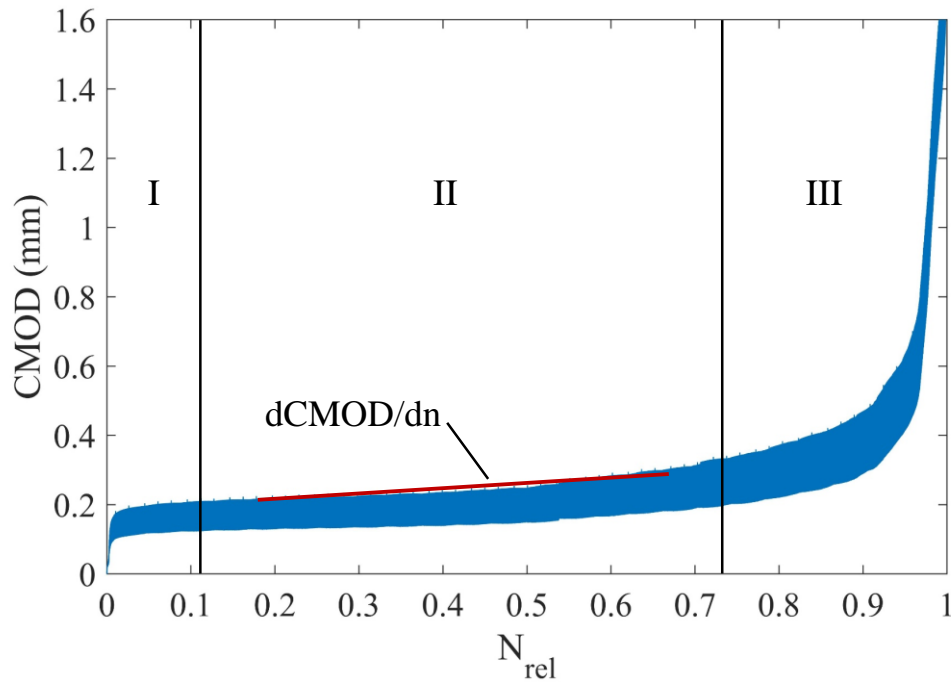


Figure 2.2-13. CMOD-N diagram in flexural fatigue test in SFRC, showing damage stages and secondary crack opening rate.

The few publications on this subject indicate that in flexural fatigue the Sparks and Menzies' law is also fulfilled, so that there is a clear correlation between the crack opening rate ($d\text{CMOD}/dn$) and the fatigue life [37,54]. It is noteworthy to mention the work of Germano et al. [54], who showed that this relationship holds true for plain concrete and SFRC with different fiber contents, and that it is independent of the levels of fatigue loads (Figure 2.2-14). Furthermore, they also concluded that the presence of fibers increases $d\text{CMOD}/dn$ by up to an order of magnitude, probably due to their higher ductility and energy absorption capacity.

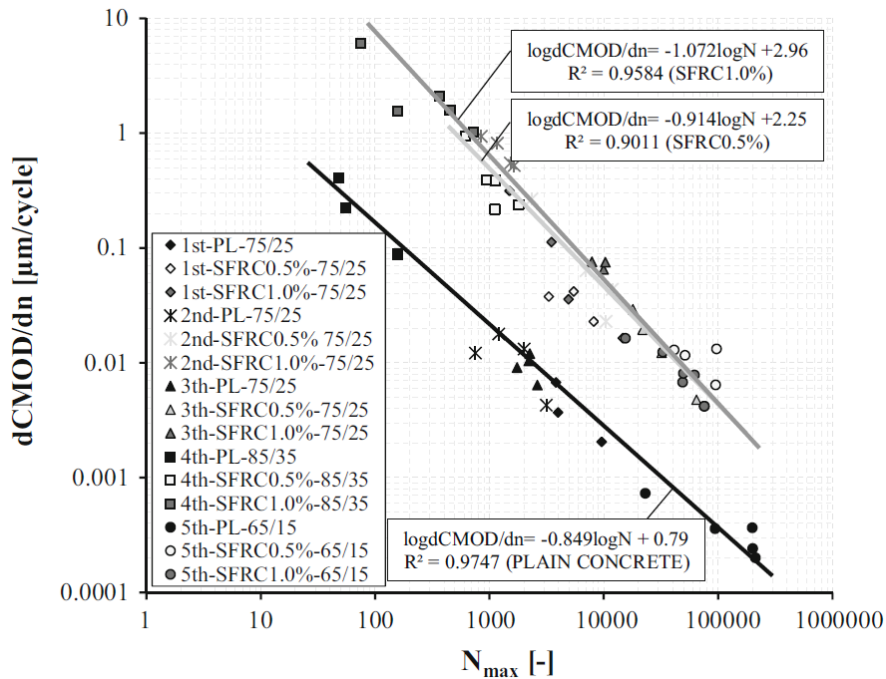


Figure 2.2-14. Crack opening rate versus fatigue life in concretes with fiber contents of 0, 0.5 and 1.0% [54].

Sometimes, the CMOD-N curve in flexural fatigue in SFRC looks like Figure 2.2-15; i.e., two distinct fatigue damage mechanisms appear, each with the characteristic shape (stages I, II and III) and its $dCMOD/dn$ explained in Figure 2.2-13. The first mechanism comprises the fatigue of uncracked concrete, equivalent to the crack initiation stage proposed by Zhang et al. [63] (see 2.2.4.1), and is characterized by a very small increase in CMOD due to higher stiffness. This type of fatigue is fundamentally governed by the concrete matrix, so the fibers are hardly involved. On the other hand, the second mechanism consists of fatigue of cracked concrete, corresponding to the crack growth stage described in Zhang et al. (again, see 2.2.4.1). This fatigue type presents a much higher $\Delta CMOD$, since the cyclic loads are mainly supported by the fibers, which provide higher ductility. Between the two fatigue mechanisms, there is a stiffness transition zone; i.e., a period in which the fatigue loads are progressively transmitted from the matrix to the fibers.

This dual behavior does not always occur, since it depends on the response of the SFRC in static flexural bending (strain hardening and softening phenomena) and on the loading levels of the fatigue cycles, among other aspects. Moreover, there are very few works in the literature that address this phenomenon (Gebuhr et al. [70]). In part, this is explained by the fact that in a good part of the investigations pre-cracked specimens are

tested, so the first mechanism is eliminated. Consequently, further research is required in this field to determine under which conditions it occurs, whether one of the two mechanisms is predominant (in terms of N), whether there is any relationship between the two crack growth rates, etc.

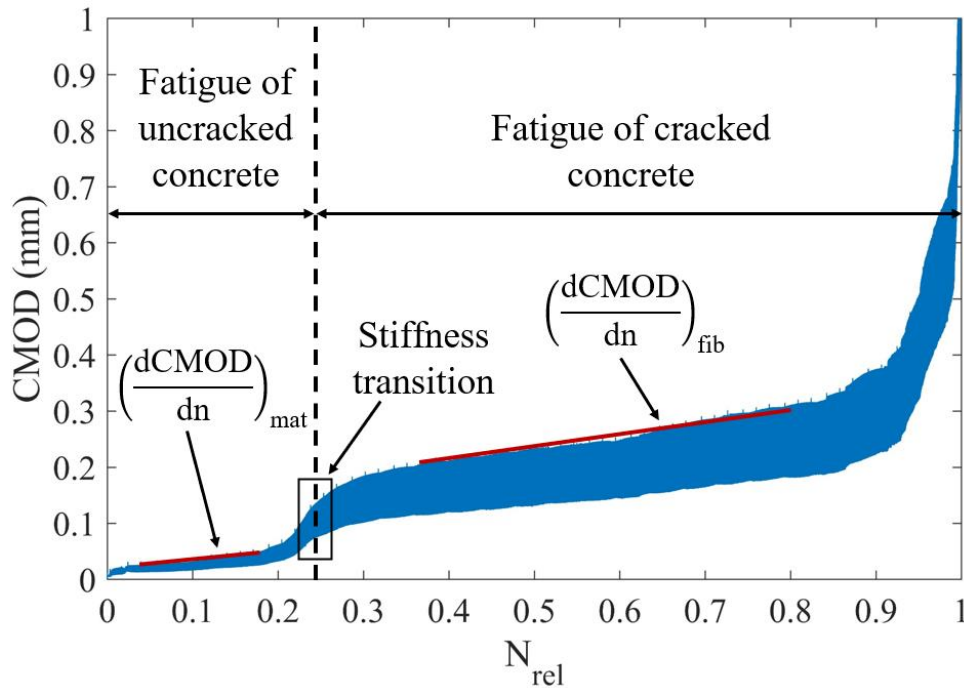


Figure 2.2-15. CMOD- N curve in flexural fatigue test in SFRC, showing the fatigue mechanisms of uncracked and cracked concrete.

Variation of stiffness

Another damage indicator in flexural fatigue that is commonly studied is the stiffness degradation over the loading cycles [32,57,65,66]. This parameter can be considered equivalent to the dynamic modulus of elasticity in compressive fatigue, whose behavior is well known [71]. The stiffness, also called residual stiffness at each loading cycle (k_i), is calculated as [65,72]:

$$k_i = \frac{F_i}{\text{CMOD}_{\text{tot},i} - \text{CMOD}_{\text{pl},i}} \quad (2.2-14)$$

Where $\text{CMOD}_{\text{tot},i}$ is the CMOD corresponding to the lower point of load reversal, $\text{CMOD}_{\text{pl},i}$ is the CMOD associated with the point of intersection of the loading and unloading branches, and F_i is the difference between the loads corresponding to $\text{CMOD}_{\text{tot},i}$ and $\text{CMOD}_{\text{pl},i}$. The determination of the stiffness k_i is illustrated in Figure 2.2-16.

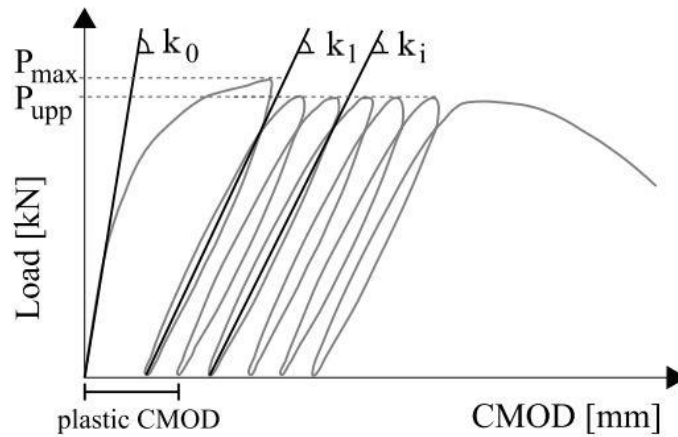


Figure 2.2-16. Schematic representation of the determination of residual stiffness for each load cycle [65].

As with the CMOD, the stiffness degradation with the number of cycles specimens shows three phases (Figure 2.2-17). In the first, there is a considerable decrease in stiffness as a result of cracking at the notch face. In the second phase, an approximately linear reduction in stiffness is observed, associated with the period of stable crack growth. Finally, in the last phase, there is an accelerated drop in stiffness due to the unstable crack growth that culminates in the failure of the element.

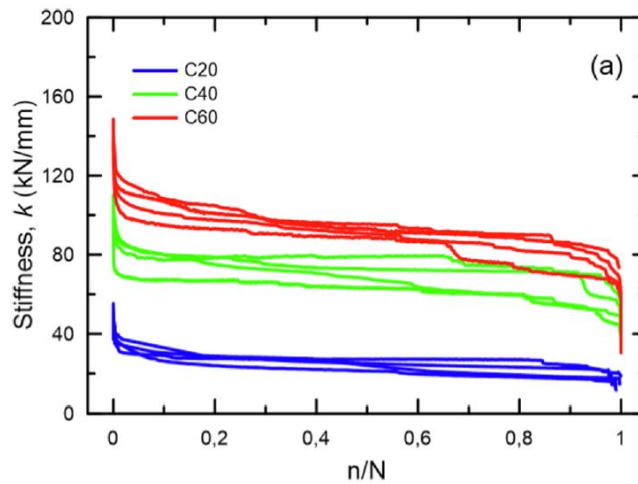


Figure 2.2-17. Variation of stiffness with the number of cycles in SFRC with different fiber contents (0.25% or 20 kg/m³, 0.50% or 40 kg/m³ and 0.75% or 60 kg/m³) [57].

Considering that stiffness is used as a damage indicator, some authors define the damage of each D_i load cycle as [57,65]:

$$D_i = 1 - \frac{k_i}{k_0} \quad (2.2-15)$$

Where k_i is the stiffness of load cycle i and k_0 is the stiffness of the first load cycle, corresponding to the undamaged material. The sum of the damage accumulated by successive cycles ΣD_i can range from 0 (intact material) to 1 (exhausted material).

Finally, another way to evaluate the decrease in stiffness due to fatigue loading is the stiffness vs CMOD curve (Figure 2.2-18). In this regard, it is worth mentioning the work of Gebuhr et al. [66], where it is shown that, both in plain concrete and SFRC with different fiber contents (0.3, 0.7 and 1.5%), most of the stiffness loss (of the order of 70%) is concentrated at very low CMOD values (0-0.05 mm).

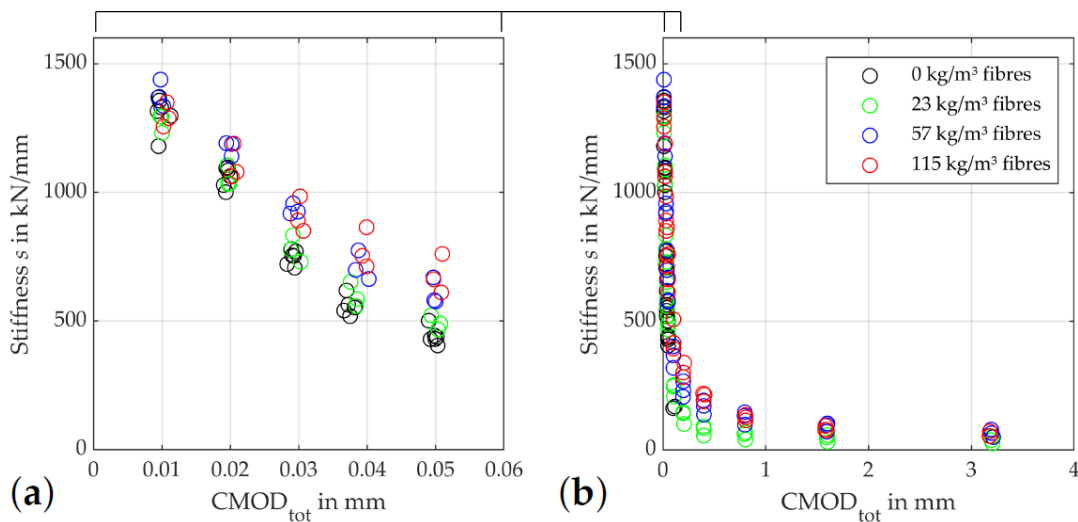


Figure 2.2-18. Stiffness vs CMOD for SFRC with different fiber contents: (a) zoom in the range 0-0.06 mm, (b) general view [66].

Post-fatigue flexural strength

Post-fatigue flexural strength is also occasionally used to evaluate damage due to flexural fatigue loading [37,55,73]. Gonzalez et al. [73] studied the residual flexural strengths ($f_{R,1}$ to $f_{R,3}$, according to [33]) in SFRC specimens that had previously been subjected to different levels of damage, calculated as percentages of the characteristic fatigue life. The results revealed that the residual strengths decreased significantly proportional to the applied damage. In a later work, Vicente et al. [55] carried out a similar investigation, but considering SFRC with different fiber contents (1 and 2%). They concluded that the post-fatigue flexural strength is highly dependent on the fiber dosage. The series with more fibers not only showed higher residual strengths for all crack openings, but also a smaller decrease of their values with increasing damage inflicted.

A very interesting phenomenon with regard to post-fatigue strength is the so-called fatigue maturation, i.e., the increase in the strength of concrete after it has been subjected

to a certain number of cycles. In compressive fatigue, this phenomenon has been observed both at low stress levels ($\approx 50\%$ of f_c), where it is supposed to be below the endurance limit, and at high stress levels ($\approx 80\%$ of f_c) [41,42]. However, fatigue maturation depends not only on the strain levels, but also on the percentage of fatigue life consumed (Figure 2.2-19). This is due to the action of two opposing mechanisms: microcracking of the concrete, which contributes to a decrease in strength, and another series of mechanisms that are not well understood and that improve strength (concrete recompaction, rehydration of the cement paste, autogenous repair, etc.). Consequently, more research is needed in this field.

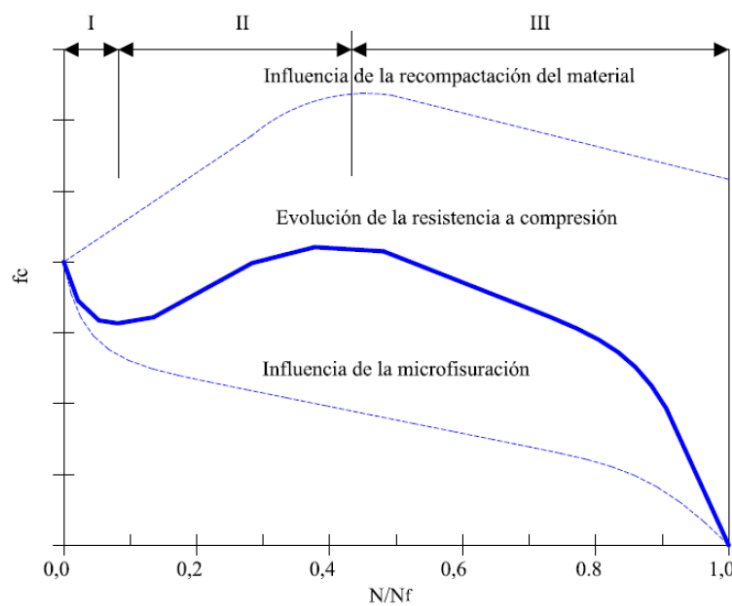


Figure 2.2-19. Model proposed by Mínguez [41] for the evolution of the residual compressive strength over the fatigue life.

In flexural fatigue, fatigue maturation has been studied even less. Carlesso et al. [37] performed monotonic tests on SFRC specimens that had exceeded the runout limit, concluding that cyclic loading appeared to have affected the CMOD, but not the post-fatigue flexural strength. In fact, in most cases the maximum post-fatigue load was about 4% higher than the $P_{0.5\text{mm}}$ load taken as a reference to establish the fatigue cycles (Figure 2.2-20). These results occurred in the specimens subjected to the lowest load levels (65% and 70% of $P_{0.5\text{mm}}$), which could indicate that they were below the endurance limit. Further study of this phenomenon is necessary, since the mechanisms that in principle explain fatigue maturation in compression (recompaction, etc.) do not seem to be compatible with the stresses generated in flexural fatigue.

(a) $P_{0.5\text{mm}} = 20.4 \text{ kN}$, $S = 0.65$, $P_{\text{res,cycl}} = 22.7 \text{ kN}$

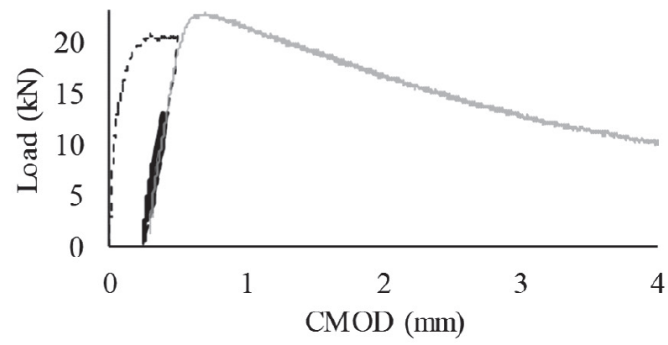


Figure 2.2-20. Increased post-fatigue flexural strength in specimens that have exceeded the runout limit [37].

2.3 Size effect on the mechanical response of concrete

This subsection deals with the size effect on the mechanical behavior of structural concrete. First, the phenomenon is defined, highlighting its interest, and some related concepts are introduced. Secondly, the causes of the size effect on concrete strength are discussed, summarizing on the one hand the main universally recognized theories, and describing on the other hand other second-order causes, such as the wall effect. Next, a literature review of the main experimental works on the size effect in concrete subjected to flexural, compressive and fatigue loads is carried out, paying special attention to those related to SFRC. Finally, the influence of the mesostructure on the size effect is described.

2.3.1 Introduction

The size effect, also called the scale effect, basically consists of the decrease in strength observed in geometrically similar elements as their size increases. This phenomenon is characteristic of quasi-brittle materials, such as concrete, and has important implications for structural design. Normally, the resistance of concrete to compressive stresses, flexural stresses, etc. is determined experimentally using small specimens, easily manageable in the laboratory. The results obtained are applied to the design of real structures, whose size can be up to two orders of magnitude larger. However, since the size range considered is affected by the size effect, this implies that the strength of the concrete in the specimens is higher than in the real structures, thus overestimating its value.

In order to establish comparisons between elements of different scales and hence characterize the size effect, it is taken as a reference the nominal stress at the moment of failure σ_N , defined as [74]:

$$\sigma_N = c_n \cdot \frac{P_{\max}}{b \cdot h} \quad (2.3-1)$$

Where P_{\max} is the maximum or ultimate load, b is the thickness of the element, h is a characteristic dimension (edge, span, etc.) and c_n is a coefficient introduced conveniently so that σ_N represents any suitable value of the stress. For example, when studying the size effect on the 3-point bending strength, it is usual that σ_N represents the maximum normal stress in the central section of the element, so that one has:

$$\sigma_N = \frac{3 \cdot P_{\max} \cdot l}{2 \cdot b \cdot h^2} = c_n \cdot \frac{P_{\max}}{b \cdot h}, \text{ con } c_n = \frac{3 \cdot l}{2 \cdot h} \quad (2.3-2)$$

Where P_{\max} is the ultimate flexural load, l is the span between supports, b is the width of the specimen and h is the depth at the center section.

The size effect occurs when geometrically similar elements of different dimensions do not have the same nominal stress at failure. This is the case for brittle and quasi-brittle materials, such as glass and concrete. In other cases, however, the nominal stress at failure is independent of the size of the element. This behavior is observed in ductile materials with plasticization, such as steel.

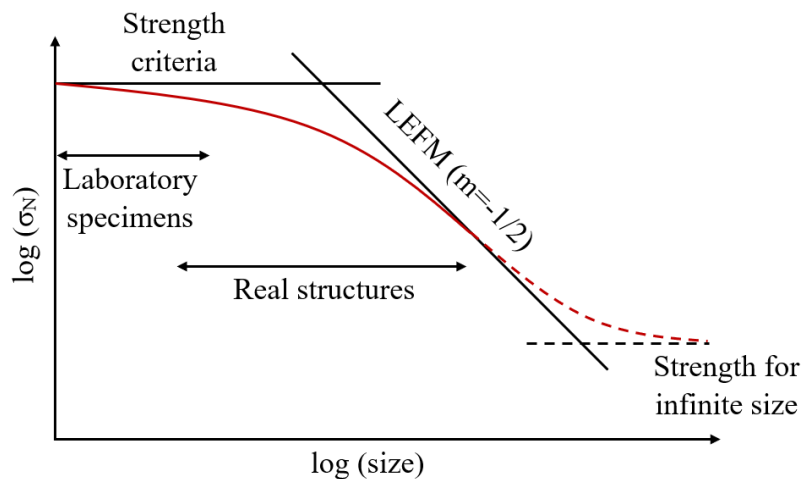


Figure 2.3-1. Strength-size curve in concrete structures (adapted from [24]).

Figure 2.3-1 shows the strength-size curve for concrete structures. The upper horizontal asymptote represents a ductile type of behavior in which no size effect occurs. In these elements, an elastic or plastic analysis is applicable according to allowable strength criteria. On the other hand, the asymptote with inclination $m=-1/2$ corresponds to a brittle type of behavior in which a strong size effect is observed. In these structures, the theory of linear elastic fracture mechanics (LEFM) is applied. In addition, some authors propose that a second horizontal asymptote exists, i.e., that the strength tends to a finite value for a theoretically infinite element size, which could be considered as the real intrinsic strength of the concrete [75].

As can be seen in Figure 2.3-1, the resistance behavior of concrete in real structures is in the transition zone, so that small elements (laboratory specimens) have a more ductile behavior, while large elements (real structures) have a more brittle response (Figure 2.3-2).

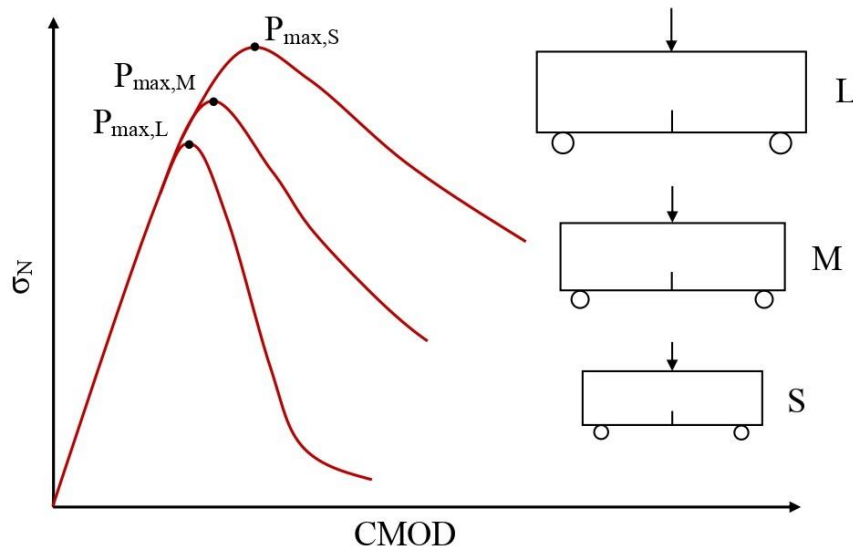


Figure 2.3-2. Transition from ductile to brittle behavior with increasing size in concrete subjected to flexural stress (adapted from [24]).

2.3.2 Causes of the size effect in concrete

There are different causes that make the nominal strength of concrete dependent on the size of the elements. Bažant and Planas [74] propose six sources of the size effect: (1) boundary layer effect or wall effect; (2) diffusion phenomena, such as heat conduction or water transfer between pores; (3) heat of hydration or other phenomena associated with chemical reactions; (4) statistical size effect; (5) size effect related to fracture mechanics; and (6) size effect due to the fractal nature of cracking surfaces. The last three causes correspond to the three scientifically accepted theories for the study of the size effect in concrete, while the rest are other causes of different nature.

2.3.2.1 Size effect theories

The first studies on the size effect in concrete were approached from a probabilistic point of view, which can be illustrated by the chain model. The maximum load that a chain is capable of supporting is determined by the strength of its weakest link. Due to the randomness of the strength of the material, the longer the chain, the lower the value of strength that its weakest link is likely to have. In other words, the heterogeneity of concrete implies a higher probability that larger specimens will contain defects that can accelerate material failure. This statistical theory of the size effect was initially proposed by Mariotte in the early 18th century, although it was Weibull in 1939 [76] who made a decisive contribution, proposing the so-called Weibull distribution to describe the phenomenon.

Decades later, attempts to explain the size effect in concrete from the viewpoint of fracture mechanics began. At that time, the theory of linear elastic fracture mechanics (LEFM), proposed by Griffith [77], was known. This theory was able to explain the strong size effect observed in brittle materials, such as glass or crystal, based on the existence of discontinuities and microscopic defects. However, the application of LEFM to structural concrete did not provide good results, concluding that the size effect in concrete was less aggressive than in brittle materials [78]. As a result, the need arose to develop a nonlinear fracture mechanics theory applied to quasi-brittle materials.

The probabilistic theory of the size effect prevailed until the mid-1980s, when Bažant presented the size effect law in quasi-brittle materials [79]. It was the first deterministic theory to explain the size effect, making it possible to define a law of evolution of the failure nominal stress with respect to the size of the element. This first law was applicable to geometrically similar notched concrete specimens subjected to flexural bending, although years later he proposed its generalization with the universal size effect law [79].

This theory is based on the process of crack growth in concrete. When concrete fissures, a micro-cracking zone called fracture process zone (FPZ) is generated at the crack face. These micro-cracks are capable of transmitting traction to each other up to a certain limit, represented by the cohesive forces of the concrete in the inter-crack zone. When a certain load limit is reached, the micro-cracks interconnect with each other, so that they are no longer able to transmit cohesive forces. The connection between the micro-cracks constitutes the crack advance (Figure 2.3-3).

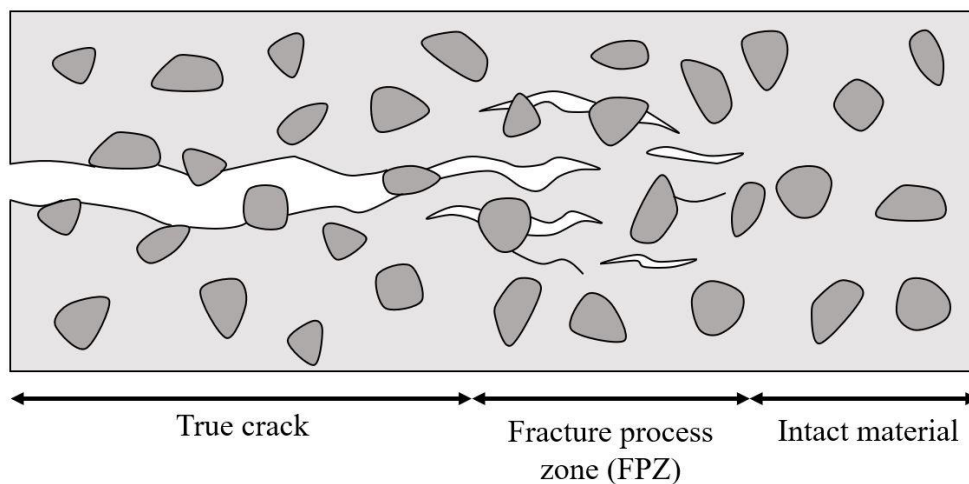


Figure 2.3-3. Fracture process in plain concrete with identification of main zones.

The importance of this fact in relation to the size effect lies in the fact that the length of the FPZ is a property of the material, so that the same concrete has the same FPZ regardless of the size of the element. Moreover, the length of the FPZ is not negligible compared to the dimensions of the structures. Consequently, the proportion of energy released in the FPZ for a given crack length increment varies with respect to the element size. This fact affects the crack development and the value of the failure stress, causing a size effect.

The fracture response of a material is strongly related to the size of the FPZ. Figure 2.3-4 depicts the fracture process zones for a brittle, ductile and quasi-brittle material, where F indicates the fracture process zone and N the zone of nonlinear/ductile behavior of the advancing FPZ. It is observed that, at equal element size, materials with a shorter FPZ length present a more brittle behavior. Continuing with the reasoning, for the same material, the smaller the ratio between the FPZ length and the element size, the more brittle its behavior will be. This is the reason why small concrete structures have a more ductile response and large ones a more brittle response.

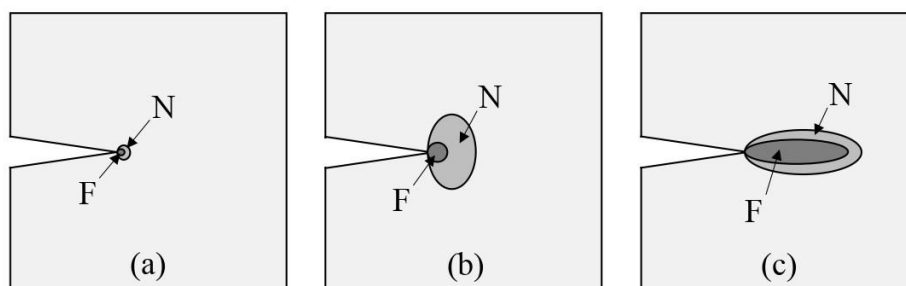


Figure 2.3-4. FPZ in materials with brittle (a), ductile (b) and quasi-brittle (c) behavior (adapted from [24]).

After the publication of Bažant's size effect law, new theories of the size effect emerged, also deterministic. However, in the mid-1990s Carpinteri put forward a theory based on fractals [76]. This researcher suggests that the process of crack formation and growth is conditioned by the fractal properties of the crack surface. Thus, as the fractal dimension (or roughness) of a crack varies depending on the scale considered, this causes a size effect on the tensile strength and fracture energy of concrete.

Carpinteri's fractal theory has some acceptance in the scientific world, although it has also received several criticisms about its lack of physical or mathematical basis. Some authors point out that the fractal size effect cannot embody the nature of the size effect in

concrete because most of the energy is consumed in the propagation of microcracks and friction between surfaces, rather than in the formation of the surfaces themselves [80].

In conclusion, there are currently three globally recognized theories applicable to the study of the size effect in concrete: a probabilistic one, a deterministic one and a fractal-based one. The most widely accepted is the deterministic theory proposed by Bažant through his size effect law in quasi-brittle materials.

2.3.2.2 Other causes

In addition to the size effect theories discussed in the previous subsection, other causes that may explain, at least partially, this phenomenon should be mentioned.

The boundary layer effect or wall effect is the result of the fact that the concrete layer in contact with the wall of the mold or formwork has different properties from those inside the element, namely a lower content of coarse aggregate and therefore a higher amount of cement paste and fine aggregate. The size effect occurs because the thickness of the surface layer is independent of the size of the specimens, and also of the same order of magnitude as the coarse aggregate [74]. Consequently, in small specimens the surface layer occupies a large proportion of the cross section, while in large specimens it occupies a small part.

In plain concrete, in most cases the contribution of the wall effect to the size effect on concrete strength is not very significant [74]. However, in SFRC it plays an essential role since it conditions the position and orientation of the fibers. Under bending, the fibers determine the residual behavior of the concrete, and even the ultimate strength if strain-hardening occurs when the right conditions of dosage and fiber properties are met. The higher the ratio between the fiber length and the minimum element dimension, the more aggressive the wall effect will be, causing the fibers to tend to align preferentially in the direction of the specimen length, resulting in better flexural behavior (Figure 2.3-5). This is the reason why flexural testing standards set a maximum fiber length to minimum mold dimension ratio between 0.3 and 0.4 [6,7].

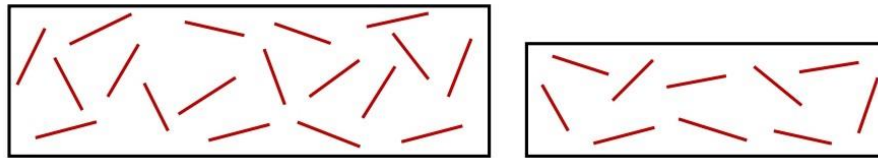


Figure 2.3-5. Wall effect on fiber orientation in different size specimens with the same fiber dosage and fiber length.

The influence of the wall effect on the size effect in SFRC is not limited exclusively to flexural stresses. It is also observed that small cylindrical specimens give higher values of compressive strength, since they accentuate a preferential alignment of the fibers.

Another possible cause of the size effect in SFRC subjected to bending is that, for the same nominal stress σ_N , the crack opening or CMOD increases with the specimen depth. Consequently, in large specimens, it is expected that the anchorage capacity of the fibers close to the most stressed edge is exhausted before the fibers close to the neutral fiber of the section fully cooperate, leading to a worsening of the flexural response.

In concrete subjected to compression, the confinement due to friction between the plates of the testing machine and the faces of the specimen is greater as the element size decreases, which causes an increase in strength. Moreover, this effect is more pronounced in cubic specimens than in cylindrical ones, due to their lower relative slenderness [42].

Finally, other causes of the size effect in concrete are diffusion phenomena and heat of hydration [74]. On the one hand, the average diffusion times (i.e., cooling, heating, drying, etc.) are proportional to the square of the size of the structure. At the same time, diffusion processes modify the material properties, introducing residual stresses that in turn lead to inelastic deformation and cracking. For example, drying can lead to surface shrinkage cracking. Due to different drying times, the extent and density of cracking can vary between large and small elements, generating a different response. On the other hand, similar to the above, the mean hydration heat dissipation time in a concrete element is proportional to the square of its thickness. Therefore, larger elements heat up at higher temperatures, suffering non-uniform temperature increases that result in the appearance of cracks and desiccation, altering the properties of the material.

2.3.3 Size effect in bending

Size effect in concrete subjected to flexural stresses is a well-known phenomenon [74,79], for several reasons. First, the size effect is a direct consequence of the theory of fracture mechanics applied to concrete; therefore, its analysis is an effective way to calibrate the parameters of any fracture model. Secondly, the development of fracture mechanics in concrete is based on the study of tensile cracks. Pure tensile tests in concrete are complex, so that bending tests of various types (at 3 or 4 points, in notched or unnotched specimens) are usually used to obtain fracture properties (fracture energy, tensile strength, etc.).

However, in the particular case of SFRC, experimental work on size effect is relatively scarce [81–86]. This fact may partly explain why the development of fracture mechanics in SFRC is still low compared to that of plain concrete [87–89].

The addition of steel fibers generates a bridging effect in the cracks, increasing the length of the fracture process zone of the material (Figure 2.3-6). This results in improved fracture behavior, i.e., an increase in the fracture energy and ductility of the concrete. Consequently, the size effect is expected to be smaller in SFRC than in plain concrete.

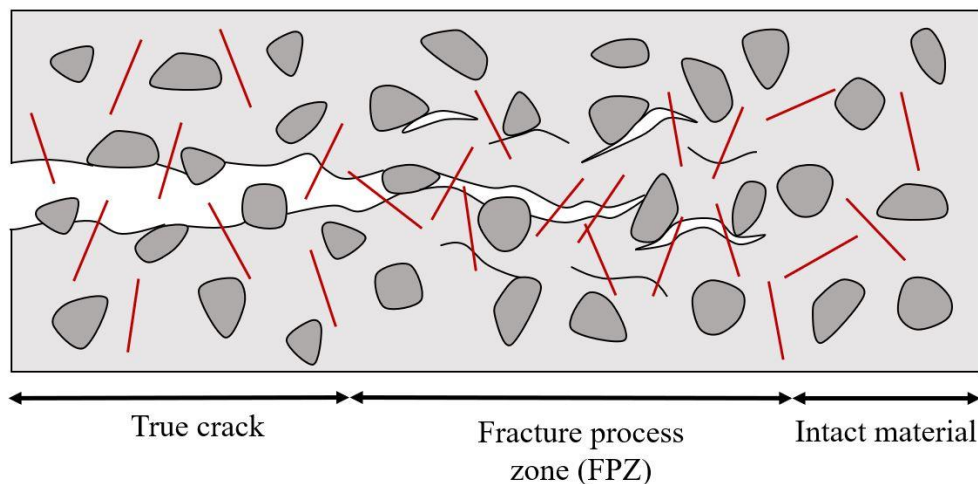


Figure 2.3-6. Fracture process in SFRC with identification of main zones.

Li et al. [81] observed that the incorporation of fibers reduces the structural size effect of concrete, shifting the size range in which the transition of brittle-ductile behaviors occurs. Thus, when ductile failure is reached due to sufficient fiber bridging, the nominal stress depends mainly on the fibers and the properties of the fiber-matrix interface. Nguyen et al. [86] investigated the size effect on the flexural behavior of high-strength hybrid SFRC. He noticed that not only size effect is produced on the ultimate flexural strength

(P_{\max} or P_{MOR}), but also on the other parameters studied (normalized displacement, normalized energy absorption capacity, etc.). Furthermore, he observed that the series with fewer fibers was more sensitive to the size effect, although he only compared two contents (1.5% and 2.0%) (Figure 2.3-7).

Yoo et al. [85] studied the size effect in normal and high strength SFRC, considering different fiber contents and types (hooked-end and amorphous). The results showed that high-strength concrete is more sensitive to the size effect on flexural strength than normal concrete. In addition, the size effect decreased with increasing fiber volume, being more effective the addition of fibers in high-strength concrete than in normal concrete, which is explained by a better fiber-matrix adhesion. In another work by the same author [84], it was observed that a greater fiber slenderness reduced the size effect of SFRC, having a higher yield and providing more ductility. Likewise, it was determined that a possible explanation of the size effect is the worse fiber orientation in the larger specimens.

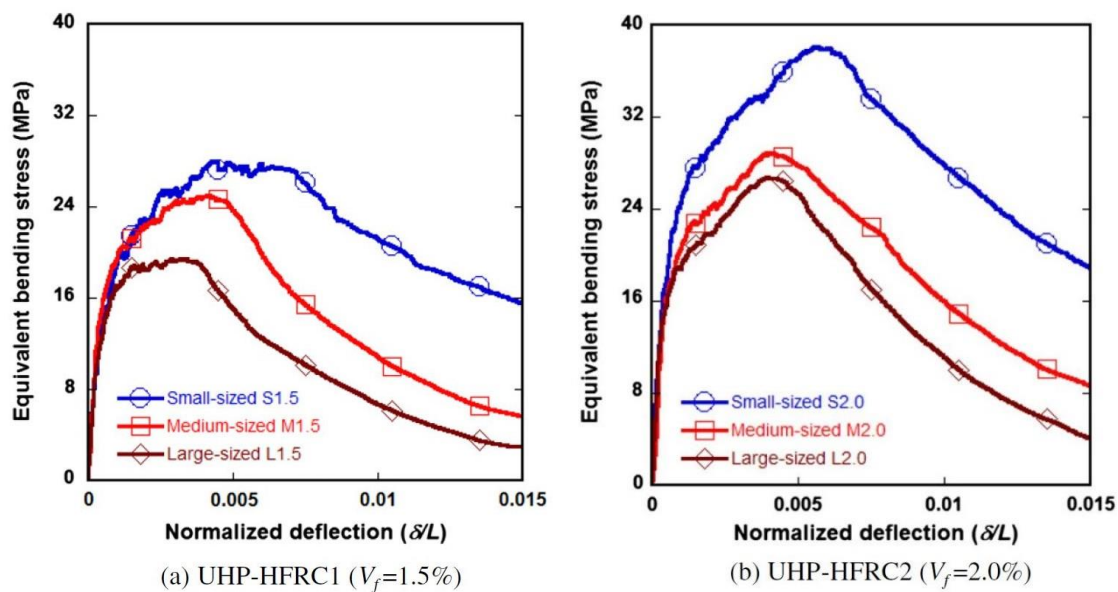


Figure 2.3-7. Size effect on flexural strength in SFRC with different fiber content [86].

2.3.4 Size effect in compression

The size effect in compressive failure of concrete has been studied much less than in the case of failure under tensile or flexural loads. This is explained by the fact that the damage mechanisms in compression are complex, since they are not controlled by a material strength criterion but are mainly due to the release of energy stored in the structure [90]. Despite this, this failure mode is of great interest since its high brittleness makes it unpredictable and therefore dangerous. At present, there are not too many models to

describe the size effect in compressive concrete, the most accepted being Bažant's size effect law for compression (CSEL) [90]. However, the accessibility and simplicity of compressive strength testing has led to an extensive literature on experimental work in this field [91–96].

In SFRC, publications are still limited [42,83,97]. Fládr & Bílý [83] carried out an extensive experimental study on the size effect in high-strength SFRC. They fabricated six different series with compressive strengths ranging from 100 to 175 MPa, using cubic specimens of four sizes, from 40 to 200 mm on a side. They observed that the size effect decreased with increasing matrix strength and fiber content (Figure 2.3-8). This fact may be due to the fact that the higher relative stiffness of the matrix was counteracted and overcome by the increase in ductility due to the significant volume of fibers, up to 2.0%. Ortega et al. [42] analyzed the size effect in SFRC under both static and fatigue compressive loads. For this purpose, they tested three series of cubic specimens (40, 80 and 150 mm) made with the same concrete, which contained 0.3% of steel fibers. The results revealed that there was no size effect on the static strength in compression, which was attributed to the fact that the fibers provided ductility, inducing a plastic failure behavior in the material.

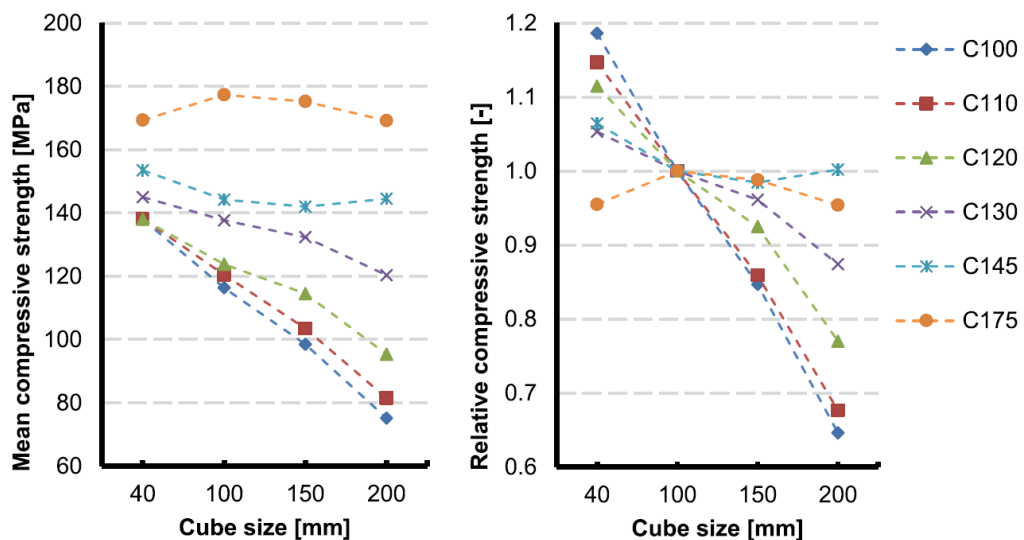


Figure 2.3-8. Size effect on SFRC compressive strength. The dosages of the series vary in cement and fiber content; as an example, the C100 series has 500 kg/m³ and 0.75%, while the C175 has 750 kg/m³ and 1.75%.

2.3.5 Size effect in fatigue

The size effect is a property of all failures in quasi-brittle materials; consequently, it affects not only the static strength, but also the fatigue response [98]. Most research focuses on the size effect in concrete under static loading since these tests are simple to perform and most structural design procedures are based on static properties. However, as mentioned in subsection 2.2, the fatigue strength of concrete is critical in certain applications, and therefore it is very interesting to know its interaction with the size effect.

The most common way to approach the study of the size effect in fatigue, particularly in flexural fatigue in notched elements, is by adapting the well-known Paris-Erdogan law [22]. The Paris law states that the increase in crack length per cycle is a power function of the amplitude of the stress intensity factor. However, in concrete this is only true for one element size, so it is necessary to make the necessary adjustments to include the size effect, thus obtaining a general Paris law [23]. Typically, these generalizations are based on the determination of the equivalent elastic crack propagation rate. Other approaches to this phenomenon seek to model the fatigue crack propagation through a nonlinear analysis, considering the cohesive stresses in the fracture process zone [99].

Most of the publications in this field deal with the flexural fatigue of plain concrete by examining the size effect on crack propagation arising from the notch. Bažant & Xu [23] were the first to propose the application of the Paris law to the study of the size effect in fatigue; to do so, they combined it with the size effect law for quasi-brittle materials under monotonic loading, previously developed by Bažant [79]. This led to a law in which the crack propagation rate per cycle is a power function of the amplitude of a size-adjusted stress intensity factor. Subsequently, Carpinteri & Spagnoli [100] did the equivalent, adapting Paris' law to their fractal-based size effect theory, called the multi-fractal scaling law. Zhang et al. [99] presented a semi-analytical method to predict the flexural fatigue behavior of concrete, based on the cohesive forces (cyclic bridging law) as the constitutive relation of the material in tension. This model is applicable when the maximum bending moment is higher than the cracking moment; that is, it assumes that a crack already exists from the beginning of the fatigue life. Other notable works on the prediction of the size effect in fatigue are those of Ray & Kishen [101], who proposed a fatigue crack propagation model by means of a dimensional analysis, and Brake & Chatti [102], who performed an inverse analysis to calculate the bridging forces induced by fatigue cycles along a dominant crack.

It is worth mentioning that the applicability of the Paris law to predict the fatigue response of concrete has been criticized by several authors [99,103,104], claiming that, due to the significant size of the fracture process zone, this material normally exhibits nonlinear fracture mechanisms. Kirane & Bažant [104] introduced some modifications to the size-adjusted Paris law. In particular, they improved the estimation of the FPZ size, since they showed that the length of the cyclic FPZ was smaller than that of the monotonic FPZ. However, they recognized that the Paris law has certain problems, indicating that it is not able to model the continuous transition between crack growth under cyclic loads, a function of N , and crack growth under static loads, a function of time.

Regarding SFRC, the works on this subject are very scarce, particularly in the case of flexural fatigue, where practically no relevant publications have been found in the available literature [105]. In compressive fatigue, the available articles deal with experimental campaigns [42,97,106,107]. Sinaie et al. [106] studied the fatigue response of cylindrical specimens of different diameters and slenderness, performing tests with displacement control. Ortega et al. [42] analyzed the size effect on the fatigue behavior by compression of cubic specimens of three sizes (40, 80 and 150 mm), containing 0.3% of steel fibers. A clear size effect on fatigue life was observed, attributed to the differences in the stress states of the specimens as a result of the different relationship between the macroscopic size of the specimen and the mesoscopic size of the internal structure of the concrete. Furthermore, another interesting conclusion is that the relationship between secondary strain rate and fatigue life, known as Sparks and Menzies' law [49], is not affected by the size effect, suggesting that it is an intrinsic relationship of the material. This same conclusion was reached by González et al. [97] in a subsequent study carried out with the same SFRC, but in this case with cylindrical specimens of the same slenderness (75x150, 100x200 and 150x300 mm). In this experimental campaign, a marked size effect on fatigue life was also detected, with different causes being proposed to explain it (statistical distribution of large pores, maturation or improvement of the compressive strength induced by cyclic loading, etc.). Figure 2.3-9 shows the fit to the Weibull distribution of the fatigue life results of all the series tested in both papers.

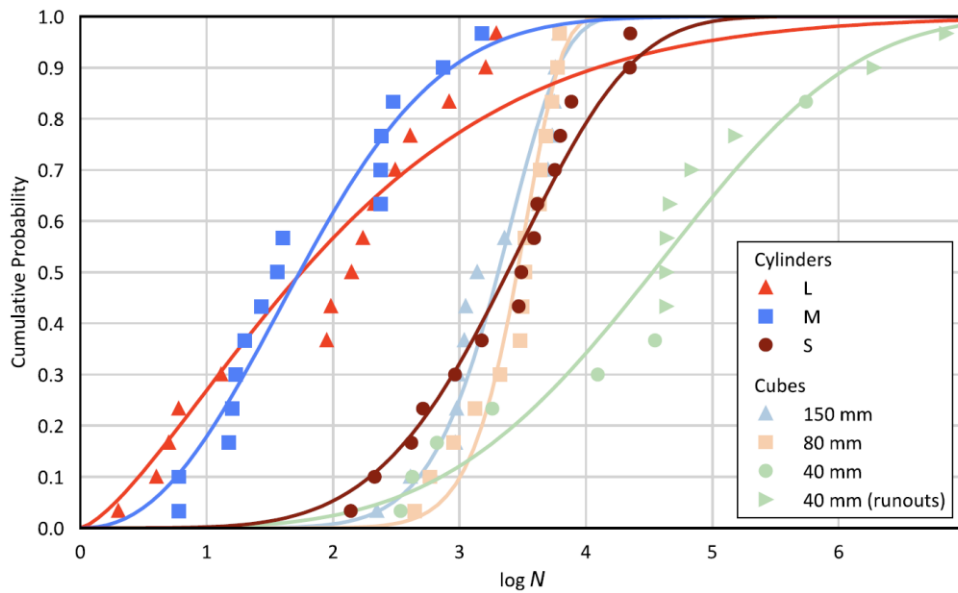


Figure 2.3-9. Weibull fit of the fatigue life of series of cubic and cylindrical specimens of different sizes. All specimens were fabricated with the same SFRC and subjected to the same stress levels (20%-85% f_c) [42,97].

2.3.6 Influence of mesostructure on size effect

As indicated above, concrete is a strongly heterogeneous material. Since the size of its components is not negligible in comparison with the dimensions of the elements, it is to be expected that the properties of the concrete mesostructure have a significant influence on the size effect. For this reason, the study of concrete heterogeneities depending on specimen size and its relation to the mechanical response is a field of scientific interest.

One of the most researched properties of the mesostructure is the coarse aggregate particle size distribution; specifically, the maximum aggregate size [82,92,93,108–110]. The reason is that this parameter is closely related to the length of the fracture process zone (Figure 2.3-3), which in turn determines the brittle-ductile behavior of the material, and consequently the size effect. In the late 1970s, Tanigawa & Yamada [92] already concluded that the specimen diameter/maximum aggregate size ratio significantly affected the size effect on compressive strength. Alam et al. [108] studied the size effect on the flexural response of quasi-brittle materials, but instead of scaling the specimens, he scaled the maximum aggregate size (which he calls the heterogeneity size). He proposed a size effect law, based on Bažant's SEL, which included the ratio of element size to maximum aggregate size (D/d_{max}). In a later work by the same group, Zhu et al. [109] performed an experimental study in which they not only considered different specimen sizes and maximum aggregate sizes, but also scaled the entire aggregate particle size

distribution curve. They concluded that the behavior was more ductile as d_{\max} increased, i.e., the size effect was reduced. In addition, they determined that the fracture energy increased linearly with increasing d_{\max} , while the stiffness number decreased.

In addition to the aforementioned components, an undesirable constituent is always present in concrete that significantly affects its mechanical response: pores. Several publications can be consulted that demonstrate the influence of porosity on the strength, stiffness or fatigue behavior of concrete, among other aspects [111,112]. However, to date, few works have studied the influence of pores on the scale effect [42,97,113,114]. This is largely explained by the fact that it is a non-controllable and random parameter by nature. Moreover, porosity analysis requires the use of complex techniques, such as micro-computed tomography (microCT) (Figure 2.3-10) or mercury intrusion porosimetry. Róžański et al. [114] used microCT to analyze porosity and pore size distribution in cylindrical specimens of mortar and gypsum, which were then subjected to compression tests. Gonzalez et al. [97] also used microCT to study the influence of the wall effect on the size effect in compression of SFRC. He concluded that the outer layer of the smaller specimens, despite having a similar thickness to that observed in the larger specimens, presented more porosity and larger pores, which could perhaps explain the inverse size effect obtained in the compressive strength.

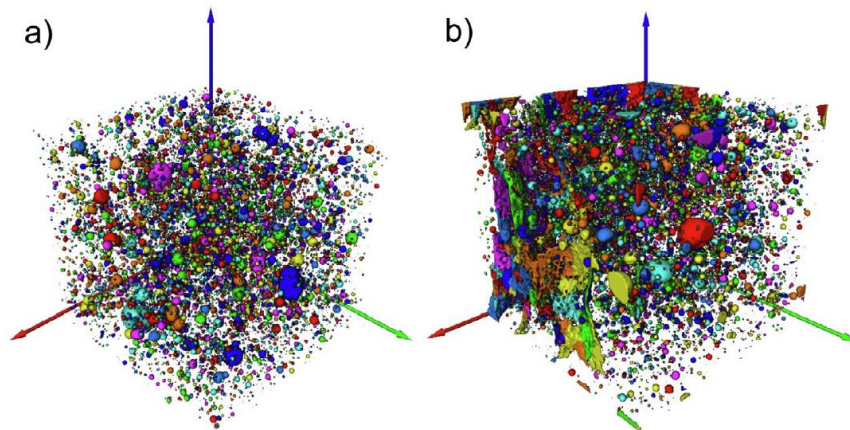


Figure 2.3-10. MicroCT analysis of a concrete specimen subjected to compressive fatigue: (a) pores before testing, (b) pores and cracks after testing [31].

In the specific case of SFRC, fibers largely determine the fracture behavior of concrete; therefore, it is very interesting to study the influence of fiber distribution and orientation as a function of specimen size. However, publications on this subject are still scarce. González et al. [97] analyzed by microCT the fiber orientation in SFRC specimens

of different sizes subjected to compressive fatigue. A certain wall effect was observed, although no significant results were obtained in relation to the size effect. Yoo et al. [84] carried out experimental work on the size effect under bending stresses in plain concrete and SFRC, varying the fiber type and slenderness. He analyzed the fiber orientations using image analysis techniques from high resolution photographs of crack surfaces. He concluded that the main reason explaining the size effect on the compressive strength of SFRC is the worse fiber orientation in the larger specimens, proposing different parameters to characterize the fiber distribution.

In addition to experimental work, several numerical studies on the influence of mesostructure on the size effect have also been carried out [113,115–117]. Wang et al. [113] analyzed by the finite element method (FEM) specimens of different sizes subjected to pure tension, considering coarse aggregates and pores with different contents, shapes and size distributions. Man & van Mier [116,117] used microCT to obtain the real mesostructure of concrete. Based on it, they studied the scale effect in bending and improved the fracture network model in concrete. Suchorzewski et al. [115] used microCT images to model the mesostructure of concrete and study the scale effect in cylindrical concrete specimens subjected to indirect tension (Figure 2.3-11).

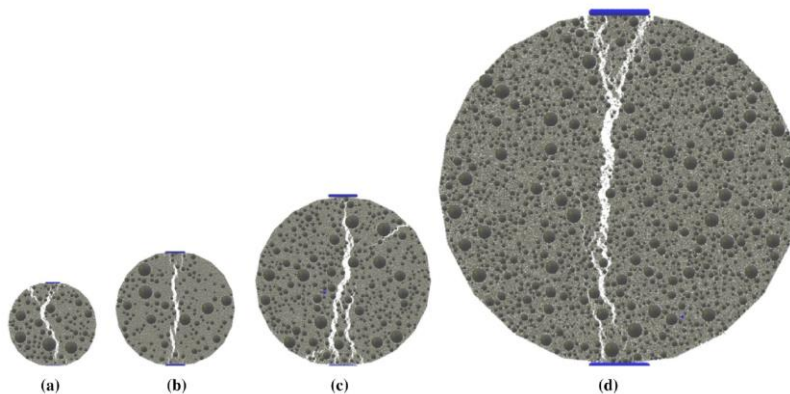


Figure 2.3-11. Crack patterns in indirect tensile test on cylindrical specimens with diameters ranging from 74 to 290 mm [115].

2.4 Analysis of the mesostructure of concrete with micro-computed tomography

The purpose of this subsection is to present the applications of micro-computed tomography (microCT) for the study of concrete components. First, an introduction to computed tomography (CT) technology is given, highlighting its combination with image analysis techniques, which is where its potential really lies. Then, the possibilities of microCT for the analysis of the concrete mesostructure, in particular, of the fibers in SFRC, porosity and cracks, are discussed. For this purpose, the most relevant publications are reviewed in each case, with special emphasis on those related to fatigue.

2.4.1 Introduction

2.4.1.1 Introduction to computed tomography

Computed tomography is a non-destructive technology that makes it possible to explore the internal structure of matter. It is based on the attenuation or loss of energy experienced by X-rays when they pass through a body, which is governed by the Beer-Lambert law (Eq. (2.4-1)):

$$I=I_0 \cdot \exp \left[- \int \mu(s) ds \right] \quad (2.4-1)$$

Where I is the final intensity of the X-ray beam, I_0 is the initial intensity and $\mu(s)$ is the linear attenuation coefficient along its trajectory. The latter parameter depends mainly on the density ρ of matter along the X-ray path. It is found that the ratio μ/ρ is approximately proportional to Z^3 , where Z is the atomic number of the element.

Consequently, the basic operating principle of CT is the direct relationship between the attenuation of X-rays and the density of the material they pass through. A CT scanner consists of three basic elements: an X-ray source, a flat-panel detector and a rotation base (Figure 2.4-1). The specimen is placed on the moving base, which rotates and moves vertically, so that each spot is traversed by X-rays in multiple directions. The CT scanner measures the attenuation of the beams (i.e., the difference between the intensity emitted by the source and that received by the panel), and finally calculates by interpolation the density at all points of the specimen.

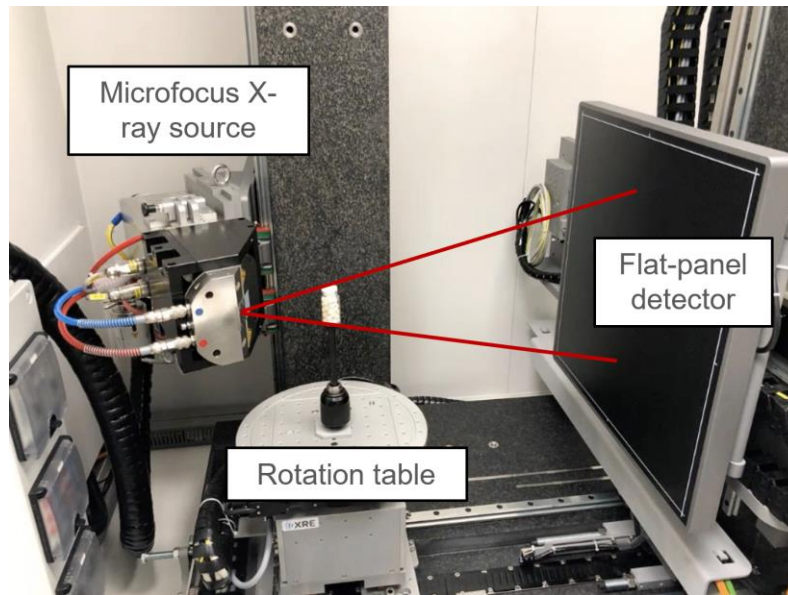


Figure 2.4-1. Interior of a microCT unit and identification of main elements.

CT technology has progressively improved over time. The conventional solution consisted of a source emitting linear X-ray beams (fan beam), which were received by a linear detector. Nowadays, most CT equipment in industry and research uses cone beam sources emitting X-ray beams incident on a flat detector panel. Among its main advantages are shorter acquisition time, increased image resolution and improved results in the 3D reconstruction process.

The practical result of a CT scan is a set of images (stack) in which each image represents a cross-section of the specimen at a given elevation. The software incorporated in CT scanners allows the reconstruction of the stack images, creating a three-dimensional image of the specimen. The resolution of a CT scan is defined by the size of the voxel (volumetric pixel), whose X and Y dimensions are given by the stack images, and whose Z dimension is the separation between consecutive images. Normally, voxels are cubic, so the resolution is indicated by a single value, given in microns. In addition, each voxel has a gray level that is associated with the average density of the specimen point it represents; for example, in 16-bit images, the gray range is between 0 and 65,535. Lower (darker) gray levels correspond to low densities, while higher (lighter) gray levels indicate high densities.

It is worth mentioning that, for the same CT device, the resolution depends on the size of the specimen; specifically, on its cross-section. The smaller its dimensions, the higher the resolution. In any case, each CT scanner has a maximum achievable resolution, and this is where the difference between conventional CT and microCT lies. While in

traditional CT the maximum resolution is about 100 μm , microCT scanners are equipped with X-ray sources with microfocus tubes, capable of achieving resolutions of the order of 10 μm , or even less.

On the other hand, the CT has certain limitations that should be pointed out. First, the specimen size is limited. Dense and very thick specimens absorb a large amount of energy, so the X-ray flux received by the detector is very low, resulting in poor quality images. On average, in microCT equipment the maximum cross-sectional dimensions of the specimens are about 15-20 cm, although it depends on the energy of the microfocus tube and the density of the material. Secondly, as already discussed, the resolution is a function of the specimen size and the type of scanner used. Consequently, when analyzing the mesostructure of a material, the maximum detectable defect size (pores, cracks, etc.) must be taken into account. Finally, since the basis of CT relies on the difference in density of the materials, the more similar the densities of the components of a specimen, the more difficult it will be for the CT equipment to differentiate between them; i.e., the gray level of the voxels representing each material will be very similar. In concrete, this can be a problem when, for example, distinguishing the coarse aggregate from the matrix. Possible alternatives in these cases are to improve the resolution (with smaller specimens, or with better scanners), or to use advanced segmentation procedures, such as those based on artificial intelligence (AI).

2.4.1.2 Image analysis

As mentioned, the result of a CT scan is a set of grayscale images, from which the 3D reconstruction of the specimen can be made. In materials engineering, the mere observation of CT images does not offer many possibilities, since what is really interesting is to quantitatively characterize the components of the internal structure of the specimen. This is precisely the goal of image analysis techniques.

The post-processing of a CT stack by image analysis can be broadly divided into two stages: image preparation and segmentation of the specimen components or phases. On the one hand, the sample preparation tasks consist of: selecting the volume of interest, discarding what is irrelevant (surrounding air, etc.) and thus optimizing the computation time; repositioning the images according to the desired coordinate system, so as to facilitate the interpretation of the results; and applying filters to improve some aspect of the images (sharpness, etc.). On the other hand, the fundamental step is segmentation, i.e. the

separation of the different components of the specimen in order to determine their geometrical properties. For example, the segmentation of the fibers in SFRC allows not only to obtain the real volume of fibers, but also to characterize them at the individual level, obtaining from each one its position, orientation, etc. There are different segmentation techniques, which are described below, ranging from the simplest to the most complex:

- a) **Thresholding:** This is the most immediate method and consists of selecting the voxels whose gray level is between certain values, so that this range of gray is associated with the density of a given component of the specimen. For example, in the SFRC specimens in this thesis, the fibers fit reasonably well in the range 40,000-65,535 (Figure 2.4-2). However, there are several drawbacks to this technique. One of them is that the selection of the gray band responds to subjective criteria. In this regard, automatic methods have been developed to identify the components of a specimen from the shape of the gray distribution histogram; however, they are not very versatile and are successful only in certain situations. Another problem is that, when elements of the same material are in close proximity, thresholding groups them together because it is not able to recognize that they are different elements (Figure 2.4-2). Consequently, these problems reduce the quality of the analysis, making it difficult to interpret the results.

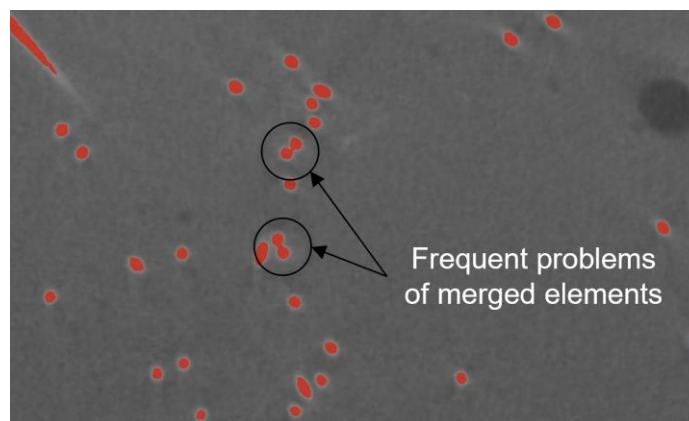


Figure 2.4-2. Simple thresholding of fibers in a SFRC specimen and identification of errors due to connected fibers.

- b) **Watershed transform:** This technique interprets grayscale images as a topographic map, in which the gray level of each voxel represents its height. Using auxiliary techniques, such as the distance transform, erosion/dilation processes, etc., it is possible to isolate the voxels of higher intensity to finally define the dividing lines. These lines divide adjacent "watersheds", i.e., elements that are theoretically in

contact. Figure 2.4-3 summarizes the watershed transformation process. This technique largely solves the drawbacks of simple thresholding. On the one hand, the level of objectivity is higher since the boundaries of the elements are defined automatically by the distance transform. On the other hand, it is able to differentiate elements of the same material that a priori are in contact.

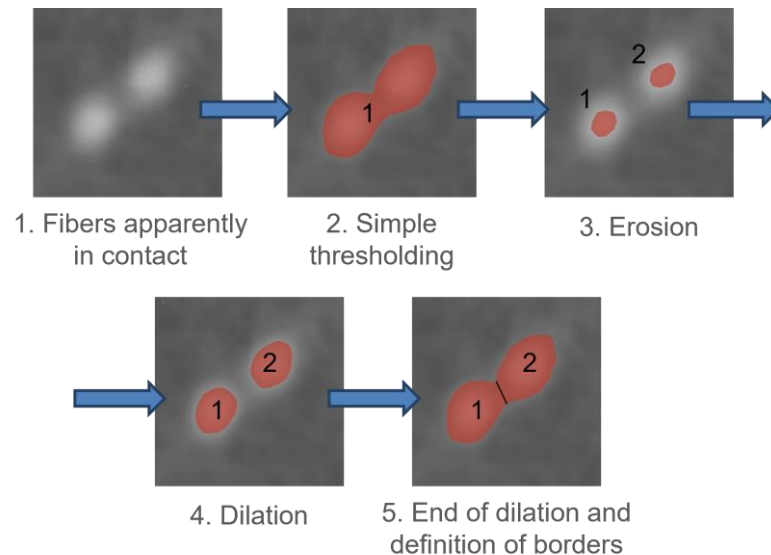


Figure 2.4-3. Process of the segmentation technique of watershed transform.

- c) Artificial intelligence (AI) models: There are particularly complex situations in which even the watershed transform does not give good results. For example, this is the case of fiber segmentation in the A3 series specimens of this work. Due to the large accumulation of fibers, false absorption halos appear in these specimens [118]. This is a type of artifact that appears when X-rays pass through highly absorbing elements (high density) that are in low absorption media (low density). This causes that at the interface between closely spaced fibers there is no clear decrease in the intensity of the voxels, making the dividing transformation ineffective. The result is the formation of clusters of a large number of fibers that greatly distort the results obtained (Figure 2.4-4).

AI models are capable of segmenting components based on geometrical shape. For example, in the case of fibers, in a first step several fibers are manually identified. This information is incorporated into the model, which then seeks to adapt the acicular geometry of the fibers to the voxels of interest, obtained from previous thresholding and/or watershed transform processes. When a set of voxels containing several fibers appears, the model detects that this geometry is anomalous and

tries to adjust the optimal number of individual fiber geometries to this volume. Finally, it separates the fibers that form it (Figure 2.4-4). It is worth mentioning that usually several iterations have to be performed to adjust the AI model for optimal results. Another application of segmentation with AI models is to differentiate components whose density is very similar, such as matrix and coarse aggregate, or pores and polypropylene fibers.

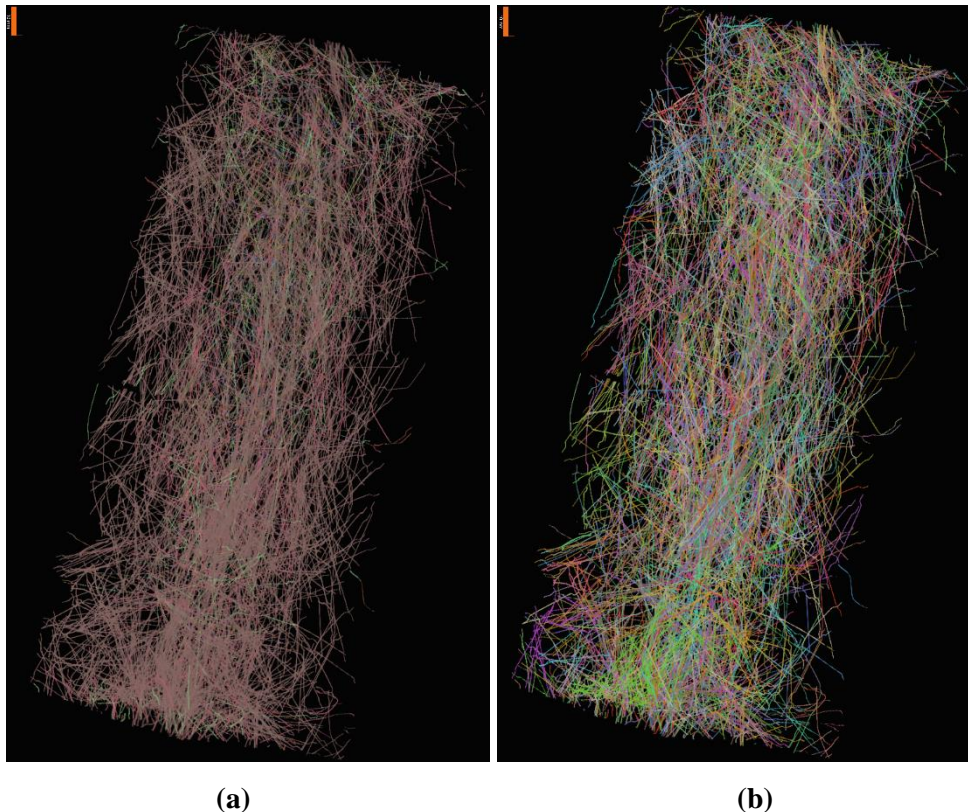


Figure 2.4-4. Fiber segmentation: (a) applying watershed transform and (b) applying watershed transform together with an artificial intelligence model.

2.4.1.3 MicroCT in concrete analysis

As is well known, CT is closely related to medicine, since it emerged in the 1970s as a noninvasive technique to study and detect pathologies in the internal parts of the human body. However, nowadays its use is widespread in many fields of science. The state of the art of microCT applied to the analysis of engineering materials can be found in [119,120]. With respect to concrete, it is known that its mechanical behavior at the macroscopic level depends largely on its mesostructure. However, it is a heterogeneous material in which the distribution of its components is random and therefore difficult to control. In this context, microCT offers many possibilities, since it makes it possible to

analyze the phases of the concrete mesostructure (matrix, coarse aggregate, pores, fibers, cracks, etc.), so that correlations can be established with the mechanical response.

One of the first works in which CT was applied for the exploration of concrete mesostructure was that of Morgan et al. [121], in which they analyzed reinforced concrete specimens, determining the location and volume of rebars, as well as the proportions of coarse aggregate and matrix. The accuracy was in the order of 1 mm. Today, the use of microCT in concrete analysis is widespread. Among its applications, three concrete components that are usually studied with microCT can be highlighted: steel fibers in SFRC, porosity and cracking.

2.4.2 Fibers in SFRC

One of the main applications of microCT to concrete is the analysis of the distribution of steel fibers in SFRC. The difference in density between steel and the other materials in the concrete makes the fiber segmentation process relatively straightforward. The major drawback is usually separating the fibers themselves when the content is high, in which case advanced segmentation techniques, such as those described in the previous subsection, can be used. Although less common, micro CT is also used in other fiber-reinforced concretes, such as those made of polypropylene or carbon.

The most representative parameters of the fibers are position and orientation; therefore, in many works these parameters are studied, trying to establish correlations with the behavior in bending, compression, etc. [122–125]. Zhou & Uchida [125] fabricated high-performance SFRC slabs and analyzed the fiber orientation as a function of mix fluidity, mixing time and formwork geometry. In addition, they extracted prismatic specimens that they then subjected to flexure, finding a strong correlation between the ultimate flexural strength and some fiber distribution parameters; in particular, the orientation factor and the number of fibers in the crack plane (Figure 2.4-5). Groeneveld et al. [124] studied the dynamic response in compression in SFRC cores extracted from a beam according to different directions, such that the specimens had different preferred fiber orientations. They concluded that, although the dynamic compressive strength was independent of orientation, ductility increased with the proportion of fibers oriented perpendicular to the direction of applied load.

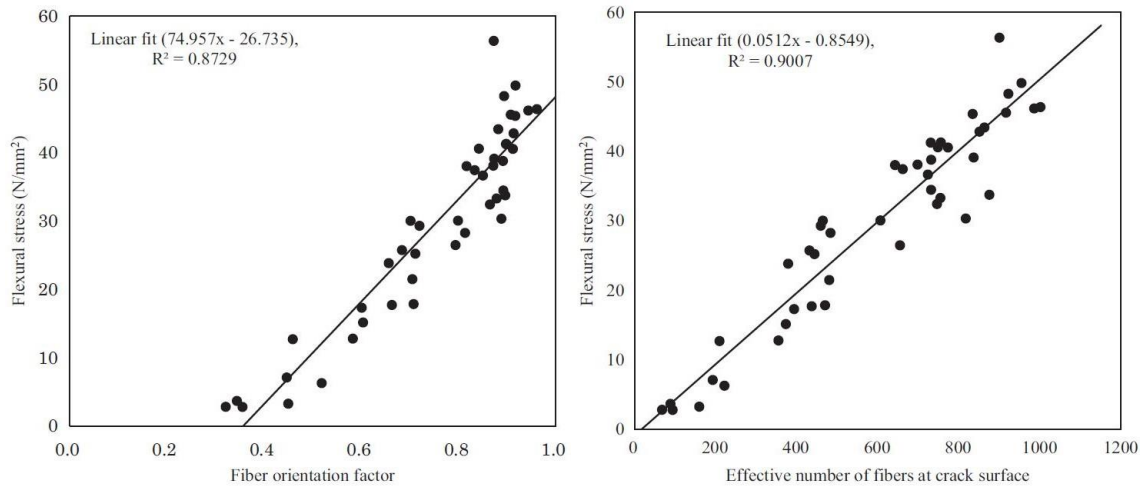


Figure 2.4-5. Correlation between fiber distribution and orientation, and flexural strength. [125].

MicroCT is also used to study the influence of fibers on the fatigue response of concrete [55,61,126,127]. Vicente et al. [61] examined the effects of fiber content and orientation in concrete subjected to both static and fatigue compressive loading. For this purpose, they scanned the specimens with microCT after the tests, so that they could study the interaction between the fibers and the crack patterns (Figure 2.4-6). They concluded that the observed scatter in the compressive fatigue life can be partially explained by the scatter in the fiber distribution itself.

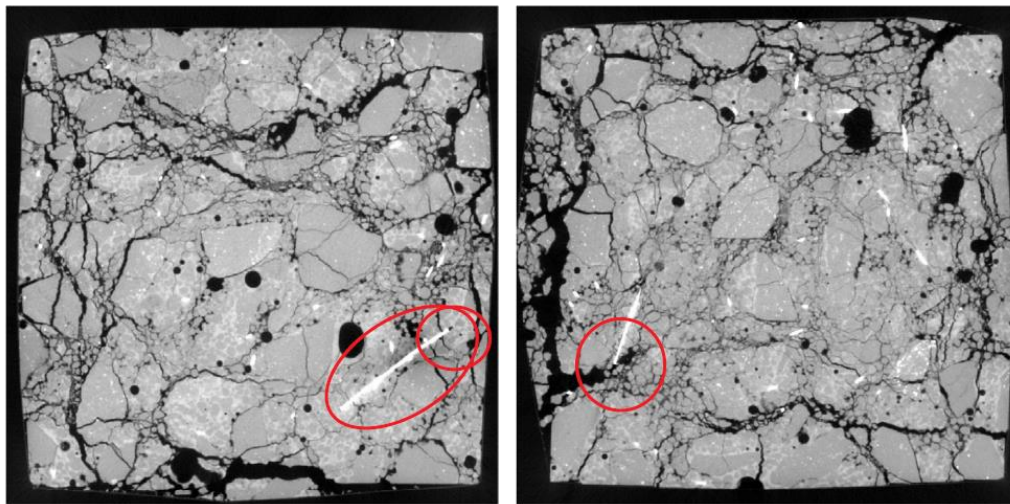


Figure 2.4-6. MicroCT images showing the bridging effect of fibers on cracks caused by compressive fatigue [61].

On the other hand, a particular case of mechanical testing in SFRC is the pull-out testing in fibers, consisting of pulling fibers partially embedded in concrete until failure. This is especially interesting for the study of SFRC under flexural stress (both static and

dynamic), since in those cases the fibers govern the behavior. MicroCT technology can also be useful in these situations, as demonstrated by Fataar et al. [127], who analyzed the failure mechanisms in fibers subjected to fatigue pull-out tests, in which certain levels of pre-slip had been previously induced.

2.4.3 Porosity

Another application of microCT is the study of concrete porosity; that is, the determination of parameters such as pore volume and position, pore size distribution, etc. In this regard, it is worth mentioning that some authors criticize this use of microCT, arguing that the macroscopic response of concrete is governed by micropores ($< 1 \mu\text{m}$), undetectable for current microCT scanners. For this reason, in certain cases it is advisable to combine microCT with other techniques that allow the detection of smaller pores, such as mercury intrusion porosimetry (MIP). MIP is capable of detecting pores in the nanometer range, although it has the disadvantages that it only offers the statistical distribution of the pore size and the specimen size is very limited. In any case, considering the resolution of current scanners, and in anticipation of the continuous development of the technology, microCT offers many possibilities for the exploration of concrete porosity, as reported in this review article by Vicente et al. [128].

One of the most widely followed lines of research in this field is the study of the influence of certain admixtures on the final porosity of concrete [129,130]. In this regard, the work of Kang et al. [130], who analyzed the effects of the addition of superabsorbent polymer (SAP) in high-strength concrete, stands out. They combined microCT with MIP to study a wide range of pore sizes (from 3 nm to 10 mm), examining two opposing effects on pore structure: matrix densification due to internal curing and the increase of large pores as a result of retained SAP particles. On the other hand, Gonzalez et al. [129] fabricated specimens with various contents of air-entraining agent (AEA), which they scanned with microCT to examine the porosity (Figure 2.4-7). They concluded that the addition of AEA not only increases the total porosity, but also the number of pores, their size and their shape factor. Furthermore, they observed that the effects of AEA are only effective up to a certain content (in this case, 0.3%), after which the porosity begins to decrease.

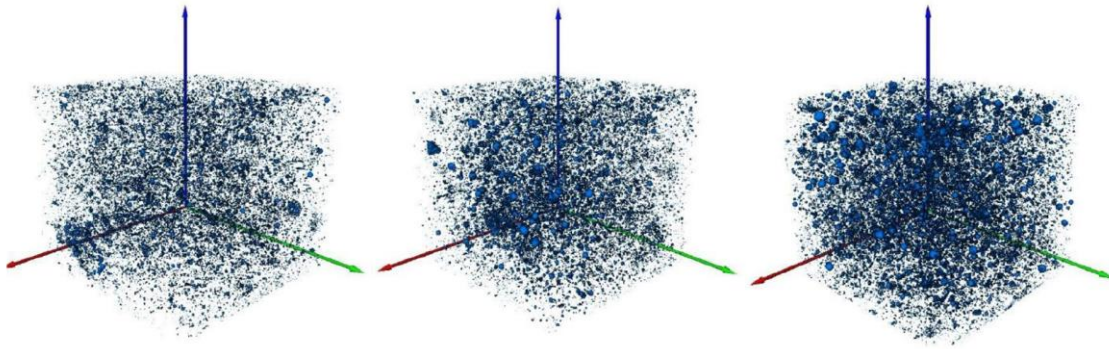


Figure 2.4-7. Porosity in specimens with different content of air-entraining agent; from left to right, 0, 0.1% and 0.2%. [129].

In the specific case of SFRC, some investigations focus on the influence of fiber addition on porosity [131,132]. Mínguez et al. [131] studied the evolution of porosity at early ages of high-strength mortar with and without fibers. They determined that the presence of fibers increased pore volume as well as pore size.

Other applications of microCT are the analysis of porosity in special concretes, such as permeable concrete or concrete made with recycled aggregates, the study of the evolution of pore structure with curing time [131], or the evaluation of the wall effect on porosity [97].

On the other hand, several works have been published using microCT to analyze the influence of porosity on the fatigue behavior of concrete [97,132,133]. Vicente et al. [133] studied the effects of pore morphology on the compressive fatigue response of concrete. The results revealed an inverse relationship between porosity and fatigue life. In addition, they observed that the most harmful pores were the large ones, which favored stress concentration phenomena and predictably the initiation of cracks. On the other hand, thermal fatigue also arouses some scientific interest [129,134]. Grubeša et al. [134] evaluated the porosity in mortar specimens subjected to freeze-thaw cycles and then to compression and flexural tests. They concluded that the most determinant factor in freeze-thaw strength is the connectivity between pores.

2.4.4 Cracking

The last application of microCT to be addressed is the study of cracking in concrete, which can be due to multiple causes, such as mechanical stresses, shrinkage, high temperatures, freeze-thaw action, etc. Post-processing of CT images for cracking analysis requires advanced knowledge of image analysis, since both cracks and pores are "formed"

by air. Consequently, if both phases are to be separated, complex segmentation processes have to be carried out, as described in subsection 2.4.1.

In the scientific literature there are a number of papers studying concrete cracking by microCT [123,135–137]. Skarżyński & Suchorzewski [123] performed wedge splitting tests on cubic specimens of plain concrete and reinforced with various types of steel fibers. The major novelty of this work is that they were able to perform microCT scans during the test, without the need to unload the specimens (Figure 2.4-8). In this way, they were able to evaluate the progress of the fracture process zone, calculating the properties of the crack at each moment (volume, width variation along its length, etc.).

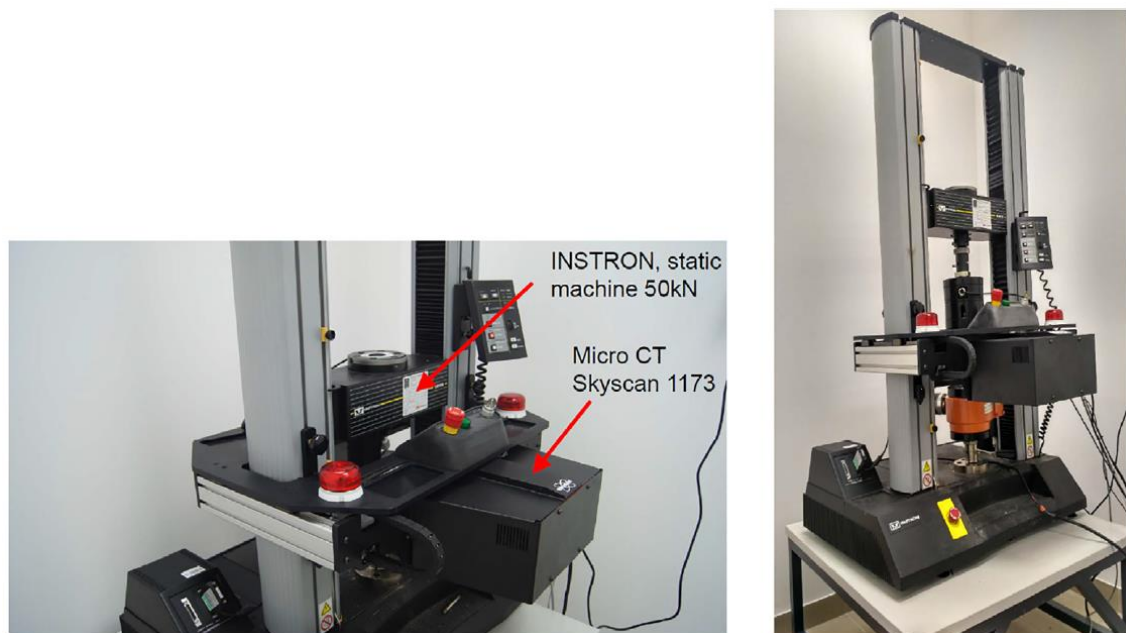


Figure 2.4-8. In situ microCT system, with Skyscan 1173 microCT scanner mounted on an Instron 5569 50 kN testing machine [123].

MicroCT images are sometimes used to calibrate fracture mechanics models so that they are able to predict the behavior of concrete [135,137]. Yang et al. [135] studied the evolution of cracking in cubic concrete specimens subjected to indirect tension (splitting test). They performed in situ microCT scans, which allowed them to analyze the evolution of the different phases of the concrete (matrix, coarse aggregate, pores and cracks) (Figure 2.4-9). Finally, with the results they created finite element models of the real specimens and adjusted them to predict the fracture behavior of the concrete. Nitka & Tejchman [137] analyzed the development of the fracture process zone in notched concrete specimens subjected to flexural stress. In addition, based on microCT images, they developed

DEM (discrete element method) models with which they obtained very satisfactory results in terms of load vs CMOD response.

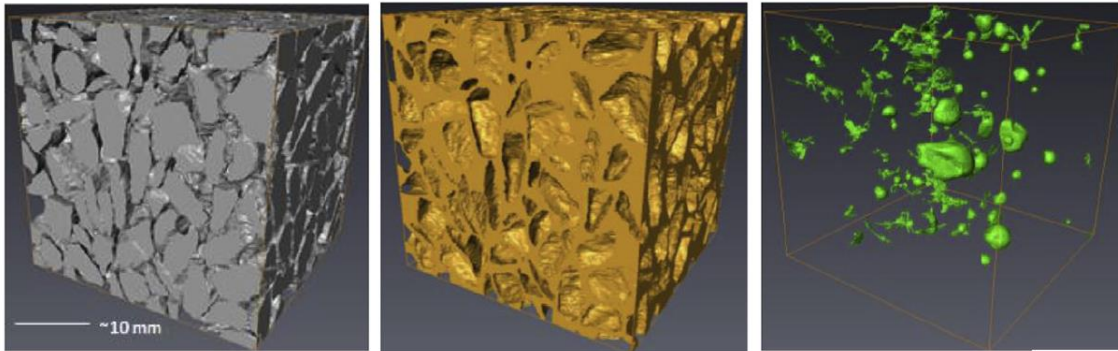


Figure 2.4-9. Segmentation of the different concrete phases (coarse aggregate, matrix and pores) for the development of finite element models [135].

The assessment of cracking under fatigue loading is also a line of research of great interest [55,68,126,138]. Skarżyński et al. [68] studied the increase of cracking under cyclic compressive loads in plain concrete specimens, which were scanned with microCT at different times throughout their fatigue life (Figure 2.4-10). They concluded that the evolution of crack volume with increasing fatigue damage, understood as the percentage over the total number of cycles, has a strongly nonlinear character. Furthermore, they observed that the total crack volume in the fatigue tests was 30% higher in comparison with the static tests. Vicente et al. [55] performed flexural fatigue tests on SFRC pre-cracked specimens with 1% and 2% fibers, respectively. After the tests, they extracted cores from the crack plane zone, which were scanned with microCT to analyze cracking, failure mechanisms of the fibers, etc.

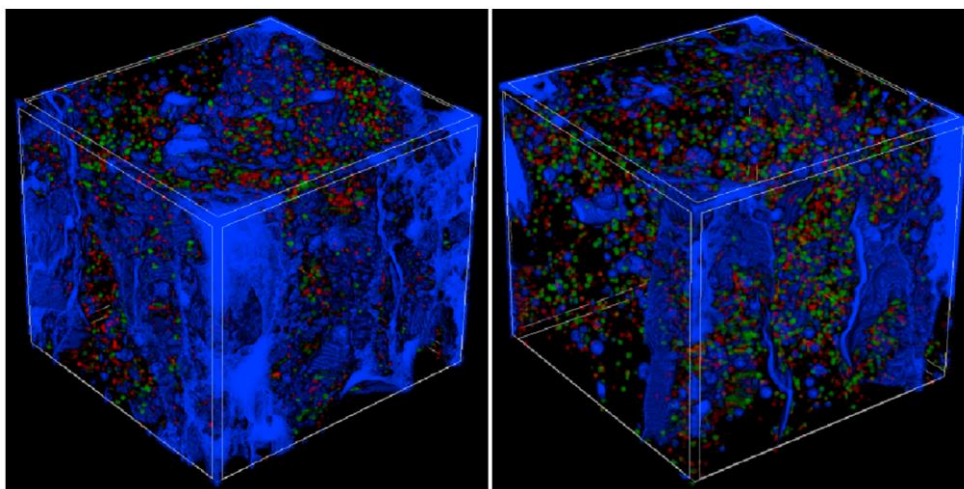


Figure 2.4-10. Identification of pores and cracks in cubic specimens subjected to compressive fatigue (pores < 1 mm in red, 1-2 mm in green and > 2 mm in blue) [68].

3 MATERIALS AND METHODS

3.1 Concrete manufacturing

3.1.1 Materials

In this subsection, the components used for the manufacture of the different concrete series are described, justifying the reasons for their choice.

First, the cement used is CEM I 52.5 R type, produced by the company Portland Valderrivas (Pamplona, Spain) at its factory in Venta de Baños (Palencia). Class I cement has been chosen because it is the most generic and thus eliminates any uncertainty that one or another addition could introduce in the results. The characteristic strength of 52.5 MPa is essential to achieve a high-strength concrete. In addition, rapid hardening is desirable to speed up the demolding and concentrate the manufacturing campaign in the shortest possible time.

Secondly, as coarse aggregate, rolled siliceous gravel of the 4/10 fraction was used, and as fine aggregate, washed siliceous sand of the 0/4 fraction. Both materials were supplied by the company Fenorte (Burgos, Spain). It is worth mentioning that the maximum size of the coarse aggregate is only 10 mm because the steel fibers are 30 mm and, according to Annex 7 of the Spanish Structural Code [3], it is recommended that the length of the fibers be at least 2 times the size of the larger aggregate, with values of 2.5 to 3 times being usual.

Since the sand is washed and therefore has a low fines content (1.7% according to the technical data sheet), filler has also been used; specifically, limestone filler I-50 manufactured by the company Industrial Mediavilla Cordero (Guardo, Palencia, Spain). This material is obtained from high-purity marble limestone, with a calcium carbonate content of over 98% and a particle size of less than 63 μm .

Third, two additives were used. First, MasterEase 5025 superplasticizer from BASF (Ludwigshafen am Rhein, Germany). This is a latest-generation superplasticizer admixture based on the novel technology of PAE polymers (polyaryl ether phosphonic condensates). It is especially indicated for the manufacture of high-strength self-compacting concretes since it makes it possible to achieve very fluid consistencies while maintaining relatively low water/cement ratios. On the other hand, MasterRoc MS 685 nanosilica, also

from BASF, has been added. It consists of an amorphous nanosilica suspension with very interesting properties: it improves workability, prevents water migration (critical for achieving optimum consistencies in self-compacting concretes) and reduces porosity (it reacts by creating a stable microscopic mineral).



Figure 3.1-1. Superplasticizer admixture (left) and nanosilica suspension (right).

Finally, Dramix RC-80/30-CP steel fibers, produced by Bekaert (Zwevegem, Belgium), were used in the fiber-reinforced concrete series. These are hooked-end fibers of 30 mm length and an aspect ratio of approximately 80. Table 3.1-1 shows its main characteristics.



Figure 3.1-2. Dramix RC-80/30-CP steel fibers.

Table 3.1-1. Characteristics of the steel fibers used.

Geometry	Length (mm)	30.0
	Diameter (mm)	0.38
	Aspect ratio l/d	78.9
Material prop- erties	Density (kN/m ³)	78.5
	Tensile strength (MPa)	3,070
	Modulus of elasticity (MPa)	210,000

The length of the fibers was chosen taking into account the requirements of the American standard ASTM C1609 [6], which indicates that the length of the fibers should not exceed 1/3 of the minimum dimension of the concrete specimens. In this case, the minimum dimension of the S-size specimens is 75 mm, so the maximum length of the fibers should be 25 mm. However, the manufacturers consulted have not offered commercial fibers of that length, with a gap between the small ones of the order of 13 mm and the larger ones of 30 mm. In view of this situation, 30 mm fibers have been chosen for several reasons. First, because with the smaller fibers the maximum recommended aggregate size [3] would be around 5 mm, falling within the range of mortars, rather than concretes. Second, because the ratio fiber length / minimum dimension of 0.4 obtained for 30 mm fibers coincides with the maximum recommended, implicitly, by the UNE-EN 14651 standard [7]. And third, because the longer the fiber length, the larger the cross-section and therefore the greater the definition of the images in the analysis with micro-computed tomography.

Finally, other properties of the fibers used are that they are made of high carbon steel ($0.55 < \%C < 2$) and that they have undergone a galvanizing process. The choice of these latter characteristics is not intentional and is purely in response to the availability of the supplier's stock.

Finally, a table summarizing the materials used for the manufacture of concrete is included.

Table 3.1-2. Materials used in the manufacture of concrete, together with their typology.

Material	Tipo
Cement	CEM I 52,5 R
Coarse aggregate	Rolled siliceous gravel 4/10
Fine aggregate	Washed siliceous sand 0/4
Filler	Limestone filler (100% vol. < 63 μ m)
Water	
Superplasticizer	MasterEase 5025 (BASF)
Nanosilica	MasterRoc MS 685 (BASF)
Steel fibers	Dramix RC-80/30-CP (Bekaert)

3.1.2 Concrete mix design

Self-compacting concrete is a type of concrete with very particular characteristics. This implies that traditional batching methods for the design of conventional concretes, such as Fuller, Bolomey, ACI [139], De la Peña, etc., are not valid. Normally, the application of such methods would lead to concretes with an insufficient amount of fines, and therefore with a low segregation resistance, being very complicated to reach the self-compacting condition.

On the other hand, the dosage of self-compacting concretes is highly sensitive to small variations in the quality and proportions of their components. This is due to the fact that the admissible range of properties (slump, etc.) for these concretes is quite narrow, and many other variables also come into play: origin of the aggregates, granulometry of the filler, type of superplasticizer, compatibility between admixtures, etc. This aspect has aroused great scientific interest during the last decades, with very interesting proposals for the design of self-compacting concretes [9,140]. However, there are still no universal batching methods. Instead, it is common for standards to indicate certain guideline recommendations [3,141].

Considering the above, an experimental study of dosages has been planned. Four series of concretes have been proposed: a reference one without fibers and three more with increasing fiber content. As will be justified later, the amounts of fibers considered are 0.3%, 0.6% and 1% by volume of concrete, respectively. The objective is to ensure that the only difference between the four dosages is the fiber content. Therefore, in all of them, the self-compacting condition must be achieved without the need to vary any other component, such as superplasticizer, etc.

To validate the self-compactness condition, the flowability (by means of the slump test according to UNE-EN 12350-8 [142]) and the resistance to segregation will be evaluated. The following table shows the admissible ranges of flowability in the slump test. As for segregation, there is no standardized method to measure it, but it can be analyzed qualitatively from the slump test. In general, it is accepted that concrete is not segregated when a uniform distribution of the coarse aggregate and no exudation is observed around the perimeter of the final slump flow.

Table 3.1-3. Requirements for self-compactness in the slump test [3].

Measured parameter	Permissible range
T_{50}	$T_{50} \leq 8 \text{ s}$
d_f	$550 \text{ mm} \leq d_f \leq 850 \text{ mm}$

There are other tests to evaluate the performance of self-compacting concretes, such as the V-funnel, the L-box and the slump with J-ring. However, the first one measures the flowability, as does the slump test, and the other two measure the resistance to blockage when passing between rebars, which is irrelevant in this case, since we are dealing with fiber-reinforced concrete.

For the experimental study of dosages, the series with the most fibers has been taken as the starting point, i.e., that of 1% by volume of concrete. It is reasonable to assume that this series will be the least fluid, due to the interlocking effect caused by the fibers, and therefore the most difficult to achieve self-compacting properties. Consequently, if this series achieves self-compactness, it is to be expected that the rest will also do so. However, care must be taken to ensure that they are not too fluid and exceed the limit of Table 3.1-3.

The initial dosage has been established following the recommendations of Annex 17 of EHE-08 [5]. The standard indicates certain limitations regarding the content and proportion of the materials. The most important ones are the following:

- The total fines content (particles $< 0.125 \text{ mm}$), i.e., cement and filler, should be in the range $450\text{-}600 \text{ kg/m}^3$ of concrete.
- The cement content should be in the range $250\text{-}500 \text{ kg/m}^3$.
- The volume of the concrete paste (water, cement, filler and admixtures) should be more than 350 L/m^3 .

- The proportion of coarse aggregate to total aggregate should not exceed 50%, and its maximum size should be less than 25 mm.

The following tables show, on one side, the initial dosage and, on the other side, the verification of the requirements of Annex 17.

Table 3.1-4. Initial dosage of the experimental dosage study.

Material	Dosage per m ³		
	Weight (kg)	Volume (L)	
Cement	400.0	129.0	
Coarse aggregate	748.9	288.0	
Fine aggregate	915.6	352.1	
Filler	180.0	69.2	
Water	160.0	160.0	0.40 w/c ratio
Superplasticizer	6.0	5.7	1.5% wgt. cem.
Nanosilica	16.0	14.2	4.0% wgt. cem.
Steel fibers	78.5	10.0	1.0% vol. conc.
	2504.9	1028.3	

Table 3.1-5. Verification of the criteria of Annex 17 in the initial dosage.

Material	Content	Permissible range
Fines	595.6 kg/m ³	450-600 kg/m ³
Cement	400.0 kg/m ³	250-500 kg/m ³
Paste	378.1 L	> 350 L/m ³
Coarse aggregate	45.0%	< 50% aggregates

The quantities of each component are justified below. As mentioned above, the content of cement, water, aggregates and filler has been calculated considering the criteria of Annex 17. The amount of cement is higher than the minimum recommended because the objective is to obtain a high-strength concrete, in the range of 80 MPa $f_{ck,28}$. For the same reason, the water/cement ratio is 0.40, which is rather low. As for the admixtures, the maximum dosage recommended by the manufacturer (1.5%) has been used for the superplasticizer admixture, and for the nanosilica, a value a little lower than the recommended maximum of 5%. Finally, the fiber content is 1%, since, as mentioned above, the series with the most fibers has been taken as the starting point.

Once the initial dosage was determined, the concreting tests began. For this purpose, small-volume batches (about 18 L) were made, together with the corresponding slump

tests. If the batch did not meet the self-compacting requirements in terms of fluidity and resistance to segregation, a new batch was made, slightly modifying the quantities of the components. The initial dosage was not adequate, and about four more tests had to be carried out until the optimum consistency was achieved. In summary, the modifications that were made were: increase of the superplasticizer (exceeding the maximum recommended), slight increase of the nanosilica, increase of the filler (exceeding the limit of Annex 17) and reduction of the coarse aggregate and the fine aggregate.

The table below shows the final dosage. In addition, comparative photos of the slump tests for the initial and final dosages are included.

Table 3.1-6. Definitive dosage after the experimental dosage study.

Material	Dosage per m ³		
	Weight (kg)	Volume (L)	
Cement	400.0	129.0	
Coarse aggregate	538.2	207.0	
Fine aggregate	847.1	325.8	
Filler	448.8	172.6	
Water	160.0	160.0	0.40 w/c ratio
Superplasticizer	16.0	15.1	4.0% wgt. cem.
Nanosilica	20.0	17.7	5.0% wgt. cem.
Steel fibers	78.5	10.0	1.0% vol. conc.
	2508.5	1037.2	

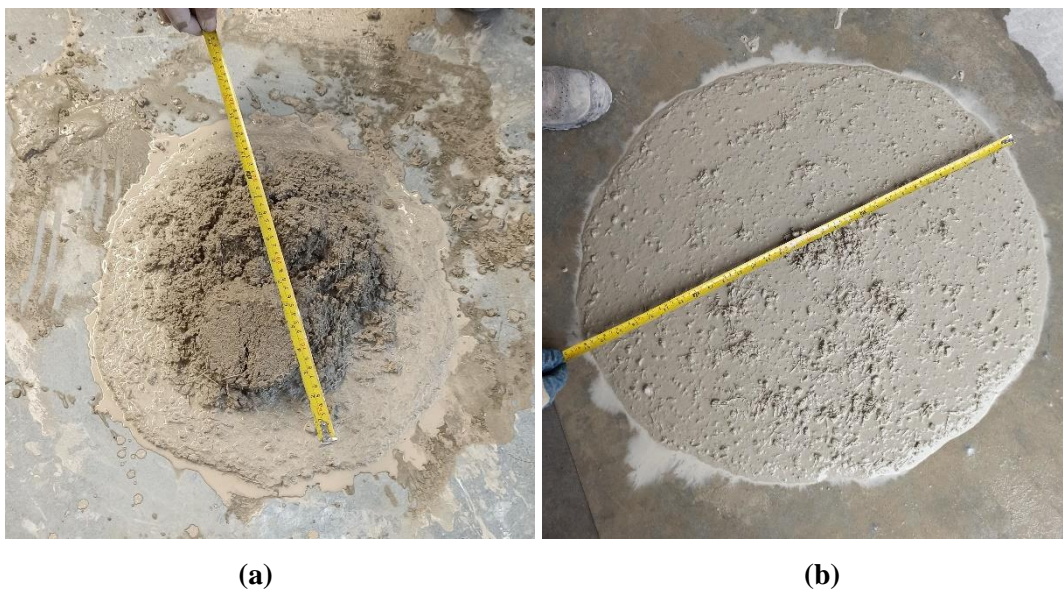


Figure 3.1-3. Comparison of the slump flow: (a) starting dosage and (b) final dosage.

After determining the final dosage with 1% fibers, an identical batch was made, but with 0% fibers. As expected, the fluidity of this batch was higher, although without exceeding the limits of the standard (Table 3.1-3). Thus, the dosages of the four series of concrete were defined, which are shown in this table.

Table 3.1-7. Final dosages (per m³) for the four series of concrete.

Material	Series			
	A0	A1	A2	A3
Cement	400.0			
Coarse aggregate	538.2			
Fine aggregate	847.1			
Filler	448.8			
Water	160.0			
Superplasticizer	16.0			
Nanosilica	20.0			
Steel fibers	0.0	23.6	47.1	78.5
w/c ratio	0.4			
Superpl. (% wgt. cem.)	4.0%			
Nanos. (% wgt. cem.)	5.0%			
Fibers (% vol. conc.)	0.0%	0.3%	0.6%	1.0%

A table with the verification of the criteria of Annex 17 of the EHE-08 for the final dosage is included below. In general, it can be concluded that the recommendations of the standard are reasonably in line with the results obtained. The exception is the amount of fines, which greatly exceeds the recommended range. This can be explained by the fact that, being a high-strength concrete, the cement content is very high (400 kg/m³). Therefore, no matter how little filler is added, it is relatively easy to exceed the upper limit of 600 kg/m³.

Table 3.1-8. Verification of the criteria of Annex 17 in the final dosage.

Material	Content	Permissible range
Fines	863.2 kg/m ³	450-600 kg/m ³
Cement	400.0 kg/m ³	250-500 kg/m ³
Paste	494.4 L	> 350 L/m ³
Coarse aggregate	38.9%	< 50% aggregates

Finally, with respect to the fiber dosages chosen, it should be mentioned that the minimum dosage corresponds to that marked by the manufacturer, which according to the

technical data sheet is 25 kg/m^3 ($\approx 0.32\%$). As for the maximum, 1% was considered because it is a usual dosage that is often chosen as the upper limit in experimental campaigns, as has been verified in the literature consulted. Thus, the three fiber dosages were defined: 0.3% (low), 0.6% (medium) and 1% (high).

3.1.3 Concreting of test specimens

The manufacture of the concrete was carried out in the Laboratory of Large Structures of Civil Works of the University of Burgos during the months of November and December 2020. The ambient temperature and relative humidity were systematically controlled during all the concreting days, with mean values of $16.6 \pm 1.1 \text{ }^\circ\text{C}$ and $42.0 \pm 7.4 \%$, respectively. The variations were considered to be minor and did not significantly affect the concreting conditions. Therefore, no special measures were taken in this respect.

A vertical-axis concrete mixer model C0199/11, manufactured by Controls (Liscate, Italy), with a useful capacity of approximately 100 L, was used for concreting.



Figure 3.1-4. Vertical-axis concrete mixer used.

Each series consists of a total of 40 specimens: 8 cylindrical ones of 150x300 mm (named CL), 16 prismatic ones of 75x75x300 mm (named PR-S, or simply S) and 16 prismatic ones of 150x150x600 mm (named PR-L, or simply L). Taking into account the capacity of the concrete mixer, 4 batches per series were carried out, divided as shown in Table 3.1-9.

Table 3.1-9. Distribution of specimens per batch, in each series.

Batch No.	CL 150x300	PR-S 75x75x300	PR-L 150x150x600	Volume (L)
1	2	4	4	71.4
2	2	4	4	71.4
3	2	4	4	71.4
4	2	4	4	71.4
	8	16	16	285.4

It is observed that the volume of concrete produced in each batch is the same. This ensures that the energy per unit volume provided by the concrete mixer is always constant, thus avoiding possible alterations in the consistency or other final characteristics of the concrete. The volume of concrete per series is 285 L, so the total volume of concrete produced in the 4 series is 1.14 m³.

As for the specimen molds, traditional steel molds were used. In the case of the 75x75x300 mm specimens, since this was not a standard size, molds of 100x100x400 mm were used, reduced with pieces of three-layer formwork board.



Figure 3.1-5. Types of molds used: cylindrical 150x300 mm, prismatic 150x150x600 mm and prismatic 100x100x400 mm with reductions.

Below is a step-by-step description of the concreting process of the batches of each series:

1. First, the materials are weighed. Given the volume of the batches, the solid components are weighed using a wheelbarrow attached to the laboratory bridge crane by means of a crane scale (Figure 3.1-6). The scale has a maximum capacity of 200 kg and an accuracy of 0.5 kg. The rest of the materials (water, additives and fibers) are weighed on a traditional scale with a capacity of 20 kg and an accuracy of 0.01 kg.

It is worth mentioning that no correction was made for moisture in the aggregates, since at that time the bags of aggregate had been stored in laboratory conditions for more than 3 months, so it was reasonable to assume that the moisture was constant throughout the volume of material. In addition, the material from these same bags was the material that had been used to adjust the dosages (Table 3.1-7).



Figure 3.1-6. Weighing of solid materials and pouring into the concrete mixer.

2. Next, the inside of the concrete mixer is slightly moistened and the materials are introduced. First the solids are added in decreasing order of particle size (gravel, sand, filler and cement) and mixed for 2-3 minutes until a homogeneous appearance is achieved. Water is then added progressively, at which point the mixing time begins. The additives are added diluted in the last part of the water. Finally, the steel fibers (if any) are added after 1-2 minutes of mixing, when the water has been integrated and the superplasticizer is starting to act.



Figure 3.1-7. Mixing of solid materials and addition of water with admixtures.

3. The total mixing time is between 5 and 7 minutes. The greater the amount of fibers, the higher the viscosity of the mix and therefore the more time it needs to reach an adequate consistency. However, there are other factors that also affect the mixing time and that are not easily controllable, such as variations in environmental conditions at any given time, a certain dispersion in the humidity of the materials, etc. All this means that it is not possible to establish a fixed mixing time, even for batches of the same series. Therefore, the criterion for determining the end of the mixing is the appearance of the mixture, which must be homogeneous throughout its volume, without accumulations or balls of fibers, and with a liquid consistency. The latter occurs when the superplasticizer acts and the mixture "breaks"; that is, in a short space of time it goes from being plastic in appearance to being very fluid.



Figure 3.1-8. Appearance of concrete with fibers at the end of the mixing time.

4. Once the concrete has reached the optimum consistency, a small volume is removed and a slump test is performed. It is checked that the self-compactness requirements (Table 3.1-3) are met and that segregation does not occur. The molds are then randomly trowel-filled. Since this is a self-compacting concrete, no vibration is applied.
5. The molds are placed in a curing chamber, where they remain at a temperature of $20 \pm 1^\circ\text{C}$ and $95 \pm 2\%$ humidity. The molds are demolded after approximately 24 hours, after which the specimens are returned to the chamber.



Figure 3.1-9. Curing chamber used.

All specimens were stored in the same curing chamber, where they remained for 1 year. The specimens were then removed and kept in laboratory conditions until the time of testing. In total, approximately 1 year and 4 months elapsed from the fabrication of the specimens to the beginning of the experimental campaign.

The reason for storing the specimens for one year is to avoid that the increase in the mechanical capacity of the concrete, especially significant at early ages, introduces uncertainty in the results of the fatigue tests. As an example, it is possible to determine the error that would be made in an experimental fatigue campaign when determining the stress levels at 28 and 365 days, respectively. To simplify the calculation, the compressive strength (f_c) has been taken as a reference, considering the formula proposed by the Spanish Structural Code [3]. In addition, a characteristic strength ($f_{ck,28}$) of 60 MPa and a campaign duration of 2 months were assumed, which is reasonable in fatigue. Figure 3.1-10 shows a graph of the evolution of the f_c of the concrete with time. Finally, Table 3.1-10 shows the maximum relative error that would occur with the last specimen tested.

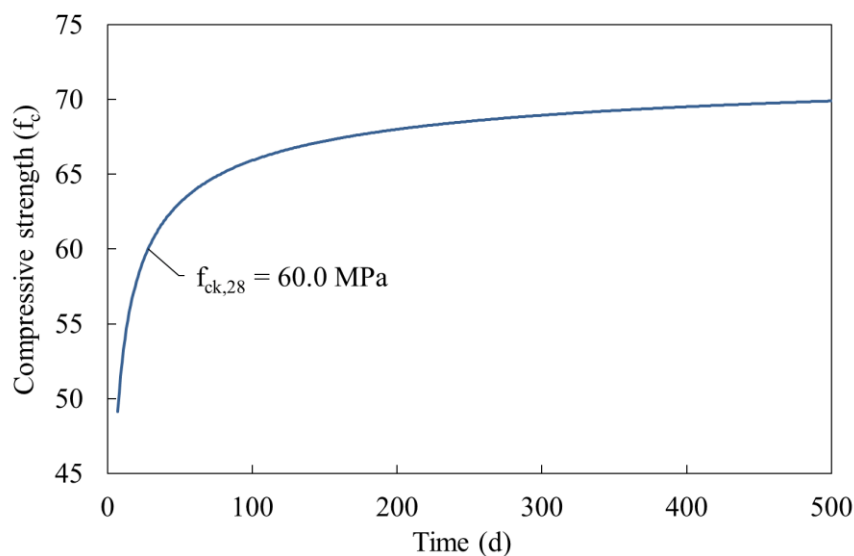


Figure 3.1-10. Evolution of the compressive strength with time in HA-60 concrete, according to the formulation proposed in [3].

Table 3.1-10. Relative error in a 2-month experimental campaign when taking $f_{c,28}$ and $f_{c,365}$ as reference, respectively.

Reference value		Value of the last specimen tested		Relative error (%)
$f_{c,28}$	60.00	$f_{c,88}$	65.47	+ 9.1%
$f_{c,365}$	69.34	$f_{c,425}$	69.62	+ 0.4%

The results reveal that the error is much higher when calculating the compressive strength at 28 days than at one year. The latter specimens would have a 9.1% higher strength than the first ones, so the range of fatigue loads applied would be lower in relative terms. In short, the fatigue life of the latter specimens would be overestimated. On the contrary, if the campaign were started one year later, the variation in resistance throughout the campaign would be minimal, barely 0.4%.

It should be remembered that the law of temporal evolution of the compressive strength considered is an approximation, since it depends on many factors (type of cement, admixtures, presence of fibers, etc.). Moreover, this evolution is not identical for all concrete parameters, such as tensile or flexural strength. Therefore, to eliminate this uncertainty, it was decided to wait for one year, which is accepted as sufficient time, before starting the tests.

3.2 Experimental campaign

3.2.1 Description

This research work focuses on the analysis of the flexural fatigue behavior of fiber-reinforced concrete. Therefore, the main tests are obviously the fatigue tests. However, it is essential to carry out other preliminary tests in order to, on the one hand, characterize the material and, on the other hand, determine the parameters of the fatigue tests. The tests that make up the experimental campaign are described below:

Slump test

It is conducted according to UNE-EN 12350-8 [142]. This test is performed with the concrete in its fresh state and its objective is to verify that it meets the self-compactness criteria (Table 3.1-3). For this purpose, at the end of the mixing time, a small volume is removed from the concrete mixer. The test is carried out with the classic Abrams cone used to measure the consistency of conventional concrete, and with a steel plate. At the

end, the diameter of the slump flow determines its level of self-compactness. A slump test is performed on each batch.



Figure 3.2-1. Example of a slump test.

This test is a good indication of the quality of the mix, since it allows detecting at a glance whether there are problems such as segregation of the aggregates, exudation of mortar or grout, etc.

Determination of compressive strength

Compressive strength is one of the main parameters to characterize the mechanical response of concrete. This test is performed according to UNE-EN 12390-3 [143] on standardized cylindrical specimens of 150x300 mm. A 300 T testing machine has been used.

It is usual for the compressive strength of concrete to be calculated at 28 days of age, since this is the characteristic reference value used in structural codes. However, for the purpose of this research it is more relevant to know the mechanical properties of the concrete at the time when its fatigue response is to be evaluated. For this reason, the tests were carried out when the concrete was 1 year and 4 months old.

To ensure a flat contact surface between the testing machine plate and the top face of the specimens, the specimens were faced with ChrysoSurf mortar, manufactured by Chryso (Issy-les-Moulineaux, France). This is a high-performance sulfur mortar suitable for high-strength concrete up to 120 MPa.

Normally, a minimum of 3 tests are recommended to determine the average value of the compressive strength. In this case, 4 tests have been performed for each series.



Figure 3.2-2. Compressive strength test on a fiber-reinforced concrete specimen.

Determination of the secant modulus of elasticity in compression

The modulus of elasticity is, together with compressive strength, the other parameter most used to characterize any concrete. Specifically, it defines its behavior in the elastic regime since it is the slope of the stress-strain diagram.

This test is carried out according to UNE-EN 12390-13 [144], also with cylindrical specimens of 150x300 mm. A 300 T testing machine was used. It is worth mentioning that the compressive strength must be previously determined, since the load cycles applied in this test are a function of this parameter.

The method used to measure the strain of concrete is the strain gauges method. Three 60 mm long strain gauges were placed on the side of each specimen, arranged longitudinally to the specimen axis, approximately at the height of its median plane and 120° apart in the circumferential direction.

To determine the average value of the modulus of elasticity, 3 tests were performed for each series.

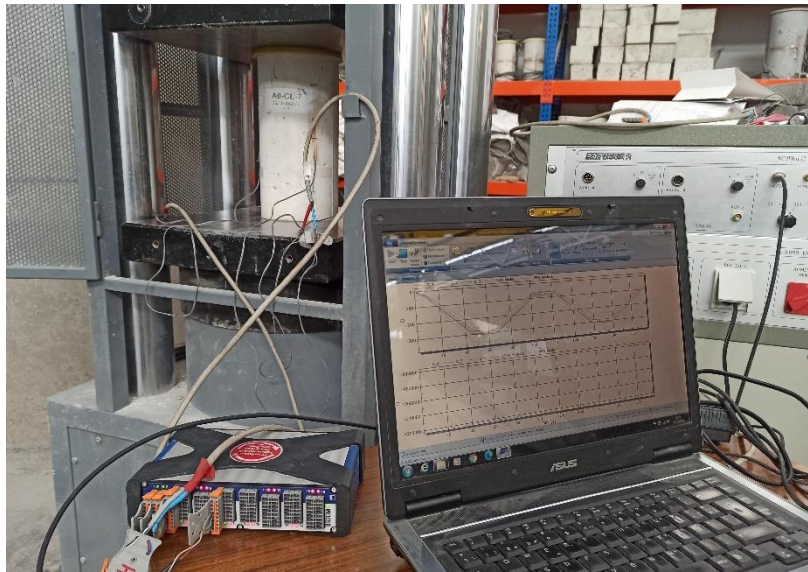


Figure 3.2-3. Test to determine the modulus of elasticity in compression.

Determination of flexural tensile strength

This test was performed in accordance with UNE-EN 14651 [7], specifically indicated for fiber-reinforced concrete. The purpose of these tests is to determine the static strength in 3-point bending, which in turn allows defining the load range of the fatigue tests. Therefore, they were carried out just before the fatigue tests.



Figure 3.2-4. Flexural strength test on a specimen of size S.

The type of specimens used in flexural tests is prismatic with notch. In particular, the standard is indicated for specimens of 150x150x600 mm, which coincides with the largest size of prismatic specimens manufactured, denominated as PR-L or L. In the case of the

smaller specimens, designated as PR-S or S, the test configuration has been calculated following a proportional relationship. Below is a table with the main geometrical parameters of the flexure test for both types of specimens, including the criteria considered.

Table 3.2-1. Geometric parameters of the 3-point bending tests for the two sizes of prismatic specimens.

Test parameter	Criteria	Type of specimen	
		PR-L	PR-S
b (mm)		150	75
h (mm)	b:h:l = 1:1:4	150	75
l (mm)		600	300
h_{ent} (mm)	$h_{ent}:h = 1:6$	25	12.5
l_{ap} (mm)	$h:l_{ap} = 0.3$	500	250

In Table 3.2-1, b, h and l are the dimensions of the specimens, i.e. width, depth and length, respectively. For the rest, h_{ent} is the notch depth and l_{ap} is the span between supports.

Three static bending tests were conducted for each type of concrete and specimen size. The notches were made with a 2.8 mm thick diamond cutting disc.

Figure 3.2-5 shows an image of a flexural tensile test, indicating the main elements and the instrumentation. It is worth mentioning that in this case the tests have been performed in the reverse position as indicated in the standard, i.e. the specimen rests on the central support and the load is applied through the lateral rollers. This method has some advantages (basically, protection of the sensor system), although the truth is that there are no significant differences, so it is indifferent to perform them in one way or another.

Another aspect to point out is that the specimen rests on the rollers with its two flat parallel faces, leaving the more irregular face (the one that is free in the mold) on one of the sides. This ensures a good contact with the rollers and therefore a correct transmission of the loads, avoiding residual local stresses.

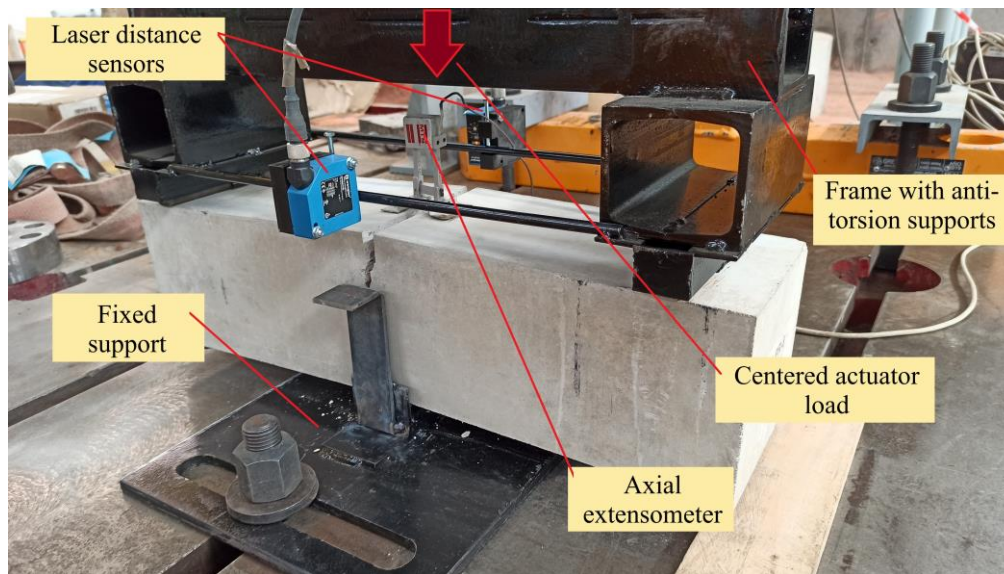


Figure 3.2-5. Flexural strength test on a specimen of size L, with identification of the main elements.

The parameters monitored were the vertical displacement at the center of the span, the CMOD (crack mouth opening displacement) and the load. As for the instrumentation, the displacement was measured with two laser distance meters placed on either side of the specimen, the CMOD by means of a clip-on extensometer and the load by means of the load cell incorporated in the actuator itself.

The load was applied with a dynamic hydraulic actuator with a maximum load of 50 kN. The tests are performed with displacement control. The speed is 0.08 mm/min until a CMOD of 0.10 mm is reached, after which it is increased to 0.21 mm/min. Due to the large plastic deformation that fibers can take on, total failure of the specimen (understood as the separation of its two parts) is rare, even for relatively low fiber contents. Therefore, the test is usually terminated when the clip-on extensometer goes out of range, which happens for a CMOD of about 8-10 mm. Logically, in plain concrete specimens (A0 series) this does not occur, resulting in brittle failure for relatively low CMODs.

3-point flexural fatigue test

Flexural fatigue tests have the same configuration as static flexural strength tests. Therefore, everything mentioned in the previous subsection regarding the type of specimens, geometrical arrangement of the test, instrumentation and equipment is still valid. However, as these are dynamic tests, the major difference lies in the type of loads to which the specimens are subjected.

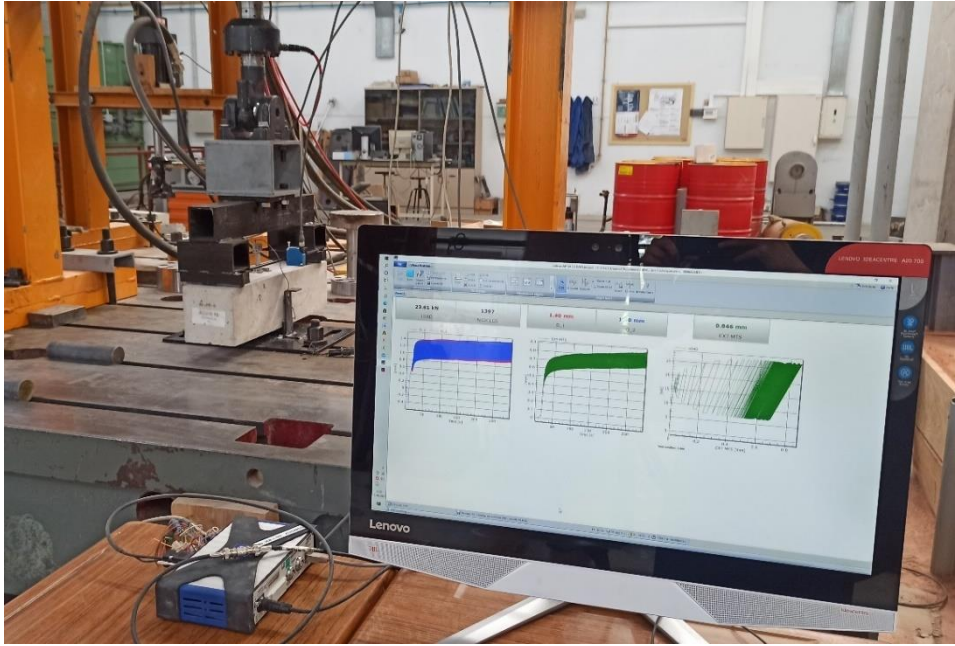


Figure 3.2-6. Flexural fatigue test, showing the data acquisition system in the foreground.

Fatigue testing is not governed by a standardized procedure, since it is a complex phenomenon that depends on multiple factors, such as the magnitude of the load cycles. Therefore, the scope of the campaign and the particular characteristics of the fatigue tests will depend on the objectives of the research work. It is considered that the detailed description of the fatigue tests deserves to be dealt with in a separate subsection.

3.2.2 Flexural fatigue test design

The main parameters of the flexural fatigue tests are described below, including the appropriate justifications.

Static reference parameter

The fatigue strength of concrete, understood as the number of cycles it is capable of withstanding until failure, depends directly on the load levels or stresses of these cycles. Normally, these levels are defined according to a parameter of the equivalent static tests. An obvious case is fatigue in compression, where the compressive static strength f_c is taken as a reference. For example, a common range of stresses in compressive fatigue is between 20% and 80% of f_c .

However, in the case of flexural fatigue in fiber-reinforced concrete, the situation is not so simple since there are several possibilities when choosing the static reference

parameter. Figure 3.2-7 shows the load vs CMOD plot of a static flexural test indicating some of these parameters, which are defined below:

- Ultimate bending strength or maximum load (P_{ult} or P_{max}). This is the maximum load that is reached throughout the entire bending test.
- Load corresponding to the limit of proportionality (P_L). This is the maximum load reached in the CMOD range of 0 to 0.05 mm, where a linear stress distribution is assumed and the concrete has not yet cracked. It is the representative parameter proposed by UNE-EN 14651 [7].
- Other criteria. It is also common to take as a reference the load corresponding to a given CMOD (e.g., $P_{0.1mm}$) or the maximum load up to the moment at which there is a decrease of a given percentage of its value (e.g., $P_{max,\downarrow 10\%}$).

In fact, all these parameters, except the first one, seek to objectively determine the cracking load, the moment at which loads are transmitted from the matrix to the fibers.

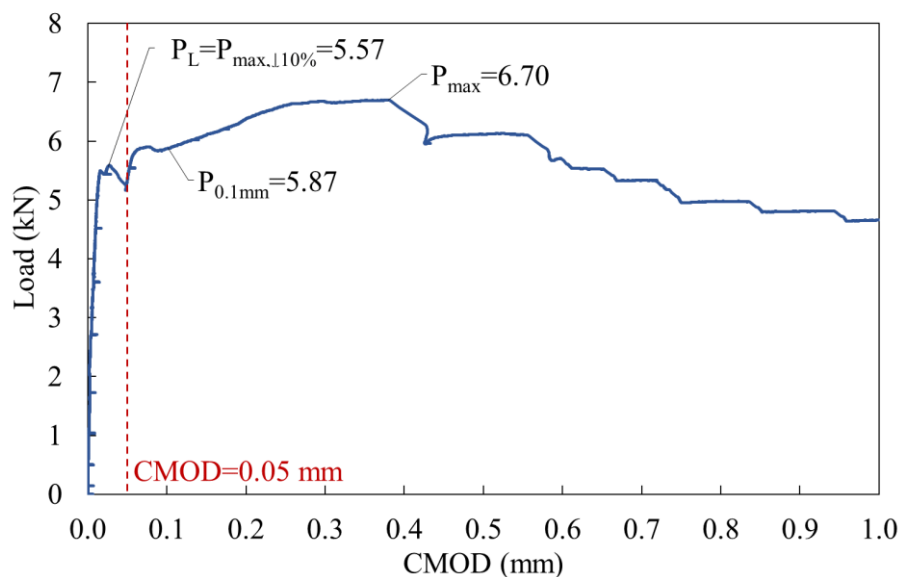


Figure 3.2-7. Identification of reference parameters in a static flexural tensile test.

Note that all or some of these parameters may be coincident, depending on the resulting load vs CMOD graph.

When choosing the most appropriate reference parameter, it should be taken into account that concrete with a high fiber content, up to 1%, will be used. Under these conditions, it is to be expected that a very important supercritical behavior will appear in the static flexural test. That is, after cracking of the concrete, the fibers will be able to assume

a high load, resulting in strain-hardening, with P_{max}/P_L ratios of 1.5 or even higher (Figure 3.2-8).

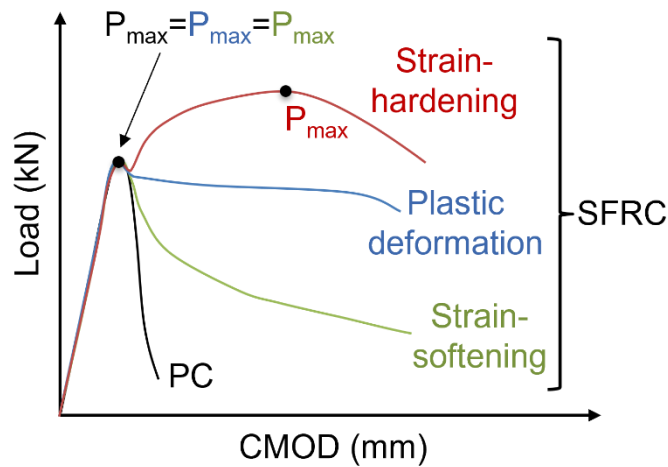


Figure 3.2-8. Load vs CMOD diagram in static flexural test with the behaviors that plain concrete (PC) and fiber-reinforced concrete (SFRC) can show.

Consequently, if P_L or any other criterion that does not take into account the possible supercritical behavior of the fibers is taken as a reference, there is a risk that the loading levels will be too low, with very high fatigue life results and even close to the fatigue limit. For this reason, P_{max} has been considered as a reference parameter when establishing load levels or stresses in fatigue. In this way, the stresses will always be within or close to the cracked condition, so the fatigue life will not be excessively high.

Stress levels

Once the reference static parameter has been determined, the next step is to define the stress levels of the fatigue cycles. The maximum (S_{max}) and minimum (S_{min}) stress levels are defined as:

$$S_{max} = \frac{\sigma_{eq,max,fat}}{\sigma_{eq,max}} \quad (3.2-1)$$

$$S_{min} = \frac{\sigma_{eq,min,fat}}{\sigma_{eq,max}} \quad (3.2-2)$$

Where $\sigma_{eq,max,fat}$ and $\sigma_{eq,min,fat}$ are the maximum and minimum equivalent stresses in each fatigue cycle, and $\sigma_{eq,max}$ is the maximum equivalent stress in the static bending test, obtained from P_{max} .

If the fatigue behavior were to be fully characterized, it would be necessary to perform tests combining different levels of maximum and minimum stresses, in order to determine the set of S-N curves for each material.

However, this is beyond the scope of this work, whose objective is to compare the fatigue response of concrete with different fiber contents and specimen sizes. Therefore, it has been considered sufficient to analyze a single stress range, i.e., to carry out a single type of fatigue tests with fixed stress levels S_{\max} and S_{\min} .

In order to choose the S_{\max} and S_{\min} values, a target fatigue life of 10^4 cycles has been set as a criterion. The reason is that this is an average value, on the boundary between low and high cycle fatigue. Thus, assuming a dispersion of the results of about 2 orders of magnitude, the expected range will be between 10^2 and 10^6 cycles. These limits are considered reasonable since the minimum is sufficiently far from static failure and the maximum is not so high that the tests would be too long in time.

Next, an intensive literature search of experimental flexural fatigue campaigns on steel fiber-reinforced concrete was carried out, noting those load levels that resulted in an average fatigue life of 10^4 cycles. Obviously, fatigue life depends not only on stress levels, but also on many other factors, such as specimen size, whether or not the specimens were pre-cracked, concrete dosage, fiber length, content and shape, etc. Therefore, the objective of this search was to determine approximate stress levels. Without being exhaustive, Table 3.2-2 shows some of the works studied, summarizing the parameters of the series with a fatigue life of about 10^4 cycles.

Table 3.2-2. Bibliographic consultation of experimental work on flexural fatigue of fiber-reinforced concrete.

Reference	Type of specimen			Fatigue test			
	Size (mm)	¿Notch?	¿Pre-cracked?	S_{\max}	S_{\min}	f (Hz)	N_{avg}
[37]	75x75x275	Yes	Yes	0.75	0.23	6	11,510
[73]	150x150x600	No	Yes	0.65	0.05	6	95,708
[132]	100x100x440	Yes, h/6	No	0.70	0.14	4	12,500
[54]	150x150x550	Yes, h/6	Yes	0.75	0.25	3	10,304
[32]	100x100x500	Yes, h/5	No	0.85	0.20	5	11,807
[30]	100x100x500	No	No	0.85	0.26	12	45,580

Finally, taking into account the results of the consultation, values for S_{\max} and S_{\min} have been set at 0.80 and 0.16, respectively; that is, with a load ratio R , defined as the quotient between S_{\max} and S_{\min} , of 0.20.

Frequency

The frequency of load cycles affects the fatigue life. However, some authors suggest that the frequency range between 1 Hz and 15 Hz hardly affects fatigue strength, as long as the peak stresses do not exceed 75% of f_c [48,49]. In the case of flexural fatigue, although some work has been published, there is no clear agreement on which frequency ranges have little impact on fatigue life.

In any case, the objective of this research work is to establish comparisons between different types of concrete and specimen sizes. Therefore, it is essential that the loading frequency be the same in all tests, regardless of its value. Consequently, a frequency of 5 Hz has been chosen, a common value in experimental fatigue campaigns, as observed in the works reviewed (Table 3.2-2).

Runout or survival limit

Given the large dispersion of fatigue results, it is usual to consider a maximum number of cycles after which, if the specimen has not failed, the test is stopped. These incomplete fatigue tests, in which the fatigue life exceeds the maximum dispersion to be expected, are called runouts. The specimen is also said to have "survived".

The number of limit cycles to consider a runout should be chosen with caution. Normally, when many runouts appear in a campaign, it is an indication that the fatigue life has not been estimated correctly. In addition, it is a problem in terms of data processing since the fatigue life values of these test specimens are not valid. Therefore, very few or no runouts are recommended.

In this case, taking into account that the estimated average fatigue life is 10^4 cycles, and assuming a dispersion of about 2 orders of magnitude, a runout limit of 10^6 cycles has been set. With a frequency of 5 Hz, this means that each fatigue test can last a maximum of 2.3 days, which is logistically feasible.

Specimen characteristics

As mentioned above, the specimens subjected to flexural fatigue are prismatic and of two different sizes: 75x75x300 mm (S) and 150x150x300 mm (L). Prior to testing, all specimens were notched in their midplane to a depth of $h/6$.

The specimens were not pre-cracked, since the aim is to study the two possible fatigue mechanisms that can occur, namely fatigue of uncracked concrete and fatigue of cracked concrete (see 2.2.4). The former occurs when the concrete has not yet cracked, with very low CMOD values (≤ 0.05 mm). Therefore, if the specimens were pre-cracked, this mechanism would be eliminated. On the other hand, it would not make sense for the purposes of the A0 series either: since we are dealing with plain concrete, pre-cracking would directly imply the breaking of the specimens.

Number of specimens

In order to obtain representative results considering the fatigue dispersion, it is advisable to test a sufficient number of specimens. In this work, 12 specimens have been tested for each type of concrete and size. Due to time and cost limitations, in most experimental concrete fatigue campaigns between 10 and 15 tests per series are performed.

Measured results

The parameters measured in the bending fatigue tests are given below:

- Vertical displacement at the mid-span of the specimen, calculated as the average of the displacements measured by the two laser distance meters placed on either side of the specimen.
- CMOD (i.e. crack mouth opening displacement), measured with a clip-on extensometer placed in the notch.
- Load, through the load cell incorporated in the actuator itself.
- Fatigue life or number of cycles to specimen rupture.

It is worth mentioning that the tests are performed with force control, applying sinusoidal load cycles according to the load levels established for each series and specimen size.

Summary of test parameters

Finally, a table is included with the fatigue test parameters for all series and specimen sizes.

Table 3.2-3. Parameters of flexural fatigue tests.

Series	Size	P_{\max} (kN)	Load range	$P_{\max,\text{fat}}$ (kN)	$P_{\min,\text{fat}}$ (kN)	f (Hz)	N_{runout}
A0	S	6.41		5.13	1.03		
	L	16.33		13.06	2.61		
A1	S	6.86	(80%-16%) $\cdot P_{\max}$	5.49	1.10	5	1,000,000
	L	18.54		14.83	2.97		
A2	S	9.21		7.37	1.47		
	L	35.53		28.42	5.68		
A3	S	15.35		12.28	2.46		
	L	51.27		41.02	8.20		

3.2.3 Facilities and equipment

All the tests have been carried out in the Laboratory of Large Structures of Civil Works, belonging to the School of Engineering of the University of Burgos (Spain). These facilities were inaugurated in 2005 and, thanks to its modern equipment and the technological impulse provided by the various research groups of the UBU, it has become a reference in the region to perform static or dynamic tests on structural elements of any type.

The laboratory has a surface area of 940 m² and has a reaction slab completely isolated from the rest of the building and designed to carry out high-capacity dynamic tests. In addition, the slab incorporates a reaction wall, two steel reaction frames and a test table.

In terms of equipment, a wide range of dynamic hydraulic actuators is available, from 15 kN to 1,000 kN capacity. Pressure is supplied to the actuators by a hydraulic unit with a capacity of 200 L/min and a working pressure of 280 bar. Between the hydraulic unit and the actuators there is a manifold, i.e. a hydraulic control unit.



Figure 3.2-9. Main entrance of the School of Engineering and access to the Laboratory of Large Structures of Civil Works.



Figure 3.2-10. Inside view of the Large Structures of Civil Works Laboratory.

The specific equipment used to carry out the experimental campaign of this research work is described below:

300 T universal testing machine

The compressive strength and modulus of elasticity tests were carried out with a universal testing machine, model MES 300, manufactured by the company Servosis (Pinto, Madrid, Spain). This hydraulic press has a load capacity of 300 tons.



Figure 3.2-11. 300 T testing machine.

50 kN dynamic actuator

In the 3-point bending tests, both static and fatigue, the force was applied with a dynamic hydraulic actuator, model 244.21, manufactured by MTS (Eden Prairie, MN, USA). This is a double-acting actuator, which allows both compressive and tensile loads to be applied, with a range of ± 50 kN and a displacement amplitude of 150 mm.



Figure 3.2-12. 50 kN actuator positioned in its reaction frame.

The hydraulic supply of the actuator is carried out through the manifold and the hydraulic unit of the laboratory.

Test fixtures

As noted above, the 50 kN hydraulic actuator was used in the bending tests. This actuator is located on the laboratory test table, fixed to an adjustable metal frame.

To perform the tests, it was necessary to design ad hoc two bending fixtures, one for each specimen size. The fixtures were designed using Inventor Professional software from Autodesk (San Rafael, CA, USA) and were made of S275 steel. The design followed the requirements of the UNE-EN 14651 standard [7].

Each fixture consists of two parts. On the one hand, the upper part, connected to the actuator, is the one with the two end supports, positioned according to a ratio $h:l_{ap} = 0.3$. The main span is formed by an HEB profile. Each support is made up of two box-shaped UPN profiles, under which the support cylinders are located. The UPN profiles provide sufficient space for the clip-on extensometer in the center of the specimen. The cylinders can rotate freely with respect to their midpoint to avoid transmitting any residual torsional stresses caused by possible warping of the specimen face. In addition, bars connecting the supports at the height of the cylinders are arranged on each side; it is at this point that the displacement sensors are placed. On the other hand, the lower part, anchored to the test table, is the one with the central support. It consists of a fixed cylinder that acts as a support and two angular profiles on each side. The upper face of the angular profiles is the fixed reference for the measurement of the displacement sensors. Figure 3.2-13 shows the fixture models for the two specimen sizes.

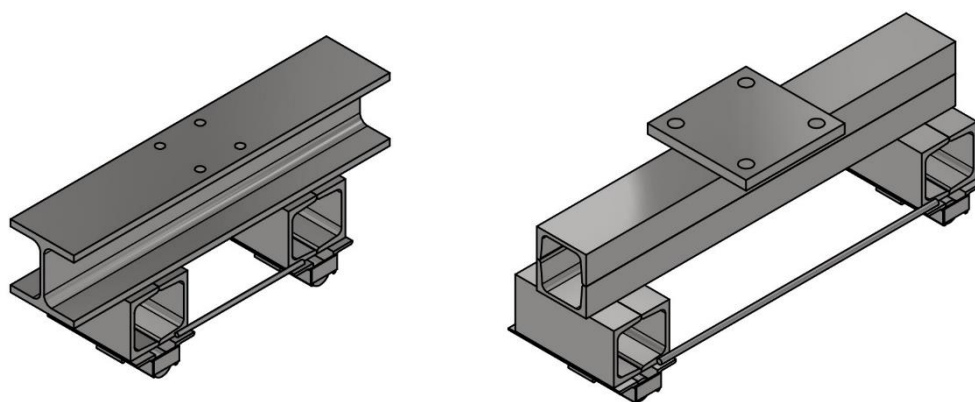


Figure 3.2-13. Bending fixtures for size S (left) and L (right) specimens.



Figure 3.2-14. Fixture for size S specimens.

Test control

The 50 kN hydraulic actuator is monitored through a control module, using the MultiPurpose TestWare 793 software from MTS. Specifically, the Station Manager application is used, whose main utilities are:

- Perform tuning of the actuator. Tuning is a procedure in which, as its name suggests, the actuator parameters are adjusted so that its control is as accurate as possible, i.e., so that it is able to reproduce the signal (load or displacement) sent to it with the minimum error. The actuator control is very sensitive to the stiffness of the set of elements that make up the test (frame, specimen, etc.). Therefore, it is advisable to do it every time the type of material or test is changed, or even routinely from time to time. In dynamic tests this process is indispensable.
- Configure cyclic and monotonic tests. With this software, the control of the hydraulic actuator for the two types of bending tests can be configured. On the one hand, in static bending tests, which are performed with displacement control, the displacement speed of the piston in mm/min is displayed. On the other hand, in the flexural fatigue tests, which are performed with load control, the load range, frequency, wave type and number of cycles of survival limit are set.

In load-controlled tests, such as flexural fatigue tests, it is very important for safety reasons to set an interlock. An interlock is simply a value of a parameter (usually load or displacement) which, if exceeded, automatically stops the test. In this case a displacement interlock has been set, whose value is large enough to be sure that, if the actuator piston reaches that value, the specimen has already failed. If an interlock is not set, when the probe breaks, the piston will continue to move forward to seek the indicated load. This is very dangerous, as it could end up damaging sensors, the actuator itself or any of its components (ball joint, etc.).

Sensors and data acquisition

The sensors used in the bending tests, both static and fatigue, are described below. Firstly, to register the load, the load cell incorporated in the actuator, model 661.20F-02, manufactured by MTS, with a range of ± 50 kN, is used.

Secondly, the relative displacement between the two end supports and the central support is measured with two high-precision laser distance meters, model CP08MHT80, manufactured by Wenglor (Tettngang, Germany). These sensors have a measuring range of 50 mm and an accuracy of 8 μm . They are placed on the bending fixture itself by means of ad hoc designed brackets made of PLA polymer with an additive manufacturing 3D printer. It is worth mentioning that the actuator has a built-in displacement transducer that tracks the piston movements. However, these data have not been taken into account, since the piston motion comprises not only the displacement of the specimen, but also other uncontrolled phenomena, such as the deformation of the frame and the fixture. Therefore, the measurement provided by laser distance meters is much more accurate.

Finally, the crack opening (i.e. the CMOD) is measured with an axial extensometer with a measuring range of 25 mm, model 634.12F-24, manufactured by MTS. The sensor and the stop piece are placed on either side of the notch with a cyanoacrylate adhesive.



Figure 3.2-15. Laser distance meters and axial extensometer placed on a specimen of size L.

Test control and data acquisition are two systems that are managed completely independently. All sensors are connected to a data acquisition system (DAQ) that receives their electrical signals and digitizes them so that they can be interpreted by a computer. In this case, the DAQ used is a QuantumX module, model MX840B, from the company HBM (Darmstadt, Germany). Finally, the data are collected, analyzed and visualized in real time with HBM's Catman DAQ software.



Figure 3.2-16. Data acquisition with QuantumX module and Catman software.

The data capture frequency is 50 Hz. This means that, in flexural fatigue tests, whose loading frequency is 5 Hz, 10 data are recorded for each complete cycle. The reason for choosing such an apparently tight ratio is to facilitate subsequent post-processing of the data, since, in the worst-case scenario with a specimen reaching the runout limit, the number of data rows would be 10^7 , generating files of several gigabytes.

In any case, the error obtained by determining the extreme points (maximum and minimum) of each cycle has been calculated. If the ratio between the data acquisition frequency and the loading frequency were an integer (in this case, 10), the error would be constant throughout the test. However, it is observed that there is a slight offset in the data acquisition frequency, which causes the error to vary between 0 and a maximum value periodically (Figure 3.2-17). This maximum error only depends on the ratio between the frequencies, and can therefore be calculated theoretically as:

$$e_{\max} = 1 - \sin\left(90^\circ - \frac{360^\circ/2}{f_{\text{data}}/f_{\text{load}}}\right) = 4.89\% \tag{1.2-3}$$

Therefore, the average error in determining the extreme values of the load cycles due to the frequency of data collection is 2.45%. This value is considered acceptable, taking into account the characteristics of the fatigue results to be obtained.

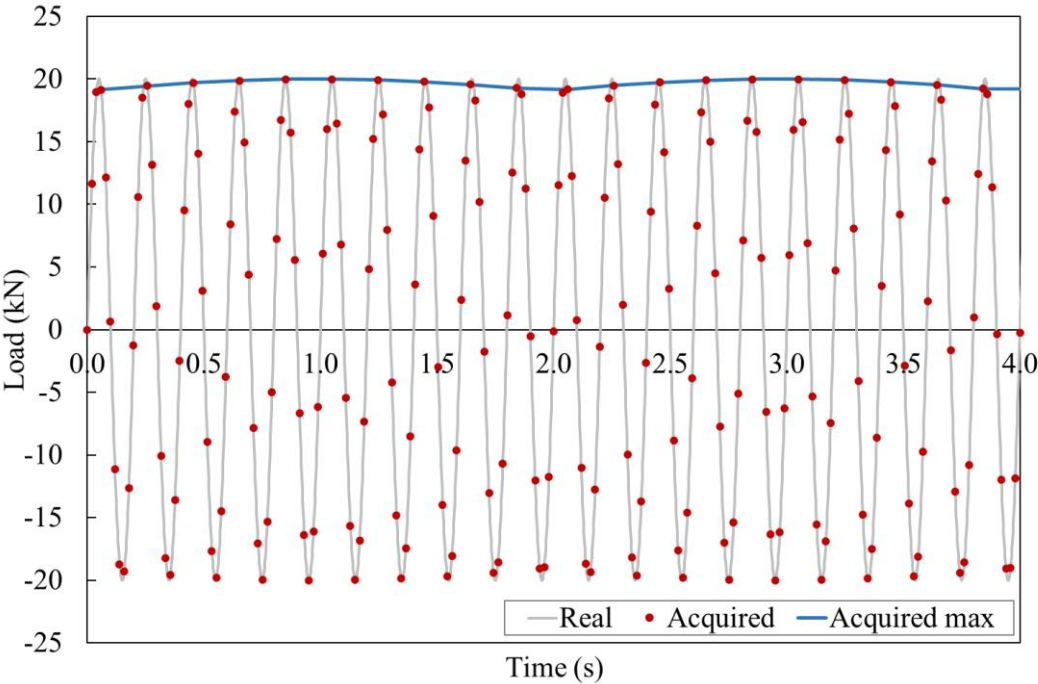


Figure 3.2-17. Example of the error due to the ratio between data acquisition frequency and loading frequency in a fatigue test.

3.2.4 Test plan

A summary table of the experimental campaign is shown below, including the number of specimens of each type of test, both per series and in total. The tests started when the concrete was 1 year and 4 months old, and the total duration of the campaign was 5 months, from March to July 2022.

The table does not contain the slump tests, performed with fresh concrete. Four tests were carried out per series (one per batch), i.e. 16 in total. In addition, one more specimen of each type per series was produced and kept in reserve.

Table 3.2-4. Summary table of the experimental campaign.

Test	Specimens per series			Specimens in total			Σ
	CL	PR-S	PR-L	CL	PR-S	PR-L	
Compressive strength	4	0	0	16	0	0	16
Secant modulus of elasticity	3	0	0	12	0	0	12
Static flexural strength	0	3	3	0	12	12	24
Flexural fatigue	0	12	12	0	48	48	96
			Σ	28	60	60	148

3.2.5 Post-processing of results

In this subsection, the process of analysis of the test results of the experimental campaign is described, distinguishing between characterization tests and flexural fatigue tests.

Characterization tests

Characterization tests allow determining the main characteristics of each material, and in this case they include slump, compressive strength, modulus of elasticity and flexural strength tests. The following is a description of the most relevant aspects in terms of obtaining results for each type of test:

- Slump test. In this test, the two parameters that characterize the self-compaction of concrete are measured: d_f (final diameter of the slump flow) and t_{50} (time it takes for the slump flow to reach a diameter of 50 cm). In fact, this test, rather than determining whether the self-compacting concrete is of one type or another, is used as a quality control. In other words, the objective is to verify that the concretes of all series actually have self-compacting properties

and that there is no segregation of the aggregates or any other pathology of the fresh concrete that could affect the results of the investigation.

The slump parameters are calculated at the series level as the average values of the 4 concrete batches. In this case, it is especially interesting to calculate the dispersion (standard deviation and coefficient of variation) in order to verify that there were no significant differences between the batches of the same series.

- Determination of compressive strength. In this test, the software incorporated in the 300 T hydraulic press directly provides the stress-strain curve up to rupture. However, this curve is not very interesting, since the strain measurement is calculated with the transducer incorporated in the piston and is therefore imprecise. Consequently, the maximum stress, i.e. the compressive strength f_c , is taken as the only representative value for each test.

The compressive strength is calculated at the series level as the average value of the strengths of the 4 specimens tested. In addition, to study the possible dispersion of the results, the standard deviation and the coefficient of variation are also calculated.

- Determination of the secant modulus of elasticity in compression. In the modulus tests, the stress-strain graph is obtained as a result. The stress is calculated from the load of the hydraulic press, while the strain is the average value of the 3 strain gauges. The modulus of elasticity E_c is calculated as the slope of the upward branch of the last loading cycle.

The modulus of elasticity, like the compressive strength, is calculated at the series level as the average of the moduli of the 3 tested specimens. In addition, the statistical dispersion variables are also obtained.

- Determination of flexural tensile strength. The static flexural tensile tests are fundamental since they are used to determine the load cycles of the flexural fatigue tests. The result obtained in each test is the load-CMOD curve. From this, the ultimate flexural load (P_{max}) is calculated, i.e., the maximum load reached in the entire test.

The ultimate flexural strength is calculated at the series and prismatic specimen size level, and is obtained as the average value of the 3 tests performed in each case. It is very important that the dispersion of results is as low as possible, otherwise we would be adding uncertainty to the fatigue tests.

Flexural fatigue tests

In fatigue tests, the data of the measured parameters are obtained, i.e., time, load, relative displacement between the center of the specimen and the ends, and crack opening or CMOD. With these data, very interesting graphs can be plotted that allow a qualitative evaluation of the test, such as load-CMOD, CMOD-time, load-time, etc. However, to quantify the fatigue response it is necessary to calculate some parameters that are not obtained directly. For this purpose, a routine has been developed in Matlab software, from Mathworks (Natick, MA, USA). The main functionalities of this algorithm are described below:

- Differentiate between the two types of fatigue observed: matrix fatigue and fiber fatigue. In those SFRC series in which both fatigue mechanisms appear, by means of a semi-automatic process, the data set is divided into two subsets corresponding to the two types of fatigue.
- Calculate the fatigue life. The number of cycles is obtained, both the total and those corresponding to the two types of fatigue, if any. It is worth mentioning that the Catman DAQ software is capable of calculating the number of cycles. However, it is not able to distinguish between the two types of fatigue, so this process is redone with Matlab code.
- Calculate the secondary crack opening rate ($d\text{CMOD}_{\text{upp}}/dn$, or simply $d\text{CMOD}/dn$). The secondary crack opening rate is the slope of the upper envelope of the CMOD-N plot in phase II, i.e. when stabilized fatigue damage occurs. To calculate this parameter, the upper envelope of the CMOD-N curve, denoted $\text{CMOD}_{\text{upp-N}}$, is first determined. Then, the data corresponding to phases I and III are discarded. Finally, a linear least squares regression is performed, the slope of the line being the value of $d\text{CMOD}/dn$. In cases where there are two fatigue mechanisms, this process is repeated to calculate $(d\text{CMOD}/dn)_{\text{mat}}$ and $(d\text{CMOD}/dn)_{\text{fib}}$ (Figure 3.2-18).

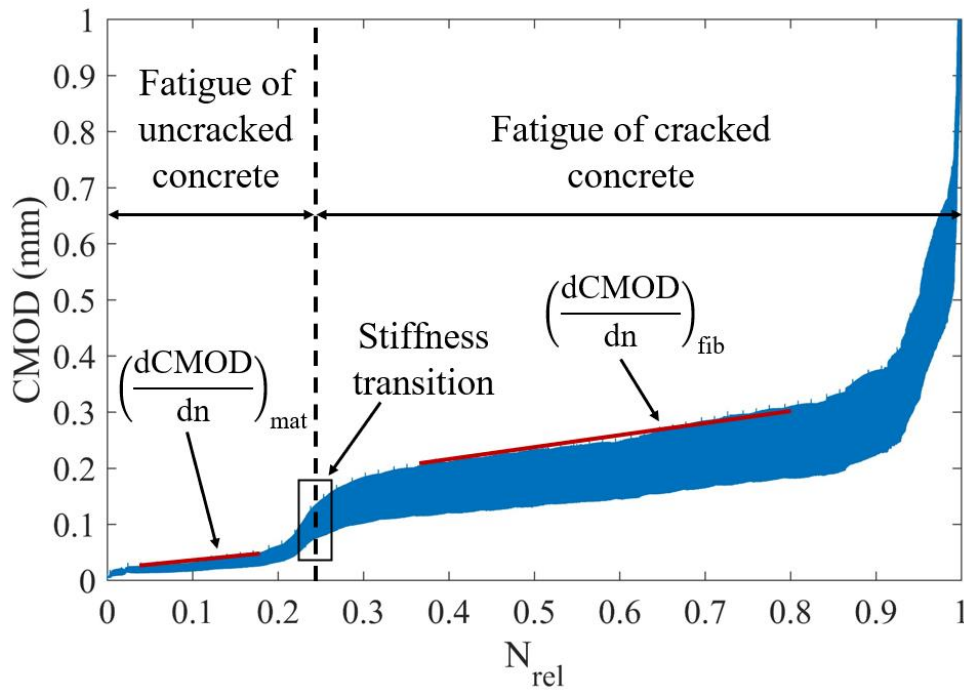


Figure 3.2-18. CMOD-N curve in flexural fatigue test in SFRC, showing the fatigue mechanisms of uncracked and cracked concrete.

In summary, the individual parameters obtained in each flexural fatigue test are the total number of cycles N_{tot} , the number of cycles corresponding to matrix fatigue N_{mat} , the number of cycles corresponding to fiber fatigue N_{fib} , the secondary crack opening rate of matrix fatigue $(dCMOD_{upp}/dN)_{mat}$, and the secondary crack opening rate of fiber fatigue $(dCMOD_{upp}/dN)_{fib}$. Depending on the type of concrete (plain concrete or fiber-reinforced concrete) and, in the case of SFRC, whether both fatigue mechanisms are observed, all or part of the above results are calculated. Subsequently, with these parameters, correlations with the properties of the concrete mesostructure will be attempted.

Finally, at the series and specimen size level, the fatigue life results are adjusted following a Weibull distribution, which proves to be reasonably well adapted to the fatigue phenomenon in concrete.

3.3 Mesostructural study with micro-computed tomography and image analysis

3.3.1 Scanning of specimens

The scanning of the concrete samples by micro-computed tomography was carried out at the facilities of the National Center for Research on Human Evolution (CENIEH), located in Burgos (Spain). This is a center of special importance, since it is one of the 29 Singular Scientific and Technical Infrastructures (ICTS) of the Spanish territory, whose mission is to carry out innovative research and technological development of the highest quality. Specifically, the CENIEH develops research in the field of human evolution during the upper Neogene and Quaternary. It is also responsible for the management of the archaeological and paleontological collections of the Atapuerca site (Burgos), among others.

In its Laboratory of Microscopy and Micro-computed tomography, CENIEH has a CoreTOM microCT from the company TESCAN (Brno, Czech Republic). It is a versatile X-ray inspection equipment consisting of a micro-focus tube with a maximum power of 300 W and a maximum resolution of 2 μm . The mobile system consisting of the micro-focus and the flat-panel detector allows the analysis of large samples. The maximum size of the sample to be scanned is 60 cm in diameter and 1 m in height, with a maximum weight of 45 kg.

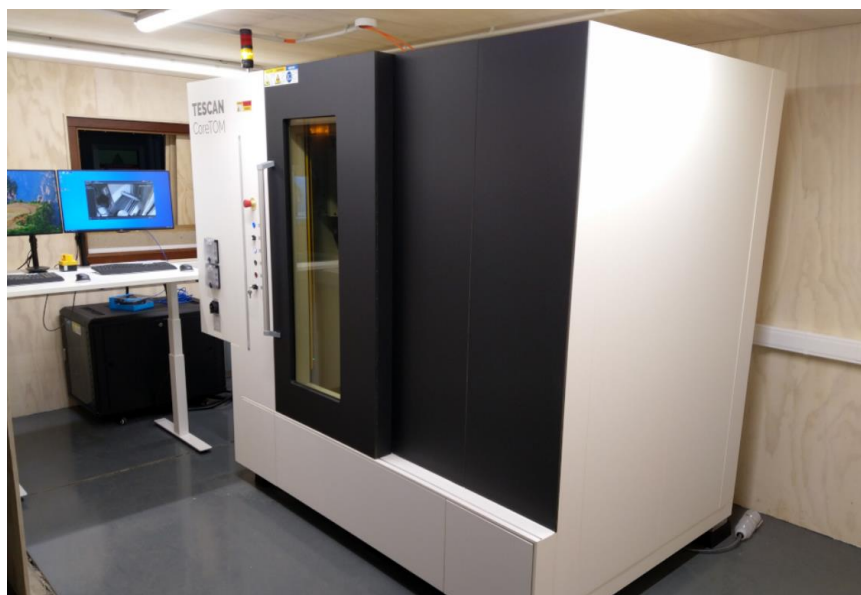


Figure 3.3-1. TESCAN CoreTOM microCT equipment.

All specimens of size S, i.e. those corresponding to the A0-S, A1-S, A2-S and A3-S series, were scanned in the microCT. Both the specimens that were tested for static flexural strength and those that were subjected to flexural fatigue were treated; in total, 64 specimens were analyzed before the tests, when the concrete was 1 year old. The reason for this is that the objective is to correlate the mesostructure of the concrete with the fatigue response; therefore, our interest is to study the intact material, not the one damaged after the tests. The resolution achieved was equal in all samples, with a value of 65 μm .

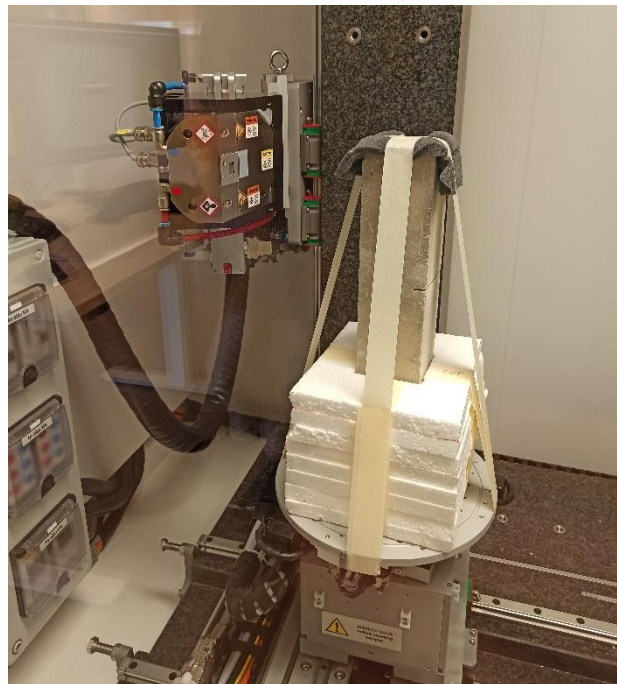


Figure 3.3-2. Specimen inside the microCT equipment.

As for the L-size specimens, they cannot be analyzed in this microCT. Although they meet the dimensional requirements, in this case the limiting factor is the combination of a large cross-section and the high density of concrete. While in the S specimens their 75x75 mm² cross-section allows obtaining reasonable results, for the 150x150 mm² cross-section of the L specimens the power of the microfocus is insufficient, resulting in low resolution and poor quality images.

The result of the microCT scanning process is a stack of images of all the slices of the sample. As already explained, these are grayscale images in which the gray level of each voxel is directly related to the density of the material it represents. As the images are 16-bit, the gray scale ranges from 0 (pure black), corresponding to the lightest material, to 65.535 (pure white), corresponding to the densest material.

The number of images obtained in each specimen depends on the resolution and the dimension of its vertical axis. Therefore, about 4,600 images are obtained on these specimens. The average time of the complete analysis process with micro-computed tomography is about 3 hours.

3.3.2 Image post-processing

The stack of images obtained from the micro-computed tomography scan allows for a 3D reconstruction of the specimen, as shown in Figure 3.3-3.

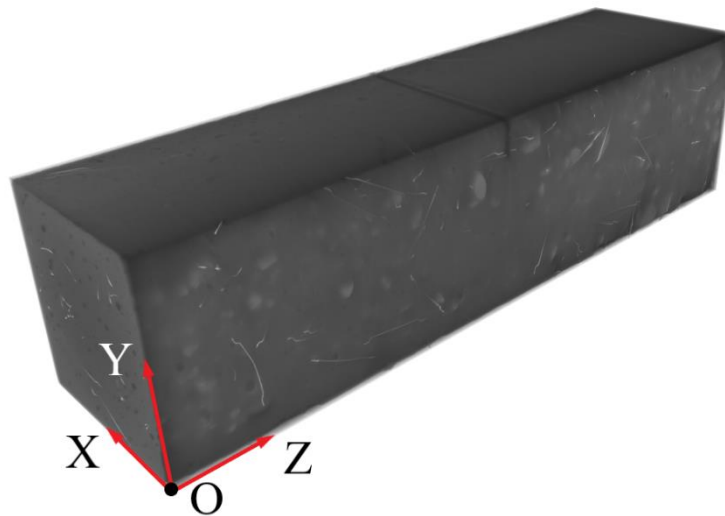


Figure 3.3-3. 3D reconstruction of specimen with indication of the coordinate axis system.

However, for the purpose of this research, the real potential of microCT lies in its combination with post-processing through image analysis. From the images obtained by microCT, digital image processing techniques can be applied to segment the different components of concrete mesostructure.

In this case, the objective of post-processing with image analysis is to obtain the main geometrical parameters of the fibers in the SFRC series (A1-S, A2-S and A3-S) and of the pores in the A0-S series of plain concrete. As addressed in more detail in Section 2, these components have been chosen because they are proven to have a notable impact on the flexural response, both static and fatigue, in each type of concrete. In addition, both pores and fibers have much difference in density with respect to the concrete matrix, which makes them more easily identifiable with this technology. The pores, being occupied by air, have practically zero density compared to that of concrete ($\rho_{\text{air}} = 1 \text{ kg/m}^3 \ll 2,400 \text{ kg/m}^3 = \rho_h$), while the fibers are made of steel, with a clearly higher density ($\rho_s = 7,850 \text{ kg/m}^3 > 2,400 \text{ kg/m}^3 = \rho_h$).

For the segmentation process, it has been used Dragonfly, an image analysis software, freely available for research purposes, developed by the company ORS (Whitesboro, NY, USA). A specific procedure adapted to the particularities of the material and the objectives of the research has been implemented in this program, for which the previous experience in image analysis of AUSINCO research group, to which the PhD candidate belongs, has been fundamental. The following is a step-by-step summary of this procedure:

1. First, CT images are imported, generating the 3D reconstruction of the specimen. Then, a prism-shaped volume of interest is created and adjusted as well as possible to the contour of the specimen, leaving the entire concrete volume inside it. The volume outside the prism, which is ultimately the air surrounding the specimen, is eliminated. In this way, the processing time is reduced.
2. Secondly, the coordinate system is repositioned so that it is always the same for all specimens (Figure 3.3-3). This step is essential for a correct interpretation of the results.
3. Thirdly, the segmentation process of fibers and pores, as appropriate, is performed. To segment a component by image analysis, the most immediate technique is thresholding. It basically consists of selecting voxels whose gray level is between certain values. However, this technique has several drawbacks. On the one hand, the selection of the range of voxels responds to subjective criteria. On the other hand, when elements of the same material are very close, thresholding merges them, as it is not able to recognize that they are distinct elements. This reduces the quality of the analysis.

To solve these problems, advanced segmentation techniques, such as the watershed transform (see subsection 2.4), must be used. Metaphorically, this technique interprets grayscale images as a topographic map, in which the gray level of each voxel represents its height. The implemented routine is able to identify the boundary lines dividing adjacent "watersheds", i.e., the elements that are theoretically in contact.

Therefore, the watershed transform technique has been applied to segment the pores and fibers of the samples.

In addition, in particularly complex cases, artificial intelligence (AI) models can be developed. This has been the case for the segmentation of fibers in the A3 series specimens, the one with the highest fiber content. Due to the high

volume of fibers, artifacts appear in these samples that result in the formation of groups of a large number of fibers that greatly distort the results obtained. Consequently, an AI model that segments the fibers according to their geometry can be implemented in the image analysis software itself. The model seeks to adapt the geometry of the fibers to each voxel cluster. When a set of voxels containing several fibers appears, the model detects that this geometry is anomalous and tries to adjust the optimal number of individual fiber geometries to this volume. As a result, it separates the different fibers that form it. Figure 2.4-4 shows the difference in results of segmenting the fibers without applying the AI model and applying it, for a specimen of the A3 series. Each color indicates a different element or group of voxels. It is clear that the watershed transform is insufficient in this case, creating a massive element of voxels (maroon tone). On the other hand, the AI model, even grouping a few fibers, achieves very acceptable results.

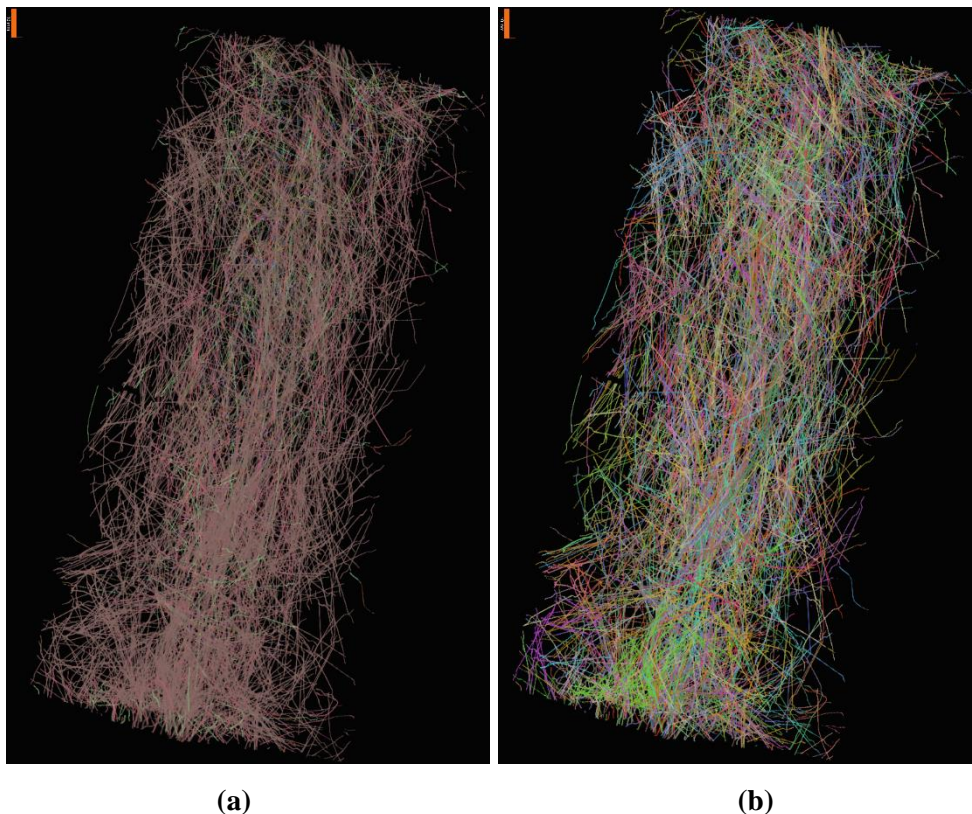


Figure 3.3-4. Fiber segmentation: (a) applying watershed transform and (b) applying watershed transform together with an artificial intelligence model.

Finally, the result of the segmentation process are elements or voxel sets that correspond to the individual fibers or pores of the sample, depending on the component under study.

4. Lastly, the individual geometrical parameters of each group of voxels are determined; that is, of the pores or fibers of the specimen studied, as applicable. This process is carried out automatically by means of a tool incorporated in the software itself. The geometrical parameters that are calculated for each type of component are briefly indicated below:
- Fibers: volume, length, thickness, coordinates of the center of gravity, coordinates of the extreme points along the XYZ axes, orientation with respect to the XYZ axes.
 - Pores: volume, surface area, length, width, coordinates of the center of gravity.

The results are exported for further statistical processing.

4 RESULTS

This section presents the results of the characterization tests, the flexural fatigue tests and the study of the microstructure by means of micro-computed tomography. The objective is to present the direct test results, making only a first brief and general analysis of them.

Therefore, this section serves as a starting point for the following chapter (5. ANALYSIS OF RESULTS AND DISCUSSION), where an in-depth analysis is carried out, second level results are extracted and, in short, the main conclusions of this doctoral thesis are drawn.

4.1 Characterization tests

This subsection contains the results of the preliminary tests, whose objectives are to characterize the material and determine the parameters of the fatigue tests. The characterization tests that have been carried out are: slump, compressive strength, modulus of elasticity and flexural strength.

4.1.1 Slump test

The slump test was carried out in accordance with UNE-EN 12350-8 [142]. The two parameters that assess the self-compactness are the final diameter of the concrete poured (d_f) and the time it takes to reach a diameter of 500 mm (t_{50}). Table 3.1-3 contains the mean values of the 4 batches of each series, including the standard deviation. In addition, comparative graphs are shown.

Table 4.1-1. Results of the slump test.

Series	d_f (mm)	t_{50} (s)
A0	843 [13]	4.8 [0.5]
A1	768 [13]	5.1 [0.5]
A2	739 [37]	4.9 [0.4]
A3	648 [44]	5.5 [0.4]

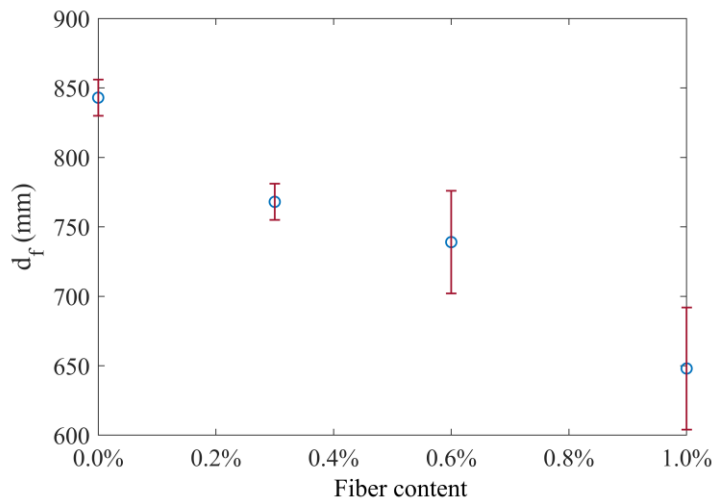


Figure 4.1-1. Slump vs fiber content.

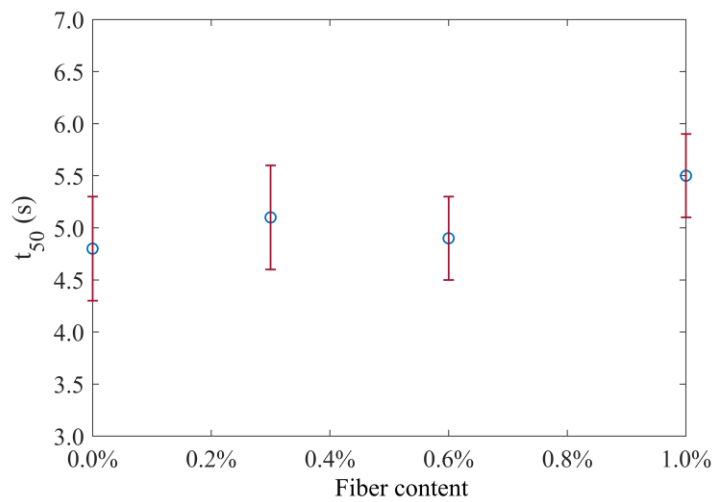


Figure 4.1-2. Time t_{50} vs fiber content.

It can be seen that in all cases the general requirements for self-compactness set by the Spanish Structural Code are met (see Table 3.1-3). However, the presence of fibers significantly affects the consistency of the concrete. Figure 4.1-1 reveals that the slump decreases roughly proportionally with increasing fiber content. As for the time t_{50} , its value increases slightly, although this parameter is less sensitive to the dosage of fibers.

With respect to the slump classes set by the Structural Code, the A0 and A1 series are classified as AC-SF3 ($760 \text{ mm} \leq d_f \leq 850 \text{ mm}$), the A2 series as AC-SF2 ($660 \text{ mm} \leq d_f \leq 750 \text{ mm}$) and the A3 series as AC-SF1 ($550 \text{ mm} \leq d_f \leq 650 \text{ mm}$).

The slump test also allows a qualitative evaluation of the segregation resistance of the concrete. Figure 4.1-3 shows the final appearance of the slump flow from one of the batches in each series.

In general, a uniform distribution of fibers and coarse aggregate is observed in all the series, and no significant exudation phenomena occur in the perimeter of the slump flow. It is worth mentioning that the A3 series has a slightly different appearance, which can be explained by the fact that, for this type of concrete, the fiber content begins to be high. If more fibers were added, the dosage would probably have to be corrected to avoid problems of segregation, formation of fiber balls, etc.

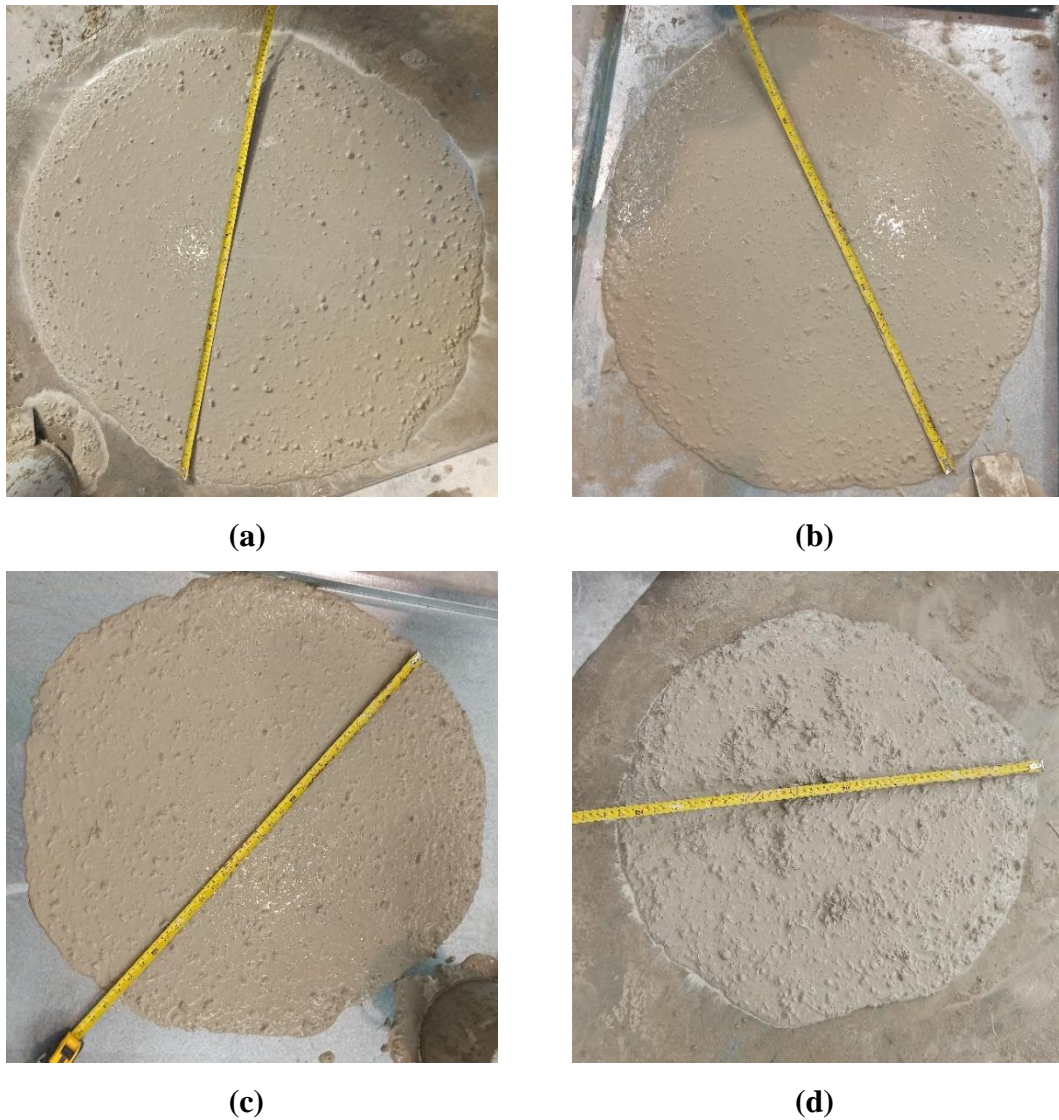


Figure 4.1-3. Appearance of the slump flow: (a) A0, (b) A1, (c) A2 and (d) A3.

4.1.2 Compressive strength

The compressive strength was determined according to UNE-EN 12390-3 [143]. The tests were carried out when the concrete was 1 year and 4 months old, i.e., just before the fatigue campaign began. Table 4.1-2 shows the results of the 4 specimens tested per series, including the mean value and the deviation. The comparative graph is also included.

It is worth mentioning that, for information purposes, in order to know the compressive strength at 28 days, 3 additional specimens of the plain concrete dosage (A0) were tested, with the result of 79.41 ± 1.75 MPa.

Table 4.1-2. Compressive strength.

Series	Specimen	$f_{c,i}$ (MPa)	f_c (MPa)	$f_{c,tot}$ (MPa)
A0	A0-CL-1	106.90	107.13 [1.73]	
	A0-CL-2	104.83		
	A0-CL-3	108.88		
	A0-CL-7	107.91		
A1	A1-CL-1	107.35	106.62 [3.41]	106.78 [2.06]
	A1-CL-2	106.28		
	A1-CL-3	102.28		
	A1-CL-4	110.55		
A2	A2-CL-1	106.58	106.22 [2.01]	
	A2-CL-2	103.73		
	A2-CL-3	108.60		
	A2-CL-7	105.96		
A3	A3-CL-1	107.05	107.17 [1.30]	
	A3-CL-2	107.53		
	A3-CL-3	108.62		
	A3-CL-7	105.48		

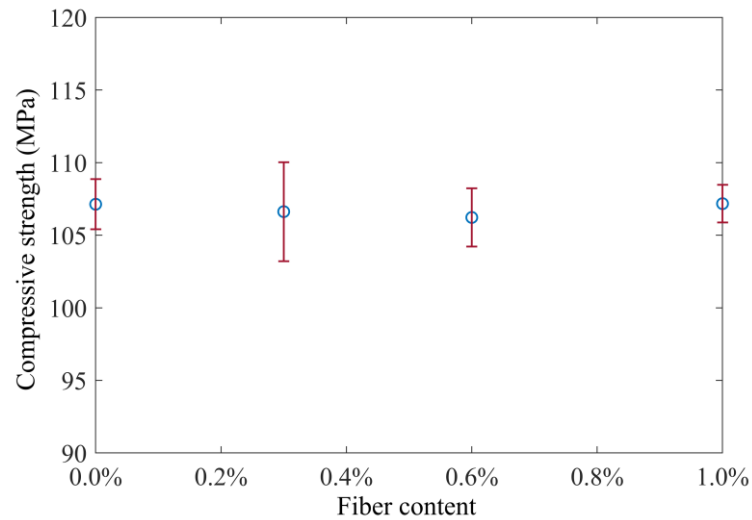


Figure 4.1-4. Compressive strength vs fiber content.

The results agree with the already known fact that the presence of fibers, for the usual contents, hardly affects the compressive strength of the concrete.

The mean value of the compressive strength considering all series is 106.78 MPa, with a deviation of ± 2.06 MPa. Therefore, it is clearly a high-strength concrete.

Figure 4.1-5 contains the stress-strain curves of all compression tests. The strain has been calculated from the displacement of the testing machine plate, so the results should be interpreted purely for comparative purposes.

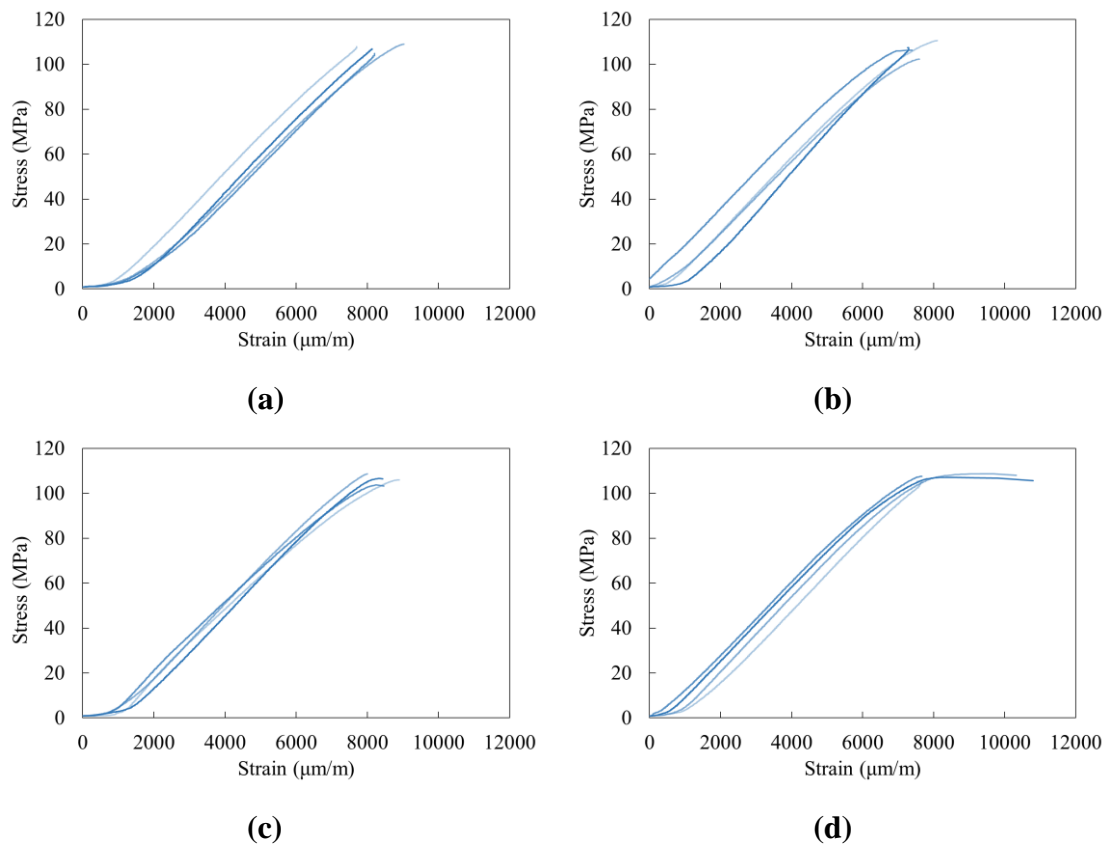


Figure 4.1-5. Stress-strain curves in compressive strength tests: (a) A0, (b) A1, (c) A2 and (d) A3.

Figure 4.1-5 reveals that the behavior is very similar in all series. The major difference is observed in two specimens of the A3 series, which show post-peak plasticization due to the ductility provided by the fibers. The specimens of the other SFRC series do not show this post-peak plasticization phenomenon, possibly because the ductility provided by the fibers is not sufficient to counteract the high brittleness of high-strength concrete.

4.1.3 Modulus of elasticity

The modulus of elasticity tests were performed according to UNE-EN 12390-13 [144]. Strain gauges were used to measure the strain of concrete, and 3 tests per series were performed. Table 4.1-3 contains the results, including mean values and deviations. In addition, the comparative graph is shown.

Table 4.1-3. Modulus of elasticity in compression.

Series	Specimen	E_i (MPa)	E (MPa)	E_{tot} (MPa)
A0	A0-CL-4	47,358	44,283 [2,703]	45,092 [1,486]
	A0-CL-5	43,203		
	A0-CL-6	42,286		
A1	A1-CL-4	45,733	45,156 [645]	
	A1-CL-5	44,460		
	A1-CL-6	45,275		
A2	A2-CL-4	45,341	44,866 [935]	
	A2-CL-5	43,788		
	A2-CL-6	45,468		
A3	A3-CL-4	47,213	46,063 [1,033]	
	A3-CL-5	45,212		
	A3-CL-6	45,764		

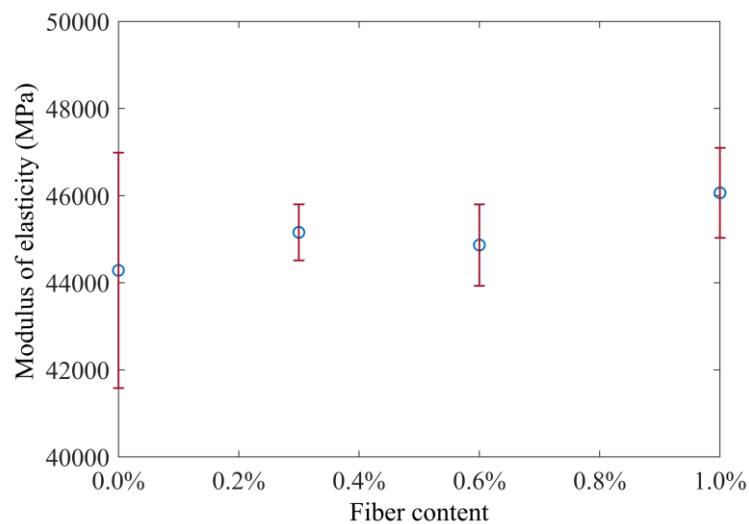
**Figure 4.1-6. Modulus of elasticity vs fiber content.**

Figure 4.1-6 shows that the modulus of elasticity tends to increase slightly with fiber content, although considering the deviations of the results, this increase is statistically negligible. Again, this is in agreement with the scientific literature.

The average modulus of elasticity in the whole sample is $45,092 \pm 1,486$ MPa. The plain concrete series (A0) has the greatest dispersion of results, with a coefficient of variation greater than 6%. It seems that the presence of fibers has the beneficial effect of reducing the dispersion of the modulus of elasticity.

4.1.4 Flexural strength

The flexural static strength was evaluated according to UNE-EN 14651 [7], equivalent to RILEM TC 162-TDF [17]. The main test results are shown below, differentiating between the two specimen sizes.

4.1.4.1 S-size specimens

Figure 4.1-7 to 4.1-10 show the nominal stress vs CMOD plots of the 4 series of specimens of size S (A0-S, A1-S, A2-S and A3-S). Each plot contains the average curve and the deviation in shading.

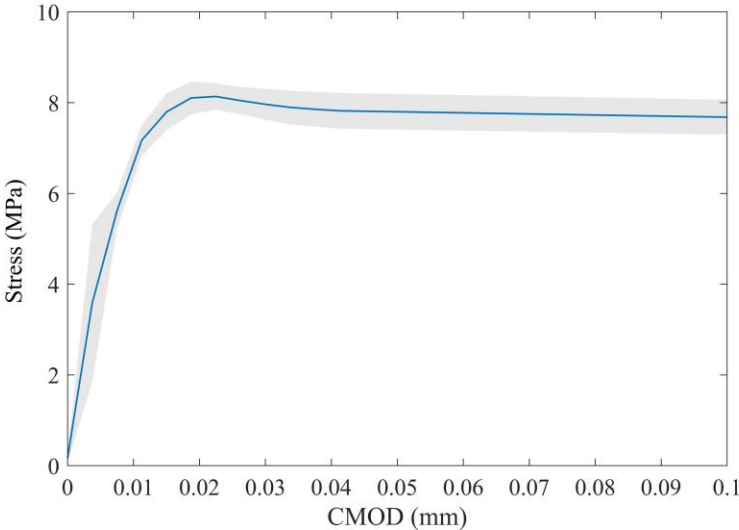


Figure 4.1-7. Nominal stress vs CMOD diagram of A0-S series.

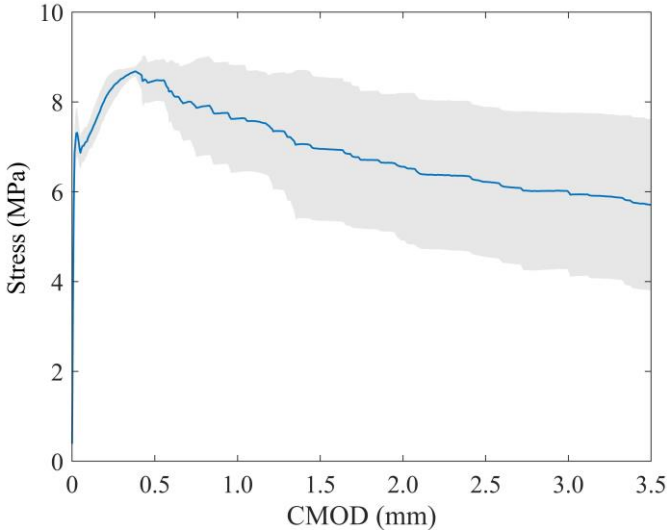


Figure 4.1-8. Nominal stress vs CMOD diagram of A1-S series.

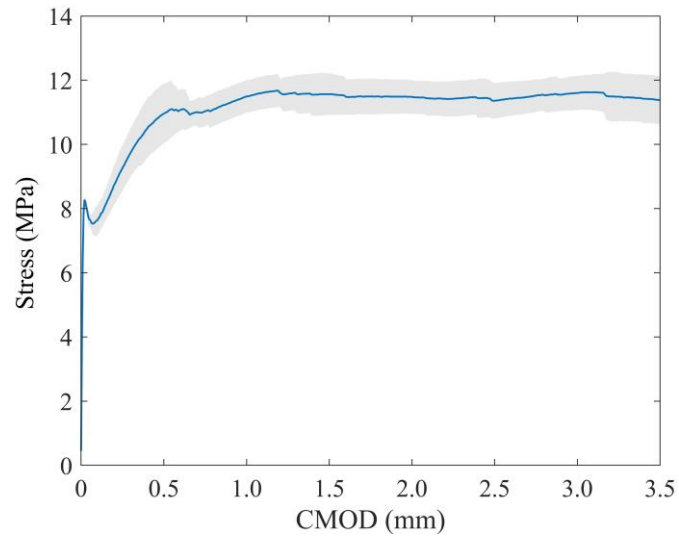


Figure 4.1-9. Nominal stress vs CMOD diagram of A2-S series.

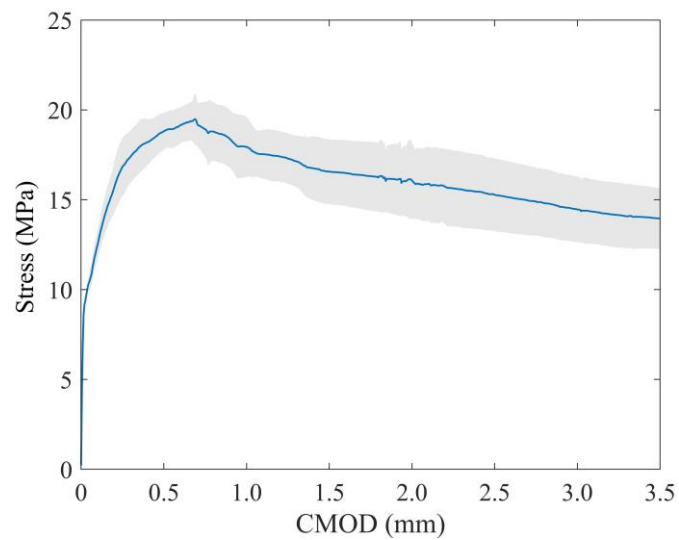


Figure 4.1-10. Nominal stress vs CMOD diagram of A3-S series.

The comparative graph with the average curves of the four series is shown below.

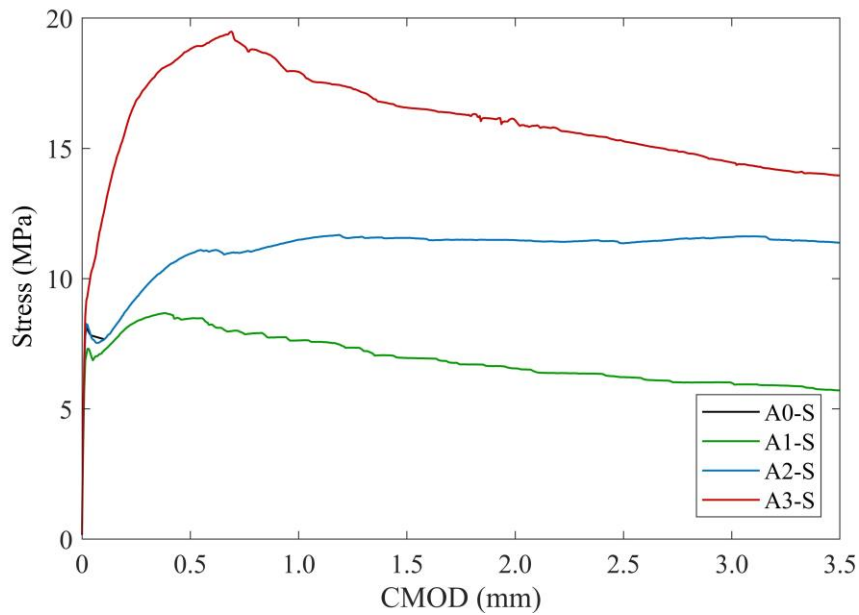


Figure 4.1-11. Comparison of the nominal stress vs CMOD diagrams for the series of S-size specimens.

Table 4.1-4 shows the maximum flexural strength, expressed both in terms of load (P_{max}) and nominal or equivalent stress (σ_{max}). Individual results are included, as well as average values and deviations.

Table 4.1-4. Maximum flexural strength.

Series	Specimen	$P_{max,i}$ (kN)	P_{max} (kN)	$\sigma_{max,i}$ (MPa)	σ_{max} (MPa)
A0-S	A0-S-1	6.11		7.82	
	A0-S-2	6.37	6.41 [0.33]	8.15	8.21 [0.42]
	A0-S-3	6.76		8.66	
A1-S	A1-S-1	6.93		8.87	
	A1-S-2	6.70	6.86 [0.14]	8.57	8.78 [0.18]
	A1-S-3	6.95		8.90	
A2-S	A2-S-1	9.53		12.19	
	A2-S-2	8.57	9.21 [0.55]	10.97	11.78 [0.7]
	A2-S-3	9.52		12.19	
A3-S	A3-S-1	16.75		21.44	
	A3-S-2	14.85	15.35 [1.22]	19.00	19.65 [1.57]
	A3-S-3	14.46		18.51	

Another parameter that characterizes the response of SFRC in bending is the strength corresponding to the limit of proportionality (LOP), which is defined as the maximum load or stress reached in the CMOD range from 0 to 0.05 mm. This parameter can be considered equivalent to the so-called first crack resistance. Table 4.1-5 lists the values

of this strength, expressed both in terms of load (P_L) and stress (f_L). The individual results are included, and finally the average values and deviations. The data of the A0-S series are not included, since in plain concrete the maximum strength and that of the LOP coincide.

Table 4.1-5. Strength corresponding to the limit of proportionality.

Series	Specimen	$P_{L,i}$ (kN)	P_L (kN)	$f_{L,i}$ (MPa)	f_L (MPa)
A1-S	A1-S-1	5.34		6.83	
	A1-S-2	5.59	5.75 [0.52]	7.15	7.36 [0.66]
	A1-S-3	6.33		8.10	
A2-S	A2-S-1	6.56		8.39	
	A2-S-2	6.35	6.52 [0.15]	8.13	8.35 [0.19]
	A2-S-3	6.65		8.51	
A3-S	A3-S-1	8.70		11.13	
	A3-S-2	7.86	8.16 [0.46]	10.06	10.45 [0.59]
	A3-S-3	7.94		10.16	

Next, a graph comparing the maximum flexural stress and the stress corresponding to LOP versus fiber content is shown.

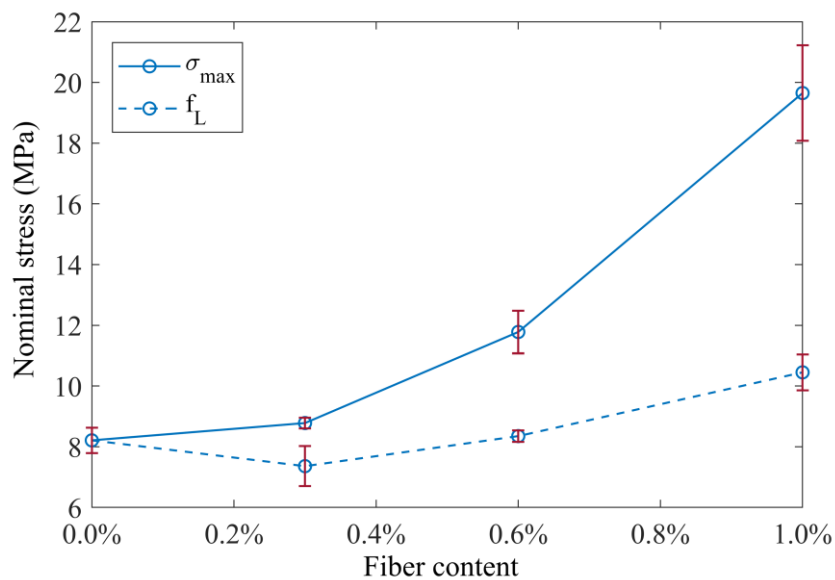


Figure 4.1-12. Maximum stress and stress corresponding to the LOP in the flexural tensile test, vs fiber content.

Several conclusions can be drawn from the results shown. First, Figure 4.1-11 shows that the addition of fibers modifies the fracture behavior of concrete from brittle to clearly ductile. Consequently, the fracture toughness increases significantly. Secondly, the fibers also cause an increase in the ultimate flexural strength, i.e., strain-hardening behavior

occurs, characterized by the fact that the strength mechanism of the fibers is able to take on more load than that of the matrix. Due to the ductility provided by the fibers, maximum strengths are reached at high CMOD values.

Third, Figure 4.1-12 reveals that the increase in ultimate strength is not proportional to the fiber dosage, but follows an exponential trend. Compared to plain concrete, the increases are 7%, 43% and 240% for fiber contents of 0.3%, 0.6% and 1.0%, respectively. Finally, the corresponding LOP strength remains constant for fiber amounts up to 0.6%, while it only increases with 1%. This is to be expected, since the first-crack strength of concrete is primarily governed by the matrix. When the concrete starts to crack, there is a progressive transfer of tensile stresses from the matrix to the fibers. As for the behavior of the A3-S series, due to the high volume of fibers, the stress drop after the first crack is practically imperceptible, with the result that the fibers assume stress from low CMODs, less than 0.05 mm.

The flexural response of fiber-reinforced concrete can also be evaluated through the residual strength. Below is a table with the values of residual strengths f_{R1} , f_{R2} , f_{R3} and f_{R4} according to MC 2010 [33], corresponding to crack openings of 0.5, 1.5, 2.5 and 3.5 mm, respectively. The comparative bar chart is shown in Figure 4.1-13. Again, the data of the A0-S series are not included because in plain concrete, when f_L is reached, collapse occurs and the residual strength is zero.

Table 4.1-6. Residual flexural strengths of SFRC series.

Series	f_L (MPa)	f_{R1} (MPa)	f_{R2} (MPa)	f_{R3} (MPa)	f_{R4} (MPa)
A1-S	7.36 [0.66]	8.47 [0.56]	6.95 [1.96]	6.22 [2.05]	5.71 [2.33]
A2-S	8.35 [0.19]	10.96 [1.13]	11.56 [0.79]	11.36 [0.68]	11.38 [0.92]
A3-S	10.45 [0.59]	18.82 [1.27]	16.57 [2.21]	15.27 [2.47]	13.96 [2.07]

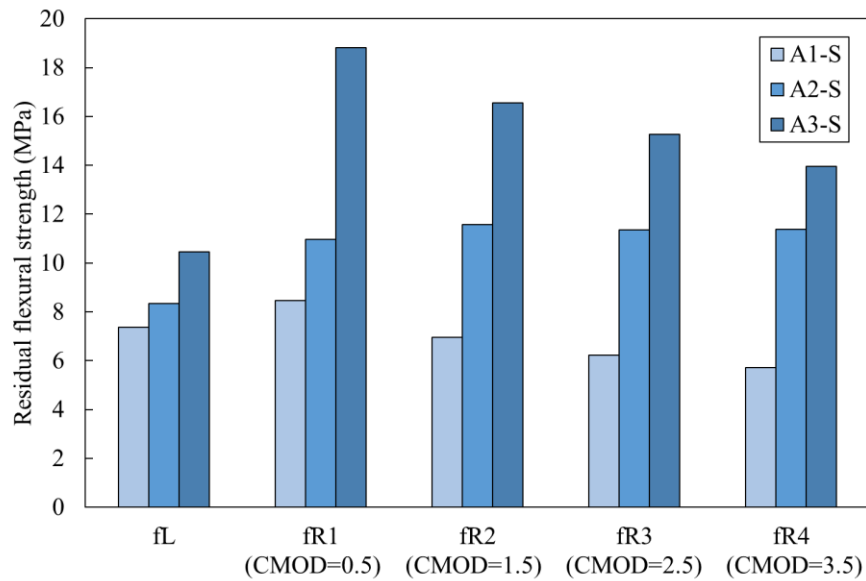


Figure 4.1-13. Residual flexural strengths of SFRC series.

Once again, strain-hardening behavior is evident, since the maximum strength is not f_L , but f_{R1} in the A1-S and A3-S series, and f_{R2} in the A2-S series. The SFRC strength classes according to MC 2010 are 8b, 10c and 18b for A1-S, A2-S and A3-S series, respectively. The first component is a number representing the residual resistance f_{R1} , while the second is a letter that is assigned based on the ratio f_{R3}/f_{R1} . The higher the ratio, the "higher" the letter and the better the post-peak performance of the SFRC. For example, the A2-S series is classified as c and clearly experiences a smaller decrease in residual strength with increasing CMOD.

4.1.4.2 L-size specimens

Figure 4.1-14 to 4.1-17 show the nominal stress vs CMOD plots of the 4 series of L-size specimens (A0-L, A1-L, A2-L and A3-L). Each plot contains the average curve and the deviation in shading.

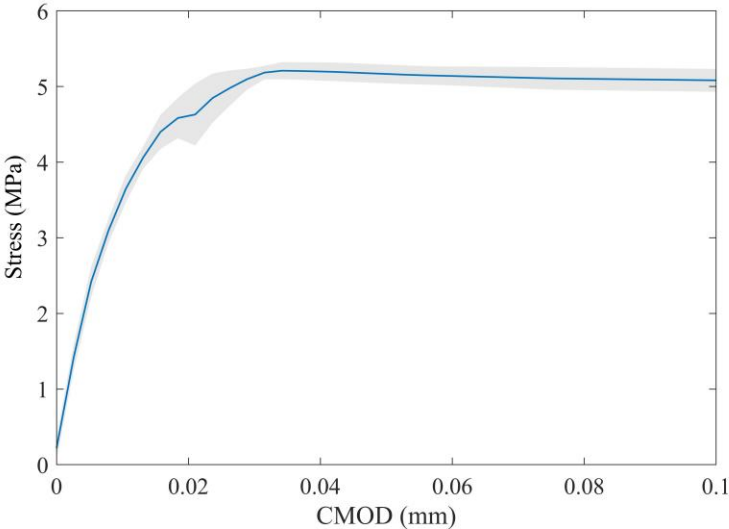


Figure 4.1-14. Nominal stress vs CMOD diagram of A0-L series.

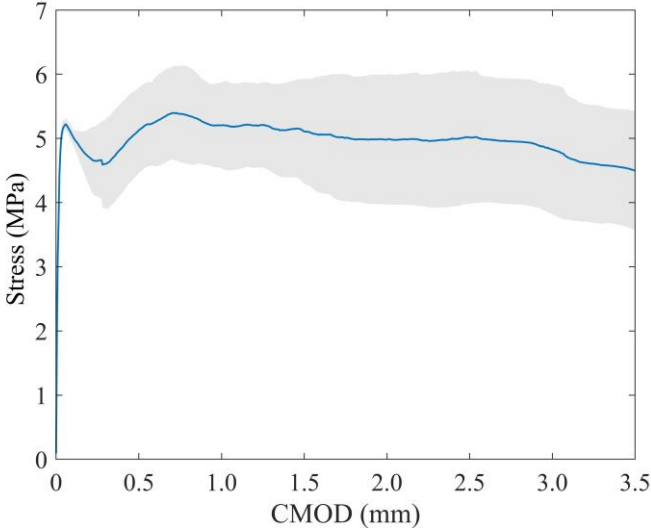


Figure 4.1-15. Nominal stress vs CMOD diagram of A1-L series.

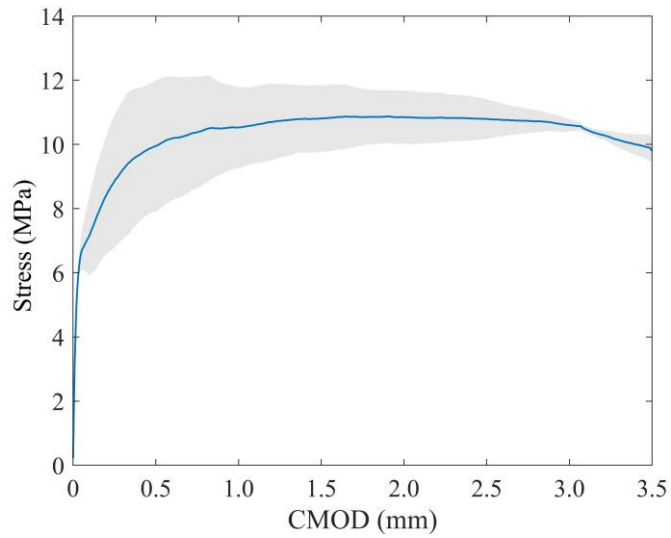


Figure 4.1-16. Nominal stress vs CMOD diagram of A2-L series.

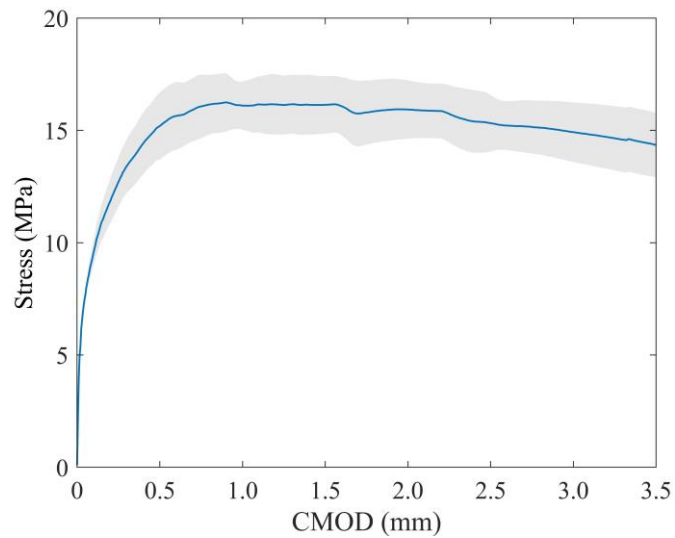


Figure 4.1-17. Nominal stress vs CMOD diagram of A3-L series.

The comparative graph with the average curves of the four series is shown below.

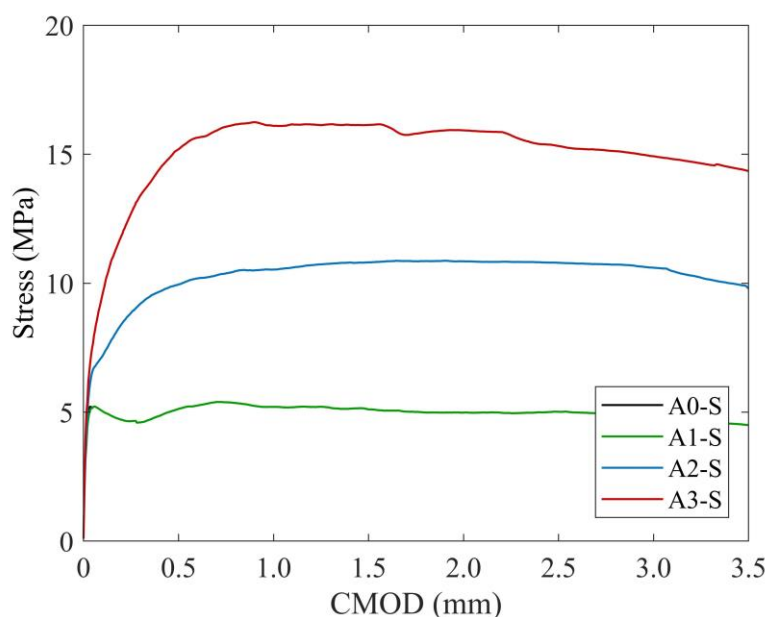


Figure 4.1-18. Comparison of the nominal stress vs CMOD diagrams for the L-size specimen series.

Table 4.1-7 shows the maximum flexural strength, expressed both in terms of load (P_{max}) and nominal or equivalent stress (σ_{max}). Individual results are included, as well as average values and deviations.

Table 4.1-7. Maximum flexural strength.

Series	Specimen	$P_{max,i}$ (kN)	P_{max} (kN)	$\sigma_{max,i}$ (MPa)	σ_{max} (MPa)
A0-L	A0-L-8	16.48		5.27	
	A0-L-11	16.69	16.33 [0.45]	5.34	5.23 [0.14]
	A0-L-12	15.82		5.06	
A1-L	A1-L-1	19.77		6.33	
	A1-L-7	19.89	18.54 [2.23]	6.36	5.93 [0.71]
	A1-L-8	15.96		5.11	
A2-L	A2-L-4	33.42		10.70	
	A2-L-11	40.41	35.53 [4.24]	12.93	11.37 [1.36]
	A2-L-14	32.76		10.48	
A3-L	A3-L-9	56.52		18.09	
	A3-L-11	48.36	51.27 [4.55]	15.48	16.41 [1.46]
	A3-L-15	48.94		15.66	

Table 4.1-8 below lists the strength values corresponding to the limit of proportionality, expressed both in terms of load (P_L) and stress (f_L). Individual results are included, as well as averages and deviations. As in the case of S specimens, the values of A0-L are not added because in plain concrete σ_{max} coincides with f_L .

Table 4.1-8. Strength corresponding to the limit of proportionality.

Series	Specimen	$P_{L,i}$ (kN)	P_L (kN)	$f_{L,i}$ (MPa)	f_L (MPa)
A1-L	A1-L-1	16.76		5.36	
	A1-L-7	16.17	16.3 [0.41]	5.18	5.22 [0.13]
	A1-L-8	15.96		5.11	
A2-L	A2-L-4	18.94		6.06	
	A2-L-11	23.32	20.83 [2.25]	7.46	6.67 [0.72]
	A2-L-14	20.23		6.47	
A3-L	A3-L-9	25.30		8.09	
	A3-L-11	24.05	24.18 [1.06]	7.70	7.74 [0.34]
	A3-L-15	23.19		7.42	

Next, a graph comparing the maximum flexural stress and the stress corresponding to the LOP versus fiber content is shown.

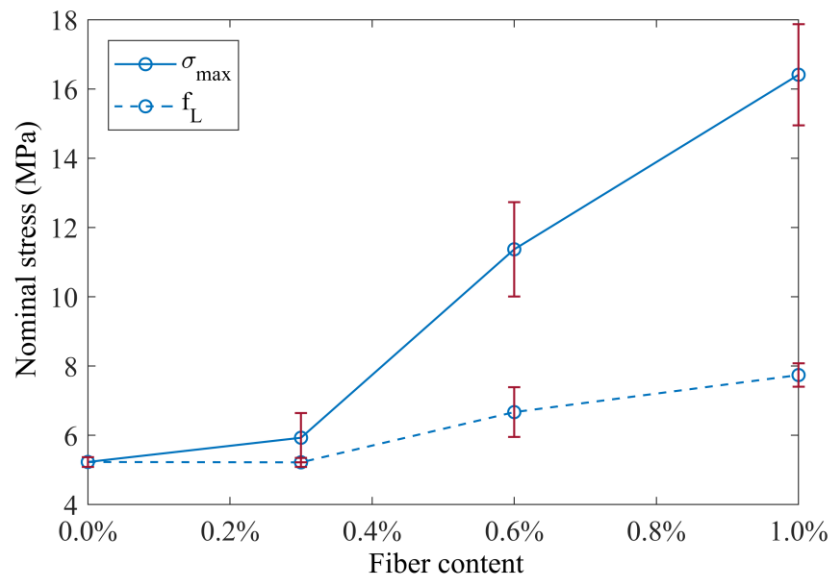


Figure 4.1-19. Maximum stress and stress corresponding to LOP in the flexural tensile test, vs fiber content.

The results yield some interesting conclusions. First, as already mentioned, fibers introduce a strength mechanism quite different from that of plain concrete, leading to a strongly ductile failure (Figure 4.1-18). Second, SFRC series experience an increase in ultimate flexural strength. In fact, this increase occurs in the series with more fibers (A2-L and A3-L), where a clear strain-hardening behavior is observed. On the other hand, in the A1-L series, the strength at first crack is practically identical to that reached by the fibers a posteriori, showing an evident plastic deformation behavior, consisting of an increase in the CMOD under constant load (Figure 4.1-18).

Third, Figure 4.1-19 shows that the maximum flexural strength increases significantly with fiber content. In relation to plain concrete, in the A1-L series the increase is insignificant, while the most notable increase is between the A1-L and A2-L series. Specifically, the strength improves by 13%, 117% and 214% for fiber dosages of 0.3%, 0.6% and 1.0%, respectively. Finally, as for the strength corresponding to the LOP, it remains constant for the lowest fiber content, from which it increases slightly.

On the other hand, it is interesting to know the residual strength of SFRC series. Below is a table with the values of the residual strengths f_{R1} , f_{R2} , f_{R3} and f_{R4} according to MC 2010, corresponding to CMODs of 0.5, 1.5, 2.5 and 3.5 mm, respectively. The comparative bar chart is shown in Figure 4.1-20.

Table 4.1-9. Residual flexural strengths of SFRC series.

Series	f_L (MPa)	f_{R1} (MPa)	f_{R2} (MPa)	f_{R3} (MPa)	f_{R4} (MPa)
A1-L	5.22 [0.13]	5.12 [0.82]	5.11 [1.00]	5.02 [1.27]	4.50 [1.14]
A2-L	6.67 [0.72]	9.95 [2.50]	10.81 [1.27]	10.79 [0.76]	9.79 [0.38]
A3-L	7.74 [0.34]	15.19 [1.82]	16.14 [1.56]	15.32 [1.54]	14.34 [1.76]

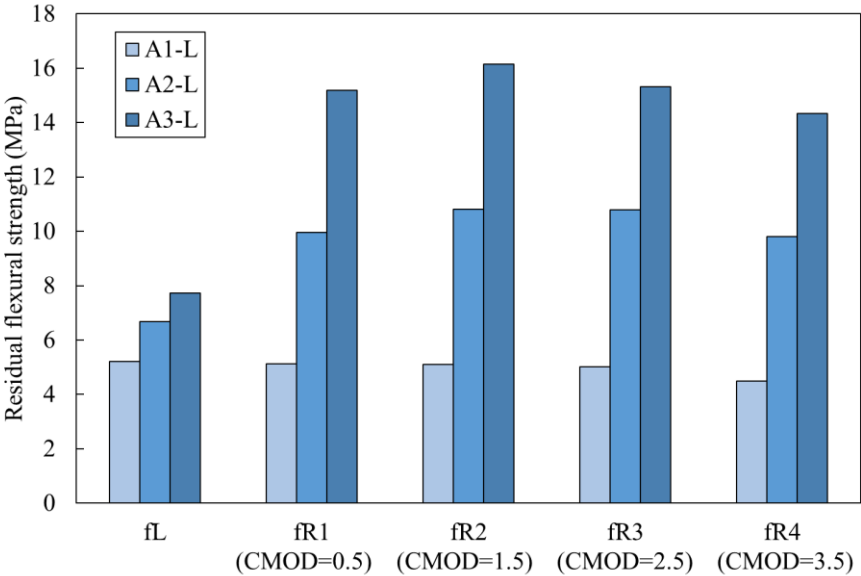


Figure 4.1-20. Residual flexural strengths of SFRC series.

Again, Figure 4.1-20 reflects the different behaviors of SFRC series. On the one hand, series A2-L and A3-L show strain-hardening, since the maximum strength is reached at f_{R2} , with a CMOD of 1.5 mm, starting to decrease from this value. On the other hand, A1-L series experiences plastic deformation; in this case, the maximum strength is reached at f_L , but only decreases by 4% up to f_{R3} . The SFRC strength classes according to MC

2010 are 5c, 9c and 15c for A1-L, A2-L and A3-L series, respectively. The index c corresponds to a plastic-type behavior, where the strength hardly decreases with increasing CMOD. This is clearly seen in Figure 4.1-18.

4.2 Flexural fatigue tests

The flexural fatigue tests were carried out as described in Section 3. In particular, the test parameters for each of the series can be found in Table 3.2-3. The main results are presented below, distinguishing between the two specimen sizes. It is worth mentioning that an appendix with all the individual fatigue test data sheets is included at the end of the document.

4.2.1 S-size specimens

4.2.1.1 Fatigue life

Table 4.2-1 shows the fatigue life for all tests on specimens of size S. Twelve tests were performed in each series.

Table 4.2-1. Fatigue life N.

Test No.	A0-S	A1-S	A2-S	A3-S
1	1,000,000*	6,121	3,522	18,889
2	99,976	4,838	10,316	918
3	511,248	3,696	40,858	30
4	243,232	43	19,401	3,176
5	139,687	2,642	22,481	12,888
6	456,365	2,791	1,000,000*	7,195
7	82,695	9,226	26,308	15,225
8	2,674	3,956	20,746	12
9	16,155	1,512	5,156	31
10	1,304	5,263	5,068	3,090
11	44,497	4,015	14,233	3,743
12	6,153	48	5,024	2,219

The results indicate that the series without fibers (A0-S) is the one with the longest fatigue life, visibly distancing itself from SFRC series. Only two specimens have reached the runout limit of 1,000,000 cycles: one from the A0-S series and the other from the A2-S series.

As discussed above, the Weibull distribution function is usually used to statistically describe the fatigue life data, since it fits its high dispersion reasonably well. Figure 4.2-1 to 4.2-4 show, for each series, the fit of the results to the Weibull function of two parameters. It should be mentioned that these parameters were determined by the graphical method.

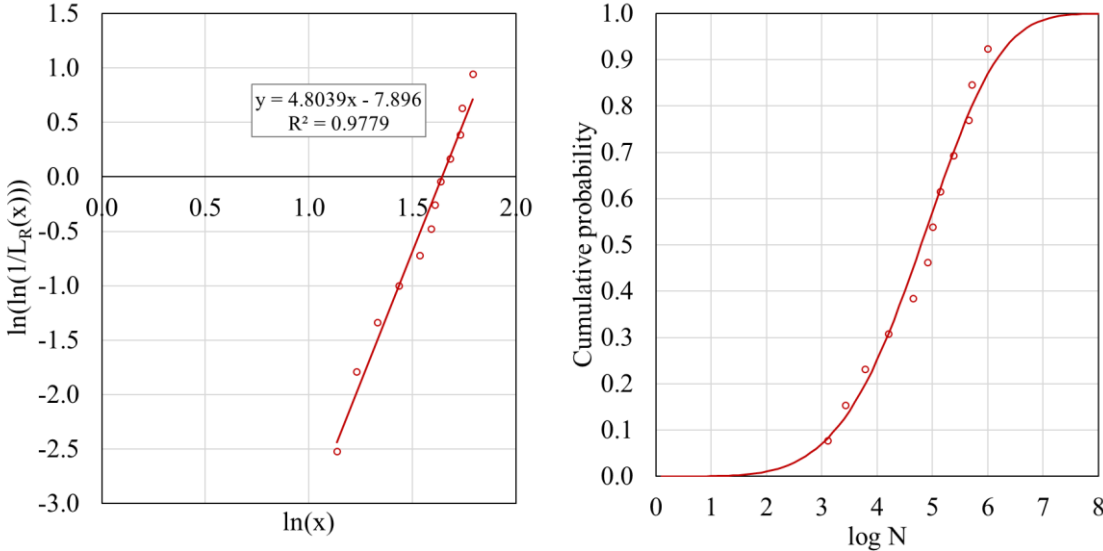


Figure 4.2-1. Fit to the Weibull distribution of the fatigue life of A0-S series.

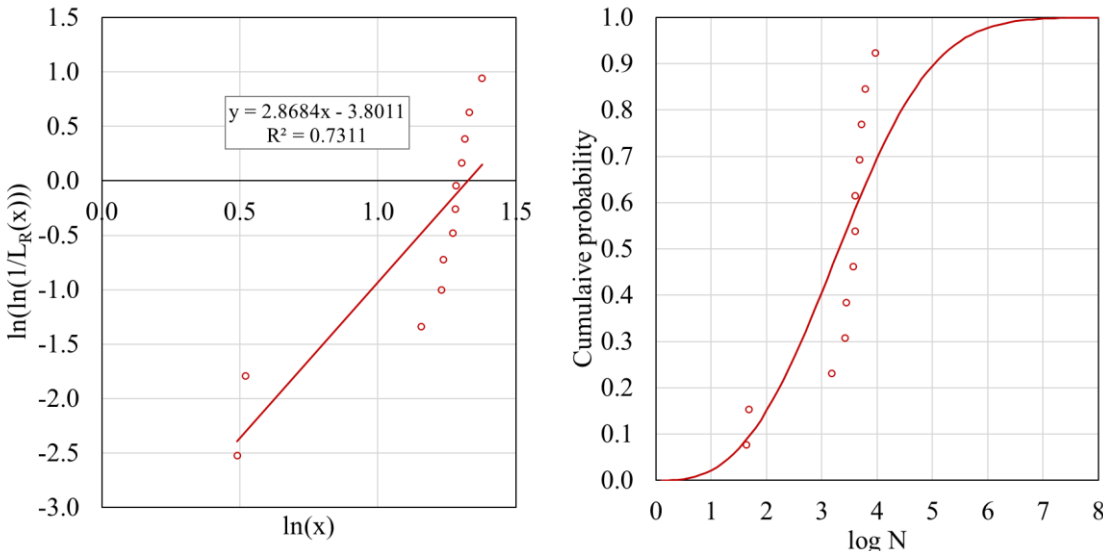


Figure 4.2-2. Fit to the Weibull distribution of the fatigue life of A1-S series.

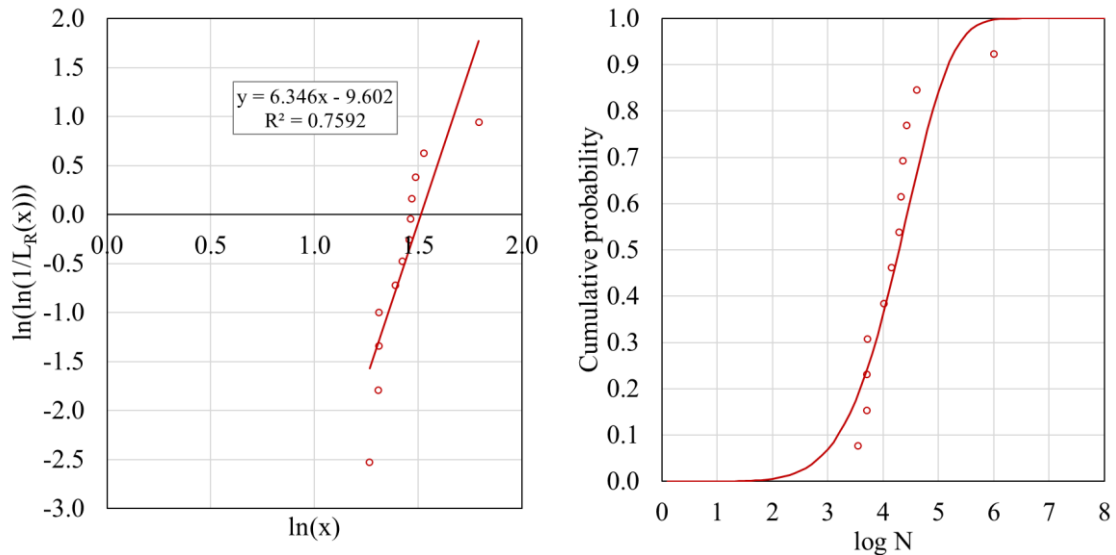


Figure 4.2-3. Fit to the Weibull distribution of the fatigue life of A2-S series.

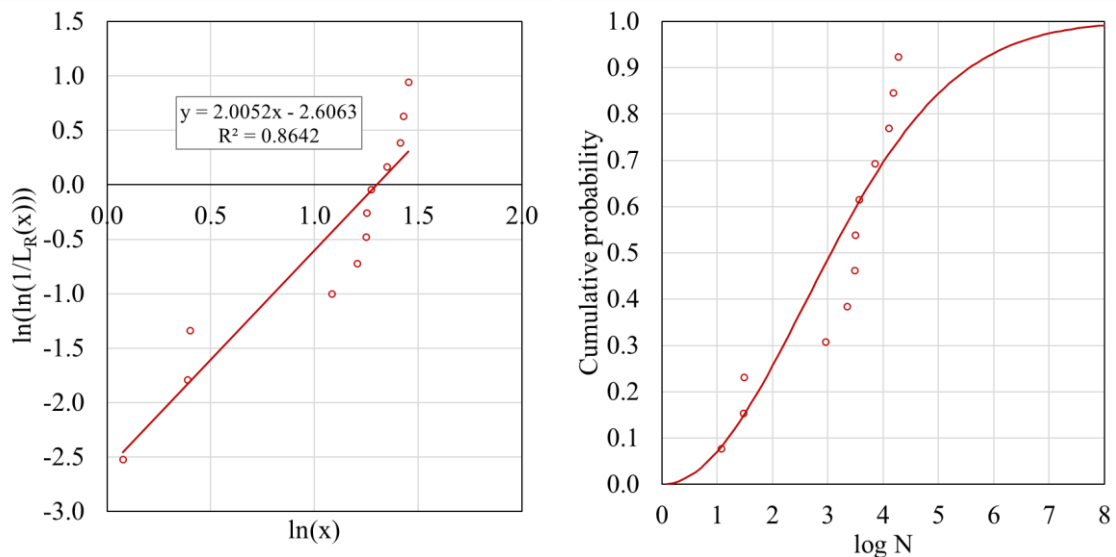


Figure 4.2-4. Fit to the Weibull distribution of the fatigue life of A3-S series.

In general, it is concluded that the results of the 4 series fit well to the Weibull distribution function. The A0-S series, for plain concrete, has the highest correlation coefficient R^2 , reaching 0.98. For the rest, its value is 0.73, 0.76 and 0.86 for the A1-S, A2-S and A3-S series, respectively. It is observed that, in the particular case of the A1-S and A3-S series, lower values of fatigue life (below 10^2 cycles) clearly alter the fit. In the case of the A2-S series, it is the highest fatigue value that shows a dissonant behavior with respect to the rest.

Figure 4.2-5 plots the Weibull distribution functions of the fatigue life of the 4 series, including the points representing each test. In addition, Table 4.2-2 shows the values of the fit parameters λ and β .

Table 4.2-2. Fit parameters λ and β of the Weibull distribution function.

Series	λ	β
A0-S	5.17	4.80
A1-S	3.76	2.87
A2-S	4.54	6.35
A3-S	3.67	2.01

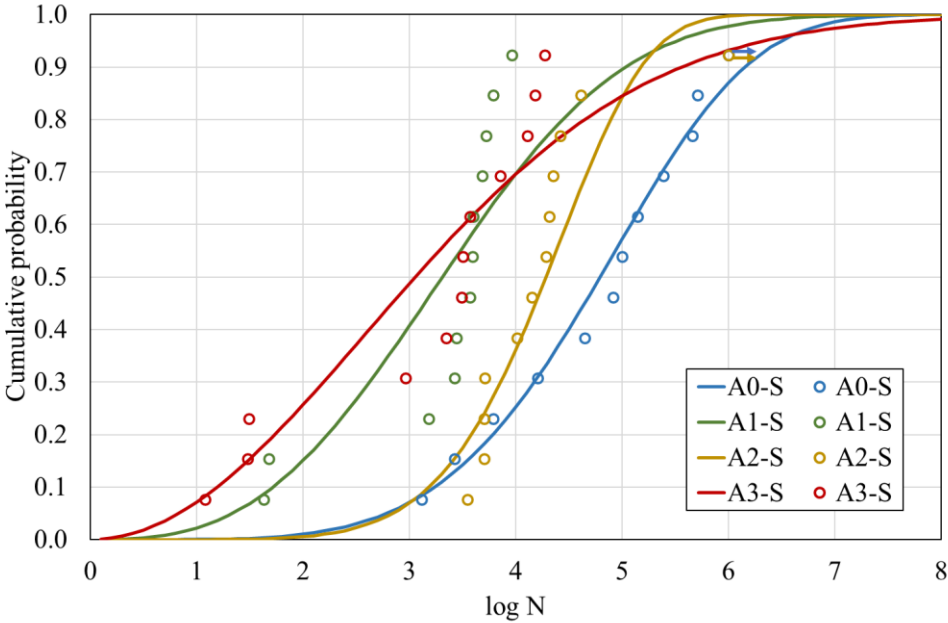


Figure 4.2-5. Fit to the Weibull distribution of the fatigue life of the S-size series.

The scale parameter λ is related to the characteristic fatigue life, so that the higher the fatigue life, the higher its value. In Figure 4.2-5, this means that the distribution function curve is more to the right. Therefore, the series with the highest fatigue life is A0-S, plain concrete. It is followed by the A2-S series and finally by the A1-S and A3-S series, whose fatigue life is very similar.

At this point, it should be remembered that the range of loads applied in the fatigue tests are percentages of the maximum load in the static flexural tests (in this case, between 16% and 80%). This implies that the range of fatigue loads to which the A3-S series specimens have been subjected is much greater than that of the A0-S series; specifically, 2.5-12.3 kN versus 1.0-5.1 kN. Consequently, caution should be exercised when interpreting the results. The A0-S series (without fibers) has a higher fatigue strength than A3-S (with 1.0% fibers) taking the maximum flexural load as a reference. However, if the A3-S series specimens were subjected to the same loads as the A0-S series, it is very

likely that their fatigue life would be much higher, being close to the endurance limit or infinite life.

On the other hand, the shape parameter β is an indicator of dispersion, so that the lower the variability of the results, the higher its value. In Figure 4.2-5, this is reflected in the slope of the curve being higher. Consequently, the series with the lowest dispersion is A2-S, followed by A0-S, and finally A1-S and A3-S. To get an overall idea of the fatigue dispersion, considering all the tests, it is observed that the results cover 5 orders of magnitude, from 10^1 to 10^6 cycles.

4.2.1.2 CMOD vs N diagrams

Figure 4.2-6 to 4.2-19 show the CMOD versus fatigue life and CMOD versus relative fatigue life diagrams of all fatigue tests on S-size specimens, divided by series. In reality, these diagrams represent the upper envelope of the CMOD, or equivalently, the maximum CMOD in each cycle. However, for simplicity they will be referred to as CMOD vs N diagrams.

It should be noted that in some tests of the A1-S and A2-S series, two fatigue mechanisms have been detected: fatigue of uncracked concrete, governed by the matrix, and fatigue of cracked concrete, dominated by the fibers (see Figure 2.2-15). In these cases, the fatigue life section corresponding to the non-cracked situation has been plotted as a dashed line. In addition, N sections shorter than 50 cycles are not plotted.

The specimens have been numbered from index 4 because the first three are the ones that have been tested in static bending. In some cases index 16 is used because there has been a problem with one of the 12 main specimens and the reserve one has been used.

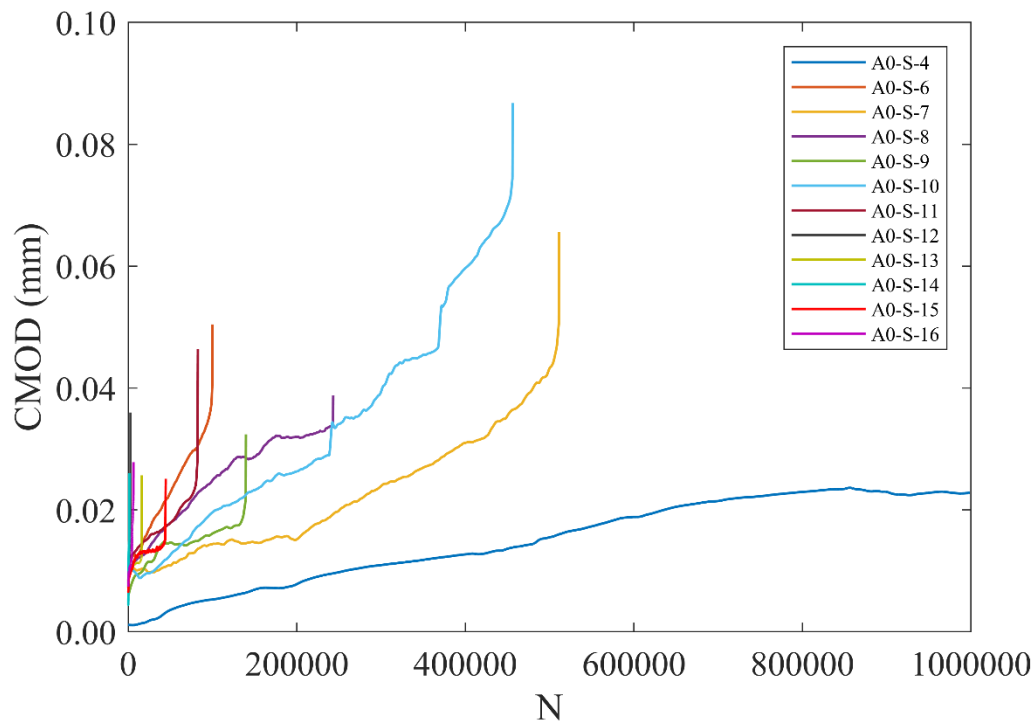


Figure 4.2-6. CMOD vs fatigue life in A0-S series fatigue tests.

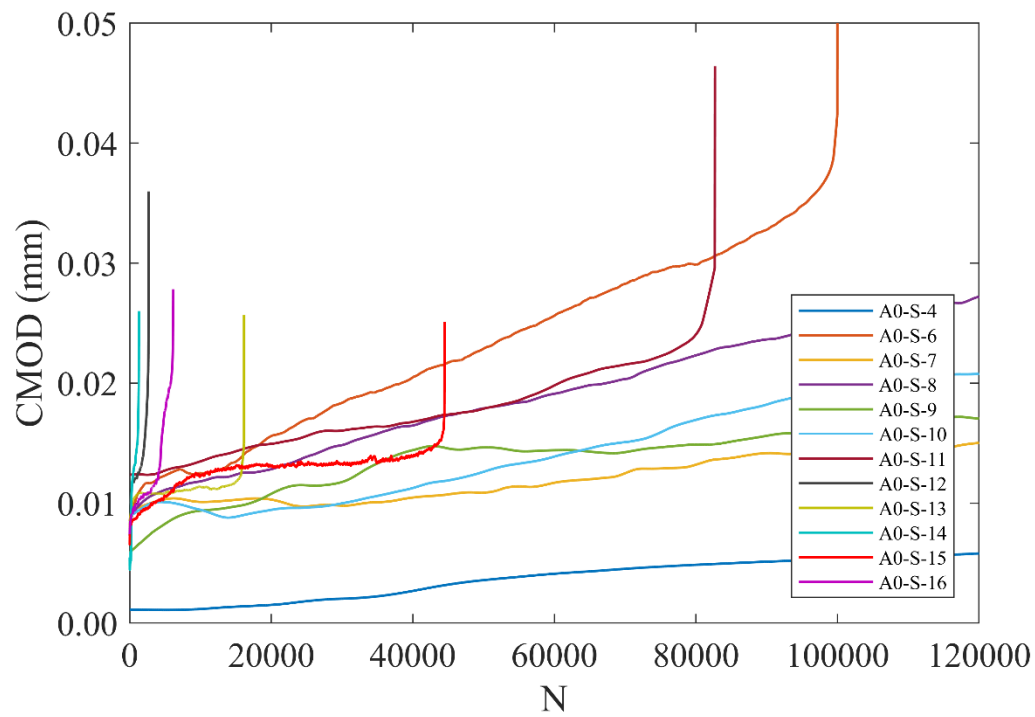


Figure 4.2-7. CMOD vs fatigue life in A0-S series fatigue tests (detail view).

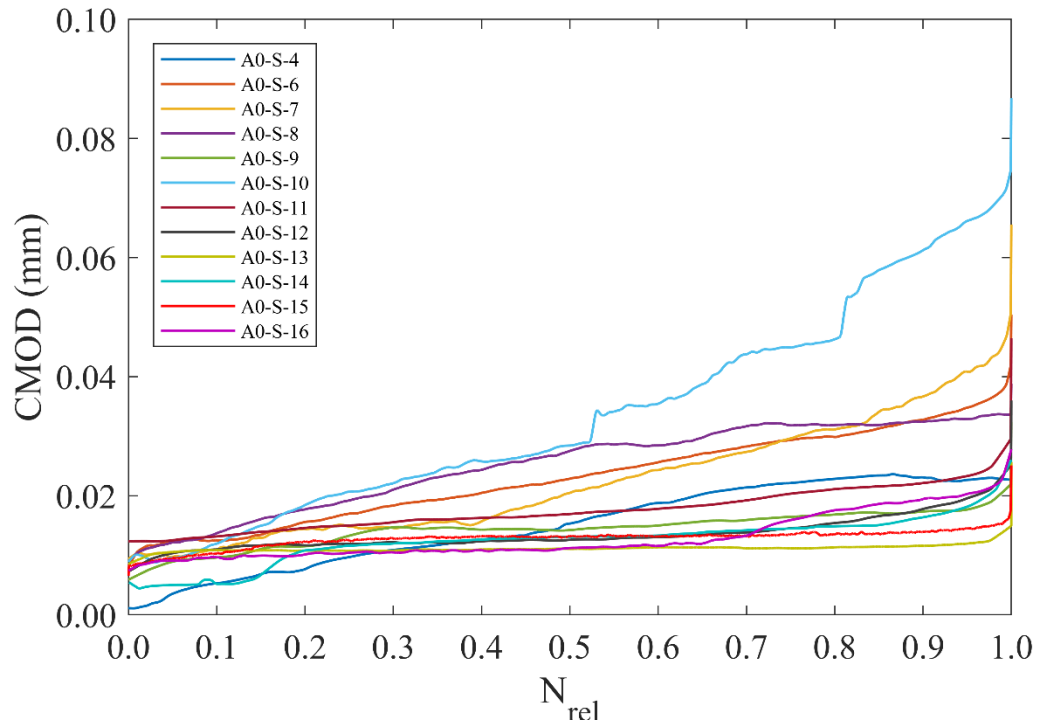


Figure 4.2-8. CMOD vs relative fatigue life in A0-S series fatigue tests.

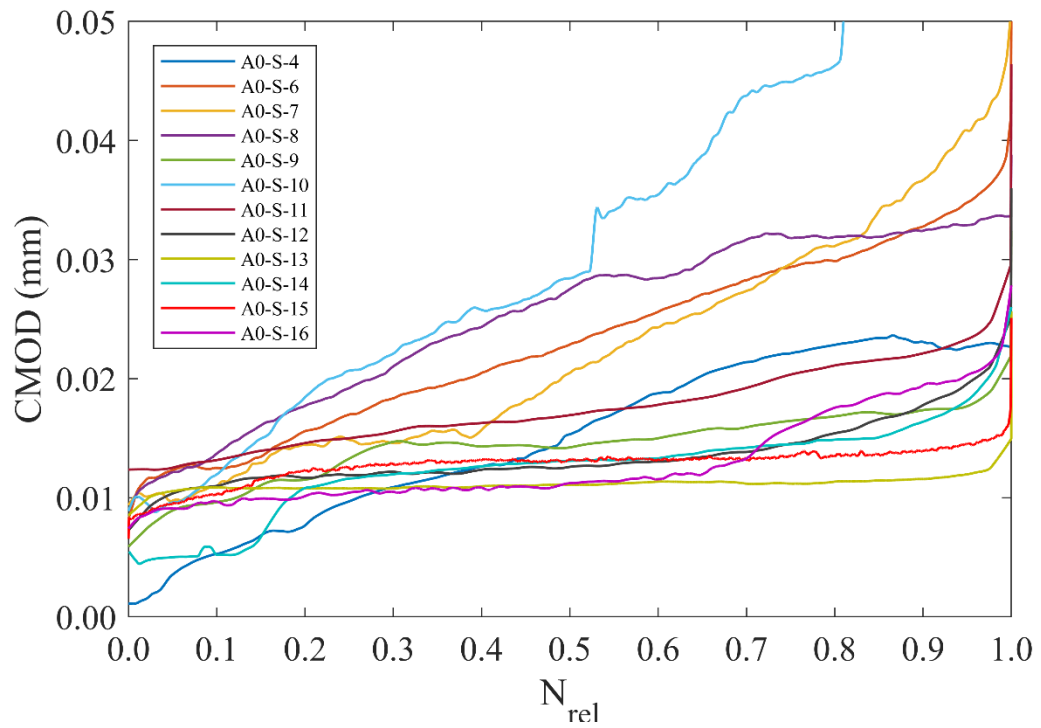


Figure 4.2-9. CMOD vs relative fatigue life in A0-S series fatigue tests (detail view).

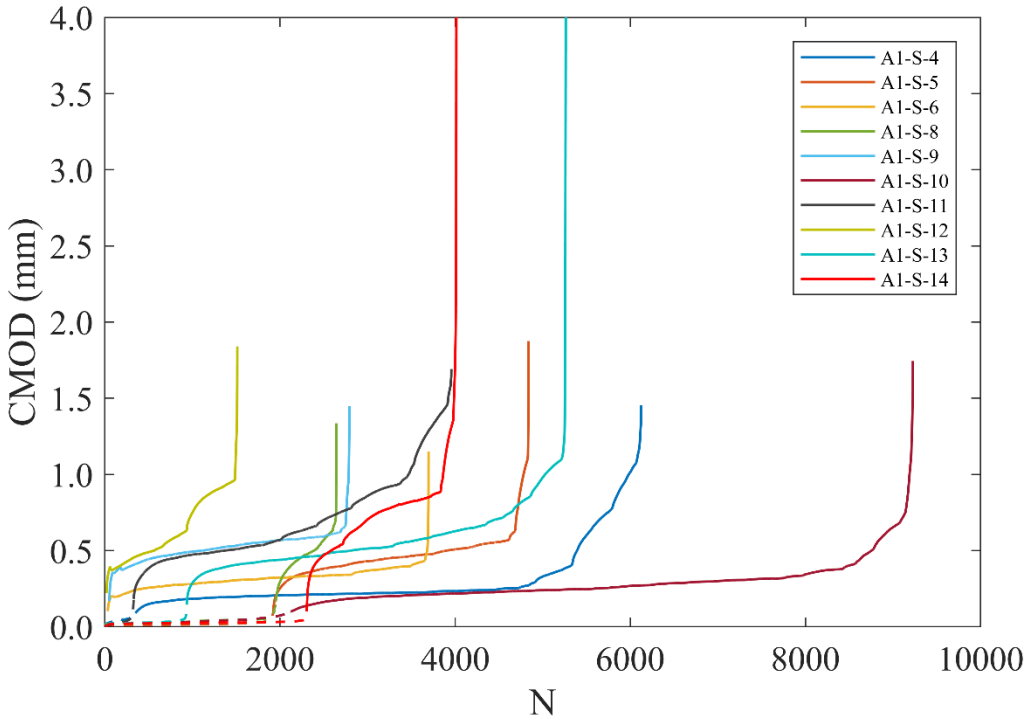


Figure 4.2-10. CMOD vs fatigue life in A1-S series fatigue tests.

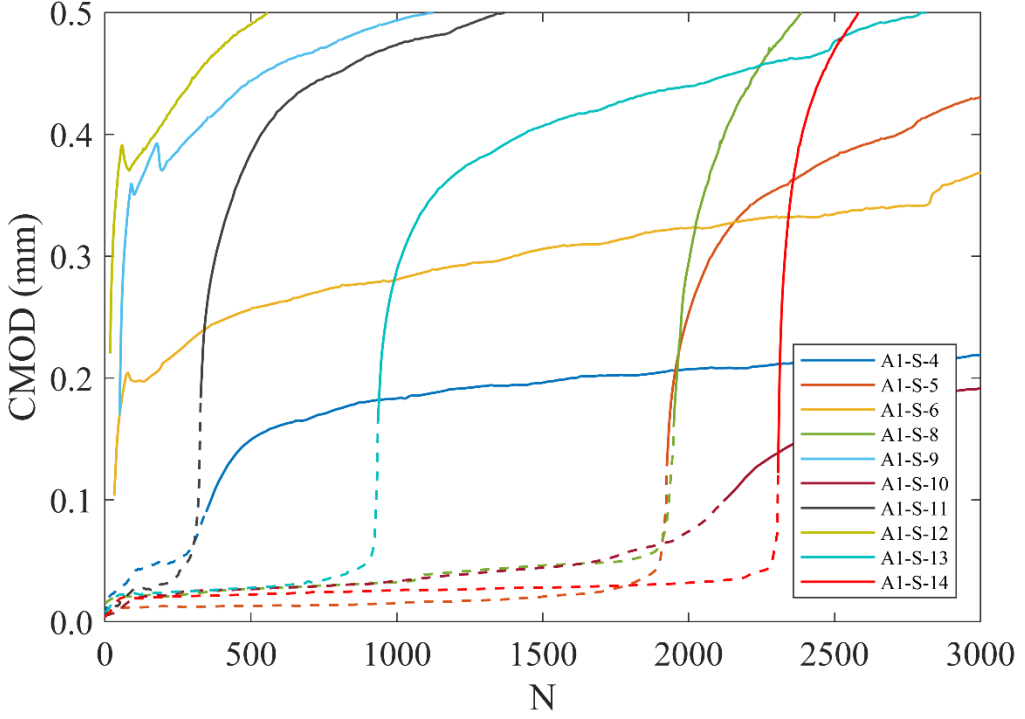


Figure 4.2-11. CMOD vs fatigue life in A1-S series fatigue tests (detail view).

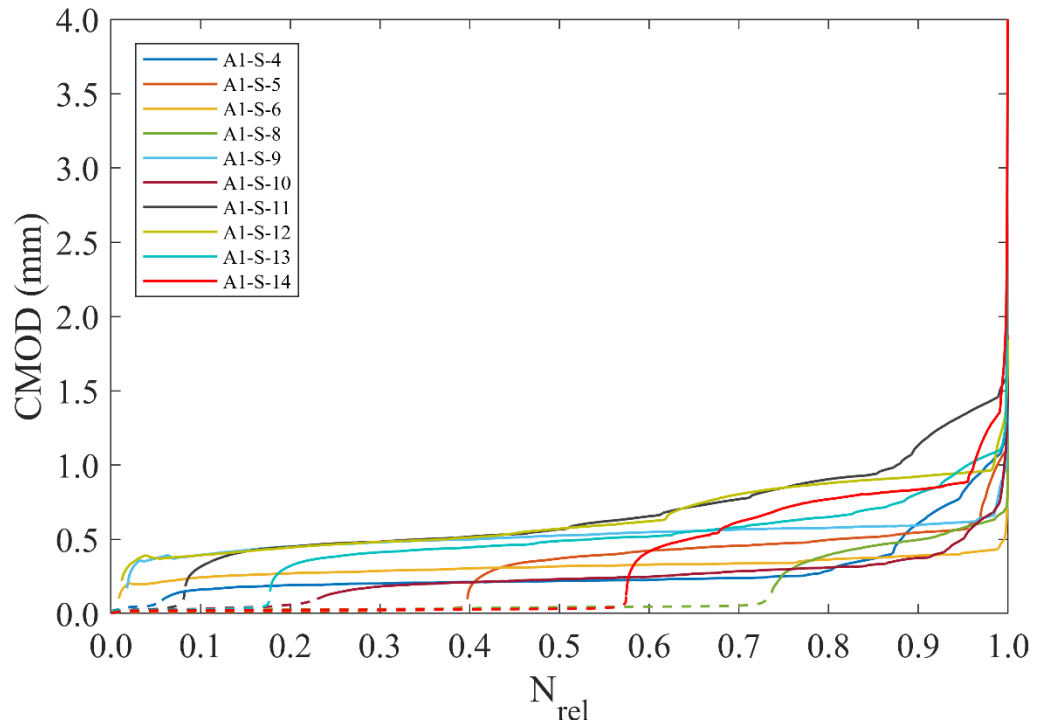


Figure 4.2-12. CMOD vs relative fatigue life in A1-S series fatigue tests.

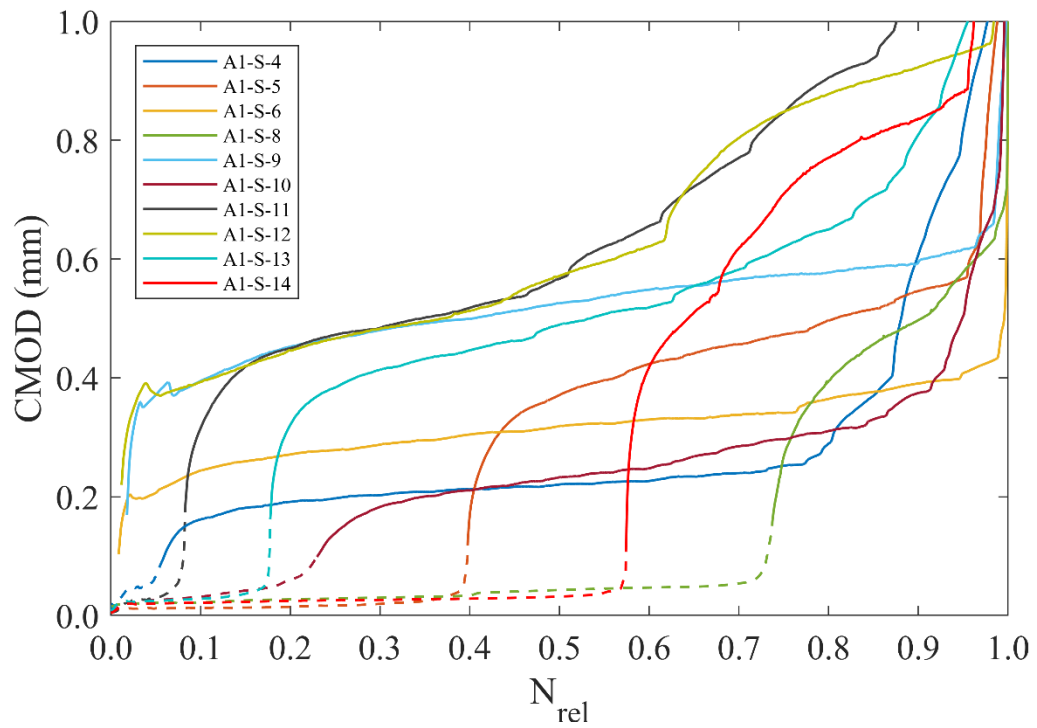


Figure 4.2-13. CMOD vs relative fatigue life in A1-S series fatigue tests (detail view).

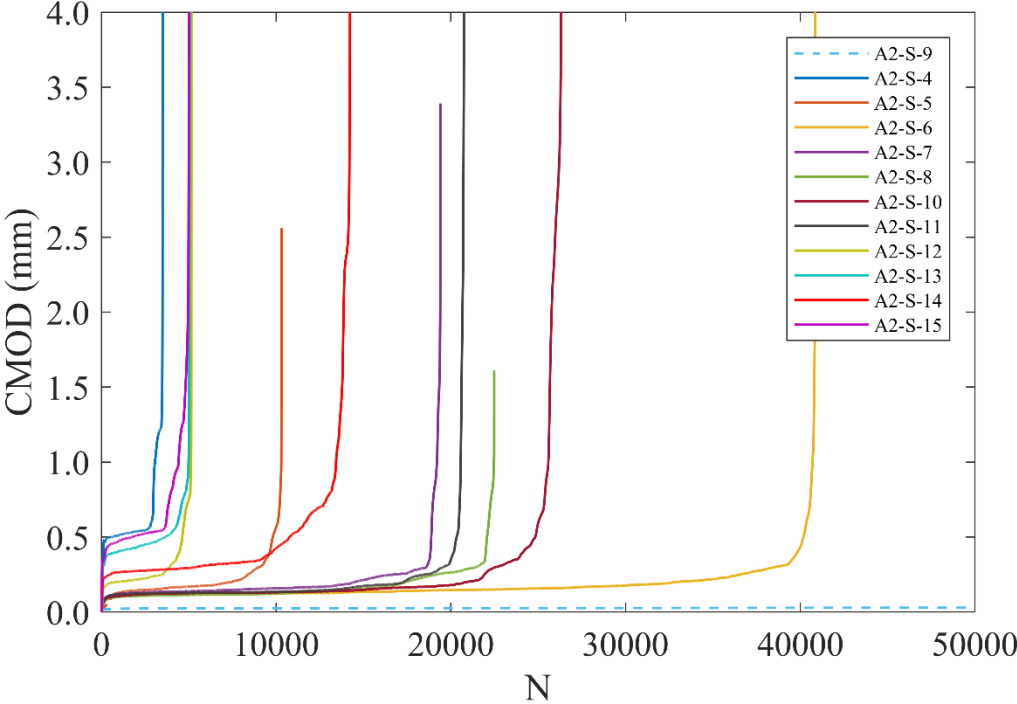


Figure 4.2-14. CMOD vs fatigue life in A2-S series fatigue tests.

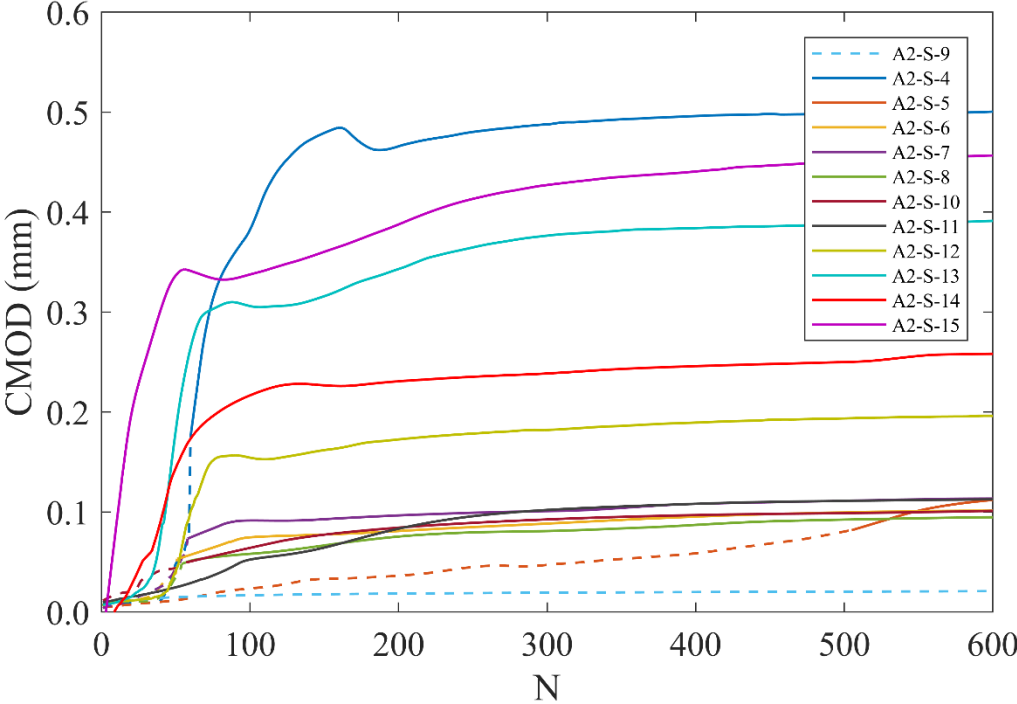


Figure 4.2-15. CMOD vs fatigue life in A2-S series fatigue tests (detail view).

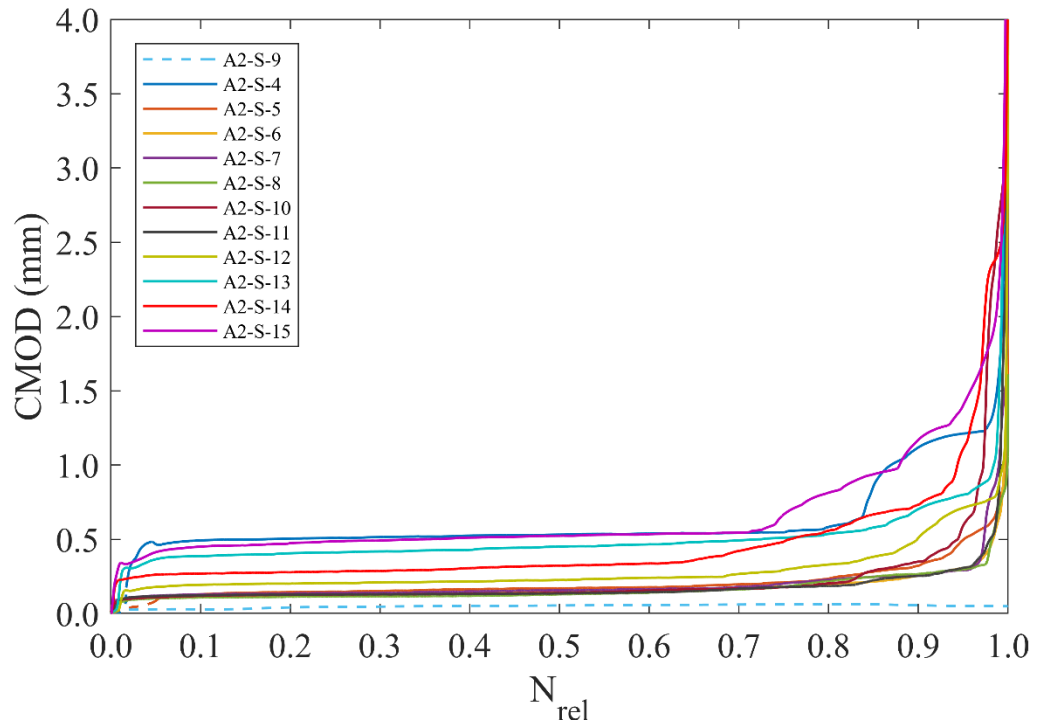


Figure 4.2-16. CMOD vs relative fatigue life in A2-S series fatigue tests.

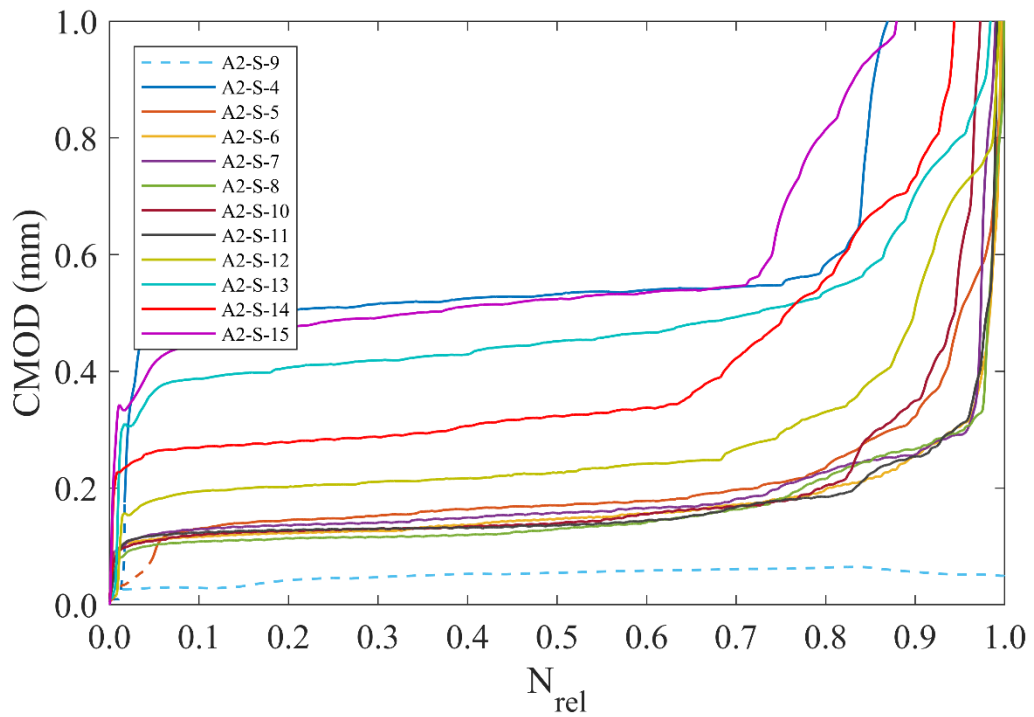


Figure 4.2-17. CMOD vs relative fatigue life in A2-S series fatigue tests (detail view).

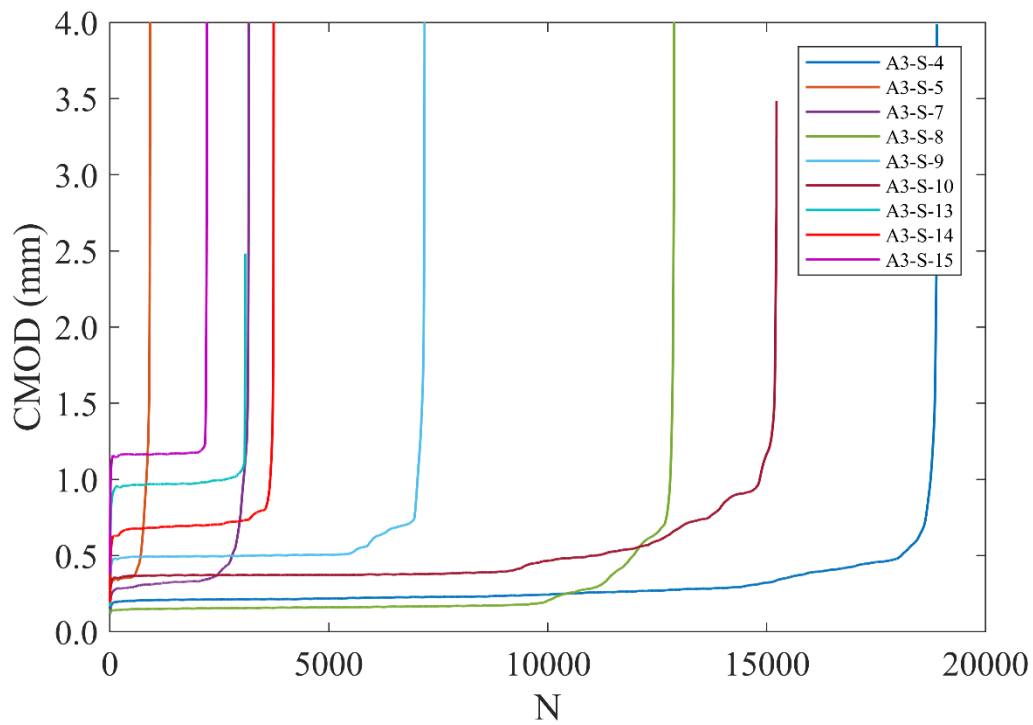


Figure 4.2-18. CMOD vs fatigue life in A3-S series fatigue tests.

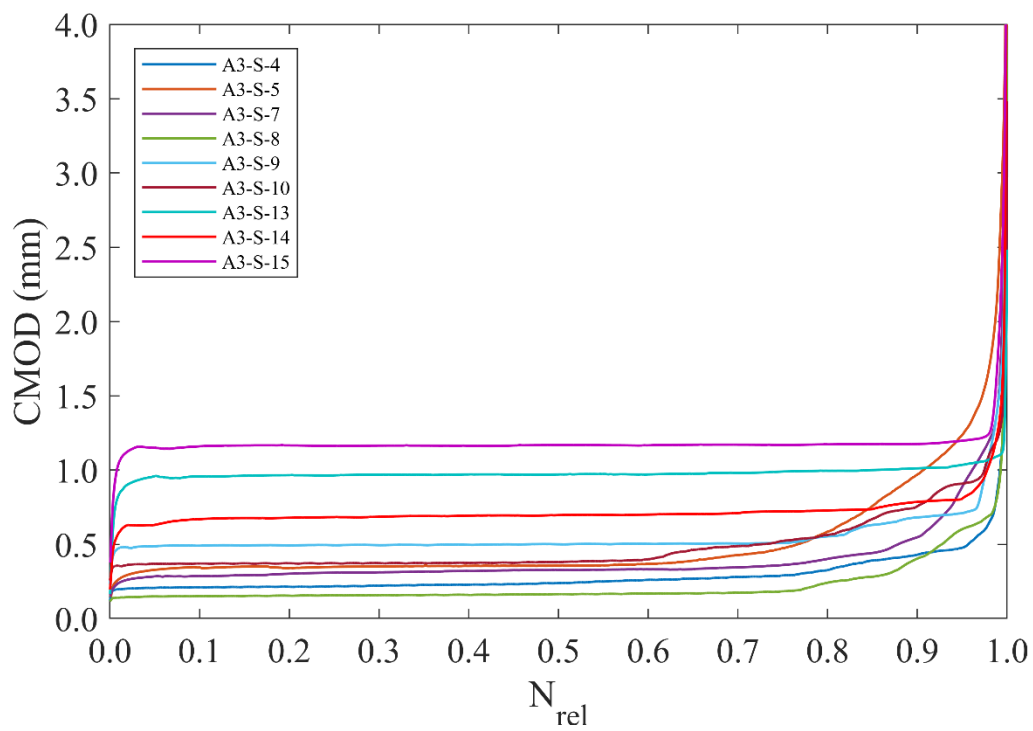


Figure 4.2-19. CMOD vs relative fatigue life in A3-S series fatigue tests.

Below is a table with the fatigue life of all specimens broken down according to the two fatigue mechanisms. That is, on the one hand, the number of cycles corresponding to the fatigue of uncracked concrete (or fatigue of the matrix) and on the other hand, the cycles associated with the fatigue of cracked concrete (or fatigue of the fibers).

Table 4.2-3. Fatigue life, distinguishing between the part corresponding to matrix fatigue (N_{mat}) and that associated with fiber fatigue (N_{fib}).

Series	Spec.	N_{mat}	N_{fib}	N_{tot}	Series	Spec.	N_{mat}	N_{fib}	N_{tot}		
A0-S	A0-S-4	1,000,000	-	1,000,000	A2-S	A2-S-4	59	3,463	3,522		
	A0-S-6	99,976	-	99,976		A2-S-5	504	9,812	10,316		
	A0-S-7	511,248	-	511,248		A2-S-6	50	40,808	40,858		
	A0-S-8	243,232	-	243,232		A2-S-7	57	19,344	19,401		
	A0-S-9	139,687	-	139,687		A2-S-8	53	22,428	22,481		
	A0-S-10	456,365	-	456,365		A2-S-9	1,000,000	-	1,000,000		
	A0-S-11	82,695	-	82,695		A2-S-10	56	26,252	26,308		
	A0-S-12	2,674	-	2,674		A2-S-11	-	20,746	20,746		
	A0-S-13	16,155	-	16,155		A2-S-12	-	5,156	5,156		
	A0-S-14	1,304	-	1,304		A2-S-13	-	5,068	5,068		
	A0-S-15	44,497	-	44,497		A2-S-14	-	14,233	14,233		
	A0-S-16	6,153	-	6,153		A2-S-15	-	5,024	5,024		
	A1-S	A1-S-4	346	5,775		6,121	A3-S	A3-S-4	-	18,889	18,889
		A1-S-5	1,924	2,914		4,838		A3-S-5	-	918	918
		A1-S-6	31	3,665		3,696		A3-S-6	-	30	30
		A1-S-7	27	16		43		A3-S-7	-	3,176	3,176
A1-S-8		1,948	694	2,642	A3-S-8	-		12,888	12,888		
A1-S-9		49	2,742	2,791	A3-S-9	-		7,195	7,195		
A1-S-10		2,118	7,108	9,226	A3-S-10	-		15,225	15,225		
A1-S-11		327	3,629	3,956	A3-S-11	-		12	12		
A1-S-12		17	1,495	1,512	A3-S-12	-		31	31		
A1-S-13		934	4,329	5,263	A3-S-13	-		3,090	3,090		
A1-S-14		2,305	1,710	4,015	A3-S-14	-		3,743	3,743		
A1-S-15		42	6	48	A3-S-15	-		2,219	2,219		

Several conclusions can be drawn from the diagrams of crack opening versus number of cycles. Firstly, the only series in which both fatigue mechanisms are observed together are A1-S and A2-S. In particular, A1-S series is the one that offers the most interesting results, since significant sections of fatigue of cracked concrete, of the order of 10^3 cycles, are observed. The reason why in some SFRC series both mechanisms appear and in others only fatigue of cracked concrete lies in the nominal stress vs CMOD curve of the static

flexural tensile tests, and specifically, in the relationship between the stress corresponding to the LOP (f_L) and the maximum fatigue stress ($\sigma_{\max,f}$) (Table 4.2-4). When $\sigma_{\max,f} > f_L$, the concrete cracks immediately during the first fatigue cycle, so no matrix fatigue appears. Conversely, when $\sigma_{\max,f} < f_L$, the concrete does not crack from the beginning, resulting in matrix fatigue. After a certain number of cycles, this mechanism is exhausted and the fibers assume the tensile stresses, and fiber fatigue is observed.

Table 4.2-4. Stress corresponding to LOP and maximum stress from loading cycles in flexural fatigue tests.

Series	f_L (MPa)	$\sigma_{\max,f}$ (MPa)
A0-S	8.21	6.57
A1-S	7.36	7.03
A2-S	8.35	9.43
A3-S	10.45	15.72

Secondly, the percentage over the total fatigue life occupied by the fatigue of cracked concrete seems to be related to the ratio $\sigma_{\max,f} / f_L$. The lower its value, the farther the maximum fatigue load is from the first crack strength, and therefore the greater the fatigue life resisted by the matrix. This explains why in the A2-S series the fatigue of the matrix extends over very few cycles (except for the anomalous case of specimen A2-S-4), while in the A1-S series it can reach several thousand cycles. Moreover, within each series, the percentage of fatigue of cracked concrete has a certain dispersion, which can be explained in part by the variability of the static parameter f_L .

Third, the CMOD vs N curves clearly distinguish the three phases of damage; namely, (I) emergence of microcracks at the notch edge, (II) stable crack growth and (III) unstable crack propagation to failure. These phases are independent of the fatigue mechanism, so that they are observed both when fatigue of uncracked concrete (A0-S series, Figure 4.2-8) and fatigue of cracked concrete (A3-S series, Figure 4.2-19) occur. In cases where both mechanisms appear, the three damage phases are also observed independently in each of them. This can be seen quite well in the A1-S series (Figure 4.2-13). Finally, the percentage of the fatigue life occupied by phase II of stable crack growth is very similar in the two types of fatigue. In the case of matrix fatigue, it ranges on average from 14% to 82% of the total life, while in fiber fatigue the range is from 9% to 84%. In addition, it is worth mentioning that the dispersion of these values is significant.

4.2.1.3 Secondary crack opening rate

In CMOD versus number of cycles curves, the upper envelope of phase II of stable crack growth can be approximated as a straight line, the slope of which is called the secondary crack opening rate ($d\text{CMOD}/dn$). This parameter is of great interest as it is related to the fatigue life. This is known as Sparks and Menzies' law [49], which was originally proposed in compressive fatigue, showing that there is a linear correlation between the logarithms of the secondary strain rate ($d\varepsilon/dn$) and the fatigue life.

In cases where fatigue of uncracked concrete and fatigue of cracked concrete appear, CMOD vs N diagrams are actually formed by two curves, each one associated to a mechanism and divided into its three corresponding phases. Consequently, two secondary crack opening rates are observed in these situations, one related to the stable fatigue degradation of the matrix $(d\text{CMOD}/dn)_{\text{mat}}$, and the other to the stable fatigue degradation of the fibers $(d\text{CMOD}/dn)_{\text{fib}}$.

In relation to the above, it should be mentioned that it is not quite accurate to call $(d\text{CMOD}/dn)_{\text{mat}}$ as "crack opening rate", since in fatigue of cracked concrete, by definition it is assumed that there is no cracking. In this case, the displacement measured at the notch mouth is due to concrete tensile strain, as well as to a primary state of micro-cracking in which the main macro-crack has not yet been generated. However, for simplicity and by analogy with the parameter $(d\text{CMOD}/dn)_{\text{fib}}$ in fatigue of cracked concrete, the name will be retained.

Figure 4.2-20 to 4.2-29 show the correlation between the secondary crack opening rate and the fatigue life for all series of size S. The two parameters, $(d\text{CMOD}/dn)_{\text{mat}}$ and $(d\text{CMOD}/dn)_{\text{fib}}$ have been correlated both with their corresponding number of cycles (N_{mat} or N_{fib}) and with the total fatigue life N_{tot} .

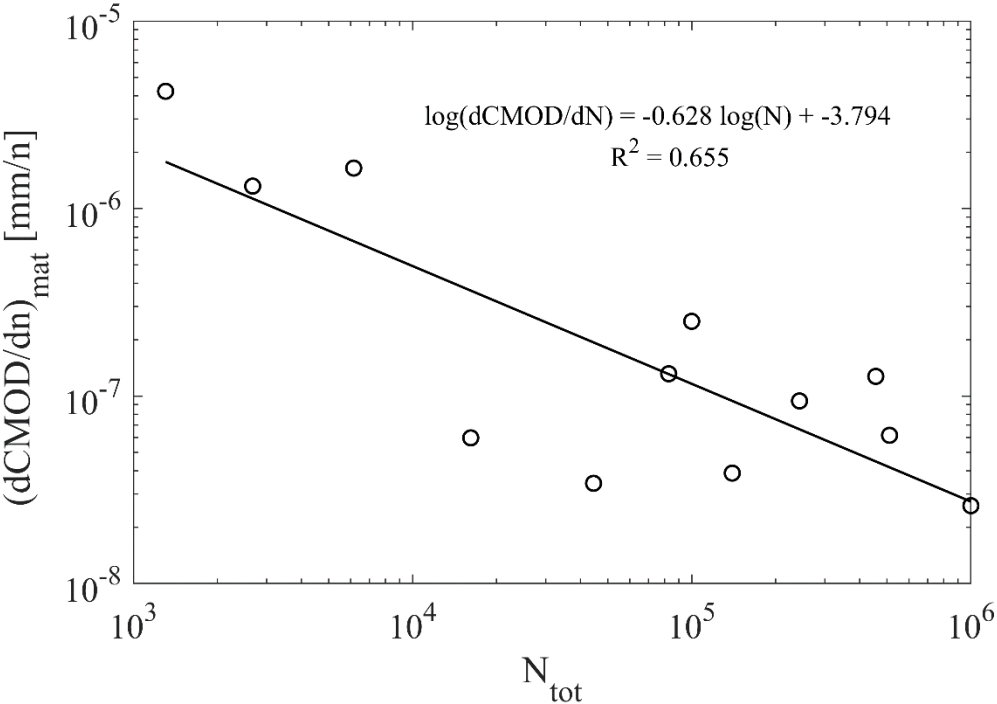


Figure 4.2-20. Secondary crack opening rate due to matrix fatigue versus total number of cycles. A0-S series.

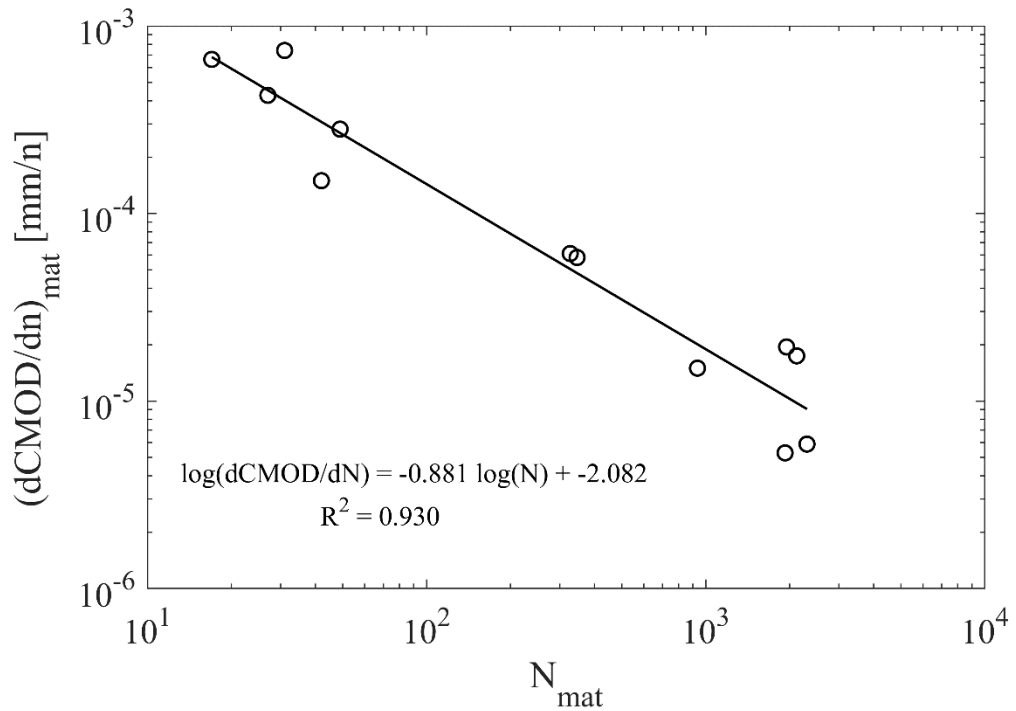


Figure 4.2-21. Secondary crack opening rate due to matrix fatigue vs number of cycles due to matrix fatigue. A1-S series.

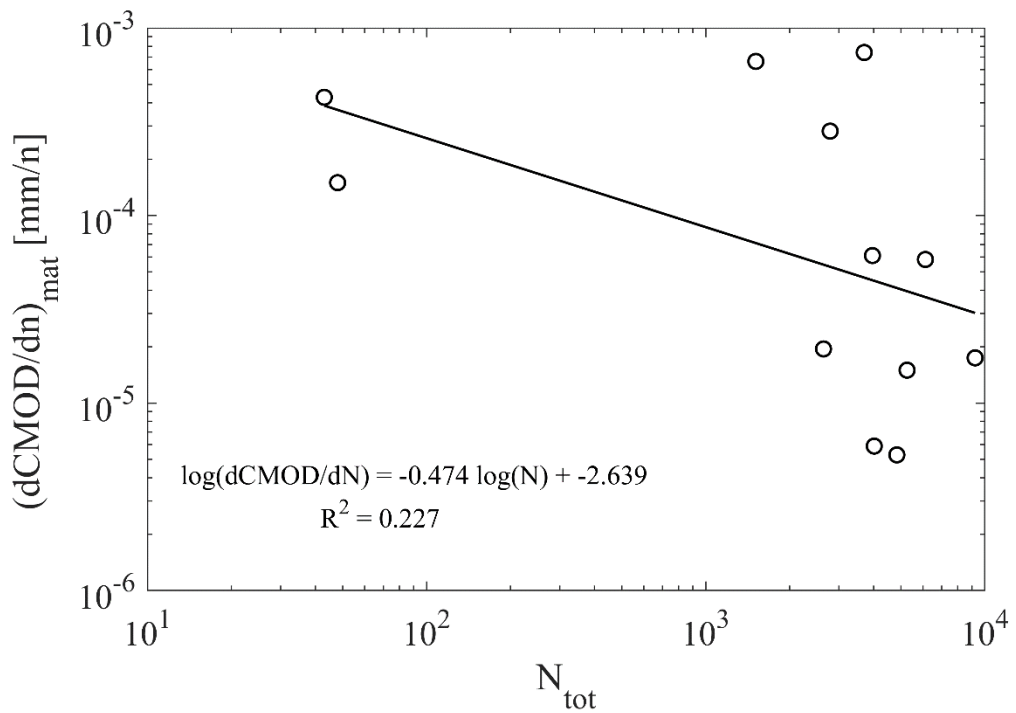


Figure 4.2-22. Secondary crack opening rate due to matrix fatigue versus total number of cycles. A1-S series.

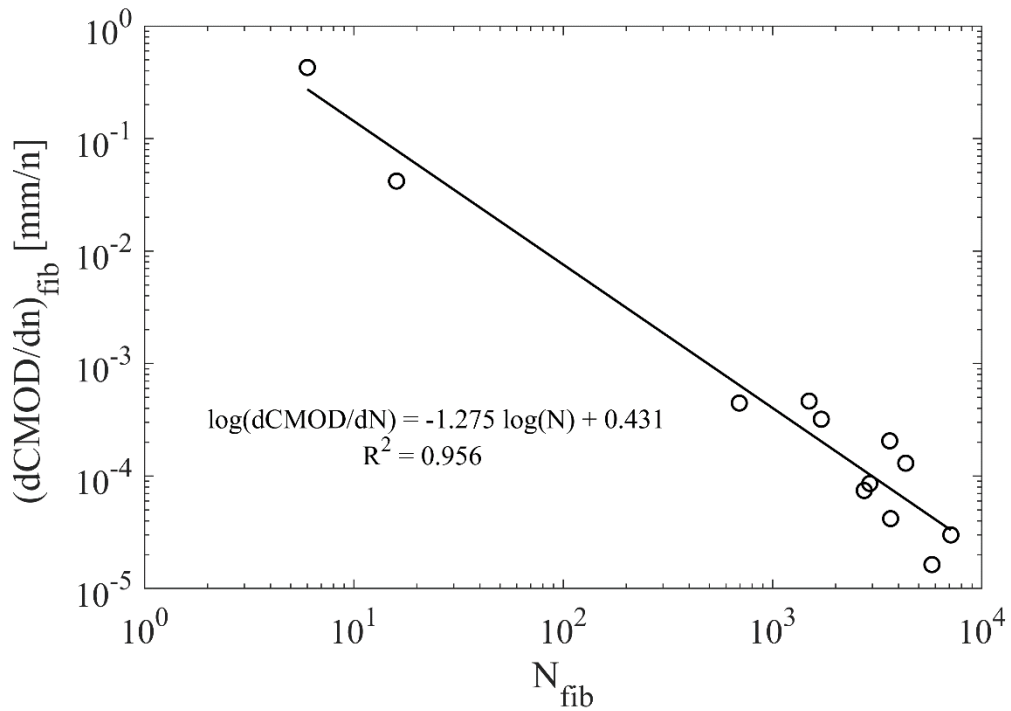


Figure 4.2-23. Secondary crack opening rate due to fiber fatigue vs number of cycles due to fiber fatigue. A1-S series.

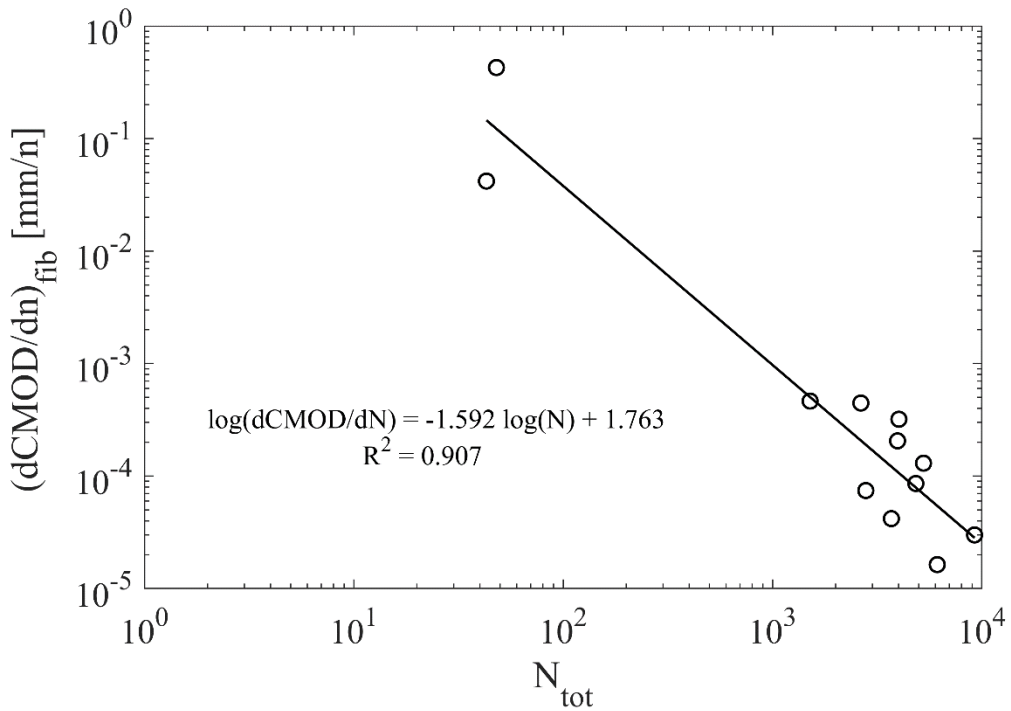


Figure 4.2-24. Secondary crack opening rate due to fiber fatigue versus total number of cycles. A1-S series.

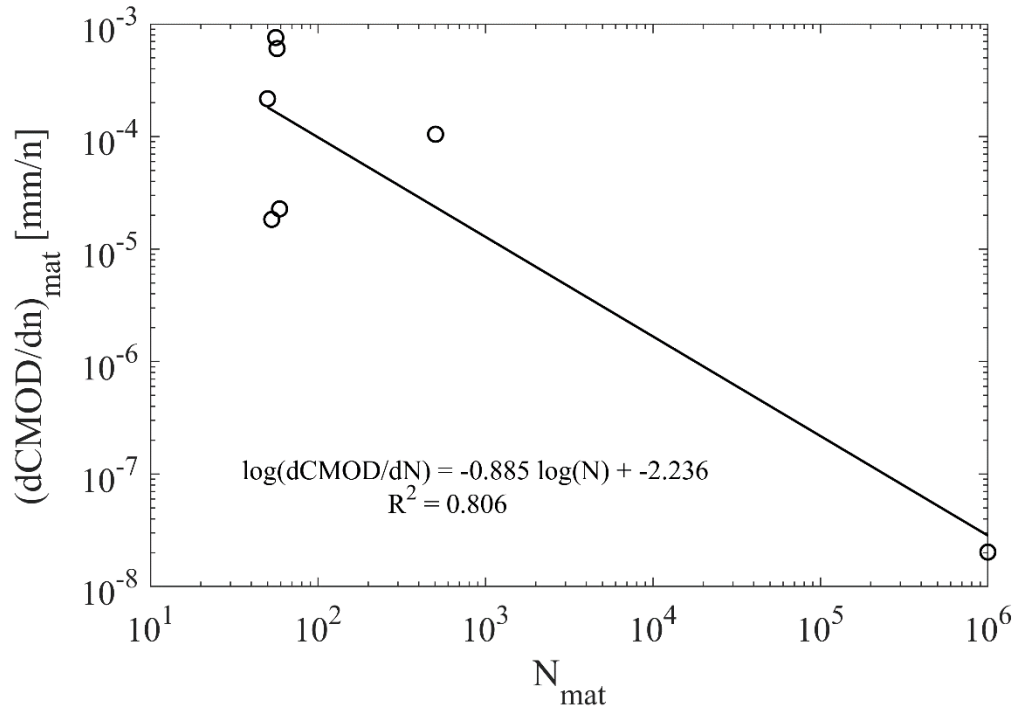


Figure 4.2-25. Secondary crack opening rate due to matrix fatigue vs number of cycles due to matrix fatigue. A2-S series.

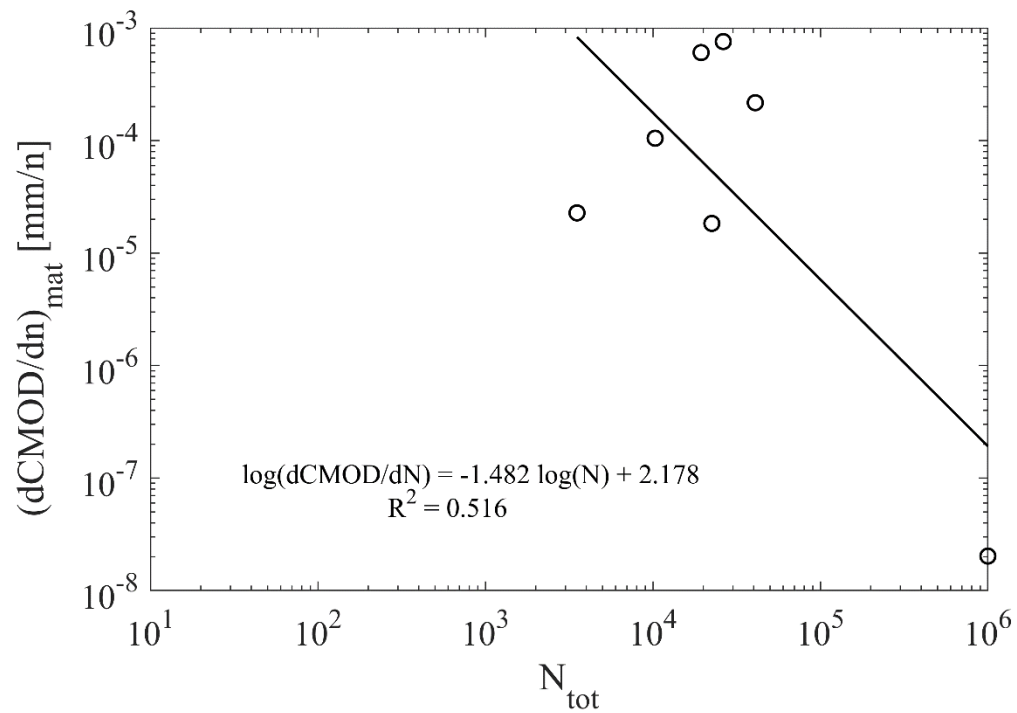


Figure 4.2-26. Secondary crack opening rate due to matrix fatigue versus total number of cycles. A2-S series.

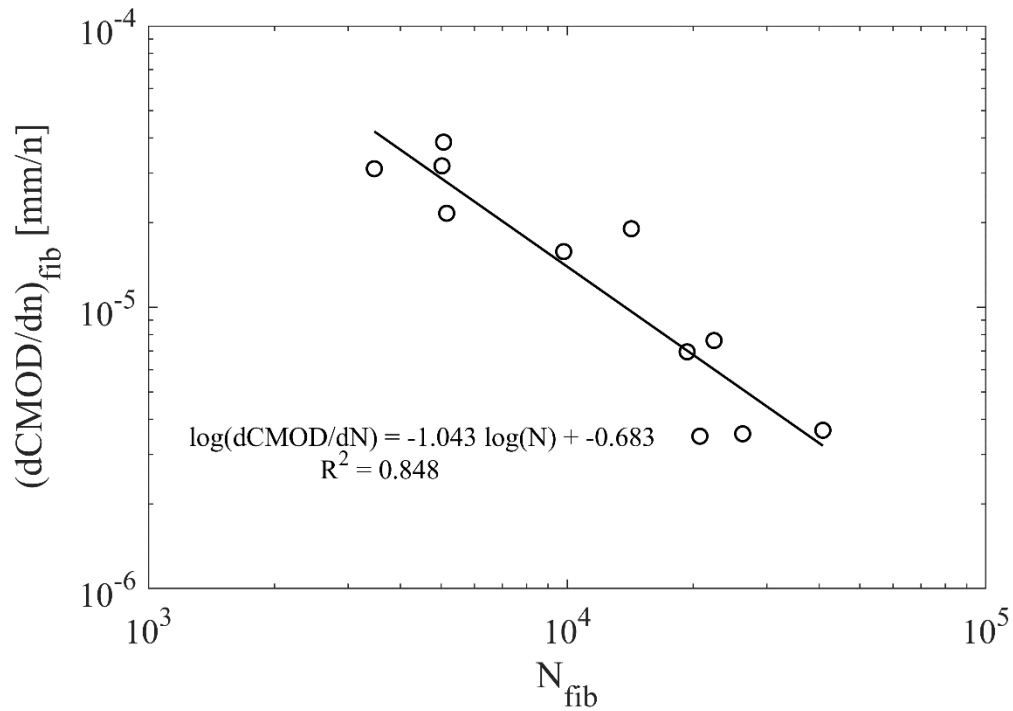


Figure 4.2-27. Secondary crack opening rate due to fiber fatigue versus number of cycles due to fiber fatigue. A2-S series.

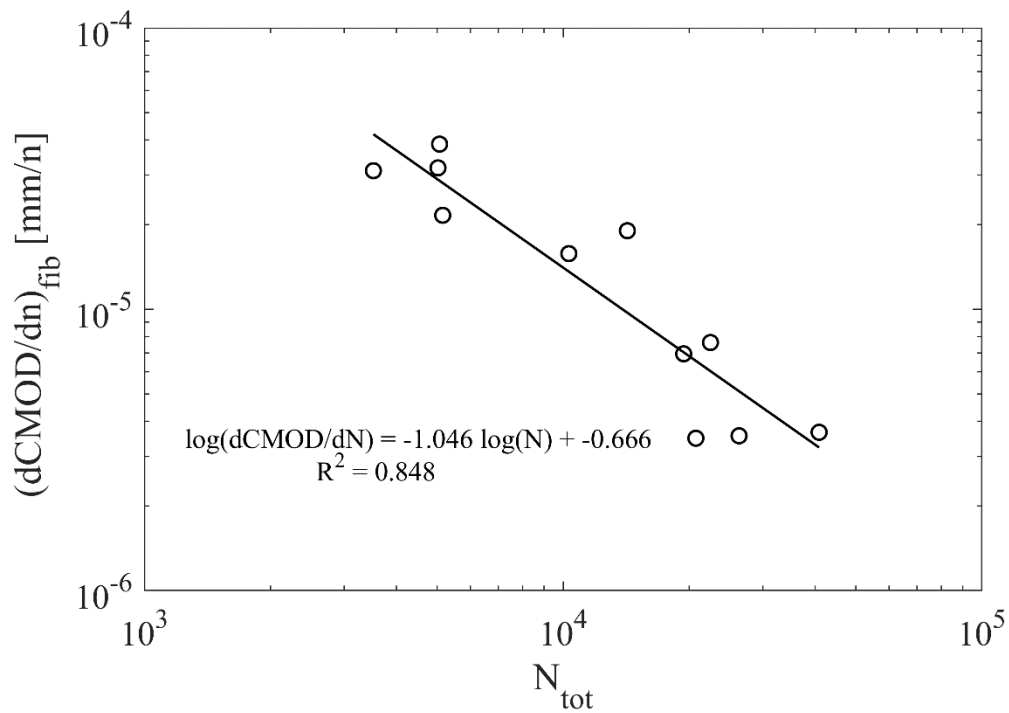


Figure 4.2-28. Secondary crack opening rate due to fiber fatigue versus total number of cycles. A2-S series.

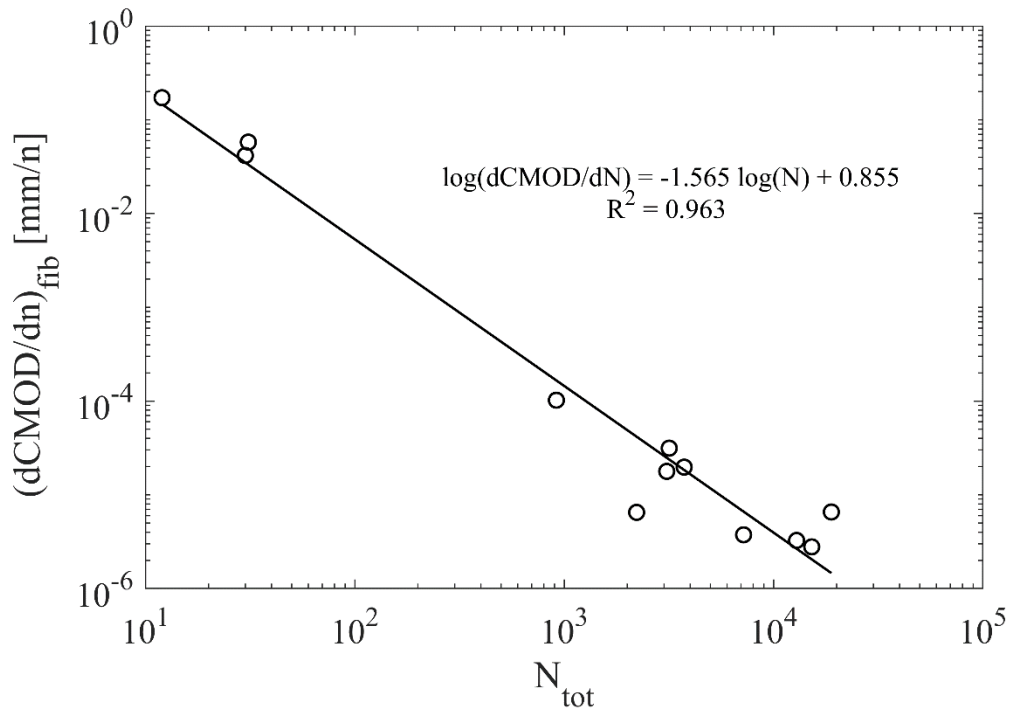


Figure 4.2-29. Secondary crack opening rate due to fiber fatigue versus total number of cycles. A3-S series.

The figures reveal that the correlation between the secondary crack opening rate and fatigue life is very strong. Therefore, it is concluded that Sparks and Menzies' law also holds true in flexural fatigue, both in plain concrete and fiber-reinforced concrete. In the series where both matrix fatigue and fiber fatigue appear (A1-S and A2-S), the fit is clearly better when each $dCMOD/dn$ is related to its corresponding number of cycles (N_{mat} or N_{fib}), rather than the total. This suggests that the two damage mechanisms are independent.

Finally, Figure 4.2-30 groups the correlations between the secondary crack opening rate, $(dCMOD/dn)_{mat}$ or $(dCMOD/dn)_{fib}$, and the associated fatigue life, N_{mat} or N_{fib} , across all series. Fits for matrix fatigue are plotted in dashed line, while those for fiber fatigue are shown in solid line.

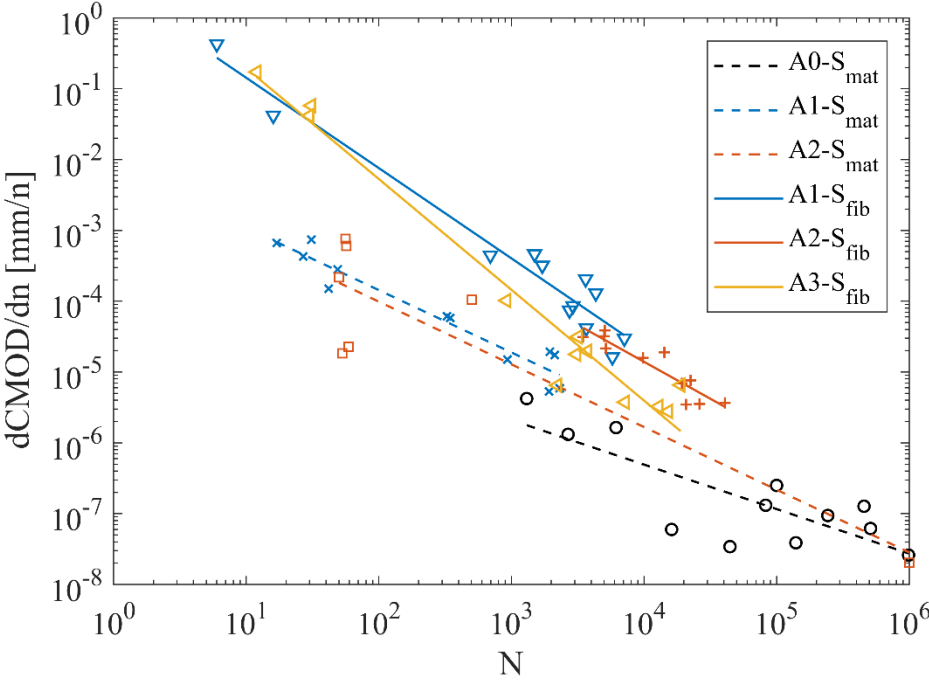


Figure 4.2-30. Secondary crack opening rate versus number of cycles, distinguishing between the two fatigue mechanisms.

In Figure 4.2-30 it is observed that the fitting lines associated with fiber fatigue are above those of matrix fatigue. This implies that the increase in crack opening per cycle is higher, concluding that the fatigue mechanism governed by the fibers damages the concrete faster. On the other hand, it appears that the fiber content does not significantly affect the relationship between $dCMOD/dn$ and N . In the case of matrix fatigue, this is to be expected because the fibers hardly interfere. However, it is also observed in fiber fatigue, where the straight lines are very similar. Consequently, it follows that the development of fatigue damage is independent of fiber content, at least for the dosages used.

4.2.2 L-size specimens

4.2.2.1 Fatigue life

Table 4.2-5 shows the fatigue life of all tests on specimens of size L. Twelve tests were performed in each series, except for A2-L, where one specimen was lost due to an incidence in the test control.

Table 4.2-5. Fatigue life N.

Test No.	A0-L	A1-L	A2-L	A3-L
1	767	2,626	25,926	15
2	90	899	37	23,308
3	143	1,830	3,476	13
4	200	109	2,004	3,335
5	263	21,892	6,597	15
6	594	1,255	32	5,747
7	129	134	8,851	9,604
8	137	284	46	3,498
9	373	69	84	5,634
10	200	102	2,415	102
11	117	18,876	4,264	1,618
12	258	42,491	-	12,964

At first glance, the results indicate that the plain concrete series (A0-L) has the lowest fatigue life, since no test exceeded 1,000 cycles. On the other hand, in the SFRC series the fatigue lives are higher; in fact, in the three cases there was always at least one test in which 10,000 cycles were exceeded. It is observed that none of the specimens reached the runout limit.

Figure 4.2-31 to 4.2-34 show, for each series, the fit of the results to the two-parameter Weibull distribution function. It should be mentioned that these parameters were determined by the graphical method.

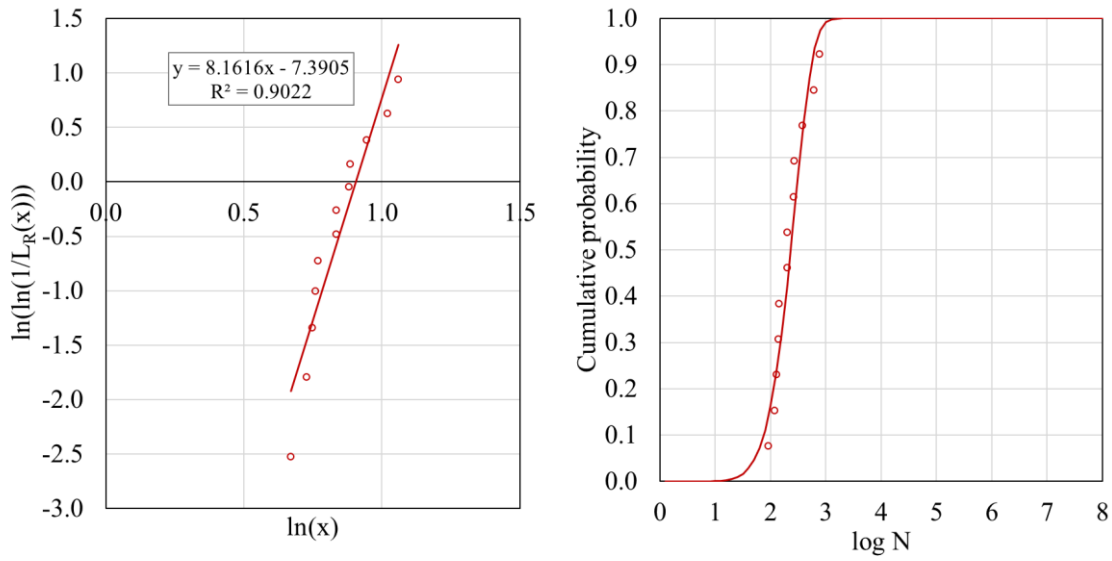


Figure 4.2-31. Fit to the Weibull distribution of the fatigue life of A0-L series.

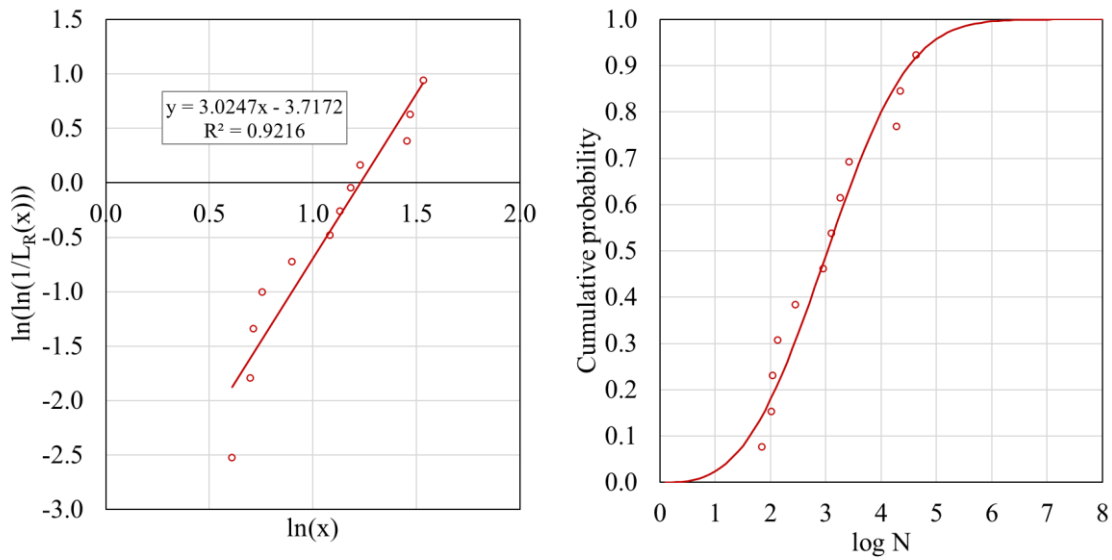


Figure 4.2-32. Fit to the Weibull distribution of the fatigue life of A1-L series.

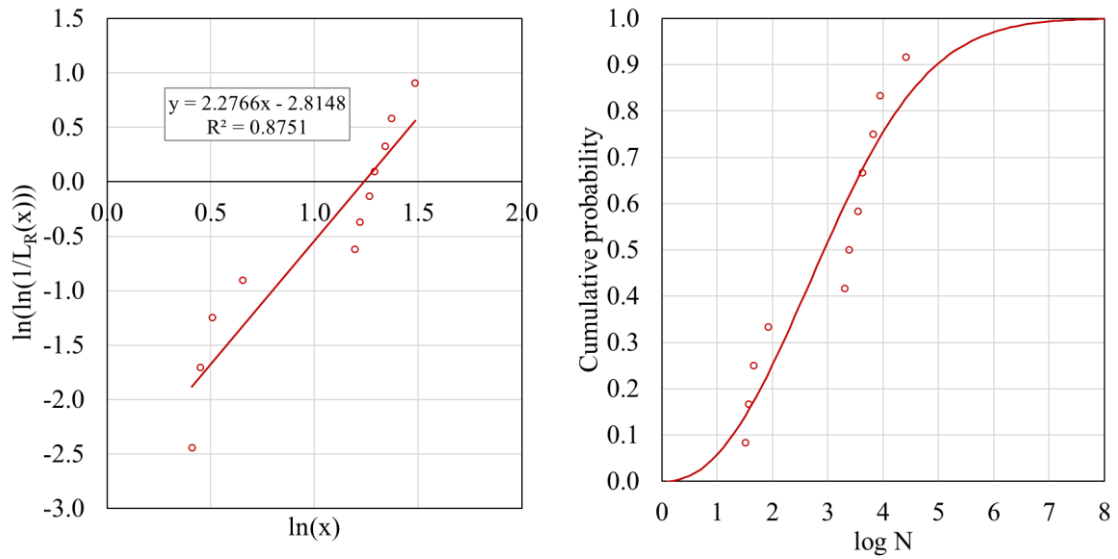


Figure 4.2-33. Fit to the Weibull distribution of the fatigue life of A2-L series.

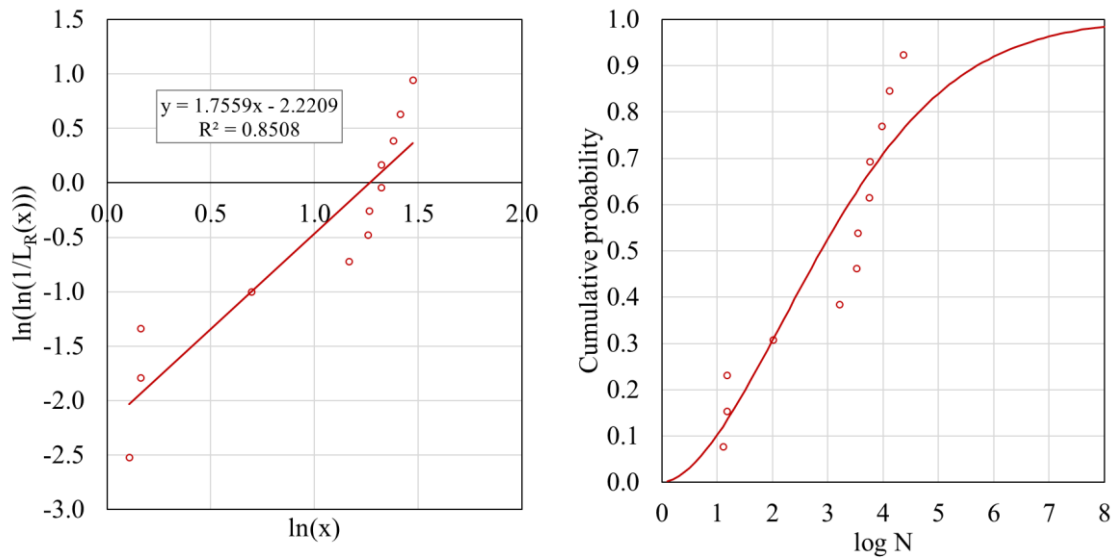


Figure 4.2-34. Fit to the Weibull distribution of the fatigue life of A3-L series.

In general, it can be stated that the results of the 4 series fit the Weibull distribution function very well. The values of the correlation coefficient R^2 range from 0.92 for A1-L series to 0.85 for A3-L series. It can be seen that, in series A2-L and A3-L, very low N values ($< 10^2$ cycles) disturb the fit.

Figure 4.2-35 plots the Weibull distribution functions of the fatigue life of the 4 series, including the points representing each test. In addition, Table 4.2-6 gives the values of the fit parameters λ and β .

Table 4.2-6. Fit parameters λ and β of the Weibull distribution function.

Series	λ	β
A0-L	2.47	8.16
A1-L	3.42	3.02
A2-L	3.44	2.28
A3-L	3.54	1.76

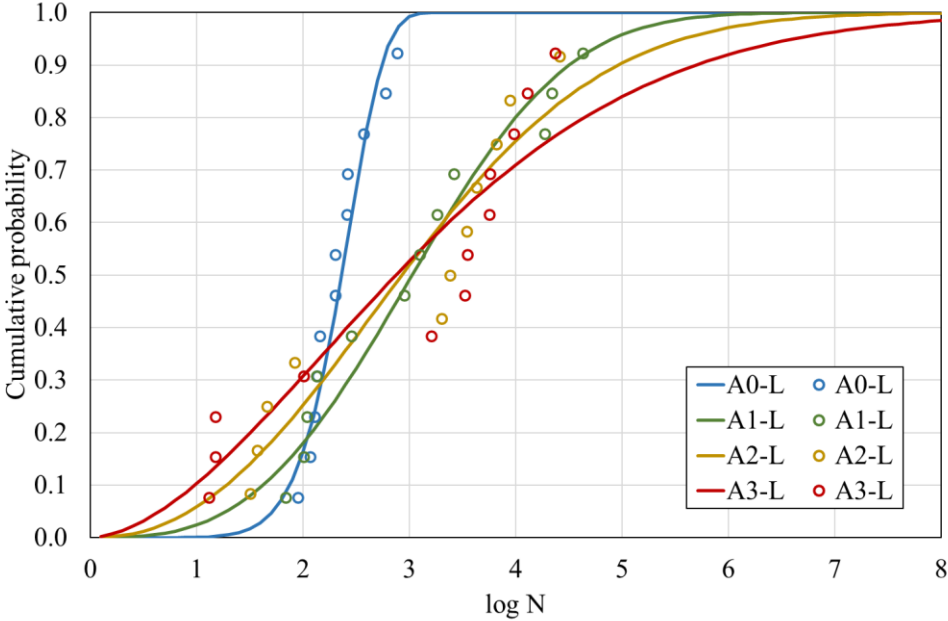


Figure 4.2-35. Fit to the Weibull distribution of the fatigue life of the L-size specimen series.

It can be seen that SFRC series show more fatigue life (higher λ) than plain concrete series; in particular, the difference is about one order of magnitude. There are no significant variations in the number of cycles of the series with fibers; at most, it seems to be slightly higher in the A3-L series for higher probabilities (above 0.55).

Again, caution is recommended in the interpretation of the results since the fatigue loads of each series are determined on the basis of its static flexural strength. One reason that could explain the shorter fatigue life of plain concrete is that, although the matrix fatigue mechanism has a slower development than that of fiber fatigue, the CMOD for which failure is reached is much lower than in SFRC. This will be discussed in more detail in the next section.

Regarding the variability of the results, the series with less dispersion (higher β) is clearly A0-L, whose N values cover only one order of magnitude. SFRC series have more

dispersion, and it is observed that this increases progressively with fiber content. If all tests are considered, the fatigue lives range over 4 orders of magnitude, from 10^1 to 10^5 .

4.2.2.2 CMOD vs N diagrams

Figure 4.2-36 to 4.2-45 show the CMOD versus fatigue life and CMOD versus relative fatigue life diagrams of all tests on L-size specimens, divided by series. It should be remembered that these diagrams actually represent the maximum CMOD in each cycle, and not the complete CMOD cycles.

Again, in some tests, two fatigue mechanisms have been detected: fatigue of the matrix or uncracked concrete, and fatigue of the fibers or cracked concrete. This behavior has only been observed in the A1-L series. In these cases, the section of N associated with matrix fatigue is shown as a dashed line. In addition, the sections of N less than 50 cycles have not been plotted.

The specimens are numbered starting at index 4 because the first three specimens are those tested in static. In some cases, index 16 is used because one of the 12 main specimens has been lost and the reserve specimen has been used.

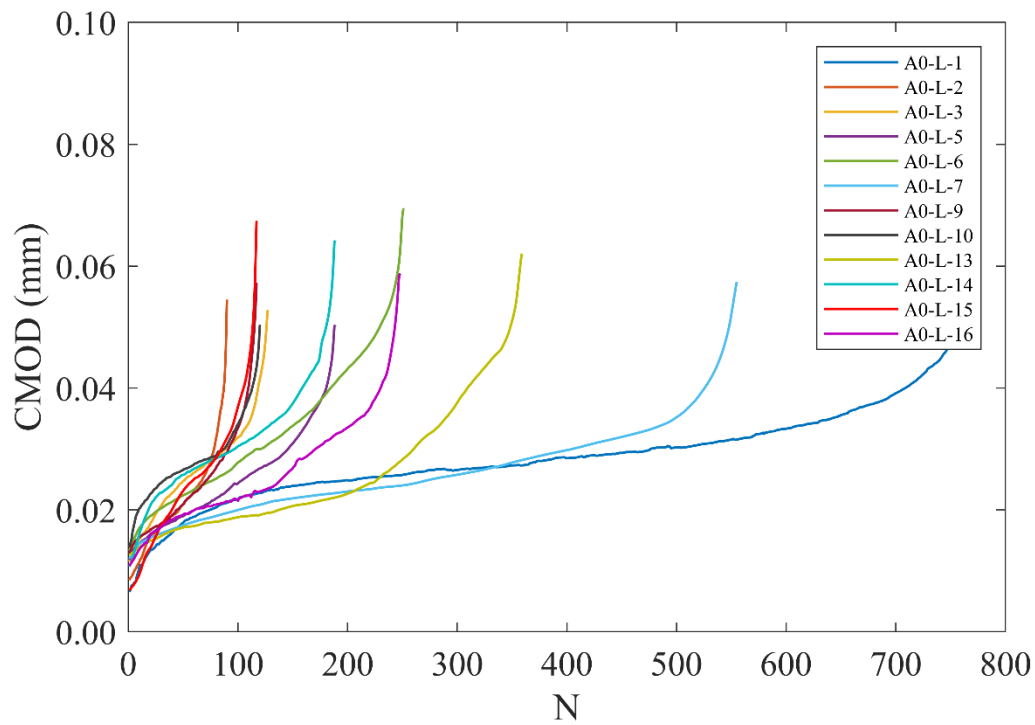


Figure 4.2-36. CMOD vs fatigue life in A0-L series fatigue tests.

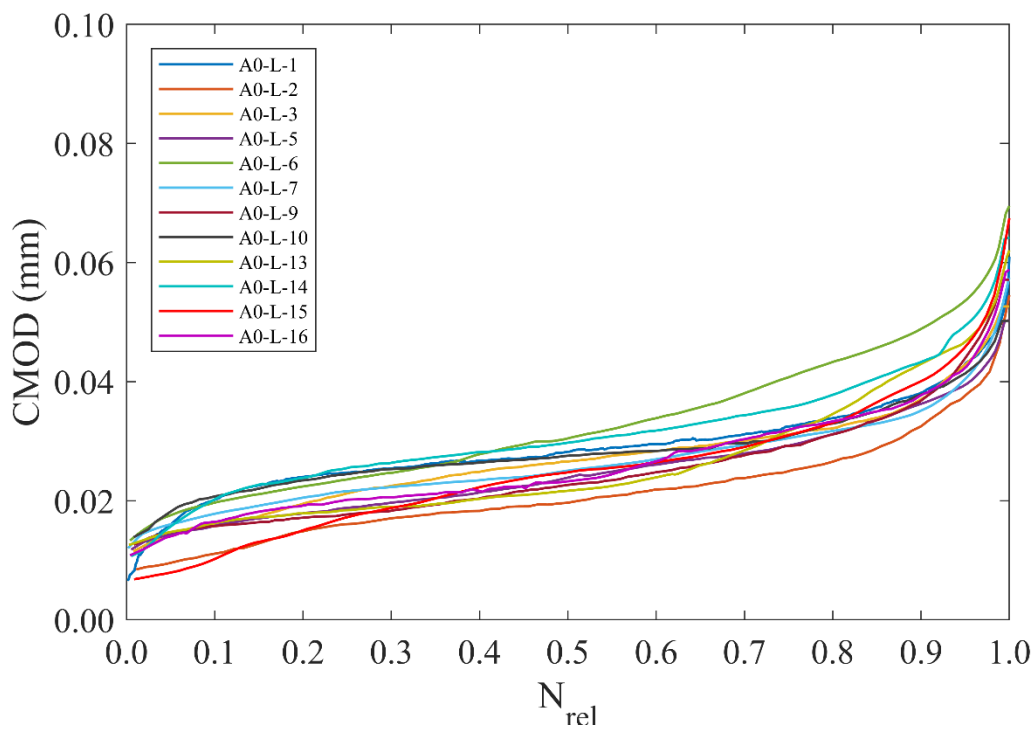


Figure 4.2-37. CMOD vs relative fatigue life in A0-L series fatigue tests.

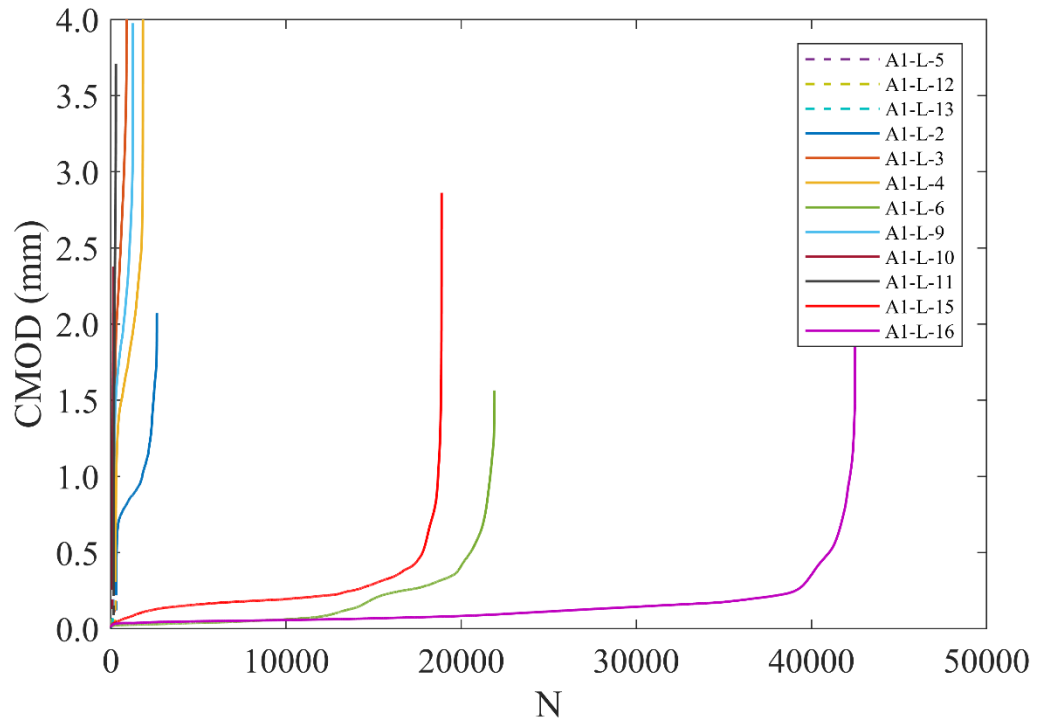


Figure 4.2-38. CMOD vs fatigue life in A1-L series fatigue tests.

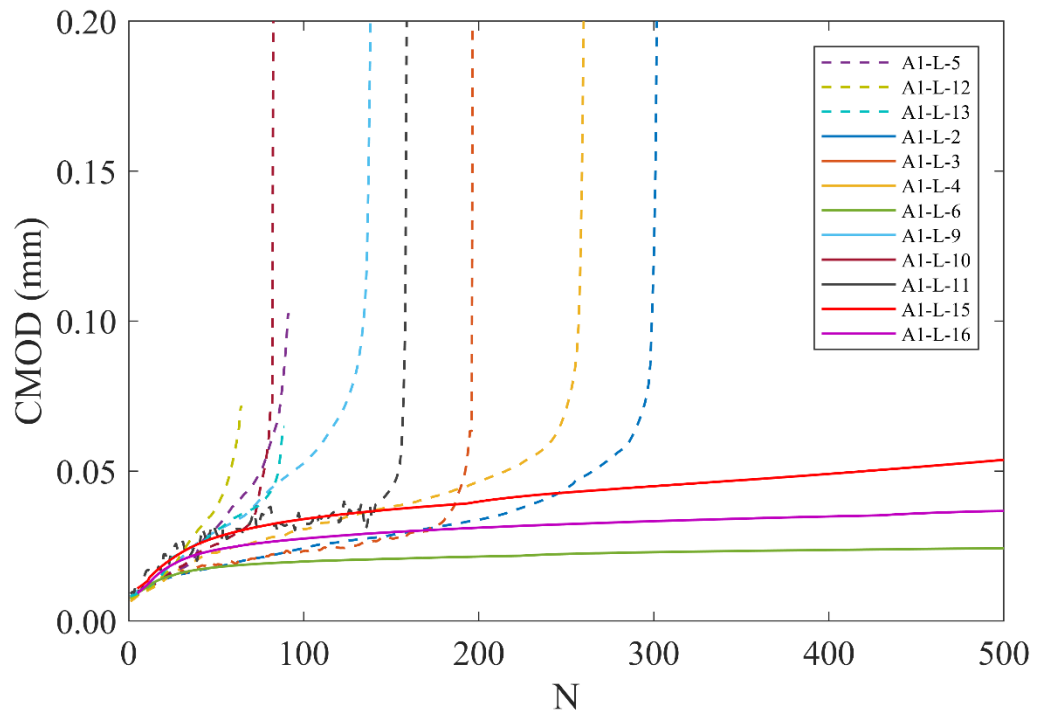


Figure 4.2-39. CMOD vs fatigue life in A1-S series fatigue tests (detail view).

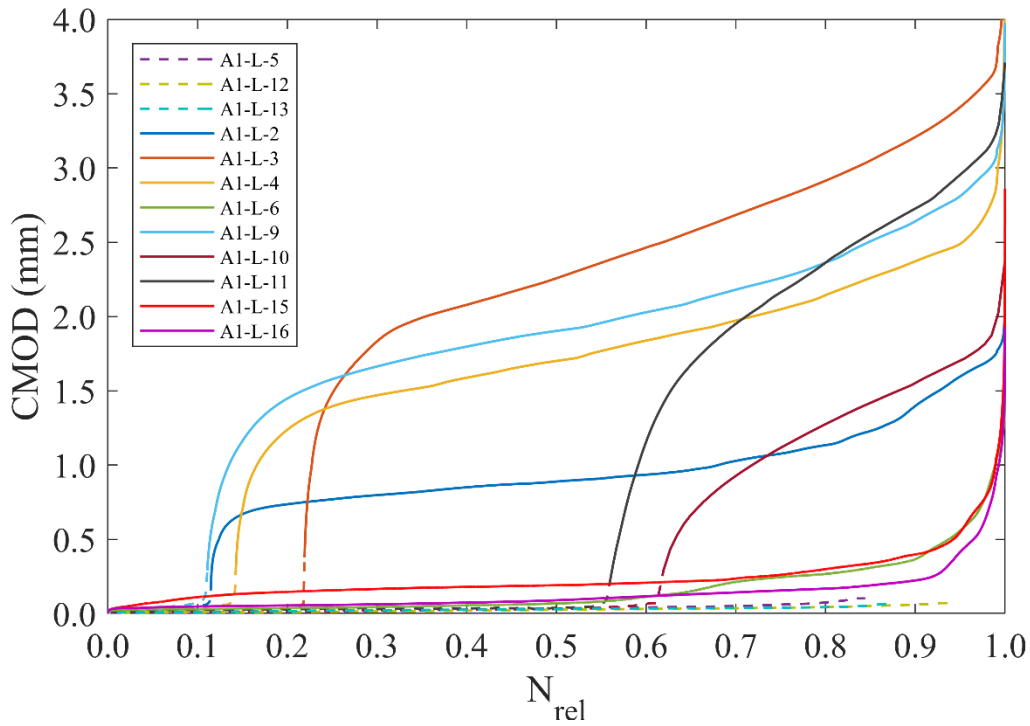


Figure 4.2-40. CMOD vs relative fatigue life in A1-L series fatigue tests.

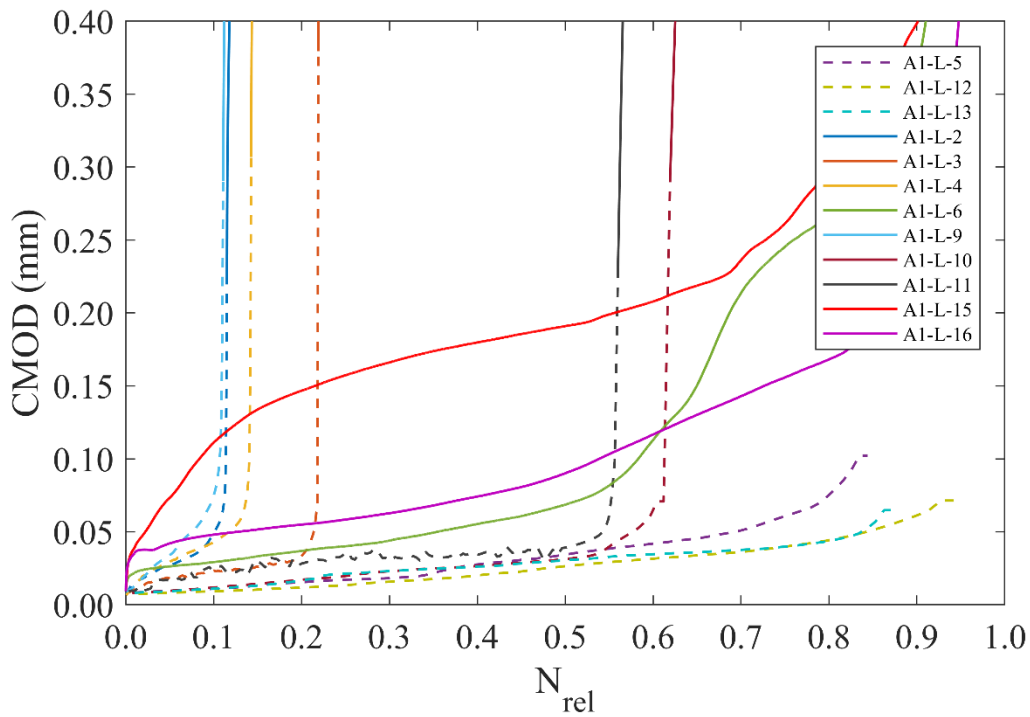


Figure 4.2-41. CMOD vs relative fatigue life in A1-L series fatigue tests (detail view).

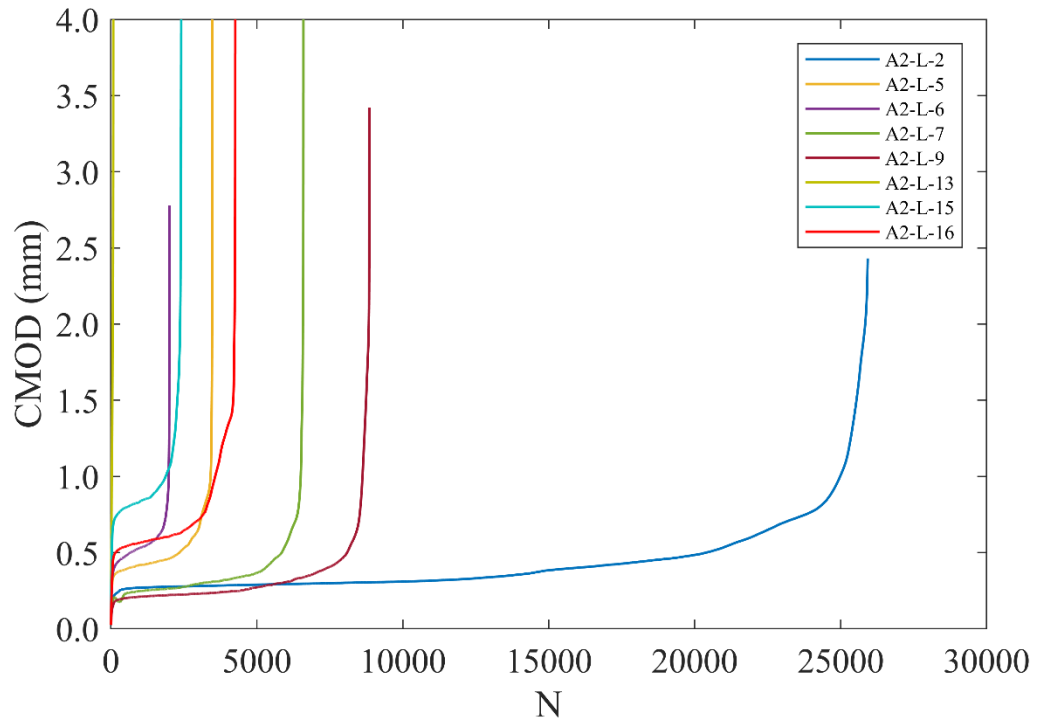


Figure 4.2-42. CMOD vs fatigue life in A2-L series fatigue tests.

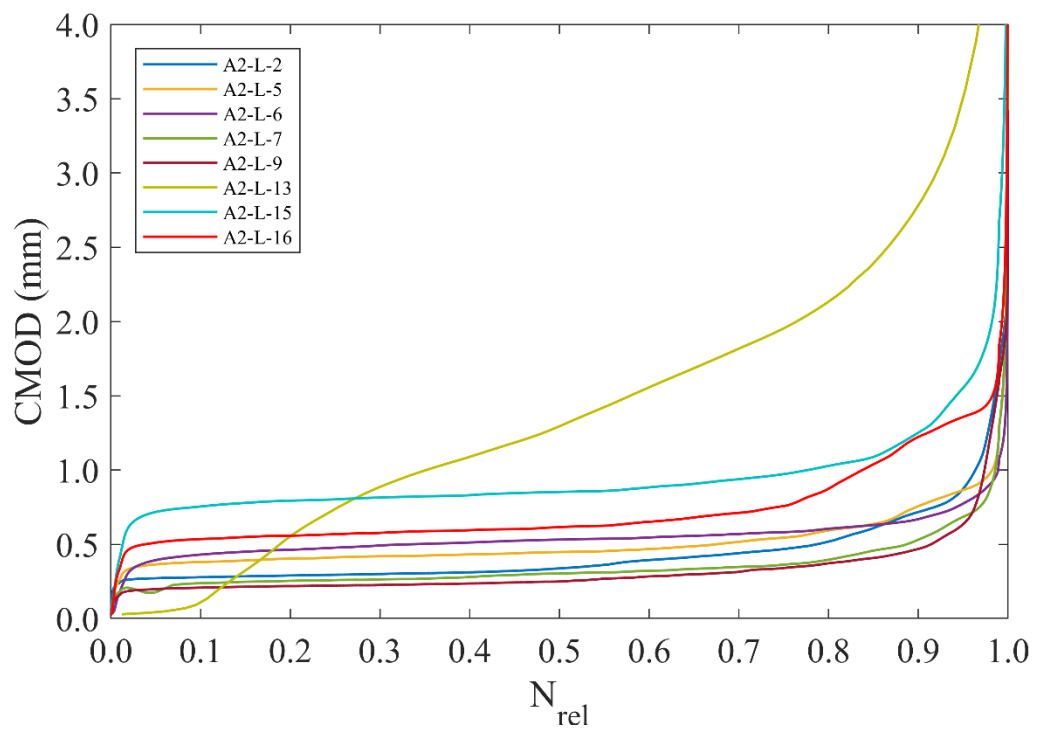


Figure 4.2-43. CMOD vs relative fatigue life in A2-L series fatigue tests.

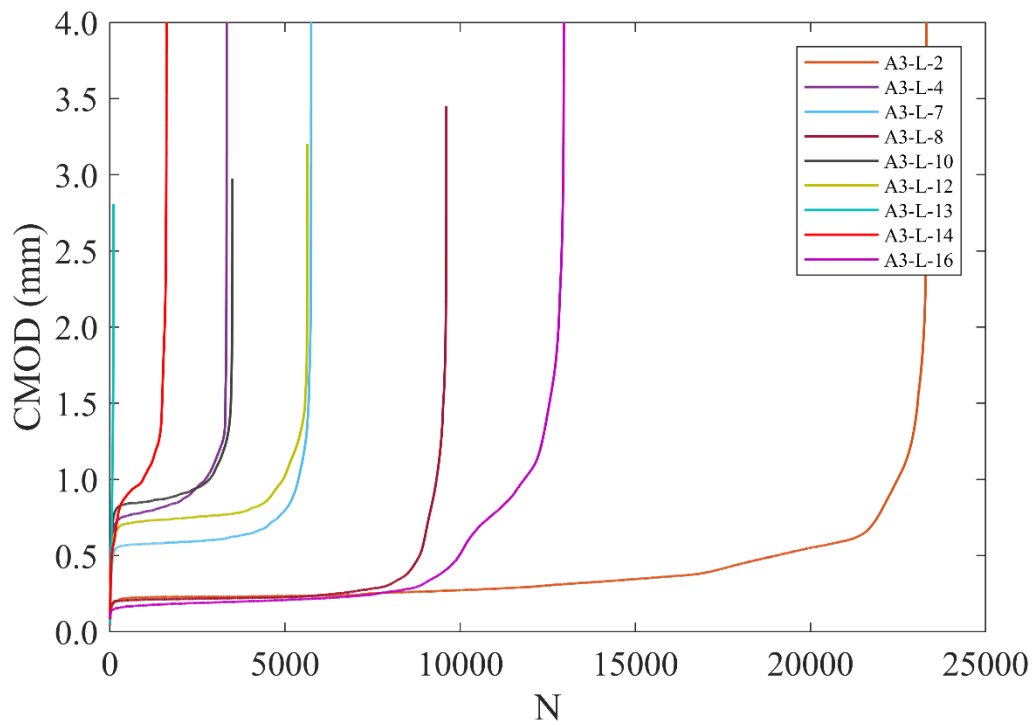


Figure 4.2-44. CMOD vs fatigue life in A3-L series fatigue tests.

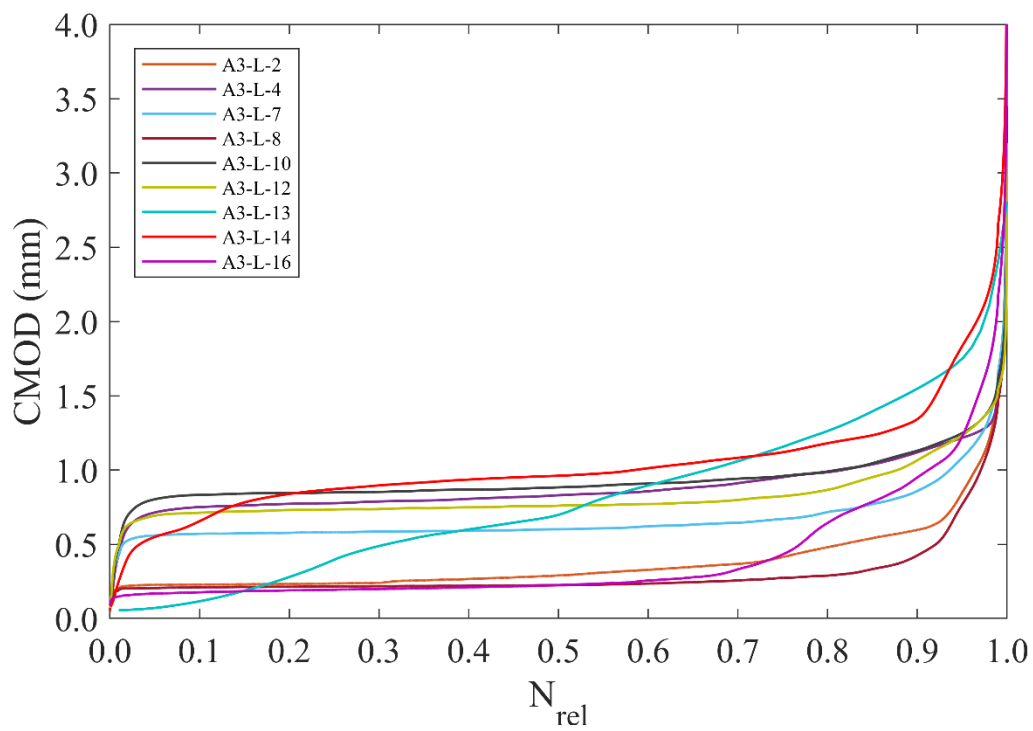


Figure 4.2-45. CMOD vs relative fatigue life in A3-L series fatigue tests.

Below is a table with the fatigue life of all specimens broken down according to the two fatigue mechanisms. That is, on the one hand the number of cycles corresponding to the fatigue of the matrix (uncracked concrete) and on the other hand the cycles associated with the fatigue of the fibers (cracked concrete).

Table 4.2-7. Fatigue life, distinguishing between the part corresponding to matrix fatigue (N_{mat}) and that associated with fiber fatigue (N_{fib}).

Series	Spec.	N_{mat}	N_{fib}	N_{tot}	Series	Spec.	N_{mat}	N_{fib}	N_{tot}		
A0-L	A0-L-1	767	-	767	A2-L	A2-L-2	-	25,926	25,926		
	A0-L-2	90	-	90		A2-L-3	-	37	37		
	A0-L-3	143	-	143		A2-L-5	-	3,476	3,476		
	A0-L-5	200	-	200		A2-L-6	-	2,004	2,004		
	A0-L-6	263	-	263		A2-L-7	-	6,597	6,597		
	A0-L-7	594	-	594		A2-L-8	-	32	32		
	A0-L-9	129	-	129		A2-L-9	-	8,851	8,851		
	A0-L-10	137	-	137		A2-L-12	-	46	46		
	A0-L-13	373	-	373		A2-L-13	-	84	84		
	A0-L-14	200	-	200		A2-L-15	-	2,415	2,415		
	A0-L-15	117	-	117		A2-L-16	-	4,264	4,264		
	A0-L-16	258	-	258							
	A1-L	A1-L-2	301	2,325		2,626	A3-L	A3-L-1	-	15	15
		A1-L-3	196	703		899		A3-L-2	-	23,308	23,308
		A1-L-4	260	1,570		1,830		A3-L-3	-	13	13
		A1-L-5	92	17		109		A3-L-4	-	3,335	3,335
A1-L-6		-	21,892	21,892	A3-L-6	-		15	15		
A1-L-9		138	1,117	1,255	A3-L-7	-		5,747	5,747		
A1-L-10		82	52	134	A3-L-8	-		9,604	9,604		
A1-L-11		158	126	284	A3-L-10	-		3,498	3,498		
A1-L-12		65	4	69	A3-L-12	-		5,634	5,634		
A1-L-13		89	13	102	A3-L-13	-		102	102		
A1-L-15		-	18,876	18,876	A3-L-14	-		1,618	1,618		
A1-L-16		-	42,491	42,491	A3-L-16	-		12,964	12,964		

It can be noted that the only series in which both fatigue mechanisms appear is A1-L; however, the matrix fatigue sections are not too important, not exceeding 500 cycles in any case. To try to explain why matrix fatigue appears in this series and not in the other SFRC ones, again it is possible to resort to the relationship between the stress corresponding to the LOP (f_L) and the maximum fatigue stress ($\sigma_{max,f}$) (Table 4.2-8). In A1-L series, $\sigma_{max,f}$ is 91% of f_L , so it is to be expected that the concrete will not fissure during the first

few cycles, resulting in matrix fatigue. However, in A2-L and A3-L series, $\sigma_{\max,f}$ is 136% and 170% of f_L , respectively. That is to say, the maximum fatigue stress is much higher than the first crack strength, which causes only fiber fatigue to occur.

Table 4.2-8. Stress corresponding to LOP and maximum stress from loading cycles in flexural fatigue tests.

Series	f_L (MPa)	$\sigma_{\max,f}$ (MPa)
A0-L	5.23	4.18
A1-L	5.22	4.75
A2-L	6.67	9.10
A3-L	7.74	13.13

In A1-L series, the percentage occupied by matrix fatigue with respect to the total fatigue life has a large dispersion, ranging from approximately 10% (specimens A1-L-2 and A1-L-9) to 90% (A1-L-5, A1-L-12 and A1-L-13). This fact could be partly associated with the dispersion of the f_L parameter itself.

On the other hand, the CMOD vs N curves have the characteristic shape, clearly differentiating the three damage phases. These phases are independent of the fatigue mechanism, so that they are seen both when matrix fatigue (A0-L series, Figure 4.2-37) and fiber fatigue (A2-L series, Figure 4.2-43, and A3-L series, Figure 4.2-45) occur. Again, when the two mechanisms appear, the three damage phases are also observed independently in each of them (Figure 4.2-40). Finally, the percentage of the fatigue life occupied by the second phase is very similar in the two types of fatigue. In the case of matrix fatigue, it extends on average between 11% and 84%; with respect to fiber fatigue, the range spans between 9% and 86%. It should be noted that there is a certain dispersion in these limits.

4.2.2.3 Secondary crack opening rate

Figure 4.2-46 to 4.2-52 show the correlation between secondary crack opening rate and fatigue life for all L-size series.

Since both fatigue mechanisms are observed in A1-L series, $(dCMOD/dn)_{mat}$ and $(dCMOD/dn)_{fib}$, calculated from the sections of the CMOD vs N diagram associated with each type of fatigue, have been obtained. Both parameters were correlated with their corresponding number of cycles (N_{mat} or N_{fib}) as well as with the total fatigue life N_{tot} .

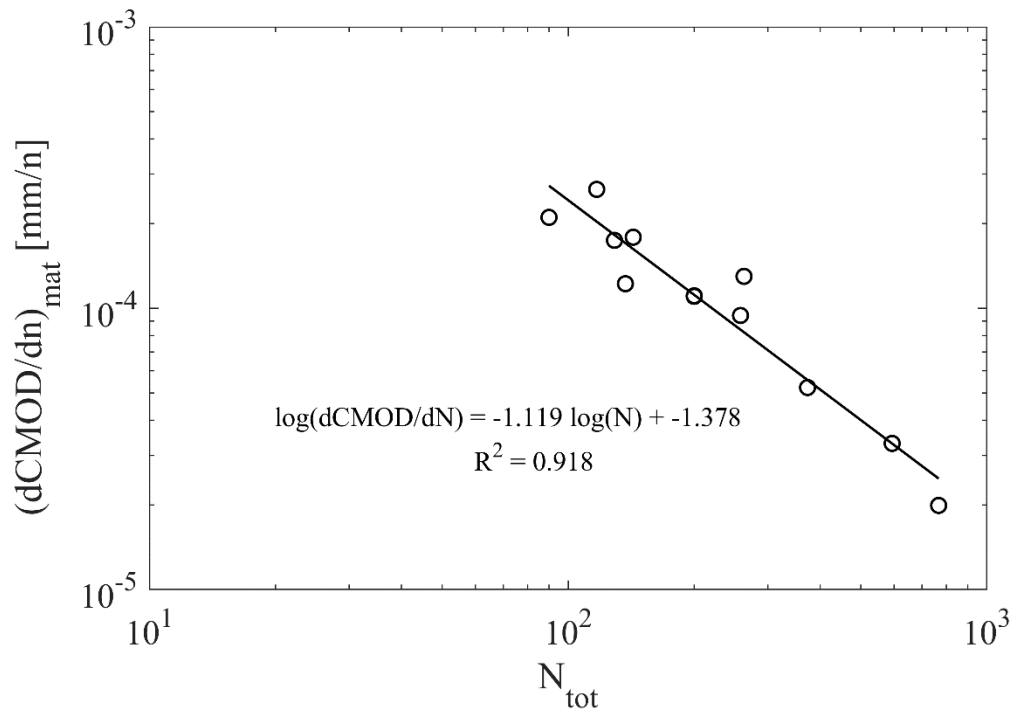


Figure 4.2-46. Secondary crack opening rate due to matrix fatigue versus total number of cycles. A0-L series.

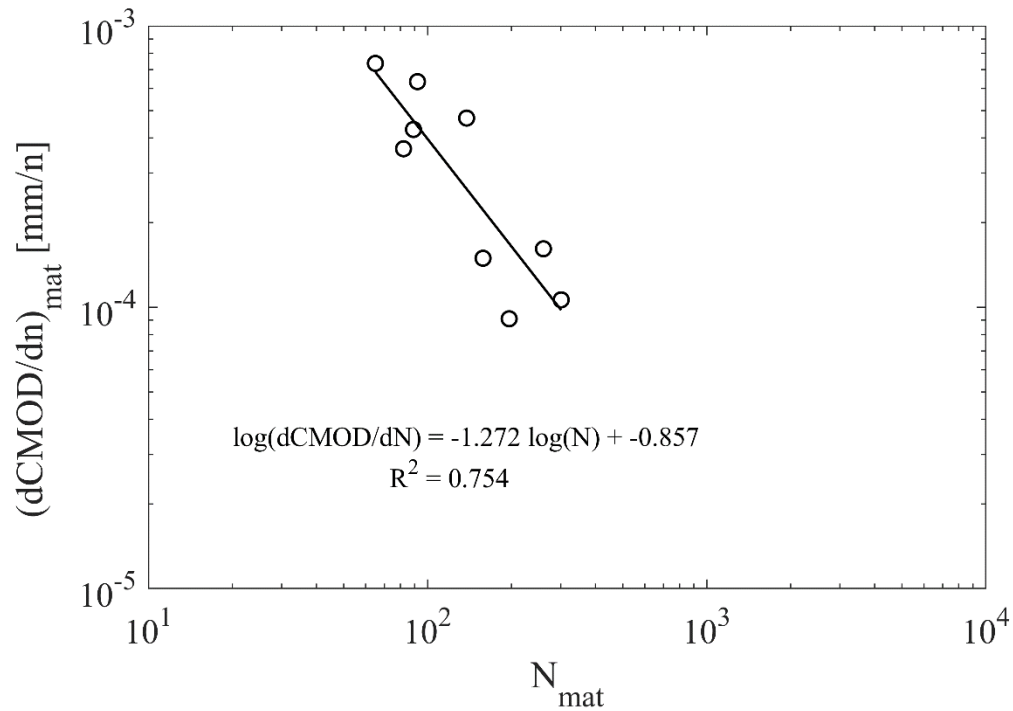


Figure 4.2-47. Secondary crack opening rate due to matrix fatigue vs number of cycles due to matrix fatigue. A1-L series.

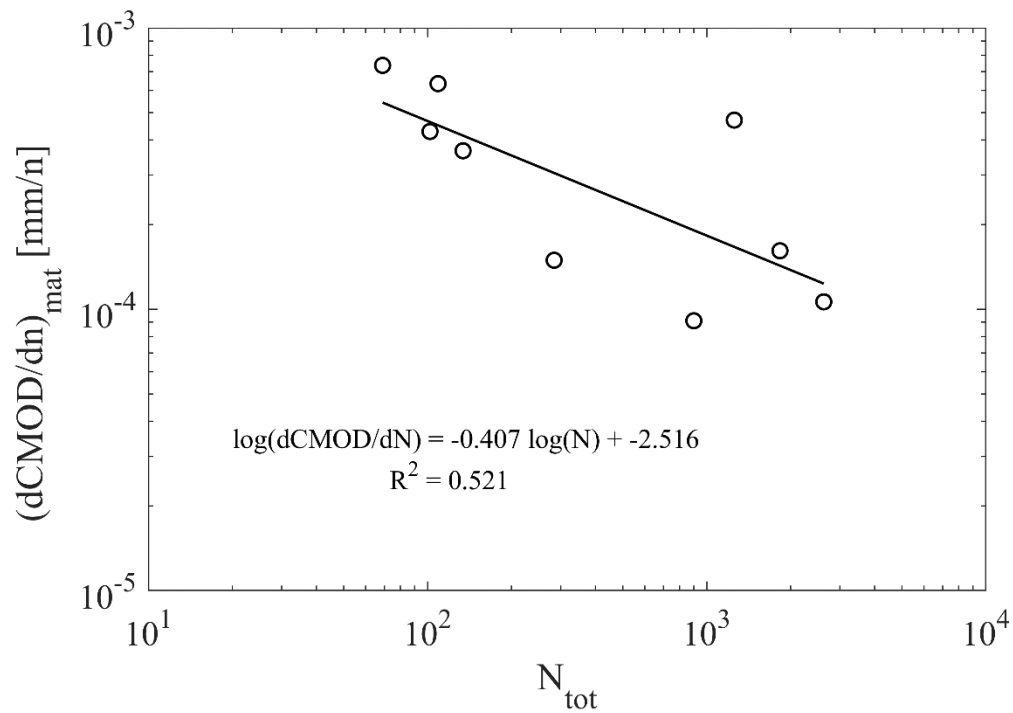


Figure 4.2-48. Secondary crack opening rate due to matrix fatigue versus total number of cycles. A1-L series.

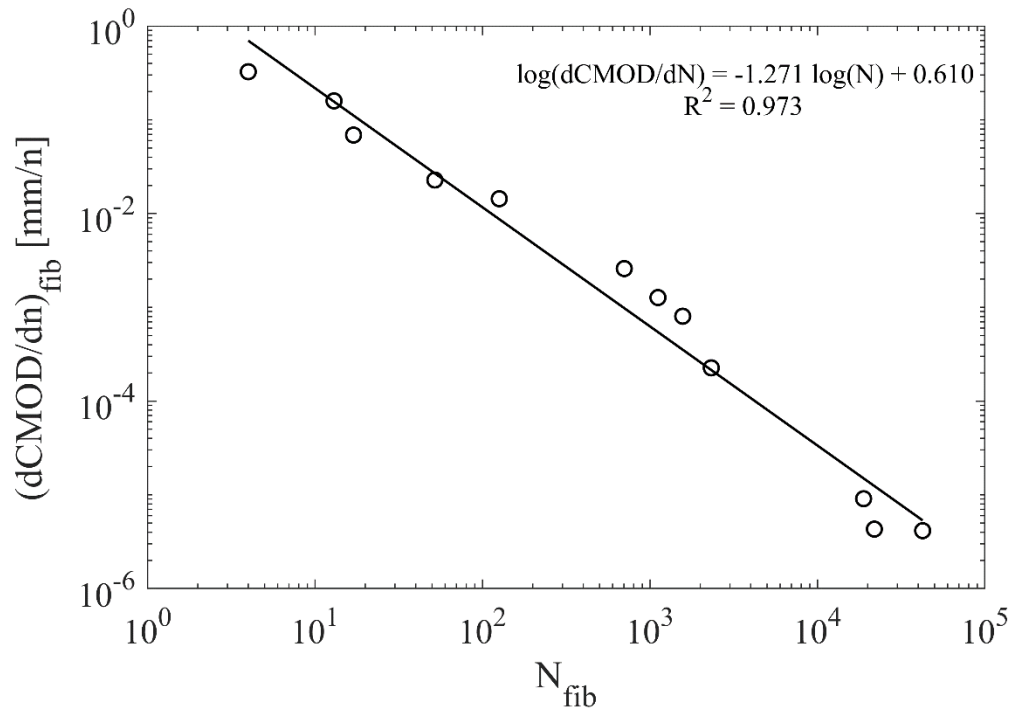


Figure 4.2-49. Secondary crack opening rate due to fiber fatigue vs number of cycles due to fiber fatigue. A1-L series.

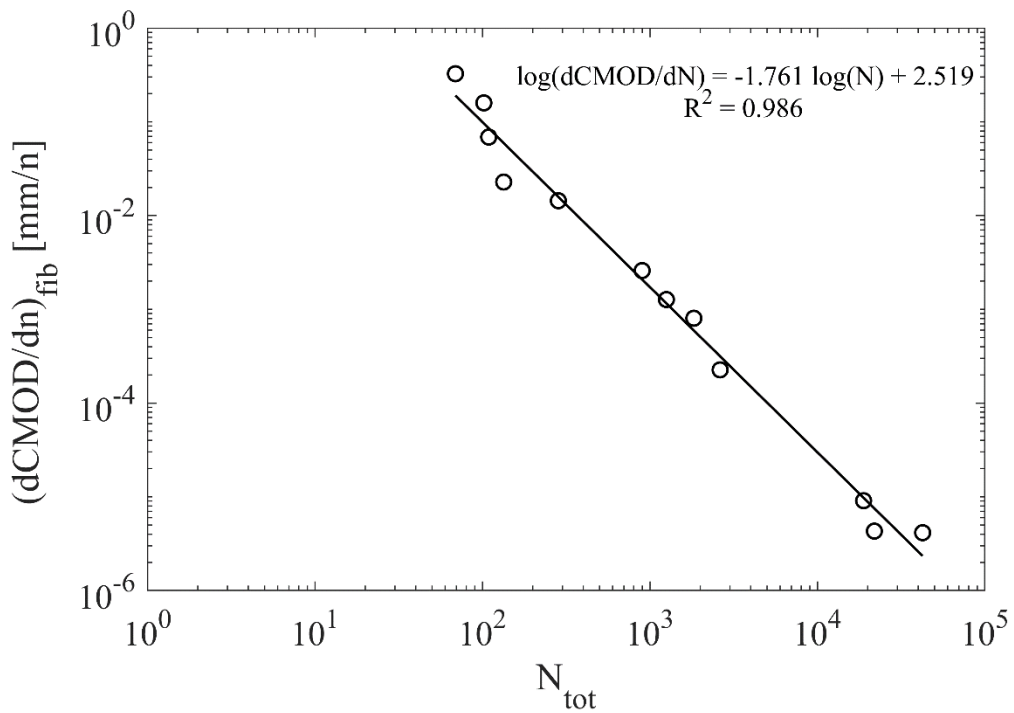


Figure 4.2-50. Secondary crack opening rate due to fiber fatigue versus total number of cycles. A1-L series.

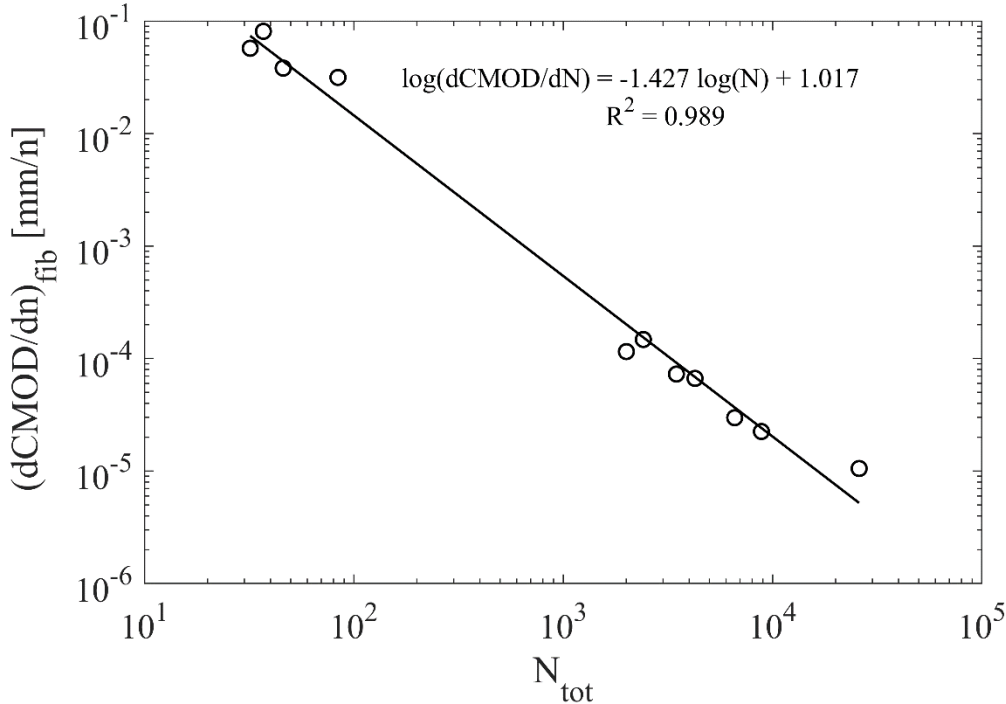


Figure 4.2-51. Secondary crack opening rate due to fiber fatigue versus total number of cycles. Series A2-L.

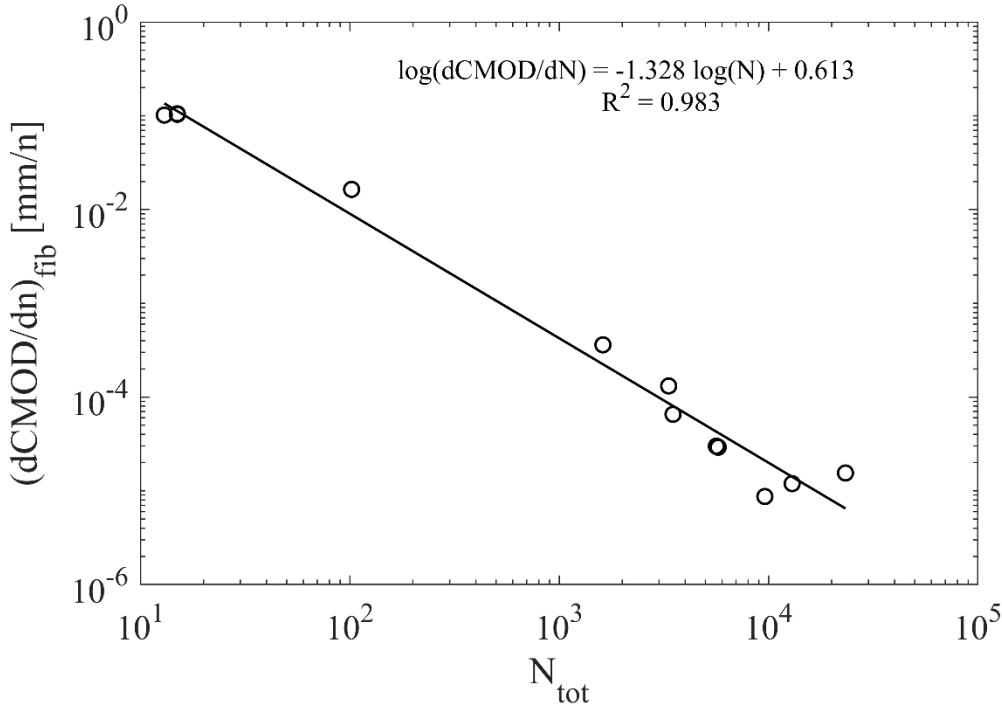


Figure 4.2-52. Secondary crack opening rate due to fiber fatigue versus total number of cycles. A3-L series.

The figures show a strong correlation between secondary crack opening rate and fatigue life, both in cases where fatigue of uncracked and cracked concrete occurs. In A1-L series, where both mechanisms appear, the fit is better when each $dCMOD/dn$ is related

to its corresponding number of cycles (N_{mat} or N_{fib}). In the fiber fatigue situation this is less evident because $N_{\text{tot}} \approx N_{\text{fib}}$.

Finally, Figure 4.2-53 groups the correlations between the secondary crack opening rate, $(d\text{CMOD}/dn)_{\text{mat}}$ or $(d\text{CMOD}/dn)_{\text{fib}}$, and the associated fatigue life, N_{mat} or N_{fib} , across all series. The fits for matrix fatigue are plotted in dashed line, while those for fiber fatigue are shown in solid line.

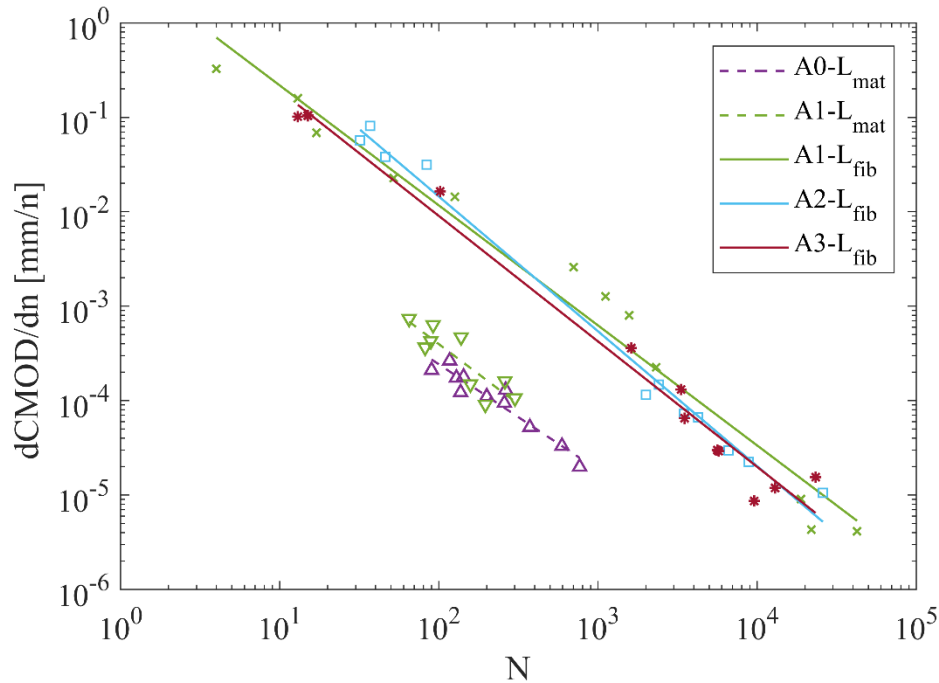


Figure 4.2-53. Secondary crack opening rate versus number of cycles, distinguishing between the two fatigue mechanisms.

Interesting conclusions can be derived from Figure 4.2-53. First, the fitting lines associated with fiber fatigue are above those for matrix fatigue, again inferring that fatigue damage progresses more rapidly when governed by the fibers. The difference between $(d\text{CMOD}/dn)_{\text{fib}}$ and $(d\text{CMOD}/dn)_{\text{mat}}$ is about one order of magnitude. This is in agreement with the results of the work of Germano et al. [54], who performed flexural fatigue tests on plain concrete (fatigue of uncracked concrete) and SFRC pre-cracked specimens with 0.5% and 1.0% fibers (fatigue of cracked concrete).

Moreover, it is observed that the fiber content does not influence the relationship between $d\text{CMOD}/dn$ and N ; in fact, the straight lines are practically coincident in both the case of matrix fatigue and fiber fatigue. In the particular situation of fiber fatigue, this points to the fact that the progress of fatigue damage is independent of fiber content,

considering the dosages used. Again, this is in agreement with what was concluded in Germano et al. [54], where the lines of fit in the concrete series with 0.5% and 1.0% fibers are also very similar.

4.3 Study of the mesostructure

S-size specimens subjected to flexural fatigue were scanned with micro-computed tomography to analyze the mesostructure of concrete. In total, 52 specimens were treated. In plain concrete specimens (A0-S series), the geometrical properties of the pores were obtained, while in SFRC specimens (A1-S, A2-S and A3-S series), only the fibers were examined.

The objective of this subsection is to demonstrate the possibilities offered by microCT for the analysis of concrete mesostructure, both pores and steel fibers. Therefore, this is a preliminary study in which some of the geometrical parameters of these components that can be obtained are shown. In any case, in Section 5. ANALYSIS OF RESULTS AND DISCUSSION, a more detailed study is made, focused on looking for correlations between the dispersion of concrete mesostructure (through its most significant parameters) and the dispersion of fatigue results themselves.

In this demonstration study, the area of interest has been restricted to the central 30 mm of the specimens in the longitudinal direction, i.e., 15 mm on each side of the notch. The reason is that the flexural failure is local in nature, being concentrated in the mid-span section.

4.3.1 Geometric parameters of the fibers

In the specimens of series A1-S, A2-S and A3-S, some of the most relevant geometrical parameters of the fibers in relation to orientation and spatial distribution have been studied. The results are shown below.

4.3.1.1 Orientation

Figure 4.3-1 to 4.3-3 show the histograms of fiber orientation with respect to the three coordinate axes. For each series, the average histograms, calculated from the results of the 13 constituent specimens (12 for flexural fatigue and 1 for reserve), are plotted. In addition, to facilitate the interpretation of the results, Figure 4.3-4 is included with the indication of the coordinate system used.

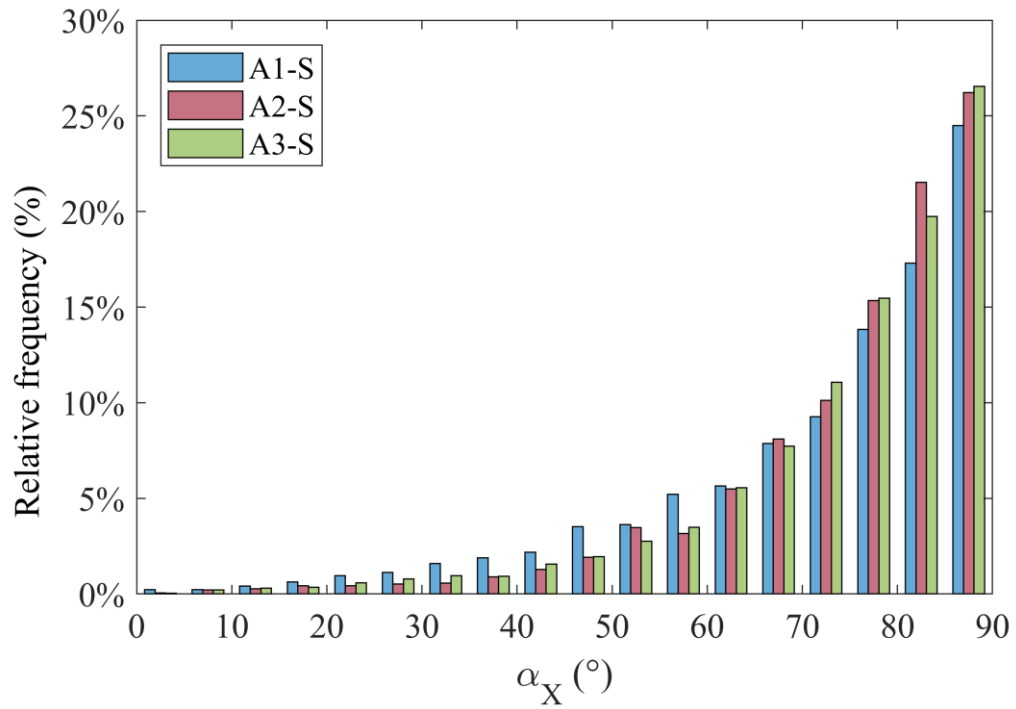


Figure 4.3-1. Histogram of fiber orientation with respect to the X-axis.

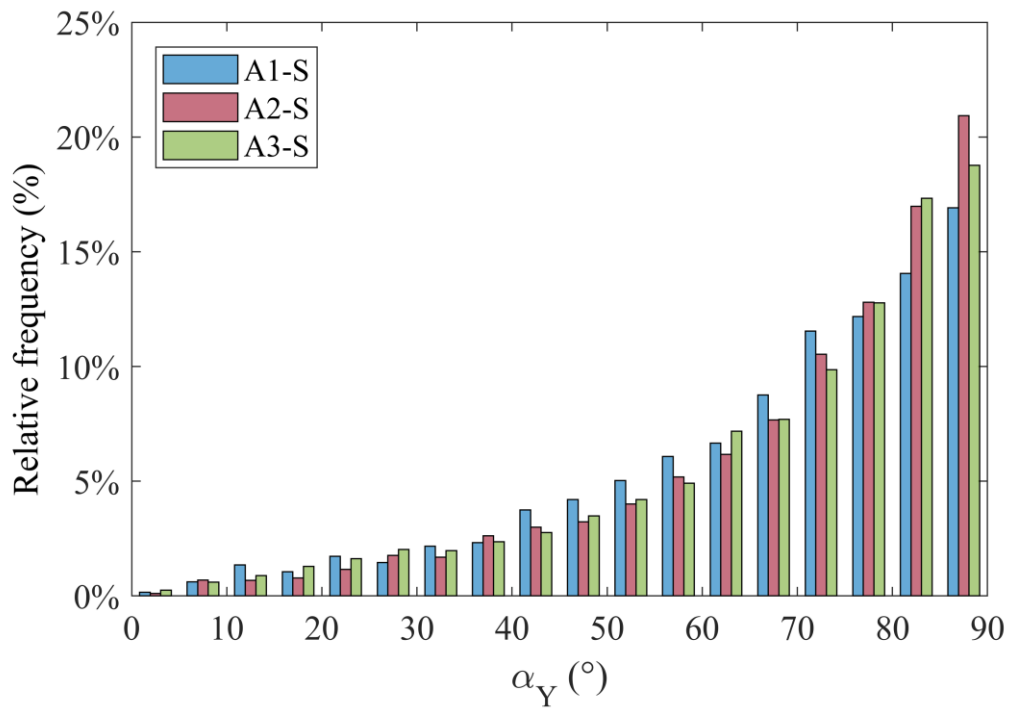


Figure 4.3-2. Histogram of fiber orientation with respect to the Y-axis.

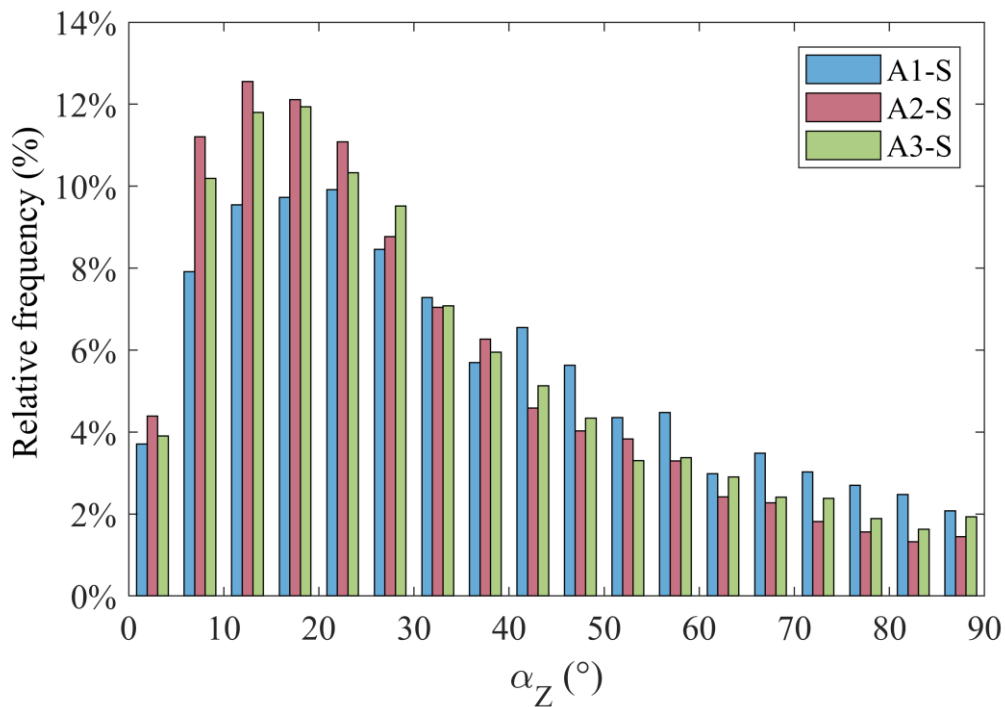


Figure 4.3-3. Histogram of fiber orientation with respect to the Z-axis.

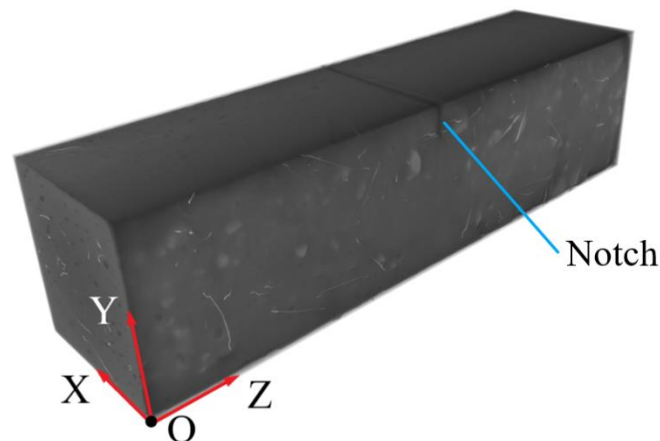


Figure 4.3-4. Indication of the coordinate system used.

The histograms reveal that the fibers are not randomly oriented, but that there are preferred directions. With respect to the X and Y axes, in all series the most frequent range of orientations is between 85° and 90°, so it is concluded that the fibers tend to orient perpendicular to the XY plane. This is explained by the wall effect, which is more significant the higher the ratio of fiber length / minimum element dimension. Since in this case this ratio is rather high (0.40), it is expected that the wall effect is significant. As for the Z-axis, it seems that the fibers are not arranged perfectly parallel, but with a certain inclination. It is observed that the most frequent orientations vary slightly according to the series, being 20-25°, 15-20° and 10-15° for series A1-S, A3-S and A2-S, respectively.

The orientation of the fibers of a specimen with respect to an axis can be characterized by the mean value of the angle they form, or by the average of the so-called orientation efficiency indexes, or simply efficiency indexes [97,128]. These are defined according to the following expression (Eq. (4.3-1)):

$$ei_{u,m} = \frac{\sum_{i=0}^n \cos \alpha_{u,i}}{n} \quad u := X, Y, Z \quad (4.3-1)$$

Where $\alpha_{u,i}$ is the angle formed by each fiber with respect to the corresponding coordinate axis and n is the number of fibers in the study area. The efficiency index takes values between 0 and 1, where 1 indicates that the fibers are perfectly oriented with respect to the reference axis, while 0 means that they are arranged perpendicular to it. Table 4.3-1 shows the mean values of the efficiency indexes for each series, including the deviations.

Table 4.3-1. Fiber orientation efficiency indexes.

Series	$ei_{X,m}$	$ei_{Y,m}$	$ei_{Z,m}$
A1-S	0.30 [0.05]	0.37 [0.05]	0.76 [0.07]
A2-S	0.25 [0.05]	0.33 [0.04]	0.82 [0.04]
A3-S	0.25 [0.04]	0.34 [0.05]	0.80 [0.04]

The results of Table 4.3-1 confirm what was observed in the orientation histograms: fibers are arranged orthogonally to the X and Y axes, preferentially aligned with the Z axis, which defines the largest dimension of the specimens. Although a priori the orientations are similar in the three series, there are some differences that should be highlighted. Series A2-S and A3-S have practically identical efficiency indexes, while in series A1-S they vary slightly; in particular, ei_Z is lower, suggesting that the fibers are less well oriented to resist bending stresses. This may indicate that orientation improves with fiber content, although to some extent. The optimum content is reached at 0.6%, since at 1.0% the ei_Z index does not increase. In any case, it is expected that this optimum value is strongly dependent on the ratio of fiber length / minimum element dimension, as well as other factors such as the maximum size of the coarse aggregate.

4.3.1.2 Spatial distribution

Figure 4.3-5 to 4.3-7 show the histograms of the position of the centers of gravity of the fibers with respect to the coordinate axes. The average histograms of each series are plotted.

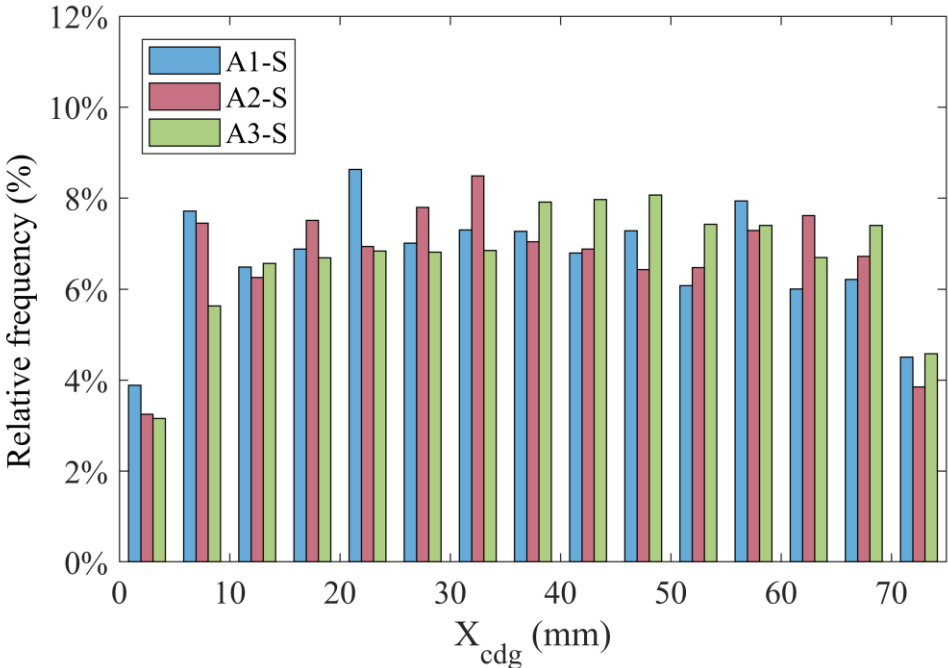


Figure 4.3-5. Histogram of X-coordinate of the center of gravity of the fibers.

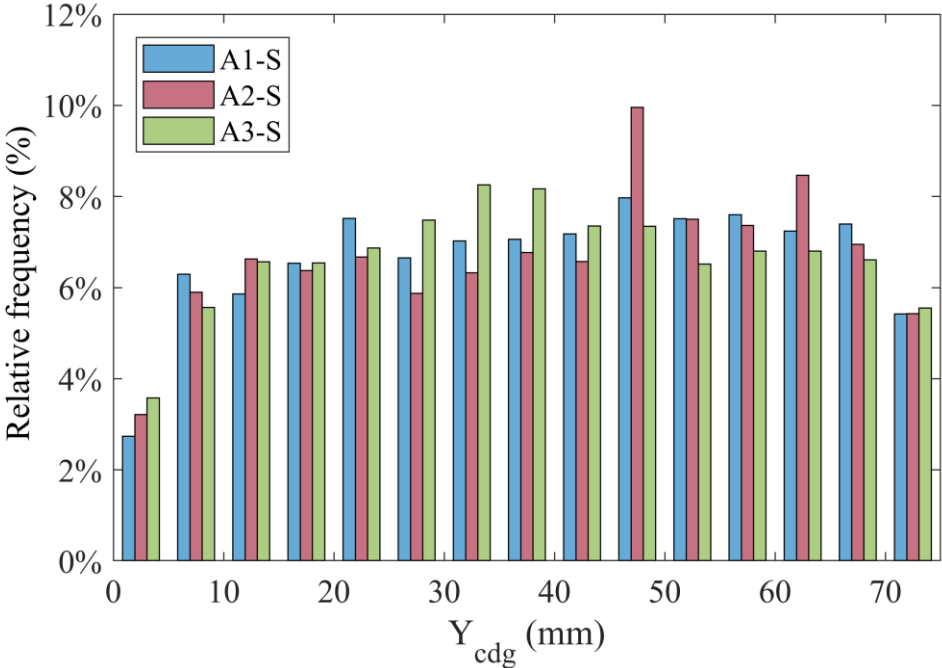


Figure 4.3-6. Histogram of Y-coordinate of the center of gravity of the fibers.

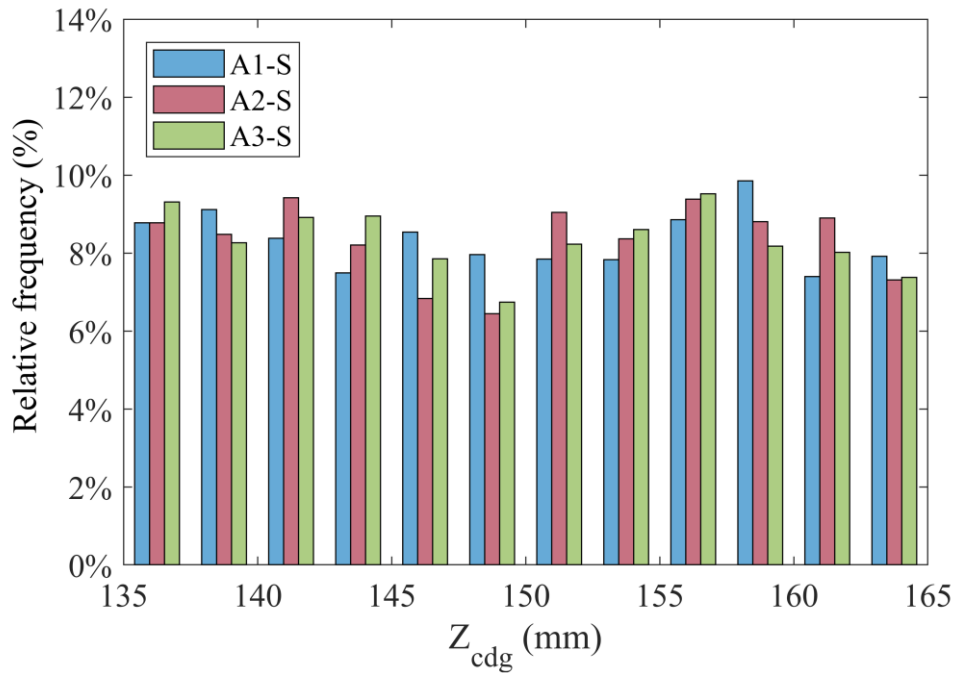


Figure 4.3-7. Histogram of Z-coordinate of the center of gravity of the fibers.

Figure 4.3-5 and 4.3-6 show the wall effect caused by the mold, which leads to a decrease in fiber concentration in the contour of the specimens. In this case, in both X and Y axes, the thickness of the outer layer affected is about 5 mm, while in the inner layer the fiber distribution remains approximately uniform. With respect to the Z-axis, Figure 4.3-7 does not show this phenomenon, since only the central region has been studied. On the other hand, no significant differences are observed between the three series. There are some peaks of fiber concentration, but the dispersion is high and could be due to some accumulation of fibers in certain specimens.

One parameter that may be of interest in correlating the mesostructure with the macroscopic response of the concrete is the number of fibers passing through the crack plane (mid-span section), or their density. Table 4.3-2 lists the mean values of both parameters, including their dispersion.

Table 4.3-2. Number of fibers and density in the crack plane.

Series	$n_{\text{fib},\text{fis}}$	$\rho_{\text{fib},\text{fis}} \text{ (cm}^{-2}\text{)}$
A1-S	73.8 [13.3]	1.3 [0.2]
A2-S	153.8 [30.6]	2.7 [0.5]
A3-S	297.2 [64.4]	5.3 [1.1]

As expected, the fiber density in the midplane increases substantially proportional to the content.

4.3.2 Geometric parameters of the pores

A porosity study was carried out on the A0-S series specimens, obtaining the main geometrical parameters of the pores: volume, length, etc. Since the resolution of the microCT scans is 65 μm , a preliminary filtering was performed. Pores whose volume is less than 0.008 mm^3 , the equivalent of a cube whose side is defined by 3 voxels, have been discarded. Smaller pores are considered to have insufficient definition to determine their properties accurately.

The most relevant results of the study are shown below.

4.3.2.1 Porosity and pore size distribution

The pore size distribution can be evaluated by two types of diagrams: the porosity curve and the cumulative pore volume curve [128,133].

Figure 4.3-8 shows the porosity curve, which represents, for each pore length, the porosity summed by pores of equal or smaller length. The length of a pore is defined as the distance between its two farthest voxels. As for the porosity, it is the ratio between the accumulated volume of the pores considered and the volume of the specimen (in this case, of the central region). The blue solid line shows the average curve, while the shading represents the deviation.

The results show that the average porosity of the series is 1.24%, although there is a large dispersion. In addition, it is observed that the larger pores ($\geq 5 \text{ mm}$) contribute almost nothing to the final porosity.

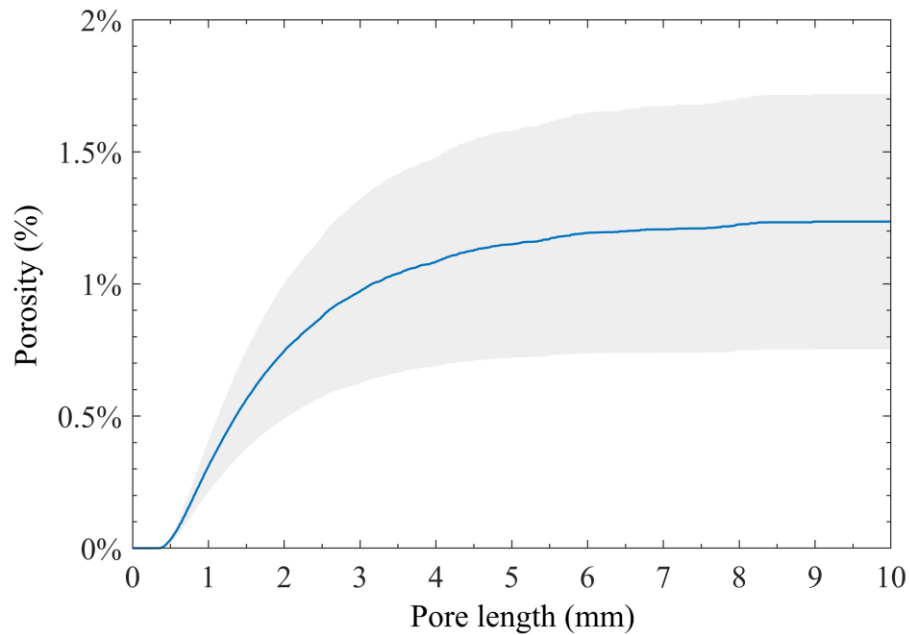


Figure 4.3-8. Porosity curve of A0-S series.

Figure 4.3-9 shows the cumulative pore volume curve, which represents, for each pore length, the percentage of the total pore volume constituted by pores of equal or smaller length. Again, the mean curve is shown in solid line and the deviation in shading.

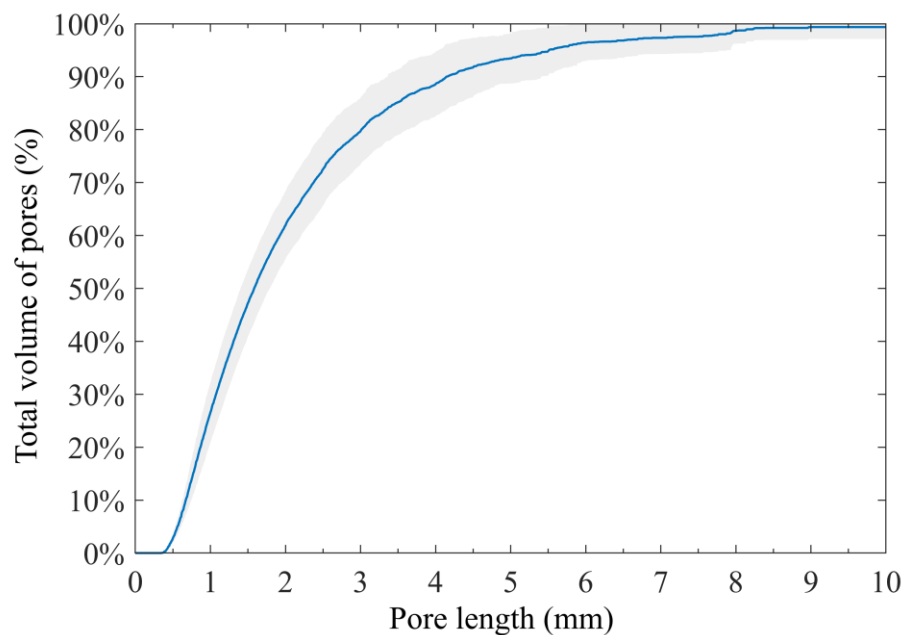


Figure 4.3-9. Cumulative pore volume curve of A0-S series.

It can be observed that the cumulative pore volume curve has much less dispersion than the porosity curve. This indicates that, although the total porosity of the specimens may vary, the pore size distribution is very similar. Figure 4.3-9 confirms that most of the

pore volume is concentrated in the smallest pores; in fact, 50% of this volume corresponds to pores of length equal to or less than 1.59 mm.

Finally, Table 4.3-3 contains the mean value of total porosity (p) and pore density (ρ_p).

Table 4.3-3. Porosity and pore density in A0-S series.

p (%)	1.24 [0.48]
ρ_{por} (cm⁻³)	95.1 [23.8]

4.3.2.2 Pore volume and length

Figure 4.3-10 and 4.3-11 show the pore volume histograms, represented in relation to the number of pores and total volume of pores, respectively.

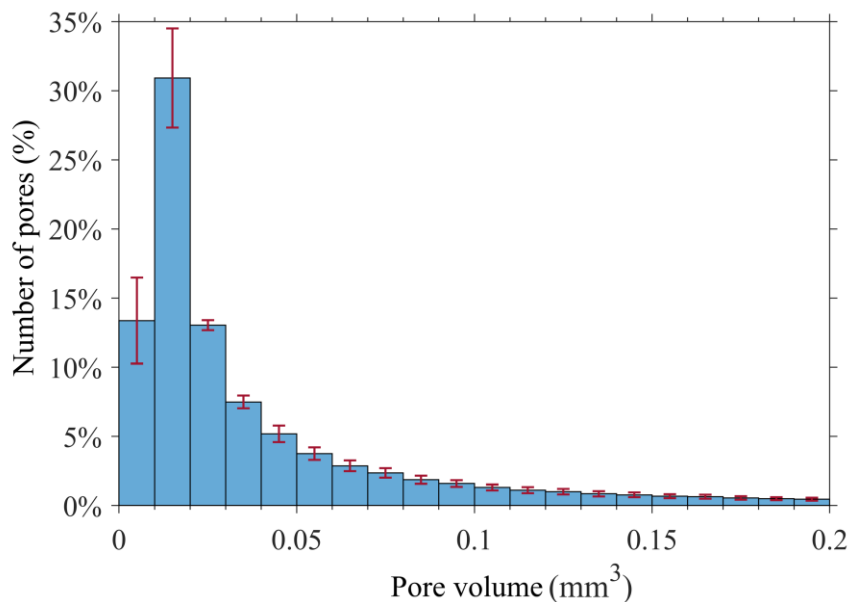


Figure 4.3-10. Histogram of pore volume versus number of pores. A0-S series.

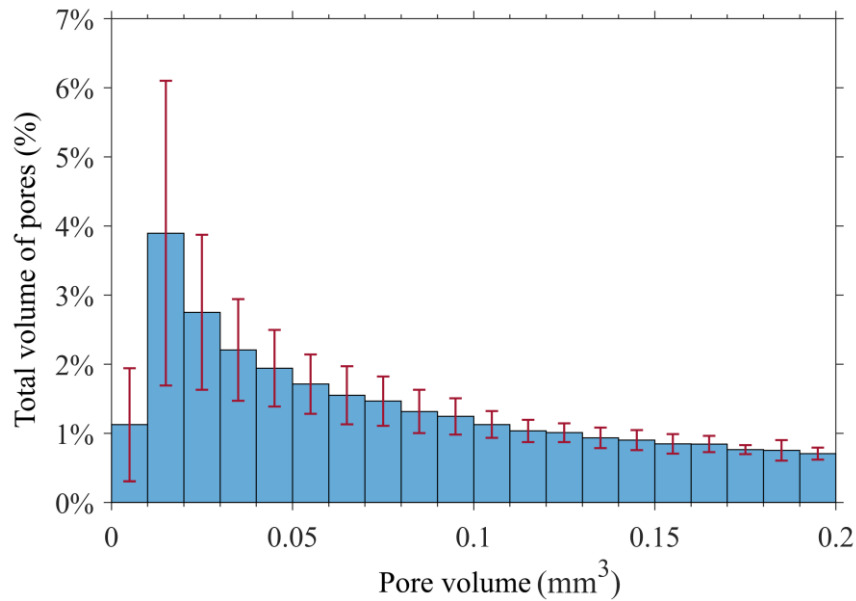


Figure 4.3-11. Histogram of pore volume versus total volume of pores. A0-S series.

Figure 4.3-10 shows that most of the pores have a very small volume; in fact, pores smaller than 0.02 mm^3 account for 44% of the total. Taking into account that only those larger than 0.008 mm^3 have been considered, it is foreseeable that this percentage is higher. On the other hand, Figure 4.3-11 reveals that the smallest pores are also those that represent the largest volume of the total. In this case, pores smaller than 0.02 mm^3 account for 5% of the total pore volume. From this it can be concluded that the incidence of smaller pores is much greater in terms of number than volume. Moreover, in the latter case the dispersion is high.

Next, Figure 4.3-12 and 4.3-13 show the histograms of pore length, plotted against the number of pores and the total volume of pores, respectively.

The figures yield similar results to those of the pore volume histograms. It is observed that the smallest pores, under 0.9 mm , represent 79% in relation to the total number of pores, and 21% in relation to the total volume of pores.

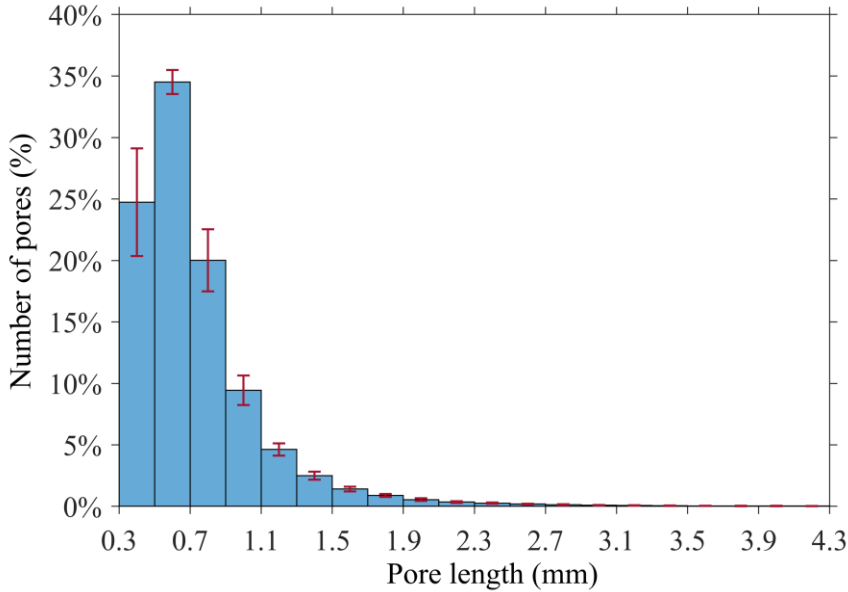


Figure 4.3-12. Histogram of pore length in relation to the number of pores. A0-S series.

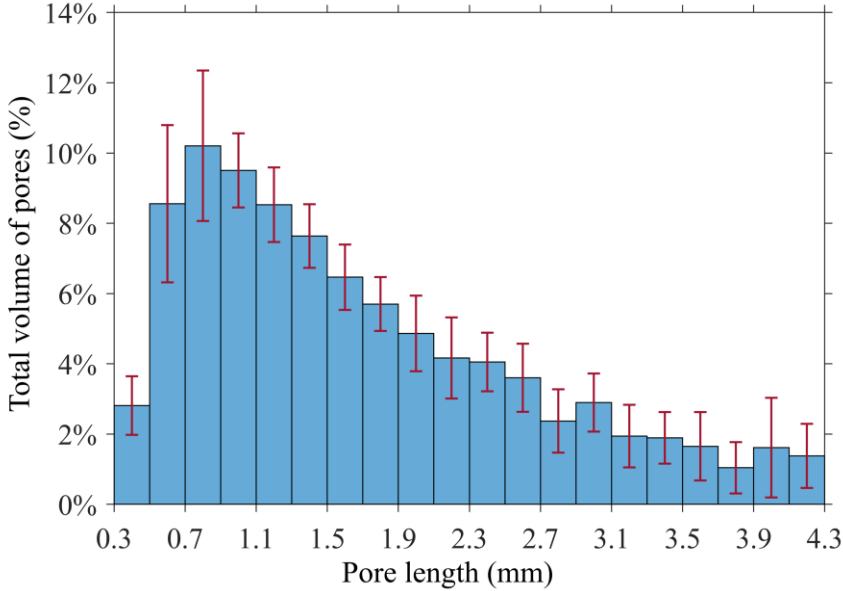


Figure 4.3-13. Histogram of pore length in relation to the total volume of pores. A0-S series.

5 ANALYSIS OF RESULTS AND DISCUSSION

This section discusses the results presented in the previous section, thus addressing the general objectives of this research.

The first two objectives consist of studying the relationship between the dispersion of concrete mesostructure properties and the dispersion of fatigue results. For this purpose, first of all, correlations are established between the geometric parameters of the fibers and the results of the flexural fatigue tests. Therefore, only A1-S, A2-S and A3-S series are considered here; i.e., SFRC specimens of size S. Secondly, the geometrical parameters of the pores are related to the fatigue results. In this case, only A0-S series of plain concrete of size S is considered. In order to facilitate the interpretation of the results, the following figure shows the coordinate system used.

The second objective is to study the size effect on the flexural fatigue behavior of concrete. Consequently, the fatigue results of the two specimen sizes, both in plain concrete and fiber-reinforced concrete, are compared.

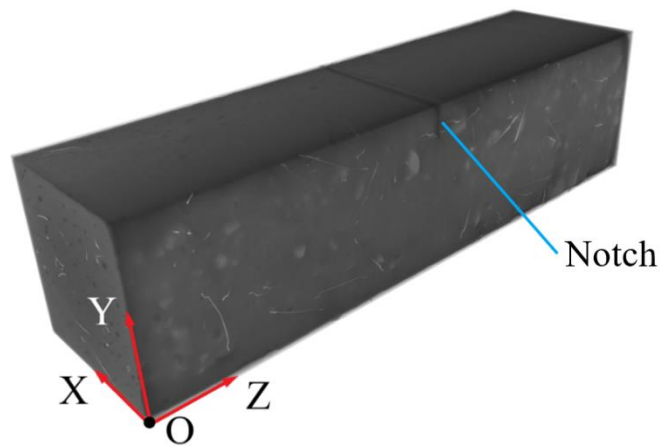


Figure 4.3-1. Indication of the coordinate system used.

5.1 Influence of fibers on the flexural fatigue response of SFRC

This subsection studies the effect of the dispersion of fiber properties on the dispersion of fatigue behavior. Consequently, it is important to clarify that the aim is not to compare the differences in fatigue response between series; what is intended is, within each series or type of concrete, to explain how slight variations in the mesostructure affect the variability of the results.

The fact that different types of SFRCs have been tested is because it is also intended to check whether the influence of the mesostructure on the fatigue response is affected in any way by the fiber content.

To achieve this goal, correlations are first established between the fatigue life and some fiber parameters related to their orientation and spatial distribution. For each parameter, it is studied how its dispersion affects the dispersion of the fatigue life, both in each series and considering the data of all series in global. Furthermore, correlations are defined not only with the fatigue life, but also with the secondary crack opening rate, another variable representative of the fatigue response. Then, using the most significant parameters, empirical formulas are developed to estimate the fatigue results.

A study region limited to the central 30 mm of the specimens, i.e., the equivalent of one fiber length, has been established. Therefore, the dimensions are 75 mm in the X-axis, 75 mm in the Y-axis and 30 mm in the Z-axis. The reason is that bending failure is local, concentrated in the notch section (mid-span), while the rest of the specimen remains practically intact. Therefore, it is the fibers in this zone that can potentially influence the fatigue response.

On the other hand, the specimen of the A2-S series that has exceeded the survival limit (A2-S-9) has not been included, since it has not even cracked ($CMOD < 0.05$ mm) and therefore fatigue of cracked concrete has not occurred. This is considered an anomalous result.

Finally, it is convenient to advance that, in general terms, the correlations between the fatigue response and the geometrical parameters considered present low values of the coefficient of determination R^2 . This shows that fatigue dispersion is a multi-parametric problem of great complexity, with no single parameter being dominant. In fact, many

more parameters have been considered in a previous phase of the study, and the ones presented here are the most significant.

5.1.1 Orientation

Linear regressions between the mean fiber orientation with respect to the Z-axis (normal to the crack plane) and the fatigue response are shown below. The main fatigue results considered are the total number of cycles (N_{tot}), the number of cycles associated with fiber fatigue (N_{fib}) and the secondary crack opening rate corresponding to fiber fatigue ($(dCMOD/dn)_{fib}$). The latter parameter is very interesting since it characterizes the evolution of fatigue damage in concrete. The variables related to the fatigue of uncracked concrete (N_{mat} and $(dCMOD/dn)_{mat}$) have not been included, since this mechanism is mainly governed by the matrix and not by the fibers.

The fatigue parameters have been plotted on a logarithmic scale. The individual regressions per series are shown, as well as the global regression with all the data.

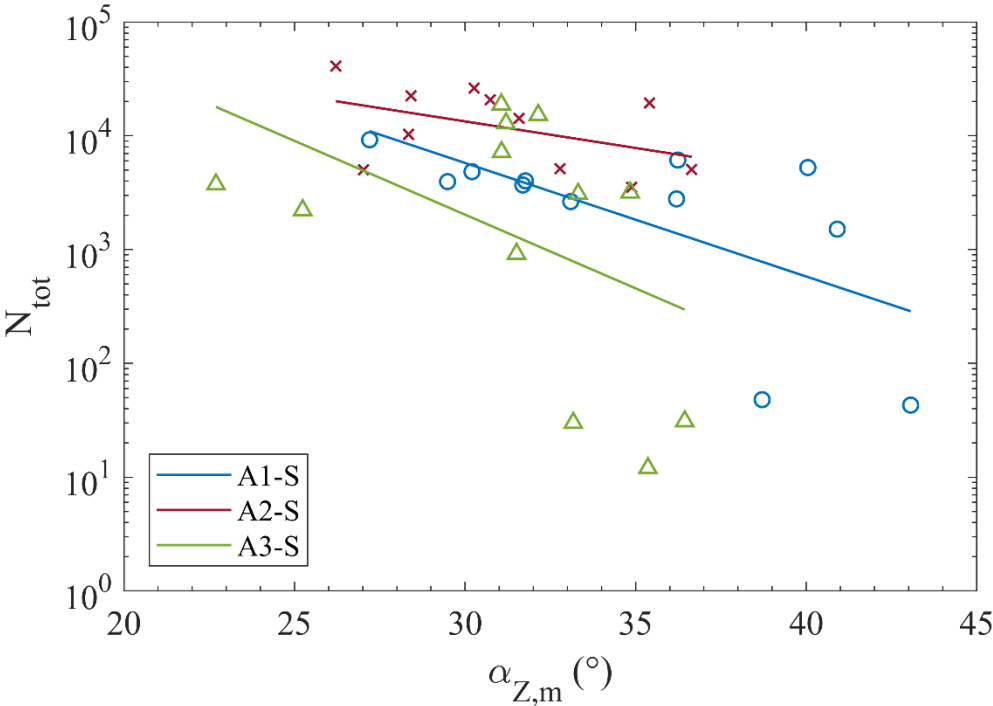


Figure 5.1-1. Linear regression (per series) between the mean fiber orientation with respect to the Z-axis and the total number of cycles.

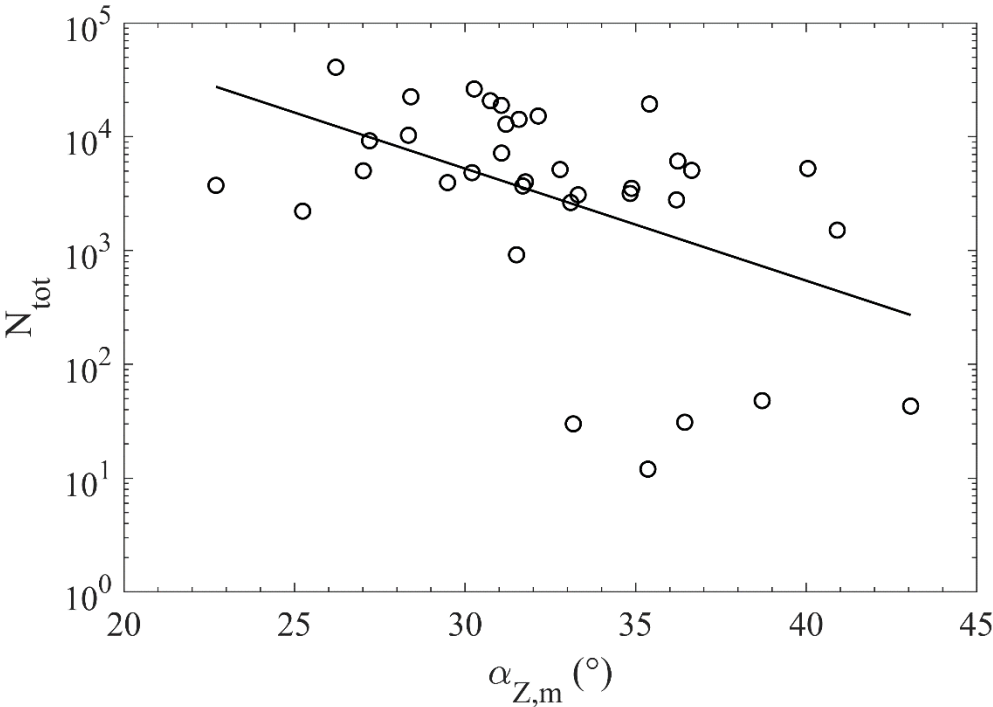


Figure 5.1-2. Linear regression (global) between the mean fiber orientation with respect to the Z-axis and the total number of cycles.

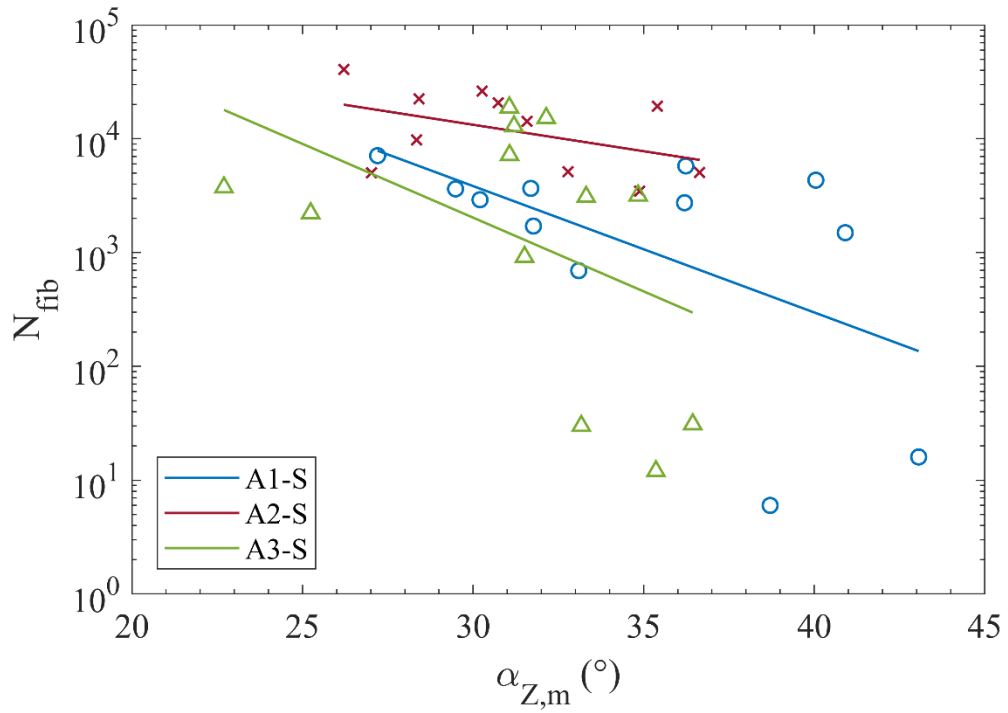


Figure 5.1-3. Linear regression (per series) between the mean fiber orientation with respect to the Z-axis and the number of fiber fatigue cycles.

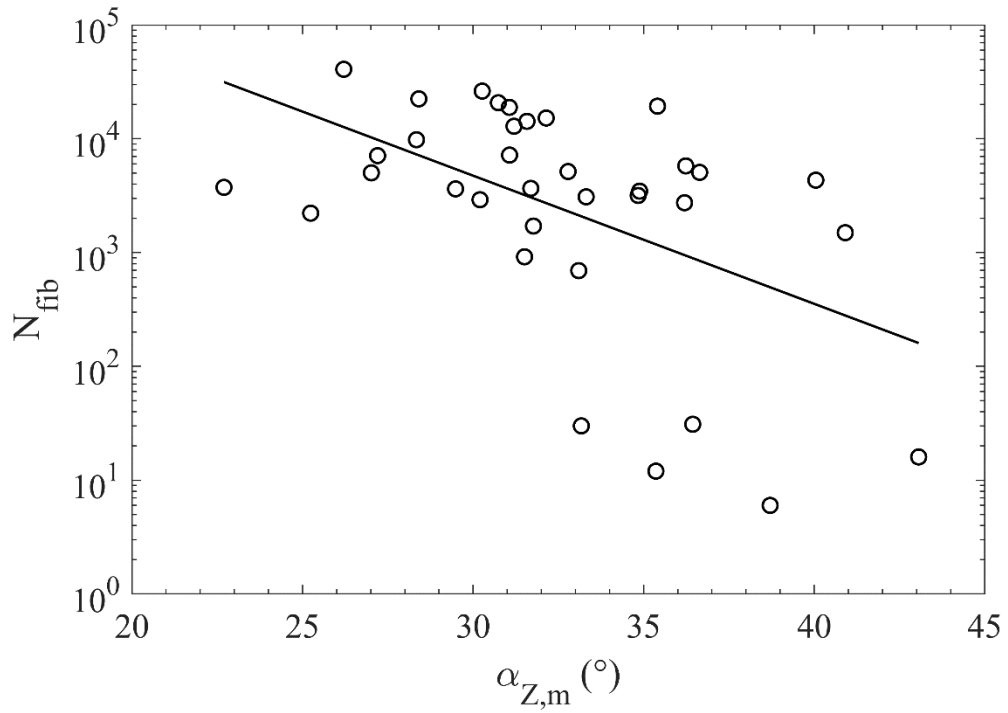


Figure 5.1-4. Linear regression (global) between the mean fiber orientation with respect to the Z-axis and the number of fiber fatigue cycles.

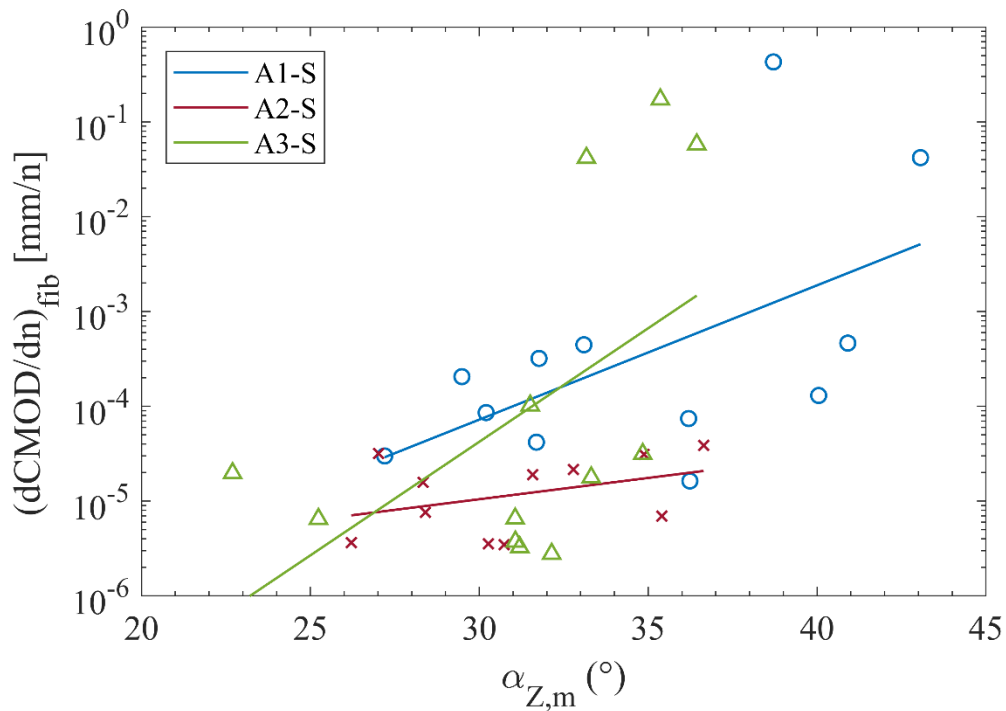


Figure 5.1-5. Linear regression (per series) between the mean fiber orientation with respect to the Z-axis and the secondary crack opening rate of fiber fatigue.

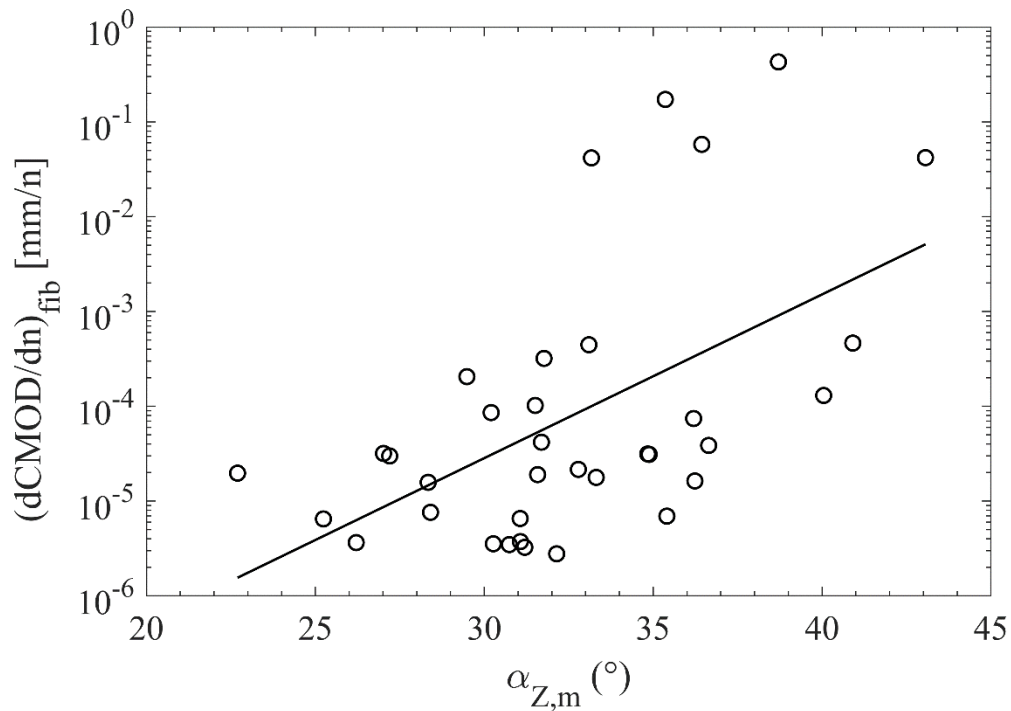


Figure 5.1-6. Linear regression (global) between the mean fiber orientation with respect to the Z-axis and the secondary crack opening rate of fiber fatigue.

Figure 5.1-1 and 5.1-3 reveal that there is a certain correlation between fiber orientation and fatigue life, both total N_{tot} and that associated with fiber fatigue N_{fib} . In all series, it is observed that, as the angle $\alpha_{z,m}$ decreases (and therefore the fibers are more perpendicular to the crack plane), the fatigue life increases. The R^2 coefficients range from 0.21 (A2-S and A3-S series for N_{tot} and N_{fib}) to 0.42 (A1-S series for N_{tot}). The A1-S series is the one with the highest values on average.

If the data are analyzed as a whole (Figure 5.1-2 and 5.1-4), the correlation is similar, both in trend and R^2 , being 0.24 and 0.26 for N_{tot} and N_{fib} , respectively.

Figure 5.1-5 also shows a relationship between fiber orientation and secondary crack opening rate. The more perpendicular the fibers are to the crack plane (lower $\alpha_{z,m}$), the lower is $(dCMOD/dn)_{fib}$. In other words, better fiber orientation causes the development of fatigue damage to be slower. In this case, A1-S and A3-S series have the highest coefficients of determination, being 0.30 and 0.28, respectively. Considering all data, the linear regression model fits relatively well, with an R^2 of 0.29 (Figure 5.1-6).

Although the coefficients of determination are low, it is considered that there is an evident trend and that the relationship is reasonably robust considering the complexity of the dispersion in fatigue.

On the other hand, the following figures show the linear regressions between the mean efficiency index on the Z-axis ($ei_{z,m}$), calculated according to Eq. (4.3-1), and the fatigue response. Again, the results considered have been N_{tot} , N_{fib} and $(dCMOD/dn)_{fib}$.

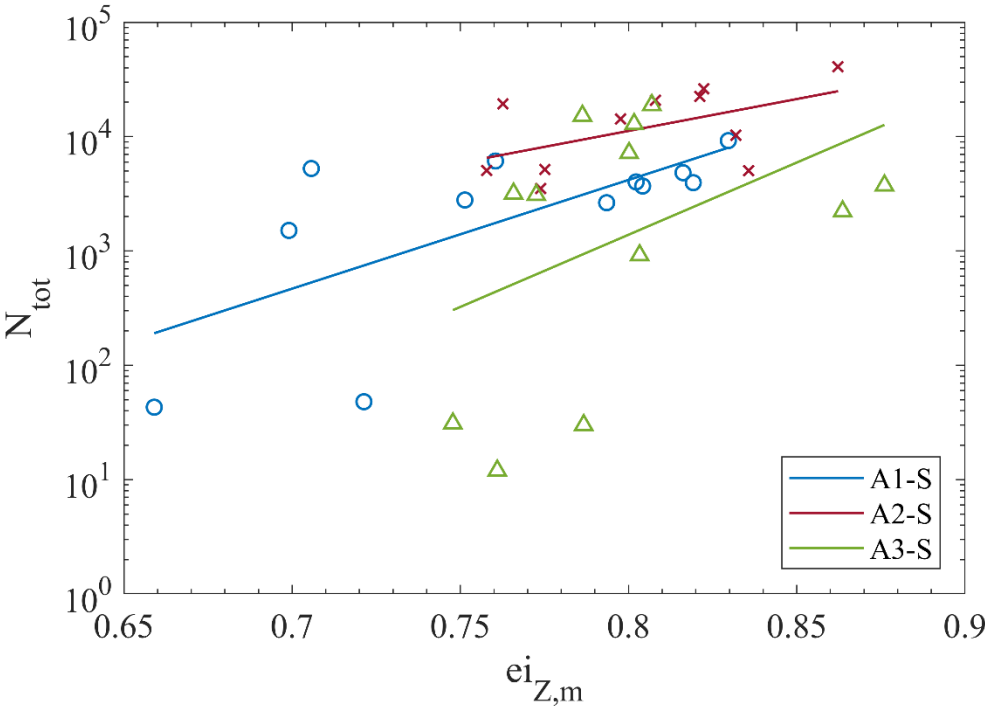


Figure 5.1-7. Linear regression (per series) between the mean efficiency index on the Z-axis and the total number of cycles.

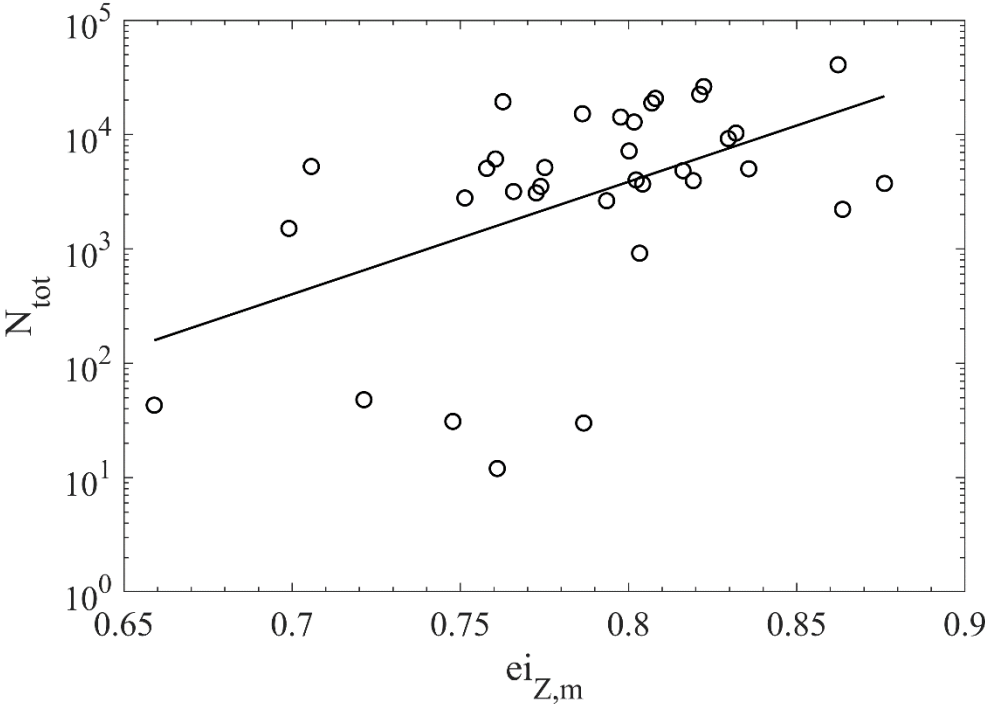


Figure 5.1-8. Linear regression (global) between the mean efficiency index on the Z-axis and the total number of cycles.

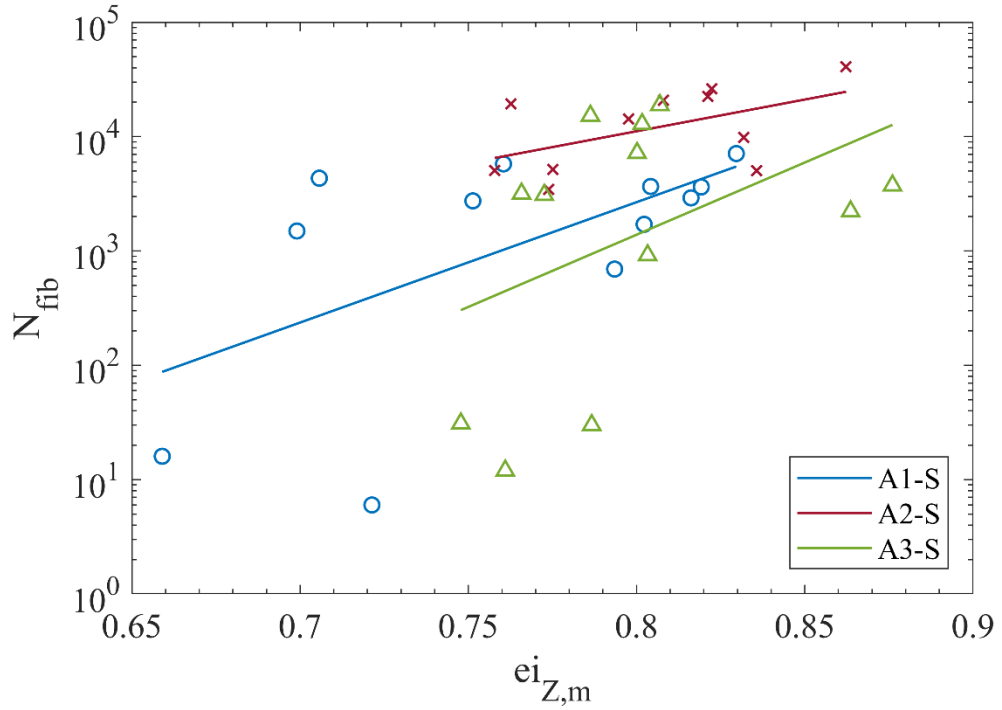


Figure 5.1-9. Linear regression (per series) between the mean efficiency index on the Z-axis and the number of fiber fatigue cycles.

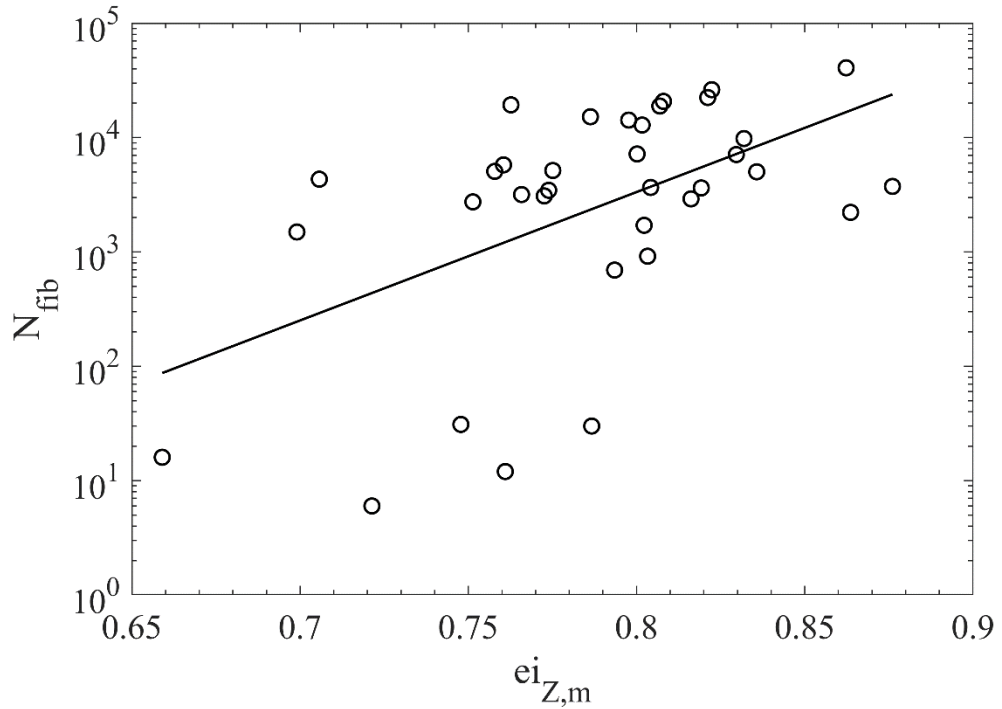


Figure 5.1-10. Linear regression (global) between the mean efficiency index on the Z-axis and the number of fiber fatigue cycles.

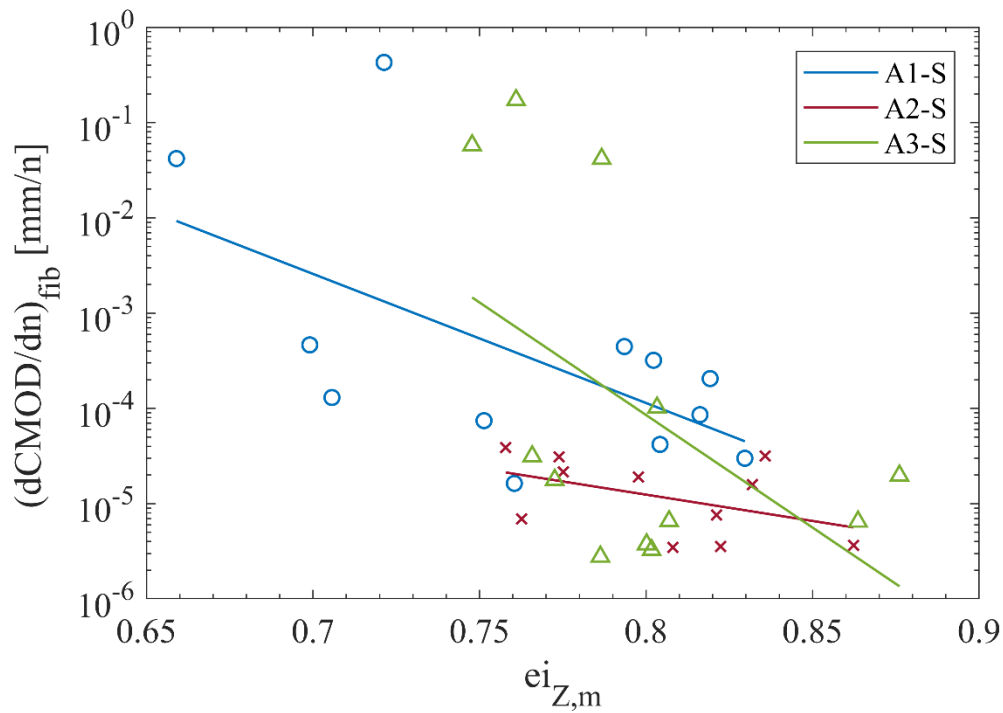


Figure 5.1-11. Linear regression (per series) between the mean efficiency index on the Z-axis and the secondary crack opening rate of fiber fatigue.

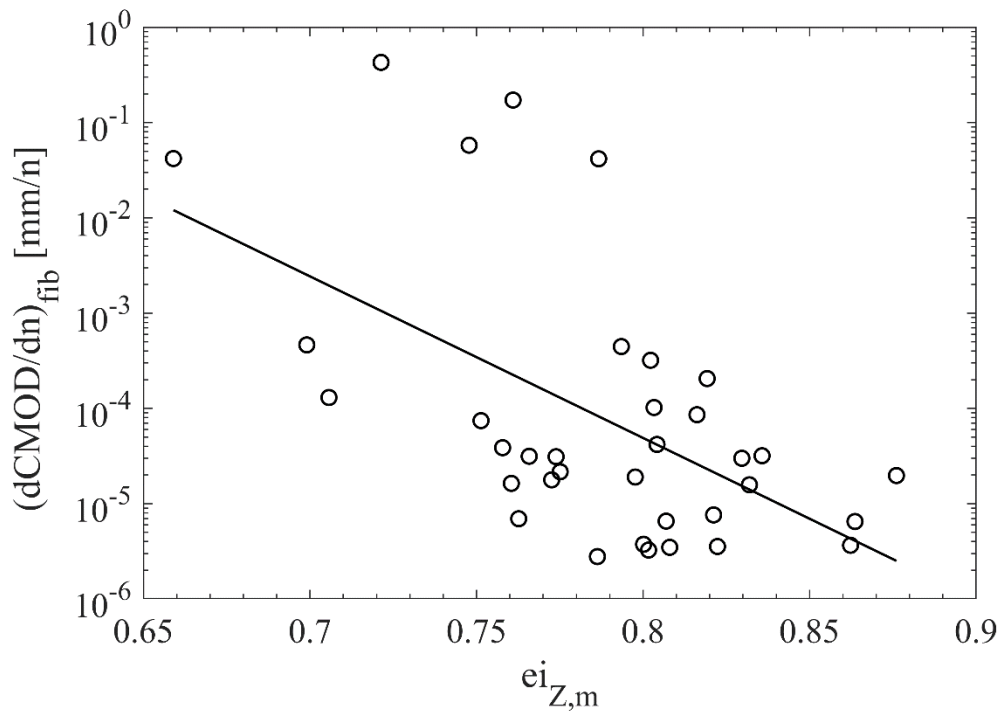


Figure 5.1-12. Linear regression (global) between the mean efficiency index on the Z-axis and the secondary crack opening rate of fiber fatigue.

Figure 5.1-7 and 5.1-9 show appreciable trends between the mean efficiency index and fatigue life. As $ei_{Z,m}$ increases and thus the fibers are more perpendicular to the crack plane, fatigue life increases. The values of R^2 coefficients vary between 0.19 (A3-S series with respect to N_{tot} and N_{fib}) and 0.47 (A1-S series with respect to N_{tot}). Again, the A1-S series is the one with the best fit.

It seems that the behavior of the three series is similar, as shown by the slopes of the straight lines. If the linear regression model is applied to all data, the resulting coefficients of determination are 0.28 and 0.25 for N_{fib} and N_{tot} , respectively (Figure 5.1-8 and 5.1-10).

As for the correlation with the secondary crack opening rate, Figure 5.1-11 and 5.1-12 show that the fits are relatively acceptable, both considering the series individually and jointly. In the first case, the mean value of R^2 is 0.27, while in the second case it is 0.31. The conclusions drawn in this case are equivalent to those obtained by relating $\alpha_{Z,m}$ to $(dCMOD/dn)_{fib}$.

From the figures it is clear that, although the R^2 coefficients are not particularly high, the mean efficiency index is a reasonably predictive parameter of fatigue dispersion. Therefore, despite the fact that it does not explain by itself this very complicated phenomenon, it is evident that its influence is not negligible.

In general terms, it is observed that the mean efficiency index in Z ($ei_{Z,m}$) has a slightly better correlation with the fatigue response than the mean orientation in Z ($\alpha_{Z,m}$). This could be explained by the pull-out behavior of hooked-end fibers. As already discussed (see subsection 2.1.4), in this fiber type the pull-out strength can be kept practically constant for low inclinations (0° - 30°). Precisely, the efficiency index, following a cosine relationship with the orientation, gives a higher weighting to lower angles (Figure 5.1-13); for example, for 30° ei_Z takes a value of 0.87. Therefore, this behavior represents better the failure of the fibers as a function of orientation.

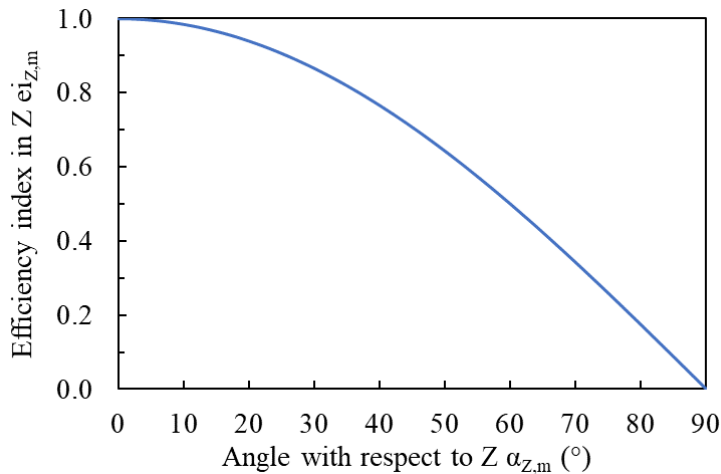


Figure 5.1-13. Relationship between orientation and efficiency index.

5.1.2 Spatial distribution

One parameter that is likely to influence the fatigue response is the density of fibers passing through the mid-span section. However, what is really interesting to know in each specimen is the dispersion of its fiber density with respect to the theoretical or average density of its series.

That is, it is not intended to determine how the average density (in short, the content) of fibers affects the fatigue life. In fact, fatigue loads have been calculated based on the average flexural strength of each series, thus eliminating the effect of fiber content (since mean fiber density directly affects mean flexural strength).

Therefore, instead of the density of fibers passing through the mid-span section or crack plane, it is more suitable to calculate the relative density of these fibers, which is expressed according to Eq. (5.1-1):

$$\rho_{\text{fib,rel},i} = \frac{\rho_{\text{fib},i}}{\rho_{\text{fib},m}} \quad (5.1-1)$$

Where $\rho_{\text{fib},i}$ is the fiber density of the specimen and $\rho_{\text{fib},m}$ is the mean fiber density of the corresponding series (A1-S, A2-S or A3-S).

Figure 5.1-14 to 5.1-19 plot the linear regressions between the relative fiber density at the crack plane and the fatigue results: the total number of cycles N_{tot} , the number of cycles associated with fiber fatigue N_{fib} and the secondary crack opening rate of fiber fatigue $(\text{dCMOD}/\text{dn})_{\text{fib}}$.

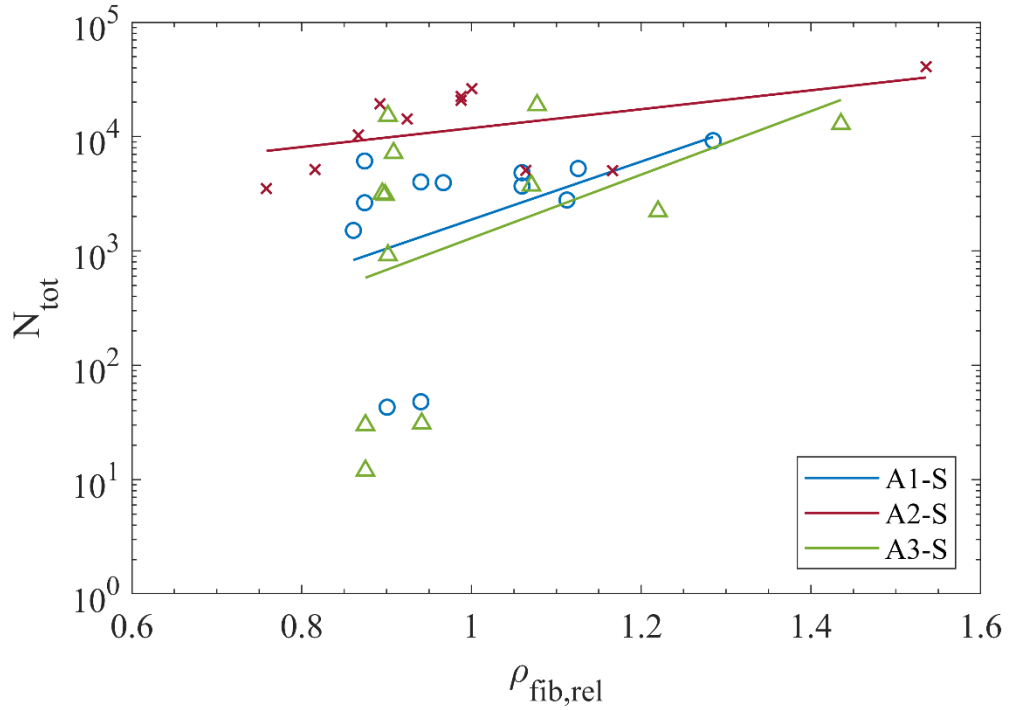


Figure 5.1-14. Linear regression (per series) between the relative density of fibers passing through the crack plane and the total number of cycles.

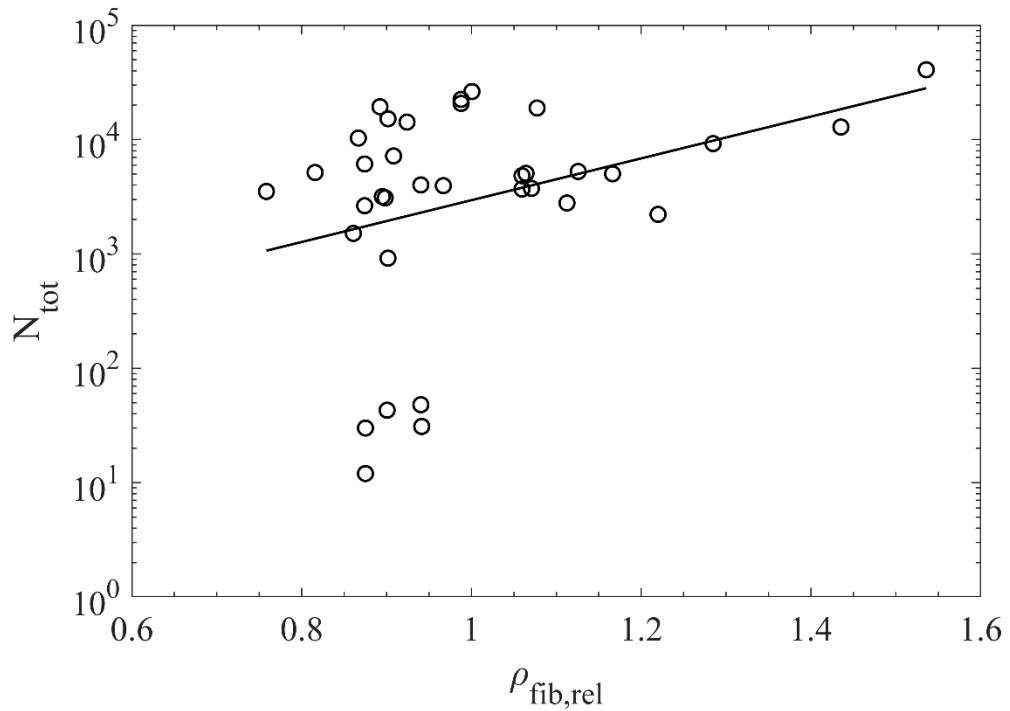


Figure 5.1-15. Linear regression (global) between the relative density of fibers passing through the crack plane and the total number of cycles.

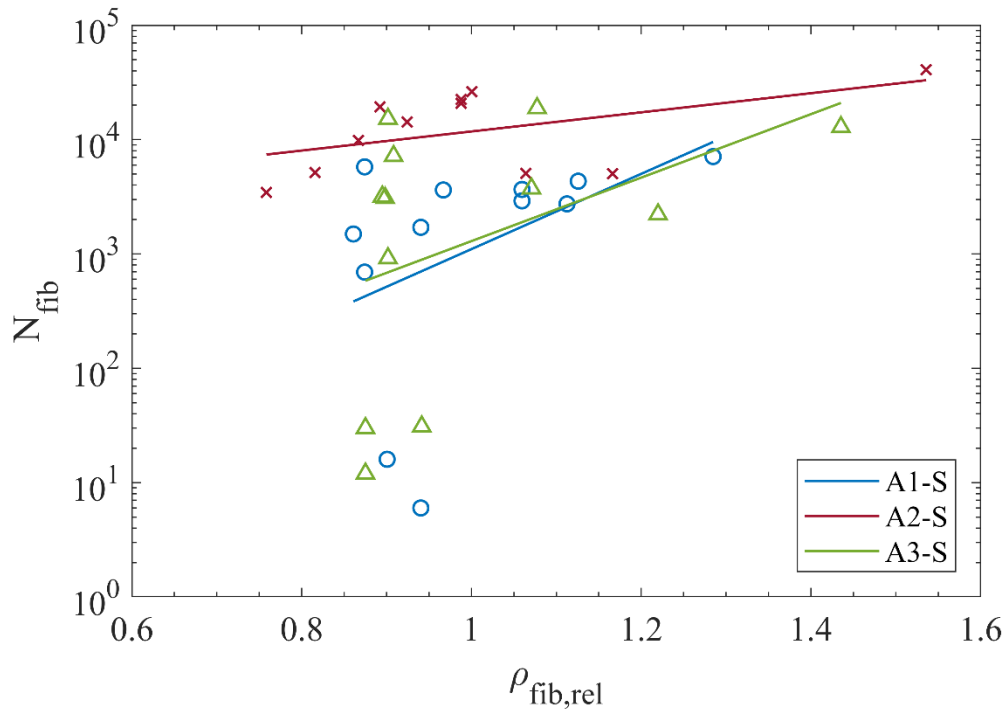


Figure 5.1-16. Linear regression (per series) between the relative density of fibers passing through the crack plane and the number of fiber fatigue cycles.

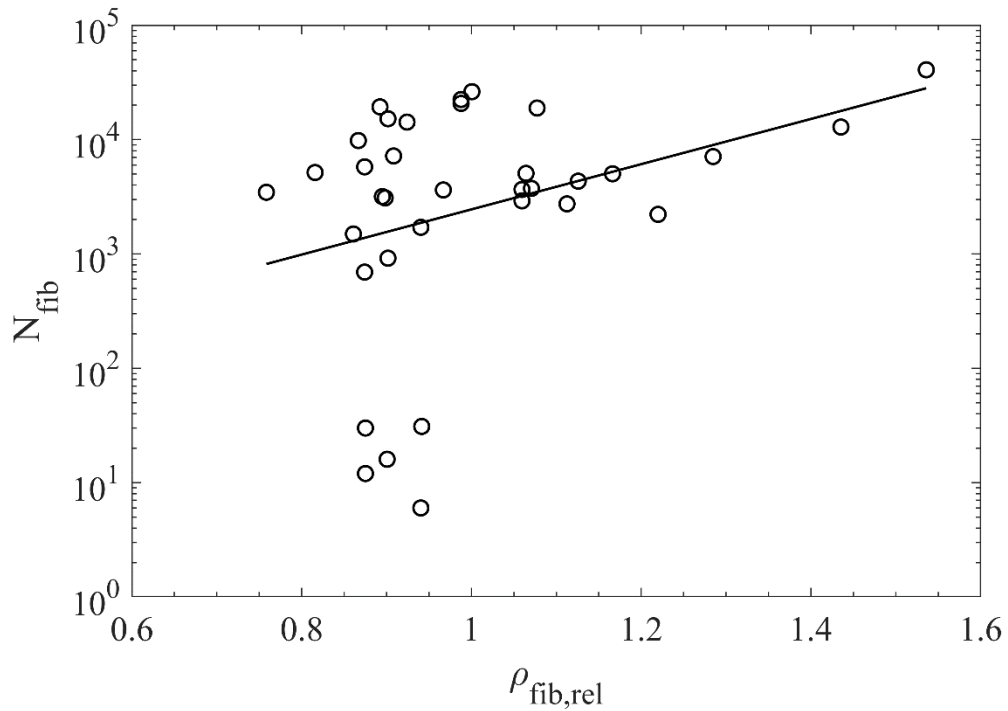


Figure 5.1-17. Linear regression (global) between the relative density of fibers passing through the crack plane and the number of fiber fatigue cycles.

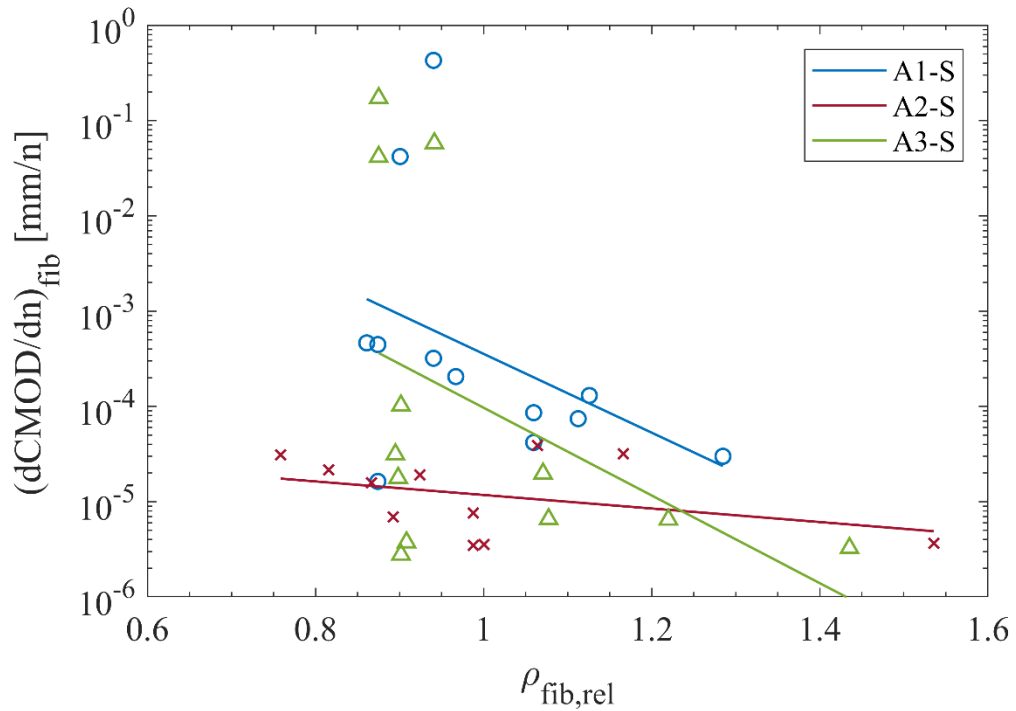


Figure 5.1-18. Linear regression (per series) between the relative density of fibers crossing the crack plane and the secondary crack opening rate of fiber fatigue.

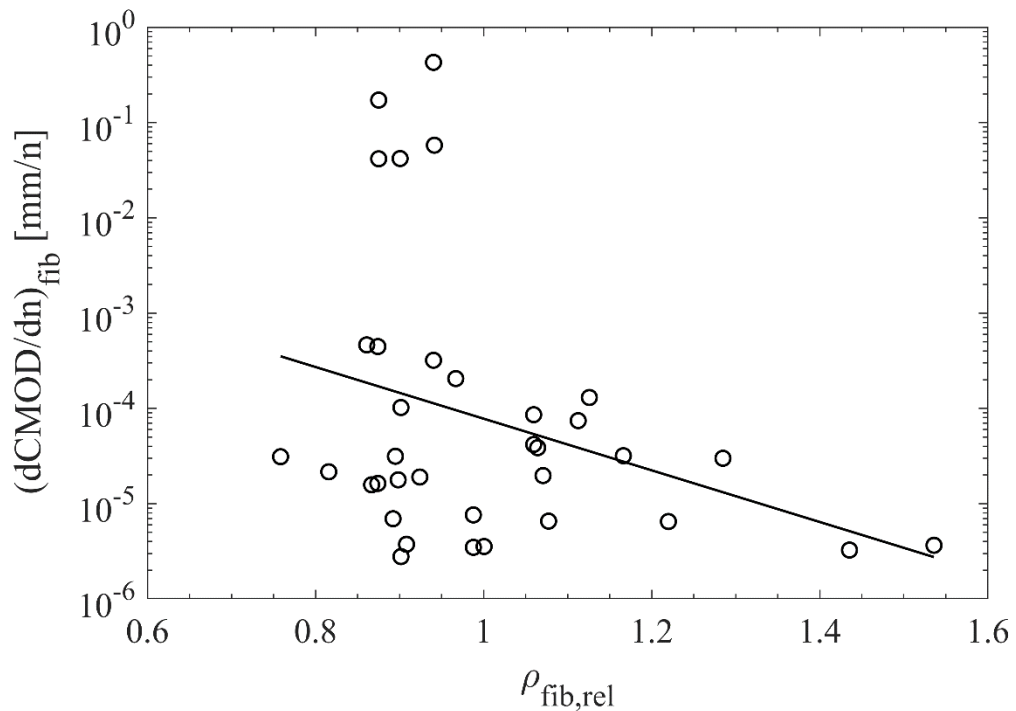


Figure 5.1-19. Linear regression (global) between the relative density of fibers crossing the crack plane and the secondary crack opening rate of fiber fatigue.

Although in each series the fiber content is the same, it is noted that the fiber density at the crack plane presents a significant dispersion, ranging from approximately 75% to 155% of the average density. Figure 5.1-14 and 5.1-16 reveal that, as the fiber density

increases, so does the fatigue life, both N_{tot} and N_{fib} . The R^2 coefficients take values from 0.18 (A1-S and A3-S series for N_{tot} and N_{fib}) to 0.24 (A3-S series for N_{tot} and N_{fib}).

When considering all data together, the linear regression model does not improve, with R^2 being 0.12 and 0.11 for N_{tot} and N_{fib} , respectively (Figure 5.1-15 and 5.1-17).

Equivalently, Figure 5.1-18 and 5.1-19 show that $(dCMOD/dn)_{fib}$ decreases with increasing density; i.e., the higher the density of fibers passing through the midplane, the higher the bridging forces in the central crack and therefore the slower the progression of fatigue damage. The R^2 coefficients are similar, obtaining the best regression for the A3-S series, with a value of 0.20.

It can be seen that the correlations are not very robust. However, it should be remembered that the aim of this subsection is to find fiber-related geometrical parameters that fit to some extent the dispersion of the fatigue results. Thus, by combining them and considering their joint effect, the correlations are expected to be reasonably better.

Another parameter of the spatial distribution of the fibers that may have some correlation with the fatigue response is their vertical position; that is, the Y-coordinate of their center of gravity, according to the proposed axis system (Figure 4.3-4). It is reasonable to assume that the closer a fiber is to the notch edge (higher Y_{cdg}), the greater its contribution to resisting flexural fatigue stresses. However, Y_{cdg} is an individual parameter at the fiber level, so it is necessary to define global parameters at the specimen level to perform linear regressions with the fatigue results.

Two global parameters are proposed. First, there is the weighted average fiber height $Y_{cdg,mp}$. It is calculated as the average of the weighted fiber heights $Y_{cdg,p}$ (Eq. (5.1-2)), which in turn are determined according to the expressions Eq. (5.1-3) to Eq. (5.1-5).

$$Y_{cdg,mp} = \frac{\sum_{i=0}^n Y_{cdg,p,i}}{n} \quad (5.1-2)$$

$$Y_{cdg,p,i} = Y_{cdg,i} \cdot f \quad (5.1-3)$$

$$f = \frac{Y_{cdg,i}}{H_s - h_n} \quad 0 \leq Y_{cdg,i} < H_s - h_n \quad (5.1-4)$$

$$f = 0 \quad H_s - h_n \leq Y_{cdg,i} < H_s \quad (5.1-5)$$

Where n is the number of fibers in the study region, $Y_{cdg,i}$ is the height or Y-coordinate of each fiber, f is the weighting factor, H_s is the depth of the specimen (75 mm) and h_n is

the depth of the notch (12.5 mm). This parameter gives greater importance to the fibers located in the tensioned part of the central section, where the crack progresses and therefore the bridging forces are mobilized. On the other hand, it reduces the value of the fibers in the compressed zone, which barely contribute to resisting the fatigue stresses. Thus, note that the weighting factor is 1 when the fiber is at the notch edge ($Y_{cdg} = 62.5$ mm), decreasing linearly to 0 when it is in the most compressed point ($Y_{cdg} = 0$). This is a simplified way of evaluating the contribution of each fiber to withstand the fatigue tensions, since evidently as the cycles progress the position (Y-coordinate) of the neutral axis decreases; that is, the resistant section is depleted by the advance of the crack and the failure of the fibers. Finally, the fibers located above the edge of the notch do not cooperate to resist the stresses, so their weighting factor is 0.

Next, linear regressions between the weighted average fiber height $Y_{cdg,mp}$ and the representative fatigue parameters N_{tot} , N_{fib} and $(dCMOD/dn)_{fib}$ are shown. Correlations per series and as a whole are included.

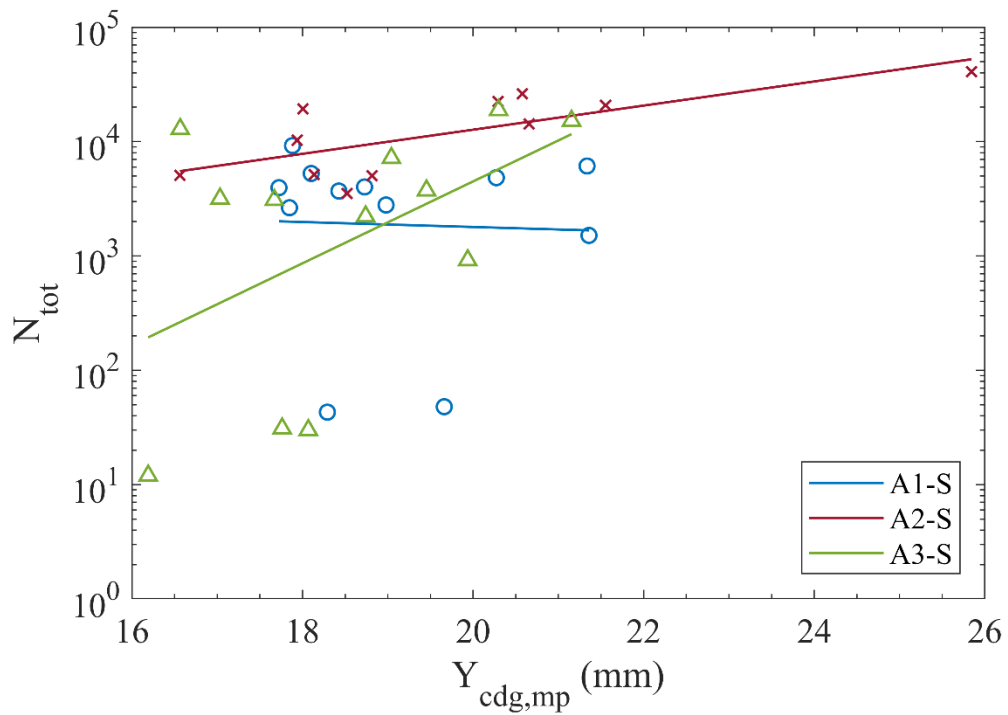


Figure 5.1-20. Linear regression (per series) between weighted average fiber height and total number of cycles.

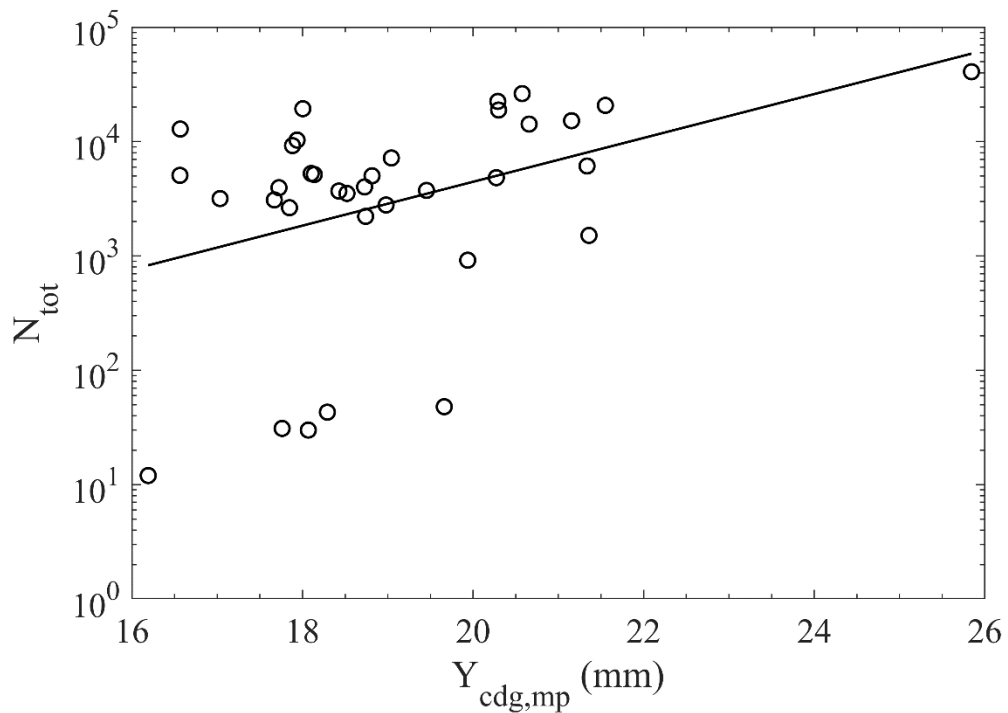


Figure 5.1-21. Linear regression (global) between weighted average fiber height and total number of cycles.

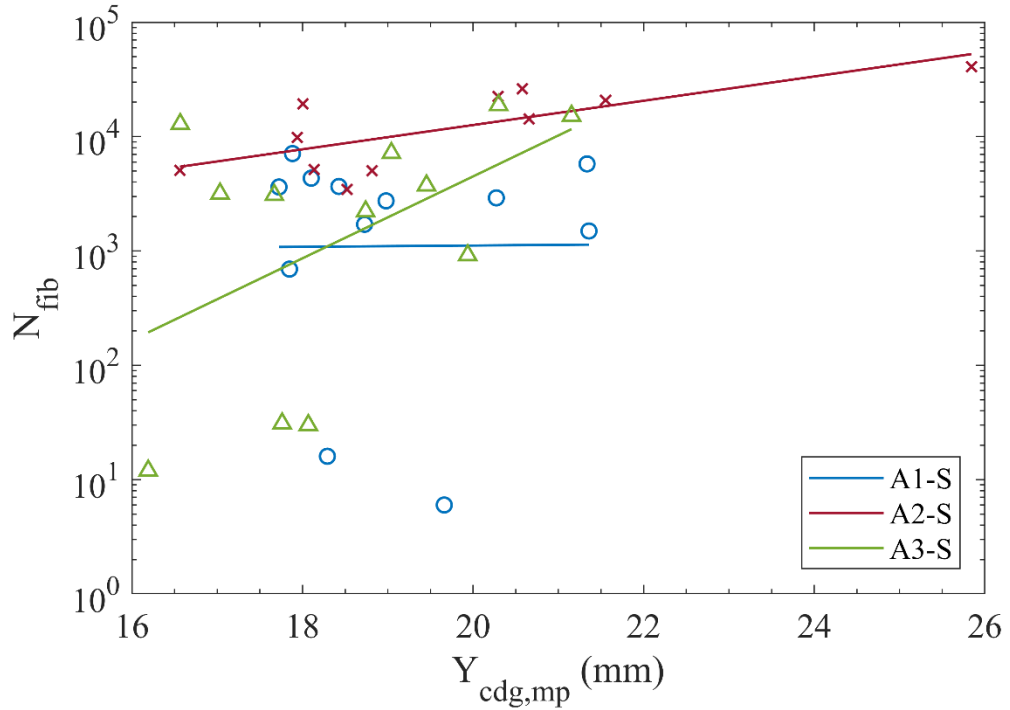


Figure 5.1-22. Linear regression (per series) between the weighted average fiber height and the number of fiber fatigue cycles.

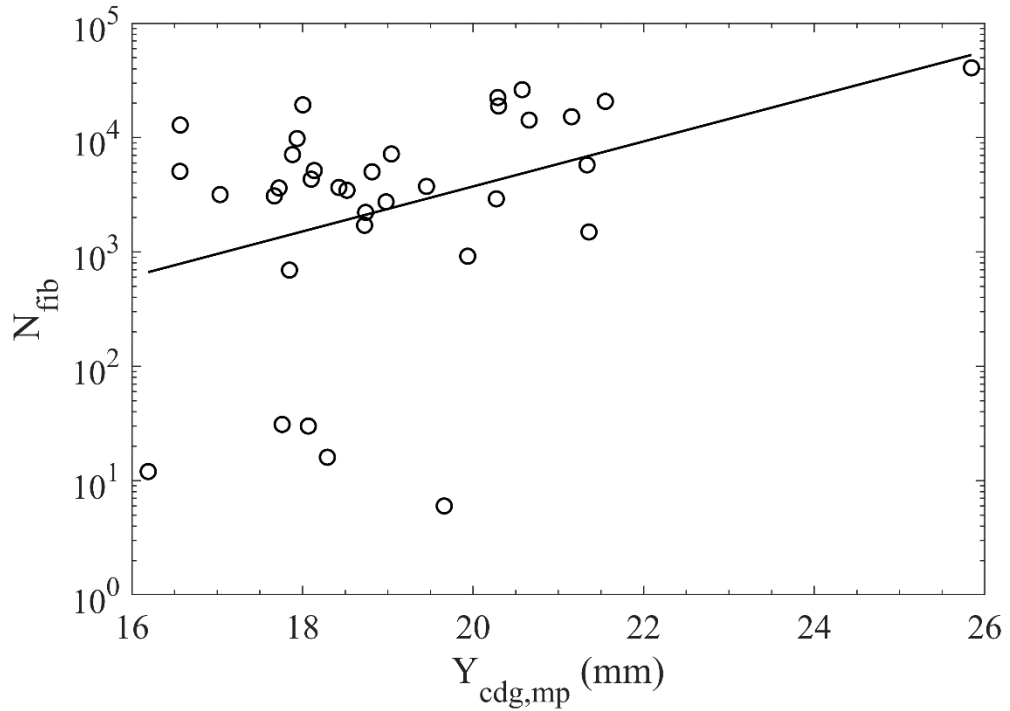


Figure 5.1-23. Linear regression (global) between the weighted average fiber height and the number of fiber fatigue cycles.

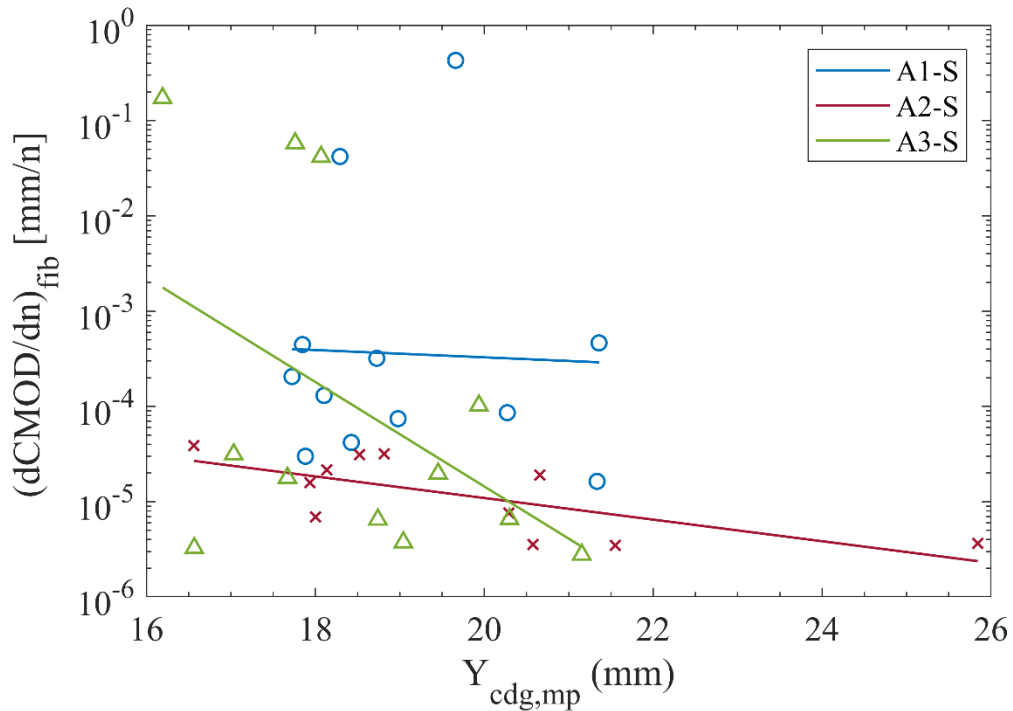


Figure 5.1-24. Linear regression (per series) between weighted average fiber height and secondary crack opening rate of fiber fatigue.

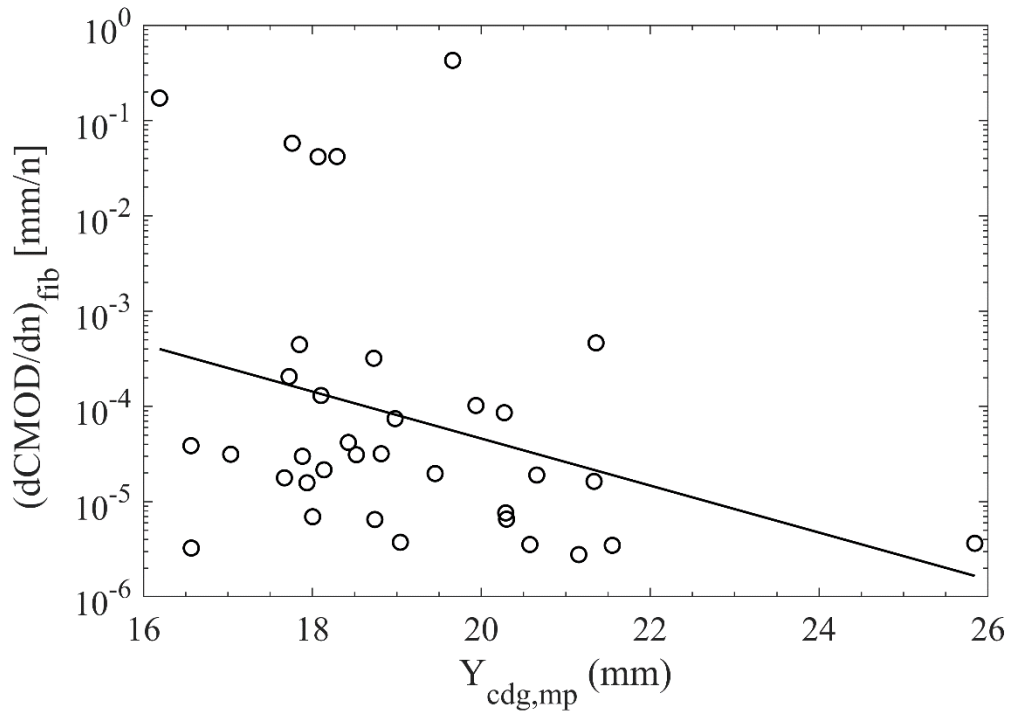


Figure 5.1-25. Linear regression (global) between weighted average fiber height and secondary crack opening rate of fiber fatigue.

Figure 5.1-20 and 5.1-22 show that in A2-S and A3-S series the weighted average fiber height is a reasonably predictive variable of the fatigue life dispersion, so that the closer the fibers are to the notch edge (higher $Y_{cdg,mp}$), the higher the number of cycles to

failure. Specifically, the coefficients of determination are 0.55 and 0.24 for A2-S and A3-S, respectively. However, in the A1-S series the regression line is practically horizontal, which indicates that in that series the fatigue life is not sensitive to $Y_{cdg,mp}$.

This could be explained because, having a low fiber content (0.3%), its distribution is more irregular, resulting in that a few fibers can determine the fracture behavior of the material. Under these conditions, it is possible that $Y_{cdg,mp}$ does not represent well the strength contribution of the fibers. On the contrary, in the other series there are many more fibers, their distribution is more uniform and the fracture behavior is more ductile. In this case, the weighting function proposed for $Y_{cdg,mp}$ better matches the real response of the fibers.

Applying the linear regression model to the whole data set, we obtain coefficients of determination of 0.14 and 0.15 for N_{fib} and N_{tot} , respectively (Figure 5.1-21 and 5.1-23). In this situation the correlation is not very good due in part to the scatter introduced by the results of the A1-S series.

Figure 5.1-24 and 5.1-25 reveal that the results are analogous when performing linear regressions between weighted mean fiber height and secondary crack opening rate. Again, the A2-S and A3-S series show a visible correlation, with R^2 of 0.49 and 0.22, respectively; in contrast, in the A1-S series it is imperceptible.

In second place, the other parameter related to the vertical position of the fibers that is proposed is the median fiber height $Y_{cdg,50\%}$. As its name indicates, it is defined as the Y-coordinate that divides the number of fibers in half; that is, 50% of the fibers are positioned below, and 50% above. The purpose of this parameter is to detect eventual accumulations of fibers around the notch edge (higher $Y_{cdg,50\%}$) that may result in better fatigue behavior. The median was chosen instead of the arithmetic mean because it is a more sensitive statistical parameter.

The following figures show the linear regression models between the median fiber height $Y_{cdg,50\%}$ and the fatigue test results. Correlations per series and as a whole are included.

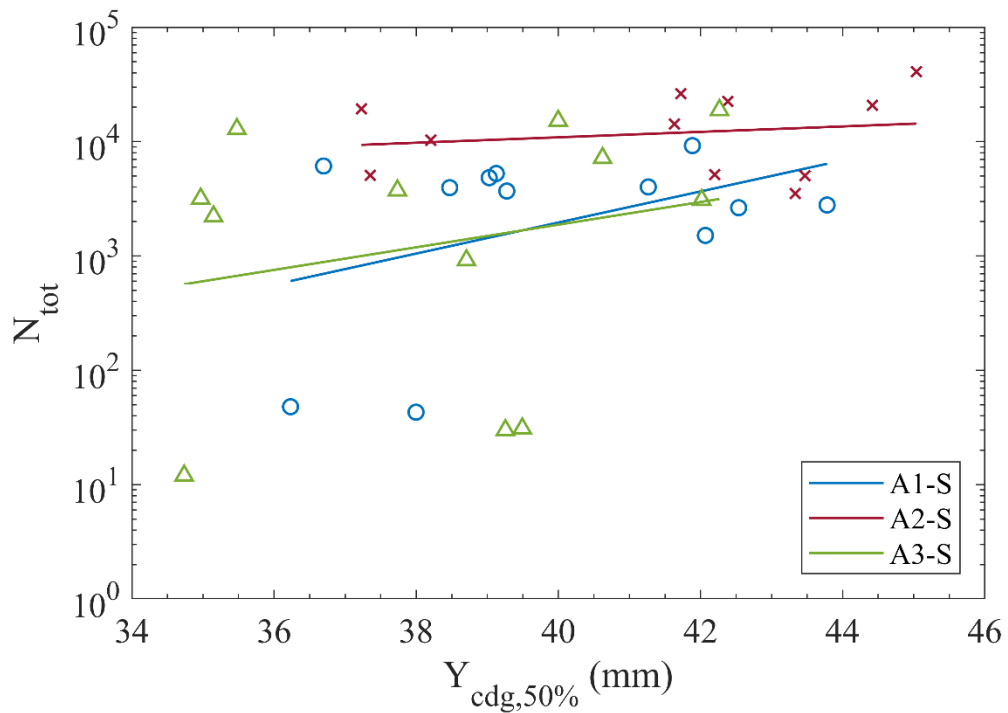


Figure 5.1-26. Linear regression (per series) between median fiber height and total number of cycles.

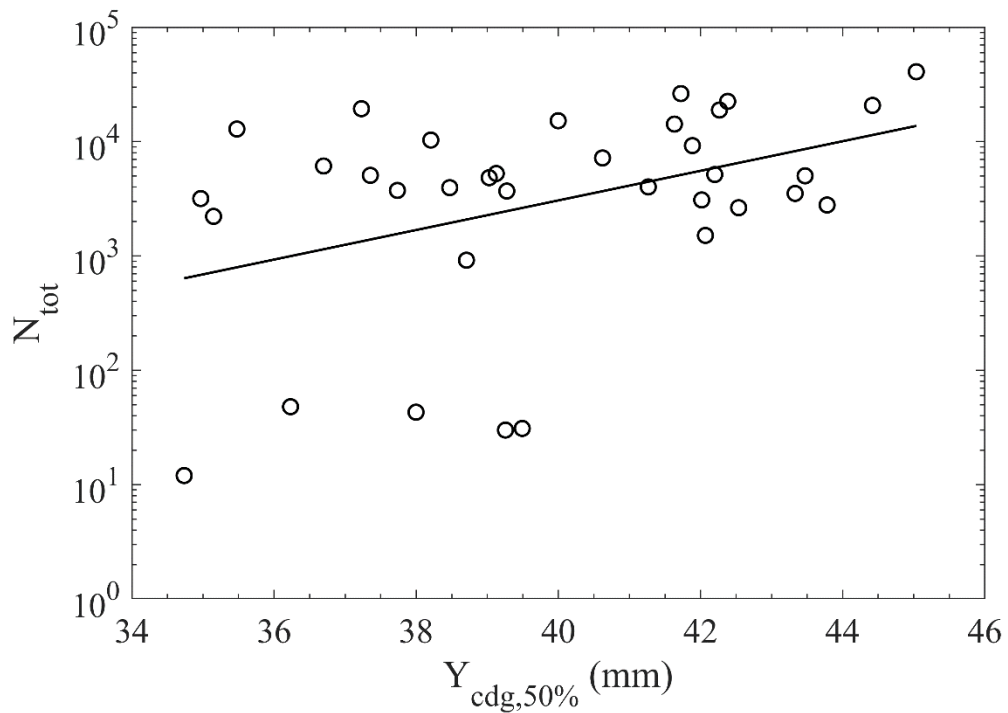


Figure 5.1-27. Linear regression (global) between median fiber height and total number of cycles.

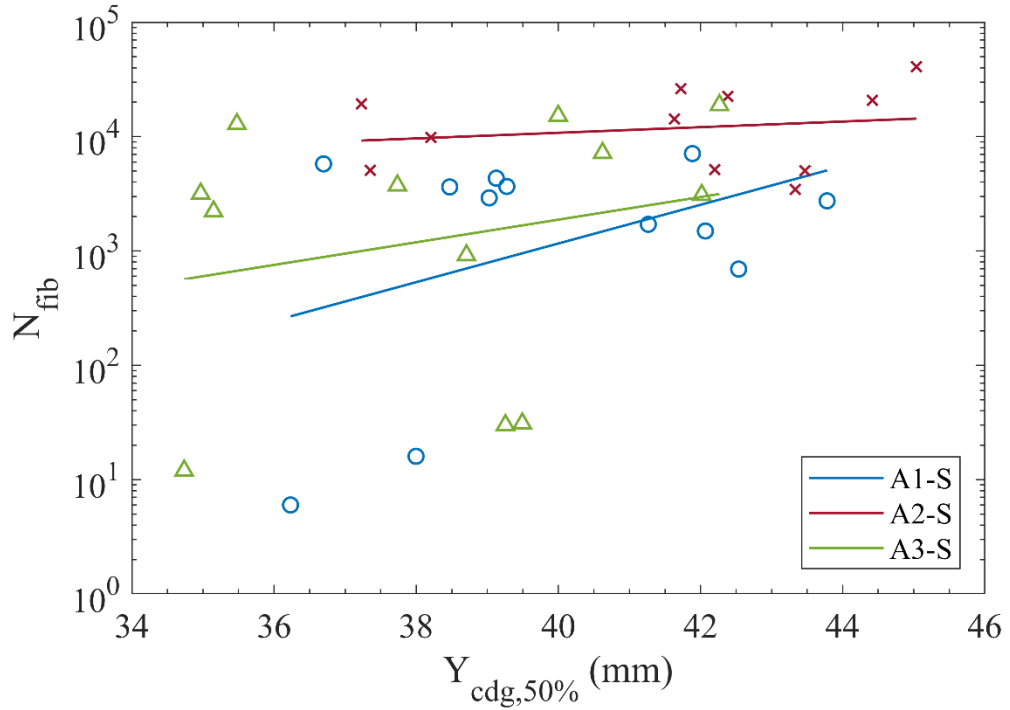


Figure 5.1-28. Linear regression (per series) between median fiber height and number of fiber fatigue cycles.

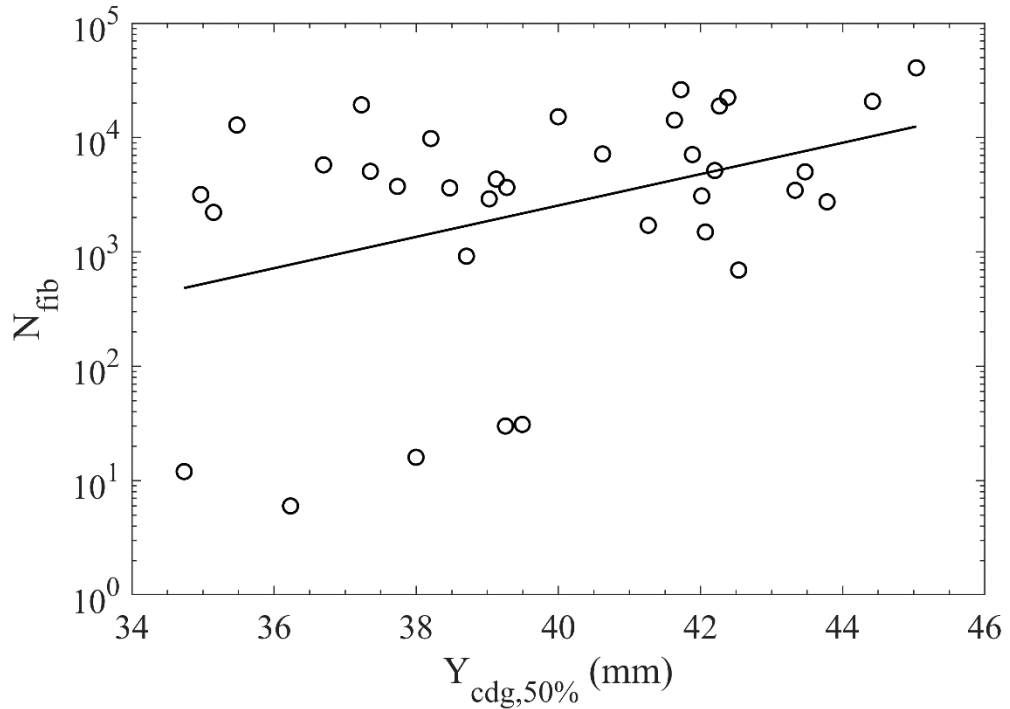


Figure 5.1-29. Linear regression (global) between median fiber height and number of fiber fatigue cycles.

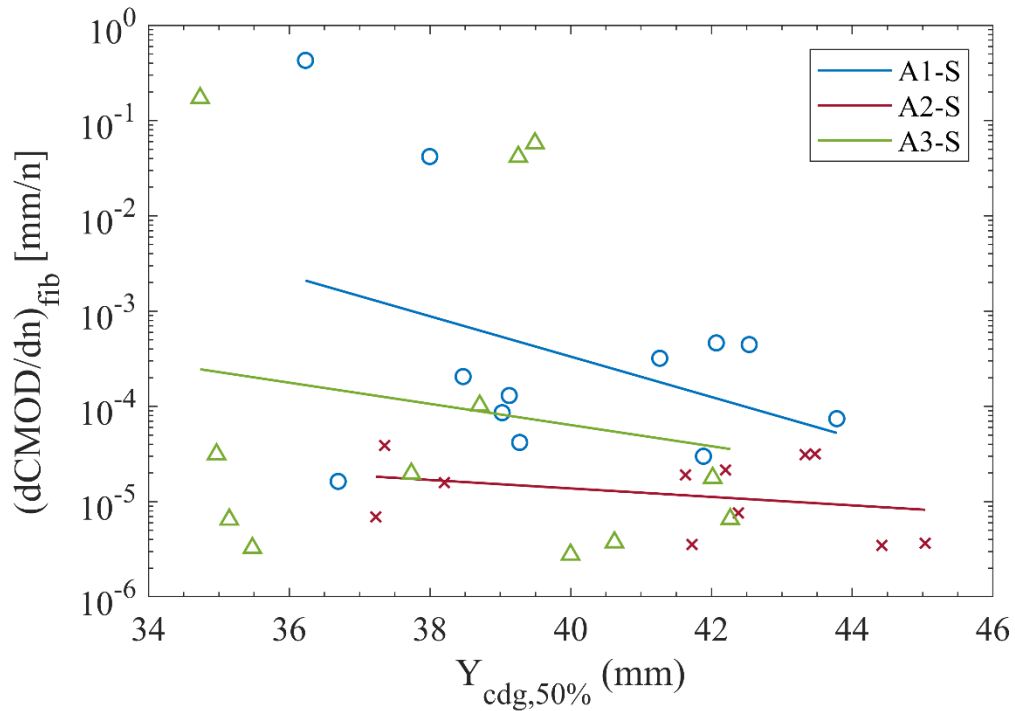


Figure 5.1-30. Linear regression (per series) between median fiber height and secondary crack opening rate of fiber fatigue.

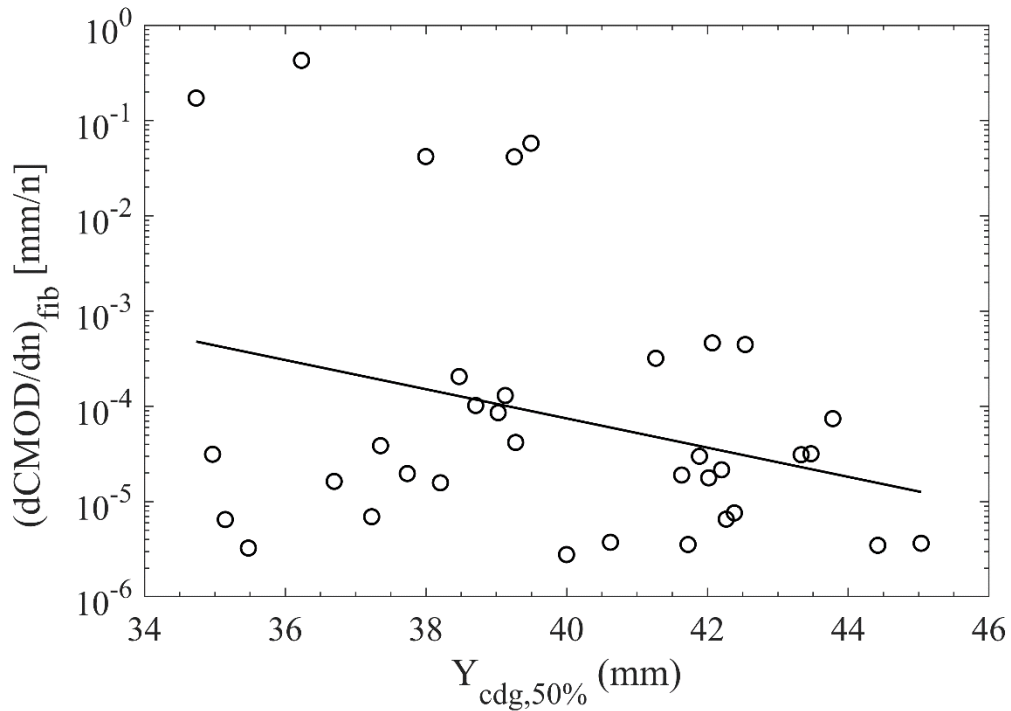


Figure 5.1-31. Linear regression (global) between median fiber height and secondary crack opening rate of fiber fatigue.

Figure 5.1-26 and 5.1-28 show a certain relationship between median fiber height and fatigue life. In all three series the trend is the same: the closer the fibers are to the notch

edge (higher $Y_{cdg,50\%}$), the higher the number of cycles. However, the correlation is weak, with R^2 less than 0.20 in all cases.

When the linear regression model is applied to all data, the resulting coefficients of determination are 0.16 and 0.17 for N_{fib} and N_{tot} , respectively (Figure 5.1-27 and 5.1-29).

With respect to the secondary crack opening rate, the results of the linear regression models are equivalent, as shown in Figure 5.1-30 and 5.1-31. It is seen that $(dCMOD/dn)_{fib}$ decreases with increasing $Y_{cdg,50\%}$. Again, the R^2 coefficients are quite low, taking a value of 0.10 when considering all the data together.

The correlations of the parameters related to fiber height are not particularly robust, which is reflected in the low R^2 values. A certain relationship with the dispersion of the fatigue results is observed, although it seems to be less significant than in the case of the other parameters considered. Nevertheless, it is worth taking them into account, since it is possible that by introducing them in the multiple linear regression models the predictive capacity improves and the R^2 increase.

5.1.3 Fatigue life estimation

The geometrical parameters of the fibers presented in the previous subsections have been shown to have a certain correlation with the fatigue response individually. Consequently, it is proposed to adjust empirical formulas to predict the fatigue results by combining these parameters. Since linear regressions have been applied for the individual correlations, in this work it is proposed, as a first approximation, to apply multiple linear regression models, whose formulation is of the form (Eq. (5.1-6)):

$$\log y = a \cdot x_1 + b \cdot x_2 + c \cdot x_3 + d \quad (5.1-6)$$

Where y is the fatigue parameter to be estimated; x_1 , x_2 and x_3 are the geometric parameters of the fibers; and finally, a , b , c and d are the adjustment coefficients. The fatigue variables are N_{tot} , N_{fib} and $(dCMOD/dn)_{fib}$. As for the fiber parameters, they have been divided according to their typology: x_1 is the relative density of fibers in the central section ($\rho_{fib,rel}$), x_2 is an orientation parameter ($\alpha_{Z,m}$ or $ei_{Z,m}$) and x_3 is a parameter of the vertical position ($Y_{cdg,mp,rel}$ or $Y_{cdg,50\%,rel}$). It is worth mentioning that the latter have been normalized, dividing by the specimen depth H_s , so that the formulation can be extrapolated to any specimen size.

It is possible to develop specific formulas for each series, or general formulas independent of fiber content.

In order to determine the most significant fiber parameters, multiple linear regression models have been fitted in a preliminary study with all possible combinations (4 in total). The best results are obtained for the efficiency index $ei_{Z,m}$ as variable x_2 and the median fiber height $Y_{cdg,50\%}$ as variable x_3 (as x_1 there is only the relative fiber density $\rho_{fib,rel}$). Therefore, the prediction formula for the fatigue results will have the form shown in Eq. (5.1-7):

$$\log y = a \cdot \rho_{fib,rel} + b \cdot ei_{Z,m} + c \cdot Y_{cdg,50\%,rel} + d \quad (5.1-7)$$

Considering the three fatigue variables, the complete formulation will be as given in Eqs. (5.1-8) to (5.1-10):

$$\log N_{tot} = a_1 \cdot \rho_{fib,rel} + b_1 \cdot ei_{Z,m} + c_1 \cdot Y_{cdg,50\%,rel} + d_1 \quad (5.1-8)$$

$$\log N_{fib} = a_2 \cdot \rho_{fib,rel} + b_2 \cdot ei_{Z,m} + c_2 \cdot Y_{cdg,50\%,rel} + d_2 \quad (5.1-9)$$

$$\log ((dCMOD/dn)_{fib}) = a_3 \cdot \rho_{fib,rel} + b_3 \cdot ei_{Z,m} + c_3 \cdot Y_{cdg,50\%,rel} + d_3 \quad (5.1-10)$$

A table with the values of the adjustment coefficients obtained from the linear regression models is shown below:

Table 5.1-1. Adjustment coefficients for prediction formulation of fatigue results.

		A1-S	A2-S	A3-S	General
N_{tot}	a_1	0.82	0.43	2.89	0.79
	b_1	8.01	4.65	7.78	7.47
	c_1	6.11	-1.46*	13.46	7.82
	d_1	-6.92	0.71	-12.87	-7.37
N_{fib}	a_2	1.41	0.46	2.89	0.77
	b_2	8.30	4.46	7.78	8.85
	c_2	7.84	-1.36*	13.46	8.11
	d_2	-8.87	0.78	-12.87	-8.67
$(dCMOD/dn)_{fib}$	a_3	-1.72	-0.22	-4.01	-0.84
	b_3	-10.82	-4.17	-16.77	-14.49
	c_3	-9.70	-0.80	-17.60	-8.09
	d_3	11.68	-0.92	22.38	12.45

Table 5.1-1 shows that the adjustment coefficients accompanying the fiber parameters (a, b and c) maintain the physical sense of the simple linear regressions shown in

subsections 5.1.1 and 5.1.2. On the one hand, in the fatigue life formulation (both N_{tot} and N_{fib}), coefficients a, b and c have positive sign because the parameters they multiply ($\rho_{fib,rel}$, $e_{iZ,m}$ and $Y_{cdg,50\%,rel}$) increase with fatigue life. In contrast, the opposite is true for the secondary crack opening rate formulas: the sign of the coefficients is negative because the relationship between the geometrical parameters of the fibers and $(dCMOD/dn)_{fib}$ is inversely proportional. The only exceptions are the two coefficients marked with an asterisk, associated with the parameter $Y_{cdg,50\%,rel}$ in the A2-S series. One possible reason for this inconsistency in the sign of the coefficient is that the correlation between median fiber height and fatigue life is particularly weak in this series, as seen in Figure 5.1-26 and 5.1-28.

It is noteworthy that the linear regression models have been designed to achieve the optimal fit for the results of this research. To this end, among other aspects, it has been chosen to include an independent term (d), instead of forcing the regression lines to pass through the origin (0,0). Consequently, it should be borne in mind that the range of application of the formulation is limited to that of the data used, so a good fit cannot be guaranteed when extrapolating.

Finally, a table with the coefficients of determination of each formula or multiple linear regression model is included.

Table 5.1-2. R² coefficients of determination for prediction formulation of fatigue results.

	A1-S	A2-S	A3-S	General
N_{tot}	0.56	0.33	0.41	0.38
N_{fib}	0.46	0.32	0.41	0.38
$(dCMOD/dn)_{fib}$	0.44	0.22	0.41	0.36

Table 5.1-2 reveals that the goodness of fit of the multiple linear regression models, although small, is comparatively better than in the individual-level correlations. The series with the highest R² is A1-S, reaching 0.56 for total fatigue life. As for the general formulas, the coefficients of determination are close to 0.4.

At this point, it is worth remembering that dispersion in fatigue is a tremendously complex phenomenon that has not been addressed too often. The starting point is a variability of results of several orders of magnitude. Consequently, it is considered that the predictive capacity of the proposed formulation is reasonably acceptable.

However, it is also evident that not all aspects of the mesostructure of fiber-reinforced concrete that are likely to affect this phenomenon have been studied. For example, the different anchorage length of the fibers along the crack plane, which determines their failure and therefore the progress of cracking. Or the effect of other components, such as coarse aggregate or porosity. It is likely that more advanced models that take into account all these variables can more accurately estimate the dispersion of fatigue results.

5.2 Influence of pores on the flexural fatigue response of plain concrete

This subsection studies the impact of the dispersion of pore properties on the dispersion of the fatigue response. Therefore, similarly to the previous subsection, it should be specified that the aim is not to compare the fatigue results between series, but to explain, within each series, how slight variations in the pore structure affect the variability of these results.

To achieve this objective, first, some pore parameters (related to porosity, spatial distribution, etc.) are correlated with the fatigue results; specifically, with the fatigue life N and the secondary crack opening rate $dCMOD/dn$. Finally, empirical formulas are adjusted to estimate the results as a function of the most significant parameters.

At this point, it should be recalled that $dCMOD/dn$, the slope of the phase II of stable damage increment in the $CMOD$ vs N diagrams, in the case of plain concrete is not exactly a "crack opening rate". The measured displacement at the notch mouth is actually due to tensile strain of concrete as well as to a primary state of microcracking. However, by analogy with $dCMOD/dn$ in fiber-reinforced concrete, the designation is retained.

It is reminded that only the A0-S series, the only one of plain concrete scanned with microCT, has been analyzed.

Figure 5.2-1 shows the pore study region, limited to dimensions of 75 mm in the X-axis, 12.5 mm in the Y-axis and 20 mm in the Z-axis. The reason is that plain concrete has a much more brittle fracture behavior than SFRC, with a smaller fracture process zone (FPZ). Consequently, the pores that can potentially influence fatigue failure are those located in a small area of the tensioned part of the central section. In this case, this zone has been limited to 20% of the depth of the center section, which is 62.5 mm.

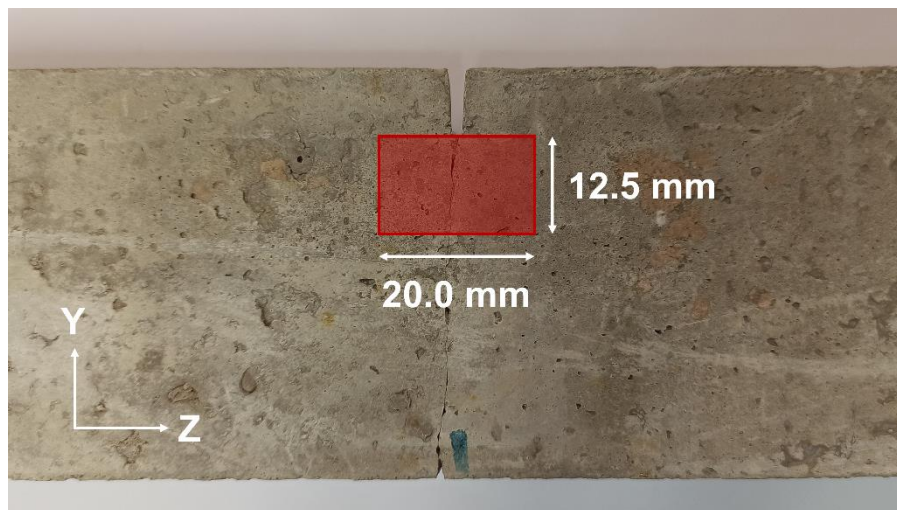


Figure 5.2-1. View of the pore study region in a A0-S series specimen tested under fatigue.

Moreover, although microCT can detect pores down to 0.008 mm^3 with sufficient resolution, it was decided to limit the minimum pore volume to 0.1 mm^3 . This is based on the hypothesis that larger pores determine fatigue failure, since they cause stress concentrations, marking a preferential path to cracking development. In this sense, several works published have concluded that the larger the pore size, the lower the fatigue life [133,145,146].

Finally, equivalent to the previous subsection, it should be mentioned that in general the correlations between the fatigue results and the pore parameters considered do not present very high R^2 coefficients. It can be deduced from this that many parameters with different levels of importance are involved in the fatigue dispersion, but probably none of them is predominant. This subsection includes those parameters that have proved to be the most significant.

5.2.1 Porosity and pore distribution

The following figures show the linear regressions relating fatigue response to porosity and pore density, respectively. Since it is plain concrete, only the so-called fatigue of uncracked concrete or matrix fatigue is observed in this series. Consequently, the fatigue test results considered are the total number of cycles (N_{tot} , here the same as N_{mat} and abbreviated as N) and the secondary crack opening rate due to matrix fatigue (formerly $(d\text{CMOD}/dn)_{\text{mat}}$, and now abbreviated as $d\text{CMOD}/dn$).

As in the previous subsection, the fatigue results have been plotted on a logarithmic scale.

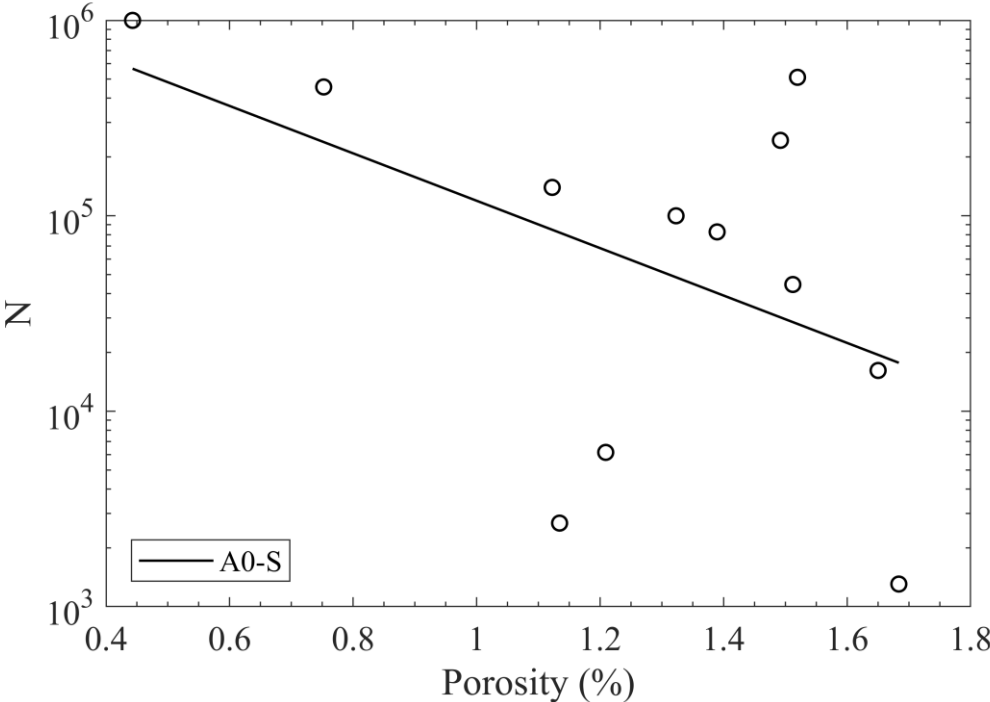


Figure 5.2-2. Linear regression between porosity and number of cycles.

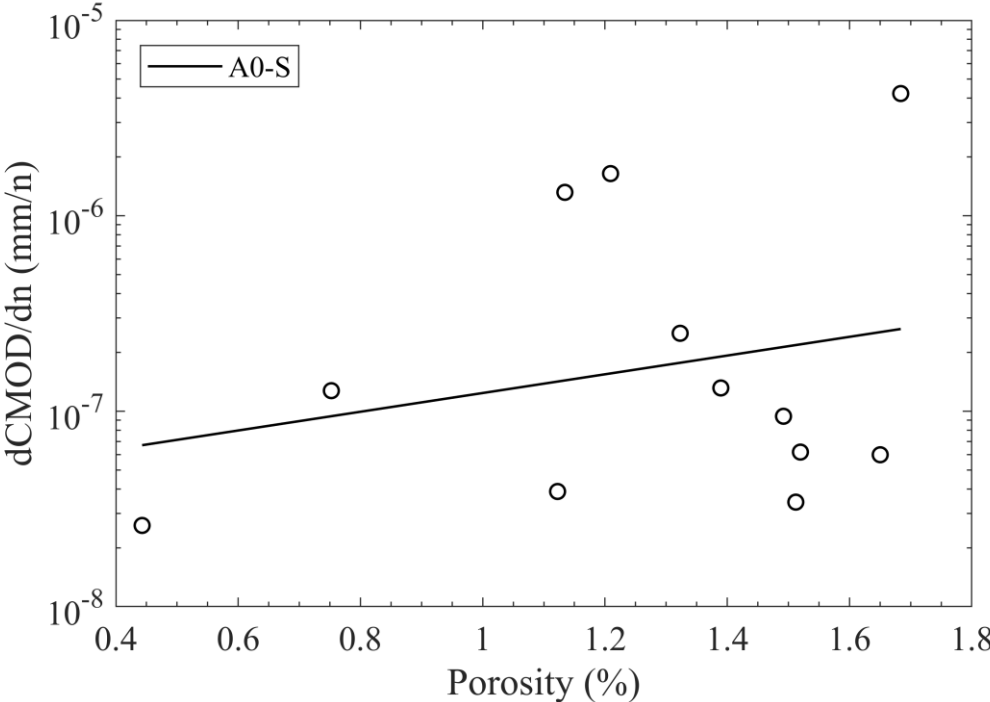


Figure 5.2-3. Linear regression between porosity and secondary crack opening rate.

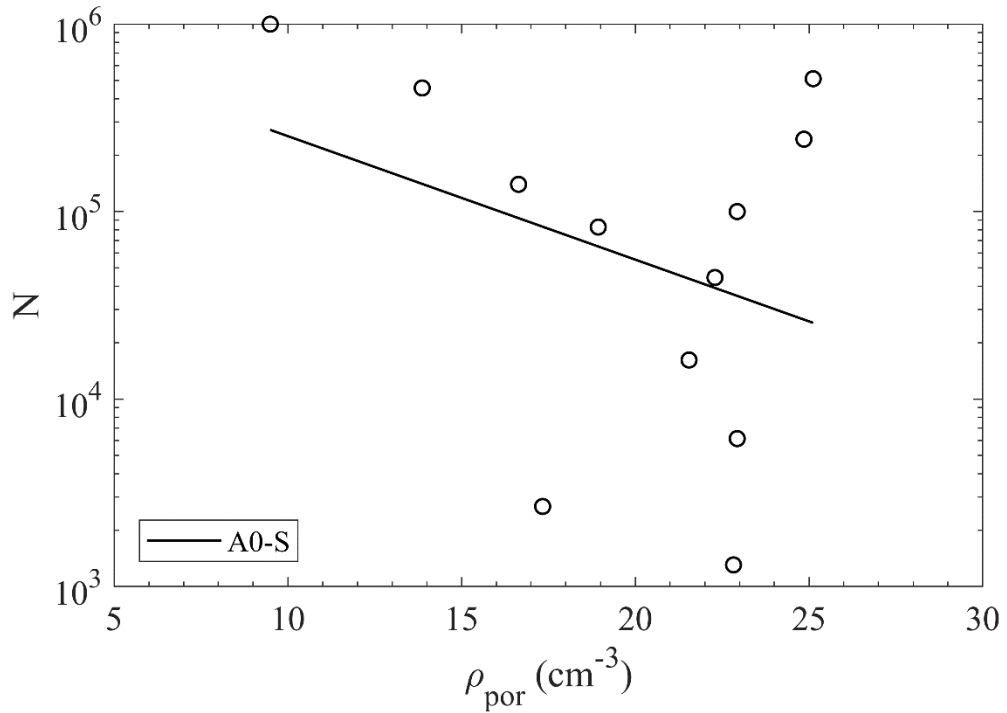


Figure 5.2-4. Linear regression between pore density and number of cycles.

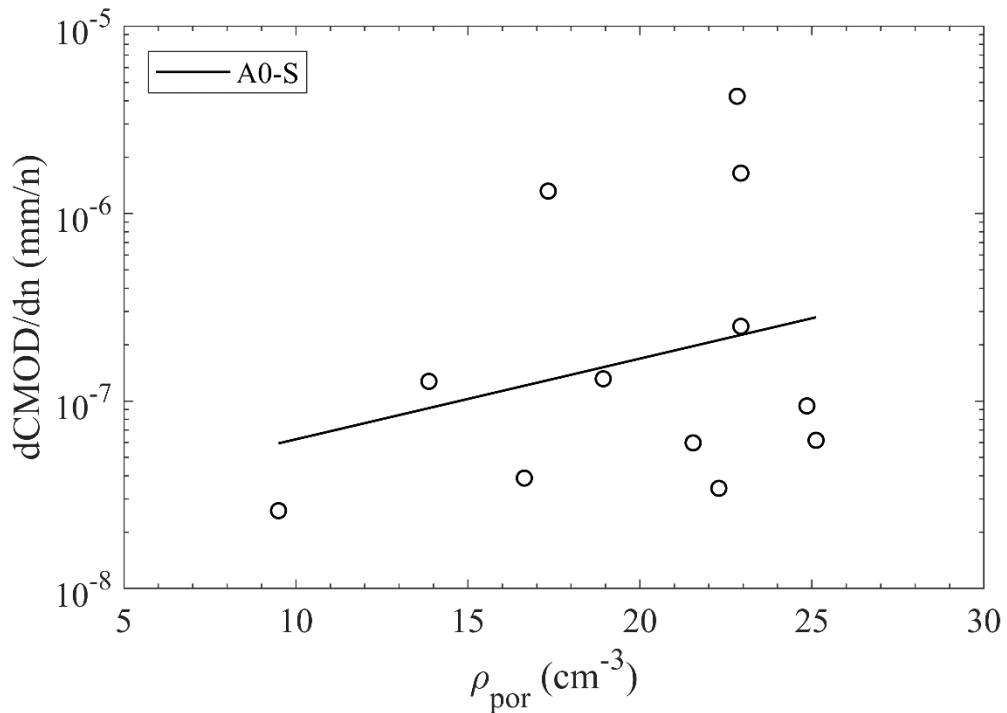


Figure 5.2-5. Linear regression between pore density and secondary crack opening rate.

Figure 5.2-2 reveals a general trend between porosity and fatigue life, such that the larger the volume of pores, the lower the number of cycles. It is striking that, although all specimens have the same dosage and have been manufactured under similar conditions, the resulting porosity (due to larger pores) is very uneven, ranging from 0.44% to 1.68%.

In any case, the figure shows some apparently anomalous results that affect the correlation, causing the R^2 coefficient to be only 0.23.

As for Figure 5.2-4, it is observed that as the pore density increases, the fatigue life decreases. The observed trend is similar to that of Figure 5.2-2, and again there are some outliers that worsen the regression. In this case, R^2 has a value of 0.11.

Consequently, it is concluded that the dispersion of porosity affects the fatigue life to some extent, so that a larger volume of pores and a higher number of them results in a decrease in the number of cycles.

With respect to the secondary crack opening rate, Figure 5.2-3 and 5.2-5 show equivalent results: the higher the porosity and the pore density, the higher the $dCMOD/dn$; i.e., the faster the development of fatigue damage. However, in this case the trend is less evident and the coefficients of determination are worse, without reaching 0.1.

Although the fit of the regressions is weak, it is clear from the figures that porosity and pore density have a non-negligible influence on the dispersion of the fatigue results, particularly in N .

In addition to porosity and pore density, it is interesting to study the pore distribution. For this purpose, based on the neighborhood test proposed by Vicente et al. [128], it is suggested to calculate the neighborhood distance (d_{nbh}). This parameter is defined as the distance from a pore to the nearest pore. Thus, the average neighborhood distance $d_{nbh,m}$ is adopted as a representative variable for the complete specimen. A higher value of $d_{nbh,m}$ indicates a greater uniformity in the pore distribution; on the contrary, a small value indicates that the pores are more concentrated. Linear regressions between mean neighborhood distance and fatigue response are presented in the following figures.

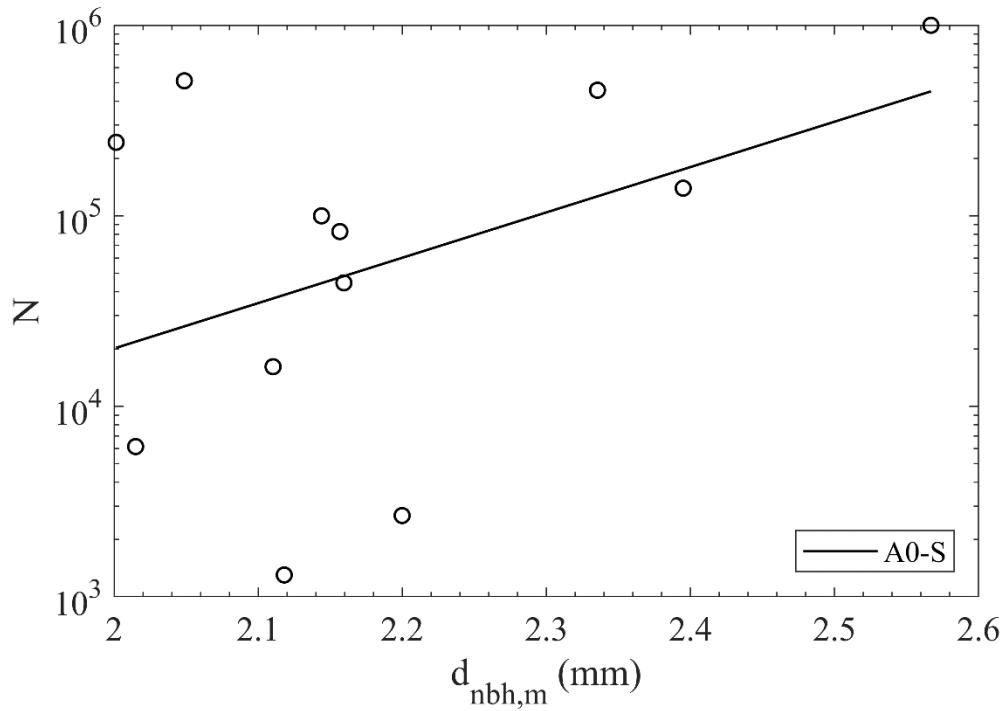


Figure 5.2-6. Linear regression between mean neighborhood distance and number of cycles.

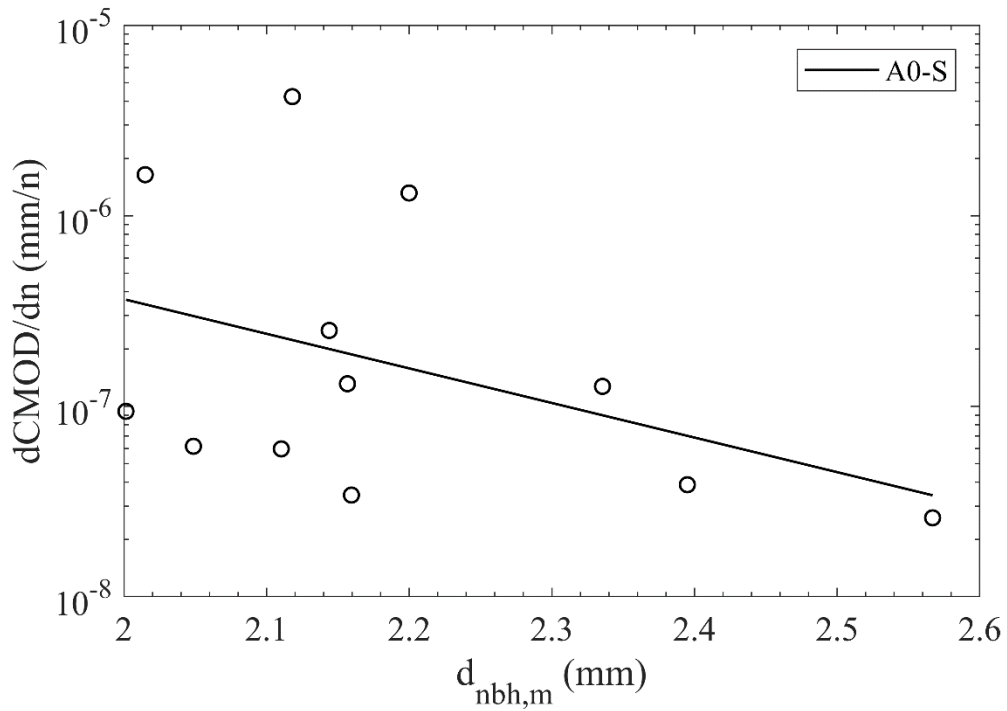


Figure 5.2-7. Linear regression between mean neighborhood distance and secondary crack opening rate.

Figure 5.2-6 reveals that, as the mean neighborhood distance decreases, so does the number of cycles; that is, the fatigue behavior worsens as the large pores are closer together. Equivalent results are obtained from Figure 5.2-7: $dCMOD/dn$ increases as $d_{nbh,m}$

decreases. The R^2 coefficients are low, being 0.18 in both cases. Nevertheless, it is clear from the figures that there is a trend, so it can be stated that the mean neighborhood distance is reasonably predictive of the fatigue response.

The parameter $d_{nbh,m}$ may decrease for two main reasons. On the one hand, because there are more pores ($> \rho_{por}$) and therefore the distance between them under a theoretically uniform distribution is necessarily smaller. In this regard, the relationship between pore density and fatigue response has already been addressed (Figure 5.2-4 and 5.2-5). On the other hand, because the distribution is more irregular, with possible accumulations of pores. In this context, if two specimens have the same number of pores but the distribution in one of them is more heterogeneous, $d_{nbh,m}$ will be smaller while ρ_{por} will remain the same.

Consequently, when the pores are closer together (due to a greater number, a more irregular distribution or a combination of both), the probability of generating planes of weakness that accelerate the development of fatigue cracking may increase.

5.2.2 Pore volume

The pore size distribution has some influence on the fatigue response of plain concrete, as pointed out by numerous investigations [97,133,145,146]. In this case, the average pore volume ($V_{por,m}$) and the maximum pore volume ($V_{por,max}$) have been chosen as representative parameters. The latter is defined as the volume greater than that of 90% of the pores. The following figures show the linear regressions between these variables and the fatigue results.

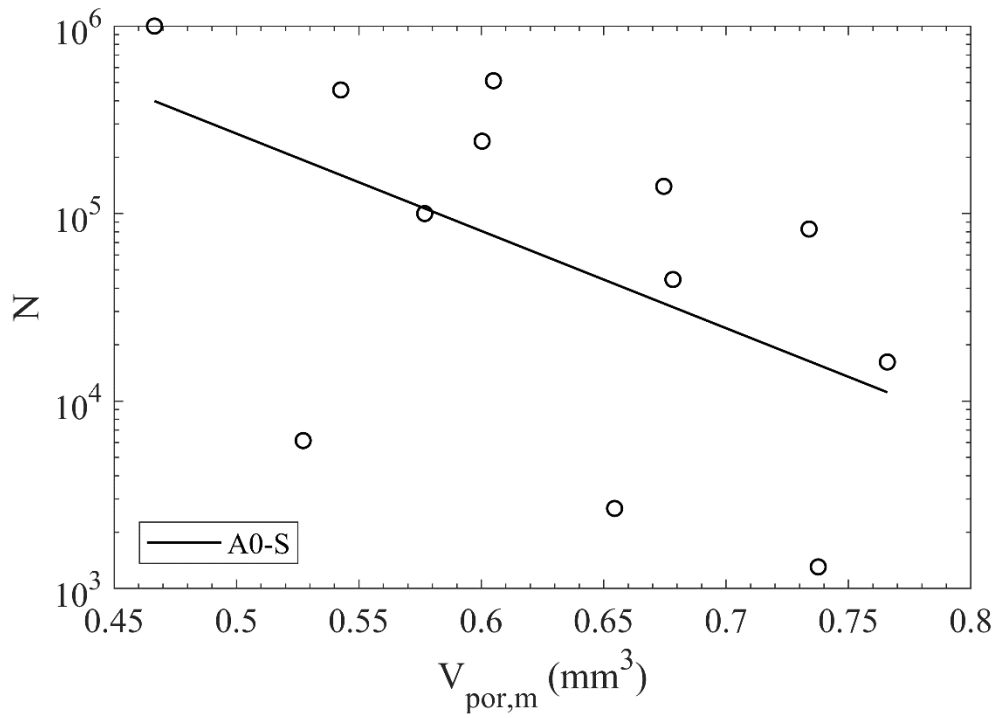


Figure 5.2-8. Linear regression between mean pore volume and number of cycles.

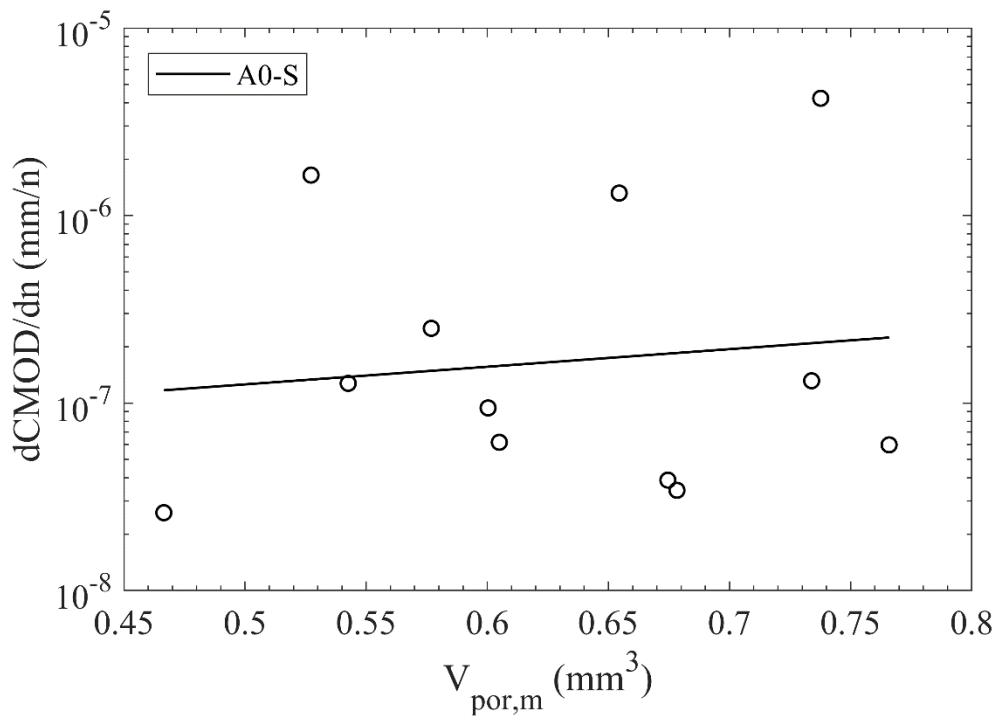


Figure 5.2-9. Linear regression between mean pore volume and secondary crack opening rate.

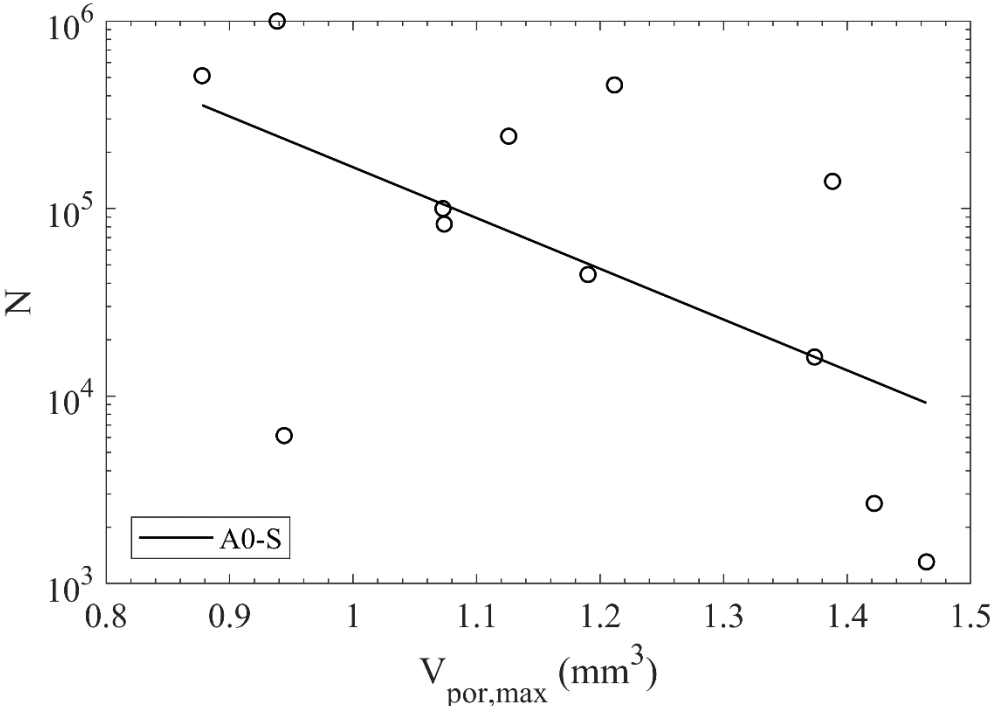


Figure 5.2-10. Linear regression between maximum pore volume and number of cycles.

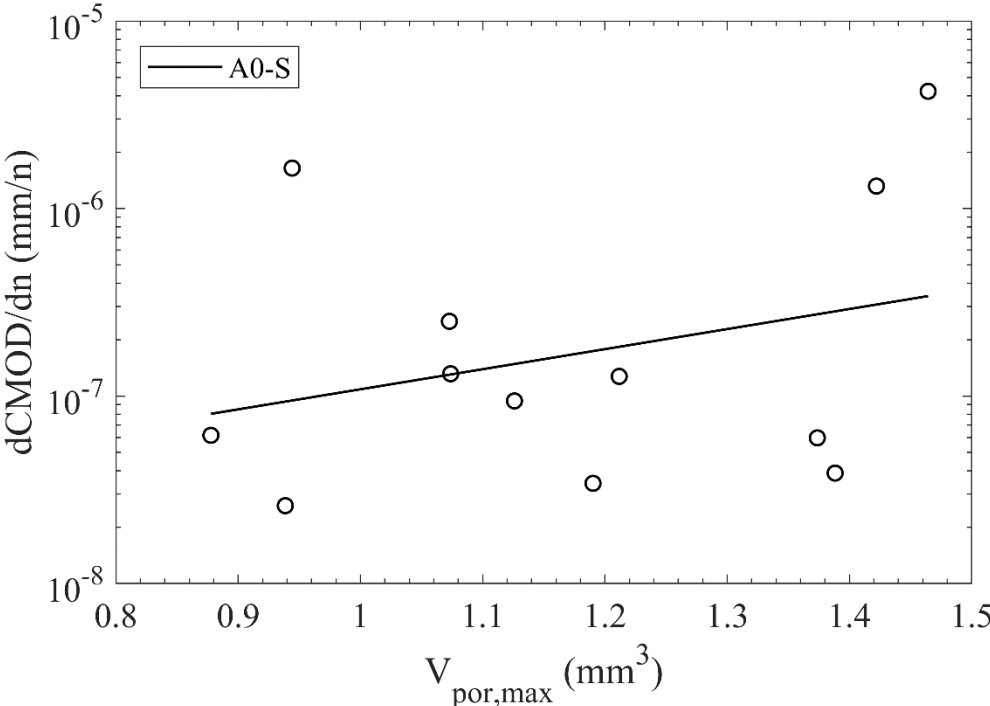


Figure 5.2-11. Linear regression between maximum pore volume and secondary crack opening rate.

Figure 5.2-8 and 5.2-10 show that the fatigue life decreases as both the mean pore volume and the maximum pore volume increase. The fits are reasonably robust to fatigue, with R^2 of 0.27 and 0.35, respectively. A few anomalous results are present again, which,

without affecting the perception of the overall trend, substantially reduce the coefficient of determination.

It is observed that the correlation is slightly better with $V_{\text{por,max}}$, which represents the highest pore sizes. This could be explained by the fact that macropores have more influence on fatigue behavior than small pores, as pointed out by several publications [133,145,146]. Large pores introduce heterogeneities in the concrete matrix, favoring stress concentration phenomena and preferential pathways for cracking progress due to cyclic tensile stresses.

On the other hand, it is found that the secondary crack opening rate is much less sensitive to pore volume parameters than the fatigue life. In particular, the regression models are weak, with R^2 barely reaching 0.1 (Figure 5.2-9 and 5.2-11). A slight trend of increasing $d\text{CMOD}/dn$ with pore size is observed.

The results are consistent with those of subsection 5.2.1, from which it is concluded that larger pores, in greater number and closer together reduce the fatigue life. Or, in other words, small variations in pore properties (such as porosity, pore size distribution or pore spatial distribution) can partially explain the dispersion in N of a priori identical specimens. Although considering each parameter individually the R^2 are not high, it is expected that, given the clear trends detected, the introduction of these parameters in multiple linear regression models will result in formulas with a reasonable predictive capacity.

5.2.3 Fatigue life estimation

Some of the pore parameters studied in the previous subsections show a clear trend with the fatigue response individually. Therefore, it is suggested to adjust empirical formulas to estimate the fatigue results from the combination of these parameters. As for the fibers, in this paper, it is proposed to fit multiple linear regression models according to the following expression (Eq. (5.2-1)):

$$\log y = a \cdot x_1 + b \cdot x_2 \quad (5.2-1)$$

Where y is the fatigue result to be estimated; x_1 and x_2 are the pore geometric parameters; and finally, a and b are the adjustment coefficients. The results considered are N (here equal to N_{tot} and N_{mat}) and $d\text{CMOD}/dn$ (here equal to $(d\text{CMOD}/dn)_{\text{mat}}$). Regarding the pore parameters, they have been divided according to their typology: x_1 is a parameter

related to porosity and pore distribution (porosity p , ρ_{por} or $d_{\text{nbh,m}}$) and x_2 is a parameter associated with pore volume ($V_{\text{por,m}}$ or $V_{\text{por,max}}$).

In the same way as with the fibers, a preliminary study has been carried out consisting of fitting multiple linear regression models with all possible parameter combinations; in this case, 9 in total. The best results have been achieved for the mean neighborhood distance $d_{\text{nbh,m}}$ as variable x_1 and the maximum pore volume $V_{\text{por,max}}$ as variable x_2 . Thus, the prediction formulas for the fatigue results will be as follows in (Eq. (5.2-2) and Eq. (5.2-3)):

$$\log N = a_1 \cdot d_{\text{nbh,m}} + b_1 \cdot V_{\text{por,max}} \quad (5.2-2)$$

$$\log (d\text{CMOD}/dn) = a_2 \cdot d_{\text{nbh,m}} + b_2 \cdot V_{\text{por,max}} \quad (5.2-3)$$

A table with the values of the adjustment coefficients obtained from the linear regression models is included below.

Table 5.2-1. Adjustment coefficients for prediction formulation of fatigue results.

N	a₁	3.54
	b₁	-2.56
dCMOD/dn	a₂	-3.46
	b₂	0.68

Table 5.2-1 shows that the adjustment coefficients are physically consistent with the correlations discussed in subsections 5.2.1 and 5.2.2. On the one hand, in the expression of the number of cycles the coefficient a_1 is positive because N increases with the distance between the pores (Figure 5.2-6). On the other hand, b_1 is negative because the relationship between N and the maximum pore size is inversely proportional (Figure 5.2-10). The opposite situation occurs in the secondary crack opening rate formula: $d\text{CMOD}/dn$ increases as the pores are closer together and their volume is larger (Figure 5.2-7 and 5.2-11).

It should be remembered that the aim of the proposed formulation is to obtain the best fit for the results of this work. Therefore, in this case it has been decided not to include an independent term, forcing the passage through the origin. It is also worth mentioning that the range of application of the expressions is in principle limited to that of the data used, without being able to ensure good results when extrapolating.

Finally, a table with the coefficients of determination of the multiple linear regression models is shown.

Table 5.2-2. R² coefficients of determination for the prediction formulation of fatigue results.

N	0.58
dCMOD/dn	0.43

The results in Table 5.2-2 demonstrate that the fit of the models is acceptable, considering the complexity of the dispersion in fatigue. The R² coefficients are comparatively higher than those of the individual correlations. Furthermore, it is observed that the coefficient of determination of the N expression is higher, being 0.58 versus 0.43. This is explained by the fact that individually the parameters also fit N better than dCMOD/dn.

In this subsection, the influence of pore structure dispersion on fatigue response dispersion has been analyzed. However, it is worth mentioning that there are other components of the mesostructure that are also important in the fracture process of concrete and have not been taken into account; in particular, the coarse aggregate, the aggregate-paste interface (ITZ, interfacial transition zone) and the smaller pores (gel pores, capillary pores and air voids below the fixed boundary) [147,148]. Current microCT technology does not allow to detect with sufficient quality and resolution such components, mainly due to the combination of large specimen size and high absorption of the concrete due to its high density.

Although pores alone cannot explain the dispersion of fatigue results in plain concrete, as shown by the modest values of the coefficients of determination obtained, it is undeniable that the variability of their size and spatial distribution plays a significant role. It is likely that, with the future development of microCT, more complex models that take into account the geometrical properties of the various components of the concrete mesostructure will be able to explain more accurately the dispersion of the fatigue response.

5.3 Size effect on the flexural fatigue behavior of concrete

This subsection deals with the size effect on the fatigue response of high strength plain and fiber-reinforced concrete. Therefore, the results of the flexural fatigue tests of all series (A0, A1, A2 and A3) and the two specimen sizes (S and L) are compared. The results have been structured in the same way as in subsection 4.2: first fatigue life is discussed, then CMOD vs N diagrams, and finally the relationship between $dCMOD/dn$ and N is studied.

It is recalled that all series have been tested to fatigue under the same relative load levels: between 16% and 80% of their corresponding flexural static strength. The test parameters for each series can be found in Table 3.2-3.

5.3.1 Fatigue life

The following tables show the number of fatigue cycles to failure for all tests, distinguishing between plain and fiber-reinforced concrete series. It is reminded that 12 tests have been performed per series, except for A2-L, where one specimen was lost due to an incidence in the control.

Table 5.3-1. Fatigue life N of plain concrete series.

Test	A0-S	A0-L
1	1,000,000*	767
2	99,976	90
3	511,248	143
4	243,232	200
5	139,687	263
6	456,365	594
7	82,695	129
8	2,674	137
9	16,155	373
10	1,304	200
11	44,497	117
12	6,153	258

Table 5.3-2. Fatigue life N of fiber-reinforced concrete series.

Test	0.3% fibers		0.6% fibers		1.0% fibers	
	A1-S	A1-L	A2-S	A2-L	A3-S	A3-L
1	6,121	2,626	3,522	25,926	18,889	15
2	4,838	899	10,316	37	918	23,308
3	3,696	1,830	40,858	3,476	30	13
4	43	109	19,401	2,004	3,176	3,335
5	2,642	21,892	22,481	6,597	12,888	15
6	2,791	1,255	1,000,000*	32	7,195	5,747
7	9,226	134	26,308	8,851	15,225	9,604
8	3,956	284	20,746	46	12	3,498
9	1,512	69	5,156	84	31	5,634
10	5,263	102	5,068	2,415	3,090	102
11	4,015	18,876	14,233	4,264	3,743	1,618
12	48	42,491	5,024	-	2,219	12,964

Table 5.3-1 reveals that there is a strong size effect in the plain concrete series. The larger specimens have a significantly lower fatigue life than the smaller ones, the difference being several orders of magnitude. While no test in the A0-L series exceeded 10^3 cycles, in the A0-S series 10^5 cycles were exceeded up to 5 times; in fact, one of the specimens reached the survival limit of 10^6 cycles.

On the other hand, Table 5.3-2 shows that the size effect in fiber-reinforced concrete is much less pronounced. The most significant differences are observed in the A2-S and A2-L series, with 0.6% of fibers. It is worth mentioning that in one test of the A2-S series the survival limit has been exceeded; however, this result can be considered anomalous, since the next longest lasting specimen has a fatigue life that is 2 orders of magnitude lower.

To compare the fatigue life of the various series in a more rigorous manner, Weibull distribution functions can be used. As seen in subsection 4.2, this function has proven to be adequate to describe the results statistically, fitting relatively well to their large scatter. Figure 5.3-1 to 5.3-4 represent the fit to the Weibull distribution of all series, divided by fiber content.

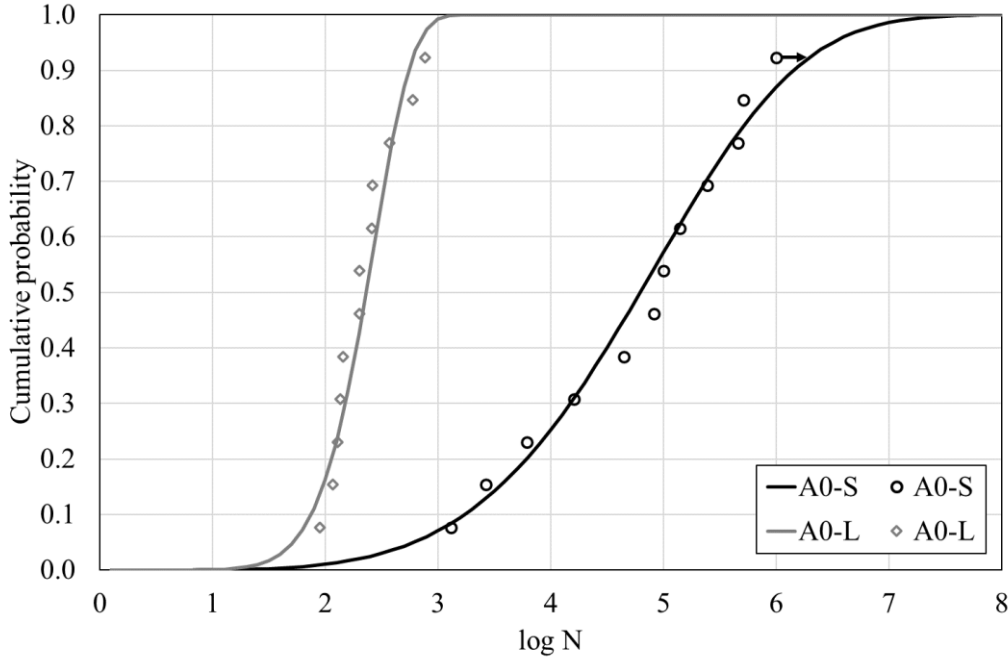


Figure 5.3-1. Weibull fitting of fatigue life of plain concrete series.

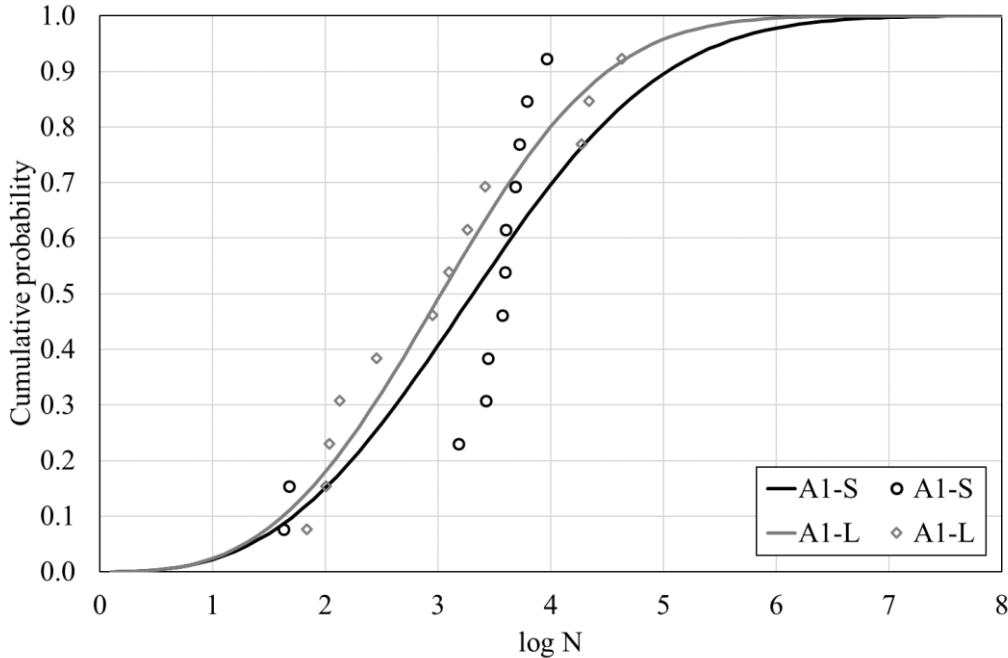


Figure 5.3-2. Weibull fitting of fatigue life of SFRC series with 0.3% fibers.

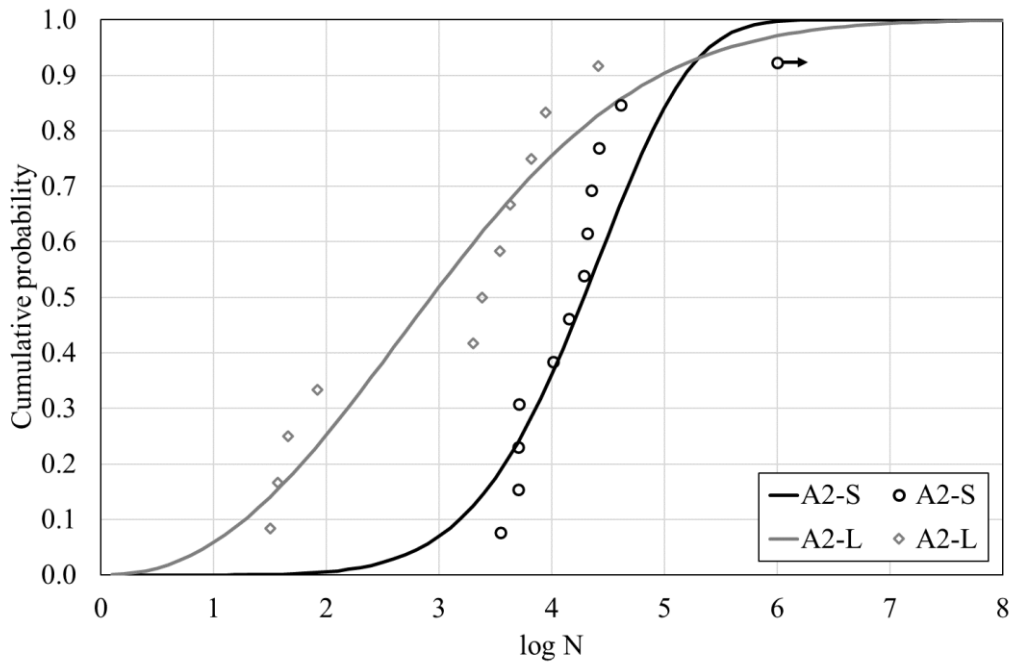


Figure 5.3-3. Weibull fitting of fatigue life of SFRC series with 0.6% fibers.

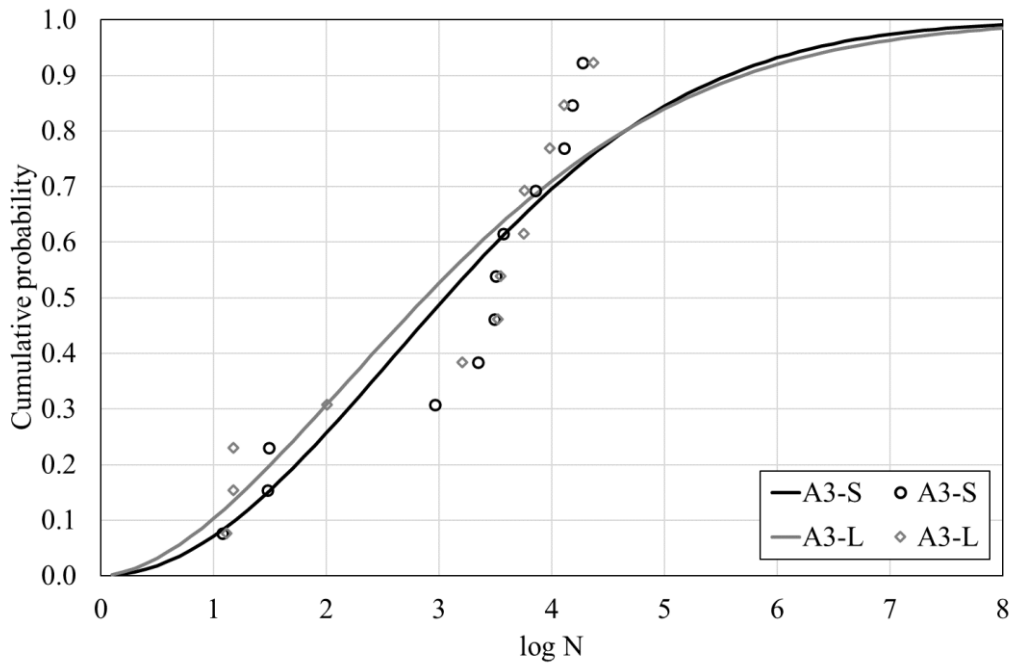


Figure 5.3-4. Weibull fitting of fatigue life of SFRC series with 1.0% fibers.

Below is a table with the fit parameters λ and β , as well as the R^2 correlation coefficients that characterize the quality of the fit of the data to the Weibull distribution.

Table 5.3-3. Fit parameters λ and β , and correlation coefficient R^2 of the Weibull distribution function.

Fibers (%)	Series	λ	β	R^2
0%	A0-S	5.17	4.80	0.97
	A0-L	2.47	8.16	0.88
0.3%	A1-S	3.76	2.87	0.74
	A1-L	3.42	3.02	0.90
0.6%	A2-S	4.54	6.35	0.76
	A2-L	3.44	2.28	0.87
1.0%	A3-S	3.67	2.01	0.87
	A3-L	3.54	1.76	0.87

Figure 5.3-1 shows that the fatigue strength of the small plain concrete specimens is markedly higher than that of the large specimens. The difference is close to 3 orders of magnitude, as pointed out by the values of the scale parameter λ (Table 5.3-3), indicative of the characteristic fatigue life. With respect to the dispersion of the results, it is noteworthy that in A0-L series it is particularly low; in fact, it is the series with the lowest dispersion (highest β), with almost all its data being grouped in one order of magnitude (between 10^2 and 10^3). In contrast, A0-S series presents a higher variability, although within what is usual in concrete fatigue.

As for the series with the lowest fiber content, Figure 5.3-2 shows that the fatigue life of A1-S series is only slightly higher than that of A1-L series, as also seen in the similar values of λ (Table 5.3-3). In addition, the dispersion is a little higher in A1-S series, with a more flattened curve and consequently a lower β . In this regard, it is worth mentioning that in this series the two tests with a lower N (43 and 48 cycles) alter the fit, since the rest of the values are comprised between 10^3 and 10^4 cycles.

The series with a fiber dosage of 0.6% show the most pronounced size effect among all the SFRC series, as Figure 5.3-3 reveals. It can be seen that A2-S series has a characteristic fatigue life about one order of magnitude higher than that of A2-L series (Table 5.3-3). On the other hand, the dispersion of the results is relatively low in A2-S series, hardly altered by the anomalous test that exceeded the survival limit. On the other hand, A2-L series presents a higher variability, and it is observed that the fit is perturbed by a group of tests with particularly low fatigue lives ($< 10^2$ cycles).

Finally, Figure 5.3-4 shows that the series with higher fiber quantity have practically identical fatigue lives, with a λ of 3.67 and 3.54 for A3-S and A3-L, respectively (Table

5.3-3). Therefore, in practice, it can be stated that no size effect is observed in the SFRC series with 1% fibers. With respect to the dispersion, it is again very similar, being slightly lower in A3-S series. Once again the fits are disturbed by the lower fatigue life results, although it affects both series equally.

Next, in Figure 5.3-5 the Weibull fittings of all the series are grouped together, although this time without representing the individual results in order to facilitate the interpretation of the results.

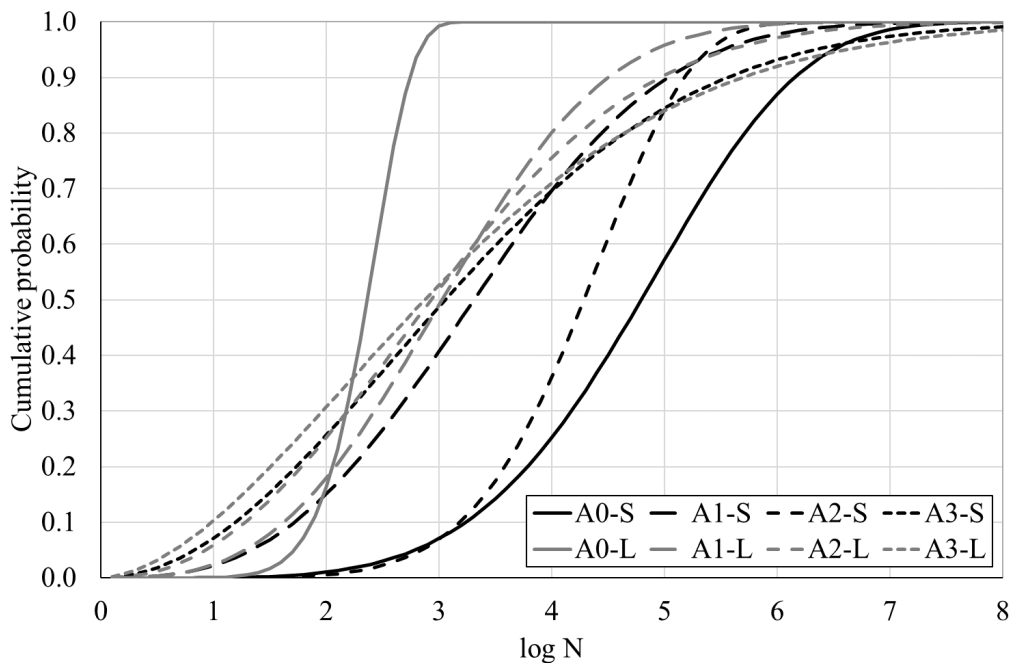


Figure 5.3-5. Weibull fitting of fatigue life of all series.

Figure 5.3-5 yields some interesting conclusions. First, the addition of fibers reduces the size effect. In fact, it could even be said that it eliminates it, since the difference in N between the two specimen dimensions goes from being 3 orders of magnitude in plain concrete to practically zero with 0.3% and 1.0% fibers (series A1 and A3, respectively). Only in A2 series with 0.6% fibers is there a noticeable size effect, with the smaller specimens having a characteristic fatigue life of about one order of magnitude greater than that of the larger specimens.

In relation to the above, it seems that the decrease in the size effect is not proportional to the fiber content. It is possible that 0.3% of fibers is sufficient to nullify the size effect, and that thereafter an increase in the dosage does not cause substantial improvements. As for the size effect of A2 series, it is explained by the fact that A2-S series behaves

differently from the rest of the SFRC series; in particular, in this series no result is less than 10^3 cycles, which therefore increases the characteristic fatigue life.

The reduction of the size effect due to the incorporation of fibers is a known fact, although in concrete subjected to bending it has been studied mostly in static condition. There are numerous studies that indicate that the difference in flexural static strength between specimens of different sizes decreases with the addition of fibers [81,85,86]. The reason is that fibers generate a bridging effect, increasing the fracture process zone and therefore the ductility of the material. In other words, in fact the fibers do not eliminate the size effect, but rather shift the size range in which the ductile-brittle behavior transition occurs, where this phenomenon really intervenes. This leads to the fact that the specimen dimensions considered are little sensitive to the size effect.

Another relevant conclusion drawn from Figure 5.3-5 is that the addition of fibers does not necessarily improve the fatigue strength. Actually, the trend changes depending on the specimen size. While in S-size specimens the plain concrete series has the highest fatigue life and its value worsens in all SFRC series, the opposite situation occurs in L-size specimens.

Furthermore, the fitting curves of all SFRC series, regardless of size, are very similar (with the exception of the A2-S series). At the same time, the curves of the plain concrete series act as upper (A0-S) and lower (A0-L) envelopes. The envelopes have characteristic fatigue lives of about 300 (A0-L) and 150,000 cycles (A0-S), while the value for the SFRC series is about 3,700 cycles. Consequently, this could indicate that there is a specimen size, intermediate between S and L, for which the characteristic fatigue life does not change with the addition of fibers.

Following the above, it is concluded that the fiber content hardly influences the flexural fatigue life, at least for the dosages used, ranging from 0.3% to 1.0%. Except for A2-S series, whose results differ from the rest, the fitting curves of the SFRC series are practically coincident, with no clear trends observed in any of the two specimen sizes.

Finally, when interpreting the results and conclusions above, it should be remembered that the fatigue stress levels are calculated as percentages of the maximum nominal stress σ_{\max} of flexural bending. Consequently, these levels are different in each series, increasing with fiber content and being higher in specimens of size S than L. The latter is due to the

size effect on the static flexural strength, which has not been directly addressed in this document.

5.3.2 CMOD vs N diagrams

In this subsection, the diagrams of (maximum) crack opening versus number of cycles, which are fundamental for understanding the development of fatigue damage in concrete, are analyzed. Two types of curves are shown because the fatigue life is represented both in absolute and relative terms. The results are presented divided by series with the same fiber content (0%, 0.3%, 0.6% and 1.0%). In addition, since the objective is to study the differences between the two specimen sizes, the diagrams are identified at the series level, and not at the individual specimen level.

On the other hand, it is worth mentioning that in some tests of the SFRC series, the two fatigue mechanisms already mentioned appear: fatigue of uncracked concrete, governed by the matrix, and fatigue of cracked concrete, dominated by the fibers. In these cases, the section of N associated with uncracked concrete is shown as a dashed line. Finally, sections below 50 cycles, as they are not representative, have not been included.

First, the diagrams of the plain concrete series are shown, as well as a table with the fatigue lives ordered from highest to lowest.

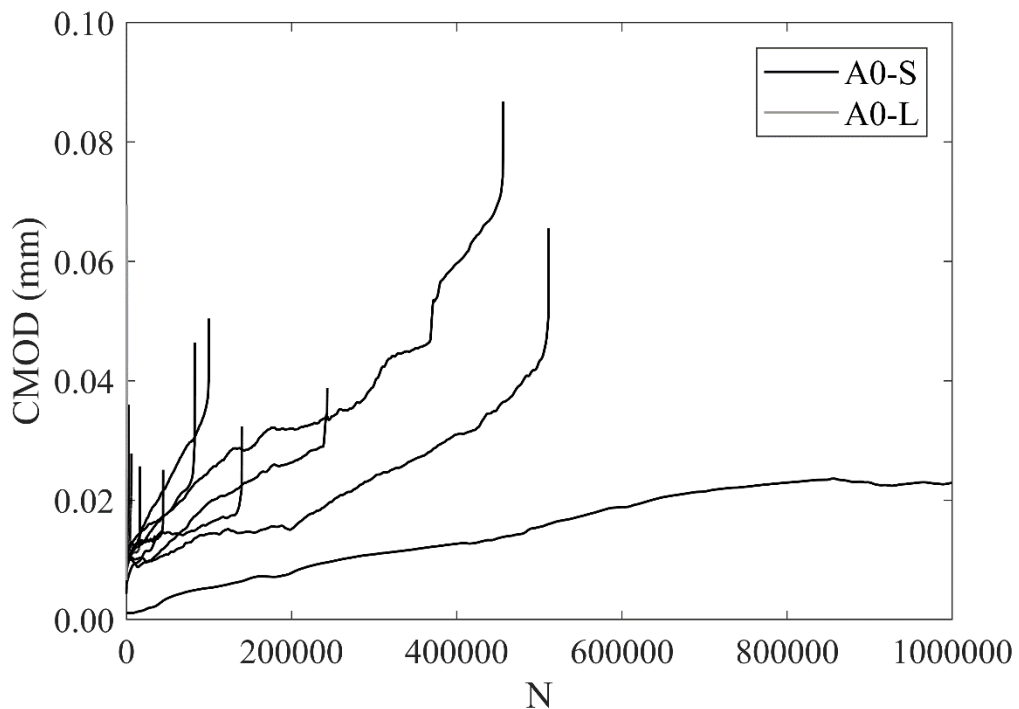


Figure 5.3-6. CMOD vs fatigue life in A0-S and A0-L series.

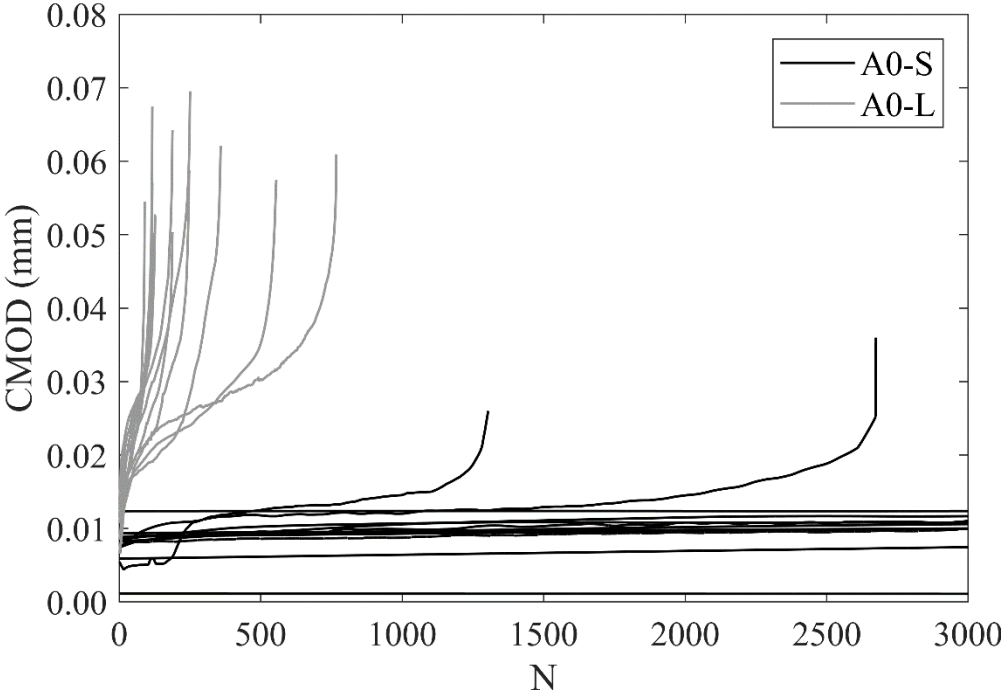


Figure 5.3-7. CMOD vs fatigue life in A0-S and A0-L series (detail view).

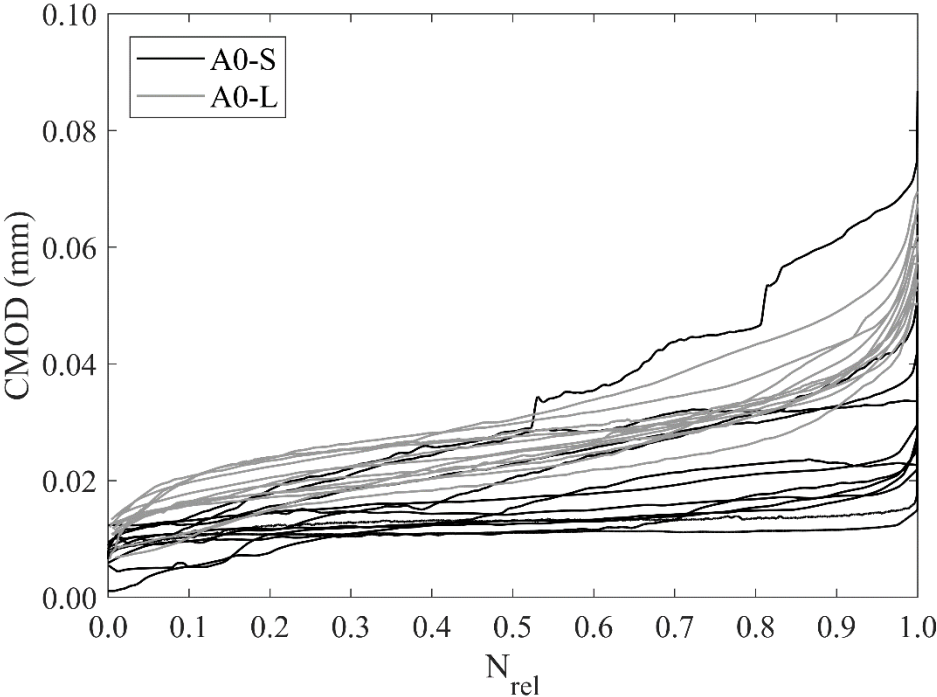


Figure 5.3-8. CMOD vs relative fatigue life in A0-S and A0-L series.

Table 5.3-4. Fatigue lives in A0-S and A0-L series.

A0-S	A0-L
N_{tot}	N_{tot}
1,000,000	767
511,248	594
456,365	373
243,232	263
139,687	258
99,976	200
82,695	200
44,497	143
16,155	137
6,153	129
2,674	117
1,304	90

A first aspect observed in the figures is that, as is well known, due to the high brittleness of plain concrete, flexural failure occurs with small crack openings, of the order of 0.05 mm. Figure 5.3-6 and 5.3-7 show that the fatigue life of A0-S series is much higher than that of A0-L series, showing an evident size effect. At the same time, the dispersion in the large specimens is clearly smaller than in the small ones; in fact, it is surprisingly low for the usual in concrete fatigue.

Due to the large difference in the number of cycles between the two series, it is more useful to analyze the results in Figure 5.3-8. Here it can be seen that all the curves have the characteristic S-shape, divided into three phases or stages of damage. However, the phenomena occurring in each phase change depending on the fatigue mechanism. In the case of fatigue of uncracked concrete, they are divided as follows: (I) plastic tensile strain and birth of scattered microcracking around the notch edge, (II) stable growth of microcracking and (III) convergence to a main microcrack that triggers failure.

The S-shape of the curves is more evident in the A0-L series. It is possible that in the A0-S series, due to the considerable duration of the tests and such low CMOD (around 0.01 mm), the thermal variations during the days may have slightly affected the concrete. As a result, these actions would be the cause of the noise observed during phase II, which causes it not to have a uniform slope, as is the case in the A0-L series. Regardless, the observed thermal effects are of a very small magnitude compared to the fatigue-induced

damage, and do not change the fact that the fatigue strength is notably higher in A0-S series than in A0-L series.

On the other hand, although the three damage phases are observed in both series, the proportions of the total fatigue life they occupy are different. While on average in A0-L series phase II extends between 15% and 81% of N, in A0-S series it extends between 9% and 90%. Another aspect that differs between the two specimen sizes is that, whereas the initial CMOD is very similar at approximately 0.01 mm, the CMOD corresponding to the beginning of phase II is higher in A0-L series (0.018 mm vs 0.011 mm). This indicates that the damage caused by phase I is greater in the larger specimens, which would contribute to shortening their fatigue life. However, it should be noted that the CMOD associated with the end of phase II, for which fatigue failure is triggered, is also higher in A0-L series (0.035 mm vs 0.025 mm). In this regard, it should be mentioned that in A0-S series its value has a lot of dispersion.

Additionally, it is noted that the secondary phase, being the most extensive, is the one that governs the evolution of fatigue damage. Returning to Figure 5.3-6 and 5.3-7, it can be seen that the slope of the nearly linear section that defines this phase is greater in the large specimens than in the small ones. This parameter is known as the secondary crack opening rate ($dCMOD/dn$), and will be discussed in depth in the next subsection. However, as a preliminary conclusion, a higher $dCMOD/dn$ in A0-L series indicates a faster increase in damage due to cyclic loading, which is the reason for the shorter fatigue life recorded in that series.

Second, CMOD vs N diagrams of the SFRC series with the lowest fiber content (0.3%) are shown, including a table with the fatigue lives.

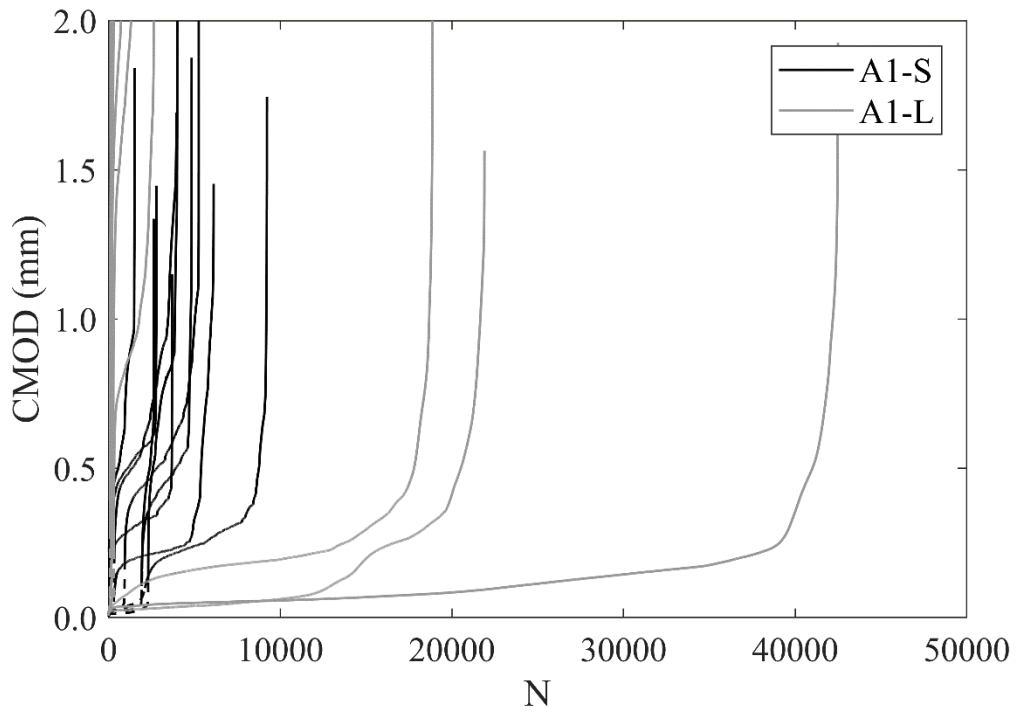


Figure 5.3-9. CMOD vs fatigue life in A1-S and A1-L series.

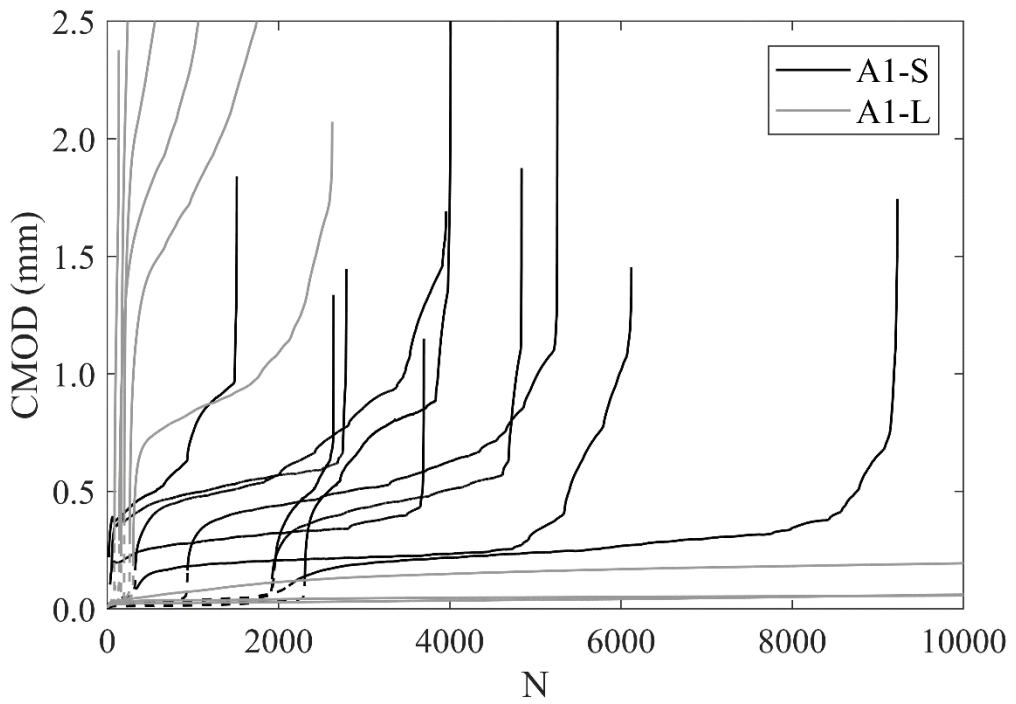


Figure 5.3-10. CMOD vs fatigue life in A1-S and A1-L series (detail view).

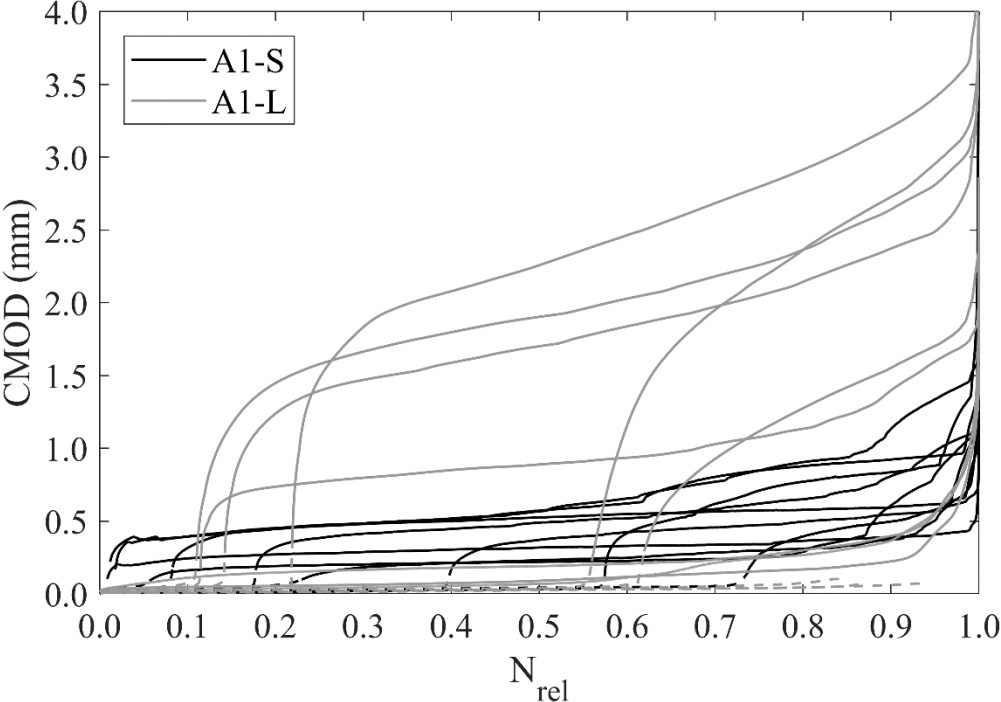


Figure 5.3-11. CMOD vs relative fatigue life in A1-S and A1-L series.

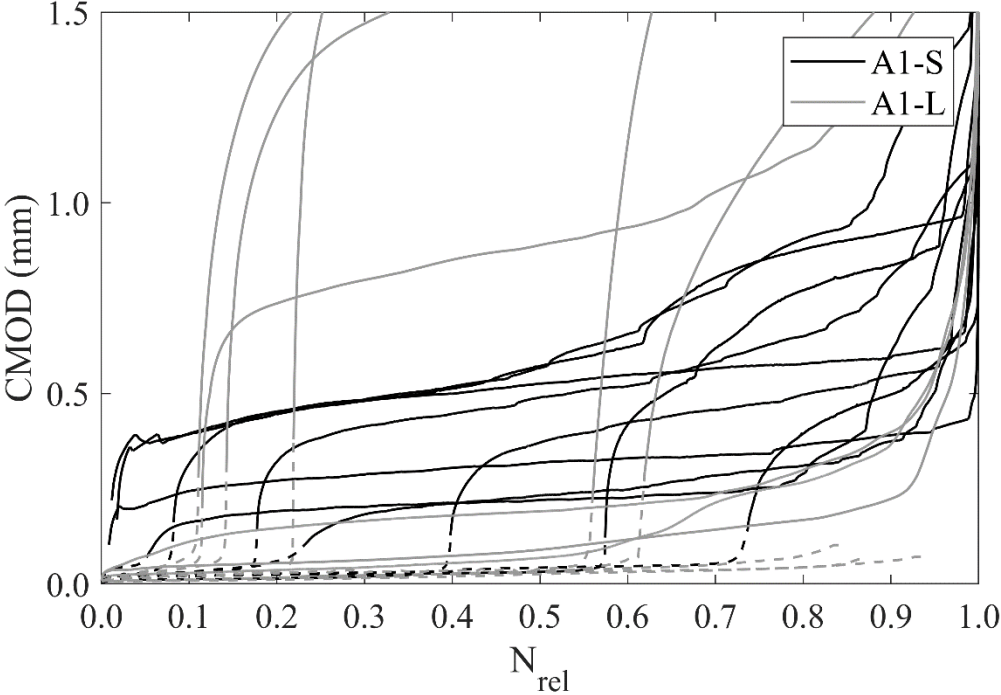


Figure 5.3-12. CMOD vs relative fatigue life in A1-S and A1-L series (detail view).

Table 5.3-5. Fatigue lives in A1-S and A1-L series.

A1-S			A1-L		
N_{mat}	N_{fib}	N_{tot}	N_{mat}	N_{fib}	N_{tot}
2,118	7,108	9,226	0	42,491	42,491
346	5,775	6,121	0	21,892	21,892
934	4,329	5,263	0	18,876	18,876
1,924	2,914	4,838	301	2,325	2,626
2,305	1,710	4,015	260	1,570	1,830
327	3,629	3,956	138	1,117	1,255
31	3,665	3,696	196	703	899
49	2,742	2,791	158	126	284
1,948	694	2,642	82	52	134
17	1,495	1,512	92	17	109
42	6	48	89	13	102
27	16	43	65	4	69

The figures reveal that in practically all the tests of these series, the two fatigue mechanisms explained appear: fatigue of uncracked concrete and fatigue of cracked concrete. The former develops at reduced CMOD values (< 0.1 mm), since it is ultimately equivalent to that observed in the plain concrete series. After its exhaustion with the birth of a main macro-crack, the second mechanism intervenes, governed by the bridging forces of the fibers. As these provide high ductility, the CMOD oscillates in high values, even several millimeters. Consequently, the resulting fatigue life can be divided into the two sections corresponding to the fatigue of uncracked concrete (N_{mat}) and cracked concrete (N_{fib}), respectively (Table 5.3-5).

With respect to the total fatigue life, it can be seen that it is higher on average in the small specimens. However, it is noteworthy that the three tests that have lasted the longest belong to A1-L series, widely exceeding 10^4 cycles. Moreover, precisely these specimens are the only ones in the series in which only the fatigue of cracked concrete has been involved. In other words, in these tests it took just one load cycle for the crack to appear and the fibers to begin to mobilize.

Regarding the proportion of the total fatigue life occupied by each damage mechanism, no significant differences are detected between the two specimen sizes. The average percentages over which the fatigue of uncracked concrete (N_{mat}) extends are 32% and 37% in A1-S and A1-L series, respectively. However, as can be seen in Figure 5.3-11, the dispersion is very high.

Figure 5.3-11 and 5.3-12 show that the curves of both series acquire a double S-shape, each with its three damage phases. The first S-shaped section (dashed line) is associated with the fatigue of uncracked concrete, while the second (solid line) corresponds to the fatigue of cracked concrete. Therefore, it is concluded that the three stages of damage evolution (I, II and III) in the CMOD vs N diagrams appear independently of the acting fatigue mechanism.

As already mentioned, phase II of the curves is very interesting, since it represents the development of fatigue damage. In the fatigue of cracked concrete (solid line), it is obtained that phase II extends on average between 13% and 89% of N_{fib} in A1-S series, and between 14% and 87% in A1-L series. Thus, there are no significant differences in this respect. However, Figure 5.3-9 and 5.3-10 show that the slope of phase II ($dCMOD/dn$) is greater in the large specimens, particularly in those with less fatigue life than the small ones. Consequently, despite the fact that phase II occupies a similar percentage of the fatigue life, damage development is faster in the large specimens, resulting in a shortening of N.

On the other hand, there is a part of the CMOD vs N diagrams that seems to have a significant impact on fatigue life: the stiffness transition zone between the fatigue of uncracked and cracked concrete. It is clearly seen that in the A1-L series specimens, the increase in CMOD that occurs from the time the concrete cracks until the fibers are mobilized is very high, of about 1 mm and reaching in some cases almost 2 mm. In contrast, in the A1-S series the CMOD jump is much smaller, practically not exceeding 0.5 mm. This has a bearing on the fact that the smaller specimens withstand more cycles than the larger ones, since it can be seen that the greater the increase in CMOD in the stiffness transition zone, the shorter the fatigue life (Figure 5.3-12). In fact, this would justify the longer fatigue life of the three specimens of the A1-L series that only have fatigue of cracked concrete, where the transition zone does not appear.

One possible cause of the larger CMOD jump in large specimens than in small ones, which in turn could partly explain the size effect in N, is the difference in fiber distribution and orientation. In the small specimens, the ratio between fiber length and minimum element dimension is higher (0.4 vs 0.2 in the large ones). This causes the wall effect to be more aggressive, i.e., the fibers are aligned more pronouncedly in the longitudinal direction. Therefore, when the concrete fissures, there will be more properly oriented fibers in

the A1-S series specimens that are able to take the stresses and resist the load, thus reducing the increase in CMOD.

Third, CMOD vs N diagrams of the SFRC series with the mean fiber content (0.6%) are shown, including a table with the fatigue lives.

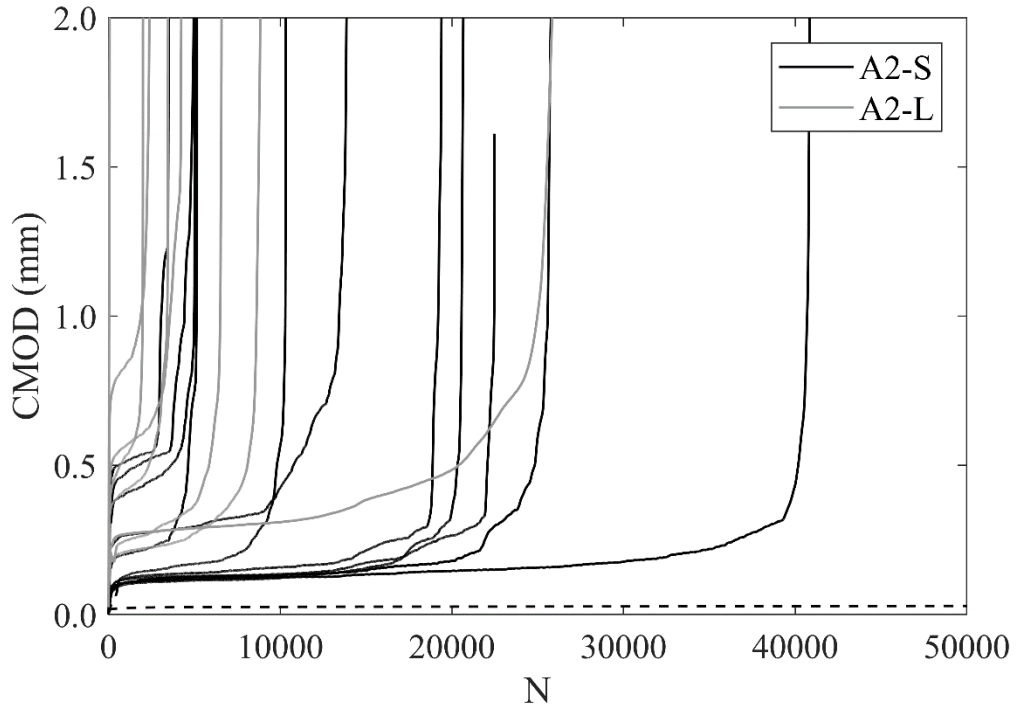


Figure 5.3-13. CMOD vs fatigue life in A2-S and A2-L series.

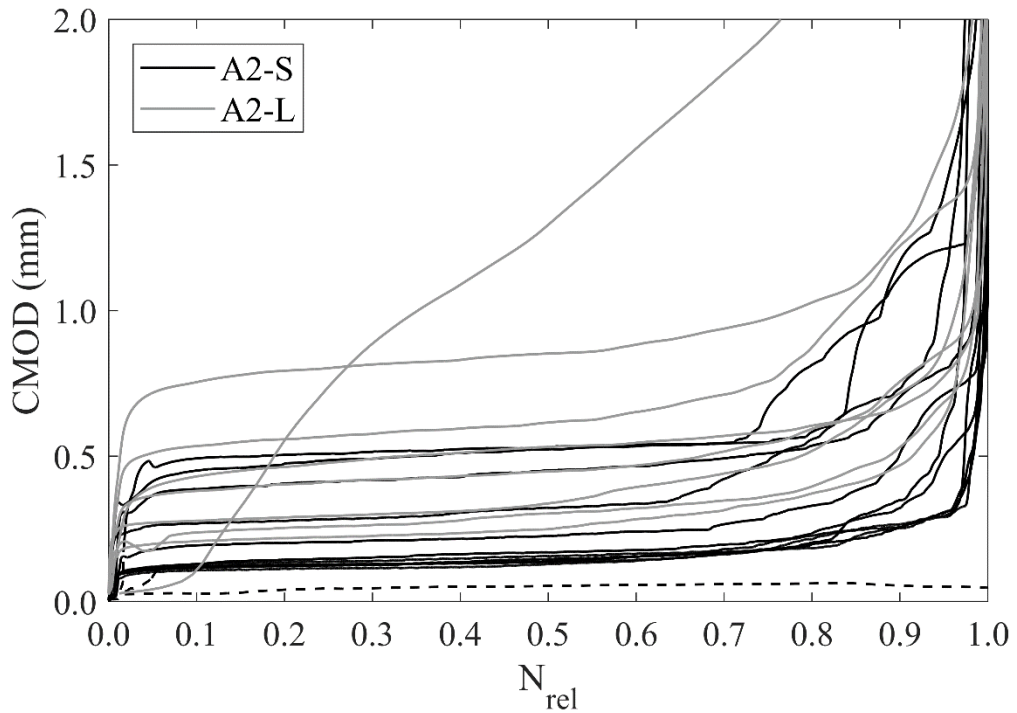


Figure 5.3-14. CMOD vs relative fatigue life in A2-S and A2-L series.

Table 5.3-6. Fatigue lives in A2-S and A2-L series.

A2-S			A2-L		
N_{mat}	N_{fib}	N_{tot}	N_{mat}	N_{fib}	N_{tot}
1,000,000	0	1,000,000	0	25,926	25,926
50	40,808	40,858	0	8,851	8,851
56	26,252	26,308	0	6,597	6,597
53	22,428	22,481	0	4,264	4,264
0	20,746	20,746	0	3,476	3,476
57	19,344	19,401	0	2,415	2,415
0	14,233	14,233	0	2,004	2,004
504	9,812	10,316	0	84	84
0	5,156	5,156	0	46	46
0	5,068	5,068	0	37	37
0	5,024	5,024	0	32	32
59	3,463	3,522	-	-	-

The figures show that in these series the dominant mechanism is the fatigue of cracked concrete, since in A2-L series all specimens crack after the first cycle ($N_{mat} = 0$) and in A2-S series the extent of fatigue cycles of uncracked concrete is very small. The only exception is a specimen from the A2-S series that reaches survival. The behavior of this test specimen is unusual because it does not even crack after 10^6 cycles, remaining at a CMOD of about 0.03 mm.

It can be noticed that the fatigue life is higher in the small specimens than in the large ones. In fact, Table 5.3-6 shows that none of the A2-S series specimens is below 10^3 cycles, a situation that is only repeated in A0-S series, which has the best fatigue behavior of all. At the same time, A2-L series has up to four specimens with a very low number of cycles, less than 100.

On the other hand, the S-shape of the curves is noticeable in both figures. Their appearance is very similar for the two specimen sizes, both qualitatively and quantitatively. However, it should be noted that in A2-S series, at the end of phase II, there are steps produced by the successive collapse of resistant "layers" of fibers as the crack progresses. In A2-L series they also appear, but are less accentuated. With respect to the proportion of the total fatigue life occupied by phase II, Figure 5.3-14 reveals that in the two series it is very similar; in fact, in A2-S series it comprises on average between 7% and 84% of N , while in A2-L, between 7% and 83%.

There are two reasons that can help to understand, through the CMOD vs N diagrams, why the number of cycles is lower in large specimens than in small specimens. On the one hand, when the initial CMOD of phase II (hereafter, $CMOD_{II,i}$) is larger, the fatigue life is reduced. This is evident in Figure 5.3-13, where it can be seen that the tests of both series with less N are those with a higher $CMOD_{II,i}$, above 0.3-0.4 mm. In general terms, the value of this parameter is markedly higher in the A2-L series. On the other hand, when the secondary crack opening rate (phase II slope) increases, the fatigue life decreases. This is the well-known Sparks and Menzies law already discussed. Again, $dCMOD/dn$ appears to be higher in large specimens than in small specimens. Consequently, it is concluded that the combination of higher $CMOD_{II,i}$ and $dCMOD/dn$ are responsible for the size effect on the fatigue life of these series.

In addition, it could be intuited that there is a certain relationship between the two parameters, so that the higher the $CMOD_{II,i}$, the higher the $dCMOD/dn$; that is, if the crack is stabilized with a higher CMOD and the effective strength section is reduced, the speed of fatigue damage increases, which has a certain logic. However, this is not exactly true, since specimens with a given $CMOD_{II,i}$ have higher $dCMOD/dn$ than others with a higher $CMOD_{II,i}$, both within the same series and comparing between the two sizes (Figure 5.3-13).

Fourth, the CMOD vs N diagrams of the SFRC series with the highest fiber content (1.0%) are shown, including a table with the fatigue lives.

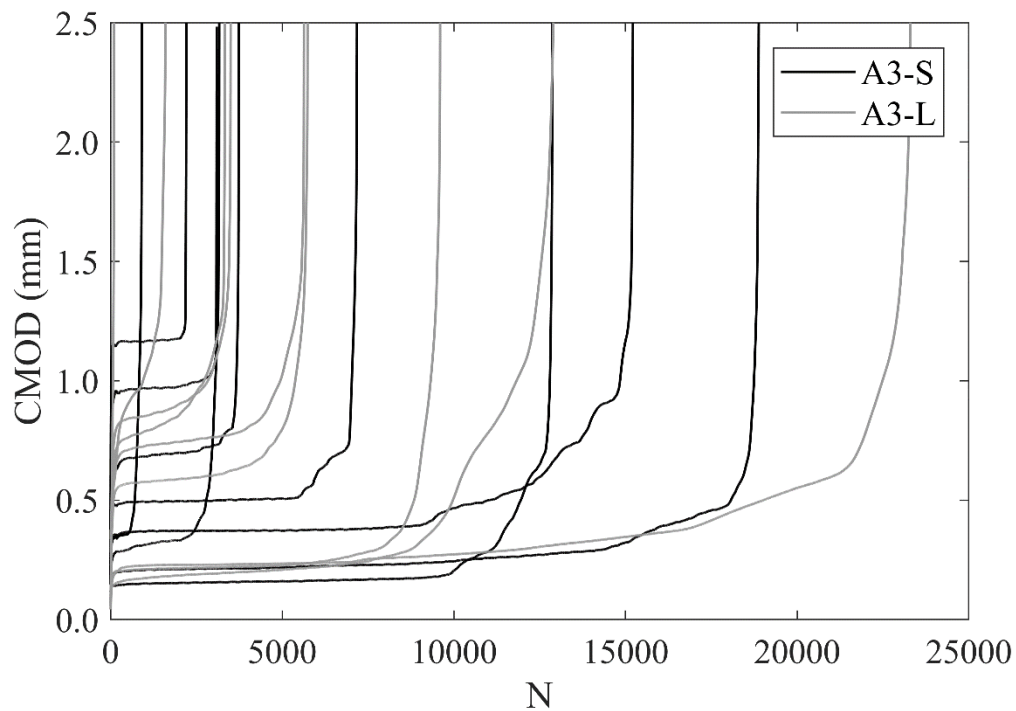


Figure 5.3-15. CMOD vs fatigue life in A3-S and A3-L series.

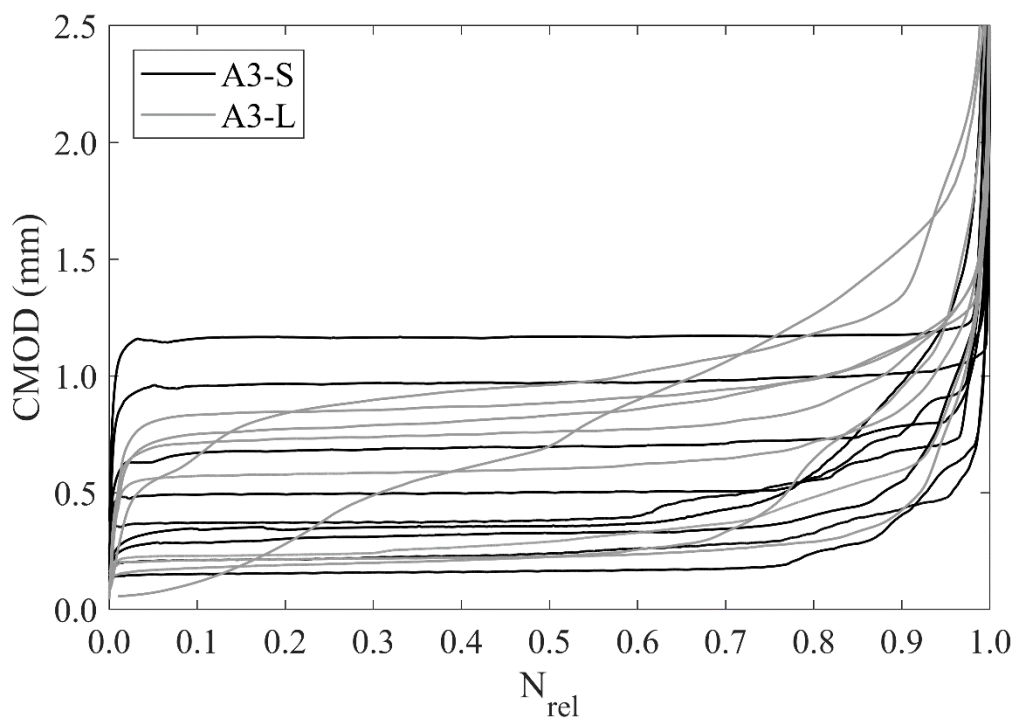


Figure 5.3-16. CMOD vs relative fatigue life in A3-S and A3-L series.

Table 5.3-7. Fatigue lives in A3-S and A3-L series.

A3-S			A3-L		
N_{mat}	N_{fib}	N_{tot}	N_{mat}	N_{fib}	N_{tot}
0	18,889	18,889	0	23,308	23,308
0	15,225	15,225	0	12,964	12,964
0	12,888	12,888	0	9,604	9,604
0	7,195	7,195	0	5,747	5,747
0	3,743	3,743	0	5,634	5,634
0	3,176	3,176	0	3,498	3,498
0	3,090	3,090	0	3,335	3,335
0	2,219	2,219	0	1,618	1,618
0	918	918	0	102	102
0	31	31	0	15	15
0	30	30	0	15	15
0	12	12	0	13	13

The figures reveal that in the series with 1.0% fibers only the fatigue mechanism of cracked concrete appears; that is, all specimens crack after the first cycle ($N_{mat} = 0$).

Table 5.3-7 shows that the number of cycles is very similar in the two series: in each, in 8 tests a fatigue life between 1,000 and 25,000 cycles is reached, and in the remaining 4 it is relatively low, below 1,000 cycles.

Additionally, the figures show that the S-curves are similar. As for phase II, Figure 5.3-16 shows that it ranges between 6% and 79% in A3-S series, and between 6% and 87% in A3-L series. Its lower amplitude in the small specimens is explained by the steps in the final part, due in turn to fiber depletion. As already mentioned in the previous series, this behavior is more accentuated in the small specimens, while in the large specimens the transitions are more moderate.

Although in this case there is no size effect on fatigue life, the reasons given in A2-S and A2-L series can be used to explain the dispersion of the results, i.e., why some specimens withstand more cycles than others. Again, it is observed that the fatigue life depends on two parameters: the initial CMOD of phase II ($CMOD_{II,i}$) and the secondary crack opening rate ($dCMOD/dn$). The higher their values, the lower the fatigue strength. In some cases, such as the specimen of the A3-S series with an N of 2,219 cycles (Figure 5.3-15), the low fatigue life is explained by a high $CMOD_{II,i}$ (1.16 mm), while its $dCMOD/dn$ is lower even than that of other specimens of the same series that have lasted

more cycles. In other cases, such as the A3-L series specimen with an N of 1,618 cycles, the low fatigue life is due to a high $dCMOD/dn$, since its $CMOD_{II,i}$ is comparatively moderate (0.75 mm). Consequently, this could indicate that the two parameters have a certain degree of independence, their combination being what determines the fatigue response of each specimen.

5.3.3 Secondary crack opening rate

As discussed several times throughout the document, in the $CMOD$ vs N diagrams, the envelope of phase II of stable crack growth can be approximated by a straight line whose slope is called the secondary crack opening rate ($dCMOD/dn$). This parameter is associated with the fatigue life, a relationship known as Sparks and Menzies' law, originally proposed in compressive fatigue.

In this subsection the linear regressions between the logarithms of $dCMOD/dn$ and N , which is the form in which this law is usually expressed, are studied. Since two types of fatigue are observed in the tests performed (fatigue of uncracked concrete and fatigue of cracked concrete), each with its characteristic S-curve, its phase II and therefore its own $dCMOD/dn$, the two mechanisms will be analyzed separately. Thus, in fatigue of uncracked concrete, the results of the series of plain concrete (A0-S and A0-L) will be treated, as well as those of the SFRC series in which there are sections of this type of fatigue (A1-S, A1-L and A2-S). On the other hand, in fatigue of cracked concrete, the results of all SFRC series will be reviewed. In addition, all the data will be studied together.

First, tables are shown with the crack opening rates, divided by series with the same fiber content (0, 0.3%, 0.6% and 1.0%). In the cases where both types of fatigue appear, the values of $(dCMOD/dn)_{mat}$, associated with the fatigue of uncracked concrete, and $(dCMOD/dn)_{fib}$, corresponding to the fatigue of cracked concrete, are included. The data have been ordered from highest to lowest. These tables are presented for information purposes only, as the results will be analyzed in detail through the linear regression plots.

Table 5.3-8. Crack opening rate in A0-S and A0-L series.

A0-S		A0-L	
$(dCMOD/dn)_{mat}$		$(dCMOD/dn)_{mat}$	
4.22E-06		2.65E-04	
1.64E-06		2.11E-04	
1.32E-06		1.79E-04	
2.50E-07		1.75E-04	
1.31E-07		1.30E-04	
1.27E-07		1.22E-04	
9.42E-08		1.11E-04	
6.18E-08		1.10E-04	
5.98E-08		9.43E-05	
3.88E-08		5.23E-05	
3.42E-08		3.31E-05	
2.60E-08		1.99E-05	

Table 5.3-9. Crack opening rate in A1-S and A1-L series.

A1-S		A1-L	
$(dCMOD/dn)_{mat}$	$(dCMOD/dn)_{fib}$	$(dCMOD/dn)_{mat}$	$(dCMOD/dn)_{fib}$
7.41E-04	4.28E-01	7.37E-04	3.26E-01
6.64E-04	4.19E-02	6.35E-04	1.59E-01
4.27E-04	4.64E-04	4.71E-04	6.88E-02
2.82E-04	4.46E-04	4.29E-04	2.28E-02
1.50E-04	3.20E-04	3.66E-04	1.44E-02
6.12E-05	2.06E-04	1.61E-04	2.59E-03
5.83E-05	1.30E-04	1.49E-04	1.27E-03
1.94E-05	8.58E-05	1.06E-04	8.03E-04
1.74E-05	7.43E-05	9.10E-05	2.26E-04
1.50E-05	4.18E-05	-	9.08E-06
5.89E-06	3.00E-05	-	4.30E-06
5.29E-06	1.63E-05	-	4.14E-06

Table 5.3-10. Crack opening rate in A2-S and A2-L series.

A2-S		A2-L	
$(dCMOD/dn)_{mat}$	$(dCMOD/dn)_{fib}$	$(dCMOD/dn)_{mat}$	$(dCMOD/dn)_{fib}$
7.59E-04	3.87E-05	-	8.11E-02
6.06E-04	3.18E-05	-	5.73E-02
2.17E-04	3.11E-05	-	3.82E-02
1.05E-04	2.16E-05	-	3.16E-02
2.28E-05	1.90E-05	-	1.48E-04
1.84E-05	1.58E-05	-	1.15E-04
2.02E-08	7.62E-06	-	7.28E-05
-	6.95E-06	-	6.66E-05
-	3.65E-06	-	2.98E-05
-	3.55E-06	-	2.25E-05
-	3.48E-06	-	1.05E-05

Table 5.3-11. Crack opening rate in A3-S and A3-L series.

A3-S	A3-L
$(dCMOD/dn)_{fib}$	$(dCMOD/dn)_{fib}$
1.72E-01	1.05E-01
5.78E-02	1.04E-01
4.17E-02	1.02E-01
1.02E-04	1.64E-02
3.14E-05	3.61E-04
1.97E-05	1.31E-04
1.78E-05	6.54E-05
6.55E-06	2.99E-05
6.49E-06	2.92E-05
3.74E-06	1.55E-05
3.26E-06	1.19E-05
2.78E-06	8.69E-06

Secondly, the following figure shows the linear regressions between the secondary crack opening rate and the number of cycles associated with the fatigue of uncracked concrete. While in the plain concrete series $N_{mat} = N_{tot}$, in series A1-S, A1-L and A2-L only the cycles associated with this type of fatigue have been considered.

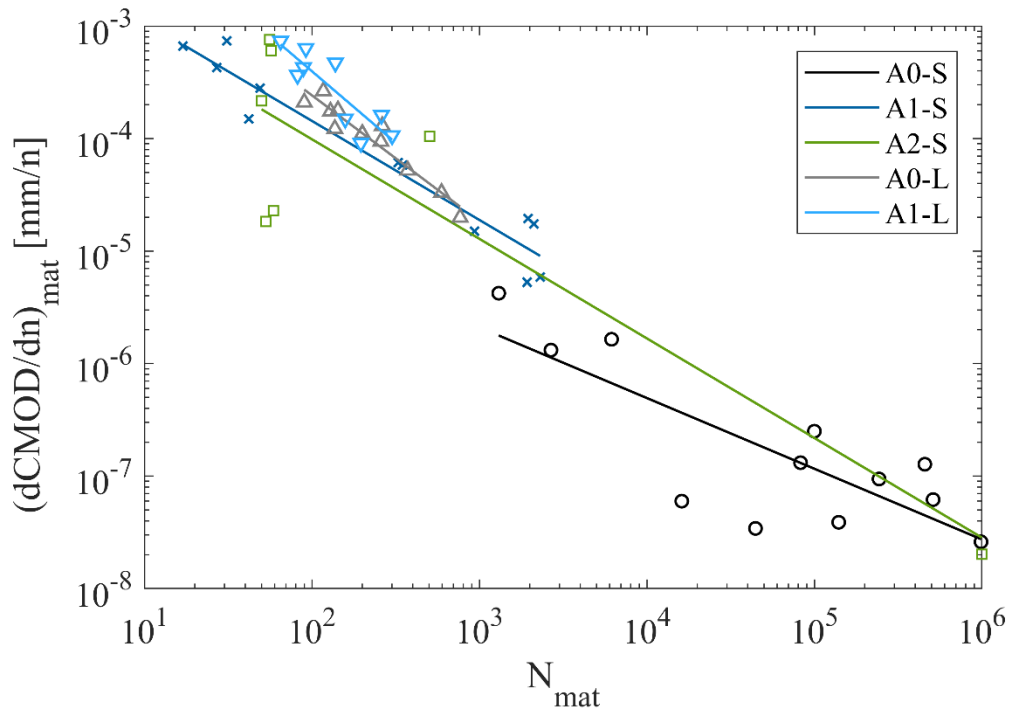


Figure 5.3-17. Secondary crack opening rate versus number of cycles, both associated with fatigue of uncracked concrete, in all series.

Several conclusions can be drawn from Figure 5.3-17. Overall, the regression lines of the SFRC series are similar, both in trend and position, to those of plain concrete. This indicates that the evolution of damage due to the fatigue of uncracked concrete is essentially the same in the two classes of concrete. Thus, it is corroborated that the presence of fibers hardly affects this type of fatigue.

With respect to the plain concrete series (in black and gray), it is noted that the considerable size effect observed is largely explained by the fact that the $dCMOD/dn$ is much smaller in the A0-S series. In other words, the damage inflicted by cyclic loading is slower in the smaller specimens, causing their fatigue life to be longer.

As for the straight lines of the series with 0.3% fibers (in blue), it can be seen that they are sensibly parallel, which means that the relationship between $dCMOD/dn$ and N follows the same proportion; that is, a certain increase in $dCMOD/dn$ produces the same decrease in N . Consequently, although in these series almost no size effect is observed, the secondary crack opening rate would explain the dispersion of the fatigue life results.

Regarding the A2-S series, no solid conclusions can be reached, since the sections of fatigue of uncracked concrete are very short, except for the specimen that exceeded the

survival limit, and the regression is not very good. Moreover, in A2-L series, this type of fatigue does not appear.

Third, the linear regressions between $dCMOD/dn$ and N corresponding to the fatigue of cracked concrete are included. Therefore, only results relative to the fiber-reinforced concrete series appear.

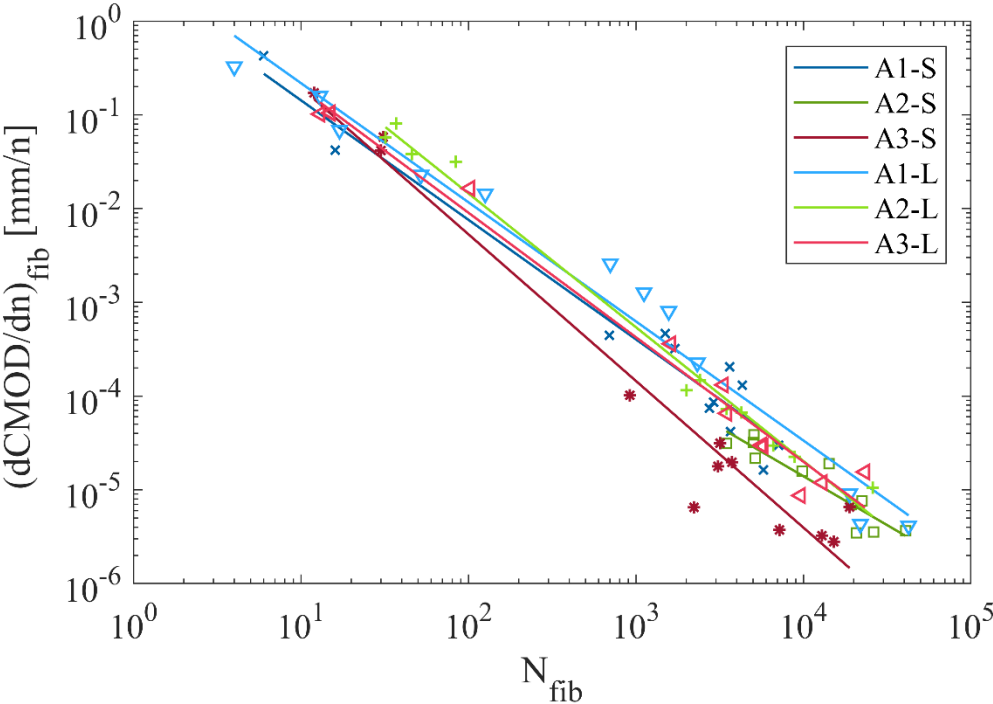


Figure 5.3-18. Secondary crack opening rate versus number of cycles, both associated with fatigue of cracked concrete, in all series.

Figure 5.3-18 reveals that all regression lines are practically coincident. Therefore, it is concluded that the relationship between $dCMOD/dn$ and N in fatigue of cracked concrete is independent of fiber content and specimen size. Evidently, this is demonstrated for the values used in this work, pending validation for wider ranges of fiber dosage and element dimensions.

Consequently, it is proved that the secondary crack opening rate is a very adequate parameter to explain the fatigue life of flexural fatigue in concrete.

With respect to the series with 0.6% fibers (in green), which are the only SFRC series in which there is a significant size effect, it can be seen that all the tests of A2-S series present reduced $dCMOD/dn$, less than 10^{-4} , and concentrated in the lower right part of the graph. Therefore, the secondary crack opening rate also explains the size effect observed in these series.

Finally, all the previous results are grouped in the following figure. The regression lines corresponding to fatigue of uncracked concrete are represented in dashed line, while those of cracked concrete are shown in solid line.

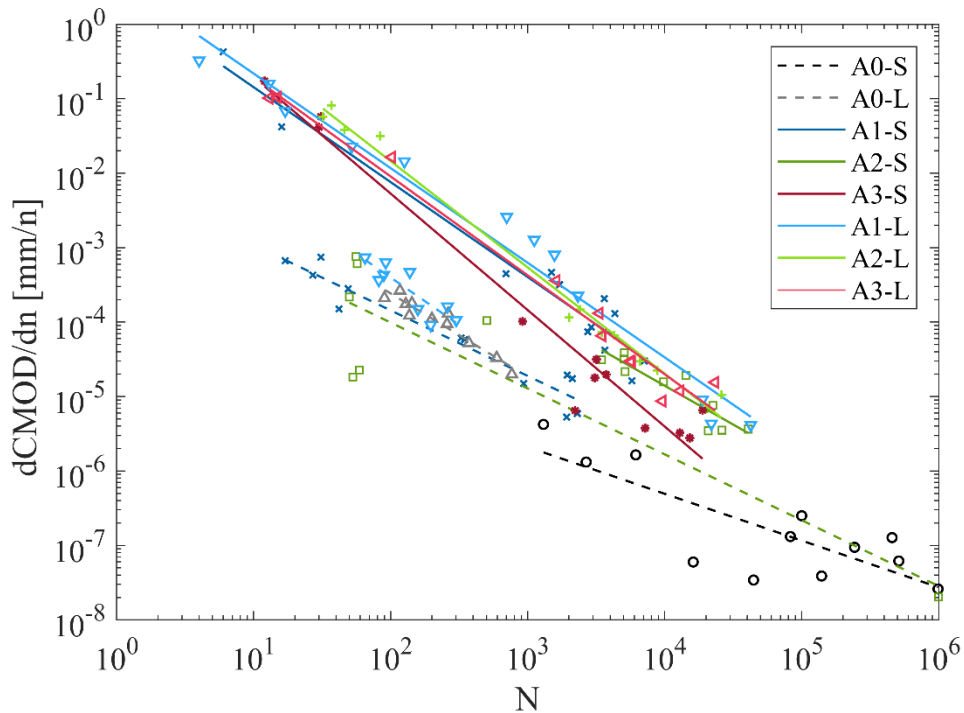


Figure 5.3-19. Secondary crack opening rate versus number of cycles in all series, distinguishing between fatigue of uncracked concrete (dashed line) and cracked concrete (solid line).

Figure 5.3-19 shows that the lines corresponding to the fatigue of cracked concrete are above those of fatigue of uncracked concrete; that is, the fatigue mechanism governed by the fibers damages the concrete faster than the one dominated by the matrix. This is to be expected, since the fibers provide much ductility, making the concrete admit large deformations, as can be seen in the CMOD vs N diagrams. Moreover, the difference between $(d\text{CMOD}/dn)_{\text{mat}}$ and $(d\text{CMOD}/dn)_{\text{fib}}$ is about one order of magnitude, remaining sensibly constant for the whole range of N observed. This is the same conclusion reached by Germano et al. [54], who performed flexural fatigue tests on plain concrete specimens and SFRC pre-cracked specimens with 0.5% and 1.0% fibers.

6 CONCLUSIONS AND FUTURE LINES OF RESEARCH

This section presents the main conclusions of this research work, extracted from the previous chapter. The section is organized in such a way that each subsection addresses one of the general objectives.

The first objective is to study the influence of the dispersion of fiber distribution and orientation on the dispersion of the flexural fatigue response of fiber-reinforced concrete. In other words, the aim is to answer whether the stochastic arrangement of the fibers within the matrix (in terms of dispersion, position, orientation, etc.) is able to explain why the fatigue life in two a priori identical specimens can differ by several orders of magnitude. For this purpose, a good number of fatigue tests with the same load levels have been performed on identical specimens, with the same size and the same dosage and fiber content. In addition, this process has been repeated with three amounts of fibers (0.3%, 0.6% and 1.0%), so that it is possible to know if the effect of fibers on the dispersion of fatigue results changes depending on their content.

Consequently, the first subsection presents, from among the multiple fiber parameters that can be determined, those that prove to have a better correlation with fatigue results. Additionally, the proposed empirical formulas that allow estimating the fatigue life from these parameters are shown.

The second objective is analogous to the previous one since it is also based on explaining the dispersion in the fatigue response of concrete through a mesostructure component. In this case, the aim is to analyze the influence of the dispersion of the geometrical and morphological parameters of the pores on the dispersion of the fatigue response of plain concrete. Therefore, it is assumed that in this type of concrete, without fibers, the pores control to a certain extent the fracture process of the concrete. Equivalently, the aim is to find out whether the stochastic nature of the pore structure (in terms of total porosity, pore size, distribution, etc.) is able to explain why the number of cycles in two equal specimens can vary greatly. To this effect, numerous identical fatigue tests with the same load levels have been carried out on plain concrete specimens of the same size and dosage.

Therefore, the second subsection presents, among all the morphological parameters of the pores, those that are best related to the fatigue results. The empirical formulas proposed to estimate the fatigue life as a function of these parameters are also included.

Finally, the third objective is to study the size effect on the flexural fatigue strength of concrete, both plain and fiber-reinforced. That is, the aim is to check whether the size effect, which significantly affects many of the macroscopic responses of concrete, also affects fatigue. To this end, fatigue tests have been carried out on two different specimen sizes and with four different concrete dosages (plain and with 0.3%, 0.6% and 1.0% fibers). In this way, it can be determined whether the size effect in fatigue changes with the presence of fibers and their content.

Thus, the third subsection summarizes the most relevant conclusions regarding the size effect obtained from the fatigue results: N, CMOD versus N diagrams and secondary crack opening rate.

Finally, the fourth and last subsection describes the future lines of research that arise to answer the new questions derived from the results of this doctoral thesis.

6.1 Influence of fibers on the flexural fatigue response of SFRC

In order to study the influence of the fibers on the dispersion of fatigue results, the geometrical parameters of the fibers of all the specimens that were subsequently tested under fatigue were obtained by means of micro-computed tomography (microCT). Then, an attempt has been made to establish correlations between these parameters and the fatigue results. Three different concrete series have been studied, the only difference between them being the fiber content: A1-S with 0.3%, A2-S with 0.6% and A3-S with 1.0%. The specimens were fatigue tested under the same relative stress levels: between 16% and 80% of their corresponding static flexural strength.

In first place, the fibers located in the central region of the specimens, around the mid-span section, have been analyzed, since this is the one that has the greatest influence on the fatigue response. Different parameters related to their orientation and spatial distribution have been obtained. Those that have shown to have a better correlation with the fatigue results are the relative density of fibers crossing the crack plane ($\rho_{\text{fib,rel}}$), the average

efficiency index in the Z-axis (normal to the crack plane) ($ei_{z,m}$) and the median fiber height ($Y_{cdg,50\%}$).

The relative density of fibers passing through the mid-span section, where the crack occurs, is calculated as the quotient between the fiber density in a specimen and the average of the fiber density in the series to which that specimen belongs (depending on the case, A1-S, A2-S and A3-S).

The average efficiency index is calculated as the average of the cosines of the angles formed by the fibers with respect to the corresponding axis. Thus, it can take values between 0 and 1, where 0 would indicate that all fibers are orthogonal to that axis, and 1 that all are parallel. In the case of the Z axis, a higher value of $ei_{z,m}$ indicates that the fibers are more aligned with the longitudinal axis, and in principle better oriented to resist bending stresses.

The median fiber height is defined as the height with respect to the bottom face of the specimen (Y-coordinate in the local axes of the specimen) that divides the number of fibers in half, with 50% of the fibers being above, and vice versa. In this way, it is intended to know if a greater accumulation of fibers near the notch, i.e. in the highest part of the specimen (and, therefore, with a higher value of $Y_{cdg,50\%}$), where there are more tensile stresses and the fibers work more, leads to a longer fatigue life.

Linear regressions between these parameters and the total number of cycles, the latter in logarithmic scale, are shown below.

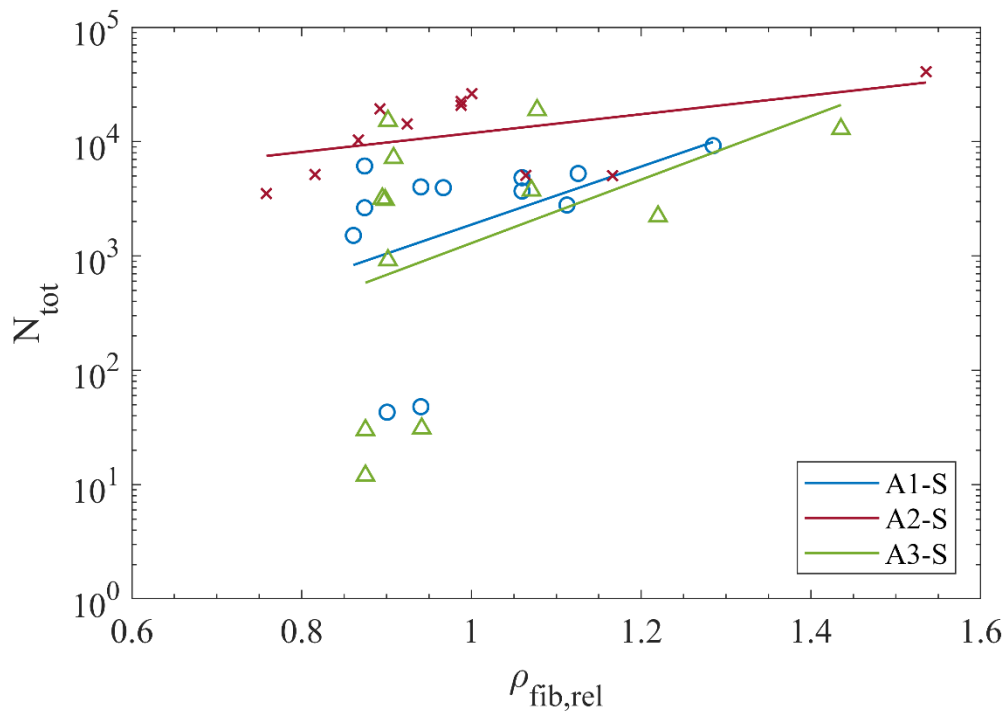


Figure 6.1-1. Linear regression between the relative density of fibers passing through the crack plane and the total number of cycles.

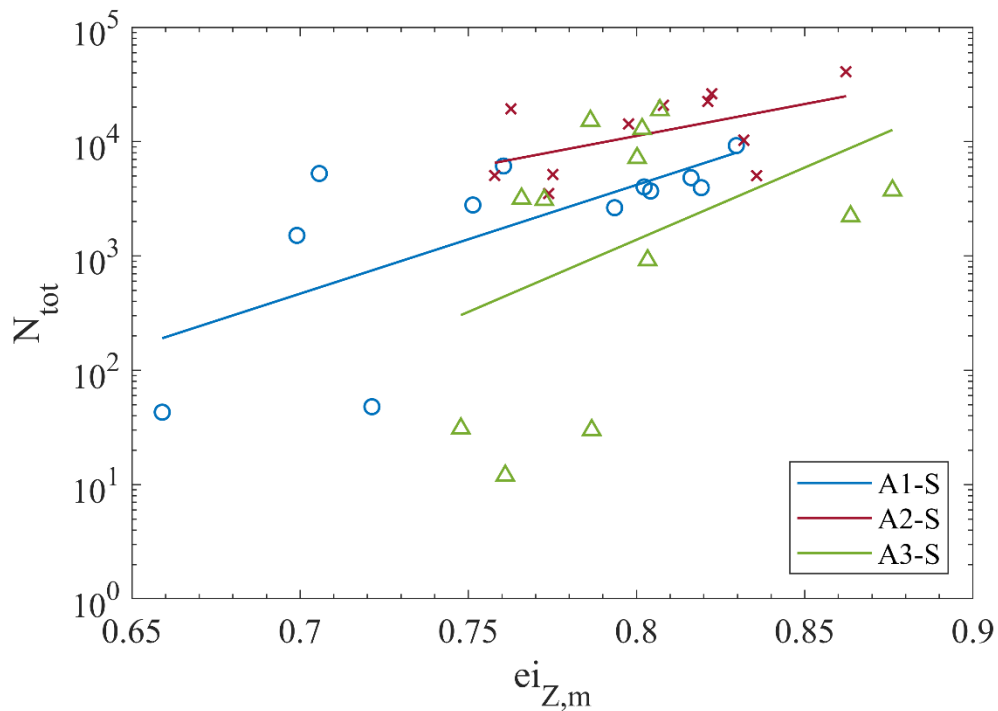


Figure 6.1-2. Linear regression between the average efficiency index on the Z-axis and the total number of cycles.

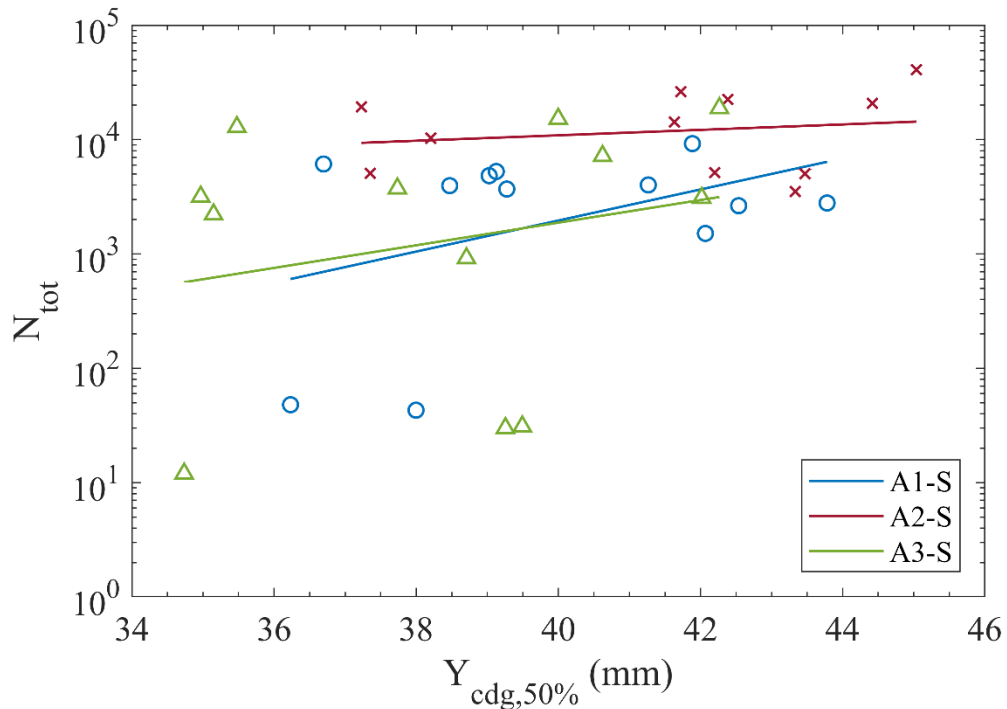


Figure 6.1-3. Linear regression between the median fiber height and the total number of cycles.

The figures show that, although in each series the specimens are apparently the same, the arrangement of the fibers shows an evident dispersion. And this randomness of the fibers influences the fatigue response. It is observed that with increasing relative fiber density (Figure 6.1-1), Z-axis efficiency index (Figure 6.1-2) and median fiber height (Figure 6.1-3), so does the fatigue life. The parameters with the highest coefficients of determination are the first two.

It should be noted that, in general terms, the correlations between fatigue response and the geometric parameters considered have low R^2 values. However, taking into account the magnitude of the problem of fatigue life dispersion, which is usually of several orders of magnitude, it is considered that the proposed parameters are reasonably predictive.

Consequently, multiple linear regression models are presented that consider these parameters simultaneously, so that the fit to the number of fatigue cycles is expected to improve. The formulas that allow estimating the fatigue life from the geometrical parameters of the fibers have the form (Eq. (6.1-1)):

$$\log N_{\text{tot}} = a_1 \cdot \rho_{\text{fib,rel}} + b_1 \cdot ei_{Z,m} + c_1 \cdot Y_{\text{cdg,50\%,rel}} + d_1 \tag{6.1-1}$$

The following table shows the values of the adjustment coefficients obtained from the model:

Table 6.1-1. Adjustment coefficients for estimation formulation of fatigue life.

	A1-S	A2-S	A3-S	General
a₁	0.82	0.43	2.89	0.79
b₁	8.01	4.65	7.78	7.47
c₁	6.11	-1.46*	13.46	7.82
d₁	-6.92	0.71	-12.87	-7.37

It can be found that the sign of the coefficients maintains the physical sense of the simple linear regressions shown above, except in the case of c_1 in the A2-S series, which accompanies $Y_{cdg,50\%}$. This is possibly because the correlation between median fiber height and fatigue life is particularly weak in this series (Figure 6.1-3).

The R^2 coefficients of determination of the multiple linear regression formulas or models are given below:

Table 6.1-2. R^2 coefficients of determination for the estimation formulation of fatigue life.

A1-S	A2-S	A3-S	General
0.56	0.33	0.41	0.38

Combining several significant fiber parameters, the fitting of the fatigue life improves substantially. The R^2 values remain relatively low, which proves that dispersion in fatigue is a complex issue, and where probably the influence of the mesostructure is not only reduced to the fibers. In any case, it is shown here that the random distribution of fibers in the concrete matrix plays a significant role in this phenomenon, laying the groundwork for multi-parametric studies of fibers and other components (pores, coarse aggregate, etc.), which together with larger samples, will allow more accurate prediction of the fatigue response of concrete.

Furthermore, to date, practically all the parameters that allow estimating the fatigue life, explaining the dispersion in a priori identical specimens, are macroscopic indicators of damage; that is, they require inflicting prior damage to the concrete. This is the case of the secondary crack opening rate $dCMOD/dn$, studied in depth in this work, or the increase in residual stiffness at each loading cycle Δk_i . Instead, here it is proposed to explain the dispersion in fatigue from the analysis of the intact mesostructure. Consequently, the

purpose of this thesis is to present a methodology that allows estimating the fatigue response of an element by studying only the mesostructure of its most critical zones.

6.2 Influence of pores on the flexural fatigue response of plain concrete

Similarly to the previous subsection, in order to study the incidence of the stochastic nature of the pores in the dispersion of the fatigue results, prior to these tests all the specimens were scanned with microCT, obtaining the geometrical parameters of the pores. Then, it has been tried to establish correlations between these parameters and the fatigue life. In this case, a single type of plain concrete (A0 series) has been used, whose dosage is the same as those of the SFRC series, but without fibers. All specimens were tested at fatigue between 16% and 80% of the average flexural strength.

The pores have only been studied in a subregion comprising in depth 20% of the central section (in the tensioned zone, next to the notch), in length 10 mm on each side of the notch and in width the entire section. Therefore, its dimensions are 12.5 x 20 x 75 mm. In addition, the minimum pore volume has been limited to 0.1 mm³, based on the fact that larger pores seem to have a higher incidence of fatigue failure.

Several parameters related to porosity, pore distribution and pore volume have been calculated. The most significant in relation to fatigue life are the mean neighborhood distance ($d_{nbh,m}$) and the maximum pore volume ($V_{por,max}$). The former is defined as the average of the distance from each pore to the nearest pore. A lower value of $d_{nbh,m}$ indicates that the pores are closer together, which could favor concrete fracture. As for the maximum pore volume, it is the volume greater than that of 90% of the pores. A higher value of $V_{por,max}$ indicates the presence of larger pores, introducing heterogeneities in the concrete matrix that could facilitate failure.

The linear regressions between these parameters and the logarithm of the number of cycles are shown below.

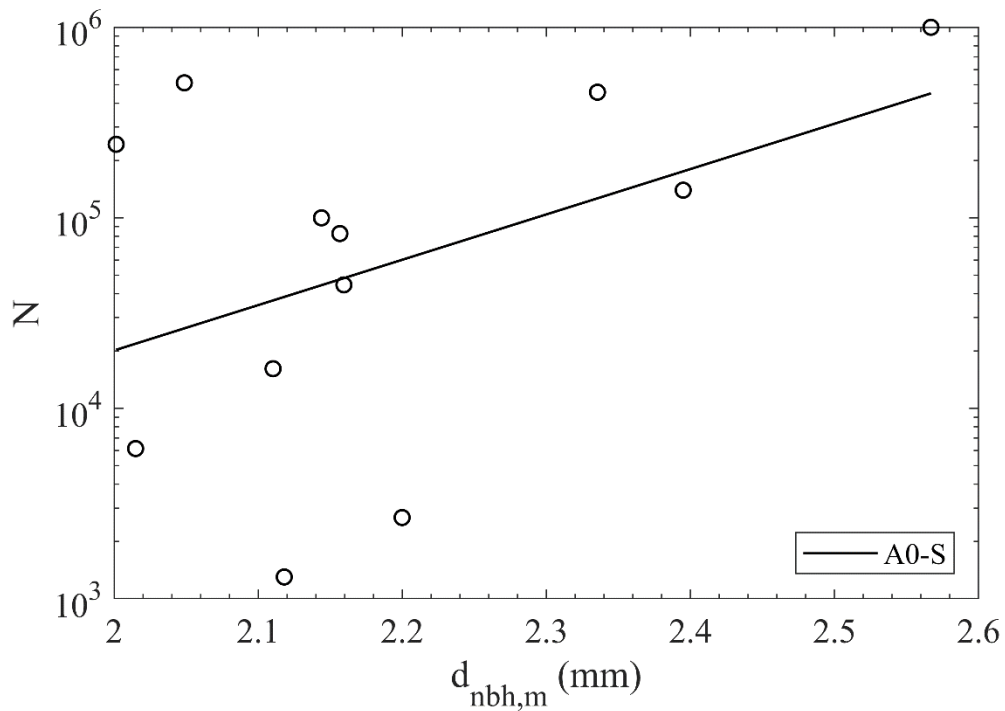


Figure 6.2-1. Linear regression between the mean neighborhood distance and the number of cycles.

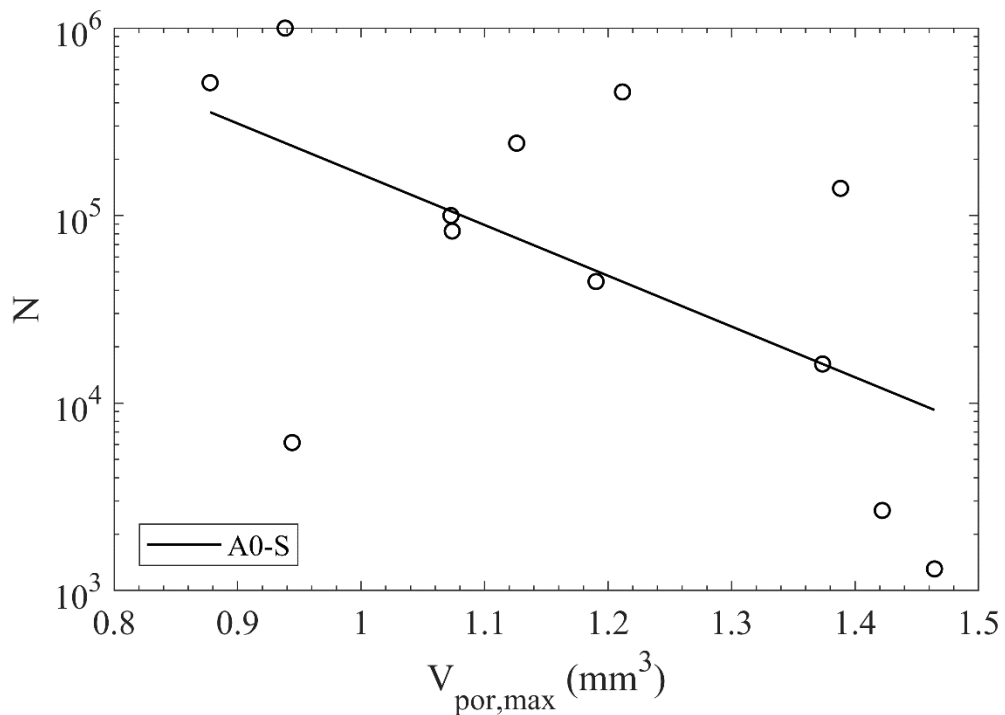


Figure 6.2-2. Linear regression between the maximum pore volume and the number of cycles.

The figures reveal that neither the spatial distribution of the pores nor the distribution of their sizes is the same in all specimens, even if they were manufactured at the same dosage and under the same conditions. This variation in the pore structure influences the

fatigue behavior. On the one hand, the larger the pore spacing (higher $d_{nbh,m}$), the higher the fatigue life (Figure 6.2-1). On the other hand, a higher proportion of large pores (higher $V_{por,max}$) results in a lower number of cycles (Figure 6.2-2). The linear regression is better with the maximum pore volume.

It can be noted that the correlations between the fatigue life and the geometric parameters calculated do not have particularly high R^2 values, which again confirms that the dispersion in fatigue is affected by multiple parameters and probably by various components of the concrete mesostructure. Nevertheless, Figure 6.2-1 and 6.2-2 show that there are clear trends.

To try to improve the fit to the number of cycles, a multiple linear regression model that takes into account the two parameters studied is proposed (Eq. (6.2-1)):

$$\log N = 3.54 \cdot d_{nbh,m} - 2.56 \cdot V_{por,max} \quad (6.2-1)$$

It is observed that the sign of the adjustment coefficients maintains the physical sense of the simple linear regressions shown above.

As for the coefficient of determination R^2 , its value is 0.58. When several pore parameters are considered together, the fatigue life fitting improves remarkably. However, R^2 is still relatively moderate, which may be due to the fact that other components that are important in the fracture process of plain concrete have not been taken into account; in particular, the coarse aggregate, the aggregate-paste interface and the smaller pores. In any case, it is clear that the randomness in the pore structure clearly influences the dispersion of the fatigue response of concrete. It is likely that complex models that take into account various parameters of several mesostructure elements can more accurately explain the variability in the fatigue behavior of concrete.

6.3 Size effect on the flexural fatigue behavior of concrete

To study the size effect on the flexural fatigue response of concrete, specimens of two different sizes were tested: 75x75x300 mm (S) and 150x150x600 mm (L). In order to make the results comparable, they have been subjected to the same relative stress levels: between 16% and 80% of their corresponding average value of the flexural static strength. In addition, 4 types of concrete were produced: plain (A0 series) and with 0.3%, 0.6% and 1.0% fibers (A1, A2 and A3 series, respectively).

The following figure compares the fit to the Weibull distribution function of the fatigue lives in the 8 series tested. This type of function proves to be very appropriate to describe statistically the fatigue results.

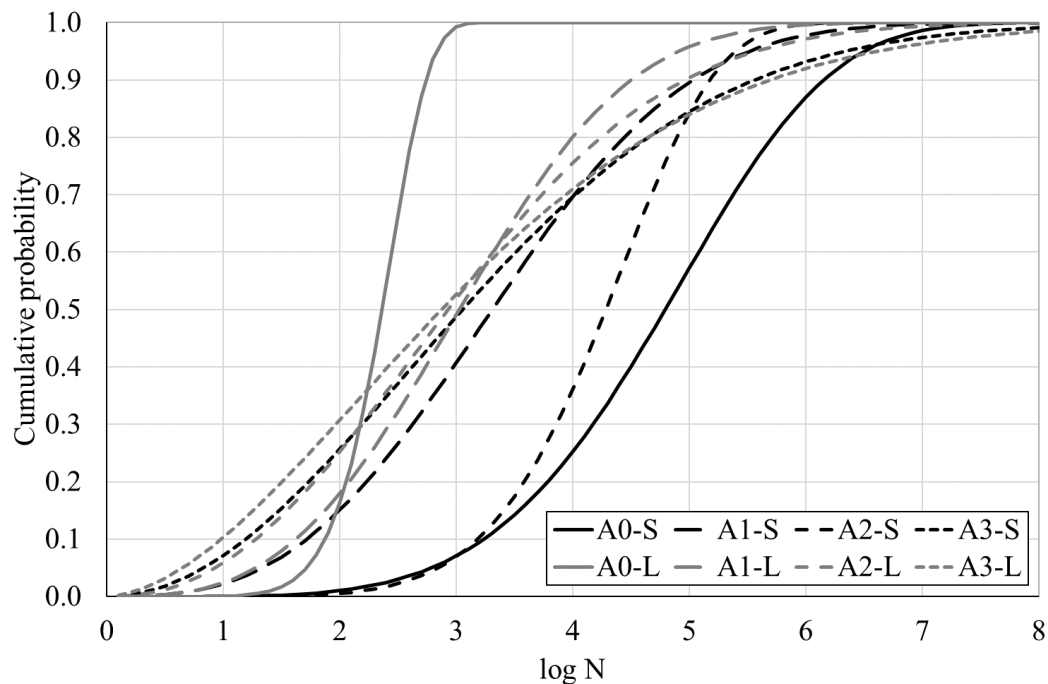


Figure 6.3-1. Weibull fitting of fatigue life of all series.

Figure 6.3-1 yields interesting conclusions. First, plain concrete has a strong size effect, with the fatigue life of small specimens being about 3 orders of magnitude higher than that of large specimens. Secondly, the addition of fibers reduces the size effect, or even cancels it out. This is especially noticeable in the series with contents of 0.3% and 1.0%. This phenomenon can be explained by the fact that fibers induce a much more ductile fracture behavior, and consequently less sensitive to specimen size. In this sense, it seems that the decrease in the size effect is not proportional to the fiber content, since the lower content (0.3%) is sufficient to practically eliminate it. Thirdly, it is observed that the addition of fibers does not necessarily improve the fatigue strength. In fact, it changes depending on the size, since in large specimens its effect is positive, and in small specimens, negative. Finally, the fiber content does not improve the fatigue life either, since all the SFRC curves, with the exception of the A2-S series, are very similar.

On the other hand, CMOD vs N diagrams are a very useful tool to understand the development of fatigue damage, explaining both the size effect (in this case, in the plain concrete series) and the dispersion of the results within each series. In fact, only the upper

envelope of the complete CMOD vs. N diagram is represented in these diagrams, i.e., the maximum CMOD in each cycle.

As a relevant aspect, it has been detected that in the specimens with the lowest fiber content, and to a lesser extent in the 0.6% specimens, two fatigue mechanisms appear: fatigue of uncracked concrete and fatigue of cracked concrete. The first is essentially the same as in plain concrete. It is governed by the matrix and develops at reduced CMOD values (< 0.1 mm). As for the second, it appears after the exhaustion of the previous one, when the concrete cracks and the bridging forces of the fibers start to mobilize. Due to the ductility contribution of the fibers, the CMODs are much higher, even up to several millimeters. Figure 6.3-2 shows the comparative CMOD vs N diagrams for A1-S and A1-L series. The fatigue of uncracked concrete is shown as a dashed line, and that of cracked concrete as a solid line.

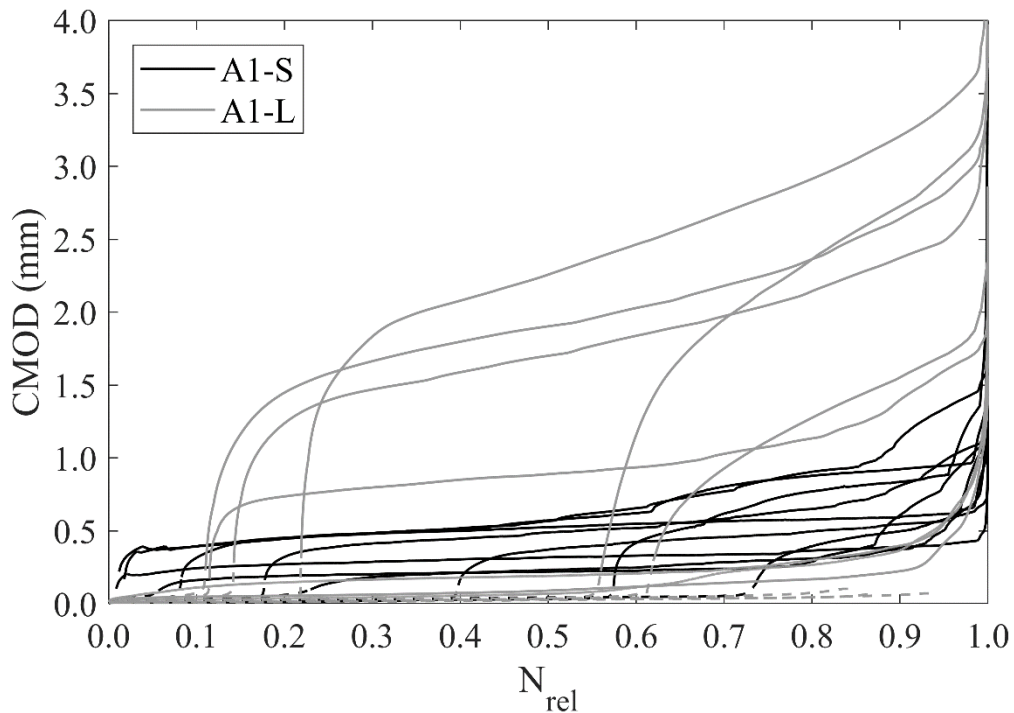


Figure 6.3-2. CMOD vs relative fatigue life in A1-S and A1-L series.

It can be seen that, when the concrete cracks, there is a sudden increase in CMOD; that is, a stiffness transition in which the stresses are shifted from being supported by the matrix to the fibers.

From the CMOD vs N diagrams, with their characteristic S-shape, it is observed that phase II, in which a stable damage progress occurs, has a great impact on the fatigue behavior. In particular, its slope, known as secondary crack opening rate ($d\text{CMOD}/dn$) is

closely related to fatigue life. This relationship is known in concrete fatigue as Sparks and Menzies' law [49], as it was originally posited by these researchers in compressive fatigue.

Linear regressions between $dCMOD/dn$ and N , both in logarithmic scale, are shown below. The results of all series are included, distinguishing between fatigue of uncracked and cracked concrete. This is because each fatigue mechanism presents its own S-curve, with its associated N and $dCMOD/dn$. It can be seen that series A1-S, A1-L and A2-S have two associated straight lines, since both types of fatigue appear in them.

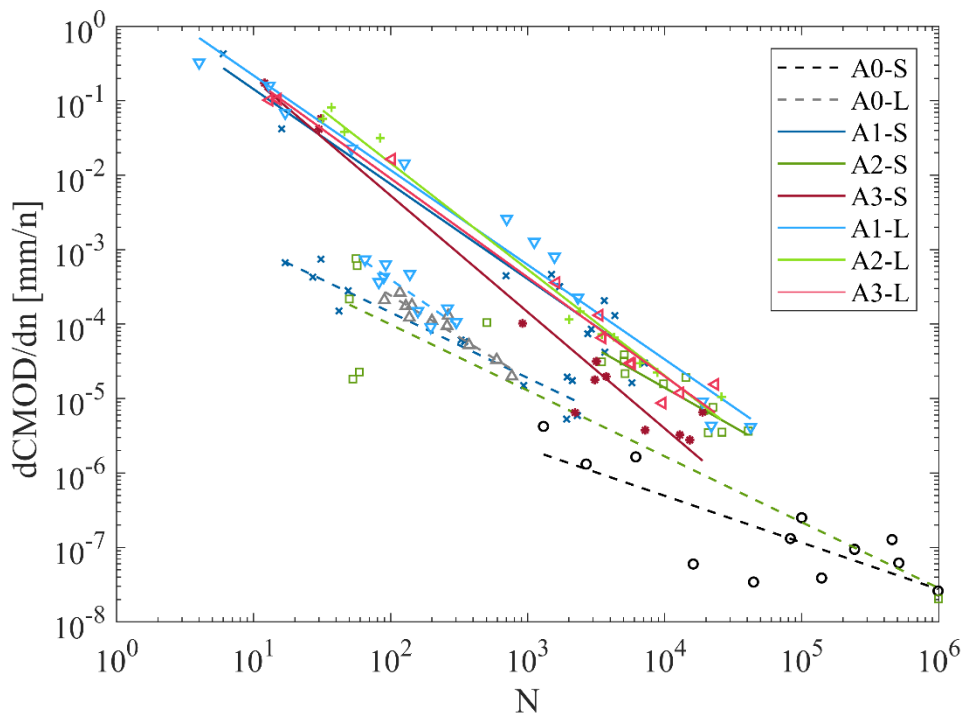


Figure 6.3-3. Secondary crack opening rate versus number of cycles in all series, distinguishing between fatigue of uncracked concrete (dashed line) and cracked concrete (solid line).

Some conclusions can be drawn from Figure 6.3-3. It is observed that in general terms the correlation between $dCMOD/dn$ and N is quite high. As for the plain concrete series (A0-S and A0-L), the size effect detected is explained by the fact that the secondary crack opening rate is lower in the smaller specimens; that is, the damage applied by the cyclic loads is slower. With respect to the fiber-reinforced concrete series, all the lines are practically coincident, indicating that the relationship between $dCMOD/dn$ and N in fatigue of cracked concrete is independent, not only of the fiber content, but also of the specimen size. Moreover, the certain size effect in the series with 0.6% fibers (A2-S and A2-L) is

again due to the fact that in large specimens the $dCMOD/dn$ are small, less than 10^{-4} , and concentrated in the lower right part of the graph.

Consequently, it is concluded that the secondary crack opening rate is a very adequate parameter to explain the fatigue life in general, and the size effect in particular.

Finally, it is observed that the regression lines associated with the fatigue of cracked concrete are above those of fatigue of uncracked concrete, from which it follows that the fiber-dominated fatigue mechanism damages concrete faster. Specifically, the difference between $(dCMOD/dn)_{mat}$ and $(dCMOD/dn)_{fib}$ is about one order of magnitude, remaining substantially constant over the whole range of N . This is to be expected, since the fibers provide ductility, causing the concrete to withstand higher deformations.

6.4 Future lines of research

From the conclusions presented in the previous subsections, new questions and lines of work arise in order to improve the knowledge of fatigue in concrete, both of the dispersion of the results and of the size effect. Some of them are presented below:

- With respect to the study of the influence of the mesostructure on the dispersion of fatigue results, to generate prediction models combining multiple geometric parameters, not only of one component (such as fibers or pores), but of several simultaneously. Develop parameters that represent the interaction between these components. In addition, extend the number of identical fatigue tests to have a better statistical understanding of the phenomenon.
- To analyze the double fatigue mechanism detected in some fiber-reinforced concrete series: under what conditions it occurs, how it affects the fatigue life, if there is any relationship between the two mechanisms, what happens in the stiffness transition zone where the load is transmitted from the matrix to the fibers, etc.
- Regarding the size effect on fatigue, to include more specimen sizes, fundamentally larger and closer to the real scale of the usual structural elements in civil works. Study whether the observed trends are maintained or change, taking into account different types of concrete (plain and fiber-reinforced concrete).
- Continuing with the size effect, to analyze whether other macroscopic damage parameters, in addition to $dCMOD/dn$, are able to predict the fatigue life of concrete. For example, in the $CMOD$ vs N diagrams, the $CMOD$ corresponding to the

onset of phase II ($CMOD_{II,i}$) or, when both fatigue mechanisms appear, the increase in CMOD occurring in the stiffness transition zone.

- Finally, to study the size effect as a particular case of the influence of the stochastic nature of the mesostructure on the fatigue response. For this purpose, the properties of the components (fibers, pores, etc.) must be compared in specimens of different dimensions, in order to finally analyze how their dispersion affects the dispersion of the fatigue life.

APPENDIX. FATIGUE TEST SHEETS

A0-S SERIES

FLEXURAL FATIGUE TEST

N.° 1

1. SERIES DATA

Code	A0-S
Size [mm]	75x75x300
Fibers [%]	0

3. SERIES STATIC STRENGTH

f_c [MPa]	107.13
$\sigma_{fl,max}$ [MPa]	8.21
$\sigma_{fl,LOP}$ [MPa]	8.21

5. FATIGUE TEST RESULTS

N_{mat}	1,000,000
N_{fib}	0
N_{tot}	1,000,000



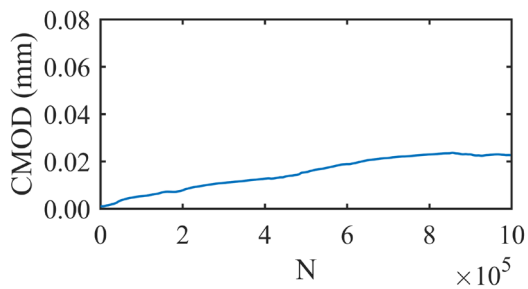
2. SPECIMEN DATA

Code	A0-S-4
Manufacture date	23/11/2020
Test date	25/04/2022

4. FATIGUE TEST PARAMETERS

Range	(16%-80%) · $\sigma_{fl,max}$
$\sigma_{max,fat}$ [MPa]	6.57
$\sigma_{min,fat}$ [MPa]	1.31

(dCMOD/dn)mat [mm/cycle]	2.60E-08
(dCMOD/dn)fib [mm/cycle]	



FLEXURAL FATIGUE TEST

N.° 2

1. SERIES DATA

Code	A0-S
Size [mm]	75x75x300
Fibers [%]	0

3. SERIES STATIC STRENGTH

f_c [MPa]	107.13
$\sigma_{fl,max}$ [MPa]	8.21
$\sigma_{fl,LOP}$ [MPa]	8.21

5. FATIGUE TEST RESULTS

N_{mat}	99,976
N_{fib}	0
N_{tot}	99,976



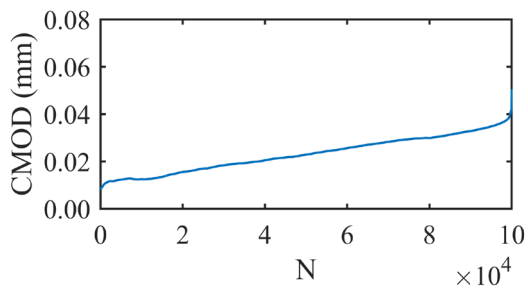
2. SPECIMEN DATA

Code	A0-S-6
Manufacture date	23/11/2020
Test date	29/04/2022

4. FATIGUE TEST PARAMETERS

Range	(16%-80%) · $\sigma_{fl,max}$
$\sigma_{max,fat}$ [MPa]	6.57
$\sigma_{min,fat}$ [MPa]	1.31

(dCMOD/dn)mat [mm/cycle]	2.50E-07
(dCMOD/dn)fib [mm/cycle]	



FLEXURAL FATIGUE TEST

N.° 3

1. SERIES DATA

Code	A0-S
Size [mm]	75x75x300
Fibers [%]	0

3. SERIES STATIC STRENGTH

f_c [MPa]	107.13
$\sigma_{fl,max}$ [MPa]	8.21
$\sigma_{fl,LOP}$ [MPa]	8.21

5. FATIGUE TEST RESULTS

N_{mat}	511,248
N_{fib}	0
N_{tot}	511,248

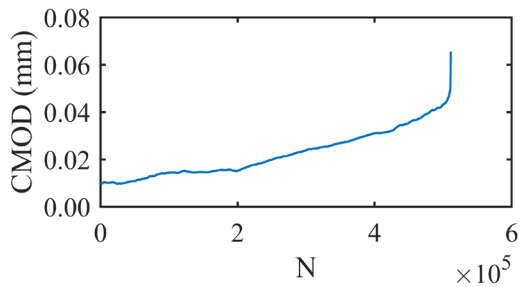
**2. SPECIMEN DATA**

Code	A0-S-7
Manufacture date	23/11/2020
Test date	04/05/2022

4. FATIGUE TEST PARAMETERS

Range	(16%-80%) · $\sigma_{fl,max}$
$\sigma_{max,fat}$ [MPa]	6.57
$\sigma_{min,fat}$ [MPa]	1.31

(dCMOD/dn)mat [mm/cycle]	6.18E-08
(dCMOD/dn)fib [mm/cycle]	

**FLEXURAL FATIGUE TEST**

N.° 4

1. SERIES DATA

Code	A0-S
Size [mm]	75x75x300
Fibers [%]	0

3. SERIES STATIC STRENGTH

f_c [MPa]	107.13
$\sigma_{fl,max}$ [MPa]	8.21
$\sigma_{fl,LOP}$ [MPa]	8.21

5. FATIGUE TEST RESULTS

N_{mat}	243,232
N_{fib}	0
N_{tot}	243,232

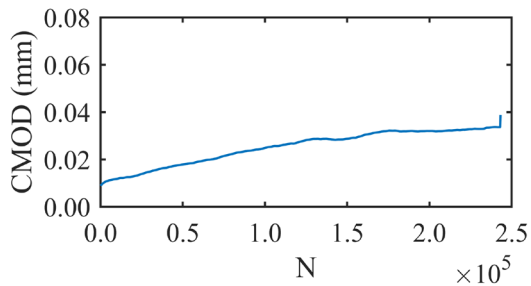
**2. SPECIMEN DATA**

Code	A0-S-8
Manufacture date	23/11/2020
Test date	04/05/2022

4. FATIGUE TEST PARAMETERS

Range	(16%-80%) · $\sigma_{fl,max}$
$\sigma_{max,fat}$ [MPa]	6.57
$\sigma_{min,fat}$ [MPa]	1.31

(dCMOD/dn)mat [mm/cycle]	9.42E-08
(dCMOD/dn)fib [mm/cycle]	



FLEXURAL FATIGUE TEST

N.° 5

1. SERIES DATA

Code	A0-S
Size [mm]	75x75x300
Fibers [%]	0

3. SERIES STATIC STRENGTH

f_c [MPa]	107.13
$\sigma_{fl,max}$ [MPa]	8.21
$\sigma_{fl,LOP}$ [MPa]	8.21

5. FATIGUE TEST RESULTS

N_{mat}	139,687
N_{fib}	0
N_{tot}	139,687



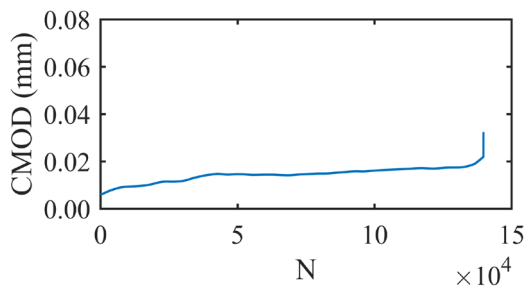
2. SPECIMEN DATA

Code	A0-S-9
Manufacture date	23/11/2020
Test date	05/05/2022

4. FATIGUE TEST PARAMETERS

Range	(16%-80%) · $\sigma_{fl,max}$
$\sigma_{max,fat}$ [MPa]	6.57
$\sigma_{min,fat}$ [MPa]	1.31

(dCMOD/dn)mat [mm/cycle]	3.88E-08
(dCMOD/dn)fib [mm/cycle]	



FLEXURAL FATIGUE TEST

N.° 6

1. SERIES DATA

Code	A0-S
Size [mm]	75x75x300
Fibers [%]	0

3. SERIES STATIC STRENGTH

f_c [MPa]	107.13
$\sigma_{fl,max}$ [MPa]	8.21
$\sigma_{fl,LOP}$ [MPa]	8.21

5. FATIGUE TEST RESULTS

N_{mat}	456,365
N_{fib}	0
N_{tot}	456,365



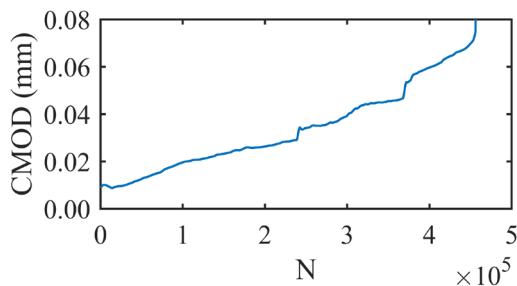
2. SPECIMEN DATA

Code	A0-S-10
Manufacture date	23/11/2020
Test date	05/05/2022

4. FATIGUE TEST PARAMETERS

Range	(16%-80%) · $\sigma_{fl,max}$
$\sigma_{max,fat}$ [MPa]	6.57
$\sigma_{min,fat}$ [MPa]	1.31

(dCMOD/dn)mat [mm/cycle]	1.27E-07
(dCMOD/dn)fib [mm/cycle]	



FLEXURAL FATIGUE TEST

N.° 7

1. SERIES DATA

Code	A0-S
Size [mm]	75x75x300
Fibers [%]	0

3. SERIES STATIC STRENGTH

f_c [MPa]	107.13
$\sigma_{fl,max}$ [MPa]	8.21
$\sigma_{fl,LOP}$ [MPa]	8.21

5. FATIGUE TEST RESULTS

N_{mat}	82,695
N_{fib}	0
N_{tot}	82,695



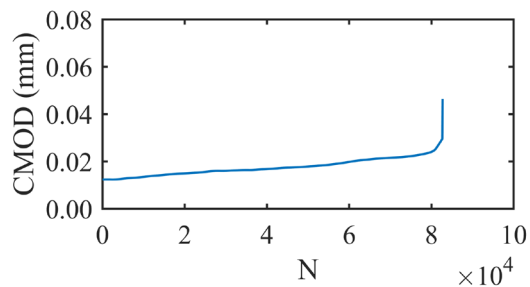
2. SPECIMEN DATA

Code	A0-S-11
Manufacture date	23/11/2020
Test date	10/05/2022

4. FATIGUE TEST PARAMETERS

Range	(16%-80%) · $\sigma_{fl,max}$
$\sigma_{max,fat}$ [MPa]	6.57
$\sigma_{min,fat}$ [MPa]	1.31

(dCMOD/dn)mat [mm/cycle]	1.31E-07
(dCMOD/dn)fib [mm/cycle]	



FLEXURAL FATIGUE TEST

N.° 8

1. SERIES DATA

Code	A0-S
Size [mm]	75x75x300
Fibers [%]	0

3. SERIES STATIC STRENGTH

f_c [MPa]	107.13
$\sigma_{fl,max}$ [MPa]	8.21
$\sigma_{fl,LOP}$ [MPa]	8.21

5. FATIGUE TEST RESULTS

N_{mat}	2,674
N_{fib}	0
N_{tot}	2,674



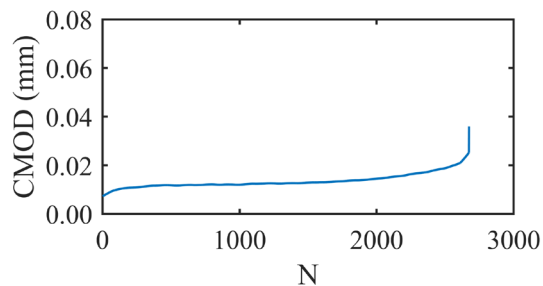
2. SPECIMEN DATA

Code	A0-S-12
Manufacture date	23/11/2020
Test date	10/05/2022

4. FATIGUE TEST PARAMETERS

Range	(16%-80%) · $\sigma_{fl,max}$
$\sigma_{max,fat}$ [MPa]	6.57
$\sigma_{min,fat}$ [MPa]	1.31

(dCMOD/dn)mat [mm/cycle]	1.32E-06
(dCMOD/dn)fib [mm/cycle]	



FLEXURAL FATIGUE TEST

N.° 9

1. SERIES DATA

Code	A0-S
Size [mm]	75x75x300
Fibers [%]	0

3. SERIES STATIC STRENGTH

f_c [MPa]	107.13
$\sigma_{fl,max}$ [MPa]	8.21
$\sigma_{fl,LOP}$ [MPa]	8.21

5. FATIGUE TEST RESULTS

N_{mat}	16,155
N_{fib}	0
N_{tot}	16,155



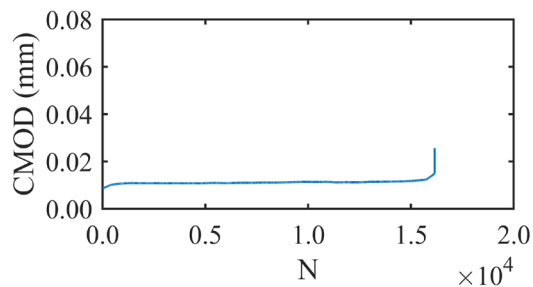
2. SPECIMEN DATA

Code	A0-S-13
Manufacture date	23/11/2020
Test date	11/05/2022

4. FATIGUE TEST PARAMETERS

Range	(16%-80%) · $\sigma_{fl,max}$
$\sigma_{max,fat}$ [MPa]	6.57
$\sigma_{min,fat}$ [MPa]	1.31

(dCMOD/dn)mat [mm/cycle]	5.98E-08
(dCMOD/dn)fib [mm/cycle]	



FLEXURAL FATIGUE TEST

N.° 10

1. SERIES DATA

Code	A0-S
Size [mm]	75x75x300
Fibers [%]	0

3. SERIES STATIC STRENGTH

f_c [MPa]	107.13
$\sigma_{fl,max}$ [MPa]	8.21
$\sigma_{fl,LOP}$ [MPa]	8.21

5. FATIGUE TEST RESULTS

N_{mat}	1,304
N_{fib}	0
N_{tot}	1,304



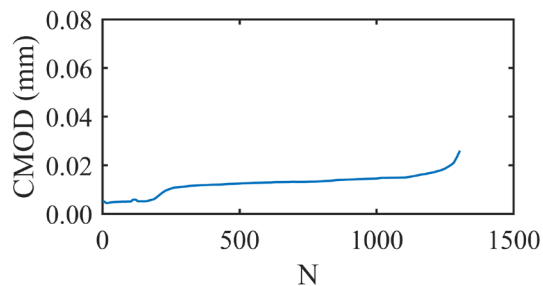
2. SPECIMEN DATA

Code	A0-S-14
Manufacture date	23/11/2020
Test date	11/05/2022

4. FATIGUE TEST PARAMETERS

Range	(16%-80%) · $\sigma_{fl,max}$
$\sigma_{max,fat}$ [MPa]	6.57
$\sigma_{min,fat}$ [MPa]	1.31

(dCMOD/dn)mat [mm/cycle]	4.22E-06
(dCMOD/dn)fib [mm/cycle]	



FLEXURAL FATIGUE TEST

N.° 11

1. SERIES DATA

Code	A0-S
Size [mm]	75x75x300
Fibers [%]	0

3. SERIES STATIC STRENGTH

f_c [MPa]	107.13
$\sigma_{fl,max}$ [MPa]	8.21
$\sigma_{fl,LOP}$ [MPa]	8.21

5. FATIGUE TEST RESULTS

N_{mat}	44,497
N_{fib}	0
N_{tot}	44,497



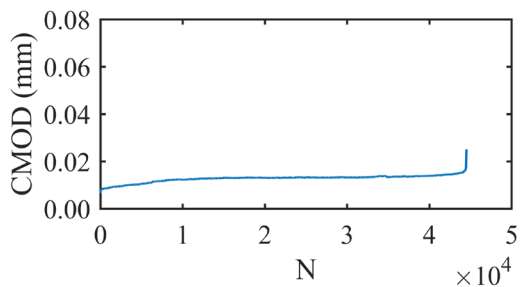
2. SPECIMEN DATA

Code	A0-S-15
Manufacture date	23/11/2020
Test date	11/05/2022

4. FATIGUE TEST PARAMETERS

Range	(16%-80%) · $\sigma_{fl,max}$
$\sigma_{max,fat}$ [MPa]	6.57
$\sigma_{min,fat}$ [MPa]	1.31

(dCMOD/dn)mat [mm/cycle]	3.42E-08
(dCMOD/dn)fib [mm/cycle]	



FLEXURAL FATIGUE TEST

N.° 12

1. SERIES DATA

Code	A0-S
Size [mm]	75x75x300
Fibers [%]	0

3. SERIES STATIC STRENGTH

f_c [MPa]	107.13
$\sigma_{fl,max}$ [MPa]	8.21
$\sigma_{fl,LOP}$ [MPa]	8.21

5. FATIGUE TEST RESULTS

N_{mat}	6,153
N_{fib}	0
N_{tot}	6,153



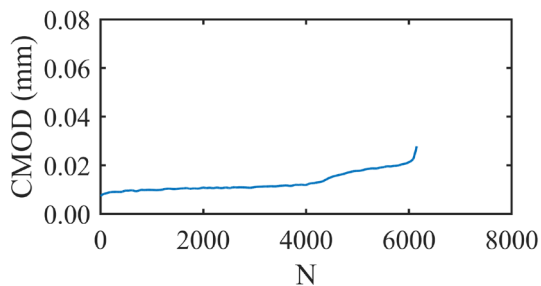
2. SPECIMEN DATA

Code	A0-S-16
Manufacture date	23/11/2020
Test date	11/05/2022

4. FATIGUE TEST PARAMETERS

Range	(16%-80%) · $\sigma_{fl,max}$
$\sigma_{max,fat}$ [MPa]	6.57
$\sigma_{min,fat}$ [MPa]	1.31

(dCMOD/dn)mat [mm/cycle]	1.64E-06
(dCMOD/dn)fib [mm/cycle]	



A1-S SERIES

FLEXURAL FATIGUE TEST

N.° 13

1. SERIES DATA

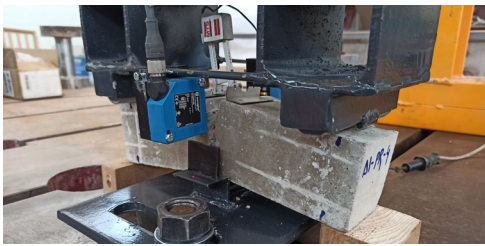
Code	A1-S
Size [mm]	75x75x300
Fibers [%]	0.3

3. SERIES STATIC STRENGTH

f_c [MPa]	106.62
$\sigma_{fl,max}$ [MPa]	8.78
$\sigma_{fl,LOP}$ [MPa]	7.36

5. FATIGUE TEST RESULTS

N_{mat}	346
N_{fib}	5,775
N_{tot}	6,121

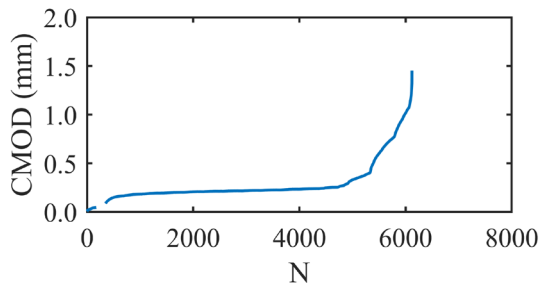
**2. SPECIMEN DATA**

Code	A1-S-4
Manufacture date	16/12/2020
Test date	04/04/2022

4. FATIGUE TEST PARAMETERS

Range	(16%-80%) · $\sigma_{fl,max}$
$\sigma_{max,fat}$ [MPa]	7.02
$\sigma_{min,fat}$ [MPa]	1.40

(dCMOD/dn)mat [mm/cycle]	5.83E-05
(dCMOD/dn)fib [mm/cycle]	1.63E-05

**FLEXURAL FATIGUE TEST**

N.° 14

1. SERIES DATA

Code	A1-S
Size [mm]	75x75x300
Fibers [%]	0.3

3. SERIES STATIC STRENGTH

f_c [MPa]	106.62
$\sigma_{fl,max}$ [MPa]	8.78
$\sigma_{fl,LOP}$ [MPa]	7.36

5. FATIGUE TEST RESULTS

N_{mat}	1,924
N_{fib}	2,914
N_{tot}	4,838

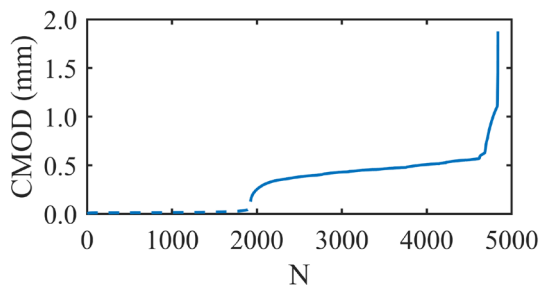
**2. SPECIMEN DATA**

Code	A1-S-5
Manufacture date	16/12/2020
Test date	04/04/2022

4. FATIGUE TEST PARAMETERS

Range	(16%-80%) · $\sigma_{fl,max}$
$\sigma_{max,fat}$ [MPa]	7.02
$\sigma_{min,fat}$ [MPa]	1.40

(dCMOD/dn)mat [mm/cycle]	5.29E-06
(dCMOD/dn)fib [mm/cycle]	8.58E-05



FLEXURAL FATIGUE TEST

N.° 15

1. SERIES DATA

Code	A1-S
Size [mm]	75x75x300
Fibers [%]	0.3

3. SERIES STATIC STRENGTH

f_c [MPa]	106.62
$\sigma_{fl,max}$ [MPa]	8.78
$\sigma_{fl,LOP}$ [MPa]	7.36

5. FATIGUE TEST RESULTS

N_{mat}	31
N_{fib}	3,665
N_{tot}	3,696

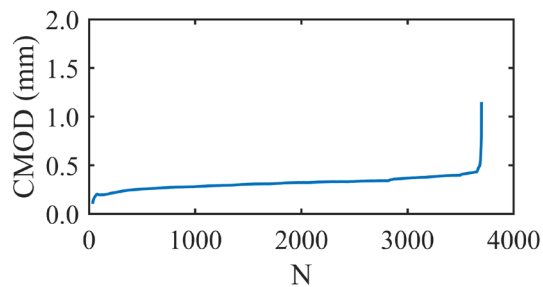
**2. SPECIMEN DATA**

Code	A1-S-6
Manufacture date	16/12/2020
Test date	04/04/2022

4. FATIGUE TEST PARAMETERS

Range	(16%-80%) · $\sigma_{fl,max}$
$\sigma_{max,fat}$ [MPa]	7.02
$\sigma_{min,fat}$ [MPa]	1.40

(dCMOD/dn)mat [mm/cycle]	7.41E-04
(dCMOD/dn)fib [mm/cycle]	4.18E-05

**FLEXURAL FATIGUE TEST**

N.° 16

1. SERIES DATA

Code	A1-S
Size [mm]	75x75x300
Fibers [%]	0.3

3. SERIES STATIC STRENGTH

f_c [MPa]	106.62
$\sigma_{fl,max}$ [MPa]	8.78
$\sigma_{fl,LOP}$ [MPa]	7.36

5. FATIGUE TEST RESULTS

N_{mat}	27
N_{fib}	16
N_{tot}	43

**2. SPECIMEN DATA**

Code	A1-S-7
Manufacture date	16/12/2020
Test date	05/04/2022

4. FATIGUE TEST PARAMETERS

Range	(16%-80%) · $\sigma_{fl,max}$
$\sigma_{max,fat}$ [MPa]	7.02
$\sigma_{min,fat}$ [MPa]	1.40

(dCMOD/dn)mat [mm/cycle]	4.27E-04
(dCMOD/dn)fib [mm/cycle]	4.19E-02

FLEXURAL FATIGUE TEST

N.° 17

1. SERIES DATA

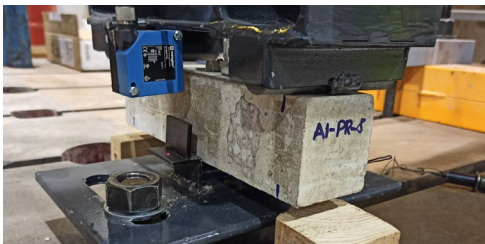
Code	A1-S
Size [mm]	75x75x300
Fibers [%]	0.3

3. SERIES STATIC STRENGTH

f_c [MPa]	106.62
$\sigma_{fl,max}$ [MPa]	8.78
$\sigma_{fl,LOP}$ [MPa]	7.36

5. FATIGUE TEST RESULTS

N_{mat}	1,948
N_{fib}	694
N_{tot}	2,642

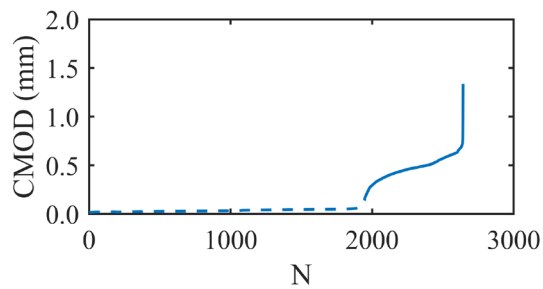
**2. SPECIMEN DATA**

Code	A1-S-8
Manufacture date	16/12/2020
Test date	05/04/2022

4. FATIGUE TEST PARAMETERS

Range	(16%-80%) · $\sigma_{fl,max}$
$\sigma_{max,fat}$ [MPa]	7.02
$\sigma_{min,fat}$ [MPa]	1.40

(dCMOD/dn)mat [mm/cycle]	1.94E-05
(dCMOD/dn)fib [mm/cycle]	4.46E-04

**FLEXURAL FATIGUE TEST**

N.° 18

1. SERIES DATA

Code	A1-S
Size [mm]	75x75x300
Fibers [%]	0.3

3. SERIES STATIC STRENGTH

f_c [MPa]	106.62
$\sigma_{fl,max}$ [MPa]	8.78
$\sigma_{fl,LOP}$ [MPa]	7.36

5. FATIGUE TEST RESULTS

N_{mat}	49
N_{fib}	2,742
N_{tot}	2,791

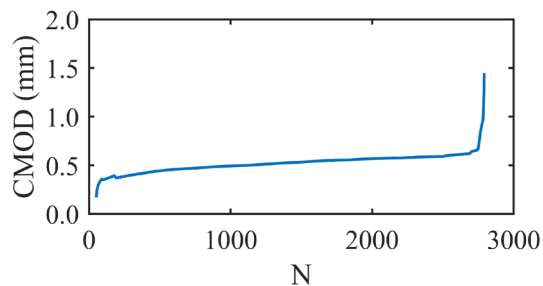
**2. SPECIMEN DATA**

Code	A1-S-9
Manufacture date	16/12/2020
Test date	05/04/2022

4. FATIGUE TEST PARAMETERS

Range	(16%-80%) · $\sigma_{fl,max}$
$\sigma_{max,fat}$ [MPa]	7.02
$\sigma_{min,fat}$ [MPa]	1.40

(dCMOD/dn)mat [mm/cycle]	2.82E-04
(dCMOD/dn)fib [mm/cycle]	7.43E-05



FLEXURAL FATIGUE TEST

N.° 19

1. SERIES DATA

Code	A1-S
Size [mm]	75x75x300
Fibers [%]	0.3

3. SERIES STATIC STRENGTH

f_c [MPa]	106.62
$\sigma_{fl,max}$ [MPa]	8.78
$\sigma_{fl,LOP}$ [MPa]	7.36

5. FATIGUE TEST RESULTS

N_{mat}	2,118
N_{fib}	7,108
N_{tot}	9,226



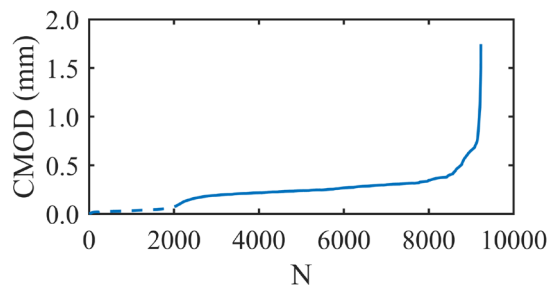
2. SPECIMEN DATA

Code	A1-S-10
Manufacture date	16/12/2020
Test date	06/04/2022

4. FATIGUE TEST PARAMETERS

Range	(16%-80%) · $\sigma_{fl,max}$
$\sigma_{max,fat}$ [MPa]	7.02
$\sigma_{min,fat}$ [MPa]	1.40

(dCMOD/dn)mat [mm/cycle]	1.74E-05
(dCMOD/dn)fib [mm/cycle]	3.00E-05



FLEXURAL FATIGUE TEST

N.° 20

1. SERIES DATA

Code	A1-S
Size [mm]	75x75x300
Fibers [%]	0.3

3. SERIES STATIC STRENGTH

f_c [MPa]	106.62
$\sigma_{fl,max}$ [MPa]	8.78
$\sigma_{fl,LOP}$ [MPa]	7.36

5. FATIGUE TEST RESULTS

N_{mat}	327
N_{fib}	3,629
N_{tot}	3,956



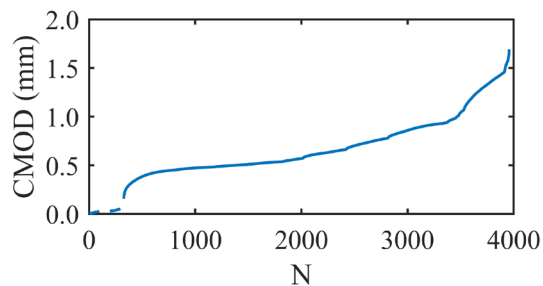
2. SPECIMEN DATA

Code	A1-S-11
Manufacture date	16/12/2020
Test date	06/04/2022

4. FATIGUE TEST PARAMETERS

Range	(16%-80%) · $\sigma_{fl,max}$
$\sigma_{max,fat}$ [MPa]	7.02
$\sigma_{min,fat}$ [MPa]	1.40

(dCMOD/dn)mat [mm/cycle]	6.12E-05
(dCMOD/dn)fib [mm/cycle]	2.06E-04



FLEXURAL FATIGUE TEST

N.° 21

1. SERIES DATA

Code	A1-S
Size [mm]	75x75x300
Fibers [%]	0.3

3. SERIES STATIC STRENGTH

f_c [MPa]	106.62
$\sigma_{fl,max}$ [MPa]	8.78
$\sigma_{fl,LOP}$ [MPa]	7.36

5. FATIGUE TEST RESULTS

N_{mat}	17
N_{fib}	1,495
N_{tot}	1,512



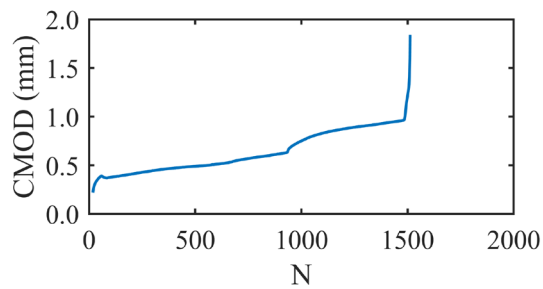
2. SPECIMEN DATA

Code	A1-S-12
Manufacture date	16/12/2020
Test date	06/04/2022

4. FATIGUE TEST PARAMETERS

Range	(16%-80%) · $\sigma_{fl,max}$
$\sigma_{max,fat}$ [MPa]	7.02
$\sigma_{min,fat}$ [MPa]	1.40

(dCMOD/dn)mat [mm/cycle]	6.64E-04
(dCMOD/dn)fib [mm/cycle]	4.64E-04



FLEXURAL FATIGUE TEST

N.° 22

1. SERIES DATA

Code	A1-S
Size [mm]	75x75x300
Fibers [%]	0.3

3. SERIES STATIC STRENGTH

f_c [MPa]	106.62
$\sigma_{fl,max}$ [MPa]	8.78
$\sigma_{fl,LOP}$ [MPa]	7.36

5. FATIGUE TEST RESULTS

N_{mat}	934
N_{fib}	4,329
N_{tot}	5,263



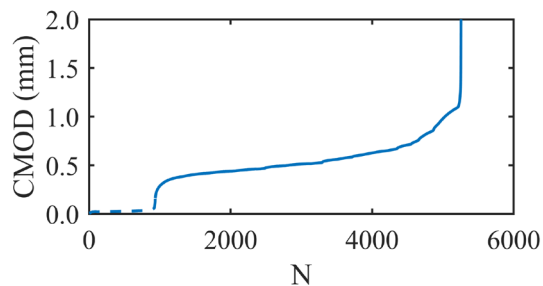
2. SPECIMEN DATA

Code	A1-S-13
Manufacture date	16/12/2020
Test date	06/04/2022

4. FATIGUE TEST PARAMETERS

Range	(16%-80%) · $\sigma_{fl,max}$
$\sigma_{max,fat}$ [MPa]	7.02
$\sigma_{min,fat}$ [MPa]	1.40

(dCMOD/dn)mat [mm/cycle]	1.50E-05
(dCMOD/dn)fib [mm/cycle]	1.30E-04



FLEXURAL FATIGUE TEST

N.° 23

1. SERIES DATA

Code	A1-S
Size [mm]	75x75x300
Fibers [%]	0.3

3. SERIES STATIC STRENGTH

f_c [MPa]	106.62
$\sigma_{fl,max}$ [MPa]	8.78
$\sigma_{fl,LOP}$ [MPa]	7.36

5. FATIGUE TEST RESULTS

N_{mat}	2,305
N_{fib}	1,710
N_{tot}	4,015

**2. SPECIMEN DATA**

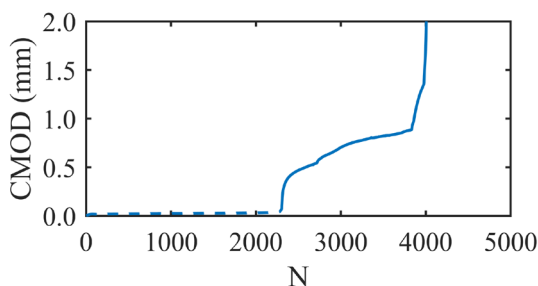
Code	A1-S-14
Manufacture date	16/12/2020
Test date	06/04/2022

4. FATIGUE TEST PARAMETERS

Range	(16%-80%) · $\sigma_{fl,max}$
$\sigma_{max,fat}$ [MPa]	7.02
$\sigma_{min,fat}$ [MPa]	1.40

(dCMOD/dn)mat [mm/cycle]	5.89E-06
--------------------------	----------

(dCMOD/dn)fib [mm/cycle]	3.20E-04
--------------------------	----------

**FLEXURAL FATIGUE TEST**

N.° 24

1. SERIES DATA

Code	A1-S
Size [mm]	75x75x300
Fibers [%]	0.3

3. SERIES STATIC STRENGTH

f_c [MPa]	106.62
$\sigma_{fl,max}$ [MPa]	8.78
$\sigma_{fl,LOP}$ [MPa]	7.36

5. FATIGUE TEST RESULTS

N_{mat}	42
N_{fib}	6
N_{tot}	48

**2. SPECIMEN DATA**

Code	A1-S-15
Manufacture date	16/12/2020
Test date	06/04/2022

4. FATIGUE TEST PARAMETERS

Range	(16%-80%) · $\sigma_{fl,max}$
$\sigma_{max,fat}$ [MPa]	7.02
$\sigma_{min,fat}$ [MPa]	1.40

(dCMOD/dn)mat [mm/cycle]	1.50E-04
--------------------------	----------

(dCMOD/dn)fib [mm/cycle]	4.28E-01
--------------------------	----------

A2-S SERIES

FLEXURAL FATIGUE TEST

N.° 25

1. SERIES DATA

Code	A2-S
Size [mm]	75x75x300
Fibers [%]	0.6

3. SERIES STATIC STRENGTH

f_c [MPa]	106.22
$\sigma_{fl,max}$ [MPa]	11.78
$\sigma_{fl,LOP}$ [MPa]	8.35

5. FATIGUE TEST RESULTS

N_{mat}	59
N_{fib}	3,463
N_{tot}	3,522

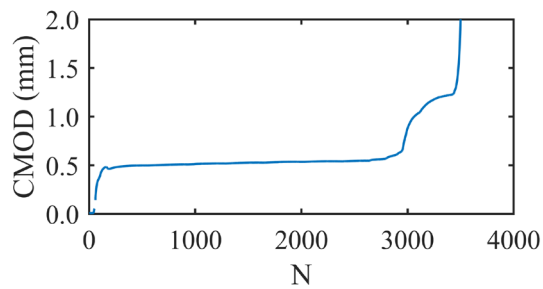
**2. SPECIMEN DATA**

Code	A2-S-4
Manufacture date	09/12/2020
Test date	13/04/2022

4. FATIGUE TEST PARAMETERS

Range	(16%-80%) · $\sigma_{fl,max}$
$\sigma_{max,fat}$ [MPa]	9.42
$\sigma_{min,fat}$ [MPa]	1.88

(dCMOD/dn)mat [mm/cycle]	2.28E-05
(dCMOD/dn)fib [mm/cycle]	3.11E-05

**FLEXURAL FATIGUE TEST**

N.° 26

1. SERIES DATA

Code	A2-S
Size [mm]	75x75x300
Fibers [%]	0.6

3. SERIES STATIC STRENGTH

f_c [MPa]	106.22
$\sigma_{fl,max}$ [MPa]	11.78
$\sigma_{fl,LOP}$ [MPa]	8.35

5. FATIGUE TEST RESULTS

N_{mat}	504
N_{fib}	9,812
N_{tot}	10,316

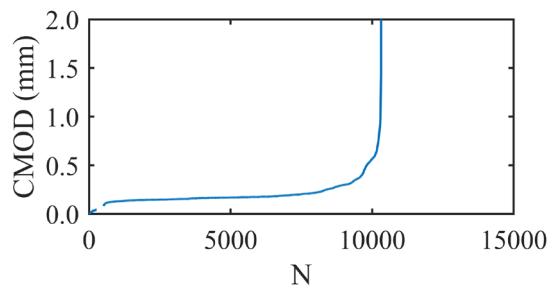
**2. SPECIMEN DATA**

Code	A2-S-5
Manufacture date	09/12/2020
Test date	13/04/2022

4. FATIGUE TEST PARAMETERS

Range	(16%-80%) · $\sigma_{fl,max}$
$\sigma_{max,fat}$ [MPa]	9.42
$\sigma_{min,fat}$ [MPa]	1.88

(dCMOD/dn)mat [mm/cycle]	1.05E-04
(dCMOD/dn)fib [mm/cycle]	1.58E-05



FLEXURAL FATIGUE TEST

N.° 27

1. SERIES DATA

Code	A2-S
Size [mm]	75x75x300
Fibers [%]	0.6

3. SERIES STATIC STRENGTH

f_c [MPa]	106.22
$\sigma_{fl,max}$ [MPa]	11.78
$\sigma_{fl,LOP}$ [MPa]	8.35

5. FATIGUE TEST RESULTS

N_{mat}	50
N_{fib}	40,808
N_{tot}	40,858

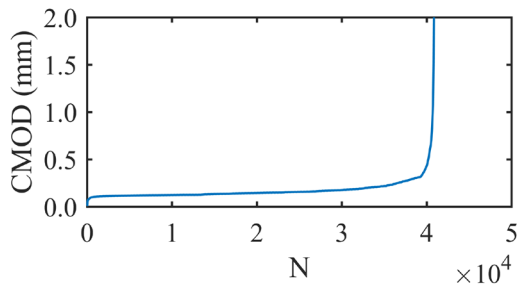
**2. SPECIMEN DATA**

Code	A2-S-6
Manufacture date	09/12/2020
Test date	13/04/2022

4. FATIGUE TEST PARAMETERS

Range	(16%-80%) · $\sigma_{fl,max}$
$\sigma_{max,fat}$ [MPa]	9.42
$\sigma_{min,fat}$ [MPa]	1.88

(dCMOD/dn)mat [mm/cycle]	2.17E-04
(dCMOD/dn)fib [mm/cycle]	3.65E-06

**FLEXURAL FATIGUE TEST**

N.° 28

1. SERIES DATA

Code	A2-S
Size [mm]	75x75x300
Fibers [%]	0.6

3. SERIES STATIC STRENGTH

f_c [MPa]	106.22
$\sigma_{fl,max}$ [MPa]	11.78
$\sigma_{fl,LOP}$ [MPa]	8.35

5. FATIGUE TEST RESULTS

N_{mat}	57
N_{fib}	19,344
N_{tot}	19,401

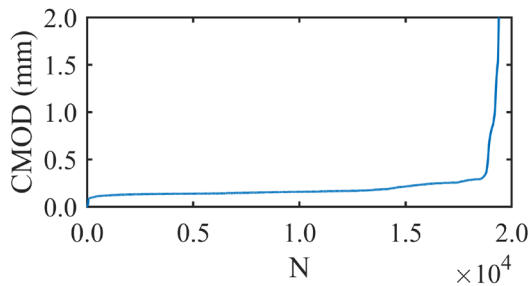
**2. SPECIMEN DATA**

Code	A2-S-7
Manufacture date	09/12/2020
Test date	13/04/2022

4. FATIGUE TEST PARAMETERS

Range	(16%-80%) · $\sigma_{fl,max}$
$\sigma_{max,fat}$ [MPa]	9.42
$\sigma_{min,fat}$ [MPa]	1.88

(dCMOD/dn)mat [mm/cycle]	6.06E-04
(dCMOD/dn)fib [mm/cycle]	6.95E-06



FLEXURAL FATIGUE TEST

N.° 29

1. SERIES DATA

Code	A2-S
Size [mm]	75x75x300
Fibers [%]	0.6

3. SERIES STATIC STRENGTH

f_c [MPa]	106.22
$\sigma_{fl,max}$ [MPa]	11.78
$\sigma_{fl,LOP}$ [MPa]	8.35

5. FATIGUE TEST RESULTS

N_{mat}	53
N_{fib}	22,428
N_{tot}	22,481

**2. SPECIMEN DATA**

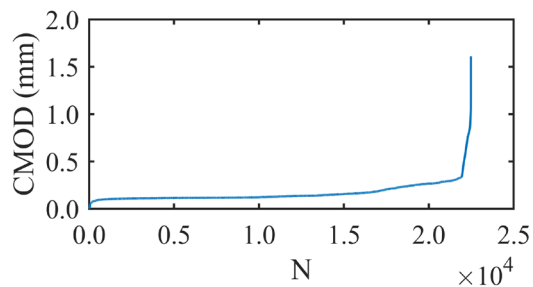
Code	A2-S-8
Manufacture date	09/12/2020
Test date	18/04/2022

4. FATIGUE TEST PARAMETERS

Range	(16%-80%) · $\sigma_{fl,max}$
$\sigma_{max,fat}$ [MPa]	9.42
$\sigma_{min,fat}$ [MPa]	1.88

(dCMOD/dn)mat [mm/cycle]	1.84E-05
--------------------------	----------

(dCMOD/dn)fib [mm/cycle]	7.62E-06
--------------------------	----------

**FLEXURAL FATIGUE TEST**

N.° 30

1. SERIES DATA

Code	A2-S
Size [mm]	75x75x300
Fibers [%]	0.6

3. SERIES STATIC STRENGTH

f_c [MPa]	106.22
$\sigma_{fl,max}$ [MPa]	11.78
$\sigma_{fl,LOP}$ [MPa]	8.35

5. FATIGUE TEST RESULTS

N_{mat}	1,000,000
N_{fib}	0
N_{tot}	1,000,000

**2. SPECIMEN DATA**

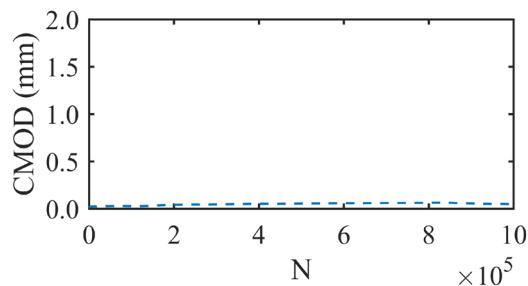
Code	A2-S-9
Manufacture date	09/12/2020
Test date	18/04/2022

4. FATIGUE TEST PARAMETERS

Range	(16%-80%) · $\sigma_{fl,max}$
$\sigma_{max,fat}$ [MPa]	9.42
$\sigma_{min,fat}$ [MPa]	1.88

(dCMOD/dn)mat [mm/cycle]	2.02E-08
--------------------------	----------

(dCMOD/dn)fib [mm/cycle]	
--------------------------	--



FLEXURAL FATIGUE TEST

N.° 31

1. SERIES DATA

Code	A2-S
Size [mm]	75x75x300
Fibers [%]	0.6

3. SERIES STATIC STRENGTH

f_c [MPa]	106.22
$\sigma_{fl,max}$ [MPa]	11.78
$\sigma_{fl,LOP}$ [MPa]	8.35

5. FATIGUE TEST RESULTS

N_{mat}	56
N_{fib}	26,252
N_{tot}	26,308



2. SPECIMEN DATA

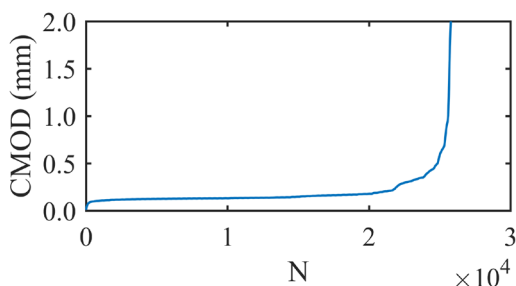
Code	A2-S-10
Manufacture date	09/12/2020
Test date	21/04/2022

4. FATIGUE TEST PARAMETERS

Range	(16%-80%) $\cdot \sigma_{fl,max}$
$\sigma_{max,fat}$ [MPa]	9.42
$\sigma_{min,fat}$ [MPa]	1.88

(dCMOD/dn)mat [mm/cycle] 7.59E-04

(dCMOD/dn)fib [mm/cycle] 3.55E-06



FLEXURAL FATIGUE TEST

N.° 32

1. SERIES DATA

Code	A2-S
Size [mm]	75x75x300
Fibers [%]	0.6

3. SERIES STATIC STRENGTH

f_c [MPa]	106.22
$\sigma_{fl,max}$ [MPa]	11.78
$\sigma_{fl,LOP}$ [MPa]	8.35

5. FATIGUE TEST RESULTS

N_{mat}	0
N_{fib}	20,746
N_{tot}	20,746



2. SPECIMEN DATA

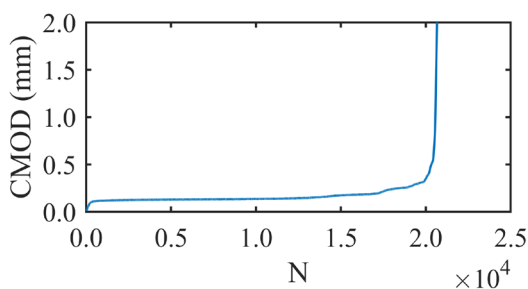
Code	A2-S-11
Manufacture date	09/12/2020
Test date	21/04/2022

4. FATIGUE TEST PARAMETERS

Range	(16%-80%) $\cdot \sigma_{fl,max}$
$\sigma_{max,fat}$ [MPa]	9.42
$\sigma_{min,fat}$ [MPa]	1.88

(dCMOD/dn)mat [mm/cycle]

(dCMOD/dn)fib [mm/cycle] 3.48E-06



FLEXURAL FATIGUE TEST

N.° 33

1. SERIES DATA

Code	A2-S
Size [mm]	75x75x300
Fibers [%]	0.6

3. SERIES STATIC STRENGTH

f_c [MPa]	106.22
$\sigma_{fl,max}$ [MPa]	11.78
$\sigma_{fl,LOP}$ [MPa]	8.35

5. FATIGUE TEST RESULTS

N_{mat}	0
N_{fib}	5,156
N_{tot}	5,156



2. SPECIMEN DATA

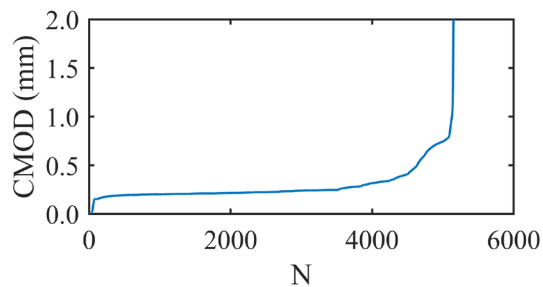
Code	A2-S-12
Manufacture date	09/12/2020
Test date	21/04/2022

4. FATIGUE TEST PARAMETERS

Range	(16%-80%) $\cdot \sigma_{fl,max}$
$\sigma_{max,fat}$ [MPa]	9.42
$\sigma_{min,fat}$ [MPa]	1.88

(dCMOD/dn)mat [mm/cycle]

(dCMOD/dn)fib [mm/cycle] 2.16E-05



FLEXURAL FATIGUE TEST

N.° 34

1. SERIES DATA

Code	A2-S
Size [mm]	75x75x300
Fibers [%]	0.6

3. SERIES STATIC STRENGTH

f_c [MPa]	106.22
$\sigma_{fl,max}$ [MPa]	11.78
$\sigma_{fl,LOP}$ [MPa]	8.35

5. FATIGUE TEST RESULTS

N_{mat}	0
N_{fib}	5,068
N_{tot}	5,068



2. SPECIMEN DATA

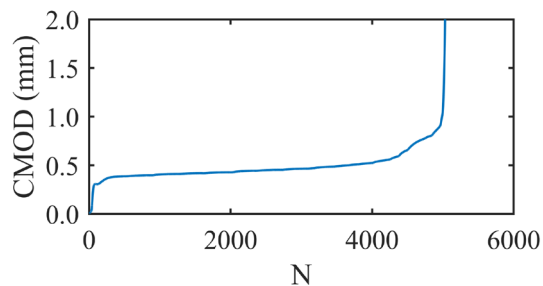
Code	A2-S-13
Manufacture date	09/12/2020
Test date	21/04/2022

4. FATIGUE TEST PARAMETERS

Range	(16%-80%) $\cdot \sigma_{fl,max}$
$\sigma_{max,fat}$ [MPa]	9.42
$\sigma_{min,fat}$ [MPa]	1.88

(dCMOD/dn)mat [mm/cycle]

(dCMOD/dn)fib [mm/cycle] 3.87E-05



FLEXURAL FATIGUE TEST

N.° 35

1. SERIES DATA

Code	A2-S
Size [mm]	75x75x300
Fibers [%]	0.6

3. SERIES STATIC STRENGTH

f_c [MPa]	106.22
$\sigma_{fl,max}$ [MPa]	11.78
$\sigma_{fl,LOP}$ [MPa]	8.35

5. FATIGUE TEST RESULTS

N_{mat}	0
N_{fib}	14,233
N_{tot}	14,233

**2. SPECIMEN DATA**

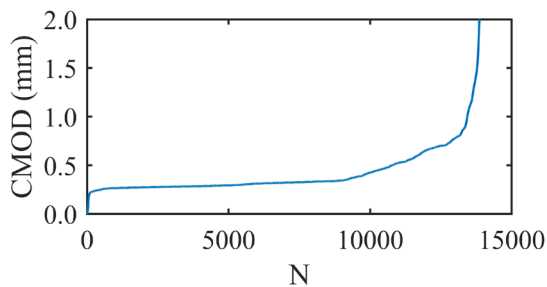
Code	A2-S-14
Manufacture date	09/12/2020
Test date	21/04/2022

4. FATIGUE TEST PARAMETERS

Range	(16%-80%) · $\sigma_{fl,max}$
$\sigma_{max,fat}$ [MPa]	9.42
$\sigma_{min,fat}$ [MPa]	1.88

(dCMOD/dn)mat [mm/cycle]

(dCMOD/dn)fib [mm/cycle] 1.90E-05

**FLEXURAL FATIGUE TEST**

N.° 36

1. SERIES DATA

Code	A2-S
Size [mm]	75x75x300
Fibers [%]	0.6

3. SERIES STATIC STRENGTH

f_c [MPa]	106.22
$\sigma_{fl,max}$ [MPa]	11.78
$\sigma_{fl,LOP}$ [MPa]	8.35

5. FATIGUE TEST RESULTS

N_{mat}	0
N_{fib}	5,024
N_{tot}	5,024

**2. SPECIMEN DATA**

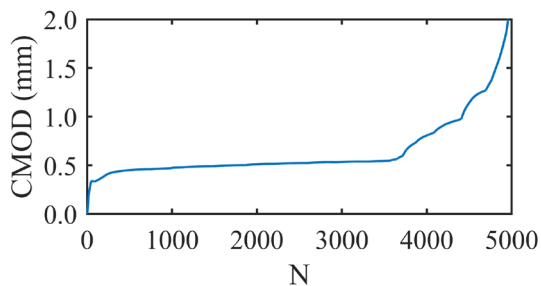
Code	A2-S-15
Manufacture date	09/12/2020
Test date	22/04/2022

4. FATIGUE TEST PARAMETERS

Range	(16%-80%) · $\sigma_{fl,max}$
$\sigma_{max,fat}$ [MPa]	9.42
$\sigma_{min,fat}$ [MPa]	1.88

(dCMOD/dn)mat [mm/cycle]

(dCMOD/dn)fib [mm/cycle] 3.18E-05



A3-S SERIES

FLEXURAL FATIGUE TEST

N.° 37

1. SERIES DATA

Code	A3-S
Size [mm]	75x75x300
Fibers [%]	1

3. SERIES STATIC STRENGTH

f_c [MPa]	107.17
$\sigma_{fl,max}$ [MPa]	19.65
$\sigma_{fl,LOP}$ [MPa]	10.45

5. FATIGUE TEST RESULTS

N_{mat}	0
N_{fib}	18,889
N_{tot}	18,889

**2. SPECIMEN DATA**

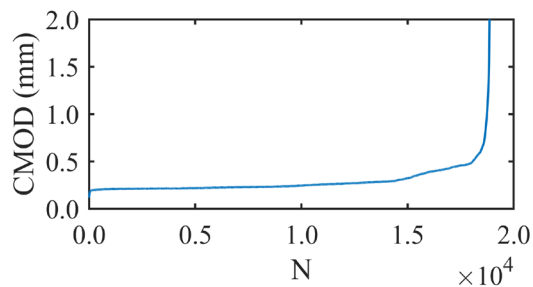
Code	A3-S-4
Manufacture date	30/11/2020
Test date	29/03/2022

4. FATIGUE TEST PARAMETERS

Range	(16%-80%) · $\sigma_{fl,max}$
$\sigma_{max,fat}$ [MPa]	15.72
$\sigma_{min,fat}$ [MPa]	3.14

(dCMOD/dn)mat [mm/cycle]

(dCMOD/dn)fib [mm/cycle] 6.55E-06

**FLEXURAL FATIGUE TEST**

N.° 38

1. SERIES DATA

Code	A3-S
Size [mm]	75x75x300
Fibers [%]	1

3. SERIES STATIC STRENGTH

f_c [MPa]	107.17
$\sigma_{fl,max}$ [MPa]	19.65
$\sigma_{fl,LOP}$ [MPa]	10.45

5. FATIGUE TEST RESULTS

N_{mat}	0
N_{fib}	918
N_{tot}	918

**2. SPECIMEN DATA**

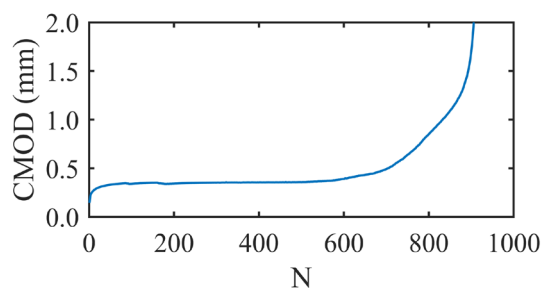
Code	A3-S-5
Manufacture date	30/11/2020
Test date	29/03/2022

4. FATIGUE TEST PARAMETERS

Range	(16%-80%) · $\sigma_{fl,max}$
$\sigma_{max,fat}$ [MPa]	15.72
$\sigma_{min,fat}$ [MPa]	3.14

(dCMOD/dn)mat [mm/cycle]

(dCMOD/dn)fib [mm/cycle] 1.02E-04



FLEXURAL FATIGUE TEST

N.° 39

1. SERIES DATA

Code	A3-S
Size [mm]	75x75x300
Fibers [%]	1

3. SERIES STATIC STRENGTH

f_c [MPa]	107.17
$\sigma_{fl,max}$ [MPa]	19.65
$\sigma_{fl,LOP}$ [MPa]	10.45

5. FATIGUE TEST RESULTS

N_{mat}	0
N_{fib}	30
N_{tot}	30

**2. SPECIMEN DATA**

Code	A3-S-6
Manufacture date	30/11/2020
Test date	30/03/2022

4. FATIGUE TEST PARAMETERS

Range	$(16\%-80\%) \cdot \sigma_{fl,max}$
$\sigma_{max,fat}$ [MPa]	15.72
$\sigma_{min,fat}$ [MPa]	3.14

(dCMOD/dn)mat [mm/cycle]

(dCMOD/dn)fib [mm/cycle] 4.17E-02

FLEXURAL FATIGUE TEST

N.° 40

1. SERIES DATA

Code	A3-S
Size [mm]	75x75x300
Fibers [%]	1

3. SERIES STATIC STRENGTH

f_c [MPa]	107.17
$\sigma_{fl,max}$ [MPa]	19.65
$\sigma_{fl,LOP}$ [MPa]	10.45

5. FATIGUE TEST RESULTS

N_{mat}	0
N_{fib}	3,176
N_{tot}	3,176

**2. SPECIMEN DATA**

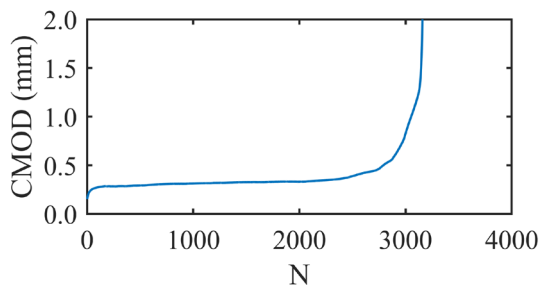
Code	A3-S-7
Manufacture date	30/11/2020
Test date	30/03/2022

4. FATIGUE TEST PARAMETERS

Range	$(16\%-80\%) \cdot \sigma_{fl,max}$
$\sigma_{max,fat}$ [MPa]	15.72
$\sigma_{min,fat}$ [MPa]	3.14

(dCMOD/dn)mat [mm/cycle]

(dCMOD/dn)fib [mm/cycle] 3.14E-05



FLEXURAL FATIGUE TEST

N.° 41

1. SERIES DATA

Code	A3-S
Size [mm]	75x75x300
Fibers [%]	1

3. SERIES STATIC STRENGTH

f_c [MPa]	107.17
$\sigma_{fl,max}$ [MPa]	19.65
$\sigma_{fl,LOP}$ [MPa]	10.45

5. FATIGUE TEST RESULTS

N_{mat}	0
N_{fib}	12,888
N_{tot}	12,888



2. SPECIMEN DATA

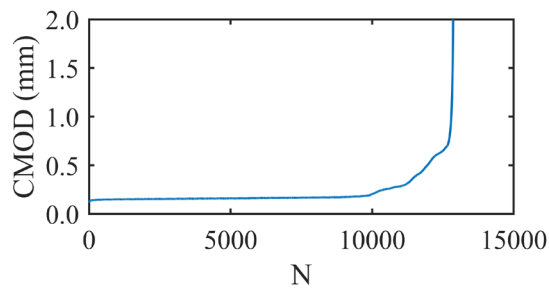
Code	A3-S-8
Manufacture date	30/11/2020
Test date	30/03/2022

4. FATIGUE TEST PARAMETERS

Range	(16%-80%) · $\sigma_{fl,max}$
$\sigma_{max,fat}$ [MPa]	15.72
$\sigma_{min,fat}$ [MPa]	3.14

(dCMOD/dn)mat [mm/cycle]

(dCMOD/dn)fib [mm/cycle] 3.26E-06



FLEXURAL FATIGUE TEST

N.° 42

1. SERIES DATA

Code	A3-S
Size [mm]	75x75x300
Fibers [%]	1

3. SERIES STATIC STRENGTH

f_c [MPa]	107.17
$\sigma_{fl,max}$ [MPa]	19.65
$\sigma_{fl,LOP}$ [MPa]	10.45

5. FATIGUE TEST RESULTS

N_{mat}	0
N_{fib}	7,195
N_{tot}	7,195



2. SPECIMEN DATA

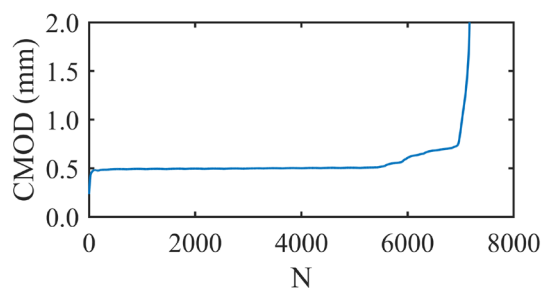
Code	A3-S-9
Manufacture date	30/11/2020
Test date	30/03/2022

4. FATIGUE TEST PARAMETERS

Range	(16%-80%) · $\sigma_{fl,max}$
$\sigma_{max,fat}$ [MPa]	15.72
$\sigma_{min,fat}$ [MPa]	3.14

(dCMOD/dn)mat [mm/cycle]

(dCMOD/dn)fib [mm/cycle] 3.74E-06



FLEXURAL FATIGUE TEST

N.° 43

1. SERIES DATA

Code	A3-S
Size [mm]	75x75x300
Fibers [%]	1

3. SERIES STATIC STRENGTH

f_c [MPa]	107.17
$\sigma_{fl,max}$ [MPa]	19.65
$\sigma_{fl,LOP}$ [MPa]	10.45

5. FATIGUE TEST RESULTS

N_{mat}	0
N_{fib}	15,225
N_{tot}	15,225

**2. SPECIMEN DATA**

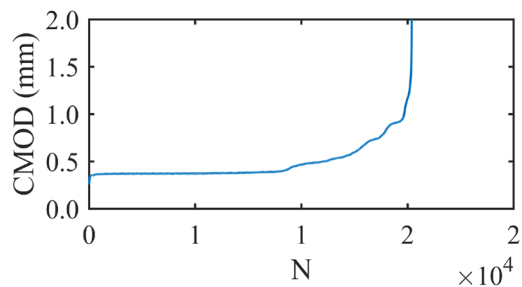
Code	A3-S-10
Manufacture date	30/11/2020
Test date	30/03/2022

4. FATIGUE TEST PARAMETERS

Range	(16%-80%) · $\sigma_{fl,max}$
$\sigma_{max,fat}$ [MPa]	15.72
$\sigma_{min,fat}$ [MPa]	3.14

(dCMOD/dn)mat [mm/cycle]

(dCMOD/dn)fib [mm/cycle] 2.78E-06

**FLEXURAL FATIGUE TEST**

N.° 44

1. SERIES DATA

Code	A3-S
Size [mm]	75x75x300
Fibers [%]	1

3. SERIES STATIC STRENGTH

f_c [MPa]	107.17
$\sigma_{fl,max}$ [MPa]	19.65
$\sigma_{fl,LOP}$ [MPa]	10.45

5. FATIGUE TEST RESULTS

N_{mat}	0
N_{fib}	12
N_{tot}	12

**2. SPECIMEN DATA**

Code	A3-S-11
Manufacture date	30/11/2020
Test date	30/03/2022

4. FATIGUE TEST PARAMETERS

Range	(16%-80%) · $\sigma_{fl,max}$
$\sigma_{max,fat}$ [MPa]	15.72
$\sigma_{min,fat}$ [MPa]	3.14

(dCMOD/dn)mat [mm/cycle]

(dCMOD/dn)fib [mm/cycle] 1.72E-01

FLEXURAL FATIGUE TEST

N.° 45

1. SERIES DATA

Code	A3-S
Size [mm]	75x75x300
Fibers [%]	1

3. SERIES STATIC STRENGTH

f_c [MPa]	107.17
$\sigma_{fl,max}$ [MPa]	19.65
$\sigma_{fl,LOP}$ [MPa]	10.45

5. FATIGUE TEST RESULTS

N_{mat}	0
N_{fib}	31
N_{tot}	31

**2. SPECIMEN DATA**

Code	A3-S-12
Manufacture date	30/11/2020
Test date	31/03/2022

4. FATIGUE TEST PARAMETERS

Range	$(16\%-80\%) \cdot \sigma_{fl,max}$
$\sigma_{max,fat}$ [MPa]	15.72
$\sigma_{min,fat}$ [MPa]	3.14

(dCMOD/dn)mat [mm/cycle]

(dCMOD/dn)fib [mm/cycle] 5.78E-02

FLEXURAL FATIGUE TEST

N.° 46

1. SERIES DATA

Code	A3-S
Size [mm]	75x75x300
Fibers [%]	1

3. SERIES STATIC STRENGTH

f_c [MPa]	107.17
$\sigma_{fl,max}$ [MPa]	19.65
$\sigma_{fl,LOP}$ [MPa]	10.45

5. FATIGUE TEST RESULTS

N_{mat}	0
N_{fib}	3,090
N_{tot}	3,090

**2. SPECIMEN DATA**

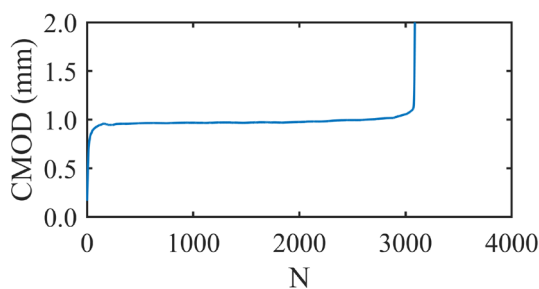
Code	A3-S-13
Manufacture date	30/11/2020
Test date	31/03/2022

4. FATIGUE TEST PARAMETERS

Range	$(16\%-80\%) \cdot \sigma_{fl,max}$
$\sigma_{max,fat}$ [MPa]	15.72
$\sigma_{min,fat}$ [MPa]	3.14

(dCMOD/dn)mat [mm/cycle]

(dCMOD/dn)fib [mm/cycle] 1.78E-05



FLEXURAL FATIGUE TEST

N.° 47

1. SERIES DATA

Code	A3-S
Size [mm]	75x75x300
Fibers [%]	1

3. SERIES STATIC STRENGTH

f_c [MPa]	107.17
$\sigma_{fl,max}$ [MPa]	19.65
$\sigma_{fl,LOP}$ [MPa]	10.45

5. FATIGUE TEST RESULTS

N_{mat}	0
N_{fib}	3,743
N_{tot}	3,743

**2. SPECIMEN DATA**

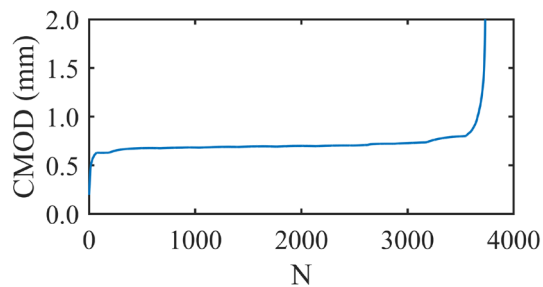
Code	A3-S-14
Manufacture date	30/11/2020
Test date	31/03/2022

4. FATIGUE TEST PARAMETERS

Range	(16%-80%) · $\sigma_{fl,max}$
$\sigma_{max,fat}$ [MPa]	15.72
$\sigma_{min,fat}$ [MPa]	3.14

(dCMOD/dn)mat [mm/cycle]

(dCMOD/dn)fib [mm/cycle] 1.97E-05

**FLEXURAL FATIGUE TEST**

N.° 48

1. SERIES DATA

Code	A3-S
Size [mm]	75x75x300
Fibers [%]	1

3. SERIES STATIC STRENGTH

f_c [MPa]	107.17
$\sigma_{fl,max}$ [MPa]	19.65
$\sigma_{fl,LOP}$ [MPa]	10.45

5. FATIGUE TEST RESULTS

N_{mat}	0
N_{fib}	2,219
N_{tot}	2,219

**2. SPECIMEN DATA**

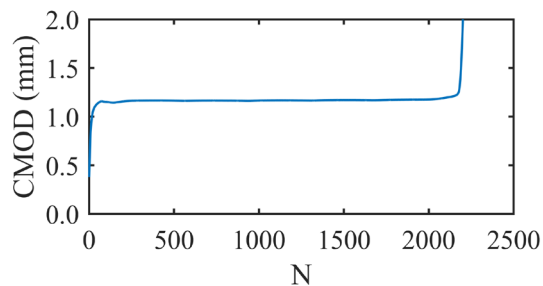
Code	A3-S-15
Manufacture date	30/11/2020
Test date	31/03/2022

4. FATIGUE TEST PARAMETERS

Range	(16%-80%) · $\sigma_{fl,max}$
$\sigma_{max,fat}$ [MPa]	15.72
$\sigma_{min,fat}$ [MPa]	3.14

(dCMOD/dn)mat [mm/cycle]

(dCMOD/dn)fib [mm/cycle] 6.49E-06



A0-L SERIES

FLEXURAL FATIGUE TEST

N.° 49

1. SERIES DATA

Code	A0-L
Size [mm]	150x150x600
Fibers [%]	0

3. SERIES STATIC STRENGTH

f_c [MPa]	107.13
$\sigma_{fl,max}$ [MPa]	5.23
$\sigma_{fl,LOP}$ [MPa]	5.23

5. FATIGUE TEST RESULTS

N_{mat}	767
N_{fib}	0
N_{tot}	767



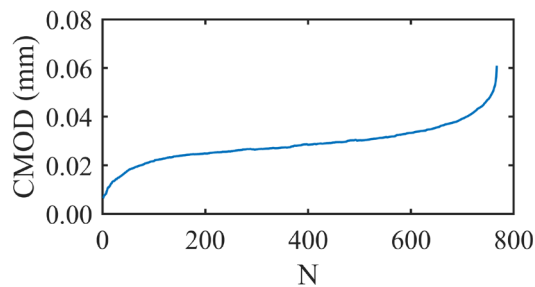
2. SPECIMEN DATA

Code	A0-L-1
Manufacture date	23/11/2020
Test date	30/06/2022

4. FATIGUE TEST PARAMETERS

Range	(16%-80%) · $\sigma_{fl,max}$
$\sigma_{max,fat}$ [MPa]	4.18
$\sigma_{min,fat}$ [MPa]	0.84

(dCMOD/dn)mat [mm/cycle]	1.99E-05
(dCMOD/dn)fib [mm/cycle]	



FLEXURAL FATIGUE TEST

N.° 50

1. SERIES DATA

Code	A0-L
Size [mm]	150x150x600
Fibers [%]	0

3. SERIES STATIC STRENGTH

f_c [MPa]	107.13
$\sigma_{fl,max}$ [MPa]	5.23
$\sigma_{fl,LOP}$ [MPa]	5.23

5. FATIGUE TEST RESULTS

N_{mat}	90
N_{fib}	0
N_{tot}	90



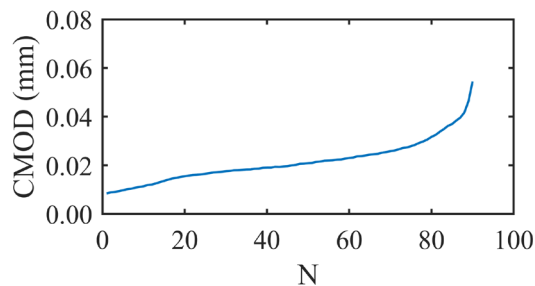
2. SPECIMEN DATA

Code	A0-L-2
Manufacture date	23/11/2020
Test date	30/06/2022

4. FATIGUE TEST PARAMETERS

Range	(16%-80%) · $\sigma_{fl,max}$
$\sigma_{max,fat}$ [MPa]	4.18
$\sigma_{min,fat}$ [MPa]	0.84

(dCMOD/dn)mat [mm/cycle]	2.11E-04
(dCMOD/dn)fib [mm/cycle]	



FLEXURAL FATIGUE TEST

N.° 51

1. SERIES DATA

Code	A0-L
Size [mm]	150x150x600
Fibers [%]	0

3. SERIES STATIC STRENGTH

f_c [MPa]	107.13
$\sigma_{fl,max}$ [MPa]	5.23
$\sigma_{fl,LOP}$ [MPa]	5.23

5. FATIGUE TEST RESULTS

N_{mat}	143
N_{fib}	0
N_{tot}	143



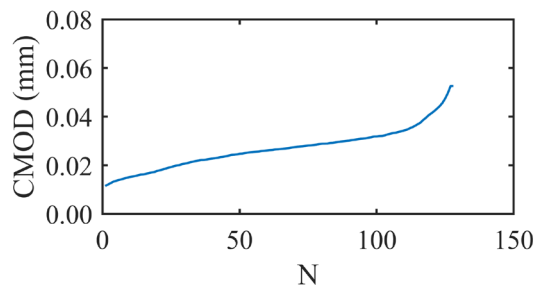
2. SPECIMEN DATA

Code	A0-L-3
Manufacture date	23/11/2020
Test date	29/06/2022

4. FATIGUE TEST PARAMETERS

Range	(16%-80%) · $\sigma_{fl,max}$
$\sigma_{max,fat}$ [MPa]	4.18
$\sigma_{min,fat}$ [MPa]	0.84

(dCMOD/dn)mat [mm/cycle]	1.79E-04
(dCMOD/dn)fib [mm/cycle]	



FLEXURAL FATIGUE TEST

N.° 52

1. SERIES DATA

Code	A0-L
Size [mm]	150x150x600
Fibers [%]	0

3. SERIES STATIC STRENGTH

f_c [MPa]	107.13
$\sigma_{fl,max}$ [MPa]	5.23
$\sigma_{fl,LOP}$ [MPa]	5.23

5. FATIGUE TEST RESULTS

N_{mat}	200
N_{fib}	0
N_{tot}	200



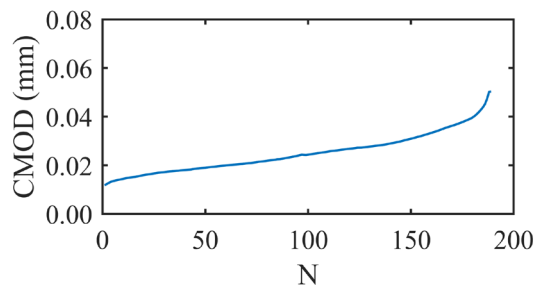
2. SPECIMEN DATA

Code	A0-L-5
Manufacture date	23/11/2020
Test date	30/06/2022

4. FATIGUE TEST PARAMETERS

Range	(16%-80%) · $\sigma_{fl,max}$
$\sigma_{max,fat}$ [MPa]	4.18
$\sigma_{min,fat}$ [MPa]	0.84

(dCMOD/dn)mat [mm/cycle]	1.10E-04
(dCMOD/dn)fib [mm/cycle]	



FLEXURAL FATIGUE TEST

N.° 53

1. SERIES DATA

Code	A0-L
Size [mm]	150x150x600
Fibers [%]	0

3. SERIES STATIC STRENGTH

f_c [MPa]	107.13
$\sigma_{fl,max}$ [MPa]	5.23
$\sigma_{fl,LOP}$ [MPa]	5.23

5. FATIGUE TEST RESULTS

N_{mat}	263
N_{fib}	0
N_{tot}	263



2. SPECIMEN DATA

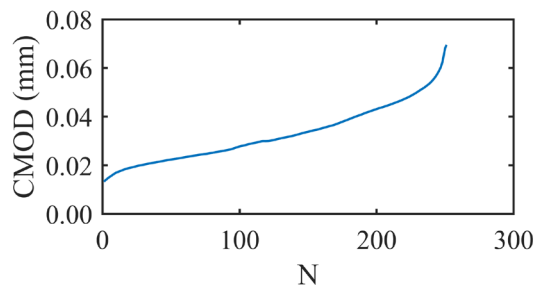
Code	A0-L-6
Manufacture date	23/11/2020
Test date	29/06/2022

4. FATIGUE TEST PARAMETERS

Range	(16%-80%) · $\sigma_{fl,max}$
$\sigma_{max,fat}$ [MPa]	4.18
$\sigma_{min,fat}$ [MPa]	0.84

(dCMOD/dn)mat [mm/cycle] 1.30E-04

(dCMOD/dn)fib [mm/cycle]



FLEXURAL FATIGUE TEST

N.° 54

1. SERIES DATA

Code	A0-L
Size [mm]	150x150x600
Fibers [%]	0

3. SERIES STATIC STRENGTH

f_c [MPa]	107.13
$\sigma_{fl,max}$ [MPa]	5.23
$\sigma_{fl,LOP}$ [MPa]	5.23

5. FATIGUE TEST RESULTS

N_{mat}	594
N_{fib}	0
N_{tot}	594



2. SPECIMEN DATA

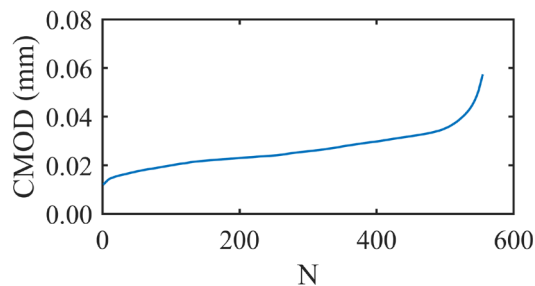
Code	A0-L-7
Manufacture date	23/11/2020
Test date	29/06/2022

4. FATIGUE TEST PARAMETERS

Range	(16%-80%) · $\sigma_{fl,max}$
$\sigma_{max,fat}$ [MPa]	4.18
$\sigma_{min,fat}$ [MPa]	0.84

(dCMOD/dn)mat [mm/cycle] 3.31E-05

(dCMOD/dn)fib [mm/cycle]



FLEXURAL FATIGUE TEST

N.° 55

1. SERIES DATA

Code	A0-L
Size [mm]	150x150x600
Fibers [%]	0

3. SERIES STATIC STRENGTH

f_c [MPa]	107.13
$\sigma_{fl,max}$ [MPa]	5.23
$\sigma_{fl,LOP}$ [MPa]	5.23

5. FATIGUE TEST RESULTS

N_{mat}	129
N_{fib}	0
N_{tot}	129



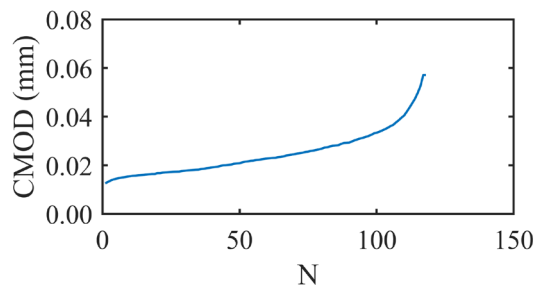
2. SPECIMEN DATA

Code	A0-L-9
Manufacture date	23/11/2020
Test date	30/06/2022

4. FATIGUE TEST PARAMETERS

Range	(16%-80%) · $\sigma_{fl,max}$
$\sigma_{max,fat}$ [MPa]	4.18
$\sigma_{min,fat}$ [MPa]	0.84

(dCMOD/dn)mat [mm/cycle]	1.75E-04
(dCMOD/dn)fib [mm/cycle]	



FLEXURAL FATIGUE TEST

N.° 56

1. SERIES DATA

Code	A0-L
Size [mm]	150x150x600
Fibers [%]	0

3. SERIES STATIC STRENGTH

f_c [MPa]	107.13
$\sigma_{fl,max}$ [MPa]	5.23
$\sigma_{fl,LOP}$ [MPa]	5.23

5. FATIGUE TEST RESULTS

N_{mat}	137
N_{fib}	0
N_{tot}	137



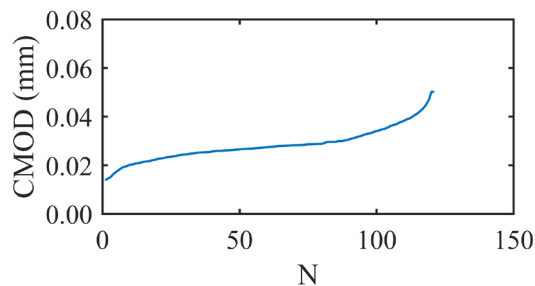
2. SPECIMEN DATA

Code	A0-L-10
Manufacture date	23/11/2020
Test date	29/06/2022

4. FATIGUE TEST PARAMETERS

Range	(16%-80%) · $\sigma_{fl,max}$
$\sigma_{max,fat}$ [MPa]	4.18
$\sigma_{min,fat}$ [MPa]	0.84

(dCMOD/dn)mat [mm/cycle]	1.22E-04
(dCMOD/dn)fib [mm/cycle]	



FLEXURAL FATIGUE TEST

N.° 57

1. SERIES DATA

Code	A0-L
Size [mm]	150x150x600
Fibers [%]	0

3. SERIES STATIC STRENGTH

f_c [MPa]	107.13
$\sigma_{fl,max}$ [MPa]	5.23
$\sigma_{fl,LOP}$ [MPa]	5.23

5. FATIGUE TEST RESULTS

N_{mat}	373
N_{fib}	0
N_{tot}	373



2. SPECIMEN DATA

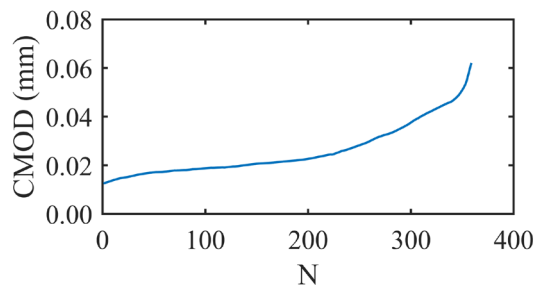
Code	A0-L-13
Manufacture date	23/11/2020
Test date	30/06/2022

4. FATIGUE TEST PARAMETERS

Range	(16%-80%) · $\sigma_{fl,max}$
$\sigma_{max,fat}$ [MPa]	4.18
$\sigma_{min,fat}$ [MPa]	0.84

(dCMOD/dn)mat [mm/cycle] 5.23E-05

(dCMOD/dn)fib [mm/cycle]



FLEXURAL FATIGUE TEST

N.° 58

1. SERIES DATA

Code	A0-L
Size [mm]	150x150x600
Fibers [%]	0

3. SERIES STATIC STRENGTH

f_c [MPa]	107.13
$\sigma_{fl,max}$ [MPa]	5.23
$\sigma_{fl,LOP}$ [MPa]	5.23

5. FATIGUE TEST RESULTS

N_{mat}	200
N_{fib}	0
N_{tot}	200



2. SPECIMEN DATA

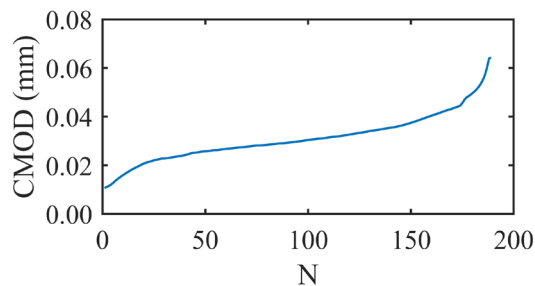
Code	A0-L-14
Manufacture date	23/11/2020
Test date	30/06/2022

4. FATIGUE TEST PARAMETERS

Range	(16%-80%) · $\sigma_{fl,max}$
$\sigma_{max,fat}$ [MPa]	4.18
$\sigma_{min,fat}$ [MPa]	0.84

(dCMOD/dn)mat [mm/cycle] 1.11E-04

(dCMOD/dn)fib [mm/cycle]



FLEXURAL FATIGUE TEST

N.° 59

1. SERIES DATA

Code	A0-L
Size [mm]	150x150x600
Fibers [%]	0

3. SERIES STATIC STRENGTH

f_c [MPa]	107.13
$\sigma_{fl,max}$ [MPa]	5.23
$\sigma_{fl,LOP}$ [MPa]	5.23

5. FATIGUE TEST RESULTS

N_{mat}	117
N_{fib}	0
N_{tot}	117

**2. SPECIMEN DATA**

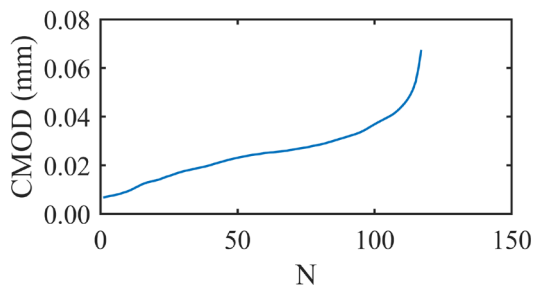
Code	A0-L-15
Manufacture date	23/11/2020
Test date	30/06/2022

4. FATIGUE TEST PARAMETERS

Range	(16%-80%) · $\sigma_{fl,max}$
$\sigma_{max,fat}$ [MPa]	4.18
$\sigma_{min,fat}$ [MPa]	0.84

(dCMOD/dn)mat [mm/cycle] 2.65E-04

(dCMOD/dn)fib [mm/cycle]

**FLEXURAL FATIGUE TEST**

N.° 60

1. SERIES DATA

Code	A0-L
Size [mm]	150x150x600
Fibers [%]	0

3. SERIES STATIC STRENGTH

f_c [MPa]	107.13
$\sigma_{fl,max}$ [MPa]	5.23
$\sigma_{fl,LOP}$ [MPa]	5.23

5. FATIGUE TEST RESULTS

N_{mat}	258
N_{fib}	0
N_{tot}	258

**2. SPECIMEN DATA**

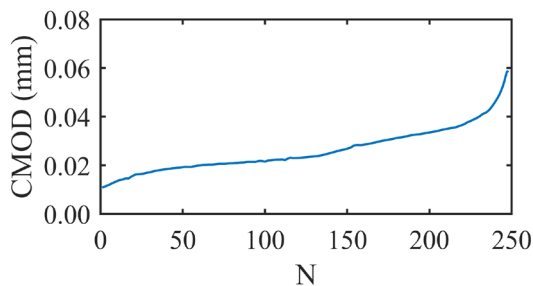
Code	A0-L-16
Manufacture date	23/11/2020
Test date	30/06/2022

4. FATIGUE TEST PARAMETERS

Range	(16%-80%) · $\sigma_{fl,max}$
$\sigma_{max,fat}$ [MPa]	4.18
$\sigma_{min,fat}$ [MPa]	0.84

(dCMOD/dn)mat [mm/cycle] 9.43E-05

(dCMOD/dn)fib [mm/cycle]



A1-L SERIES

FLEXURAL FATIGUE TEST

N.° 61

1. SERIES DATA

Code	A1-L
Size [mm]	150x150x600
Fibers [%]	0.3

3. SERIES STATIC STRENGTH

f_c [MPa]	106.62
$\sigma_{fl,max}$ [MPa]	5.93
$\sigma_{fl,LOP}$ [MPa]	5.22

5. FATIGUE TEST RESULTS

N_{mat}	301
N_{fib}	2,325
N_{tot}	2,626

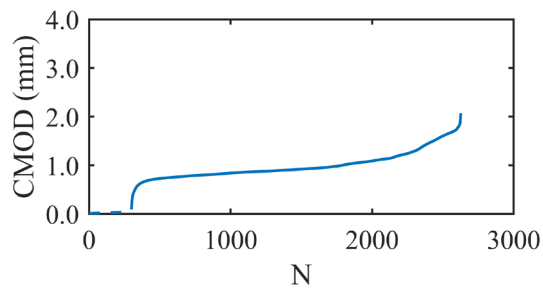
**2. SPECIMEN DATA**

Code	A1-L-2
Manufacture date	16/12/2020
Test date	27/06/2022

4. FATIGUE TEST PARAMETERS

Range	(16%-80%) · $\sigma_{fl,max}$
$\sigma_{max,fat}$ [MPa]	4.74
$\sigma_{min,fat}$ [MPa]	0.95

(dCMOD/dn)mat [mm/cycle]	1.06E-04
(dCMOD/dn)fib [mm/cycle]	2.26E-04

**FLEXURAL FATIGUE TEST**

N.° 62

1. SERIES DATA

Code	A1-L
Size [mm]	150x150x600
Fibers [%]	0.3

3. SERIES STATIC STRENGTH

f_c [MPa]	106.62
$\sigma_{fl,max}$ [MPa]	5.93
$\sigma_{fl,LOP}$ [MPa]	5.22

5. FATIGUE TEST RESULTS

N_{mat}	196
N_{fib}	703
N_{tot}	899

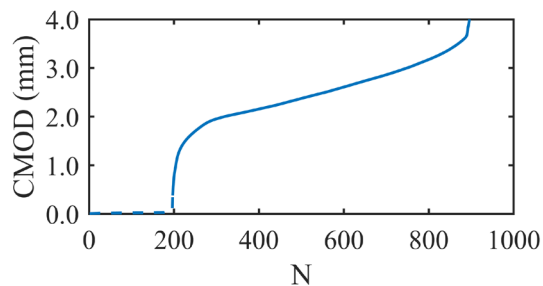
**2. SPECIMEN DATA**

Code	A1-L-3
Manufacture date	16/12/2020
Test date	28/06/2022

4. FATIGUE TEST PARAMETERS

Range	(16%-80%) · $\sigma_{fl,max}$
$\sigma_{max,fat}$ [MPa]	4.74
$\sigma_{min,fat}$ [MPa]	0.95

(dCMOD/dn)mat [mm/cycle]	9.10E-05
(dCMOD/dn)fib [mm/cycle]	2.59E-03



FLEXURAL FATIGUE TEST

N.° 63

1. SERIES DATA

Code	A1-L
Size [mm]	150x150x600
Fibers [%]	0.3

3. SERIES STATIC STRENGTH

f_c [MPa]	106.62
$\sigma_{fl,max}$ [MPa]	5.93
$\sigma_{fl,LOP}$ [MPa]	5.22

5. FATIGUE TEST RESULTS

N_{mat}	260
N_{fib}	1,570
N_{tot}	1,830

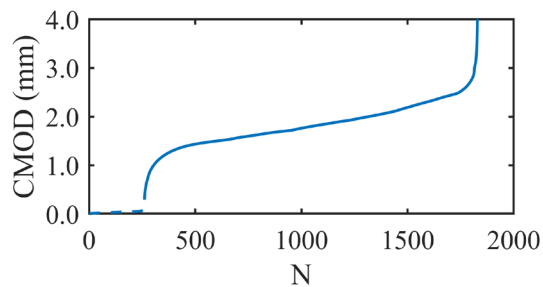
**2. SPECIMEN DATA**

Code	A1-L-4
Manufacture date	16/12/2020
Test date	29/06/2022

4. FATIGUE TEST PARAMETERS

Range	(16%-80%) · $\sigma_{fl,max}$
$\sigma_{max,fat}$ [MPa]	4.74
$\sigma_{min,fat}$ [MPa]	0.95

(dCMOD/dn)mat [mm/cycle]	1.61E-04
(dCMOD/dn)fib [mm/cycle]	8.03E-04

**FLEXURAL FATIGUE TEST**

N.° 64

1. SERIES DATA

Code	A1-L
Size [mm]	150x150x600
Fibers [%]	0.3

3. SERIES STATIC STRENGTH

f_c [MPa]	106.62
$\sigma_{fl,max}$ [MPa]	5.93
$\sigma_{fl,LOP}$ [MPa]	5.22

5. FATIGUE TEST RESULTS

N_{mat}	92
N_{fib}	17
N_{tot}	109

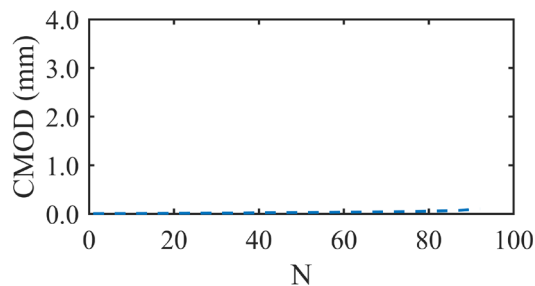
**2. SPECIMEN DATA**

Code	A1-L-5
Manufacture date	16/12/2020
Test date	28/06/2022

4. FATIGUE TEST PARAMETERS

Range	(16%-80%) · $\sigma_{fl,max}$
$\sigma_{max,fat}$ [MPa]	4.74
$\sigma_{min,fat}$ [MPa]	0.95

(dCMOD/dn)mat [mm/cycle]	6.35E-04
(dCMOD/dn)fib [mm/cycle]	6.88E-02



FLEXURAL FATIGUE TEST

N.° 65

1. SERIES DATA

Code	A1-L
Size [mm]	150x150x600
Fibers [%]	0.3

3. SERIES STATIC STRENGTH

f_c [MPa]	106.62
$\sigma_{fl,max}$ [MPa]	5.93
$\sigma_{fl,LOP}$ [MPa]	5.22

5. FATIGUE TEST RESULTS

N_{mat}	0
N_{fib}	21,892
N_{tot}	21,892



2. SPECIMEN DATA

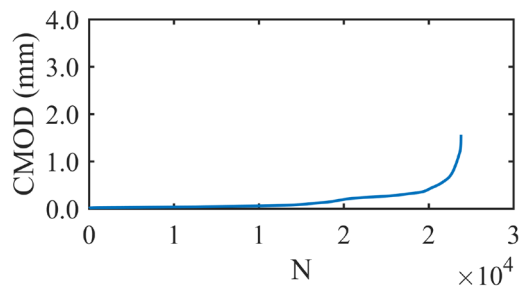
Code	A1-L-6
Manufacture date	16/12/2020
Test date	28/06/2022

4. FATIGUE TEST PARAMETERS

Range	(16%-80%) · $\sigma_{fl,max}$
$\sigma_{max,fat}$ [MPa]	4.74
$\sigma_{min,fat}$ [MPa]	0.95

(dCMOD/dn)mat [mm/cycle]

(dCMOD/dn)fib [mm/cycle] 4.30E-06



FLEXURAL FATIGUE TEST

N.° 66

1. SERIES DATA

Code	A1-L
Size [mm]	150x150x600
Fibers [%]	0.3

3. SERIES STATIC STRENGTH

f_c [MPa]	106.62
$\sigma_{fl,max}$ [MPa]	5.93
$\sigma_{fl,LOP}$ [MPa]	5.22

5. FATIGUE TEST RESULTS

N_{mat}	138
N_{fib}	1,117
N_{tot}	1,255



2. SPECIMEN DATA

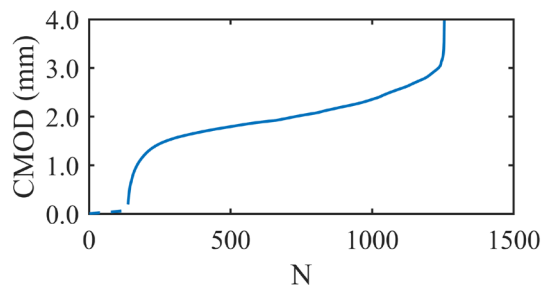
Code	A1-L-9
Manufacture date	16/12/2020
Test date	28/06/2022

4. FATIGUE TEST PARAMETERS

Range	(16%-80%) · $\sigma_{fl,max}$
$\sigma_{max,fat}$ [MPa]	4.74
$\sigma_{min,fat}$ [MPa]	0.95

(dCMOD/dn)mat [mm/cycle]

(dCMOD/dn)fib [mm/cycle] 1.27E-03



FLEXURAL FATIGUE TEST

N.° 67

1. SERIES DATA

Code	A1-L
Size [mm]	150x150x600
Fibers [%]	0.3

3. SERIES STATIC STRENGTH

f_c [MPa]	106.62
$\sigma_{fl,max}$ [MPa]	5.93
$\sigma_{fl,LOP}$ [MPa]	5.22

5. FATIGUE TEST RESULTS

N_{mat}	82
N_{fib}	52
N_{tot}	134



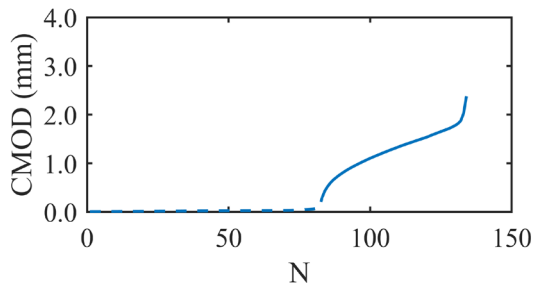
2. SPECIMEN DATA

Code	A1-L-10
Manufacture date	16/12/2020
Test date	28/06/2022

4. FATIGUE TEST PARAMETERS

Range	(16%-80%) · $\sigma_{fl,max}$
$\sigma_{max,fat}$ [MPa]	4.74
$\sigma_{min,fat}$ [MPa]	0.95

(dCMOD/dn)mat [mm/cycle]	3.66E-04
(dCMOD/dn)fib [mm/cycle]	2.28E-02



FLEXURAL FATIGUE TEST

N.° 68

1. SERIES DATA

Code	A1-L
Size [mm]	150x150x600
Fibers [%]	0.3

3. SERIES STATIC STRENGTH

f_c [MPa]	106.62
$\sigma_{fl,max}$ [MPa]	5.93
$\sigma_{fl,LOP}$ [MPa]	5.22

5. FATIGUE TEST RESULTS

N_{mat}	158
N_{fib}	126
N_{tot}	284



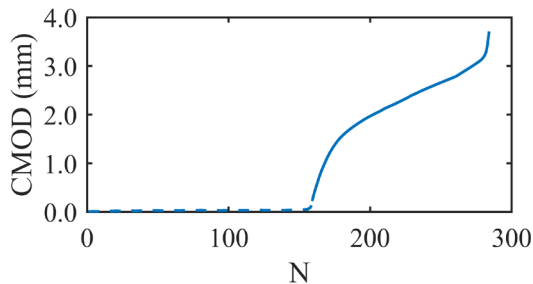
2. SPECIMEN DATA

Code	A1-L-11
Manufacture date	16/12/2020
Test date	28/06/2022

4. FATIGUE TEST PARAMETERS

Range	(16%-80%) · $\sigma_{fl,max}$
$\sigma_{max,fat}$ [MPa]	4.74
$\sigma_{min,fat}$ [MPa]	0.95

(dCMOD/dn)mat [mm/cycle]	1.49E-04
(dCMOD/dn)fib [mm/cycle]	1.44E-02



FLEXURAL FATIGUE TEST

N.° 69

1. SERIES DATA

Code	A1-L
Size [mm]	150x150x600
Fibers [%]	0.3

3. SERIES STATIC STRENGTH

f_c [MPa]	106.62
$\sigma_{fl,max}$ [MPa]	5.93
$\sigma_{fl,LOP}$ [MPa]	5.22

5. FATIGUE TEST RESULTS

N_{mat}	65
N_{fib}	4
N_{tot}	69

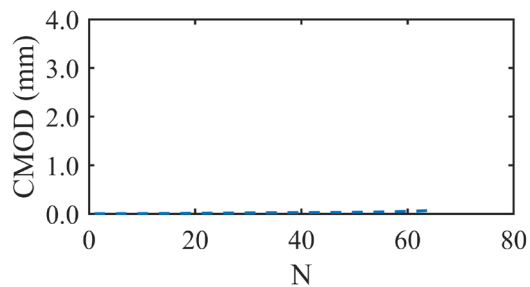
**2. SPECIMEN DATA**

Code	A1-L-12
Manufacture date	16/12/2020
Test date	28/06/2022

4. FATIGUE TEST PARAMETERS

Range	(16%-80%) · $\sigma_{fl,max}$
$\sigma_{max,fat}$ [MPa]	4.74
$\sigma_{min,fat}$ [MPa]	0.95

(dCMOD/dn)mat [mm/cycle]	7.37E-04
(dCMOD/dn)fib [mm/cycle]	3.26E-01

**FLEXURAL FATIGUE TEST**

N.° 70

1. SERIES DATA

Code	A1-L
Size [mm]	150x150x600
Fibers [%]	0.3

3. SERIES STATIC STRENGTH

f_c [MPa]	106.62
$\sigma_{fl,max}$ [MPa]	5.93
$\sigma_{fl,LOP}$ [MPa]	5.22

5. FATIGUE TEST RESULTS

N_{mat}	89
N_{fib}	13
N_{tot}	102

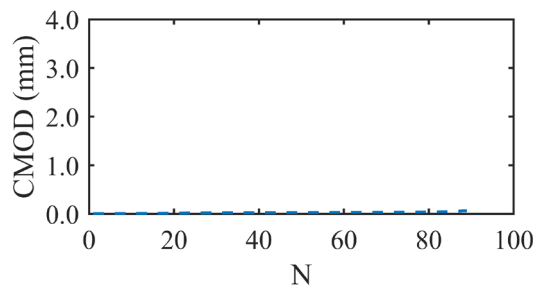
**2. SPECIMEN DATA**

Code	A1-L-13
Manufacture date	16/12/2020
Test date	28/06/2022

4. FATIGUE TEST PARAMETERS

Range	(16%-80%) · $\sigma_{fl,max}$
$\sigma_{max,fat}$ [MPa]	4.74
$\sigma_{min,fat}$ [MPa]	0.95

(dCMOD/dn)mat [mm/cycle]	4.29E-04
(dCMOD/dn)fib [mm/cycle]	1.59E-01



FLEXURAL FATIGUE TEST

N.° 71

1. SERIES DATA

Code	A1-L
Size [mm]	150x150x600
Fibers [%]	0.3

3. SERIES STATIC STRENGTH

f_c [MPa]	106.62
$\sigma_{fl,max}$ [MPa]	5.93
$\sigma_{fl,LOP}$ [MPa]	5.22

5. FATIGUE TEST RESULTS

N_{mat}	0
N_{fib}	18,876
N_{tot}	18,876



2. SPECIMEN DATA

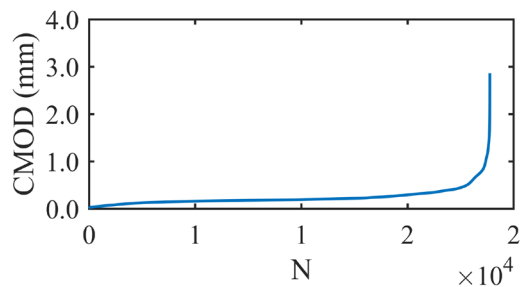
Code	A1-L-15
Manufacture date	16/12/2020
Test date	28/06/2022

4. FATIGUE TEST PARAMETERS

Range	(16%-80%) · $\sigma_{fl,max}$
$\sigma_{max,fat}$ [MPa]	4.74
$\sigma_{min,fat}$ [MPa]	0.95

(dCMOD/dn)mat [mm/cycle]

(dCMOD/dn)fib [mm/cycle] 9.08E-06



FLEXURAL FATIGUE TEST

N.° 72

1. SERIES DATA

Code	A1-L
Size [mm]	150x150x600
Fibers [%]	0.3

3. SERIES STATIC STRENGTH

f_c [MPa]	106.62
$\sigma_{fl,max}$ [MPa]	5.93
$\sigma_{fl,LOP}$ [MPa]	5.22

5. FATIGUE TEST RESULTS

N_{mat}	0
N_{fib}	42,491
N_{tot}	42,491



2. SPECIMEN DATA

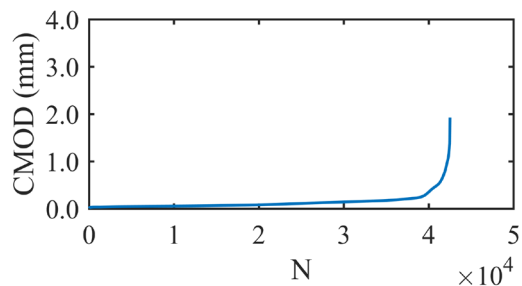
Code	A1-L-16
Manufacture date	16/12/2020
Test date	28/06/2022

4. FATIGUE TEST PARAMETERS

Range	(16%-80%) · $\sigma_{fl,max}$
$\sigma_{max,fat}$ [MPa]	4.74
$\sigma_{min,fat}$ [MPa]	0.95

(dCMOD/dn)mat [mm/cycle]

(dCMOD/dn)fib [mm/cycle] 4.14E-06



A2-L SERIES

FLEXURAL FATIGUE TEST

N.° 73

1. SERIES DATA

Code	A2-L
Size [mm]	150x150x600
Fibers [%]	0.6

3. SERIES STATIC STRENGTH

f_c [MPa]	106.22
$\sigma_{fl,max}$ [MPa]	11.37
$\sigma_{fl,LOP}$ [MPa]	6.67

5. FATIGUE TEST RESULTS

N_{mat}	0
N_{fib}	25,926
N_{tot}	25,926

**2. SPECIMEN DATA**

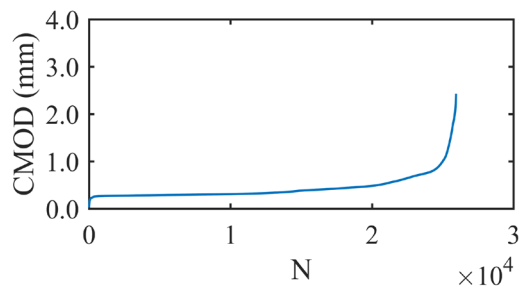
Code	A2-L-2
Manufacture date	09/12/2020
Test date	13/06/2022

4. FATIGUE TEST PARAMETERS

Range	(16%-80%) · $\sigma_{fl,max}$
$\sigma_{max,fat}$ [MPa]	9.10
$\sigma_{min,fat}$ [MPa]	1.82

(dCMOD/dn)mat [mm/cycle]

(dCMOD/dn)fib [mm/cycle] 1.05E-05

**FLEXURAL FATIGUE TEST**

N.° 74

1. SERIES DATA

Code	A2-L
Size [mm]	150x150x600
Fibers [%]	0.6

3. SERIES STATIC STRENGTH

f_c [MPa]	106.22
$\sigma_{fl,max}$ [MPa]	11.37
$\sigma_{fl,LOP}$ [MPa]	6.67

5. FATIGUE TEST RESULTS

N_{mat}	0
N_{fib}	37
N_{tot}	37

**2. SPECIMEN DATA**

Code	A2-L-3
Manufacture date	09/12/2020
Test date	13/06/2022

4. FATIGUE TEST PARAMETERS

Range	(16%-80%) · $\sigma_{fl,max}$
$\sigma_{max,fat}$ [MPa]	9.10
$\sigma_{min,fat}$ [MPa]	1.82

(dCMOD/dn)mat [mm/cycle]

(dCMOD/dn)fib [mm/cycle] 8.11E-02

FLEXURAL FATIGUE TEST

N.° 75

1. SERIES DATA

Code	A2-L
Size [mm]	150x150x600
Fibers [%]	0.6

3. SERIES STATIC STRENGTH

f_c [MPa]	106.22
$\sigma_{fl,max}$ [MPa]	11.37
$\sigma_{fl,LOP}$ [MPa]	6.67

5. FATIGUE TEST RESULTS

N_{mat}	0
N_{fib}	3,476
N_{tot}	3,476



2. SPECIMEN DATA

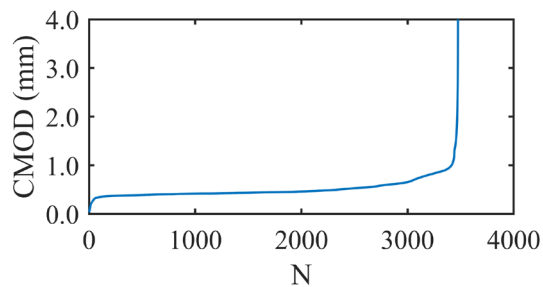
Code	A2-L-5
Manufacture date	09/12/2020
Test date	13/06/2022

4. FATIGUE TEST PARAMETERS

Range	(16%-80%) · $\sigma_{fl,max}$
$\sigma_{max,fat}$ [MPa]	9.10
$\sigma_{min,fat}$ [MPa]	1.82

(dCMOD/dn)mat [mm/cycle]

(dCMOD/dn)fib [mm/cycle] 7.28E-05



FLEXURAL FATIGUE TEST

N.° 76

1. SERIES DATA

Code	A2-L
Size [mm]	150x150x600
Fibers [%]	0.6

3. SERIES STATIC STRENGTH

f_c [MPa]	106.22
$\sigma_{fl,max}$ [MPa]	11.37
$\sigma_{fl,LOP}$ [MPa]	6.67

5. FATIGUE TEST RESULTS

N_{mat}	0
N_{fib}	2,004
N_{tot}	2,004



2. SPECIMEN DATA

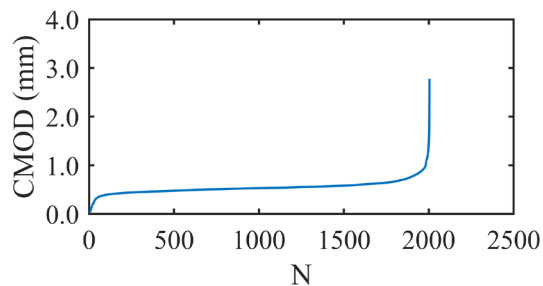
Code	A2-L-6
Manufacture date	09/12/2020
Test date	13/06/2022

4. FATIGUE TEST PARAMETERS

Range	(16%-80%) · $\sigma_{fl,max}$
$\sigma_{max,fat}$ [MPa]	9.10
$\sigma_{min,fat}$ [MPa]	1.82

(dCMOD/dn)mat [mm/cycle]

(dCMOD/dn)fib [mm/cycle] 1.15E-04



FLEXURAL FATIGUE TEST

N.° 77

1. SERIES DATA

Code	A2-L
Size [mm]	150x150x600
Fibers [%]	0.6

3. SERIES STATIC STRENGTH

f_c [MPa]	106.22
$\sigma_{fl,max}$ [MPa]	11.37
$\sigma_{fl,LOP}$ [MPa]	6.67

5. FATIGUE TEST RESULTS

N_{mat}	0
N_{fib}	6,597
N_{tot}	6,597

**2. SPECIMEN DATA**

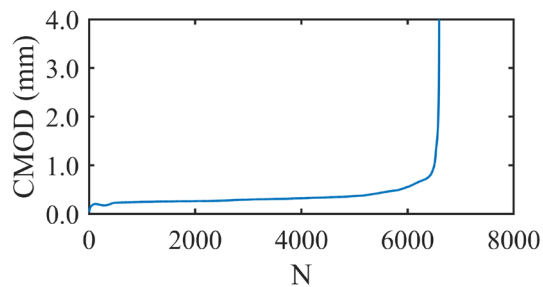
Code	A2-L-7
Manufacture date	09/12/2020
Test date	13/06/2022

4. FATIGUE TEST PARAMETERS

Range	(16%-80%) · $\sigma_{fl,max}$
$\sigma_{max,fat}$ [MPa]	9.10
$\sigma_{min,fat}$ [MPa]	1.82

(dCMOD/dn)mat [mm/cycle]

(dCMOD/dn)fib [mm/cycle] 2.98E-05

**FLEXURAL FATIGUE TEST**

N.° 78

1. SERIES DATA

Code	A2-L
Size [mm]	150x150x600
Fibers [%]	0.6

3. SERIES STATIC STRENGTH

f_c [MPa]	106.22
$\sigma_{fl,max}$ [MPa]	11.37
$\sigma_{fl,LOP}$ [MPa]	6.67

5. FATIGUE TEST RESULTS

N_{mat}	0
N_{fib}	32
N_{tot}	32

**2. SPECIMEN DATA**

Code	A2-L-8
Manufacture date	09/12/2020
Test date	13/06/2022

4. FATIGUE TEST PARAMETERS

Range	(16%-80%) · $\sigma_{fl,max}$
$\sigma_{max,fat}$ [MPa]	9.10
$\sigma_{min,fat}$ [MPa]	1.82

(dCMOD/dn)mat [mm/cycle]

(dCMOD/dn)fib [mm/cycle] 5.73E-02

FLEXURAL FATIGUE TEST

N.° 79

1. SERIES DATA

Code	A2-L
Size [mm]	150x150x600
Fibers [%]	0.6

3. SERIES STATIC STRENGTH

f_c [MPa]	106.22
$\sigma_{fl,max}$ [MPa]	11.37
$\sigma_{fl,LOP}$ [MPa]	6.67

5. FATIGUE TEST RESULTS

N_{mat}	0
N_{fib}	8,851
N_{tot}	8,851

**2. SPECIMEN DATA**

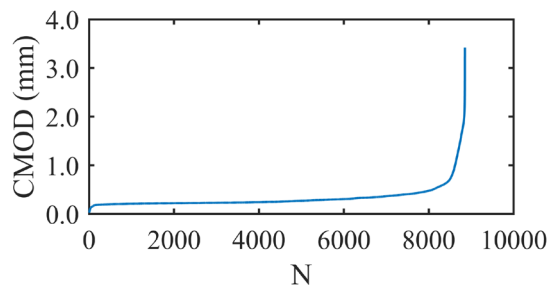
Code	A2-L-9
Manufacture date	09/12/2020
Test date	13/06/2022

4. FATIGUE TEST PARAMETERS

Range	(16%-80%) · $\sigma_{fl,max}$
$\sigma_{max,fat}$ [MPa]	9.10
$\sigma_{min,fat}$ [MPa]	1.82

(dCMOD/dn)mat [mm/cycle]

(dCMOD/dn)fib [mm/cycle] 2.25E-05

**FLEXURAL FATIGUE TEST**

N.° 80

1. SERIES DATA

Code	A2-L
Size [mm]	150x150x600
Fibers [%]	0.6

3. SERIES STATIC STRENGTH

f_c [MPa]	106.22
$\sigma_{fl,max}$ [MPa]	11.37
$\sigma_{fl,LOP}$ [MPa]	6.67

5. FATIGUE TEST RESULTS

N_{mat}	0
N_{fib}	46
N_{tot}	46

**2. SPECIMEN DATA**

Code	A2-L-12
Manufacture date	09/12/2020
Test date	13/06/2022

4. FATIGUE TEST PARAMETERS

Range	(16%-80%) · $\sigma_{fl,max}$
$\sigma_{max,fat}$ [MPa]	9.10
$\sigma_{min,fat}$ [MPa]	1.82

(dCMOD/dn)mat [mm/cycle]

(dCMOD/dn)fib [mm/cycle] 3.82E-02

FLEXURAL FATIGUE TEST

N.° 81

1. SERIES DATA

Code	A2-L
Size [mm]	150x150x600
Fibers [%]	0.6

3. SERIES STATIC STRENGTH

f_c [MPa]	106.22
$\sigma_{fl,max}$ [MPa]	11.37
$\sigma_{fl,LOP}$ [MPa]	6.67

5. FATIGUE TEST RESULTS

N_{mat}	0
N_{fib}	84
N_{tot}	84

**2. SPECIMEN DATA**

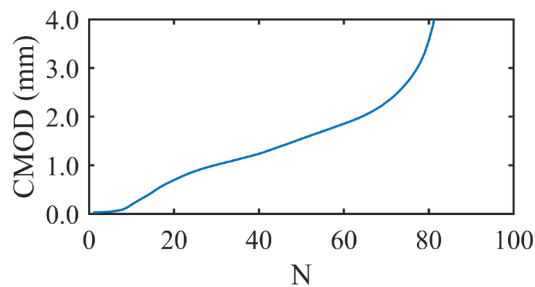
Code	A2-L-13
Manufacture date	09/12/2020
Test date	13/06/2022

4. FATIGUE TEST PARAMETERS

Range	(16%-80%) · $\sigma_{fl,max}$
$\sigma_{max,fat}$ [MPa]	9.10
$\sigma_{min,fat}$ [MPa]	1.82

(dCMOD/dn)mat [mm/cycle]

(dCMOD/dn)fib [mm/cycle] 3.16E-02

**FLEXURAL FATIGUE TEST**

N.° 82

1. SERIES DATA

Code	A2-L
Size [mm]	150x150x600
Fibers [%]	0.6

3. SERIES STATIC STRENGTH

f_c [MPa]	106.22
$\sigma_{fl,max}$ [MPa]	11.37
$\sigma_{fl,LOP}$ [MPa]	6.67

5. FATIGUE TEST RESULTS

N_{mat}	0
N_{fib}	2,415
N_{tot}	2,415

**2. SPECIMEN DATA**

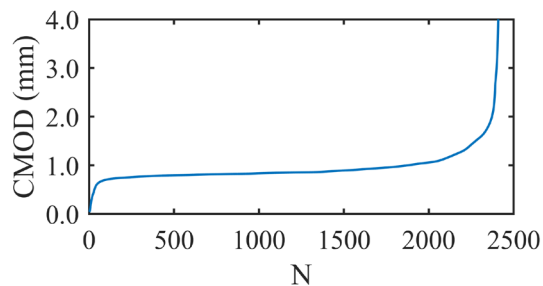
Code	A2-L-15
Manufacture date	09/12/2020
Test date	13/06/2022

4. FATIGUE TEST PARAMETERS

Range	(16%-80%) · $\sigma_{fl,max}$
$\sigma_{max,fat}$ [MPa]	9.10
$\sigma_{min,fat}$ [MPa]	1.82

(dCMOD/dn)mat [mm/cycle]

(dCMOD/dn)fib [mm/cycle] 1.48E-04



FLEXURAL FATIGUE TEST

N.° 83

1. SERIES DATA

Code	A2-L
Size [mm]	150x150x600
Fibers [%]	0.6

3. SERIES STATIC STRENGTH

f_c [MPa]	106.22
$\sigma_{fl,max}$ [MPa]	11.37
$\sigma_{fl,LOP}$ [MPa]	6.67

5. FATIGUE TEST RESULTS

N_{mat}	0
N_{fib}	4,264
N_{tot}	4,264



2. SPECIMEN DATA

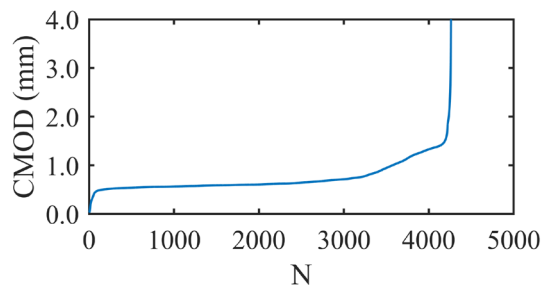
Code	A2-L-16
Manufacture date	09/12/2020
Test date	13/06/2022

4. FATIGUE TEST PARAMETERS

Range	(16%-80%) $\cdot \sigma_{fl,max}$
$\sigma_{max,fat}$ [MPa]	9.10
$\sigma_{min,fat}$ [MPa]	1.82

(dCMOD/dn)mat [mm/cycle]

(dCMOD/dn)fib [mm/cycle] 6.66E-05



A3-L SERIES

FLEXURAL FATIGUE TEST

N.° 84

1. SERIES DATA

Code	A3-L
Size [mm]	150x150x600
Fibers [%]	1

3. SERIES STATIC STRENGTH

f_c [MPa]	107.17
$\sigma_{fl,max}$ [MPa]	16.41
$\sigma_{fl,LOP}$ [MPa]	7.74

5. FATIGUE TEST RESULTS

N_{mat}	0
N_{fib}	15
N_{tot}	15

**2. SPECIMEN DATA**

Code	A3-L-1
Manufacture date	30/11/2020
Test date	27/06/2022

4. FATIGUE TEST PARAMETERS

Range	(16%-80%) · $\sigma_{fl,max}$
$\sigma_{max,fat}$ [MPa]	13.13
$\sigma_{min,fat}$ [MPa]	2.63

(dCMOD/dn)mat [mm/cycle]

(dCMOD/dn)fib [mm/cycle] 1.04E-01

FLEXURAL FATIGUE TEST

N.° 85

1. SERIES DATA

Code	A3-L
Size [mm]	150x150x600
Fibers [%]	1

3. SERIES STATIC STRENGTH

f_c [MPa]	107.17
$\sigma_{fl,max}$ [MPa]	16.41
$\sigma_{fl,LOP}$ [MPa]	7.74

5. FATIGUE TEST RESULTS

N_{mat}	0
N_{fib}	23,308
N_{tot}	23,308

**2. SPECIMEN DATA**

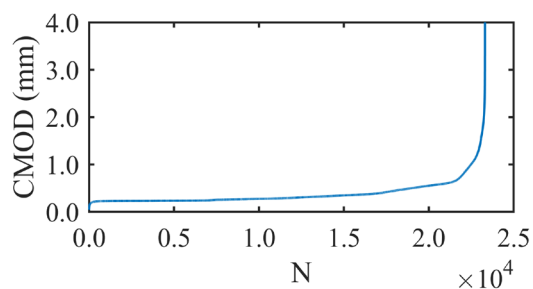
Code	A3-L-2
Manufacture date	30/11/2020
Test date	27/06/2022

4. FATIGUE TEST PARAMETERS

Range	(16%-80%) · $\sigma_{fl,max}$
$\sigma_{max,fat}$ [MPa]	13.13
$\sigma_{min,fat}$ [MPa]	2.63

(dCMOD/dn)mat [mm/cycle]

(dCMOD/dn)fib [mm/cycle] 1.55E-05



FLEXURAL FATIGUE TEST

N.° 86

1. SERIES DATA

Code	A3-L
Size [mm]	150x150x600
Fibers [%]	1

3. SERIES STATIC STRENGTH

f_c [MPa]	107.17
$\sigma_{fl,max}$ [MPa]	16.41
$\sigma_{fl,LOP}$ [MPa]	7.74

5. FATIGUE TEST RESULTS

N_{mat}	0
N_{fib}	13
N_{tot}	13

**2. SPECIMEN DATA**

Code	A3-L-3
Manufacture date	30/11/2020
Test date	27/06/2022

4. FATIGUE TEST PARAMETERS

Range	$(16\%-80\%) \cdot \sigma_{fl,max}$
$\sigma_{max,fat}$ [MPa]	13.13
$\sigma_{min,fat}$ [MPa]	2.63

(dCMOD/dn)mat [mm/cycle]

(dCMOD/dn)fib [mm/cycle] 1.02E-01

FLEXURAL FATIGUE TEST

N.° 87

1. SERIES DATA

Code	A3-L
Size [mm]	150x150x600
Fibers [%]	1

3. SERIES STATIC STRENGTH

f_c [MPa]	107.17
$\sigma_{fl,max}$ [MPa]	16.41
$\sigma_{fl,LOP}$ [MPa]	7.74

5. FATIGUE TEST RESULTS

N_{mat}	0
N_{fib}	3,335
N_{tot}	3,335

**2. SPECIMEN DATA**

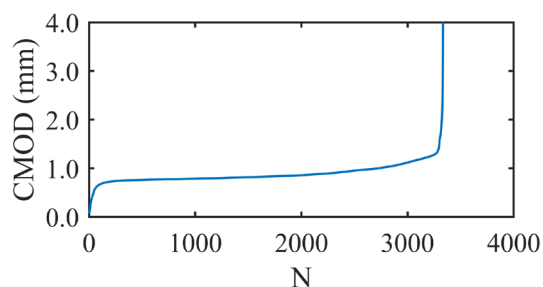
Code	A3-L-4
Manufacture date	30/11/2020
Test date	15/06/2022

4. FATIGUE TEST PARAMETERS

Range	$(16\%-80\%) \cdot \sigma_{fl,max}$
$\sigma_{max,fat}$ [MPa]	13.13
$\sigma_{min,fat}$ [MPa]	2.63

(dCMOD/dn)mat [mm/cycle]

(dCMOD/dn)fib [mm/cycle] 1.31E-04



FLEXURAL FATIGUE TEST

N.° 88

1. SERIES DATA

Code	A3-L
Size [mm]	150x150x600
Fibers [%]	1

3. SERIES STATIC STRENGTH

f_c [MPa]	107.17
$\sigma_{fl,max}$ [MPa]	16.41
$\sigma_{fl,LOP}$ [MPa]	7.74

5. FATIGUE TEST RESULTS

N_{mat}	0
N_{fib}	15
N_{tot}	15

**2. SPECIMEN DATA**

Code	A3-L-6
Manufacture date	30/11/2020
Test date	27/06/2022

4. FATIGUE TEST PARAMETERS

Range	(16%-80%) · $\sigma_{fl,max}$
$\sigma_{max,fat}$ [MPa]	13.13
$\sigma_{min,fat}$ [MPa]	2.63

(dCMOD/dn)mat [mm/cycle]

(dCMOD/dn)fib [mm/cycle] 1.05E-01

FLEXURAL FATIGUE TEST

N.° 89

1. SERIES DATA

Code	A3-L
Size [mm]	150x150x600
Fibers [%]	1

3. SERIES STATIC STRENGTH

f_c [MPa]	107.17
$\sigma_{fl,max}$ [MPa]	16.41
$\sigma_{fl,LOP}$ [MPa]	7.74

5. FATIGUE TEST RESULTS

N_{mat}	0
N_{fib}	5,747
N_{tot}	5,747

**2. SPECIMEN DATA**

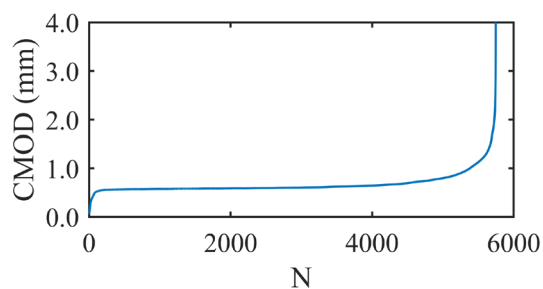
Code	A3-L-7
Manufacture date	30/11/2020
Test date	27/06/2022

4. FATIGUE TEST PARAMETERS

Range	(16%-80%) · $\sigma_{fl,max}$
$\sigma_{max,fat}$ [MPa]	13.13
$\sigma_{min,fat}$ [MPa]	2.63

(dCMOD/dn)mat [mm/cycle]

(dCMOD/dn)fib [mm/cycle] 2.92E-05



FLEXURAL FATIGUE TEST

N.° 90

1. SERIES DATA

Code	A3-L
Size [mm]	150x150x600
Fibers [%]	1

3. SERIES STATIC STRENGTH

f_c [MPa]	107.17
$\sigma_{fl,max}$ [MPa]	16.41
$\sigma_{fl,LOP}$ [MPa]	7.74

5. FATIGUE TEST RESULTS

N_{mat}	0
N_{fib}	9,604
N_{tot}	9,604



2. SPECIMEN DATA

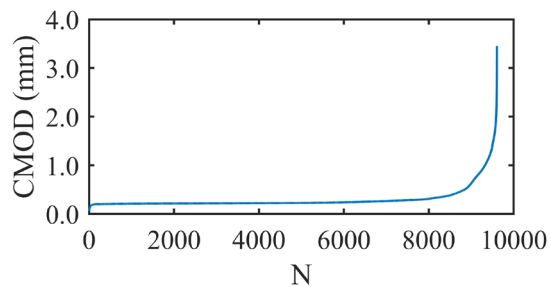
Code	A3-L-8
Manufacture date	30/11/2020
Test date	27/06/2022

4. FATIGUE TEST PARAMETERS

Range	(16%-80%) · $\sigma_{fl,max}$
$\sigma_{max,fat}$ [MPa]	13.13
$\sigma_{min,fat}$ [MPa]	2.63

(dCMOD/dn)mat [mm/cycle]

(dCMOD/dn)fib [mm/cycle] 8.69E-06



FLEXURAL FATIGUE TEST

N.° 91

1. SERIES DATA

Code	A3-L
Size [mm]	150x150x600
Fibers [%]	1

3. SERIES STATIC STRENGTH

f_c [MPa]	107.17
$\sigma_{fl,max}$ [MPa]	16.41
$\sigma_{fl,LOP}$ [MPa]	7.74

5. FATIGUE TEST RESULTS

N_{mat}	0
N_{fib}	3,498
N_{tot}	3,498



2. SPECIMEN DATA

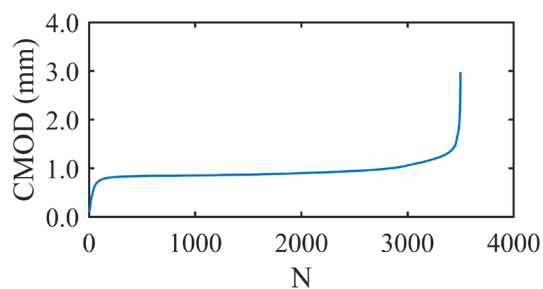
Code	A3-L-10
Manufacture date	30/11/2020
Test date	14/06/2022

4. FATIGUE TEST PARAMETERS

Range	(16%-80%) · $\sigma_{fl,max}$
$\sigma_{max,fat}$ [MPa]	13.13
$\sigma_{min,fat}$ [MPa]	2.63

(dCMOD/dn)mat [mm/cycle]

(dCMOD/dn)fib [mm/cycle] 6.54E-05



FLEXURAL FATIGUE TEST

N.° 92

1. SERIES DATA

Code	A3-L
Size [mm]	150x150x600
Fibers [%]	1

3. SERIES STATIC STRENGTH

f_c [MPa]	107.17
$\sigma_{fl,max}$ [MPa]	16.41
$\sigma_{fl,LOP}$ [MPa]	7.74

5. FATIGUE TEST RESULTS

N_{mat}	0
N_{fib}	5,634
N_{tot}	5,634



2. SPECIMEN DATA

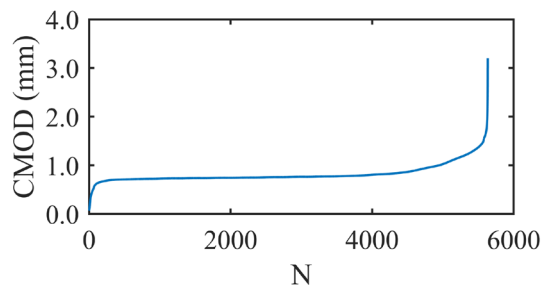
Code	A3-L-12
Manufacture date	30/11/2020
Test date	15/06/2022

4. FATIGUE TEST PARAMETERS

Range	(16%-80%) · $\sigma_{fl,max}$
$\sigma_{max,fat}$ [MPa]	13.13
$\sigma_{min,fat}$ [MPa]	2.63

(dCMOD/dn)mat [mm/cycle]

(dCMOD/dn)fib [mm/cycle] 2.99E-05



FLEXURAL FATIGUE TEST

N.° 93

1. SERIES DATA

Code	A3-L
Size [mm]	150x150x600
Fibers [%]	1

3. SERIES STATIC STRENGTH

f_c [MPa]	107.17
$\sigma_{fl,max}$ [MPa]	16.41
$\sigma_{fl,LOP}$ [MPa]	7.74

5. FATIGUE TEST RESULTS

N_{mat}	0
N_{fib}	102
N_{tot}	102



2. SPECIMEN DATA

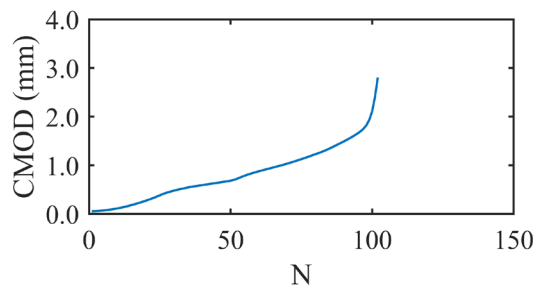
Code	A3-L-13
Manufacture date	30/11/2020
Test date	15/06/2022

4. FATIGUE TEST PARAMETERS

Range	(16%-80%) · $\sigma_{fl,max}$
$\sigma_{max,fat}$ [MPa]	13.13
$\sigma_{min,fat}$ [MPa]	2.63

(dCMOD/dn)mat [mm/cycle]

(dCMOD/dn)fib [mm/cycle] 1.64E-02



FLEXURAL FATIGUE TEST

N.° 94

1. SERIES DATA

Code	A3-L
Size [mm]	150x150x600
Fibers [%]	1

3. SERIES STATIC STRENGTH

f_c [MPa]	107.17
$\sigma_{fl,max}$ [MPa]	16.41
$\sigma_{fl,LOP}$ [MPa]	7.74

5. FATIGUE TEST RESULTS

N_{mat}	0
N_{fib}	1,618
N_{tot}	1,618



2. SPECIMEN DATA

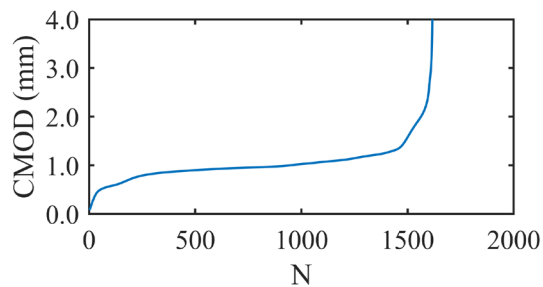
Code	A3-L-14
Manufacture date	30/11/2020
Test date	14/06/2022

4. FATIGUE TEST PARAMETERS

Range	(16%-80%) · $\sigma_{fl,max}$
$\sigma_{max,fat}$ [MPa]	13.13
$\sigma_{min,fat}$ [MPa]	2.63

(dCMOD/dn)mat [mm/cycle]

(dCMOD/dn)fib [mm/cycle] 3.61E-04



FLEXURAL FATIGUE TEST

N.° 95

1. SERIES DATA

Code	A3-L
Size [mm]	150x150x600
Fibers [%]	1

3. SERIES STATIC STRENGTH

f_c [MPa]	107.17
$\sigma_{fl,max}$ [MPa]	16.41
$\sigma_{fl,LOP}$ [MPa]	7.74

5. FATIGUE TEST RESULTS

N_{mat}	0
N_{fib}	12,964
N_{tot}	12,964



2. SPECIMEN DATA

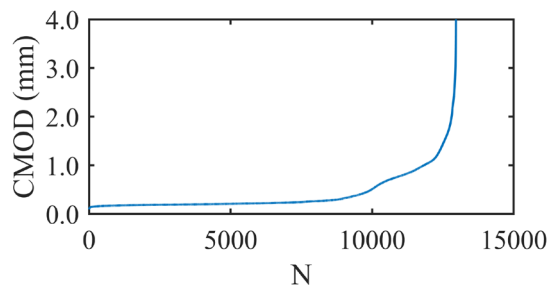
Code	A3-L-16
Manufacture date	30/11/2020
Test date	15/06/2022

4. FATIGUE TEST PARAMETERS

Range	(16%-80%) · $\sigma_{fl,max}$
$\sigma_{max,fat}$ [MPa]	13.13
$\sigma_{min,fat}$ [MPa]	2.63

(dCMOD/dn)mat [mm/cycle]

(dCMOD/dn)fib [mm/cycle] 1.19E-05



REFERENCES

- [1] EN 1992-1-1. Eurocode 2: Design of concrete structures - Part 1-1 : General rules and rules for buildings, 1991.
 - [2] C. Ríos, J.C. Lancha, M.Á. Vicente, Fatigue in Structural Concrete According to the New Eurocode 2, *Hormigón y Acero*. (2023). <https://doi.org/10.33586/hya.2023.3100>.
 - [3] Boletín Oficial del Estado (BOE) n.º 190, Real Decreto 470/2021, de 29 de junio, por el que se aprueba el Código Estructural, 2021.
 - [4] Asociación Española de Hormigón Estructural, M-2. Manual de tecnología del hormigón reforzado con fibras de acero, 2000.
 - [5] Instrucción de Hormigón Estructural (EHE-08), 2008.
 - [6] ASTM C1609/C1609M-12. Standard Test Method for Flexural Performance of Fiber-Reinforced Concrete (Using Beam With Third-Point Loading), 2012.
 - [7] UNE-EN 14651:2007+A1. Método de ensayo para hormigón con fibras metálicas. Determinación de la resistencia a la tracción por flexión (límite de proporcionalidad (LOP), resistencia residual), 2008.
 - [8] M.G. Alberti, A. Enfedaque, J.C. Gálvez, A review on the assessment and prediction of the orientation and distribution of fibres for concrete, *Compos. Part B Eng.* 151 (2018) 274–290. <https://doi.org/10.1016/j.compositesb.2018.05.040>.
 - [9] Á. de la Rosa, E. Poveda, G. Ruiz, H. Cifuentes, Proportioning of self-compacting steel-fiber reinforced concrete mixes based on target plastic viscosity and compressive strength: Mix-design procedure & experimental validation, *Constr. Build. Mater.* 189 (2018) 409–419. <https://doi.org/10.1016/j.conbuildmat.2018.09.006>.
 - [10] ACI Committee 544, ACI 544.3R-93. Guide for Specifying, Proportioning, Mixing, Placing, and Finishing Steel Fiber Reinforced Concrete, 1998.
 - [11] C.D. Johnston, Properties of steel fibre reinforced mortar and concrete, *International Symp. Fibrous Concr.* (1980).
 - [12] H. Singh, *Steel Fiber Reinforced Concrete*, Springer Singapore, Singapore, 2017. <https://doi.org/10.1007/978-981-10-2507-5>.
 - [13] F. Song, Steel fiber reinforced concrete under concentrated load [PhD thesis, Ruhr-Universität Bochum, Germany], (2017).
 - [14] E. Poveda, R.C. Yu, M. Tarifa, G. Ruiz, V.M.C.F. Cunha, J.A.O. Barros, Rate effect in inclined fibre pull-out for smooth and hooked-end fibres: a numerical study, *Int. J. Fract.* 223 (2020) 135–149. <https://doi.org/10.1007/s10704-019-00404-7>.
-

- [15] G. Gebuhr, M. Pise, M. Sarhil, S. Anders, D. Brands, J. Schröder, Analysis and evaluation of the pull-out behavior of hooked steel fibers embedded in high and ultra-high performance concrete for calibration of numerical models, *Struct. Concr.* 20 (2019) 1254–1264. <https://doi.org/10.1002/suco.201900034>.
- [16] K. Wille, S. El-Tawil, A.E. Naaman, Properties of strain hardening ultra high performance fiber reinforced concrete (UHP-FRC) under direct tensile loading, *Cem. Concr. Compos.* 48 (2014) 53–66. <https://doi.org/10.1016/j.cemconcomp.2013.12.015>.
- [17] Recommendations of RILEM TC 162-TDF: Test and design methods for steel fibre reinforced concrete: bending test, 2002.
- [18] CEB-FIP, Bulletin n.º 188. Fatigue of Concrete Structures - State-of-the-Art Report, 1988.
- [19] Asociación Española de Hormigón Estructural, M-34. Fatiga en hormigón estructural, 2020.
- [20] ACI Committee 215, ACI PRC-215-21. Concrete Structure Design for Fatigue Loading-Report, 2021.
- [21] K. Aas-Jakobsen, R. Lenschow, Behavior of Reinforced Columns Subjected to Fatigue Loading, *ACI J. Proc.* 70 (1973). <https://doi.org/10.14359/11198>.
- [22] P. Paris, F. Erdogan, A Critical Analysis of Crack Propagation Laws, *J. Basic Eng.* 85 (1963) 528–533. <https://doi.org/10.1115/1.3656900>.
- [23] Z.P. Bažant, K. Xu, Size effect in fatigue fracture of concrete, *ACI Mater. J.* 88 (1991) 390–399.
- [24] H. Cifuentes, F. Medina, *Mecánica de la fractura aplicada al hormigón. Conceptos, análisis experimental y modelos numéricos*, Secretariado de Publicaciones. Universidad de Sevilla, 2013. <https://editorial.us.es/en/detalle-libro/719434/politica-de-cookies>.
- [25] T.T.C. Hsu, Fatigue of Plain Concrete, *ACI J. Proc.* 78 (1981). <https://doi.org/10.14359/6927>.
- [26] K. Aas-Jakobsen, Fatigue of concrete beams and columns, *Div. Concr. Struct. Nor. Inst. Technol. Univ. Trondheim.* (1970).
- [27] R. Tepfers, T. Kutti, Fatigue Strength of Plain, Ordinary, and Lightweight Concrete, *ACI J. Proc.* 76 (1979). <https://doi.org/10.14359/6962>.
- [28] B.H. Oh, Fatigue Analysis of Plain Concrete in Flexure, *J. Struct. Eng.* 112 (1986) 273–288. [https://doi.org/10.1061/\(ASCE\)0733-9445\(1986\)112:2\(273\)](https://doi.org/10.1061/(ASCE)0733-9445(1986)112:2(273)).
- [29] A.E. Naaman, H. Hammoud, Fatigue characteristics of high performance fiber-reinforced concrete, *Cem. Concr. Compos.* 20 (1998) 353–363. [https://doi.org/10.1016/S0958-9465\(98\)00004-3](https://doi.org/10.1016/S0958-9465(98)00004-3).
- [30] S.P. Singh, S.K. Kaushik, Fatigue strength of steel fibre reinforced concrete in flexure, *Cem. Concr. Compos.* 25 (2003) 779–786. [https://doi.org/10.1016/S0958-9465\(02\)00102-6](https://doi.org/10.1016/S0958-9465(02)00102-6).
- [31] L. Saucedo, R.C. Yu, A. Medeiros, X. Zhang, G. Ruiz, A probabilistic fatigue model based on the initial distribution to consider frequency effect in plain and fiber reinforced concrete, *Int. J. Fatigue.* 48 (2013) 308–318. <https://doi.org/10.1016/j.ijfatigue.2012.11.013>.
-

-
- [32] N.K. Banjara, K. Ramanjaneyulu, Experimental Investigations and Numerical Simulations on the Flexural Fatigue Behavior of Plain and Fiber-Reinforced Concrete, *J. Mater. Civ. Eng.* 30 (2018) 1–15. [https://doi.org/10.1061/\(ASCE\)MT.1943-5533.0002351](https://doi.org/10.1061/(ASCE)MT.1943-5533.0002351).
- [33] International Federation for Structural Concrete (fib), Model Code 2010, 2012.
- [34] E. Castillo, A. Fernández-Canteli, M.L. Ruiz-Ripoll, A general model for fatigue damage due to any stress history, *Int. J. Fatigue.* 30 (2008) 150–164. <https://doi.org/10.1016/j.ijfatigue.2007.02.011>.
- [35] E. Castillo, A. Fernández-Canteli, R. Koller, M.L. Ruiz-Ripoll, A. García, A statistical fatigue model covering the tension and compression Wöhler fields, *Probabilistic Eng. Mech.* 24 (2009) 199–209. <https://doi.org/10.1016/j.probengmech.2008.06.003>.
- [36] V. Ramakrishnan, G.Y. Wu, G. Hosalli, Flexural fatigue strength, endurance limit, and impact strength of fiber reinforced concretes, *Transp. Res. Rec.* (1989) 17 – 24. <https://www.scopus.com/inward/record.uri?eid=2-s2.0-0024872334&partnerID=40&md5=723703fbcc8798ffbad4031500daddf>.
- [37] D.M. Carlesso, A. de la Fuente, S.H.P. Cavalaro, Fatigue of cracked high performance fiber reinforced concrete subjected to bending, *Constr. Build. Mater.* 220 (2019) 444–455. <https://doi.org/10.1016/j.conbuildmat.2019.06.038>.
- [38] M.A. Miner, Cumulative Damage in Fatigue, *J. Appl. Mech.* 12 (1945) A159–A164. <https://doi.org/10.1115/1.4009458>.
- [39] H.A.W. Cornelissen, Fatigue failure of concrete in tension, *HERON.* 29(4) (1984).
- [40] B.H. Oh, Fatigue Life Distributions of Concrete for Various Stress Levels, *ACI Mater. J.* 88 (1991). <https://doi.org/10.14359/1870>.
- [41] J. Mínguez, Análisis de la capacidad mecánica postfatiga en hormigones de altas prestaciones sometidos a cargas cíclicas axiales [PhD thesis, University of Burgos, Spain], (2012).
- [42] J.J. Ortega, G. Ruiz, E. Poveda, D.C. González, M. Tarifa, X.X. Zhang, R.C. Yu, M.Á. Vicente, Á. de la Rosa, L. Garijo, Size effect on the compressive fatigue of fibre-reinforced concrete, *Constr. Build. Mater.* 322 (2022) 126238. <https://doi.org/10.1016/j.conbuildmat.2021.126238>.
- [43] J.J. Ortega, G. Ruiz, R.C. Yu, N. Afanador-García, M. Tarifa, E. Poveda, X. Zhang, F. Evangelista, Number of tests and corresponding error in concrete fatigue, *Int. J. Fatigue.* 116 (2018) 210–219. <https://doi.org/10.1016/j.ijfatigue.2018.06.022>.
- [44] E.J. Gumbel, Parameters in the Distribution of Fatigue Life, *J. Eng. Mech. Div.* 89 (1963) 45–64. <https://doi.org/10.1061/JMCEA3.0000418>.
- [45] S.P. Singh, S.K. Khushik, Flexural Fatigue Life Distributions and Failure Probability of Steel Fibrous Concrete, *ACI Mater. J.* (2000) 1–10.
- [46] E. Poveda, G. Ruiz, H. Cifuentes, R.C. Yu, X. Zhang, Influence of the fiber content on the compressive low-cycle fatigue behavior of self-compacting SFRC, *Int. J. Fatigue.* 101 (2017) 9–
-

17. <https://doi.org/10.1016/j.ijfatigue.2017.04.005>.
- [47] J. Ríos, H. Cifuentes, R. Yu, G. Ruiz, Probabilistic Flexural Fatigue in Plain and Fiber-Reinforced Concrete, *Materials* (Basel). 10 (2017) 767. <https://doi.org/10.3390/ma10070767>.
- [48] ACI Committee 215, ACI 215R-74. Considerations for Design of Concrete Structures Subjected to Fatigue Loading, (1997).
- [49] P.R. Sparks, J.B. Menzies, The effect of rate of loading upon the static and fatigue strengths of plain concrete in compression, *Mag. Concr. Res.* 25 (1973) 73–80. <https://doi.org/10.1680/mac.1973.25.83.73>.
- [50] K. Furtak, Ein verfahren zur berechnung der betonfestigkeit unter schwellenden belastungen, *Cem. Concr. Res.* 14 (1984) 855–865. [https://doi.org/10.1016/0008-8846\(84\)90012-7](https://doi.org/10.1016/0008-8846(84)90012-7).
- [51] B. Zhang, D. V. Phillips, K. Wu, Effects of loading frequency and stress reversal on fatigue life of plain concrete, *Mag. Concr. Res.* 48 (1996) 361–375. <https://doi.org/10.1680/mac.1996.48.177.361>.
- [52] A. Medeiros, X. Zhang, G. Ruiz, R.C. Yu, M.D.S.L. Velasco, Effect of the loading frequency on the compressive fatigue behavior of plain and fiber reinforced concrete, *Int. J. Fatigue.* 70 (2015) 342–350. <https://doi.org/10.1016/j.ijfatigue.2014.08.005>.
- [53] C.D. Johnston, R.W. Zemp, Flexural fatigue performance of steel fiber reinforced concrete. Influence of fiber content, aspect ratio, and type, *ACI Mater. J.* 88 (1991) 374 – 383. <https://www.scopus.com/inward/record.uri?eid=2-s2.0-0026188936&partnerID=40&md5=c71ca67a0d0abc9796903e993c5c63a8>.
- [54] F. Germano, G. Tiberti, G. Plizzari, Post-peak fatigue performance of steel fiber reinforced concrete under flexure, *Mater. Struct.* 49 (2016) 4229–4245. <https://doi.org/10.1617/s11527-015-0783-3>.
- [55] M.A. Vicente, J. Mínguez, D.C. González, Computed tomography scanning of the internal microstructure, crack mechanisms, and structural behavior of fiber-reinforced concrete under static and cyclic bending tests, *Int. J. Fatigue.* 121 (2019) 9–19. <https://doi.org/10.1016/j.ijfatigue.2018.11.023>.
- [56] D. Gao, Z. Gu, H. Zhu, Y. Huang, Fatigue behavior assessment for steel fiber reinforced concrete beams through experiment and Fatigue Prediction Model, *Structures.* 27 (2020) 1105–1117. <https://doi.org/10.1016/j.istruc.2020.07.028>.
- [57] V. Moreira de Alencar Monteiro, D. Carlos Taissum Cardoso, F. de Andrade Silva, A novel methodology for estimating damage evolution and energy dissipation for steel fiber reinforced concrete under flexural fatigue loading, *Int. J. Fatigue.* 166 (2023) 107244. <https://doi.org/10.1016/j.ijfatigue.2022.107244>.
- [58] J. Mínguez, D.C. González, M.A. Vicente, Fiber geometrical parameters of fiber-reinforced high strength concrete and their influence on the residual post-peak flexural tensile strength, *Constr. Build. Mater.* 168 (2018) 906–922. <https://doi.org/10.1016/j.conbuildmat.2018.02.095>.
-

-
- [59] A. Mudadu, G. Tiberti, F. Germano, G.A. Plizzari, A. Morbi, The effect of fiber orientation on the post-cracking behavior of steel fiber reinforced concrete under bending and uniaxial tensile tests, *Cem. Concr. Compos.* 93 (2018) 274–288. <https://doi.org/10.1016/j.cemconcomp.2018.07.012>.
- [60] D.C. González, J. Mínguez, M.A. Vicente, F. Cambroner, G. Aragón, Study of the effect of the fibers' orientation on the post-cracking behavior of steel fiber reinforced concrete from wedge-splitting tests and computed tomography scanning, *Constr. Build. Mater.* 192 (2018) 110–122. <https://doi.org/10.1016/j.conbuildmat.2018.10.104>.
- [61] M.A. Vicente, G. Ruiz, D.C. González, J. Mínguez, M. Tarifa, X. Zhang, Effects of fiber orientation and content on the static and fatigue behavior of SFRC by using CT-Scan technology, *Int. J. Fatigue.* 128 (2019) 105178. <https://doi.org/10.1016/j.ijfatigue.2019.06.038>.
- [62] F.H. Wittmann, Structure of concrete with respect to crack formation, *Fract. Mech. Concr.* 43(5) (1983).
- [63] J. Zhang, H. Stang, V.C. Li, Fatigue life prediction of fiber reinforced concrete under flexural load, *Int. J. Fatigue.* 21 (1999) 1033–1049. [https://doi.org/10.1016/S0142-1123\(99\)00093-6](https://doi.org/10.1016/S0142-1123(99)00093-6).
- [64] J.O. Holmen, Fatigue of concrete by constant and variable amplitude loading [PhD thesis, Division of Concrete Structures, Norwegian Institute of Technology, University of Trondheim, Norway], (1979).
- [65] M. De Smedt, R. Vrijdaghs, C. Van Steen, E. Verstryngne, L. Vandewalle, Damage analysis in steel fibre reinforced concrete under monotonic and cyclic bending by means of acoustic emission monitoring, *Cem. Concr. Compos.* 114 (2020) 103765. <https://doi.org/10.1016/j.cemconcomp.2020.103765>.
- [66] G. Gebuhr, M. Pise, S. Anders, D. Brands, J. Schröder, Damage Evolution of Steel Fibre-Reinforced High-Performance Concrete in Low-Cycle Flexural Fatigue: Numerical Modeling and Experimental Validation, *Materials (Basel)*. 15 (2022) 1179. <https://doi.org/10.3390/ma15031179>.
- [67] C. Zanuy, P. de la Fuente, L. Albajar, Effect of fatigue degradation of the compression zone of concrete in reinforced concrete sections, *Eng. Struct.* 29 (2007) 2908–2920. <https://doi.org/10.1016/j.engstruct.2007.01.030>.
- [68] Ł. Skarżyński, I. Marzec, J. Tejchman, Fracture evolution in concrete compressive fatigue experiments based on X-ray micro-CT images, *Int. J. Fatigue.* 122 (2019) 256–272. <https://doi.org/10.1016/j.ijfatigue.2019.02.002>.
- [69] S. Blasón, E. Poveda, G. Ruiz, H. Cifuentes, A. Fernández Canteli, Twofold normalization of the cyclic creep curve of plain and steel-fiber reinforced concrete and its application to predict fatigue failure, *Int. J. Fatigue.* 120 (2019) 215–227. <https://doi.org/10.1016/j.ijfatigue.2018.11.021>.
- [70] G. Gebuhr, S. Anders, M. Pise, M. Sahril, D. Brands, J. Schröder, Deterioration development of steel fibre reinforced high performance concrete in low-cycle fatigue, in: *Adv. Eng. Mater. Struct. Syst. Innov. Mech. Appl.*, CRC Press, 2019: pp. 1444–1449. <https://doi.org/10.1201/9780429426506-249>.
-

- [71] J.O. Holmen, Fatigue of Concrete by Constant and Variable Amplitude loading, *ACI Symp. Publ.* 75 (1982) 71–110. <https://doi.org/10.14359/6402>.
- [72] J. Schröder, M. Pise, D. Brands, G. Gebuhr, S. Anders, Phase-field modeling of fracture in high performance concrete during low-cycle fatigue: Numerical calibration and experimental validation, *Comput. Methods Appl. Mech. Eng.* 398 (2022) 115181. <https://doi.org/10.1016/j.cma.2022.115181>.
- [73] D.C. González, R. Moradillo, J. Mínguez, J.A. Martínez, M.A. Vicente, Postcracking residual strengths of fiber-reinforced high-performance concrete after cyclic loading, *Struct. Concr.* 19 (2018) 340–351. <https://doi.org/10.1002/suco.201600102>.
- [74] Z.P. Bažant, J. Planas, *Fracture and Size Effect in Concrete and Other Quasibrittle Materials*, Taylor & Francis, 1998. <https://doi.org/10.1201/9780203756799>.
- [75] L. Saucedo, R.C. Yu, G. Ruiz, Fully-developed FPZ length in quasi-brittle materials, *Int. J. Fract.* 178 (2012) 97–112. <https://doi.org/10.1007/s10704-012-9769-0>.
- [76] TC-QFS RILEM . Quasibrittle fracture scaling and size effect -final report, *Mater. Struct.* 37 (2004) 547–568. <https://doi.org/10.1007/bf02481579>.
- [77] A.A. Griffith, VI. The phenomena of rupture and flow in solids, *Philos. Trans. R. Soc. London. Ser. A.* 221 (1921) 163–198. <https://doi.org/10.1098/rsta.1921.0006>.
- [78] B.L. Karihaloo, *Fracture mechanics & structural concrete*, Longman Scientific and Technical, 1995.
- [79] Z.P. Bažant, Size effect on structural strength: a review, *Arch. Appl. Mech.* 69 (1999) 703–725. <https://doi.org/10.1007/s004190050252>.
- [80] Z.P. Bažant, A. Yavari, Is the cause of size effect on structural strength fractal or energetic–statistical?, *Eng. Fract. Mech.* 72 (2005) 1–31. <https://doi.org/10.1016/j.engfracmech.2004.03.004>.
- [81] V.C. Li, Z.L. Lin, T. Matsumoto, Influence of fiber bridging on structural size-effect, *Int. J. Solids Struct.* 35 (1998) 4223–4238. [https://doi.org/10.1016/S0020-7683\(97\)00311-9](https://doi.org/10.1016/S0020-7683(97)00311-9).
- [82] M. Ghasemi, M.R. Ghasemi, S.R. Mousavi, Studying the fracture parameters and size effect of steel fiber-reinforced self-compacting concrete, *Constr. Build. Mater.* 201 (2019) 447–460. <https://doi.org/10.1016/j.conbuildmat.2018.12.172>.
- [83] J. Fládr, P. Bílý, Specimen size effect on compressive and flexural strength of high-strength fibre-reinforced concrete containing coarse aggregate, *Compos. Part B Eng.* 138 (2018) 77–86. <https://doi.org/10.1016/j.compositesb.2017.11.032>.
- [84] D.Y. Yoo, N. Banthia, S.T. Kang, Y.S. Yoon, Size effect in ultra-high-performance concrete beams, *Eng. Fract. Mech.* 157 (2016) 86–106. <https://doi.org/10.1016/j.engfracmech.2016.02.009>.
- [85] D.Y. Yoo, N. Banthia, J.M. Yang, Y.S. Yoon, Size effect in normal- and high-strength amorphous metallic and steel fiber reinforced concrete beams, *Constr. Build. Mater.* 121 (2016) 676–685. <https://doi.org/10.1016/j.conbuildmat.2016.06.040>.
-

-
- [86] D.L. Nguyen, D.J. Kim, G.S. Ryu, K.T. Koh, Size effect on flexural behavior of ultra-high-performance hybrid fiber-reinforced concrete, *Compos. Part B Eng.* 45 (2013) 1104–1116. <https://doi.org/10.1016/j.compositesb.2012.07.012>.
- [87] S. Mindess, F. V. Lawrence, C.E. Kesler, The J-integral as a fracture criterion for fiber reinforced concrete, *Cem. Concr. Res.* 7 (1977) 731–742. [https://doi.org/10.1016/0008-8846\(77\)90057-6](https://doi.org/10.1016/0008-8846(77)90057-6).
- [88] A. Carpinteri, R. Massabó, Continuous vs discontinuous bridged-crack model for fiber-reinforced materials in flexure, *Int. J. Solids Struct.* 34 (1997) 2321–2338. [https://doi.org/10.1016/s0020-7683\(96\)00129-1](https://doi.org/10.1016/s0020-7683(96)00129-1).
- [89] K. Visalvanich, A.E. Naaman, Fracture Model for Fiber Reinforced Concrete, *ACI J. Proc.* 80 (1983). <https://doi.org/10.14359/10712>.
- [90] Z.P. Bažant, Y. Xiang, Size Effect in Compression Fracture: Splitting Crack Band Propagation, *J. Eng. Mech.* 123 (1997) 162–172. [https://doi.org/10.1061/\(ASCE\)0733-9399\(1997\)123:2\(162\)](https://doi.org/10.1061/(ASCE)0733-9399(1997)123:2(162)).
- [91] D.C. Jansen, S.P. Shah, Effect of Length on Compressive Strain Softening of Concrete, *J. Eng. Mech.* 123 (1997) 25–35. [https://doi.org/10.1061/\(asce\)0733-9399\(1997\)123:1\(25\)](https://doi.org/10.1061/(asce)0733-9399(1997)123:1(25)).
- [92] Y. Tanigawa, K. Yamada, Size effect in compressive strength of concrete, *Cem. Concr. Res.* 8 (1978) 181–190. [https://doi.org/10.1016/0008-8846\(78\)90007-8](https://doi.org/10.1016/0008-8846(78)90007-8).
- [93] J. Il Sim, K.H. Yang, J.K. Jeon, Influence of aggregate size on the compressive size effect according to different concrete types, *Constr. Build. Mater.* 44 (2013) 716–725. <https://doi.org/10.1016/j.conbuildmat.2013.03.066>.
- [94] J.R. del Viso, J.R. Carmona, G. Ruiz, Shape and size effects on the compressive strength of high-strength concrete, *Cem. Concr. Res.* 38 (2008) 386–395. <https://doi.org/10.1016/j.cemconres.2007.09.020>.
- [95] G. Muciaccia, G. Rosati, G. Di Luzio, Compressive failure and size effect in plain concrete cylindrical specimens, *Constr. Build. Mater.* 137 (2017) 185–194. <https://doi.org/10.1016/j.conbuildmat.2017.01.057>.
- [96] P. Chen, C. Liu, Y. Wang, Size effect on peak axial strain and stress-strain behavior of concrete subjected to axial compression, *Constr. Build. Mater.* 188 (2018) 645–655. <https://doi.org/10.1016/j.conbuildmat.2018.08.072>.
- [97] D.C. González, Á. Mena, G. Ruiz, J.J. Ortega, E. Poveda, J. Mínguez, R. Yu, Á. De La Rosa, M.Á. Vicente, Size effect of steel fiber–reinforced concrete cylinders under compressive fatigue loading: Influence of the mesostructure, *Int. J. Fatigue.* 167 (2023) 107353. <https://doi.org/10.1016/j.ijfatigue.2022.107353>.
- [98] J.L. Le, Z.P. Bažant, Unified nano-mechanics based probabilistic theory of quasibrittle and brittle structures: II. Fatigue crack growth, lifetime and scaling, *J. Mech. Phys. Solids.* 59 (2011) 1322–1337. <https://doi.org/10.1016/j.jmps.2011.03.007>.
- [99] J. Zhang, V.C. Li, H. Stang, Size Effect on Fatigue in Bending of Concrete, *J. Mater. Civ. Eng.* 13
-

- (2001) 446–453. [https://doi.org/10.1061/\(ASCE\)0899-1561\(2001\)13:6\(446\)](https://doi.org/10.1061/(ASCE)0899-1561(2001)13:6(446)).
- [100] A. Carpinteri, A. Spagnoli, A fractal analysis of size effect on fatigue crack growth, *Int. J. Fatigue*. 26 (2004) 125–133. [https://doi.org/10.1016/S0142-1123\(03\)00142-7](https://doi.org/10.1016/S0142-1123(03)00142-7).
- [101] S. Ray, J.M. Chandra Kishen, Fatigue crack propagation model and size effect in concrete using dimensional analysis, *Mech. Mater.* 43 (2011) 75–86. <https://doi.org/10.1016/j.mechmat.2010.12.002>.
- [102] N.A. Brake, K. Chatti, Prediction of size effect and non-linear crack growth in plain concrete under fatigue loading, *Eng. Fract. Mech.* 109 (2013) 169–185. <https://doi.org/10.1016/j.engfracmech.2013.06.004>.
- [103] M. Ciavarella, M. Paggi, A. Carpinteri, One, no one, and one hundred thousand crack propagation laws: A generalized Barenblatt and Botvina dimensional analysis approach to fatigue crack growth, *J. Mech. Phys. Solids*. 56 (2008) 3416–3432. <https://doi.org/10.1016/j.jmps.2008.09.002>.
- [104] K. Kirane, Z.P. Bažant, Size effect in Paris law and fatigue lifetimes for quasibrittle materials: Modified theory, experiments and micro-modeling, *Int. J. Fatigue*. 83 (2016) 209–220. <https://doi.org/10.1016/j.ijfatigue.2015.10.015>.
- [105] A. Carpinteri, F. Accornero, The Bridged Crack Model with multiple fibers: Local instabilities, scale effects, plastic shake-down, and hysteresis, *Theor. Appl. Fract. Mech.* 104 (2019) 102351. <https://doi.org/10.1016/j.tafmec.2019.102351>.
- [106] S. Sinaie, A. Heidarpour, X.L. Zhao, J.G. Sanjayan, Effect of size on the response of cylindrical concrete samples under cyclic loading, *Constr. Build. Mater.* 84 (2015) 399–408. <https://doi.org/10.1016/j.conbuildmat.2015.03.076>.
- [107] S.E.D.F. Taher, T.M. Fawzy, Performance of very-high-strength concrete subjected to short-term repeated loading, *Mag. Concr. Res.* 52 (2000) 219–223. <https://doi.org/10.1680/mac.2000.52.3.219>.
- [108] S.Y. Alam, R. Zhu, A. Loukili, A new way to analyse the size effect in quasi-brittle materials by scaling the heterogeneity size, *Eng. Fract. Mech.* 225 (2020) 106864. <https://doi.org/10.1016/j.engfracmech.2019.106864>.
- [109] R. Zhu, S.Y. Alam, A. Loukili, An experimental investigation on the correlation between the aggregate size effect and the structural size effect, *Eng. Fract. Mech.* 234 (2020) 107101. <https://doi.org/10.1016/j.engfracmech.2020.107101>.
- [110] L. Jin, W. Yu, D. Li, X. Du, Numerical and theoretical investigation on the size effect of concrete compressive strength considering the maximum aggregate size, *Int. J. Mech. Sci.* 192 (2021) 106130. <https://doi.org/10.1016/j.ijmecsci.2020.106130>.
- [111] S. Zhang, K. Cao, C. Wang, X. Wang, G. Deng, P. Wei, Influence of the porosity and pore size on the compressive and splitting strengths of cellular concrete with millimeter-size pores, *Constr. Build. Mater.* 235 (2020) 117508. <https://doi.org/10.1016/j.conbuildmat.2019.117508>.
-

-
- [112] D. Liu, B. Šavija, G.E. Smith, P.E.J. Flewitt, T. Lowe, E. Schlangen, Towards understanding the influence of porosity on mechanical and fracture behaviour of quasi-brittle materials: experiments and modelling, *Int. J. Fract.* 205 (2017) 57–72. <https://doi.org/10.1007/s10704-017-0181-7>.
- [113] X. Wang, Z. Yang, A.P. Jivkov, Monte Carlo simulations of mesoscale fracture of concrete with random aggregates and pores: A size effect study, *Constr. Build. Mater.* 80 (2015) 262–272. <https://doi.org/10.1016/j.conbuildmat.2015.02.002>.
- [114] A. Rózanski, M. Rajczakowska, A. Serwicki, The influence of microstructure geometry on the scale effect in mechanical behaviour of heterogeneous materials, *Sci. Eng. Compos. Mater.* 24 (2017) 557–571. <https://doi.org/10.1515/secm-2015-0007>.
- [115] J. Suchorzewski, J. Tejchman, M. Nitka, J. Bobiński, Meso-scale analyses of size effect in brittle materials using DEM, *Granul. Matter.* 21 (2019) 9. <https://doi.org/10.1007/s10035-018-0862-6>.
- [116] H.-K. Man, J.G.M. Mier, Size effect on strength and fracture energy for numerical concrete with realistic aggregate shapes, *Int. J. Fract.* 154 (2008) 61–72. <https://doi.org/10.1007/s10704-008-9270-y>.
- [117] H.-K. Man, J.G.M. van Mier, Damage distribution and size effect in numerical concrete from lattice analyses, *Cem. Concr. Compos.* 33 (2011) 867–880. <https://doi.org/10.1016/j.cemconcomp.2011.01.008>.
- [118] J.F. Barrett, N. Keat, Artifacts in CT: Recognition and Avoidance, *RadioGraphics.* 24 (2004) 1679–1691. <https://doi.org/10.1148/rg.246045065>.
- [119] M.A. Vicente, D.C. González, J. Mínguez, Recent advances in the use of computed tomography in concrete technology and other engineering fields, *Micron.* 118 (2019) 22–34. <https://doi.org/10.1016/j.micron.2018.12.003>.
- [120] Á. Mena Alonso, J. Mínguez Algarra, D.C. González Cabrera, M.Á. Vicente Cabrera, La tomografía computerizada más allá de la medicina: Aplicaciones al estudio microestructural del hormigón y otros materiales de la ingeniería (versión inglesa), *Hormigón y Acero.* 71 (2020) e1–e12. <https://doi.org/10.33586/hya.2020.3035>.
- [121] J.N.T. I.L. Morgan, H. Ellinger, R. Klinksiek, Examination of Concrete by Computerized Tomography, *ACI J. Proc.* 77 (1980). <https://doi.org/10.14359/6987>.
- [122] G.L. Balázs, O. Czoboly, É. Lublós, K. Kapitány, Á. Barsi, Observation of steel fibres in concrete with Computed Tomography, *Constr. Build. Mater.* 140 (2017) 534–541. <https://doi.org/10.1016/j.conbuildmat.2017.02.114>.
- [123] Ł. Skarżyński, J. Suchorzewski, Mechanical and fracture properties of concrete reinforced with recycled and industrial steel fibers using Digital Image Correlation technique and X-ray micro computed tomography, *Constr. Build. Mater.* 183 (2018) 283–299. <https://doi.org/10.1016/j.conbuildmat.2018.06.182>.
- [124] A.B. Groeneveld, T.M. Ahlborn, C.K. Crane, C.A. Burchfield, E.N. Landis, Dynamic strength and
-

- ductility of ultra-high performance concrete with flow-induced fiber alignment, *Int. J. Impact Eng.* 111 (2018) 37–45. <https://doi.org/10.1016/j.ijimpeng.2017.08.009>.
- [125] B. Zhou, Y. Uchida, Influence of flowability, casting time and formwork geometry on fiber orientation and mechanical properties of UHPFRC, *Cem. Concr. Res.* 95 (2017) 164–177. <https://doi.org/10.1016/j.cemconres.2017.02.017>.
- [126] M.A. Vicente, G. Ruiz, D.C. González, J. Mínguez, M. Tarifa, X. Zhang, CT-Scan study of crack patterns of fiber-reinforced concrete loaded monotonically and under low-cycle fatigue, *Int. J. Fatigue.* 114 (2018) 138–147. <https://doi.org/10.1016/j.ijfatigue.2018.05.011>.
- [127] H. Fataar, R. Combrinck, W.P. Boshoff, An experimental study on the fatigue failure of steel fibre reinforced concrete at a single fibre level, *Constr. Build. Mater.* 299 (2021) 123869. <https://doi.org/10.1016/j.conbuildmat.2021.123869>.
- [128] M.A. Vicente, Á. Mena, J. Mínguez, D.C. González, Use of Computed Tomography Scan Technology to Explore the Porosity of Concrete: Scientific Possibilities and Technological Limitations, *Appl. Sci.* 11 (2021) 8699. <https://doi.org/10.3390/app11188699>.
- [129] D.C. González, Á. Mena, J. Mínguez, M.A. Vicente, Influence of air-entraining agent and freeze-thaw action on pore structure in high-strength concrete by using CT-Scan technology, *Cold Reg. Sci. Technol.* 192 (2021). <https://doi.org/10.1016/j.coldregions.2021.103397>.
- [130] S.H. Kang, S.G. Hong, J. Moon, The effect of superabsorbent polymer on various scale of pore structure in ultra-high performance concrete, *Constr. Build. Mater.* 172 (2018) 29–40. <https://doi.org/10.1016/j.conbuildmat.2018.03.193>.
- [131] J. Mínguez, M.A. Vicente, D.C. González, Pore morphology variation under ambient curing of plain and fiber-reinforced high performance mortar at an early age, *Constr. Build. Mater.* 198 (2019) 718–731. <https://doi.org/10.1016/j.conbuildmat.2018.12.010>.
- [132] J.D. Ríos, H. Cifuentes, S. Blasón, M. López-Aenlle, A. Martínez-De La Concha, Flexural fatigue behaviour of a heated ultra-high-performance fibre-reinforced concrete, *Constr. Build. Mater.* 276 (2021) 122209. <https://doi.org/10.1016/j.conbuildmat.2020.122209>.
- [133] M.A. Vicente, D.C. González, J. Mínguez, M.A. Tarifa, G. Ruiz, R. Hindi, Influence of the pore morphology of high strength concrete on its fatigue life, *Int. J. Fatigue.* 112 (2018) 106–116. <https://doi.org/10.1016/j.ijfatigue.2018.03.006>.
- [134] I. Netinger Grubeša, B. Marković, M. Vračević, M. Tunkiewicz, I. Szentí, Á. Kukovecz, Pore Structure as a Response to the Freeze/Thaw Resistance of Mortars, *Materials (Basel)*. 12 (2019) 3196. <https://doi.org/10.3390/ma12193196>.
- [135] Z. Yang, W. Ren, R. Sharma, S. McDonald, M. Mostafavi, Y. Vertyagina, T.J. Marrow, In-situ X-ray computed tomography characterisation of 3D fracture evolution and image-based numerical homogenisation of concrete, *Cem. Concr. Compos.* 75 (2017) 74–83. <https://doi.org/10.1016/j.cemconcomp.2016.10.001>.
-

-
- [136] Skarżyński, J. Tejchman, Experimental investigations of damage evolution in concrete during bending by continuous micro-CT scanning, *Mater. Charact.* 154 (2019) 40–52. <https://doi.org/10.1016/j.matchar.2019.05.034>.
- [137] M. Nitka, J. Tejchman, A three-dimensional meso-scale approach to concrete fracture based on combined DEM with X-ray μ CT images, *Cem. Concr. Res.* 107 (2018) 11–29. <https://doi.org/10.1016/j.cemconres.2018.02.006>.
- [138] J. Sainz-Aja, I. Carrascal, J.A. Polanco, C. Thomas, Fatigue failure micromechanisms in recycled aggregate mortar by μ CT analysis, *J. Build. Eng.* 28 (2020) 101027. <https://doi.org/10.1016/j.jobbe.2019.101027>.
- [139] ACI Committee 211, ACI PRC-211.1-91: Standard Practice for Selecting Proportions for Normal, Heavyweight, and Mass Concrete (Reapproved 2009), (2002).
- [140] C. Shi, Z. Wu, K. Lv, L. Wu, A review on mixture design methods for self-compacting concrete, *Constr. Build. Mater.* 84 (2015) 387–398. <https://doi.org/10.1016/j.conbuildmat.2015.03.079>.
- [141] ACI Committee 237, ACI PRC-237-07 Self-Consolidating Concrete (Reapproved 2019), (2007).
- [142] UNE-EN 12350-8. Ensayos de hormigón fresco. Parte 8: Hormigón autocompactante. Ensayo del escurrimiento, 2011.
- [143] UNE-EN-12390-3. Ensayos de hormigón endurecido. Parte 3: Determinación de la resistencia a compresión de probetas, 2020.
- [144] UNE-EN 12390-13. Ensayos de hormigón endurecido. Parte 13: Determinación del módulo secante de elasticidad en compresión, 2014.
- [145] A.K. Chandrappa, K.P. Biligiri, Effect of pore structure on fatigue of pervious concrete, *Road Mater. Pavement Des.* 20 (2019) 1525–1547. <https://doi.org/10.1080/14680629.2018.1464500>.
- [146] J. Shi, Y. Zhao, Pore structure of concrete under fatigue load in areas with large temperature differences, *Struct. Concr.* 23 (2022) 2132–2149. <https://doi.org/10.1002/suco.202000756>.
- [147] S. Erdem, A.R. Dawson, N.H. Thom, Impact load-induced micro-structural damage and micro-structure associated mechanical response of concrete made with different surface roughness and porosity aggregates, *Cem. Concr. Res.* 42 (2012) 291–305. <https://doi.org/10.1016/j.cemconres.2011.09.015>.
- [148] Y. Chen, J. Feng, H. Li, Z. Meng, Effect of coarse aggregate volume fraction on mode II fracture toughness of concrete, *Eng. Fract. Mech.* 242 (2021) 107472. <https://doi.org/10.1016/j.engfracmech.2020.107472>.
-